

**SORPTION OF ARSENIC, MERCURY, SELENIUM ONTO
NANOSTRUCTURED ADSORBENT MEDIA AND STABILIZATION VIA
SURFACE REACTIONS**

A Dissertation

by

DONG SUK HAN

Submitted to the Office of Graduate Studies of
Texas A&M University
in partial fulfillment of the requirements for the degree of

DOCTOR OF PHILOSOPHY

December 2009

Major Subject: Civil Engineering

**SORPTION OF ARSENIC, MERCURY, SELENIUM ONTO
NANOSTRUCTURED ADSORBENT MEDIA AND STABILIZATION VIA
SURFACE REACTIONS**

A Dissertation

by

DONG SUK HAN

Submitted to the Office of Graduate Studies of
Texas A&M University
in partial fulfillment of the requirements for the degree of

DOCTOR OF PHILOSOPHY

Approved by:

| | |
|---------------------|---------------------|
| Chair of Committee, | Bill Batchelor |
| Committee Members, | Richard H. Loeppert |
| | Daniel F. Shantz |
| | Kung-Hui Chu |
| | Ahmed Abdel-Wahab |
| Head of Department, | John Niedzwecki |

December 2009

Major Subject: Civil Engineering

ABSTRACT

Sorption of Arsenic, Mercury, Selenium onto Nanostructured Adsorbent Media and Stabilization
via Surface Reactions. (December 2009)

Dong Suk Han, B.S.; M.S., Keimyung University, Daegu, South Korea

Chair of Advisory Committee: Dr. Bill Batchelor

The overall goal of this study is to evaluate the ability of novel nanostructured adsorbent media (NTAs, iron sulfides (FeS_2 and FeS)) to remove arsenic, selenium and mercury from ash and scrubber pond effluents. The NTAs aim to enhance arsenic removal from solution compared to conventional adsorbents. The iron sulfides are expected to produce stable residuals for ultimate disposal after removing As, Se and Hg from solution, so that removal of these compounds from wastewaters will not result in contamination of soils and groundwaters. Methods for reliably and economically producing these materials were developed. The synthesized NTAs and iron sulfides were characterized by surface analysis techniques such as XRD, FT-IR, SEM-EDS, TEM, XPS, AFM and N_2 -adsorption. These analyses indicated that $\text{Ti}_{(25)}$ -SBA-15 has highly ordered hexagonal mesopores, MT has interparticle mesopores, pyrite (FeS_2) forms crystalline, nonporous rectangular nanoparticles (<500 nm), and mackinawite (FeS) forms amorphous, nonporous nanoparticles (<100 nm).

Kinetic and equilibrium tests for As(III, V) removal were conducted with NTAs over a range of pH (4, 7, 9.5). The rates of arsenic uptake were very fast and followed a bi-phasic sorption pattern, where sorption was fast for the first 10 minutes, and then slowed and was almost completed within 200 minutes. Distinct sorption maxima for As(III) removal were observed between pH 7 and pH 9.5 for MT and between pH 4 and pH 7 for $\text{Ti}_{(25)}$ -SBA-15. The

amount of As(V) adsorbed generally decreased as pH increased. In addition, a surface complexation model (SCM) based on the diffuse layer model (DLM) was used to predict arsenic adsorption envelopes by NTAs under various environmental conditions. The SCM for As(III, V) adsorption by NTAs demonstrated the role of mono- and bidentate surface complexes in arsenic adsorption.

A batch reactor system was employed in an anaerobic chamber to conduct experiments to characterize both the removal of As, Se, Hg from solution and their subsequent reactions with iron sulfides. Experiment variables for removal experiments included: contaminant valence state (As(V), As(III), Se(VI), Se(IV), Hg(II)); adsorbent/reactant type (FeS, FeS₂); adsorbent/reactant concentration; pH (7, 8, 9, 10); and competing ion (SO₄²⁻) concentration (0, 1, 10 mM). Experimental variables for reaction experiments were reaction time (up to 30 days) at pH 8 and oxidation states of contaminants. In addition, the stability of iron sulfides (FeS₂, FeS) combined with target compounds was investigated by measuring the ability of the target compounds to resist release to the aqueous phase after removal. These experiments showed that iron sulfides were good adsorbent/reactants for target contaminants in spite of the presence of sulfate. This was particularly true at intermediate concentrations of target compounds. The experiments also demonstrated that iron sulfides interacted with target contaminants in such a way to improve their resistance to being released back to solution as pH was changed.

Therefore, this study demonstrates the ability of novel nanostructured adsorbent media to remove arsenic, selenium and mercury from ash and scrubber pond effluents and the ability of iron sulfides to produce residuals that are stable when disposed in landfills.

DEDICATION

This dissertation is dedicated to God who always loves me, my parents,
my wife (“Sunhee Yoon”) and my sweetie (“Elizabeth J. Han”)

ACKNOWLEDGEMENTS

I would like to thank my committee chair, Dr. Batchelor, who invited me to be a research group member in spite of my short research background. Moreover, he has provided me with fantastic research topics and treated me kindly as if we were co-workers. Whenever we have a group meeting, he has given me good ideas and sincere comments and guidance to develop the next steps. Most of all, he has provided me financial support until the time when I am leaving Texas A&M University. Also, thanks to my committee members, Dr. Loeppert, Dr. Shantz, Dr. Chu, and Dr. Abdul-Wahab, for their guidance and support throughout the course of this research.

I would like to gratefully acknowledge the research fund for my dissertation, supported in part by TWRI (Texas Water Resource Institute) through USGS (United States Geological Survey) and in part by NETL (National Energy Technology Laboratory) through USDOE (Department of Energy).

I would like to thank the staffs in the MIC (Microscopy and Imaging Center) and the MCF (Material Characterization Facility) at Texas A&M University that taught me how to operate spectroscopic instruments. More thanks are extended to Dr. Batchelor research group members, including former students, of Dr. Saebom Ko, Dr. Jeong Yun Choi, Dr. Bahngmi Jung, Dr. Sihyun Do, Dr. Jinkun Song, Dr. Eunjung Kim, Dr. Chunwoo Lee, Mr. Sunghyuk Park, Mr. Bhanu Prakash, Mr. Adi Desai, Mr. Sanjay Tewari for discussing opinions in research as well as friendships. Sepecial thanks to Dr. DK Kim for helping me with computer-related problems.

Finally, I am grateful to my parents for their lovely concerns and encouragement. Most of all, special gratitude for my wife's love, prayers, and sincere support for me to achieve a Ph.D. degree. In spite of studying together to achieve Ph.D. degrees, she has always taken care of my health and studies rather than herself. The moment that I can not forget is when she was always

preparing or delivering breakfast, lunch and dinner to give me more time to conduct more experiments, even though she had severe morning sickness. I cannot help loving my wife and my God forever.

TABLE OF CONTENTS

| | Page |
|--|-----------|
| ABSTRACT | iii |
| DEDICATION..... | v |
| ACKNOWLEDGEMENTS | vi |
| TABLE OF CONTENTS..... | viii |
| LIST OF FIGURES | xiv |
| LIST OF TABLES | xxvii |
| 1. INTRODUCTION..... | 1 |
| 1.1 Problem Statements and Motivation..... | 1 |
| 1.2 Strategic Approaches and Objectives..... | 3 |
| 1.2.1 Task 1: Develop Techniques to Synthesize Nanostructured Adsorbent Media and Characterize Surface Properties | 3 |
| 1.2.2 Task 2: Characterize Sorption Kinetics of As, Hg, Se Uptake by Nano-Structured Adsorbent Media..... | 4 |
| 1.2.3 Task 3: Characterize Sorption of As, Hg, Se on Nanostructured Adsorbent Media | 4 |
| 1.2.4 Task 4: Characterize Adsorption Envelope of Arsenic by NTAs as Affected by Solution Composition..... | 5 |
| 1.2.5 Task 5: Characterize Reactions of As, Hg, Se on the Surfaces of Iron Sulfides (FeS/FeS ₂) | 6 |
| 1.2.6 Task 6: Evaluate Stability of Iron Sulfides (FeS/FeS ₂) Residuals..... | 6 |
| 1.3 Dissertation Organization | 7 |
| 2. BACKGROUND..... | 10 |
| 2.1 Arsenic | 10 |
| 2.1.1 Introduction | 10 |
| 2.1.2 Acid/Base and Redox Chemistry..... | 10 |
| 2.1.3 Precipitation of Arsenic Compounds..... | 11 |
| 2.1.4 Sorption of Arsenic..... | 13 |
| 2.1.5 Release of Arsenic from Arsenic-Bearing Wastes..... | 15 |
| 2.2 Selenium | 18 |
| 2.2.1 Introduction | 18 |
| 2.2.2 Aquatic Chemistry of Selenium | 19 |
| 2.2.3 Sorption of Selenium..... | 20 |
| 2.3 Mercury..... | 21 |
| 2.3.1 Introduction | 21 |
| 2.3.2 Aquatic Chemistry of Mercury..... | 22 |

| | Page |
|---|------|
| 2.3.3 Precipitation of Mercury | 25 |
| 2.3.4 Sorption of Mercury | 25 |
| 2.4 Nanostructured Adsorbents Media..... | 26 |
| 2.4.1 Mackinawite..... | 26 |
| 2.4.2 Pyrite | 30 |
| 2.4.3 Mesoporous Materials | 32 |
| 2.4.3.1 Nanoporous Titania Adsorbents (NTAs)..... | 37 |
| 2.4.3.2 Environmental Applications | 38 |
| | |
| 3. ADSORPTION OF ARSENIC(III) AND ARSENIC(V) TO NANOPOROUS TITANIA ADSORBENTS (NTAs): SYNTHESIS, KINETICS, EQUILIBRIUM | 40 |
| 3.1 Introduction..... | 41 |
| 3.2 Materials and Methods..... | 42 |
| 3.2.1 Synthesis of Nanoporous Titania Adsorbents (NTAs)..... | 42 |
| 3.2.2 Adsorption Experiments | 44 |
| 3.2.3 Spectroscopic Analyses | 47 |
| 3.2.4 Measurements of Arsenic Concentrations..... | 48 |
| 3.3 Results and Discussion | 48 |
| 3.3.1 Surface Characterization of NTAs | 48 |
| 3.3.2 Kinetics | 55 |
| 3.3.2.1 Effect of pH | 55 |
| 3.3.2.2 Effect of Arsenic Concentrations..... | 59 |
| 3.3.3 Equilibrium Isotherms for Arsenic Adsorption..... | 63 |
| 3.3.3.1 Effect of Ratio of Ti to SBA-15..... | 63 |
| 3.3.3.2 Effect of pH | 67 |
| | |
| 4. MODELING ON ADSORPTION OF ARSENIC(III) AND ARSENIC(V) ONTO NANOPOROUS TITANIA ADSORBENTS (NTAs) | 73 |
| 4.1 Introduction..... | 74 |
| 4.2 Materials and Methods..... | 76 |
| 4.2.1 Materials..... | 76 |
| 4.2.2 Equilibrium Adsorption Experiments..... | 77 |
| 4.2.3 Analytical Methods | 78 |
| 4.2.4 Potentiometric Titration..... | 78 |
| 4.2.5 Surface Complexation Model..... | 81 |
| 4.3 Results and Discussion | 82 |
| 4.3.1 Arsenic Adsorption Envelopes: Variation of Initial Arsenic Concentration..... | 82 |
| 4.3.2 Modeling Arsenic Adsorption Envelopes: Various Solid-To-Liquid Ratios..... | 89 |
| | |
| 5. SORPTION OF SELENIUM(IV) AND SELENIUM(VI) TO SYNTHETIC PYRITE (FeS ₂): 1. MICROSCOPIC AND SPECTROSCOPIC ANALYSES..... | 94 |
| 5.1 Introduction..... | 95 |
| 5.2 Materials and Method | 97 |

| | Page |
|---|------------|
| 5.2.1 Materials..... | 97 |
| 5.2.2 Synthesis of Nanoparticulate Pyrite | 97 |
| 5.2.3 Sorption/Reaction Experiments..... | 98 |
| 5.2.4 Spectroscopic Analyses | 98 |
| 5.2.5 Measurement of Aqueous Concentrations..... | 100 |
| 5.3 Results and Discussion | 100 |
| 5.3.1 Surface Characterization of Synthetic Pyrite | 100 |
| 5.3.2 XPS Investigations for Se-Contacted Pyrites..... | 103 |
| 5.3.3 SEM Investigation for Se-Contacted Pyrites..... | 117 |
| 5.3.4 AFM Investigations for Se-Contacted Pyrites..... | 119 |
| 6. SORPTION OF SELENIUM(IV) AND SELENIUM(VI) TO SYNTHETIC PYRITE (FeS₂): KINETICS, EXTENT OF REMOVAL, STABILITY | 122 |
| 6.1 Introduction..... | 123 |
| 6.2 Material and Methods | 125 |
| 6.2.1 Materials..... | 125 |
| 6.2.2 Sorption/Reaction Experiments..... | 125 |
| 6.2.3 Stability of Se-Contacted Pyrites | 126 |
| 6.2.4 Spectroscopic Analyses | 127 |
| 6.2.5 Measurements of Aqueous Concentrations | 127 |
| 6.3 Results and Discussion | 128 |
| 6.3.1 Kinetics | 128 |
| 6.3.2 Nonlinear Removal Patterns..... | 130 |
| 6.3.2.1 Effect of pH | 130 |
| 6.3.2.2 Effect of Sulfate Concentration | 133 |
| 6.3.3 Stability of Se-Contacted Pyrite..... | 135 |
| 6.3.3.1 XPS Investigation of Pure Pyrite..... | 135 |
| 6.3.3.2 Se(IV)-Contacted Pyrite | 139 |
| 6.3.3.3 Se(VI)-Contacted Pyrite | 147 |
| 7. SORPTION OF SELENIUM(IV) AND SELENIUM(VI) TO MACKINAWITE (FeS): SPECTROSCOPIC ANALYSES | 156 |
| 7.1 Introduction..... | 156 |
| 7.2 Materials and Method | 158 |
| 7.2.1 Materials..... | 158 |
| 7.2.2 Synthesis of FeS..... | 158 |
| 7.2.3 Sorption/Reaction Experiments..... | 159 |
| 7.2.4 Spectroscopic Analyses | 159 |
| 7.2.5 Measurements of Selenium Concentration..... | 160 |
| 7.3 Results and Discussion | 160 |
| 7.3.1 Surface Characterization of Synthetic Mackinawite | 160 |
| 7.3.2 Spectroscopic Investigation of Se-Contacted Mackinawite | 162 |
| 8. SORPTION OF SELENIUM(IV) AND SELENIUM(VI) TO MACKINAWITE | |

| | Page |
|---|------|
| (FeS): KINETICS, EXTENT OF REMOVAL, STABILITY | 175 |
| 8.1 Introduction..... | 176 |
| 8.2 Materials and Method | 178 |
| 8.2.1 Materials..... | 178 |
| 8.2.2 Sorption/Reaction Experiments..... | 178 |
| 8.2.3 Stability Test of Se(IV)/Se(VI)-Contacted FeS..... | 179 |
| 8.2.4 Spectroscopic Analyses | 180 |
| 8.2.5 Measurements | 180 |
| 8.3 Results and Discussion | 181 |
| 8.3.1 Kinetics | 181 |
| 8.3.2 Nonlinear Removal Patterns..... | 183 |
| 8.3.2.1 Effect of pH | 183 |
| 8.3.2.2 Effect of Sulfate Concentration | 189 |
| 8.3.2 Stability of Selenium-Contacted Mackinawite..... | 192 |
| 8.3.2.1 XPS Investigation of Pure Mackinawite..... | 192 |
| 8.3.2.2 Se(IV)-Contacted FeS..... | 197 |
| 8.3.2.3 Se(VI)-Contacted FeS..... | 201 |
| 9. SORPTION OF ARSENIC(III) AND ARSENIC(V) TO SYNTHETIC PYRITE (FeS ₂) AND MACKINAWITE (FeS): SPECTROSCOPIC INVESTIGATIONS | 206 |
| 9.1 Introduction..... | 206 |
| 9.2 Materials and Methods..... | 209 |
| 9.2.1 Materials..... | 209 |
| 9.2.2 Sorption/Reaction Experiments..... | 210 |
| 9.2.3 Spectroscopic Analyses | 210 |
| 9.3 Results and Discussion | 211 |
| 9.3.1 Spectroscopic Investigation of As-Contacted Pyrite..... | 211 |
| 9.3.2 SEM-EDS Investigation for As-Contacted Pyrites | 224 |
| 9.3.3 Spectroscopic Analyses of As-Contacted FeS..... | 227 |
| 10. SORPTION OF ARSENIC(III) AND ARSENIC(V) TO PYRITE (FeS ₂): KINETICS, EXTENT OF REMOVAL, STABILITY | 242 |
| 10.1 Introduction..... | 242 |
| 10.2 Materials and Method | 245 |
| 10.2.1 Sorption/Reaction Experiments..... | 245 |
| 10.2.2 Stability of As-Contacted Pyrites | 246 |
| 10.2.3 Measurements | 247 |
| 10.3 Results and Discussion | 247 |
| 10.3.1 Kinetics | 247 |
| 10.3.2 Nonlinear Removal Patterns..... | 250 |
| 10.3.2.1 Effect of pH | 250 |
| 10.3.2.2 Effect of Sulfate Concentration | 253 |
| 10.3.3 Stability of As-Contacted Pyrites | 256 |

| | Page |
|---|------------|
| 10.3.3.1 As(III)-Contacted Pyrite | 256 |
| 10.3.3.2 As(V)-Contacted Pyrite | 262 |
| 11. SORPTION OF ARSENIC(III) AND ARSENIC(V) TO MACKINAWITE (FeS): KINETICS, EXTENT OF REMOVAL, STABILITY | 271 |
| 11.1 Introduction..... | 271 |
| 11.2 Materials and Methods..... | 274 |
| 11.2.1 Sorption/Reaction Experiments..... | 274 |
| 11.2.2 Stability of As-Contacted FeS | 275 |
| 11.3 Results and Discussion..... | 276 |
| 11.3.1 Kinetics..... | 276 |
| 11.3.2 Nonlinear Removal Patterns..... | 278 |
| 11.3.2.1 Effect of pH | 278 |
| 11.3.2.2 Effect of Sulfate Concentration | 283 |
| 11.3.3 Stability of As-Contacted FeS | 289 |
| 11.3.3.1 As(III)-Contacted FeS..... | 289 |
| 11.3.3.2 As(V)-Contacted FeS..... | 294 |
| 12. SORPTION OF MERCURY(II) TO ADSORBENTS/REACTANTS: | |
| 1. PYRITE (FeS₂)..... | 301 |
| 12.1 Introduction..... | 302 |
| 12.2 Materials and Method | 304 |
| 12.2.1 Materials..... | 304 |
| 12.2.2 Kinetics | 304 |
| 12.2.3 Sorption/Reaction Experiments..... | 305 |
| 12.2.4 Stability of Hg(II)-Contacted Pyrite..... | 305 |
| 12.2.5 Spectroscopic Analyses | 306 |
| 12.2.6 Measurement of Aqueous Concentration | 307 |
| 12.3 Results and Discussion | 307 |
| 12.3.1 Kinetics | 307 |
| 12.3.2 Nonlinear Removal Patterns..... | 309 |
| 12.3.2.1 Effect of pH | 309 |
| 12.3.2.2 Effect of Sulfate Concentrations..... | 311 |
| 12.3.3 Surface Characterization for Hg(II)-Contacted Pyrite | 314 |
| 12.3.3.1 XPS Study | 314 |
| 12.3.3.2 SEM Study..... | 322 |
| 12.3.4 Stability of Hg(II)-Contacted Pyrite..... | 323 |
| 12.3.4.1 Low Molar Ratio of [Hg(II)]/[FeS ₂]..... | 323 |
| 12.3.4.2 High Molar Ratio of Hg(II) to Pyrite..... | 329 |
| 13. SORPTION OF MERCURY(II) TO ADSORBENTS/REACTANTS: | |
| 2. MACKINAWITE (FeS) | 337 |
| 13.1 Introduction..... | 338 |

| | Page |
|---|------|
| 13.2 Materials and Method | 341 |
| 13.2.1 Materials..... | 341 |
| 13.2.2 Kinetic Experiments..... | 341 |
| 13.2.3 Sorption/Reaction Experiments..... | 341 |
| 13.2.4 Stability of Hg(II)-Contacted FeS..... | 342 |
| 13.3 Results and Discussion | 343 |
| 13.3.1 Kinetics | 343 |
| 13.3.2 Nonlinear Removal Patterns..... | 345 |
| 13.3.2.1 Effect of pH..... | 345 |
| 13.3.2.2 Effect of Sulfate Concentrations..... | 348 |
| 13.3.3. Spectroscopic Investigations of Hg(II)-Contacted FeS..... | 350 |
| 13.3.4 Stability of Hg(II)-Contacted Mackinawite | 355 |
| 13.3.4.1 Low Molar Ratio of [Hg]/[FeS]..... | 355 |
| 13.3.4.2 High Molar Ratio of [Hg]/[FeS]..... | 361 |
| 14. CONCLUSIONS | 367 |
| 14.1 Summary and Overall Merits..... | 367 |
| 14.2 Recommendations..... | 373 |
| 14.2.1 Nanoporous Titania Adsorbents | 373 |
| 14.2.2 Nano-particulate Iron Sulfides | 373 |
| LITERATURE CITED | 375 |
| APPENDIX | 396 |
| VITA..... | 403 |

LIST OF FIGURES

| | | Page |
|------------|--|------|
| Figure 2.1 | Speciation of arsenic (III, V) as a function of pH for $[As]_T=0.1$ M and $I=0.1$ M (as NaCl). Calculations were made by chemical equilibrium program, MINEQL+. | 11 |
| Figure 2.2 | Speciation of selenium (IV, VI) as a function of pH for $[Se]_T=0.1$ M and $I=0.1$ M as NaCl. Calculations are made by MINEQL+(63). | 19 |
| Figure 2.3 | Speciation of mercury as a function of pH for $[Hg]_T=5 \times 10^{-4}$ M and $[HS^-]_T=0.1$ M. Calculations were made by MINEQL+ without considering precipitates. | 23 |
| Figure 2.4 | Aqueous speciation of mercury ($[Hg]_T=5 \times 10^{-4}$ M) in (a) the ligand-free system and in the presence of (b) $[Cl^-]_T=0.1$ M and (c) $[SO_4^{2-}]_T=0.1$ M. Calculations were made by MINEQL+ without considering precipitates. | 23 |
| Figure 2.5 | The primary pathways for formation of sedimentary iron sulfides. Circles and rectangles denote dissolved and solid species, respectively. Text in italics refers to processes that involve the activity of bacteria. (Used with permission from Pósfai and Dunin-Borkowski (96)). | 28 |
| Figure 2.6 | Schematic diagram of the preparation of mesoporous silica molecular sieve SBA-15. | 34 |
| Figure 2.7 | Schematic representation of the different types of interaction pathways between the surfactant and the inorganic framework: S=surfactant molecules, I=inorganic framework, M^+ and X^- =corresponding counterions, triangle=solvent molecules, dashed lines=H-bonding interactions (153). | 36 |
| Figure 2.8 | Schematic representation of the chemical structure of synthesized SBA-15, $Ti_{(25)}$ -SBA-15, and MT. | 38 |
| Figure 3.1 | Low angle XRD patterns of $Ti_{(15, 25, 35)}$ -SBA-15 and MT. | 49 |
| Figure 3.2 | High-angle XRD patterns for (a) MT, (b) SBA-15 and $Ti_{(15, 25, 35)}$ -SBA-15. | 50 |
| Figure 3.3 | (a) N_2 adsorption isotherms and (b) pore size distribution for $Ti_{(25)}$ -SBA-15 and MT. | 52 |
| Figure 3.4 | TEM images of (a) SBA-15, (b) $Ti_{(25)}$ -SBA-15, and (c) MT. | 53 |
| Figure 3.5 | Secondary images of SEM and EDS analysis for (a) SBA-15, (b) $Ti_{(25)}$ -SBA-15, (c) MT. | 53 |

| | Page |
|-------------|---|
| Figure 3.6 | FT-IR spectra of SBA-15, Ti _(15,25,35) -SBA-15, and MT..... 55 |
| Figure 3.7 | Percentage of As(III) adsorbed by (a) Ti ₍₂₅₎ -SBA-15 and (b) MT as a function of time at different pH values with predictions of kinetic model. 57 |
| Figure 3.8 | Percentage of As(V) adsorbed by (a) Ti ₍₂₅₎ -SBA-15 and (b) MT as a function of time at different pH values with predictions of kinetic model. 58 |
| Figure 3.9 | Percentage of (a) As(III) and (b) As(V) adsorbed by Ti ₍₂₅₎ -SBA-15 at pH 7 as affected by initial arsenic concentration with model predictions. 61 |
| Figure 3.10 | Percentage of (a) As(III) and (b) As(V) adsorbed by MT at pH 7 as affected by initial arsenic concentration with model predictions. 62 |
| Figure 3.11 | Langmuir (a) and Freundlich (b) adsorption isotherms for As(III) on Ti _(15,25,35) -SBA-15 and MT. Solid concentration is 1g/L. Curves are isotherm models obtained by nonlinear regression. 65 |
| Figure 3.12 | Langmuir (a) and Freundlich (b) adsorption isotherms for As(V) on Ti _(15,25,35) -SBA-15 and MT. Solid concentration is 1g/L. Curves are isotherm models obtained by nonlinear regression. 66 |
| Figure 3.13 | Langmuir adsorption isotherms for As(III) on (a) Ti ₍₂₅₎ -SBA-15 and (b) MT as affected by pH. Curves are isotherm models obtained by nonlinear regression. 69 |
| Figure 3.14 | Freundlich adsorption isotherms for As(III) on (a) Ti ₍₂₅₎ -SBA-15 and (b) MT as affected by pH. Curves are isotherm models obtained by nonlinear regression. 70 |
| Figure 3.15 | Langmuir adsorption isotherms for As(V) on (a) Ti ₍₂₅₎ -SBA-15 and (b) MT as affected by pH. Curves are isotherm models obtained by nonlinear regression. 71 |
| Figure 3.16 | Freundlich adsorption isotherms for As(V) on Ti ₍₂₅₎ -SBA-15 and MT as affected by pH. Curves are isotherm models obtained by nonlinear regression. 72 |
| Figure 4.1 | Fits of DLM to titration data for (a) Ti ₍₂₅₎ -SBA-15 and (b) MT in 0.01 and 0.1 M NaCl background electrolyte: The symbols represent experimental data and lines indicate the predictions of the DLM. 80 |
| Figure 4.2 | Modeling As(III) adsorption on NTAs. Effect of pH at various initial As(III) concentrations on percent adsorption by: (a1) Ti ₍₂₅₎ -SBA-15 and (b1) MT. Surface speciation predicted by DLM as function of pH for: (a2) Ti ₍₂₅₎ -SBA-15 + 7.82 μM As(III), (a3) Ti ₍₂₅₎ -SBA-15 + 45.6 μM As(III), (b2) MT + 7.82 μM As(III), (b3) MT + 45.6 μM As(III). 85 |

| | Page |
|------------|---|
| Figure 4.3 | Modeling As(V) adsorption on NTAs. Effect of pH at various initial As(V) concentrations on percent adsorption by: (a1) Ti ₍₂₅₎ -SBA-15, (b1) MT; Surface speciation predicted by DLM as function of pH for: (a2) Ti ₍₂₅₎ -SBA-15 + 9.86 μM As(V), (a3) Ti ₍₂₅₎ -SBA-15 + 39.4 μM As(V), (b2) MT + 9.86 μM As(V), (b3) MT + 39.4 μM As(V)..... 88 |
| Figure 4.4 | Modeling As(III) adsorption on NTAs. Effect of pH at various solid concentrations on adsorption of As(III) by: (a1) Ti ₍₂₅₎ -SBA-15 and (b1) MT. Surface speciation predicted by DLM as function of pH for: (a2) 1 g/L Ti ₍₂₅₎ -SBA-15, (a3) 3 g/L Ti ₍₂₅₎ -SBA-15, (b2) 1 g/L MT, (b3) 3 g/L MT. 91 |
| Figure 4.5 | Modeling As(V) adsorption on NTAs. Effect of pH at various solid concentration on adsorption of As(V) by: (a1) Ti ₍₂₅₎ -SBA-15 and (b1) MT. Surface speciation predicted by the DLM as a function of pH for: (a2) 1 g/L Ti ₍₂₅₎ -SBA-15, (a3) 3 g/L Ti ₍₂₅₎ -SBA-15, (b2) 1 g/L MT, (b3) 3 g/L MT..... 93 |
| Figure 5.1 | Surface characterization of synthetic pyrite using (a) XRD, (b) TEM, (c) SEM-EDS. 101 |
| Figure 5.2 | AFM images of synthetic pyrite before contact with selenium: (a) 3.22 μm × 3.22 μm 3D topography image (left) and height profile for cross-sectional region (right), (b) 2D phase image (left) and phase profile for cross-sectional region (right). 103 |
| Figure 5.3 | High resolution Se 3d XPS spectra of synthetic pyrite (1 g/L) reacted with (a) 3.1 mM Se(IV) and (b) 3.1 mM Se(VI) at pH 8 and various contact times. 105 |
| Figure 5.4 | High resolution Fe 2p _{3/2} XPS spectra of synthetic pyrite (1 g/L) reacted with 3.1mM Se(IV) at pH 8 for various times: (a) 1 day, (b) 15 days, (c) 30 days..... 107 |
| Figure 5.5 | High resolution Fe 2p _{3/2} XPS spectra of synthetic pyrite (1 g/L) reacted with 3.1mM Se(VI) at pH 8 for various times: (a) 1 day, (b) 15 days, (c) 30 days..... 108 |
| Figure 5.6 | High resolution S 2p XPS spectra of synthetic pyrite (1 g/L) reacted with 3.1 mM Se(IV) at pH 8 for various times: (a) 1 day, (b) 15 days, (c) 30 days..... 111 |
| Figure 5.7 | High resolution S 2p XPS spectra of synthetic pyrite (1 g/L) reacted with 3.1 mM Se(VI) at pH 8 for various times: (a) 1 day, (b) 15 days, (c) 30 days..... 112 |

| | Page |
|-------------|---|
| Figure 5.8 | High resolution of O 1s XPS spectra for synthetic pyrite (1 g/L) reacted with 3.1 mM Se(IV) at pH 8 for various times: (a) 1 day, (b) 15 days, (c) 30 days..... 114 |
| Figure 5.9 | High resolution of O 1s XPS spectra for synthetic pyrite (1 g/L) reacted with 3.1 mM Se(VI) at pH 8 for various times: (a) 1 day, (b) 15 days, (c) 30 days..... 115 |
| Figure 5.10 | Secondary images of SEM analysis for Se(IV)- and Se(VI)-contacted pyrites: (a) 1 day, (b) 15 days, (c) 30 days of contact times for Se(IV) (3.1 mM, pH 8), and (d) 1 day, (e) 15 days, (f) 30 days of contact times for Se(VI) (3.1 mM, pH 8)..... 118 |
| Figure 5.11 | AFM images of synthetic pyrite contacted with Se(IV) (3.1 mM, pH 8) for 15 days: (a) 4.0 μm \times 4.0 μm 3D topography image (left) and height profile for cross-sectional region (right), (b) 2D phase image (left) and phase profile for cross-sectional region (right)..... 120 |
| Figure 5.12 | AFM images of synthetic pyrite contacted with Se(VI) (3.1 mM, pH 8) for 15 days: (a) 1.46 μm \times 1.46 μm 3D topography image (left) and height profile for cross-sectional region (right), (b) 2D phase image (left) and phase profile for cross-sectional region (right)..... 121 |
| Figure 6.1 | Effect of time on removal of Se(IV) (100 μM) in the presence of pyrite (1 g/L) at pH 7 and 10. 129 |
| Figure 6.2 | Effect of time on removal of Se(VI) in the presence of pyrite (1 g/L) at pH 8..... 129 |
| Figure 6.3 | Amounts of Se(IV) removed per mass of solid (pyrite) as functions of concentration of Se(VI) in water for various pH. 131 |
| Figure 6.4 | Amounts of Se(VI) removed per mass of solid (pyrite) as functions of concentration of Se(VI) in water for various pH. 132 |
| Figure 6.5 | Amounts of Se(VI) removed per mass of solid (pyrite) as functions of concentration of Se(VI) in water for various pH, using only data at lower concentrations. 132 |
| Figure 6.6 | Effect of Sulfate on Solid-phase Concentration of Se(IV) on Pyrite. 134 |
| Figure 6.7 | Effect of Sulfate on Solid-phase Concentration of Se(VI) on Pyrite. 134 |
| Figure 6.8 | High resolution Fe 2p _{3/2} XPS spectra of pyrite (1 g/L) before contact with selenium at various pH (4, 8, 10). 136 |
| Figure 6.9 | High resolution S 2p XPS spectra of pyrite (1 g/L) before contact with |

| | Page |
|--|------|
| selenium at various pH (4, 8, 10)..... | 137 |
| Figure 6.10 High resolution O 1s XPS spectra of pyrite (1 g/L) before contact with selenium at various pH (4, 8, 10)..... | 138 |
| Figure 6.11 Effect of pH on removal of Se(IV) (16.5 μ M) by pyrite (1 g/L) as pH was decreased from near pH 10 and subsequently was increased..... | 140 |
| Figure 6.12 Secondary images of SEM analysis for pyrite (1 g/L) reacted with Se(IV) (16.5 μ M) at (a) pH 10 _(i) and (b) pH 4 _(a.a.t) | 141 |
| Figure 6.13 High resolution Se 3d XPS spectra for pyrite (1 g/L) after contact with Se(IV) (16.5 μ M) at (a) pH 10 _(i) and (b) pH 4 _(a.a.t) | 143 |
| Figure 6.14 High resolution Fe 2p _{3/2} XPS spectra for pyrite (1 g/L) reacted with Se(IV) (16.5 μ M) at (a) pH 10 _(i) and (b) pH 4 _(a.a.t) | 144 |
| Figure 6.15 High resolution S 2p XPS spectra for pyrite (1 g/L) reacted with Se(IV) (16.5 μ M) at (a) pH 10 _(i) and (b) pH 4 _(a.a.t) | 145 |
| Figure 6.16 High resolution O 1s XPS spectra for pyrite (1 g/L) reacted with Se(IV) (16.5 μ M) at (a) pH 10 _(i) and (b) pH 4 _(a.a.t) | 146 |
| Figure 6.17 Effect of pH on removal of Se(VI) (16.5 μ M) by pyrite (1 g/L) as pH was increased from near pH 4 and subsequently was decreased..... | 148 |
| Figure 6.18 Secondary images of SEM analysis for pyrite (1 g/L) reacted with Se(VI) (16.5 μ M) at (a) pH 4 _(i) and (b) pH 7 _(a.b.t) and (c) pH 10 _(a.b.t) as pH was increased. | 149 |
| Figure 6.19 High resolution Se 3d XPS spectra for pyrite after contact with Se(VI) (16.5 μ M) at pH 4 _(i) , 7 _(a.b.t) , 10 _(a.b.t) as pH was increased. | 150 |
| Figure 6.20 High resolution Fe 2p _{3/2} XPS spectra for pyrite (1 g/L) reacted with Se(VI) (16.5 μ M) at (a) pH 4 _(i) and (b) pH 7 _(a.b.t) and (c) pH 10 _(a.b.t) as pH increased.... | 152 |
| Figure 6.21 High resolution S 2p XPS spectra for pyrite (1 g/L) reacted with Se(VI) (16.5 μ M) at (a) pH 4 _(i) and (b) pH 7 _(a.b.t) and (c) pH 10 _(a.b.t) as pH increased.... | 153 |
| Figure 6.22 High resolution O 1s XPS spectra for pyrite (1 g/L) reacted with Se(VI) (16.5 μ M) at (a) pH 4 _(i) and (b) pH 7 _(a.b.t) and (c) pH 10 _(a.b.t) as pH increased. ... | 154 |
| Figure 7.1 X-ray diffraction patterns of synthetic FeS. | 161 |
| Figure 7.2 Transmission electron microscope (TEM) image (left) and selected area electron diffraction (SAED) pattern (right) of synthetic FeS..... | 162 |

| | Page |
|-------------|--|
| Figure 7.3 | Secondary image of scanning electron microscope (SEM) (left) and analysis of energy dispersive spectroscopy (EDS) (right) of synthetic mackinawite. 162 |
| Figure 7.4 | High resolution Se 3d spectra of synthetic mackinawite (1 g/L) at pH 8 before and at various times after contact with (a) 3.1 mM Se(IV) and (b) 3.1 mM Se(VI). 164 |
| Figure 7.5 | High resolution Fe 2p _{3/2} XPS spectra of synthetic mackinawite (1 g/L) reacted with 3.1 mM Se(IV) at pH 8 for various times: (a) 1 day, (b) 15 days, (c) 30 days. 165 |
| Figure 7.6 | High resolution Fe 2p _{3/2} XPS spectra of synthetic mackinawite (1 g/L) reacted with 3.1 mM Se(VI) at pH 8 for various times: (a) 1 day, (b) 15 days, (c) 30 days. 166 |
| Figure 7.7 | High resolution S 2p spectra of synthetic mackinawite (1 g/L) reacted with 3.1 mM Se(IV) at pH 8 for various times: (a) 1 day, (b) 15 days, (c) 30 days. 169 |
| Figure 7.8 | High resolution S 2p spectra of synthetic mackinawite (1 g/L) reacted with 3.1mM Se(VI) at pH 8 for various times: (a) 1 day, (b) 15 days, (c) 30 days. 170 |
| Figure 7.9 | High resolution of O 1s XPS spectra for synthetic mackinawite (1 g/L) reacted with 3.1 mM Se(IV) at pH 8 for various times: (a) 1 day, (b) 15 days, (c) 30 days. 172 |
| Figure 7.10 | High resolution of O 1s XPS spectra for synthetic mackinawite (1 g/L) reacted with 3.1 mM Se(VI) at pH 8 for various times: (a) 1 day, (b) 15 days, (c) 30 days. 173 |
| Figure 8.1 | Kinetics of Se(IV) uptake by FeS at pH 8 as affected by initial concentrations of FeS and Se(IV): (a) FeS = 1 g/L and Se(IV) = 6.3, 12.7, 38 μM; (b) FeS = 0.5 g/L and Se(IV) = 127 and 253 μM. 182 |
| Figure 8.2 | Effect of time on concentrations of Se(VI) in presence of 1 g/L FeS at pH 8. 183 |
| Figure 8.3 | Measured concentrations of Se(IV) on FeS (symbols) as functions of concentration in water with (a) Langmuir, (b) Freundlich, and (c) BET model predictions (lines) at various pH. 185 |
| Figure 8.4 | Measured concentrations of Se(VI) on FeS (symbols) as functions of concentration in water with (a) Langmuir, (b) Freundlich, and (c) BET model predictions (lines) at various pH. 187 |

| | Page |
|-------------|--|
| Figure 8.5 | Effect of sulfate on solid-phase concentration of Se(IV) on FeS with (a) the Langmuir and (b) Freundlich models (lines) fitted to data (symbols). ... 190 |
| Figure 8.6 | Effect of sulfate on solid-phase concentration of Se(VI) on FeS..... 191 |
| Figure 8.7 | High resolution Fe 2p _{3/2} XPS spectra for mackinawite (1 g/L) before contact with selenium at various pH (4, 8, 10). 194 |
| Figure 8.8 | High resolution S 2p XPS spectra of mackinawite (1 g/L) before contact with selenium at various pH (4, 8, 10). 195 |
| Figure 8.9 | High resolution O 1s XPS spectra of mackinawite (1 g/L) before contact with selenium at various pH (4, 8, 10). 196 |
| Figure 8.10 | Effect of pH on removal of Se(IV) (16.6 μM) by FeS (1 g/L) as pH was decreased from pH 10 and subsequently was increased. 197 |
| Figure 8.11 | High resolution Se 3d XPS spectra for FeS before and after contact with Se(IV) (16.6 μM) at pH 10 _(i) and pH 4 _(a.a.t) 198 |
| Figure 8.12 | High resolution Fe 2p _{3/2} XPS spectra for FeS reacted with Se(IV) (15.2 μM) at (a) pH 10 _(i) and (b) pH 4 _(a.a.t) 200 |
| Figure 8.13 | High resolution S 2p XPS spectra for FeS reacted with Se(IV) (15.2 μM) at (a) pH 10 _(i) and (b) pH 4 _(a.a.t) 201 |
| Figure 8.14 | Effect of pH on removal of Se(VI) (16.6 μM) by FeS (1 g/L) as pH was increased from near pH 4 and subsequently was decreased..... 202 |
| Figure 8.15 | High resolution Se 3d XPS spectra for FeS before and after contact with Se(VI) (16.6 μM) at pH 4 _(i) , 6 _(a.b.t) , and 10 _(a.b.t) 203 |
| Figure 8.16 | High resolution Fe 2p _{3/2} XPS spectra for FeS reacted with Se(VI) (15.2 μM) at (a) pH 4 _(i) and (b) pH 6 _(a.b.t) and (c) pH 10 _(a.b.t) as pH increased for sorption..... 204 |
| Figure 8.17 | High resolution S 2p XPS spectra for FeS reacted with Se(VI) (15.2 μM) at (a) pH 4 _(i) and (b) pH 6 _(a.b.t) and (c) pH 10 _(a.b.t) as pH increased for sorption. 205 |
| Figure 9.1 | High resolution As 3d _{5/2} XPS spectra of synthetic pyrite (1 g/L) reacted with 3.3 mM As(III) at pH 8 for various times: (a) 1 day, (b) 15 days, (c) 30 days..... 213 |
| Figure 9.2 | High resolution As 3d _{5/2} XPS spectra of synthetic pyrite (1 g/L) reacted with 3.3 mM As(V) at pH 8 for various times: (a) 1 day, (b) 15 days, (c) 30 days..... 214 |

| | Page |
|-------------|---|
| Figure 9.3 | High resolution Fe 2p _{3/2} XPS spectra for synthetic pyrite (1 g/L) reacted with 3.3 mM As(III) at pH 8 for various times: (a) 1 day, (b) 15 days, (c) 30 days..... 218 |
| Figure 9.4 | High resolution Fe 2p _{3/2} XPS spectra for synthetic pyrite (1 g/L) reacted with 3.3 mM As(V) at pH 8 for various times: (a) 1 day, (b) 15 days, (c) 30 days..... 219 |
| Figure 9.5 | High resolution S 2p XPS spectra for synthetic pyrite (1 g/L) reacted with 3.3 mM As(III) at pH 8 for various times: (a) 1 day, (b) 15 days, (c) 30 days..... 220 |
| Figure 9.6 | High resolution S 2p XPS spectra for synthetic pyrite (1 g/L) reacted with 3.3 mM As(V) at pH 8 for various times: (a) 1 day, (b) 15 days, (c) 30 days..... 221 |
| Figure 9.7 | High resolution O 1s XPS spectra for pyrite reacted with 3.3 mM As(III) at pH 8 for various times: (a) 1 day, (b) 15 days, (c) 30 days. 222 |
| Figure 9.8 | High resolution O 1s XPS spectra for pyrite reacted with 3.3 mM As(V) at pH 8 for various times: (a) 1 day, (b) 15 days, (c) 30 days. 223 |
| Figure 9.9 | The O 1s XPS spectra for pyrite reacted with As(III) (3.3 mM) at pH 8 and various reaction times (1, 15, 30 days). 224 |
| Figure 9.10 | Secondary SEM images and EDS analysis of pyrites after contact with As(III) (3.3 mM) as a function of reaction times: (a) 1 day, (b) 15 day, (c) 30 days..... 225 |
| Figure 9.11 | Secondary SEM images and EDS analysis of pyrites after contact with As(V) (3.3mM) as a function of reaction times: (a) 1 day, (b) 15 day, (c) 30 days..... 226 |
| Figure 9.12 | High resolution As 3d _{5/2} XPS spectra of synthetic pyrite (1 g/L) reacted with 3.3 mM As(III) at pH 8 for various times: (a) 1 day, (b) 15 days, (c) 30 days..... 228 |
| Figure 9.13 | High resolution As 3d _{5/2} XPS spectra of synthetic pyrite (1 g/L) reacted with 3.3 mM As(V) at pH 8 for various times: (a) 1 day, (b) 15 days, (c) 30 days..... 229 |
| Figure 9.14 | High resolution Fe 2p _{3/2} XPS spectra of synthetic mackinawite (1 g/L) reacted with 3.3 mM As(III) at pH 8 for various times: (a) 1 day, (b) 15 days, (c) 30 days..... 232 |
| Figure 9.15 | High resolution Fe 2p _{3/2} XPS spectra of synthetic mackinawite (1 g/L) reacted with 3.3 mM As(V) at pH 8 for various times: (a) 1 day, |

| | Page |
|--|------|
| (b) 15 days, (c) 30 days..... | 233 |
| Figure 9.16 High resolution S 2p XPS spectra of synthetic mackinawite (1 g/L) reacted with 3.3 mM As(III) at pH 8 for various times: (a) 1 day, (b) 15 days, (c) 30 days..... | 234 |
| Figure 9.17 High resolution S 2p XPS spectra of synthetic mackinawite (1g/L) reacted with 3.3 mM As(V) at pH 8 for various times: (a) 1 day, (b) 15 days, (c) 30 days..... | 235 |
| Figure 9.18 High resolution O 1s XPS spectra for pyrite reacted with 3.3 mM As(III) at pH 8 for various times: (a) 1 day, (b) 15 days, (c) 30 days..... | 239 |
| Figure 9.19 High resolution O 1s XPS spectra for pyrite reacted with 3.3 mM As(V) at pH 8 for various times: (a) 1 day, (b) 15 days, (c) 30 days..... | 240 |
| Figure 10.1 Removal of As(III) and As(V) by pyrite as a function of time at pH 8. Initial concentrations of As(III) and As(V) were 13.6 and 20.9 μM , respectively..... | 249 |
| Figure 10.2 Measured concentrations of As(III) on pyrite (symbols) as function of concentration in water with (a) Langmuir and (b) Freundlich models (lines) fitted to data at various pH..... | 251 |
| Figure 10.3 Measured concentrations of As(V) on pyrite (symbols) as function of concentration in water with Langmuir model (lines) fitted to data at various pH..... | 252 |
| Figure 10.4 Measured concentrations of As(III) on pyrite (symbols) as function of concentration in water in water with (a) Langmuir and (b) Freundlich models (lines) fitted to data at various concentrations of sulfate..... | 254 |
| Figure 10.5 Measured concentration of As(V) on pyrite (symbols) as function of concentration in water with (a) Langmuir and (b) Freundlich models (lines) fitted to data at various concentrations of sulfate..... | 255 |
| Figure 10.6 Effect of pH on removal of As(III) (15.2 μM) by pyrite (1 g/L) as pH was increased from pH 4 to pH 10 and subsequently was decreased..... | 256 |
| Figure 10.7 Secondary SEM images and EDS results for pyrite after contact with 15.2 μM As(III) at (a) pH 4 _(i) and (b) pH 10 _(a,b,t) | 257 |
| Figure 10.8 High resolution As 3d XPS spectra for pyrite after contact with As(III) (15.2 μM) at (a) pH 4 _(i) and (b) pH 10 _(a,b,t) | 258 |
| Figure 10.9 High resolution Fe 2p _{3/2} XPS spectra for pyrite after contact with As(III) (15.2 μM) at (a) pH 4 _(i) and (b) pH 10 _(a,b,t) | 259 |

| | Page |
|---|------|
| Figure 10.10 High resolution S 2p XPS spectra for pyrite after contact with As(III) (15.2 μM) at (a) pH 4 _(i) and (b) pH 10 _(a,b,t) | 260 |
| Figure 10.11 High resolution O 1s XPS spectra for pyrite after contact with As(III) (15.2 μM) at (a) pH 4 _(i) and (b) pH 10 _(a,b,t) | 261 |
| Figure 10.12 Effect of pH on removal of As(V) (15.2 μM) by pyrite (1 g/L) as pH was decreased from pH 10 and subsequently was increased. | 263 |
| Figure 10.13 Secondary images of SEM and EDS analysis for pyrite after contact with As(V) (15.2 μM) at (a) pH 10 _(i) (b) pH 4 _(a,a,t) , and (c) pH 7 _(a,b,t) | 264 |
| Figure 10.14 High resolution As 3d XPS spectra for pyrite after contact with As(V) (15.2 μM) at (a) pH 10 _(i) , (b) pH 4 _(a,a,t) , and (c) pH 7 _(a,b,t) . Expanded view shows XPS spectra at binding energy between 36 and 48 eV. | 266 |
| Figure 10.15 High resolution Fe 2p _{3/2} XPS spectra for pyrite after contact with As(V) (15.2 μM) at (a) pH 10 _(i) , (b) pH 4 _(a,a,t) , and (c) pH 10 _(a,b,t) | 267 |
| Figure 10.16 High resolution S 2p XPS spectra for pyrite after contact with As(V) (15.2 μM) at (a) pH 10 _(i) , (b) pH 4 _(a,a,t) , and (c) pH 7 _(a,b,t) | 268 |
| Figure 10.17 High resolution O 1s XPS spectra for pyrite after contact with As(V) (15.2 μM) at (a) pH 10 _(i) , (b) pH 4 _(a,a,t) , and (c) pH 7 _(a,b,t) | 269 |
| Figure 11.1 Removal of As(III) and As(V) by FeS as a function of time at pH 8. Initial concentrations of As(III) and As(V) were 13.3 μM and dose of FeS was 1 g/L. | 277 |
| Figure 11.2 Measured concentrations of As(III) on FeS as function of concentration in water with (a) Langmuir, (b) Freundlich, (c) BET equations (lines) fitted to data (symbols) at various pH. | 279 |
| Figure 11.3 Measured concentrations of As(III) on FeS as a function of concentration in water for various pH using data at lower concentrations. | 281 |
| Figure 11.4 Measured concentrations of As(V) on FeS as function of concentration in water with (a) Langmuir, (b) Freundlich, (c) BET equations (lines) fitted to data (symbols) at various pH. | 282 |
| Figure 11.5 Measured concentrations of As(III) on FeS as function of concentration in water with (a) Langmuir, (b) Freundlich, and (c) BET equations (lines) fitted to data (symbols) at various concentrations of sulfate. | 284 |
| Figure 11.6 Measured concentrations of As(V) on FeS as function of concentration in water with (a) Langmuir, (b) Freundlich, and (c) BET equations (lines) fitted to data (symbols) at various concentrations of sulfate. | 286 |

| | Page |
|--------------|---|
| Figure 11.7 | Effect of pH on removal of As(III) (15.2 μ M) by FeS (1 g/L) as pH was decreased from pH 10 to pH 4 and then increased back to pH 10. 290 |
| Figure 11.8 | High resolution As 3d XPS spectra for FeS after contact with As(III) (15.2 μ M) at (a) pH 10 _(i) and (b) pH 4 _(a.a.t) 291 |
| Figure 11.9 | High resolution Fe 2p _{3/2} XPS spectra for FeS reacted with As(III) (15.2 μ M) at (a) pH 10 _(i) and (b) pH 4 _(a.a.t) 292 |
| Figure 11.10 | High resolution S 2p XPS spectra for FeS reacted with As(III) (15.2 μ M) at (a) pH 10 _(i) and (b) pH 4 _(a.a.t) 293 |
| Figure 11.11 | Effect of pH on removal of As(V) (15.2 μ M) by FeS (1 g/L) as pH was decreased from pH 10 to pH 4 and then increased back to pH 10. 295 |
| Figure 11.12 | High resolution As 3d XPS spectra for pyrite after contact with As(V) (15.2 μ M) at (a) pH 4 _(a.a.t) , (b) pH 10 _(i) , and (c) pH 10 _(f) 297 |
| Figure 11.13 | High resolution Fe 2p _{3/2} XPS spectra for pyrite after contact with As(V) (15.2 μ M) at (a) pH 10 _(i) , (b) pH 4 _(a.a.t) , and (c) pH 10 _(f) 298 |
| Figure 11.14 | High resolution S 2p XPS spectra for pyrite after contact with As(V) (15.2 μ M) at (a) pH 10 _(i) , (b) pH 4 _(a.a.t) , and (c) pH 10 _(f) 299 |
| Figure 12.1 | Removal of Hg(II) as a function of time at pH 7 (initial concentration = 100, 250, 500 μ M, pyrite dose = 1, 0.5, 0.2 g/L). 308 |
| Figure 12.2 | Measured concentrations of Hg(II) on pyrite as function of concentration in water with (a) Langmuir, (b) Freundlich, (c) BET models (lines) fitted to data (symbols) at various pH. 310 |
| Figure 12.3 | Measured concentrations of Hg(II) on pyrite as function of concentration in water with (a) Langmuir, (b) Freundlich, and (c) BET models (lines) fitted to data (symbols) at various concentrations of sulfate. 312 |
| Figure 12.4 | High resolution Hg 4f XPS spectra for synthetic pyrite (1 g/L) reacted with 200 μ M Hg(II) at pH 8 for various times: (a) 1 day, (b) 15 days, (c) 30 days. 315 |
| Figure 12.5 | High resolution Fe 2p _{3/2} XPS spectra for synthetic pyrite (1 g/L) reacted with 200 μ M Hg(II) at pH 8 for various times: (a) 1 day, (b) 15 days, (c) 30 days. 317 |
| Figure 12.6 | High resolution S 2p XPS spectra for synthetic pyrite (1 g/L) reacted with 200 μ M Hg(II) at pH 8 for various times: (a) 1 day, (b) 15 days, (c) 30 days. 318 |

| | Page | |
|--------------|--|-----|
| Figure 12.7 | High resolution O 1s XPS spectra (Al K α) for synthetic pyrite (1 g/L) reacted with 200 μ M Hg(II) at pH 8 for various times: (a) 1 day, (b) 15 days, (c) 30 days..... | 321 |
| Figure 12.8 | Secondary images of SEM and EDS results for pyrites contacted with Hg(II) at various times: (a) 1 day, (b) 15 days, and (c) 30 days..... | 322 |
| Figure 12.9 | Effect of pH change on the stability of Hg(II)-contacted pyrite: [Hg(II)] _o =6.48 μ M, solid loading = 1 g/L, contact time = 30 minutes, pH was first increased from pH 3.4 to pH 10 and then decreased to pH 3.4. | 324 |
| Figure 12.10 | Secondary SEM images of synthetic pyrite reacted with Hg(II) (6.48 μ M) at (a) pH 3.4 (initial sample) and (b) pH 10 (after base titration). | 325 |
| Figure 12.11 | High resolution Hg 4f XPS spectra for pyrite after contact with Hg(II) (6.48 μ M) at (a) pH 3.4 _(i) and (b) pH 10 _(a,b,t) | 326 |
| Figure 12.12 | High resolution Fe 2p _{3/2} XPS spectra for pyrite after contact with Hg(II) (6.48 μ M) at (a) pH 3.4 _(i) and (b) pH 10 _(a,b,t) | 328 |
| Figure 12.13 | High resolution Fe 2p _{3/2} XPS spectra for pyrite after contact with Hg(II) (6.48 μ M) at (a) pH 3.4 _(i) and (b) pH 10 _(a,b,t) | 329 |
| Figure 12.14 | Effect of pH change on stability of Hg(II)-contacted pyrite: [Hg(II)] _o =1 mM, solid loading = 1 g/L, contact time = 30 minutes, pH was first increased from pH 2.4 to pH 10 and then decreased to pH 3.0. | 330 |
| Figure 12.15 | Secondary SEM images of pyrite after contact with Hg(II) (1.0 mM) at (a) pH 2.4 _(i) and (b) pH 10 _(a,b,t) | 331 |
| Figure 12.16 | High resolution Hg 4f XPS spectra for pyrite after contact with Hg(II) (1 mM) at (a) pH 2.4 _(i) and (b) pH 10 _(a,b,t) | 334 |
| Figure 12.17 | High resolution Fe 2p _{3/2} XPS spectra for pyrite after contact with Hg(II)(1 mM) at (a) pH 2.4 _(i) and (b) pH 10 _(a,b,t) | 335 |
| Figure 12.18 | High resolution S 2p XPS spectra for pyrite after contact with Hg(II)(1 mM) at (a) pH 2.4 _(i) and (b) pH 10 _(a,b,t) | 336 |
| Figure 13.1 | Percentage removal of Hg(II) and concentration of total Fe released as a function of time at pH 8 for three initial Hg(II) concentrations..... | 345 |
| Figure 13.2 | Measured concentrations of Hg(II) on FeS as functions of concentration in water for various pH: (a) at all Hg concentrations and (b) at lower Hg concentrations. | 347 |
| Figure 13.3 | Amounts of Hg(II) removed per mass of solid (FeS) as functions of | |

| | Page |
|---|------|
| concentration of Hg(II) in water as affected by sulfate concentration (0, 1, and 10 mM) at pH 8..... | 349 |
| Figure 13.4 High resolution Hg 4f XPS spectra for FeS (1 g/L) reacted with Hg(II) (200 μ M) at pH 8 for various times: (a) 1 day, (b) 15 days, (c) 30 days..... | 351 |
| Figure 13.5 High resolution Fe 2p _{3/2} XPS spectra for FeS (1 g/L) reacted with Hg(II) (200 μ M) at pH 8 for various times: (a) 1 day, (b) 15 days, (c) 30 days. | 352 |
| Figure 13.6 High resolution S 2p XPS spectra for FeS (1 g/L) reacted with Hg(II) (200 μ M) at pH 8 for various times: (a) 1 day, (b) 15 days, (c) 30 days. | 353 |
| Figure 13.7 Effect of pH on removal of Hg(II) (6.48 μ M) by FeS (1 g/L) as pH was decreased from pH 10.5 and subsequently increased. | 356 |
| Figure 13.8 High resolution Hg 4f XPS spectra for mackinawite after contact with Hg(II) (6.48 μ M) at (a) pH 10.5 _(i) and (b) pH 3.5 _(a.a.t) | 358 |
| Figure 13.9 High resolution Fe 2p _{3/2} XPS spectra for mackinawite after contact with Hg(II) (6.48 μ M) at (a) pH 10.5 _(i) and (b) pH 3.5 _(a.a.t) | 359 |
| Figure 13.10 High resolution S 2p XPS spectra for mackinawite after contact with Hg(II) (6.48 μ M) at (a) pH 10.5 _(i) and (b) pH 3.5 _(a.a.t) | 360 |
| Figure 13.11 Effect of pH on removal of Hg(II) (1.0 mM) by FeS (1 g/L) as pH decreased from pH 10 and subsequently increased. | 361 |
| Figure 13.12 High resolution Hg 4f XPS spectra for mackinawite after contact with Hg(II) (1 mM) at (a) pH 10 _(i) and (b) pH 3.5 _(a.a.t) | 363 |
| Figure 13.13 High resolution Fe 2p _{3/2} XPS spectra for mackinawite after contact with Hg(II) (1 mM) at (a) pH 10 _(i) and (b) pH 3.5 _(a.a.t) | 364 |
| Figure 13.14 High resolution S 2p XPS spectra for mackinawite after contact with Hg(II) (1 mM) at (a) pH 10 _(i) and (b) pH 3.5 _(a.a.t) | 365 |

LIST OF TABLES

| | | Page |
|-----------|---|------|
| Table 2.1 | Comparison of solubility constants of selected metal sulfides (121, 122)..... | 29 |
| Table 3.1 | Calculated parameters of the adsorption kinetic model for arsenic (As(III,V)) uptake by NTAs, as affected by initial pH values (pH 4, 7, 9.5)..... | 59 |
| Table 3.2 | Calculated parameters of the adsorption kinetic model for arsenic (As(III,V)) uptake by NTAs, as affected by initial As(III, V) concentrations (5.3, 9.3, 13.3 μM)..... | 63 |
| Table 3.3 | Comparison of isotherm parameters \pm 95% confidence levels for As(III) adsorption..... | 64 |
| Table 3.4 | Comparison of isotherm parameters \pm 95% confidence levels for As(V) adsorption. | 64 |
| Table 3.5 | Comparison of As(III) adsorption isotherm parameters as a function of pH..... | 68 |
| Table 3.6 | Comparison of As(V) adsorption isotherm parameters as a function of pH. | 68 |
| Table 4.1 | Intrinsic surface acidity constants for Ti ₍₂₅₎ -SBA-15 and MT using diffuse layer model. | 79 |
| Table 4.2 | Arsenic surface reactions and intrinsic surface complexation constants. | 82 |
| Table 5.1 | Binding energies (BE), full width at half maximum (FWHM), and area percentage for peaks in the Fe 2p _{3/2} XPS spectra of pyrite contacted with Se(IV) and Se(VI) for various times. | 116 |
| Table 5.2 | Binding energies (BE), full width at half maximum (FWHM), and area percentage for peaks in the S 2p XPS spectra of pyrite contacted with Se(IV) and Se(VI) for various times..... | 116 |
| Table 5.3 | Binding energies (BE), full width at half maximum (FWHM), and area percentage for peaks in the O 1s XPS spectra of pyrite contacted with Se(IV) and Se(VI) for various times. | 117 |
| Table 6.1 | Binding energies (BE), full width at half maximum (FWHM), and area percentage for peaks in the Fe 2p _{3/2} , S 2p, and O 1s XPS spectra of synthetic pyrite before contact with selenium at various pH (4, 8, 10)..... | 139 |
| Table 6.2 | Binding energies (BE), full width at half maximum (FWHM), and relative area for peaks in the Fe 2p _{3/2} , S 2p, and O 1s XPS spectra of synthetic | |

| | Page |
|--|------|
| pyrite contacted with Se(IV) at pH 10 _(i) and 4 _(a.a.t) | 147 |
| Table 6.3 Binding energies (BE), full width at half maximum (FWHM), and relative area for peaks in the Fe 2p _{3/2} , S 2p, and O 1s XPS spectra of synthetic pyrite contacted with Se(VI) at pH 4 _(i) , 7 _(a.b.t) , 10 _(a.b.t) | 155 |
| Table 7.1 Binding energies (BE), full width at half maximum (FWHM), and area percentage for peaks in the Fe 2p _{3/2} XPS spectra of mackinawite contacted with Se(IV) and Se(VI) for various times..... | 167 |
| Table 7.2 Binding energies (BE), full width at half maximum (FWHM), area percentage for peaks in the S 2p XPS spectra of mackinawite contacted with Se(IV) and Se(VI) for various times..... | 168 |
| Table 7.3 Binding energies (BE), full width at half maximum (FWHM), and area percentage for peaks in the O 1s XPS spectra of mackinawite contacted with Se(IV) and Se(VI) for various times. | 174 |
| Table 8.1 Summary of model parameters for Se(IV) removal by FeS. | 186 |
| Table 8.2 Summary of model parameters for Se(VI) removal by FeS. | 189 |
| Table 8.3 Summary of model parameters for Se(IV) removal as affected by sulfate..... | 191 |
| Table 8.4 Binding energies (BE), full width at half maximum (FWHM), and area percentage for peaks in the Fe 2p _{3/2} , S 2p, and O 1s XPS spectra of mackinawite before contact with selenium at various pH (4, 8, 10)..... | 193 |
| Table 9.1 Binding energies (BE), full width at half maximum (FWHM), and area percentage for peaks in the As 3d _{5/2} XPS spectra of pyrite contacted with As(III) and As(V) for various times..... | 212 |
| Table 9.2 Binding energies (BE), full width at half maximum (FWHM), and area percentage for peaks in the Fe 2p _{3/2} XPS spectra of pyrite contacted with As(III) and As(V) for various times..... | 216 |
| Table 9.3 Binding energies (BE), full width at half maximum (FWHM), and area percentage for peaks in the S 2p XPS spectra of pyrite contacted with As(III) and As(V) for various times..... | 217 |
| Table 9.4 Binding energies (BE), full width at half maximum (FWHM), and area percentage for peaks in the O 1s XPS spectra of pyrite contacted with As(III) and As(V) for various times..... | 217 |
| Table 9.5 Binding energies (BE), full width at half maximum (FWHM), and area percentage for peaks in the As 3d _{5/2} XPS spectra of mackinawite contacted with As(III) and As(V) for various times. | 230 |

| | Page |
|------------|--|
| Table 9.6 | Binding energies (BE), peak full width at half maximum (FWHM), peak area percentage for Fe 2p _{3/2} photoelectron spectra of mackinawite contacted with As(III) and As(V) for various times. 236 |
| Table 9.7 | Binding energies (BE), peak full width at half maximum (FWHM), peak area percentage for S 2p photoelectron spectra of mackinawite contacted with As(III) and As(V) for various times..... 237 |
| Table 9.8 | Binding energies (BE), peak fill width at half maximum (FWHM), peak area percentage for O 1s photoelectron spectra of mackinawite contacted with As(III) and As(V) over contact time. 241 |
| Table 10.1 | Calculated parameters of the sorption kinetic model for As(III) and As(V) uptake by pyrite at pH 8..... 250 |
| Table 10.2 | As(III) adsorption model parameters. 253 |
| Table 10.3 | As(V) adsorption model parameters. 253 |
| Table 10.4 | As(III) adsorption model parameters as affected by sulfate. 253 |
| Table 10.5 | As(V) adsorption model parameters as affected by sulfate. 253 |
| Table 10.6 | Binding energies (BE), full width at half maximum (FWHM), and area percentage for peaks in the Fe 2p _{3/2} , S 2p, and O 1s XPS spectra of pyrite after contact with As(III) (15.2 μM) at pH 4 _(i) and pH 10 _(a,b,t) 262 |
| Table 10.7 | Binding energies (BE), full width at half maximum (FWHM), and area percentage for peaks in the Fe 2p _{3/2} , S 2p, and O 1s XPS spectra of pyrite after contact with As(V) (15.2 μM) at (a) pH 10 _(i) , pH 4 _(a,a,t) , and pH 7 _(a,b,t) 270 |
| Table 11.1 | Calculated parameters for kinetic model of As(III) and As(V) uptake by FeS at pH 8. 277 |
| Table 11.2 | Parameters of models describing removal of As(III) by FeS as affected by pH. 279 |
| Table 11.3 | Parameters of models describing removal of As(V) by FeS as affected by pH. 282 |
| Table 11.4 | Parameters of models describing removal of As(III) by FeS as affected by sulfate concentration..... 288 |
| Table 11.5 | Parameters for models describing removal of As(V) by FeS as affected by sulfate concentration..... 288 |

| | | |
|------------|---|-----|
| Table 11.6 | Binding energies (BE), full width at half maximum (FWHM), and area percentage for peaks in the Fe 2p _{3/2} and S 2p XPS spectra of FeS after contact with As(III) at pH 10 _(i) and pH 4 _(a.a.t) | 294 |
| Table 11.7 | Binding energies (BE), full width at half maximum (FWHM), and area percentage for peaks in the Fe 2p _{3/2} and S 2p XPS spectra for pyrite after contact with As(V) (15.2 μM) at pH 10 _(i) , pH 4 _(a.a.t) , and pH 10 _(f) | 300 |
| Table 12.1 | Calculated parameters of the kinetic model for Hg(II) uptake by pyrite at pH 7. | 309 |
| Table 12.2 | Parameters of models describing removal of Hg(II) by pyrite as affected by pH. | 311 |
| Table 12.3 | Parameters of models describing removal of As(III) by FeS as affected by sulfate concentration..... | 314 |
| Table 12.4 | Binding energies (BE), peak full width at half maximum (FWHM), peak area percentage for Hg 4f _{7/2} XPS spectra of pyrite contacted with Hg(II) for various times and for reference materials | 319 |
| Table 12.5 | Binding energies (BE), full width at half maximum (FWHM), and area percentage for peaks in the Fe 2p _{3/2} XPS spectra of pyrite contacted with Hg(II) for various times..... | 320 |
| Table 12.6 | Binding energies (BE), full width at half maximum (FWHM), and area percentage for peaks in the O 1s spectra of pyrite contacted with Hg(II) for various times. | 320 |
| Table 12.7 | Binding energies (BE), full width at half maximum (FWHM), and area percentage for peaks in the Fe 2p _{3/2} XPS spectra of the pH 4 _(i) sample and the pH 10 _(f) sample..... | 327 |
| Table 12.8 | Binding energies (BE), full width at half maximum (FWHM), and area percentage for peaks in the Fe 2p _{3/2} XPS spectra of pyrite after contact with Hg(II) (1 mM) at pH 2.4 _(i) and pH 10 _(a.b.t) | 333 |
| Table 13.1 | Calculated parameters of the kinetic model for Hg(II) uptake by FeS at pH 8. | 344 |
| Table 13.2 | Binding energies (BE), peak full width at half maximum (FWHM), peak area percentage for Hg 4f _{7/2} XPS spectra of FeS contacted with Hg(II) for various times and for reference materials. | 354 |
| Table 13.3 | Binding energies (BE), peak full width at half maximum (FWHM), peak area percentage for Fe 2p _{3/2} XPS spectra of FeS contacted with Hg(II) | |

| | Page |
|---|------|
| for various times. | 354 |
| Table 13.4 Binding energies (BE), peak full width at half maximum (FWHM), peak area percentage for S 2p XPS spectra of FeS contacted with Hg(II) for various times. | 355 |
| Table 13.5 Binding energies (BE), full width at half maximum (FWHM), and area percentage for peaks in the Fe 2p _{3/2} and S 2p XPS spectra of mackinawite at pH 10.5 _(i) and pH 3.5 _(a.a.t) | 357 |
| Table 13.6 Binding energies (BE), full width at half maximum (FWHM), and area percentage for peaks in the Fe 2p _{3/2} XPS spectra of mackinawite after contact with Hg(II) at (a) pH 10.5 _(i) and (b) pH 3.5 _(a.a.t) | 366 |

1. INTRODUCTION

1.1 Problem Statements and Motivation

Efficient water management at thermo-electric power plants is becoming increasingly important in the U.S. Electric power production is a major user of water in the U.S., accounting for almost 40 % of fresh water withdrawals in 2000 (1). For example, approximately 136,000 million gallons per day (MGD) is used for thermo-electric power generation, which is as high as that used for irrigation (2). Increases in projected demands for electrical power will tend to increase water use in the future. Much of the projected increase in demand is expected in areas that are already facing water shortages, so the problem will be additionally difficult to solve. Furthermore, increased concern for release of toxic compounds is driving more stringent effluent discharge criteria. In particular, new toxicology data has led to increasingly stringent discharge criteria for some compounds.

One important area for improved water management at power plants is that of wastewaters from ash and scrubber ponds. These waters can be contaminated with toxic compounds such as arsenic, selenium and mercury and must be treated before discharge (3). The composition of these waters depends on the fuel composition, presence of control devices for NO_x and SO_x , and other factors related to how the water system is managed. Fly ash is the major sink for arsenic and selenium at a power plant (4), so it is expected to be prevalent in ash pond waters. A lower fraction of mercury is partitioned to fly ash, but it can approach half of the load to the plant (4). Scrubber waters can also carry toxic compounds as well as very high concentrations of calcium and sulfate.

A variety of techniques can be applied to removing arsenic, selenium and mercury from ash and scrubber pond waters. Probably the most commonly applied treatment method is adsorp-

This dissertation follows the style of *Environmental Science and Technology*.

tion onto iron oxy-hydroxides (5, 6), which is sometimes called coprecipitation. This process can remove arsenic, selenium and mercury, but it is limited by two important factors. First, the removal mechanism is primarily one of surface adsorption, so removal of target compounds (As, Hg, Se) can be inhibited by presence of other adsorbates. In particular, the presence of high concentrations of sulfate observed in scrubber waters would substantially reduce removals by adsorption. A second problem with treatment with iron oxy-hydroxides is that the residuals produced by the process are unstable when disposed in landfills. Landfills are typically anoxic and can support chemically reducing environments. Under reducing conditions, the ferric iron in the oxy-hydroxides would be reduced to ferrous iron, thereby destroying the solid-phase that had adsorbed the toxic compounds and releasing them to solution.

An alternative to current technology for removing arsenic, selenium and mercury from ash and scrubber pond waters is to remove them with iron sulfide (FeS) and iron disulfide (FeS₂). Initial removal would be followed by surface reactions that would convert the toxic compounds to stable solid phases. Mixtures of As, Se, and Hg are often found in minerals, which demonstrate their long-term stability in the environment (7-13). Additionally, the specific reactions between the surfaces and the target compounds mean that interference by compounds such as sulfate would be minimized or removed. Therefore, this approach has the potential to simultaneously remove arsenic, selenium, and mercury from ash and scrubber pond waters and produce inherently stable residuals.

Another approach to enhancing removal of arsenic from solution is to apply nanoporous titania adsorbents (NTAs). A new more stringent maximum contaminant level (MCL) for arsenic is 10 ppb (µg/L) and many contaminated sites and approximately 4000 water utilities in the USA are not in compliance with the new MCL and would benefit from novel treatment technology (14). Until now, adsorption technology using conventional adsorbents (e.g., iron-hydroxide,

alumina, activated carbon) has been widely employed due to their safe, easy to set-up and use, relatively cost-effective treatment. However, there are limitations for conventional adsorbents to lower arsenic concentration below the new MCL due to their physical limitations. The development of NTAs is expected to enhance adsorption capacity for arsenic because the NTAs have highly regular mesoporosity with much higher surface areas and surface functional groups that more strongly attract arsenic. Moreover, if they have longer life cycles than other adsorbents or ion exchange resins, their relative cost-effectiveness will be improved.

1.2 Strategic Approaches and Objectives

The overall goal of this study is to evaluate the ability of synthetic nano-structured adsorbents to remove arsenic, selenium, mercury from water while producing stable residuals for ultimate disposal. To achieve this goal, several tasks were conducted to evaluate novel treatment media applied to different target compounds and to investigate their chemical interactions on the surface. All experiments were conducted as part of one of the following tasks.

1.2.1 Task 1: Develop Techniques to Synthesize Nanostructured Adsorbent Media and Characterize Surface Properties

Task 1 developed techniques to synthesize nanostructured adsorbents to removal inorganic compounds (As, Hg, Se) from water. Two types of nanostructured adsorbents were used in this study and they differed in terms of porosity. One type includes nanoporous titania adsorbents (NTAs) and the other consists of iron sulfide/disulfide (FeS and FeS₂). The NTAs having titania sorption sites differed depending on the presence of mesoporous silica molecular sieve (SBA-15). Ti_(x)-SBA-15 contains SBA-15 and mesoporous titania (MT) does not. In addition, effects of reactant (Fe²⁺, Fe³⁺, HS⁻) concentrations, temperature, and presence of nuclei on extent of formation and particle sizes of iron sulfide/disulfides was evaluated. A key focus of

this task was to develop methods to increase yields of nanostructured adsorbents with high surface area that results in high sorption capacities for target compounds. After developing synthesis methods, a series of experiments described in Tasks 2-6 was conducted with three target compounds (As, Hg, Se) to insure that the solids synthesized were able to reduce concentrations of target compounds to acceptable levels and were able to produce stable solid phases, i.e. solids that were able to retain the target compounds for long periods of time. Therefore, successful completion of Task 1 provides a specific procedure that can produce cost-effective synthetic nanostructured adsorbent media at high yield.

1.2.2 Task 2: Characterize Sorption Kinetics of As, Hg, Se Uptake by Nano-Structured Adsorbent Media

Task 2 provided fundamental data to describe sorption kinetics of target compounds by NTAs ($\text{Ti}_{(x)}$ -SBA-15 and MT) and iron sulfide/disulfides (FeS and FeS_2). To predict sorption behavior and sorption rates more precisely and to understand what factors strongly affect sorption kinetics, sorption kinetic model was applied to kinetic experimental data. The important objective of this Task was to provide fundamental information for conducting Tasks 2 and 3. In the case of synthetic iron sulfides contacted with target compounds, specifying the period of reaction time provides information to evaluate the reaction steps (i.e., surface adsorption and surface precipitation).

1.2.3 Task 3: Characterize Sorption of As, Hg, Se on Nanostructured Adsorbent Media

Task 3 characterized the initial adsorption step of target compounds onto nanostructured adsorbents (NTAs and iron sulfides). Removal of arsenic (As(III) , As(V)) by NTAs was evaluated by adsorption equilibrium experiments, which provided information about the

potential applicability to and long-term performance of these materials in adsorptive filtration technology. In the case of iron sulfide/disulfide (FeS and FeS₂), experiments to evaluate removal of As, Hg, Se were conducted in a way that is similar to that used to characterize adsorption equilibrium. However, it is not believed that adsorption was the only important process affecting the behavior of target compounds in these experiments, nor is it believed that true chemical equilibrium was achieved. Characterization of adsorption of As, Hg, Se onto iron sulfides has provided fundamental information to evaluate sorption behavior that occurs prior to surface reactions. A variety of chemical equilibrium models were developed and employed to describe the interactions between target compounds and nanostructured adsorbents during sorption. Then, the best model was selected to guide the later tasks and future development of the sorption process. In addition, this task focused on quantifying the operating factors that affect surface adsorption. Therefore, successful completion of this task provided data needed to understand how target compounds adsorb onto nanostructured adsorbent media and to predict sorption behavior with chemical equilibrium models.

1.2.4 Task 4: Characterize Adsorption Envelope of Arsenic by NTAs as Affected by Solution Composition

Sorption envelopes of arsenic onto NTAs were evaluated over a range of pH and concentrations of competing anions by assuming that adsorption reactions progressed to equilibrium. Other objectives of this study were to understand the sorption trends observed during the experiments and to evaluate how environmental factors affected the adsorption envelopes. Successful completion of this task provided criteria needed to extend experimental results to different conditions.

1.2.5 Task 5: Characterize Reactions of As, Hg, Se on the Surfaces of Iron Sulfides (FeS/FeS₂)

The critical step in proposed study was characterizing surface reactions of target compounds after sorption occurred. Since each target compound (As, Hg, Se) has a specific affinity to iron or sulfur surface sites, characterizing surface reactions has important implications not only for removal from solution but also for stabilization of iron sulfides residuals. The surface reaction between target compounds and iron sulfide/disulfide was characterized by investigating the change of redox states of surface ions, by identifying the differences in redox state and binding partners of elements within the minerals (Fe, S), and by observing the differences in morphology of the surface before and after the surface reactions occur. The objectives of this task were to identify the solid phases (e.g., arsenopyrite (FeAsS) or orpiment (As₂S₃), cinnabar (HgS), ferroselite (FeSe₂)) that form as products of surface reactions. Specifically, this task determined the optimum conditions for the formation of solid phases, including reaction time and relative doses of reagents.

1.2.6 Task 6: Evaluate Stability of Iron Sulfides (FeS/FeS₂) Residuals

The goal of this work was to determine the stability of adsorbent/reactants (FeS₂, FeS) combined with target compounds (As(III), As(V), Se(IV), Se(VI), Hg(II)) and to evaluate the solid phases to better understand the chemical changes that can affect stability. In this context, “stability” is measured by the ability of the solids that have removed target compounds to resist their release back into the aqueous phase. If solids are sufficiently stable, they can be disposed to the environment without concern for subsequent release of and environmental contamination by the target compounds.

1.3 Dissertation Organization

The dissertation is divided into two major parts, according to the type of adsorbents being investigated. The first part deals with sorption behavior of arsenic (As(III), As(V)) on nanostructured titania adsorbents (NTAs). This part includes Sections 3 and 4. Section 3 focuses on surface characterization of synthetic NTAs and equilibrium and kinetic behavior of arsenic (As(III), As(V)) in batch sorption experiments. Two different synthesis methods were applied to synthesize NTAs. One method, called the “incipient wetness method”, was used to incorporate titanium into a mesoporous silica molecular sieve (SBA-15). The other method directly synthesized mesoporous titania, without using a mesoporous silica template. Surface properties of the adsorbents were characterized by spectroscopy as follows: Scanning electron microscopy (SEM) and transmission electron microscopy (TEM) for solids morphology and particle size; X-ray diffraction (XRD) for identity of solids; and Fourier transform infrared (FT-IR) spectroscopy for investigation of changes in the intensities of peaks for silanol (Si-OH) groups with changes in titanium loading ratio. Sorption kinetics for arsenic (As(III, V)) was evaluated as affected by total adsorbate concentration, solids concentration, and initial pH. Equilibrium experiments were conducted to evaluate sorption capacity of $Ti_{(x)}$ -SBA-15 and MT for arsenic (As(III, V)). The final solids concentration was 1 g/L and the initial target compound concentration varied. Experimental data was fitted to sorption equilibrium models (Langmuir and Freundlich).

Section 4 focuses on surface complexation modeling of arsenic adsorption envelopes under various solution compositions. Three factors that can affect sorption behavior were studied: 1) target compounds concentration and 2) solid concentration. In addition, the diffuse double layer model (DLM) was applied as a surface complexation model to correlate experimental results. Calculations needed to apply the DLM were made by chemical equilibrium programs such as FITEQL and MINEQL+.

The second part of the dissertation focuses on sorption, surface reactions, and stability of arsenic (As(III, V)), Hg(II), and selenium (Se(IV, VI)) combined with iron sulfide (FeS, mackinawite) and iron disulfide (FeS₂, pyrite). The results of this research are covered in Sections 5 – 13. In Section 5, batch experiments on selenium (Se(IV, VI)) removal by pyrite were conducted at various contact times (1 day to 30 days). The morphology, topography, and oxidation status of surface species was observed by surface analysis techniques (SEM-EDS, XPS, AFM). The hypothesis that the surface-facilitated redox reactions between Se(IV, VI) and the pyrite surface can lead to formation of low solubility surface precipitates, was demonstrated by interpretation of microscopic and spectroscopic analyses.

As an extension of Section 5, Section 6 describes the macroscopic sorption behavior of mixtures of Se(IV, VI) and pyrite as well as the stability of Se(IV, VI)-contacted pyrites. This Section deals with the effect of time as well as aqueous phase concentration on removals of Se(IV, VI) with or without the presence of sulfate, as a competing ion. Results of these experiments provides a method for determining the fast or slow removal step, which can be the basis for determining the reaction time required to produce stable surface compounds. Stability experiments were conducted by first contacting pyrite with solutions of target compounds and allowing the target compounds to be removed and to react with the solid surface. Then, the solution pH was changed in a series of steps and the concentration of target compound in the aqueous phase measured. The extent of release of target compounds as pH is changed is a measure of the stability of the combination of pyrite and Se(IV, VI). To understand what chemical changes occur when selenium interacts with the surface of pyrite and how those changes affect stability, the solid surfaces were characterized with different techniques, including SEM-EDS, XPS, and AFM.

Sections 7 and 8 are organized similarly to Sections 5 and 6, except that the suspensions

contain mackinawite (FeS). The results of XPS analyses of FeS contacted with Se(IV, VI) and allowed to react for up to 30 days are interpreted with those of macroscopic investigations of removals of selenium on FeS. The hypothesis that Se(IV, VI) is reduced by FeS and subsequently forms less soluble solid phases is supported by the reaction mechanism developed in Sections 5 and 6. The stability of FeS contacted with Se(IV, VI) is evaluated in Section 7.

Sections 9-11 focus on arsenic (As(III,V)) removal by both pyrite and mackinawite. These Sections follow similar patterns of organization to the Sections that described selenium removals by pyrite and mackinawite. Section 9 presents sorption behavior of As(III, V) by pyrite and mackinawite. The chemical interactions between As(III, V) and the solids surface during up to 30 days of contact were investigated by microscopic and spectroscopic analyses, including SEM-EDS, XPS, and AFM. Sections 10 and 11 discuss the kinetics and extent of removal as affected by pH and the presence of a competing ion (sulfate), as well as the stability of As-contacted pyrite and mackinawite.

Sections 12 and 13 focus on removal of mercury(II) by pyrite and mackinawite. Mercury(II) is also expected to form low solubility solid-phases such as HgS or HgS₂. A surface reaction mechanism for Hg is supported by both surface analysis techniques (SEM, XPS, AFM) and macroscopic sorption results. Results of experiments to evaluate the stability of solid-phases containing Hg give additional evidence for formation of less soluble solid phases.

Finally, Section 14 summarizes and draws conclusions based on all of the content of the dissertation.

2. BACKGROUND

2.1 Arsenic

2.1.1 Introduction

Arsenic concentrations in drinking water have been regulated for protection of public health in the U.S. since 1942. The standard of 50 $\mu\text{g/L}$ was the maximum contaminant level (MCL) for total arsenic in drinking water for over 50 years. Epidemiological evidence of arsenic carcinogenicity was taken as evidence that this standard might not be sufficiently protective of human health. The cancer risk from arsenic in drinking water at the 50- $\mu\text{g/L}$ level is estimated to be 200 times the acceptable level of 10^{-4} specified by EPA (15). Therefore, EPA promulgated a new health-based enforceable MCL of 10 $\mu\text{g/L}$ and a non-enforceable maximum contaminant level goal (MCLG) of 0.0 $\mu\text{g/L}$ (16). However, this standard might also need to be revised by regulatory agencies, because significant biological effects of As at less than the current EPA MCL of 10 ppb on the innate immune system has recently been observed in a mouse model of exposure (17). It has also been suggested that those who have a weakened immune system can be easily infected by the H1N1 flu that has recently been found in Mexico (18).

2.1.2 Acid/Base and Redox Chemistry

The two primary oxidation states of arsenic that are of importance in natural waters are the +V oxidation state (arsenate or arsenic acid) and the +III oxidation state (arsenite or arsenious acid) (19, 20). Arsenic acid (As(V)) has pK_a values at 2.20, 6.97 and 11.53 while arsenous acid (As(III)) has pK_a values of 9.22, 12.13, and 13.40 (Figure 2.1). Therefore, at pH 7, As(V) will exist primarily as negatively charged species and As(III) will exist primarily as an uncharged specie. Under oxidizing conditions, arsenate is predicted to be the stable form, while under reducing conditions, arsenite becomes the stable form. At pH 7, H_3AsO_3 and HAsO_4^{2-} will

have equal activities at $pe = 0.22$ (equilibrium data from Vink (1996))(21).

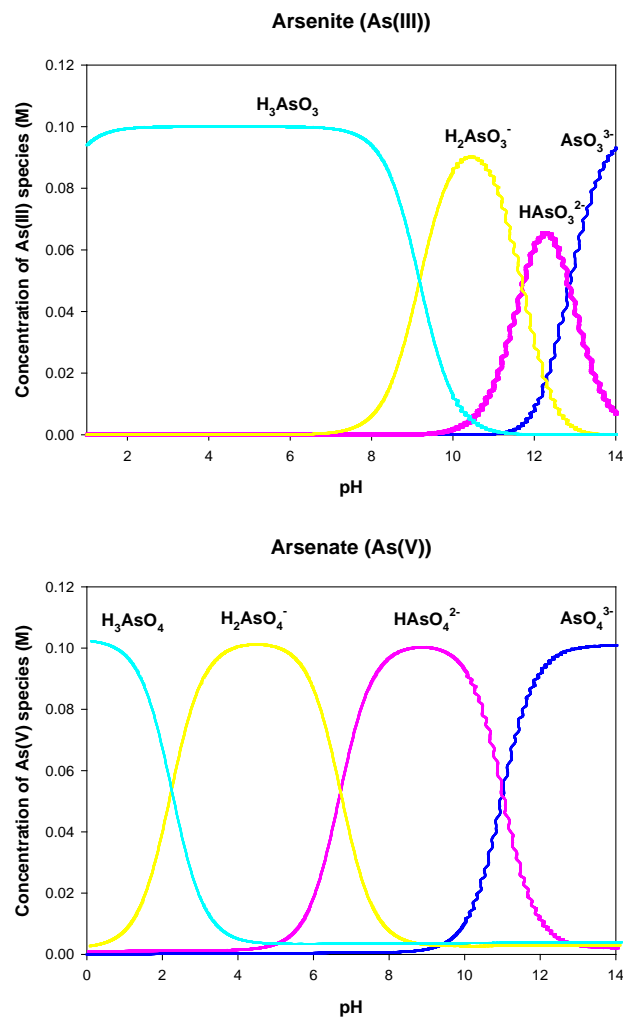


Figure 2.1 Speciation of arsenic (III, V) as a function of pH for $[As]_T=0.1$ M and $I=0.1$ M (as NaCl). Calculations were made by chemical equilibrium program, MINEQL+.

2.1.3 Precipitation of Arsenic Compounds

Arsenic readily precipitates as a sulfide (22) or co-precipitates with metal sulfides (19). The available thermodynamic data indicate that the presence of sulfide should result in the effective precipitation and removal of arsenic. Kim et al. (2000) reported that both As(V) and As(III) are quickly and reductively converted to insoluble arsenic sulfide precipitate when sulfides are present (23). Packed beds of ferrous sulfide and the addition of hydrogen sulfide or

sodium sulfide have been used in removal processes (24, 25).

Blakey (1984) investigated the behavior and attenuation of arsenical waste co-disposed with domestic solid wastes (26). Results of this study indicated that under strongly reduced conditions in the presence of hydrogen sulfide, the iron present in the solution precipitates as iron sulfide. The arsenic present is either co-precipitated with iron sulfide or is reduced to the arsenic sulfide directly, particularly at about pH 7. Attenuation of arsenic by a factor of 10 was obtained. However, under mildly reducing conditions, where hydrogen sulfide is absent, the presence of soluble ferrous iron had little effect on the mobility of the more toxic reduced As(III) ion. A study conducted by Carbonell-Barrachina et al. (1999) to evaluate the effect of redox potential and pH on arsenic chemistry in municipal sewage sludge indicated that upon reduction to $E_h = -250$ mV ($p_e = -4.2$), arsenic solubility was controlled by the formation of insoluble sulfides and as a result, soluble arsenic concentrations dramatically decreased compared to levels measured at $E_h = 0$ mV (27). Arsenic and sulfur concentrations were highly and negatively correlated ($R^2 = 0.76$). Another study by Carbonell-Barrachina et al. (1999) indicated that the concentrations of arsenic remained low and constant under both aerobic and anaerobic conditions in sludge-amended soil after dissolution of Fe and Mn-oxides (28). The As(V) was released into sludge solution, reduced to As(III) and likely precipitates with sulfide. Therefore, an organic amendment rich in sulfur compounds, such as sewage sludge, would drastically reduce the potential risks derived from potential releases of arsenic because its microbial activity would bring about lower redox conditions with the presence of sulfides. In hydrometallurgical processes, the precipitation of an amorphous form of orpiment (As_2S_3 (am)) is used as a method to remove arsenic from waste streams (29).

One of the least soluble arsenic solids is arsenopyrite ($FeAsS$). This is the primary mineral form of arsenic and it is believed to have been formed geologically under conditions of

high temperature and pressure (30). However, arsenopyrite has also been reported to be formed in natural sediments and water treatment sludges under less extreme conditions (31-33). Vlassopoulos et al. (1999) reported that arsenic was immobilized in a tidal marsh groundwater by coprecipitation with iron sulfide and formation of arsenopyrite (31). Rittle (1995) reported formation of arsenopyrite from As(III) in sediment microorganisms in which sulfide was formed by microbial sulfate reduction (32). Heinrich and Eadington (1986) describe a pathway for formation of arsenopyrite at low temperatures by reaction of As(III) and Fe(II) with Sn^{2+} (33). Even if formation of arsenopyrite is difficult, it may be possible to form arsenian pyrite ($\text{Fe}(\text{S},\text{As})_2$) (30), which may approach the low solubility of arsenopyrite.

2.1.4 Sorption of Arsenic

Zouboulis et al. (1993) investigated the application of pyrite as a sorbent for arsenic (34). The pyrite that was used was a byproduct/solid waste from an industrial process and had a median diameter of 11 μm and a specific surface area of 4.7 m^2/g . Removal of As(V) was optimal at pH 3-9, while removal of As(III) was optimal at pH 7-10. Equilibrium was observed to occur within 10 minutes. Using the data presented in that paper, linear partition coefficients can be calculated that are in the range between 100 – 200 L/kg. Farquhar et al. (2002) investigated sorption of arsenic onto ground natural pyrite (size < 32 μm) and FeS (mackinawite) (35). The data presented could be used to calculate linear sorption coefficients of 32 and 41 L/kg for As(III) and As(V), respectively, on pyrite and 1340 and 420 L/kg for As(III) and As(V), respectively, on FeS. Differences in partition coefficients with Zouboulis et al. (1993) could be due to differences in pyrite size (34). Others have reported successful removal of arsenic by adsorption/reaction with FeS (36, 37). Pyrite (FeS_2) is a mineral that often contains impurities such as arsenic in nature (38). The fact that these minerals have existed for geologic time periods attests to their stability.

Although an adsorption mechanism can be reasonably used to describe the mechanism of arsenic removal from solution, it does not completely describe the interaction of arsenic with iron sulfide and disulfides. Bostick et al. (2004) have shown that substantial arsenic removal occurs in the first 30 minutes when placed in contact with FeS and FeS₂, but that soluble arsenic concentrations continue to decrease for as long as 100 hours (39). This is much longer than would be needed for equilibration with the surface of a non-porous solid phase. They interpret the slow removal as the result of surface reactions that form a series of more insoluble solid phases that continue to remove arsenic to lower levels. Surface analysis by XANES showed that the initial solid phase was similar to arsenopyrite, which is a very insoluble solid phase and a major form of arsenic in nature (39). Therefore, the interaction of arsenic with iron sulfide and disulfide should be considered an adsorption/reaction process, not solely an adsorption process. Wolthers et al. (2005) exhibited that As(III) sorption to disordered mackinawite is explained by a Freundlich isotherm and is not strongly pH-dependent (40). The X-ray absorption spectroscopy (XAS) study showed that both As(III) and As(V) form an outer-sphere complex at the surface of mackinawite (40). This result is in accordance with those reported by Farquhar et al. (2002) and indicates that both As(III) and As(V) at pH 5.5-6.5 coordinate to four oxygen atoms (As-O: 1.69-1.76 Å) in the first coordination shell, and they coordinate with two sulfur (~3.1 Å) and three iron atoms (3.4-3.5 Å) in the second shell. This suggests interactions via outer-sphere complexation, because the distances for the As-S and As-Fe bonds are longer than that for As-O. (35). However, this result was obtained under experimental conditions of low arsenic concentration and pH in the range 5.5 – 6.5. However, when pH was lowered to pH 4.0, arsenic was coprecipitated with mackinawite. The formation of precipitates is affected by arsenic concentration as well as pH. For example, a poorly crystalline arsenic sulfide (As₂S₃) was formed at high As(III) and As(V) concentrations and low pH (35). A similar result was obtained

when pyrite reacted with arsenic at acidic pH and As_2S_3 and As_4S_4 -like precipitates were observed to form (41). Gallegos et al. (2008) studied the removal of As(III) using nanoparticulate mackinawite with the help of surface analysis techniques, including XAS and XRD (42). They found that sorption mechanisms of As(III) are very different under different solution conditions, such as initial As(III) concentration or pH. For instance, when mackinawite was reacted with 5×10^{-4} M As(III) at basic pH (5, 7, 9), a realgar-like solid phase was identified and showed that As(III) was being reduced. This identification was made by XRD and XAS, which indicated arsenic coordination environments in which arsenic was bound to sulfur (As-S: ~ 2.26 Å) and to arsenic (As-As: ~ 2.54 Å). At lower As(III) concentration (5×10^{-5} M), the realgar-like solid phase was observed below pH 5, while only adsorption of As(III) without the occurrence of reduction-mediated precipitation was observed at basic pH. Therefore, it was demonstrated that whether As(III) sorbed to mackinawite or precipitated via surface reactions is strongly affected by environmental conditions. This could be the reason why discrepant results are frequently reported in the literature, even when conditions are similar.

2.1.5 Release of Arsenic from Arsenic-Bearing Wastes

A major source of arsenic-contaminated wastes will be residuals from treatment processes that use iron oxy-hydroxides. Robins (1992) questioned the long term stability of the (oxy)hydroxide-arsenic solid material (43). He has demonstrated that arsenic removal is via adsorption and not by formation of precipitated arsenic-containing solid phase. Therefore, ripening of the (oxy)hydroxide solids after disposal could result in reduced surface area and arsenic release. Arsenic could also be released under moderately reducing environments where Fe(III) in the (oxy)hydroxides could be reduced to soluble Fe(II), releasing the sorbed arsenic. Moderately reducing conditions are found in most landfills due to high concentrations of dissolved organic carbon and bacteria, which often results in reduction of As(V) and release of

As(III) (26, 44, 45).

Barnett (1992) reported that the behavior of arsenic in engineered systems such as landfills and water distribution systems is probably influenced by many factors operative in natural systems (46). Conceptually, the mobility of arsenic below a landfill would be controlled by the redox condition of the groundwater in a manner analogous to natural waters (44). Arsenic would be expected to be immobile in the oxic zone because of adsorption onto ferric (oxy)hydroxides. However, it could become mobile upon the onset of moderately reducing conditions and then become immobile as more strongly reducing conditions developed and sulfide solid phases are generated. In laboratory leaching tests with concentrated arsenic wastes (concentrations from <1 to 121 g/wet kg), arsenic was most mobile at neutral pH under mildly reducing conditions and least mobile under neutral pH and strongly reducing conditions, possibly the result of sulfide precipitation (26).

Under reducing conditions such as found in landfills, Fe(III) is converted to Fe(II), which destroys the binding sites for arsenic. Furthermore, As(V) is reduced to As(III), which is less strongly bound to the remaining iron hydroxide sites. Thus, the solubility and mobility of arsenic is significantly increased. White and Sevee (1999) reported that landfills in southern New Hampshire contribute to the mobilization of arsenic by generating soluble total organic carbon, which creates and sustains the reductive dissolution mechanism responsible for the release of arsenic to the groundwater (47). Welch (1999) indicated that synthetic organic compounds can lead to reductive dissolution of iron oxide and arsenic release (48). Laboratory experiments by Ahmann (1997) showed that significant arsenic mobilization from contaminated sediments by microbial arsenic reduction (45). Moore et al. (1998) reported that total interstitial arsenic in sediments increased from less than 20 mg/kg of soil in the oxidized zone to > 550 mg/kg in the reduced zone, indicative of the dissolution of iron and manganese (oxy)hydroxides (49).

Laboratory experiments and modeling studies conducted by Meng et al. (2001) on a surface water treatment sludge from a California surface water treatment plant indicated that soluble arsenic increased from less than 5 $\mu\text{g/L}$ to as high as 700 $\mu\text{g/L}$ when the sludge was aged for a few weeks in closed containers (50). This release was caused by reduction of ferric (oxy)hydroxide to ferrous iron and As(V) to As(III). Experimental results and thermodynamic models showed that the effects of redox conditions on arsenic mobility can be divided into three zones: (a) an adsorption zone at oxidizing conditions ($p_e > 0$; $E_h > 0$ mV), which is characterized by strong adsorption of As(V) on ferric (oxy)hydroxide; (b) a mobilization zone at moderately reducing conditions ($-4.0 < p_e < 0$; -240 mV $< E_h < 0$ mV), where arsenic is released because of reduction of ferric (oxy)hydroxide to ferrous iron and As(V) to As(III); and (c) a reductive fixation zone at strongly reducing conditions ($p_e < -4.0$; $E_h < -240$ mV), where arsenic is immobilized by reaction with sulfides and other reduced solid phases.

Leachate from a municipal landfill in Saco, Maine resulted in a plume of anoxic groundwater containing high concentrations of As(III), ferrous iron, manganese, and dissolved organic carbon. The arsenic appears to have been released by reductive dissolution of arsenic-containing iron oxides in the landfill by dissolved organic carbon (51). The presence in landfill leachate of inorganic solutes such as phosphate, sulfates, and lower pH may also cause arsenic mobilization. The anions can directly compete for surface binding sites and may also influence the surface charge of adsorbents. This would control the degree to which arsenic remains associated with the (oxy)hydroxide surface or enters the leachate (52).

In summary, arsenic can be released from arsenic-contaminated wastes after it is disposed if moderately reducing conditions occur. It would be difficult to insure that such conditions do not occur in a landfill. Therefore, residuals may show low leachability when measured by a test such as TCLP that is conducted under aerobic/oxidizing conditions, but high

leachability in moderately reducing landfills. This means that many residuals may require further treatment before disposal in order to immobilize arsenic and prevent its release to the environment. Stabilization process should be designed so that arsenic is strongly immobilized under conditions in disposal zone, which in the case of landfills, will be reducing.

2.2 Selenium

2.2.1 Introduction

Selenium is known to be an essential nutritional element to animals and humans, although it is not essential for plant growth (53). According to the level of Se in vegetation, however, it can be toxic to animals (53). For instance, leaching of Se-rich soils by agricultural drainage in the San Joaquin valley was found to result in extremely harmful levels, with concentrations in drainage water approaching 500 µg/L, which is high enough to cause carcinogenic and teratogenic effects (54). In addition, chronic exposure to low levels of Se can cause developmental abnormalities and reproductive disorders. The difference in Se concentrations between levels that cause nutrient deficiency and toxicity is smaller than that noted for other USEPA priority or non-priority pollutant (55, 56).

Selenium is released from natural and anthropogenic sources and coal-fired power stations are one of the largest anthropogenic sources. Selenium is present in coal at small concentrations of several parts per million and most of that is associated with organic matter, but 5-10 % appears to be associated with pyrite or other mineral sulfides (3, 57). Selenium in all phases can be released to the environment if not managed continuously. Recently, selenium (^{79}Se , $t_{1/2}=1.0\times 10^6$ years) has been found in radioactive wastes resulting from processing spent fuel and in releases from operating nuclear reactors and fuel reprocessing plants.

2.2.2 Aquatic Chemistry of Selenium

Selenium is an analogue of sulfur, so they are similar in aquatic chemistry (58). The primary selenium species in oxidized water are selenate ($\text{Se}^{\text{VI}}\text{O}_4^{2-}$), selenite ($\text{Se}^{\text{IV}}\text{O}_3^{2-}$) and their protonated forms. Figure 2.2 shows that the pK_a values for selenic acid (H_2SeO_4) are <1 and 1.7 , and those for selenious acid (H_2SeO_3) are 2.75 and 8.5 (58). Therefore, at pH 7, the primary species will be SeO_4^{2-} and HSeO_3^- . Under more reducing conditions, zero-valent selenium and hydrogen selenide (H_2Se) are found. The pK_a values for hydrogen selenide are 3.89 and 15 , so HSe^- will be the primary Se(-II) species observed in the pH range of most natural waters. Se(IV) and Se(VI) are most mobile, while Se(0) and Se(-II) are relatively immobile because of the low solubility of their solid phases. Se(IV) is more toxic than other forms and that is why Se(IV) removal is extensively studied (59). In addition, zero-valent selenium and HSe^- in subsurface environments can form less soluble solid phases such as metal sulfide ores that include Fe, Cu, and Pb (60-62).

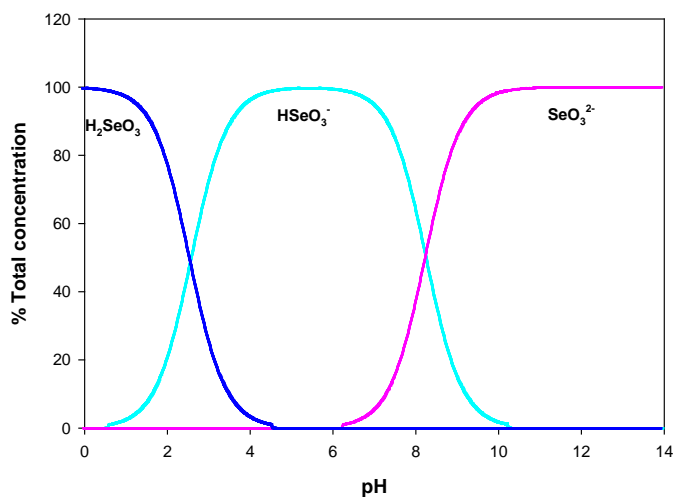


Figure 2.2 Speciation of selenium (IV, VI) as a function of pH for $[\text{Se}]_{\text{T}}=0.1\text{M}$ and $\text{I}=0.1\text{M}$ as NaCl. Calculations are made by MINEQL+(63).

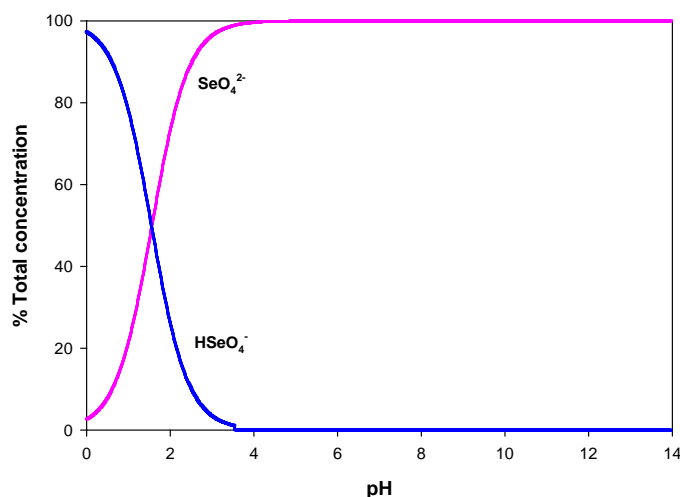


Figure 2.2 Continued.

2.2.3 Sorption of Selenium

The lowest solubility solid forms of selenium are elemental selenium (Se(0)) and metal selenides. FeSe has been proposed as a controlling solid in reduced sediments contaminated with selenium (64). The soluble concentration of Se in equilibrium with FeSe at pH 7 can be calculated as being less than 1 $\mu\text{g/L}$ using the chemical equilibrium program VMINTEQ (65). The stability of metal selenides is seen in the fact that selenium is often found in nature as the selenide substituting for sulfide in metal sulfide solids (9, 66). Interaction of oxidized forms of selenium with metal sulfide solids has also been reported (9). Transport of selenate is strongly affected by its adsorption onto FeS and subsequent reaction. Recent studies demonstrate that selenite was reduced to insoluble Se(0) after contact with Fe(II)-bearing minerals such as mackinawite and magnetite, finally forming two iron selenides (Fe_7Se_8 and FeSe) (67). Adsorption was reported to be relatively independent of pH and stronger on FeS than on FeS_2 . In addition, a kinetically limited redox reaction of Se(IV) is observed with FeS and FeS_2 , in which Se(IV) is reduced to Se(0) by nanoparticulate FeS within one day, while it takes a week with

pyrite (67). XANES analysis indicated that selenate reacted on the surface to form more reduced species, but identification of Se(-II) was not possible due to limitations of the analytical technique.

Removal of selenites and selenates from water and wastewater is most commonly achieved by adsorption onto iron oxy-hydroxides. This technology has been adopted as the Best Demonstrated Available Technology (BDAT) for selenium treatment by the EPA (68). This application of iron oxy-hydroxide adsorption has the same limitations as when applied to removal of arsenic. Removal of selenium will be inhibited by competing ions such as sulfate and the residuals will not be stable under the anoxic conditions found in landfills.

2.3 Mercury

2.3.1 Introduction

Mercury has been considered as a global contaminant of significant concern for centuries due to its high toxicity and bioaccumulation via the aquatic food chain, which seriously affects natural ecosystems and the health of humans. Historically, the first outbreak of mercury-related disaster occurred in the mid 1950s at Minamata, which is a city located in Japan on the coast of the Yatsushiro Sea. More than a few hundred people died as a result of dumping 27 tons of mercury compounds into Minamata Bay (69). Exposure to high levels of mercury can cause inhibition of enzyme activity, cell damage, impairment of pulmonary function and kidney performance, chest pain, and damage of the central nerve system (70, 71). Also, trace quantities of mercury may accumulate in the biosphere, so that many ecologists and health authorities have paid considerable attention to this problem. Mercury contamination is from anthropogenic and natural sources including chloro-alkali plants, mining and smelting activities, coal-fired power plants, electrical and electronic manufacturing plants, and a variety of incinerator facilities (72, 73). Among them, coal-fired power plants and incinerator facilities are the major source,

constituting 77 % of anthropogenic Hg emissions in the United States and emitting 120 ton of Hg per year (74). Removal of inorganic Hg from emissions is a crucial process because in aquatic ecosystem, most of inorganic Hg is transformed to methylmercury (MeHg) that leads to buildup of highly elevated concentration in aquatic fish and wildlife (75).

2.3.2 Aquatic Chemistry of Mercury

Inorganic mercury exists in the aqueous environment primarily as divalent mercury (Hg(II)), however, the zero-valent state can also exist under some conditions (76, 77). However, formation of Hg(0) is slow without biological action and it is expected to volatilize if it is produced (76, 77). Under reducing conditions, the primary soluble complexes are those formed with sulfide ($\text{Hg}(\text{HS})_2$, HgS_2H , HgS_2^{2-}) (Figure 2.3) and insoluble solids are formed depending on various solution conditions (e.g., pH, $[\text{Hg}]/[\text{sulfide}]$). Under oxic conditions, on the other hand, mercury tends to complex with hydroxide (Hg^{2+} , $\text{Hg}(\text{OH})^+$, $\text{Hg}(\text{OH})_{2(\text{aq})}$), chloride ($\text{HgClOH}_{(\text{aq})}$, $\text{HgCl}_{2(\text{aq})}$, HgCl_3^-), and sulfate (HgSO_4) (Figure 2.4) (76, 78, 79). In particular, in oxic seawater, mercury-chloro complexes (HgCl_4^{2-} , HgCl^- , HgCl_2^0 , HgCl^+) are dominant, although other mercury-halide complexes are present, because chloride ion concentration is much higher than the concentrations of other halide ions (80). In such an environment, the concentrations of mercury-hydroxide complexes are not appreciable, because the pH of sea water is about 8. Many earlier studies reported that the maximum adsorption of Hg(II) by a variety of adsorbents (SiO_2 , bentonite, goethite) was observed below pH 5, but in the presence of Cl^- ion, the extent of Hg(II) adsorption is considerably reduced because a larger fraction of mercury is present as HgCl_2 (Figure 2.4b) (81).

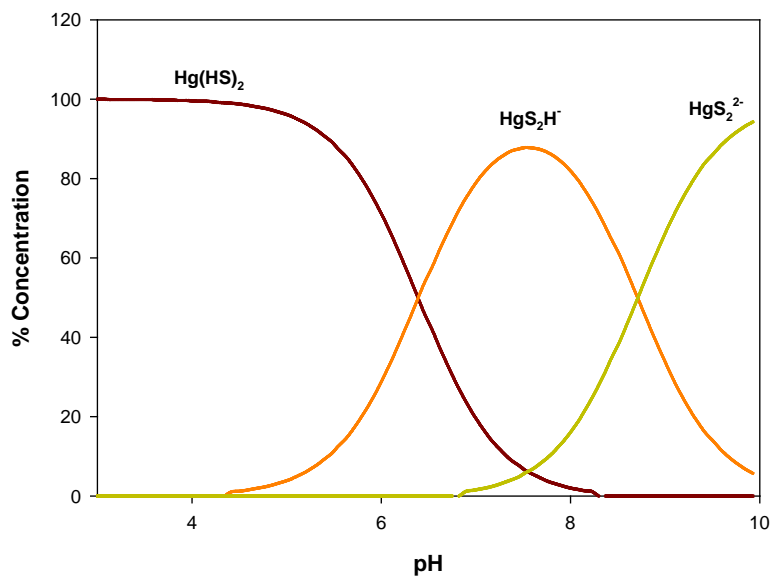


Figure 2.3 Speciation of mercury as a function of pH for $[\text{Hg}]_{\text{T}} = 5 \times 10^{-4} \text{ M}$ and $[\text{HS}^{-}]_{\text{T}} = 0.1 \text{ M}$. Calculations were made by MINEQL+ without considering precipitates.

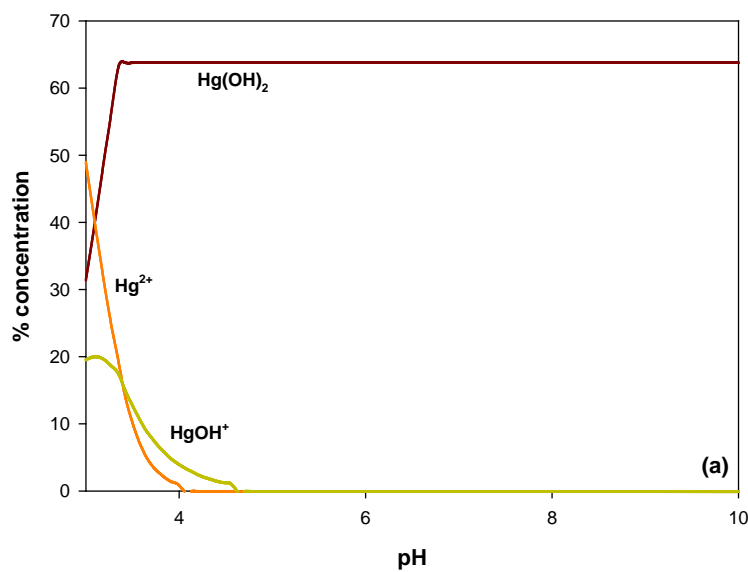


Figure 2.4 Aqueous speciation of mercury ($[\text{Hg}]_{\text{T}} = 5 \times 10^{-4} \text{ M}$) in (a) the ligand-free system and in the presence of (b) $[\text{Cl}^{-}]_{\text{T}} = 0.1 \text{ M}$ and (c) $[\text{SO}_4^{2-}]_{\text{T}} = 0.1 \text{ M}$. Calculations were made by MINEQL+ without considering precipitates.

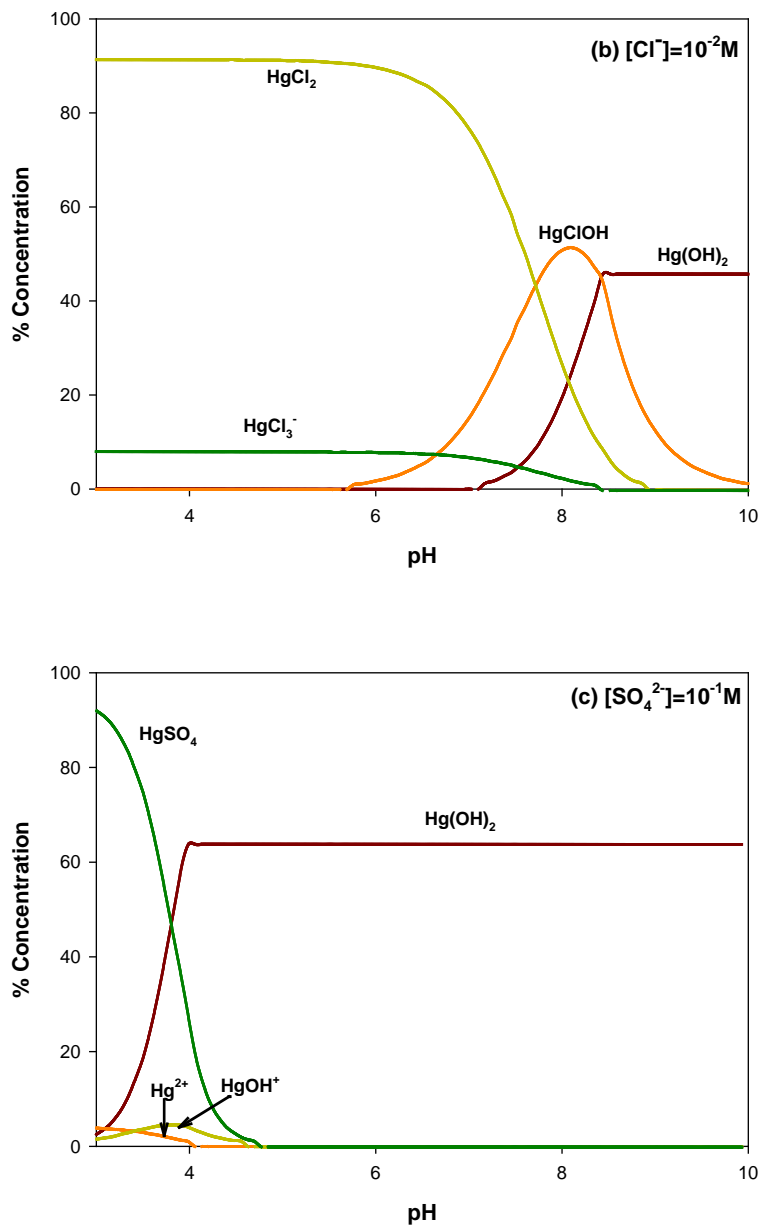


Figure 2.4 Continued.

2.3.3 Precipitation of Mercury

Since Hg(II) is a “soft” Lewis acid that is preferentially bonded with “soft” Lewis bases such as those containing a thiol functional group, the use of sulfur-containing chemicals has been widely used to remove mercury (82, 83). Thus, mercury forms a very insoluble solid with sulfide (76, 77, 84, 85). This has been the basis for the most common treatment process for removing mercury from industrial wastewaters such as those at chloro-alkali plants (86). It can typically achieve effluent concentrations in the range between 10 and 100 $\mu\text{g/L}$, but there are problems associated with controlling the sulfide dose. If excess sulfide is added, then soluble Hg-S complexes are formed and the effluent concentrations of soluble mercury increase (86). In general, the solubility of Hg-sulfide solid phases depends on pH and sulfide concentration. At low pH and low sulfide concentration, formation of insoluble mercuric sulfide solid phase (HgS) is preferred, whereas soluble Hg-S complexes occurs at high pH and high sulfide concentrations (79).

2.3.4 Sorption of Mercury

A way of avoiding the problems that occur in precipitation processes that use soluble reagents is to dose with large particles of iron sulfide, which gradually dissolves to produce the needed sulfide (76). If smaller particles are added, the removal mechanism will include sorption and surface reaction. Nano-scale iron sulfide particles have been produced microbially or abiotically and applied to removal of mercury (37, 70, 87, 88). Particle sizes around 2-5 nm and specific surface areas of 280-500 m^2/g have been reported (88). The biogenic FeS particles can adsorb and react with mercury resulting in metal loadings as high as 0.66 g Hg/g FeS (0.29 mole/mole) (87). Evidence for the reaction phase is found in the decrease in soluble mercury concentration with time (1 to 24 hr) that becomes more pronounced as the surface concentration is increased (87). Other metals besides Hg were shown to be removed by the biogenic FeS (87,

88). Chemical synthesis of nano-sized FeS has also been reported (89, 90). Others have also reported that iron sulfides are good reagents for removing mercury from solution (10-12, 70, 84, 91-93). For example, X-ray photoelectron spectroscopy (XPS) studies on interactions between Hg(II) and pyrite demonstrated that high sorption is caused by the formation of weakly or strongly bound species including Hg-chloro and Hg-sulfhydryl complexes rather than HgS(s) (11, 92-94). Bower et al (2008) conducted experiments for Hg(II) removal by pyrite in batch and column systems (11). XPS analyses indicated that during aging over two weeks at low pH, an ordered monolayer of mono-dentate Hg-Cl complexes was formed on the pyrite surface. In studies with columns packed with the mixtures of pyrite and pure quartz sand, a great retardation of Hg(II) was observed, although the system was exposed to oxygen (11). Liu et al. (2008) investigated interactions between aqueous Hg(II) and FeS in batch sorption experiments, and found that the maximum removal capacity at lower pH was approximately 0.75 mol Hg(II)/mol FeS. They also used X-ray power diffraction (XRPD) to identify the major products as metacinnabar, cinnabar, and mercury iron sulfide (10).

2.4 Nanostructured Adsorbents Media

2.4.1 Mackinawite

Mackinawite (FeS) is an ubiquitous mineral in anoxic sediments where sulfate-reducing bacteria produce sulfides that subsequently react with ferrous iron. Amorphous or a weakly crystalline tetragonal mackinawite ($\text{FeS}_{0.995-1.023}$) is known as metastable iron monosulfide and after it is precipitated, it is rapidly altered to thermodynamically stable pyrite (FeS_2). Greigite (Fe_3S_4) is an intermediate solid phase that can be formed if mackinawite is exposed to air (95). Among iron sulfides, amorphous mackinawite is known to be highly reactive with toxic metals. Figure 2.5 shows the primary pathways for formation of sedimentary iron sulfides (96). Due to its high level of reactivity (large surface area) and common occurrence in estuarine or near-shore

marine environments, mackinawite is a topic of research in many areas in environmental science and engineering.

Since most transition metals have a strong affinity for surface-bound sulfur species, elevated concentrations of various transition metals are usually found in the pyritized anoxic sediments where they tend to coprecipitate or to be incorporated with intermediates of pyrite such as mackinawite (40, 97-100). Morse (1993) indicated that mackinawite can contain up to 4.29 wt% Cu, 3.75 wt% Co, and 4.09 wt% Ni (98). In particular, many sorption experiments using mackinawite have been conducted and various surface analysis techniques have been used to characterize the chemical interactions between the mackinawite surface and toxic heavy metals, such as Cu, Cd, Co, Ni, Mn, and Au (101-103). This research shows that retention of toxic metals by mackinawite is caused by adsorption and various surface reactions, resulting in formation of discrete precipitates (CdS), mixtures of co-precipitates (CuFeS₂), depending on solution conditions (103). In addition, mackinawite is widely used to retain redox sensitive radio-nuclides (Np, U, Tc) (104-108) or reduce toxic chlorinated chemicals (PCE, TCE, CCl₄) (109-118).

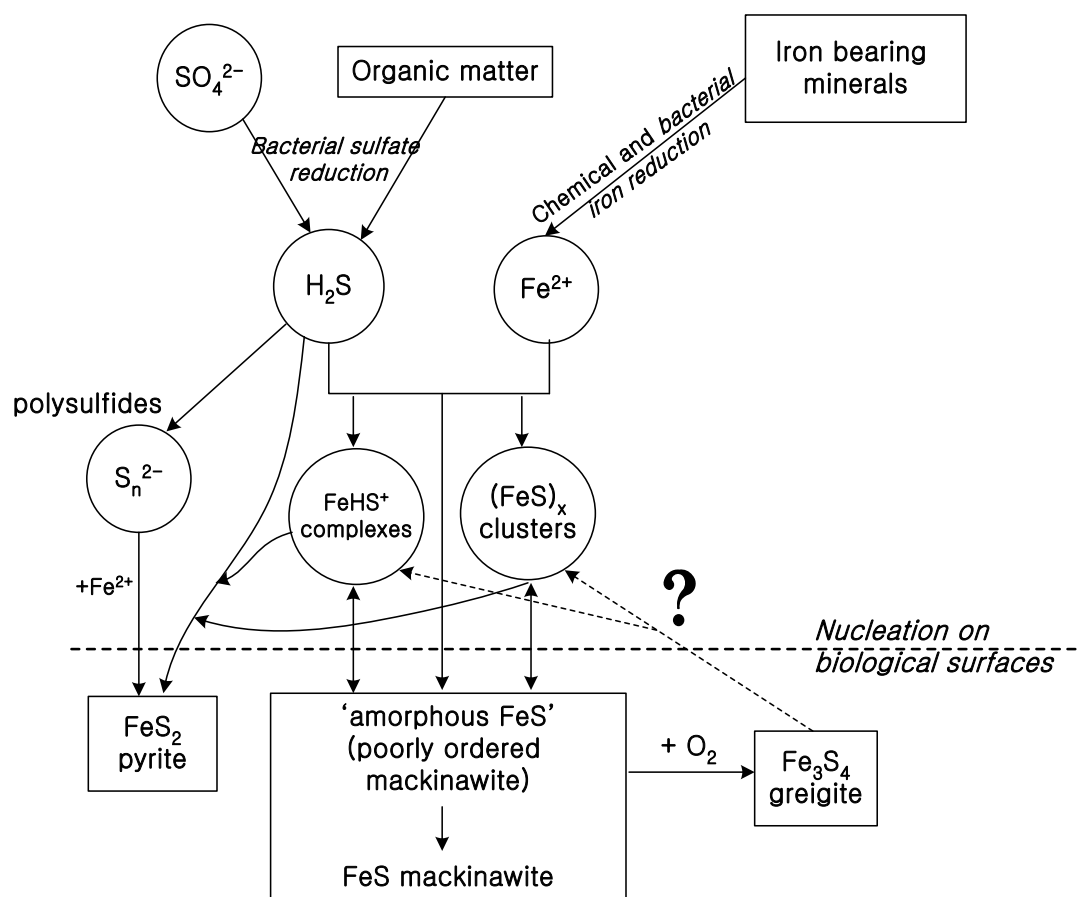
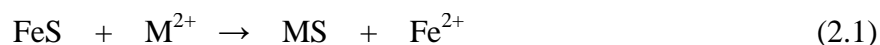


Figure 2.5 The primary pathways for formation of sedimentary iron sulfides. Circles and rectangles denote dissolved and solid species, respectively. Text in italics refers to processes that involve the activity of bacteria. (Used with permission from Pósfai and Dunin-Borkowski (96)).

In particular, removal of cationic metals by mackinawite can be explained by two reaction mechanisms. One is to form a less soluble metal sulfide (MS) than mackinawite by replacing Fe atoms with divalent metals or incorporating them into the lattice of mackinawite ((M,Fe)S). For instance, the displacement reaction of mackinawite in the presence of a divalent metal appears to occur at a 1:1 molar ratio.



where M^{2+} represents a divalent metal, such as Co, Cd, Mn, Ni, Zn, Cu, Pb, Hg, and MS

represents a less soluble metal sulfide than mackinawite. However, formation of precipitates or co-precipitates occurs only if the solubility of the metal sulfide being formed is lower than that of mackinawite and, as conditions become more reducing, the precipitates that are formed may be pyritized (119, 120). In contrast, if more divalent metals are present that have sulfides that are more soluble than mackinawite, those metals preferentially adsorb on mackinawite via electrostatic-derived attraction between divalent metals and mackinawite surface. When mackinawite is dispersed in a solution with pH higher than pH_{zpc} , the surface of mackinawite is expected to be negatively charged, so that positively charged divalent metals can adsorb on the mackinawite surface. Although the reactions discussed above are expected to occur generally, inconsistent results are sometimes reported to occur even when equivalent experimental conditions are used. For example, adsorption could act as the main removal mechanism in a system where replacement or precipitation would be expected to occur, because the metal-FeS system is highly complicated and very susceptible to reaction conditions (120).

A few studies have demonstrated that replacement and precipitation reactions of metals with mackinawite were completed over time scale of minutes to hours (119). Table 2.1 summarizes the solubility products (K_{sp}) of various metal sulfides. The insolubility of these metal sulfides is in order: $\text{HgS} \gg \text{PbS} > \text{CuS} > \text{CdS} > \text{ZnS} > \text{NiS} > \text{mackinawite}$.

Table 2.1 Comparison of solubility constants of selected metal sulfides (121, 122).

| Metal sulfides | Solubility Product (K_{sp}) |
|------------------|--|
| FeS, mackinawite | 2.3×10^{-4} |
| NiS, millerite | 5.9×10^{-10} |
| ZnS, sphalerite | 1.6×10^{-11} |
| CdS, greenockite | 7.9×10^{-15} |
| CuS, covellite | 6.3×10^{-23} |
| PbS, galena | 8.4×10^{-28} |
| HgS, cinnabar | 3.0×10^{-53} |

So far, there are three methods for synthesis of mackinawite in batch systems at ambient temperature. All methods use aqueous sulfide solutions that react with different iron(II) donors (metallic iron, ferrous iron, reduced iron(III) oxy-hydroxides via sulfate reducing bacteria). Gallegos (2007) cited that once mackinawite is synthesized, different compositions of mackinawite could occur by competition between H_2S and HS^- to react with ferrous iron, depending on pH. Wolthers (2003) described this in more detail and provided the following reaction equations (123).



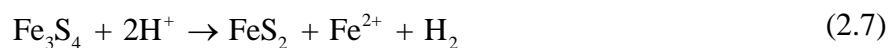
Reaction (2.2) is dominant at $\text{pH} < 7$ and reaction (2.3) is dominant at $\text{pH} > 7$.

2.4.2 Pyrite

Pyrite (FeS_2) is also formed in reducing subsurface environments where sufficient reduced sulfur species and iron(II) species are available, and it is formed through intermediates of iron sulfide. Pyrite is mostly observed in terrestrial or marine sediments and it is the most abundant type of iron sulfide on the Earth's surface (124, 125). Major factors that govern the rates of pyrite formation are carbon-to-sulfur ratio, availability of iron, redox potential, and acidity (126). For example, in the submarine environments where lack of organic carbon leads to low amounts of sulfate reducing bacteria, a slow rate of pyrite formation results in framboidal morphology (126). In contrast, salt marsh environments (e.g., the Atlantic coast of North America and northern Europe) have sufficient numbers of where sulfate reducing bacteria and other iron(II) species to form pyrite rapidly, resulting in small single pyrite crystals (126-128). Moreover, if intermediate sulfur species (e.g., polysulfides, polythionates, thiosulfate) are abundantly present, pyrite or marcasite is formed rapidly (124).

Pyrite has an octahedral molecular arrangement and can form various crystalline shapes from cubical to polyhedral (126). For example, in cubic pyrite, iron is coordinated to six S₂(-II) sulfur dianions in a slightly disordered octahedron (123). The sizes of pyrite particles vary from 400 nm to 5 μm (126). The presence of impurities in pyrite can cause it to deviate from typical stoichiometry of FeS₂ and this results in it exhibiting semiconducting behavior of *n*- or *p*-type (123).

In general, it is accepted that pyrite is formed either through FeS₂ nucleation at high temperature (129) or through replacement of an FeS precursor at low temperature environments (124). In addition, many studies suggested other possible pathways for FeS₂ formation via sulfidation of iron(III) oxy-hydroxides. In this process, the ferric iron undergoes reduction and dissolution in the presence of intermediate sulfur species (H₂S, HS⁻), followed by precipitation of an iron monosulfide precursor that subsequently proceeds to form more sulfide-rich iron disulfides such as pyrite or marcasite (124). For more details, conversion of iron monosulfide to pyrite by intermediate sulfur species can be described as occurring by three primary pathways that have been summarized by Pósfai and Dunin-Borkowski (96), based on other studies (130-133). The relevant reactions are:



In the reactions (2.4) and (2.5), the FeS precursor is oxidized by a polysulfide species or H₂S to form pyrite. Pyrite can also be formed by reaction of FeS with oxygen to form the intermediate solid phase greigite (Fe₃S₄) (Equation (2.6)), that is converted to pyrite by loss of iron and

formation of hydrogen (Equation (2.7)). The reactions described above are schematically represented in Figure 2.5. In an experimental batch system, Wei and Osseo-Asare (1996) demonstrated that pyrite crystals as small as 30 nm could be produced by reaction of FeCl_3 and NaHS (134). These smaller particles only formed at lower concentrations of FeCl_3 , so the concentration of pyrite that could be produced was limited.

Pyrite is associated with several environmental issues. One association is as a source of environmental pollution and the other is as a scavenger to remove or immobilize toxic contaminants. When pyrite is exposed to air or decomposed at coal or metal mining sites, high concentrations of protons are produced and thus acidify mine waters, forming acid mine drainage (AMD)) that deteriorates the surrounding environments (125). Simultaneously, trace metals and metalloids (As, Cd, Pb, Hg, etc.) that are associated with pyrite also can be released to surface waters and soils (135, 136). In addition, since pyrite has a relatively high electrical conductivity, it can catalyze oxidation of other sulfide minerals (PbS , CuFeS_2) by oxygen in air, resulting in release of metals into water (137). However, pyrite has been used as a beneficial reactant or scavenger to degrade toxic organic compounds (138-141), immobilize inorganic compounds (39, 92, 93, 137, 142, 143), and confine radionuclides (e.g., Sr(II), Eu(III)) (144).

2.4.3 Mesoporous Materials

Since the early 1990s, development of the M41S family of mesoporous silica molecular sieves (an Exxon/Mobil catalyst support) has stimulated the development of nanoscience and nanotechnology. It has opened potential applications to heterogeneous catalysis, sensors, biotechnology, selective adsorbents, medicine, ion exchangers and environmental remediation agents, because of the remarkable features of these materials that provide highly ordered hexagonal pore structures of a few nanometers in diameter, with wall thicknesses of about 1.2-1.4 nm and specific surface areas of about $1000 \text{ m}^2/\text{g}$ (145, 146). The M41S family of

mesoporous silica is different from zeolites, which have a regular hexagonal tubular channel framework that is not intersected (147). Furthermore, a remarkable advance in synthesis techniques for mesoporous materials has been achieved with the invention of a procedure to produce hydrothermally stable SBA-15 silica molecular sieve using a triblock copolymer surfactant as template. This material has uniform hexagonal channels ranging from 5 to 30 nm (148). Figure 2.6 shows schematic diagram for synthesis procedure of SBA-15.

According to IUPAC (International Union of Pure and Applied Chemistry) classification, porous materials are grouped into three classes depending on their pore diameters as follows: (1) microporous (< 2 nm), (2) mesoporous (2 to 50 nm), and (3) macroporous (> 50 nm). Among them, mesoporous materials are considered to be useful for hosts, supports, catalysts, or separation media, whereas microporous materials may have limited access to active sites inside pores for macromolecules or metal compounds due to pore blocking. Also, macroporous materials may be inappropriate for use as catalysts or sorbents due to their irregular pore size distribution (149, 150).

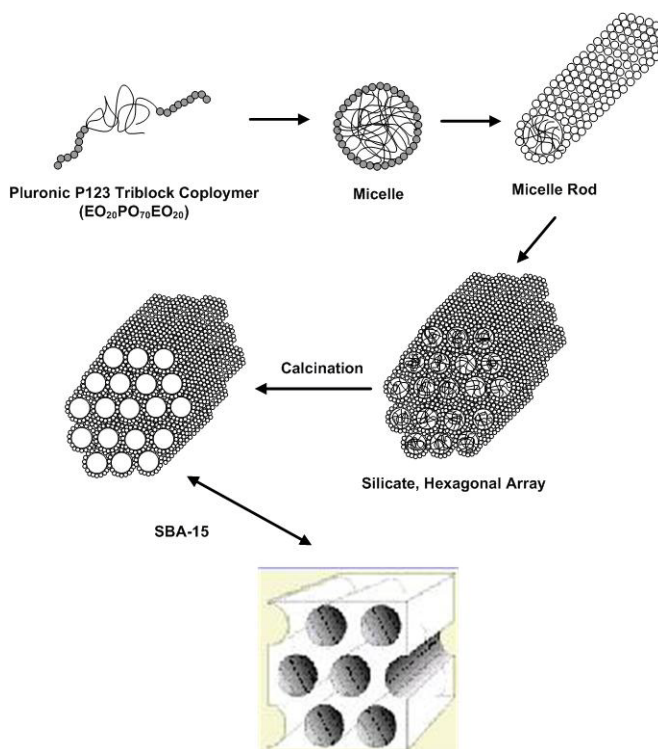


Figure 2.6 Schematic diagram of the preparation of mesoporous silica molecular sieve SBA-15.

Much work has been done to explore various structures of mesoporous silica using a variety of self-assembled, molecular arrays of surfactants as templates. For instance, hexagonal MCM-41, cubic MCM-48, lamellar MCM-50, SBA-series, FSM, HMS, and MSU-series are those that are most frequently reported in the literature. In general, mesoporous silica is prepared by two synthesis methods. One is an electrostatic assembly method and the other is a neutral templating route (151). The M41S family was synthesized by electrostatic co-assembly. For example, hexagonal MCM-41 is synthesized by the direct co-condensation (S^+I) and nucleation of the anionic inorganic precursors (I) with a cationic ammonium surfactant head group (S^+) under basic medium (152). In the case of MCM-48, the $S^+X^-I^+$ pathway is used in which another counter ion (X^-) that could be a halide such as fluoride, chloride, or bromide, mediates the interaction between the protonated surfactant (S^+) and the protonated inorganic silica (I^+), under

acidic medium (152). Other electrostatic interaction assemblies such as S^+T^- , $S^-M^+T^-$ (where $X^- = Cl^-$ or Br^- and $M^+ = Na^+$ or K^+) are also used. Another synthesis route called the neutral templating path is based on hydrogen bonding and self assembly between a neutral surfactant (S^0) as template and neutral inorganic precursors (I^0). For example, the HMS and MSU-series mesostructures are synthesized through the neutral (S^0I^0) route and their surface properties are different from those prepared by electrostatic interaction pathways. Figure 2.7 indicates different types of interaction pathways between the surfactant and the inorganic framework (153). The advantages of using non-ionic surfactants (triblock copolymers, P123 or F127) over ionic surfactants as templates are the increase in wall thickness and pore diameter, leading to improved hydrothermal stability (154). Finally, the mesoporous materials with high surface area and pore volume are obtained by eliminating organic moieties of the surfactant with thermal treatment or solvent extraction (151).

Furthermore, mesoporous silicas are functionalized with organic molecules such as organic silanes to increase the ability to control the molecular recognition properties of the porous network, so that the range of their applications to various uses for industry are expanded (154). As for functionality of mesoporous silica, two different methods, are usually employed (152). One is called grafting or post synthesis and it is based on covalent bonding between organosilane species (organotrialkoxysilanes or organotrichlorosilanes) and surface silanol group (Si-OH groups). An alternative method of surface functionality is to co-condensate functional organosilanes ($(R'O)_3Si-R$) with silica precursor (tetraethyl orthosilicate (TEOS)) via the direct assembly pathway.

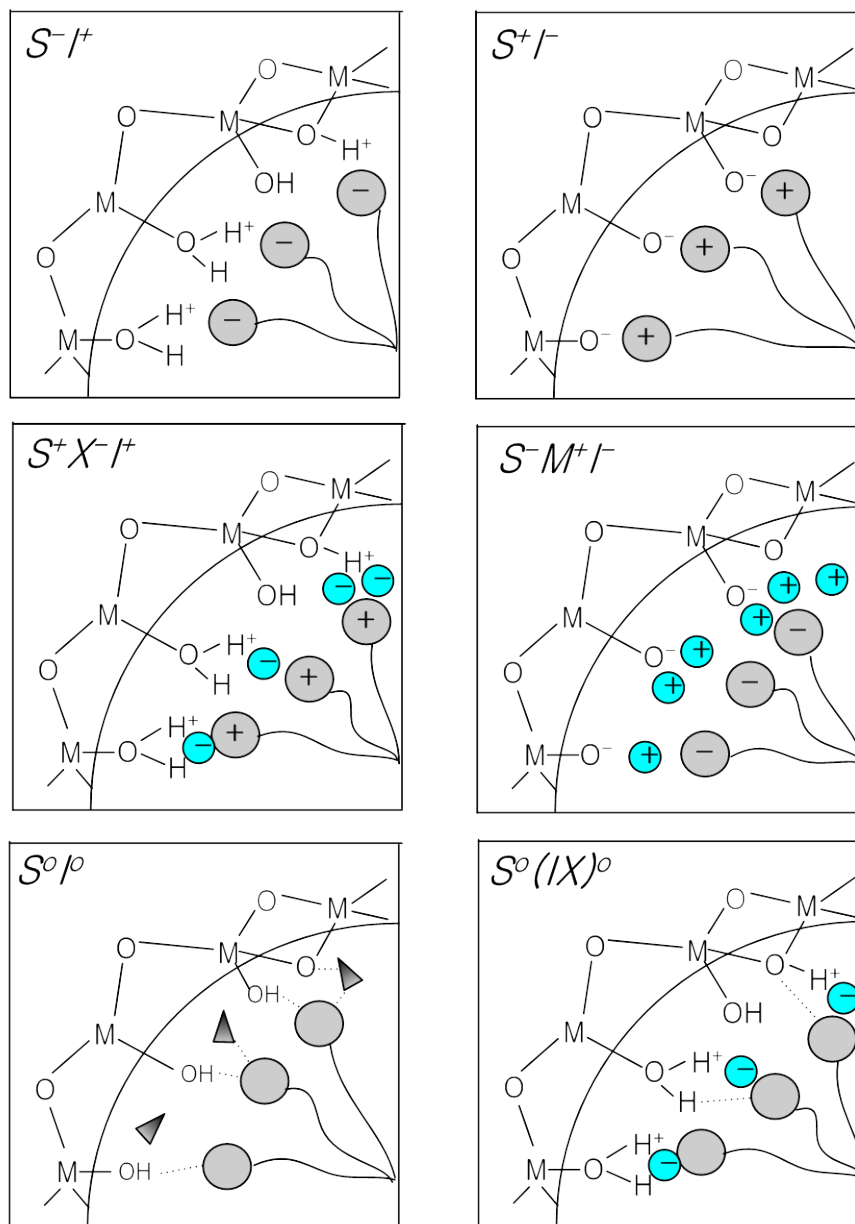


Figure 2.7 Schematic representation of the different types of interaction pathways between the surfactant and the inorganic framework: S=surfactant molecules, I=inorganic framework, M^+ and X^- =corresponding counterions, triangle=solvent molecules, dashed lines=H-bonding interactions (153).

2.4.3.1 Nanoporous Titania Adsorbents (NTAs)

Titanium dioxide (TiO_2) is a widely used material in a photocatalysis-based advanced oxidation process (AOP) that can degrade a variety of organic chemicals and produce hydrogen by water photolysis. It is also an adsorbent that can remove inorganic contaminants. Moreover, titanium dioxide is considered to be a promising, sustainable photocatalyst because of its strong redox power and high photocorrosion resistance (151). Many attempts have been made recently to enhance the physical/chemical properties of titanium dioxide by employing mesoporous synthesis techniques that were first invented by scientists at Mobil Oil Research and Development in 1992 (145). Since then, a variety of templating surfactants and oligomers have been explored under wide range of synthesis conditions, so that impressive progress has been achieved in the areas of catalysis, adsorption, separation processes, and environmental clean-up (155).

Nanoporous titania adsorbents (NTAs) made by new synthesis technology used for mesoporous materials are expected to have improved performance because of higher numbers of reactive sites, greater surface area, faster mass transfer, and more effective functionalization or surface modification in the nano-sized pore wall structures (156). Many attempts to incorporate titanium into mesoporous frameworks have been made. For example, titania-grafted MCM-41, FSM-16, and SBA-15 were synthesized with grafting techniques. Mesoporous silica MCM-41 and titanium silicate-1 (TS-1), which is a titanium-substituted microporous aluminophosphates, were synthesized via direct assembly (157-162). Specifically, titanium-substituted SBA-15 could act as a selective oxidation catalyst for large molecules (e.g., toluene or 1-butane) while other Ti-substituted mesoporous materials are limited in their ability to catalyze oxidation of large substrates due to smaller pore sizes (163). The challenge in the synthesis of Ti-substituted mesoporous materials is to avoid the formation of anatase (TiO_2), because maintaining high

content of titanium in the framework is important to having an effective catalyst. However, it could be beneficial for removal of toxic metals, because anatase-type TiO_2 exhibits high sorption capacity (164-167).

Current research in the area of the synthesis of nanostructured adsorbents has focused on incorporation of titanium dioxide into the framework of mesoporous silica molecular sieve (SBA-15) and direct synthesis of mesoporous titania using phosphoric acid medium. Figure 2.8 represents the synthesized SBA-15, Ti-SBA-15, and mesoporous titania (MT).

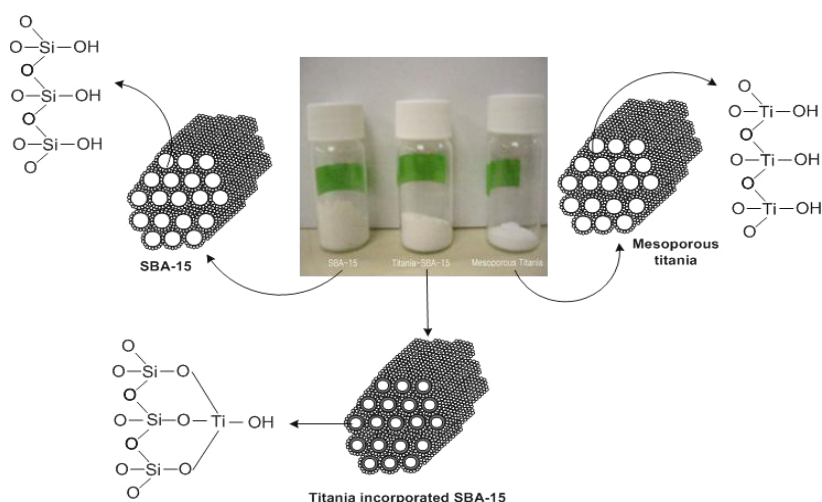


Figure 2.8 Schematic representation of the chemical structure of synthesized SBA-15, $\text{Ti}_{(25)}$ -SBA-15, and MT.

2.4.3.2 Environmental Applications

Mesoporous materials recently have attracted a great deal of attention in environmental applications. They have unique physical and chemical properties, such as a high surface-to-volume ratio that provides a much higher number of reactive sites and higher interfacial reactivity or affinity for toxic heavy metals (146). In addition, they are readily functionalized with metal-chelating groups to attract toxic pollutants such as As, Hg, and Pb that are monitored

by EPA (168, 169). In the case of functionalized mesoporous materials, a variety of chelating ligands that contain thiol, amine, and imidazol groups are grafted to the surface of mesoporous materials. Moreover, their highly regular pore structures overcome physical limitations of conventional materials (e.g., activated carbon, zeolites, clays and silica) and enable metal ions in water to access easily grafted ligand sites (169, 170). For example, sulfur-containing functional groups (benzoylthiourea, thiol, 2-mercaptothiazoline) (171-174) are “soft” Lewis acids and can be grafted on the surface to remove “soft” Lewis bases such as Hg, Pb or Cd, because of the highly affinities between them, while Cu is effectively removed by an amine group (175).

Recently, titanium-substituted or grafted mesoporous materials have been widely used in environmental remediation. Examples are removal of toxic metals by adsorption and the photocatalytic degradation of organic chlorinated chemicals, which is effective because of the semiconductive nature of titania and the photoactivity of its anatase crystal phase (176). One of the biggest problems caused by the photocatalytic activity of TiO_2 is the rapid recombination of photogenerated electrons (e^-) and holes (h^+), because this process limits redox reactions with adsorbed substrates. Like non-porous titanium dioxide, a variety of transition metals are doped on the surface of mesoporous TiO_2 to enhance photocatalytic activity by intercepting photogenerated electrons (e^-). Other studies have reported that control of particle size around 10 nm can lower the surface e^-/h^+ recombination rate and thermal treatment of the surface can also improve photocatalytic activity (151, 177, 178).

Since mesoporous titania materials are ultra-fine powders, there is a potential problem in needing to recover mesoporous powders after separating metal ions from water (169). To overcome this limitation, functionalized mesoporous materials are supported by magnetic materials (magnetite, Fe_3O_4) so that spent adsorbents can be effectively separated from multiphase suspension for safe disposal, regeneration, or recycle (179).

3. ADSORPTION OF ARSENIC(III) AND ARSENIC(V) TO NANOPOROUS TITANIA ADSORBENTS (NTAs): SYNTHESIS, KINETICS, EQUILIBRIUM

Arsenic contamination in groundwater is of major concern to many water treatment facilities in the world. Various treatment technologies have been applied to remove arsenic from drinking water. Among them, adsorption processes are often considered to be most effective forms of treatment for As(V), but they can be limited in their ability to remove As(III). To enhance removal efficiency of adsorption process for As(III) as well as As(V), this study has focused on developing two new adsorbents. One is a highly ordered mesoporous silica solids (SBA-15) that can incorporate reactive titania sorption sites ($\text{Ti}_{(x)}$ -SBA-15), and the other is mesoporous titania (MT). XRD results showed that both $\text{Ti}_{(25)}$ -SBA-15 and MT had surface properties like that of anatase (TiO_2). From nitrogen adsorption /desorption tests, mesoporosity of these solids were observed to show hysteresis loops, which is representative of a Type IV isotherm. However, TEM images showed that SBA-15 and $\text{Ti}_{(25)}$ -SBA-15 have highly ordered hexagonal mesoporosity and titania nanostructured mesopores. However, MT has disordered wormhole-like mesopores that are caused by interparticle porosity. Based on q_{max} ($\mu\text{mol As/g}$) in the Langmuir isotherm, $\text{Ti}_{(25)}$ -SBA-15 had a greater sorption capacity for As(III) than did $\text{Ti}_{(15,35)}$ -SBA-15. It was also observed by FT-IR analysis that the peak intensity of the silanol (Si-OH) peak at 960 cm^{-1} was stronger for $\text{Ti}_{(25)}$ -SBA-15. This indicates that $\text{Ti}_{(25)}$ -SBA-15 has not exceeded its capacity to incorporate Ti. The rates of arsenic uptake were very fast and followed a bi-phasic sorption pattern, where sorption was fast for the first 10 minutes, and then slowed and was almost completed within 200 minutes of contact. The Langmuir isotherm more accurately fitted experimental sorption data than did the Freundlich model. The order of maximum As(III) sorption capacity was $\text{MT (162 } \mu\text{mol/g)} > \text{Ti}_{(25)}\text{-SBA-15 (87 } \mu\text{mol/g)} > \text{Ti}_{(35)}\text{-SBA-15 (76 } \mu\text{mol/g)} > \text{Ti}_{(15)}\text{-SBA-15 (60 } \mu\text{mol/g)}$. The order of sorption capacity for As(V) was MT (pH 9.5,

285 $\mu\text{mol/g}$) > MT (pH 7, 162 $\mu\text{mol/g}$) > $\text{Ti}_{(25)}$ -SBA-15 (pH 4, 121 $\mu\text{mol/g}$) > $\text{Ti}_{(25)}$ -SBA-15 (pH 7, 87 $\mu\text{mol/g}$) > MT (pH 4, 66 $\mu\text{mol/g}$) > $\text{Ti}_{(25)}$ -SBA-15 (pH 9.5, 60 $\mu\text{mol/g}$). Distinct sorption maxima for As(III) removal were observed between pH 8 and pH 11 for MT and between pH 4 and pH 7 for $\text{Ti}_{(25)}$ -SBA-15. The amount of As(V) adsorbed generally decreased as pH increased.

3.1 Introduction

Arsenic contamination in groundwater is a serious threat to human health because of its toxicity. Arsenic contamination is found in many countries and has been caused by use of arsenical pesticides, activities related to mining, and natural geologic weathering process (180). In the US, arsenic has been ranked as the contaminant that poses the greatest risk to human health, based on its frequency of occurrence at NPL sites, toxicity, and potential for human exposure (181). In 2006, EPA has promulgated a new health-based enforceable maximum contaminant level (MCL) of 10 ppb, resulting in an increase of the number of groundwater sites where the contamination exceeds the new MCL (181). Therefore, enhanced arsenic removal technologies are needed to meet these more stringent standards for drinking water and to meet related standards for wastewater effluents.

Arsenite (As(III)) and arsenate (As(V)) are the oxidation states of arsenic that are generally found in subsurface environments. The distribution between different species of each valence state depends primarily on pH and redox potential. In reduced environments in the typical environmental pH range, nonionic arsenous acid (H_3AsO_3) is the primary species of arsenic (182). In oxidized environments, on the other hand, two ionic arsenate species (H_2AsO_4^- or HAsO_4^{2-}) exist, depending on the pH. Specifically, arsenite is more mobile, more toxic, and more difficult to remove due to its electro-neutrality.

The commonly applied processes for arsenic removal are chemical precipitation, co-precipitation, reverse osmosis, ion exchange, and oxidative filtration (182). Among them,

adsorption is considered to be the most promising process, because of its safety, ease of handling and set-up, high removal efficiency with low cost, and potential for regeneration of materials (183). Despite their wide availability, adsorption process may not be able to decrease As(III) concentrations to acceptable levels because of the physical limitations of the adsorbents, although they are able to lower As(V) concentration to acceptable levels. Traditional adsorbents have a relatively low density of surface sites that have an affinity for As(III), which leads to low removal efficiency. Also, their irregular physical structure makes it difficult for arsenic to easily access internal sorption sites.

To overcome these disadvantages, this study will synthesize nanoporous titania adsorbents (NTAs) that have higher surface area, a more highly ordered structural framework, larger pore volume and higher concentration of sorption sites in order to improve adsorption processes for removal of arsenic from water. Hence, the development of these NTAs will be expected to contribute to meeting the needs for improving POE (point of entry)/POU (point of use) devices for arsenic removal because the national drinking water advisory council (NDWAC) recommends that the EPA continue to undertake and support research that will identify affordable POE/POU devices (184). Therefore, the purpose of this study is to develop highly ordered NTAs for removing both As(III) and As(V) from water to low concentrations. Two types of NTAs were produced and characterized. The characteristics of these NTAs for sorption of As(III) and As(V) were evaluated by kinetic and equilibrium tests.

3.2 Materials and Methods

3.2.1 Synthesis of Nanoporous Titania Adsorbents (NTAs)

Two types of NTAs, $\text{Ti}_{(x)}$ -SBA-15 and mesoporous titania (MT), were used in this study. They have similar titania sorption sites, but differ in that $\text{Ti}_{(x)}$ -SBA-15 contains has as its base the silica molecular sieve (SBA-15) and MT does not. SBA-15 was synthesized by modifying the

procedure described by Zhao et al. (148). A portion (4 g) of Pluronic P123 triblock copolymer (poly(ethylene oxide)-poly(propylene oxide)-poly(ethylene oxide), $\text{EO}_{20}\text{PO}_{70}\text{EO}_{20}$, Aldrich) was dissolved in 2 M HCl solution and mixed for 30 minutes at room temperature. Then, 9 mL of tetraethyl orthosilicate (TEOS) were added and the mixture stirred using a rotary mixer for 20 hours at 45 °C. The resulting gel was allowed to age for 48 hours at 80 °C. The solid product was then filtered from the mixture with a 0.45 μm filter, washed with distilled water, and dried at room temperature. Finally, the solid was calcined at 550 °C for 6 hours to remove the polymer. Titanium was grafted on SBA-15 by generally following the incipient impregnation method (157). First, 1 g of SBA-15 was pretreated at 120 °C for 3 hours to remove adsorbed water. The pretreated SBA-15 was dispersed in 100 mL of anhydrous solvent (i.e., ethanol, Aldrich 99.8 %) and then the appropriate amount of titanium isopropoxide ($\text{Ti}(\text{OPr})_4$, Aldrich, 97 %) was slowly added to achieve the desired loading of titanium. The mixture was stirred for 24 hours, followed by filtration and washing with ethanol. Then, the resulting solids were dried at 90 °C for 3 hours and finally calcined in a furnace at 550 °C for 6 hours. The NTAs produced were identified as “ $\text{Ti}_{(x)}$ -SBA-15”, where the subscript x stands for the weight ratio of Ti to SBA-15.

The MT adsorbent was prepared with the procedure described by Huang et al (185). A portion (6.65 mL) of titanium (IV) butoxide was added to ethanol as an anhydrous solvent with a weight ratio of 1/7 and then the system was vigorously stirred. After 30 min, 0.96 mL of 0.28 M phosphoric acid was added and stirred for 3 hours. Then, 72.4 mL of distilled water was added, the mixture was continuously stirred for 2 hours, and then vaporized at 80 °C in an evaporator. The resulting solids were washed with ethanol, dried at 80 °C for 6 hours, and calcined at 550 °C for 6 hours.

3.2.2 Adsorption Experiments

Kinetic experiments for uptake of As(III) and As(V) were performed using a solids concentration of 1 g/L at pH 4, 7, and 9.5 in a solution with NaCl as background electrolyte at a concentration resulting in an ionic strength of 0.01 M. The suspension was mixed for 2 hours and then that amount of arsenic stock solution was added in order to achieve an initial arsenic concentration of 13.3 μM . The desired initial pH was adjusted by adding 0.5 M HCl or 0.5 M NaOH. The reaction vessel was mixed by an orbital shaker at 200 rpm to promote arsenic uptake. At specified sampling times, approximately 10 mL of solid suspension was filtered by cellulose nitrate membrane filter (Whatman[®]) with a pore size of 0.2 μm . Approximately 12 samples were taken over the time period of 5 min to 1 day. All filtered samples were placed into an anaerobic chamber to avoid arsenic oxidation or pH change until atomic absorption spectroscopy (AAS) analysis.

To separate kinetic effects (how rapidly q increases) from equilibrium effects (how high q becomes after a sufficiently long time), the general adsorption kinetic model (the Lagergren's equation) was suggested by

$$\frac{dq}{dt} = k(q_e - q) \quad (3.1)$$

where q ($\mu\text{mol/g}$) is the amount adsorbed at specified time, t (min) and q_e is the value of q that occurs when equilibrium is reached, and k (min^{-1}) is the rate constant for adsorption, respectively. When this kinetic model is fitted to the data, most of data is overestimated, because the experimental data show a rapid rate initially, that gradually declines. The kinetic model described by Equation 3.1 is unable to fit such biphasic behavior. Therefore, an improved model is needed to better describe the physical reality, which is that adsorption is rapid initially, because the adsorbate can adsorb to surfaces at or near the external surface of the adsorbent. As

time proceeds, those sites can fill and adsorbate needs to diffuse into the solid to find an open site and the diffusion process is slower. Alternatively, the slower adsorption kinetics could be due to surface reactions of the adsorbate that gradually provide more room for additional adsorbate to be adsorbed. Thus, an improved kinetic model was developed that assumes two types of surfaces (fast-reacting sites and slow-reacting sites) and it is described by Equations 3.2 and 3.3.

$$\frac{dq_f}{dt} = k_f (q_{f,\max} - q_f) \quad (3.2)$$

$$\frac{dq_s}{dt} = k_s (q_{s,\max} - q_s) \quad (3.3)$$

where q_f , q_s , k_f , k_s , $q_{f,\max}$, $q_{s,\max}$ indicate amount of adsorbate adsorbed, adsorption rate coefficients, maximum amount of adsorbate adsorbed on fast-reacting sites and slow-reacting sites, respectively. The total amount adsorbed is the sum of the amount adsorbed on fast-reacting sites and on slowly reacting sites ($q=q_f + q_s$). All coefficients were obtained by nonlinear regression using MATLAB[®] with its embedded functions “nlinfit and ode23s”. This approach chooses parameters to minimize the sum of squared residuals (SSR). However, a non-linear regression routine would have a difficult time searching for coefficients for both the slow and fast sites, because the structures of the models are the same and they differ only in the values of the coefficients. Therefore, a sequential approach was used in which values for “slow” coefficients were determined and then they were used in a regression to find the “fast” coefficients. This process continues until a satisfactory fit is obtained. The fitness of model to experimental data was calculated by a goodness of fit parameter (GFP) defined by Equation.3.4.

$$GFP = \frac{\sqrt{SSR/(n-2)}}{\bar{q}} \quad (3.4)$$

where SSR is sum of squared residuals, n is the number of data points, \bar{q} is average value of the amount of As adsorbed per amount of NTA. Small values of GFP represent better fits of the model to the data.

Equilibrium experiments were conducted to evaluate the sorption capacity of each adsorbent for As(III) and As(V). To start each equilibrium test, 10 mL of a 2-g/L adsorbent suspension was added to 20-mL reaction vessels and then 10 mL of a mixture of de-ionized water and arsenic stock solution (200 ppm) was added to reach a solid concentration of 1 g/L and specified initial arsenic concentration. Immediately, the desired pH was adjusted using 0.5 HCl or 0.5 M NaOH. The reaction vessels were mixed by a reciprocal shaker at 200 rpm. After 24 hours of reaction, all samples were filtered using cellulose nitrate membrane filter (Whatman®) with pore size of 0.2 μm . All filtered samples were placed into an anaerobic chamber to avoid arsenic oxidation or pH change until atomic absorption spectroscopy (AAS) analysis. In order to describe arsenic removal onto solids, two equilibrium isotherms were applied to the experimental data. One is the Langmuir model, which can be represented by

$$q_e = \frac{q_{\max} b C_e}{1 + b C_e} \quad (3.5)$$

where q_e is the equilibrium concentration of target compound on the solid ($\mu\text{mol/g}$), q_{\max} is maximum equilibrium concentration of target compound on the solid (i.e., maximum sorption capacity, $\mu\text{mol/g}$), b is the Langmuir isotherm parameter ($\text{L}/\mu\text{mol}$). The other model is the Freundlich isotherm.

$$q_e = k_f C_e^{1/n} \quad (3.6)$$

where k_f ($\mu\text{mol}^{1-1/n} \cdot \text{L}^{1/n}/\text{g}$) and n are parameters in the Freundlich isotherm.

3.2.3 Spectroscopic Analyses

X-ray diffractograms were collected using a Rigaku automated X-ray diffractometer using $\text{CuK}\alpha$ radiation (40 kV, 20 mA) with a resolution of 0.02° and a 3-s step time over the range $0.5^\circ < 2\theta < 10^\circ$. For wide angle XRD patterns, the data were collected from 6° to 60° with a 0.05° step size and 3-s step time. To characterize the porosity of NTAs, nitrogen adsorption experiments were performed on a Micrometrics ASAP 2010 micropore system using approximately 0.1 g of sample. The samples were degassed under vacuum at room temperature for 2 hours, then at 100°C for 4 hours, and then at 300°C overnight prior to analysis. The surface area was calculated by the BET method. The micropore and mesopore volumes were determined using the alpha s-method (186, 187). The mesopore size distributions were calculated from the adsorption branch of the isotherm using the BJH method with a modified equation for the statistical film thickness (188, 189). To investigate the morphology of NTAs, transmission electron microscopy (TEM) was performed using a JEOL 2010 microscope with a lanthanum hexaboride filament and an excitation voltage of 200 kV. The secondary images of scanning electron microscope (SEM) were also acquired by a JEOL 6400 Scanning Microscope equipped with energy dispersive spectrometer (EDS) to analyze surface morphology and chemical composition. Fourier transform infrared (FTIR) spectra were measured using the KBr wafer technique. Samples of 1 g were dried and KBr was mixed with 0.02 g portions of the dried sample. Appropriate amounts of the prepared samples were moved to the sample chamber and their FTIR peaks were recorded in transmission mode using a Perkin Elmer 2000 FTIR spectrophotometer. A total 64 scans were collected with a triglycine sulfate (TGS) detector at a resolution of 1 cm^{-1} .

3.2.4 Measurements of Arsenic Concentrations

Arsenic was analyzed with a model Solar M6 atomic absorption spectrometer equipped with a model V90 continuous hydride generator (Thermo Elemental). The procedure for measuring total arsenic (As(III) + As(V)) was based on Standard Method 3114C, which is a continuous hydride generation/atomic absorption spectrometer (HGAAS) method (190). Total arsenic is determined by mixing a sample flow of 7 mL/min with an equal flow of strong acid (6 M HCl) and a 3.5 mL/min flow of sodium borohydride. With these flows and pH conditions, both As(III) and As(V) can be reduced by borohydride to arsine gas (191). The arsine is transferred by argon gas with a 250 mL/min flow to the flame AA, where its absorbance is determined and used to calculate the arsenic concentration using a standard calibration curve.

3.3 Results and Discussion

3.3.1 Surface Characterization of NTAs

Figure 3.1 shows the low-angle XRD patterns for four NTAs. All samples of $\text{Ti}_{(x)}$ -SBA-15 have three peaks at around 1.0° , 1.65° and 1.9° , corresponding to reflections of (100), (110), and (200) planes of a 2D hexagonal mesoporous structure. Specifically, the reflections regarding the (100) plane at 1.0° were shown to be very high for both MT and $\text{Ti}_{(x)}$ -SBA-15, indicating that the NTAs have highly ordered features (157). These results also indicate that the incorporation of titanium did not rupture the mesoporous structure of SBA-15, regardless of titanium content. However, MT does not show reflections at (110) and (200), revealing that the highly ordered structure of MT is not related to a hexagonal mesophase.

Figures 3.2(a) and 3.2(b) show the wide-angle XRD pattern of NTAs. Comparison of the measured d -spacings of peaks shown in Figure 3.2(a) with the values in the JCPDS card (i.e., 3.516, 1.892, 2.378, 1.700, 1.666, and 1.480 nm) indicates that they are the same as those for

anatase, which is a crystalline form of TiO_2 . Figure 3.2(b) shows that the XRD patterns of SBA-15 and titanium-incorporated SBA-15 are very similar to those reported by other studies, indicating that the broad XRD reflection peak at 23° is caused by the very small size of the solid (192, 193). Also, Figure 3.2(b) shows that the highest peak for $\text{Ti}_{(25)}$ -SBA-15 is closest to 2θ equal to 25° and that peaks for $\text{Ti}_{(15,35)}$ -SBA-15 are also near 2θ equal to 25° . This is the location of a major peak for anatase. In contrast, rutile, which is another form of TiO_2 , has its highest peak at 2θ equal to about 54° or 56° . Therefore, $\text{Ti}_{(25)}$ -SBA-15 contains components with properties that are similar to those of anatase. For this reason, $\text{Ti}_{(25)}$ -SBA-15 was chosen from all $\text{Ti}_{(x)}$ -SBA-15 for additional experiments to determine its ability to remove arsenic.

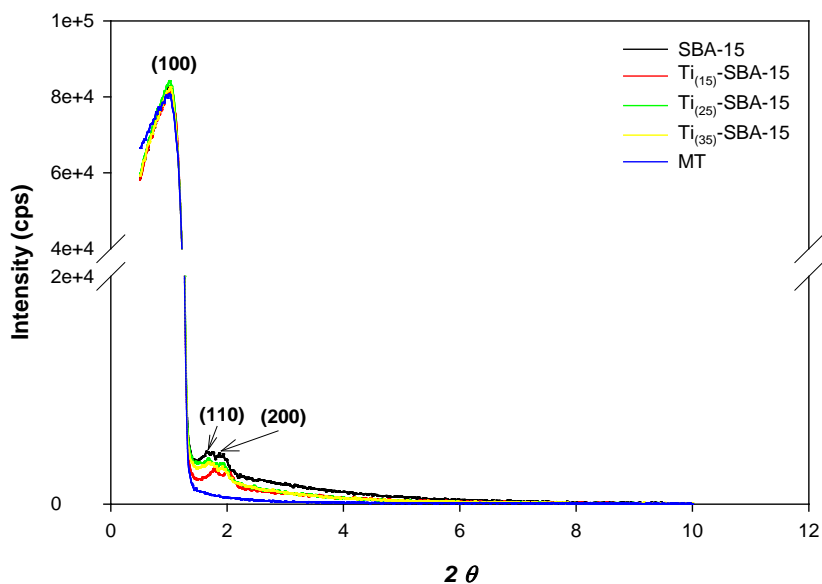


Figure 3.1 Low angle XRD patterns of $\text{Ti}_{(15, 25, 35)}$ -SBA-15 and MT.

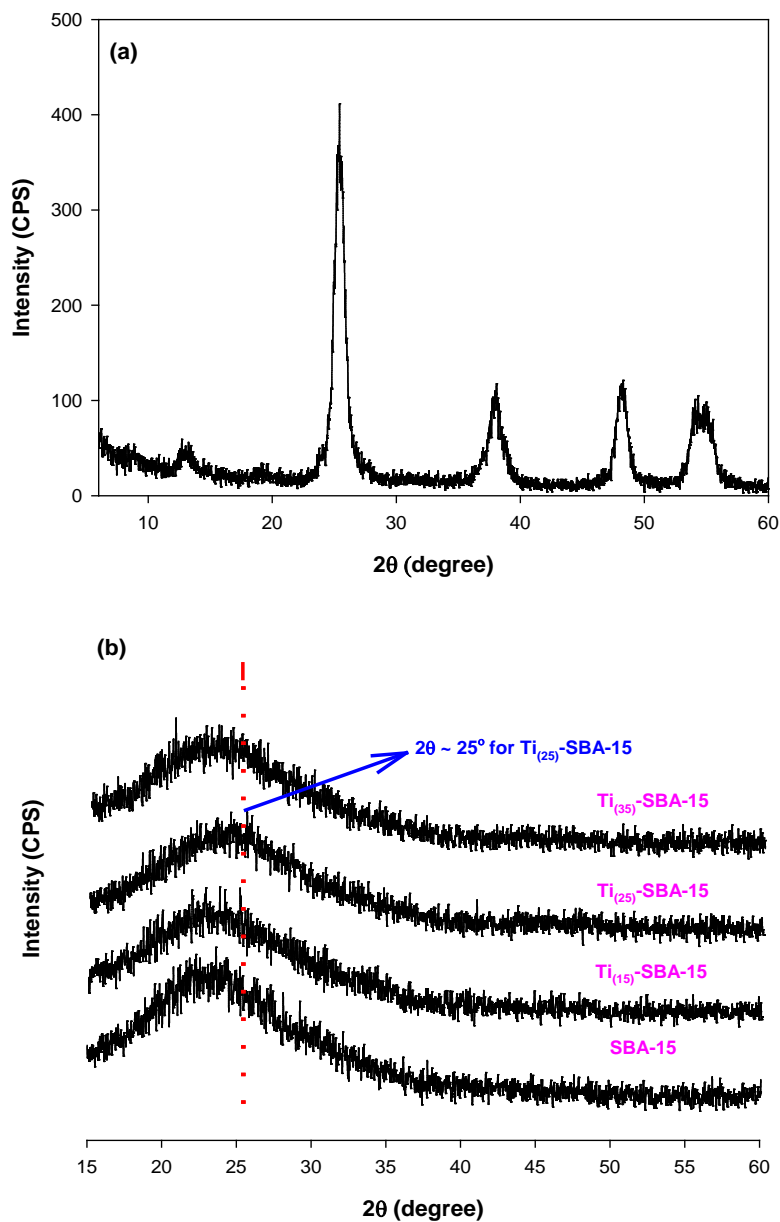


Figure 3.2 High-angle XRD patterns for (a) MT, (b) SBA-15 and $Ti_{(15, 25, 35)}$ -SBA-15.

Figure 3.3(a) shows nitrogen adsorption-desorption isotherms for MT and $Ti_{(25)}$ -SBA-15. They follow the typical irreversible type IV isotherm model as designated by IUPAC (International Union of Pure and Applied Chemistry) classification (187). These NTAs have a

H1 hysteresis loop, which is representative of mesopores (194). The sharpness of the inflection step for $\text{Ti}_{(25)}\text{-SBA-15}$ was greater than that for MT, so it appears that $\text{Ti}_{(25)}\text{-SBA-15}$ has more uniformity in its mesopores than MT. Figure 3.3(b) shows the distribution of pore volume in these NTAs and it provides further evidence of the differences in porosities. It shows a sharp peak at 7.3 nm for $\text{Ti}_{(25)}\text{-SBA-15}$, whereas MT has a broad peak at 9.4 nm. The specific surface areas (A_{BET}) and specific pore volumes (V_{BJH}) for MT were $114 \text{ m}^2/\text{g}$ and $0.28 \text{ cm}^3/\text{g}$, respectively, and for $\text{Ti}_{(25)}\text{-SBA-15}$ were $588 \text{ m}^2/\text{g}$ and $0.78 \text{ cm}^3/\text{g}$, respectively.

The TEM images in Figure 3.4 show that SBA-15 and $\text{Ti}_{(25)}\text{-SBA-15}$ have highly ordered hexagonal pores with diameters of approximately 10 nm. However, MT has a disordered wormhole-like pore structure with pore sizes in the range of 10 nm to 20 nm. This agrees with Huang et al. (185) who reported that MT was formed by the agglomeration of TiO_2 nanoparticles and had its mesoporosity caused by interparticle porosity rather than intraparticle porosity (185). Figure 3.5(a) shows the SEM image of mesoporous SBA-15 with a plate-like morphology. There are three types of morphology for SBA-15 (fiber-like, rod-like, plate-like) and the type that occurs depends on stirring and synthesis temperature (195). The rod- or plate-like SBA-15 usually has a highly-ordered hexagonal mesostructure.

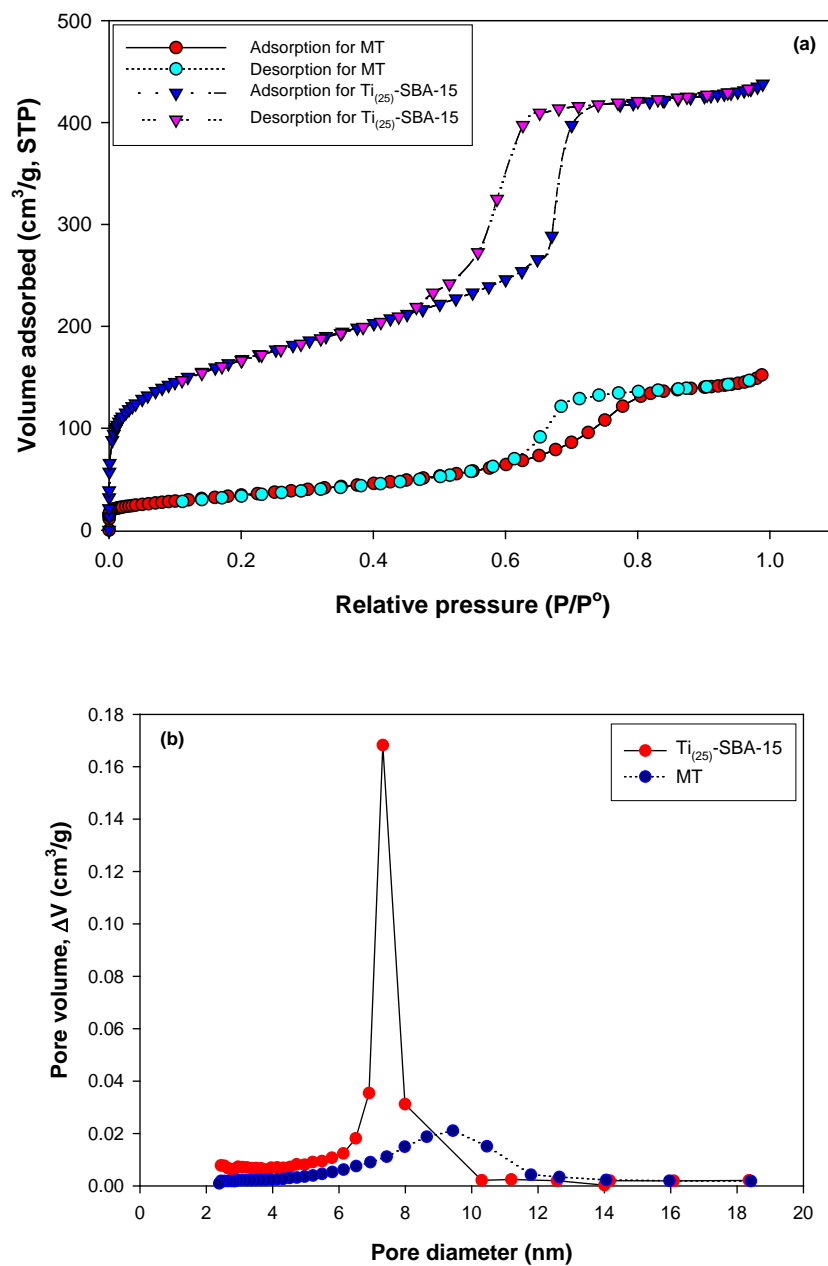


Figure 3.3 (a) N_2 adsorption isotherms and (b) pore size distribution for $Ti_{(25)}$ -SBA-15 and MT.

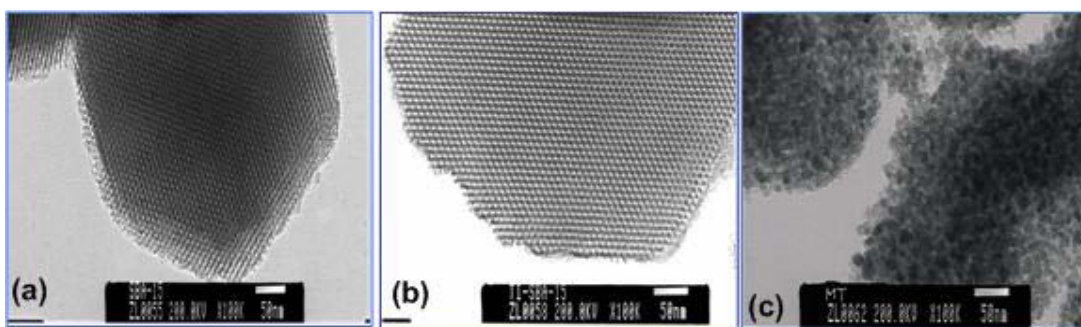


Figure 3.4 TEM images of (a) SBA-15, (b) $\text{Ti}_{(25)}$ -SBA-15, and (c) MT.

The EDS analysis shown in Figure 3.5(a) indicates that the SBA-15 is composed of Si and O. Figure 3.5(b) exhibits the morphology of $\text{Ti}_{(25)}$ -SBA-15 and comparison with Figure 3.5(a) indicates that the shape of SBA-15 was almost maintained after introducing Ti to produce $\text{Ti}_{(25)}$ -SBA-15. The EDS analysis indicated that $\text{Ti}_{(25)}$ -SBA-15 was composed of Si, O, and Ti. As shown in Figure 3.5(c), MT has also plate-like morphology and the EDS analysis shows that MT is primarily composed of Ti and O.

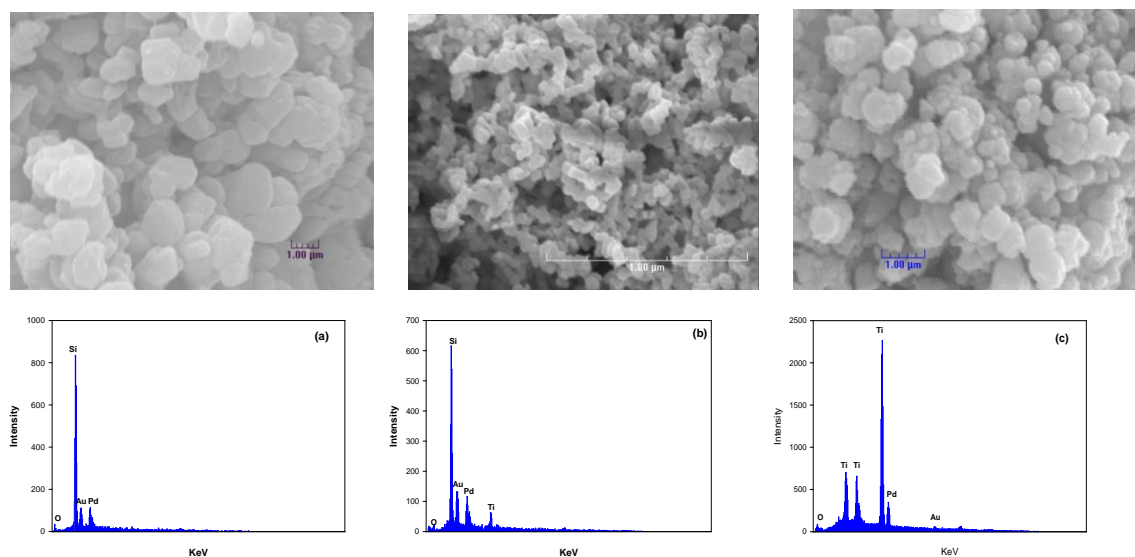


Figure 3.5 Secondary images of SEM and EDS analysis for (a) SBA-15, (b) $\text{Ti}_{(25)}$ -SBA-15, (c) MT.

Infrared spectroscopy applied to several NTAs in order to evaluate the framework of SBA-15 and the local bonding environment of titanium that was incorporated that framework. The FTIR spectra are presented in Figure 3.6 and they show three peaks at 445, 795, and 1070 cm^{-1} , which indicate rocking, bending (or symmetric stretching), and asymmetric stretching of the tetrahedral oxygen atoms in the SiO_2 structure, respectively (196). In addition, the peak at 960 cm^{-1} is assigned to the silanol group (Si-OH) in the framework of SBA-15 by the stretching of nonbridging oxygen atoms (196). This peak can be also assigned to Ti-O-Si stretching vibration (197). As the extent of titanium incorporation increases, the peak at 960 cm^{-1} gradually decreases, because of the interaction between titanium and the silanol groups. However, the peak does not disappear, which indicates that the silanol groups have not been completely consumed. Therefore, it appears possible to incorporate more titanium into the SBA-15 framework than the maximum value done in this work. However, other factors can limit the amount of titanium that can be incorporated. The decrease in intensity of the peak at 1070 cm^{-1} in the spectra for $\text{Ti}_{(35)}$ -SBA-15 indicates that Si-O-Si bonding in the mesoporous SBA-15 framework was decreased by presence of titanium. Thus, excessive impregnation of titanium can destroy the pore structure of SBA-15. The peaks at around 3600 and 1615 cm^{-1} can be attributed to the stretching vibration of hydroxyl and water, caused by humidity of KBr used as a blank sample or by humidity incorporated into sample by sample preparation techniques (197).

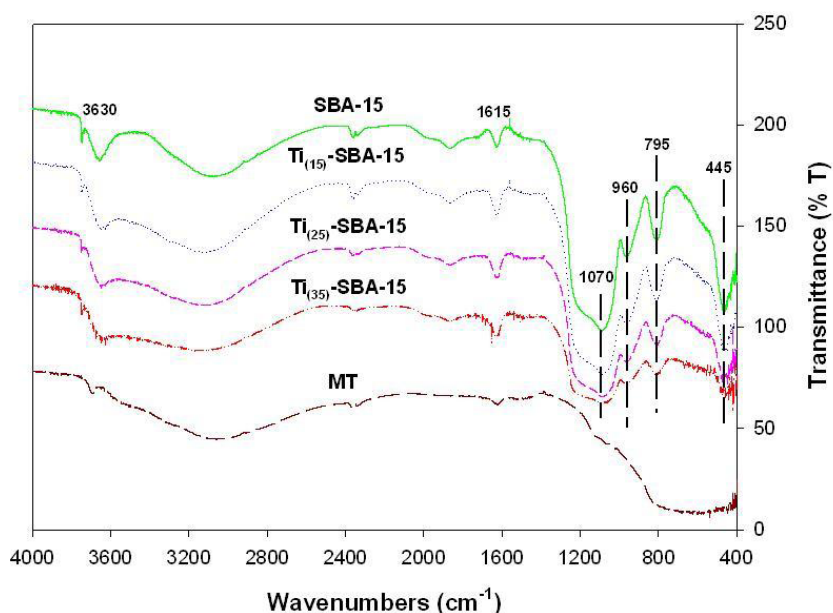


Figure 3.6 FT-IR spectra of SBA-15, $Ti_{(15,25,35)}$ -SBA-15, and MT.

3.3.2 Kinetics

3.3.2.1 Effect of pH

Kinetics of arsenic sorption by $Ti_{(25)}$ -SBA-15 and MT were investigated in batch systems at three different initial pH (4, 7, 9.5). Figures 3.7(a) and 3.7(b) show that adsorption of As(III) onto both adsorbents was rapid with most arsenic being removed within the first 10 minutes of contact, followed by slower removal rates. This behavior could be caused by transformation of arsenic species adsorbed or by other environmental factors. Specifically, the slower sorption reaction could be attributed to surface precipitation or polymerization, diffusion into interparticle or intraparticle pores, or changes in the type of surface complex (198, 199). The NTAs used in this study have much internal porosity, so it is likely that the slower rates of adsorption of arsenic are caused by intraparticle diffusion. The extent of As(III) uptake by MT increased with increasing pH over the range investigated, whereas the highest level of As(III) removal by $Ti_{(25)}$ -SBA-15 was observed at pH 7. The amount adsorbed at pH 4 was initially

much lower than that adsorbed at pH 7. However, after a longer time of reaction, the amount removed at pH 4 became nearly as high as that at pH 7. At pH 9.5, the removal efficiency of MT for As(III) was more than three times greater than that of Ti₍₂₅₎-SBA-15.

The kinetic experiments for As(V) removal were conducted similarly to those for As(III) removal. Figures 3.8(a) and (b) show that the amount of As(V) removed depends strongly on solution pH. At lower pH, higher As(V) adsorption was observed, whereas at high pH, lower removal of As(V) was observed. In spite of the similar trends of As(V) removal by each adsorbent over the pH range investigated, the extent of As(V) uptake at a specified pH was very different. For instance, As(V) at pH 4 was almost completely removed by Ti₍₂₅₎-SBA-15, whereas only 91 % removal was achieved by MT. However, at other pH, the extent of As(V) uptake by MT was much higher than that by Ti₍₂₅₎-SBA-15.

All coefficients in the kinetic model and GFP values for each experimental data set are summarized in Table 3.1. The fastest sorption rate constants for both fast-reacting and slow-reacting sites were observed at the optimal pH values, i.e., pH 4 and 9.5 for As(III)/Ti₍₂₅₎-SBA-15, pH 4 and 9.5 for As(III)/MT, pH 9.5 and 4 for As(V)/Ti₍₂₅₎-SBA-15, pH 4 for As(V)/MT, respectively. However, many rate coefficients have very large confidence limits that are often larger than the value of parameter. This is because there are few data points during the early stages of the reaction, where the fast-reacting sites would be filled, so it is very difficult to determine the values of the coefficients exactly.

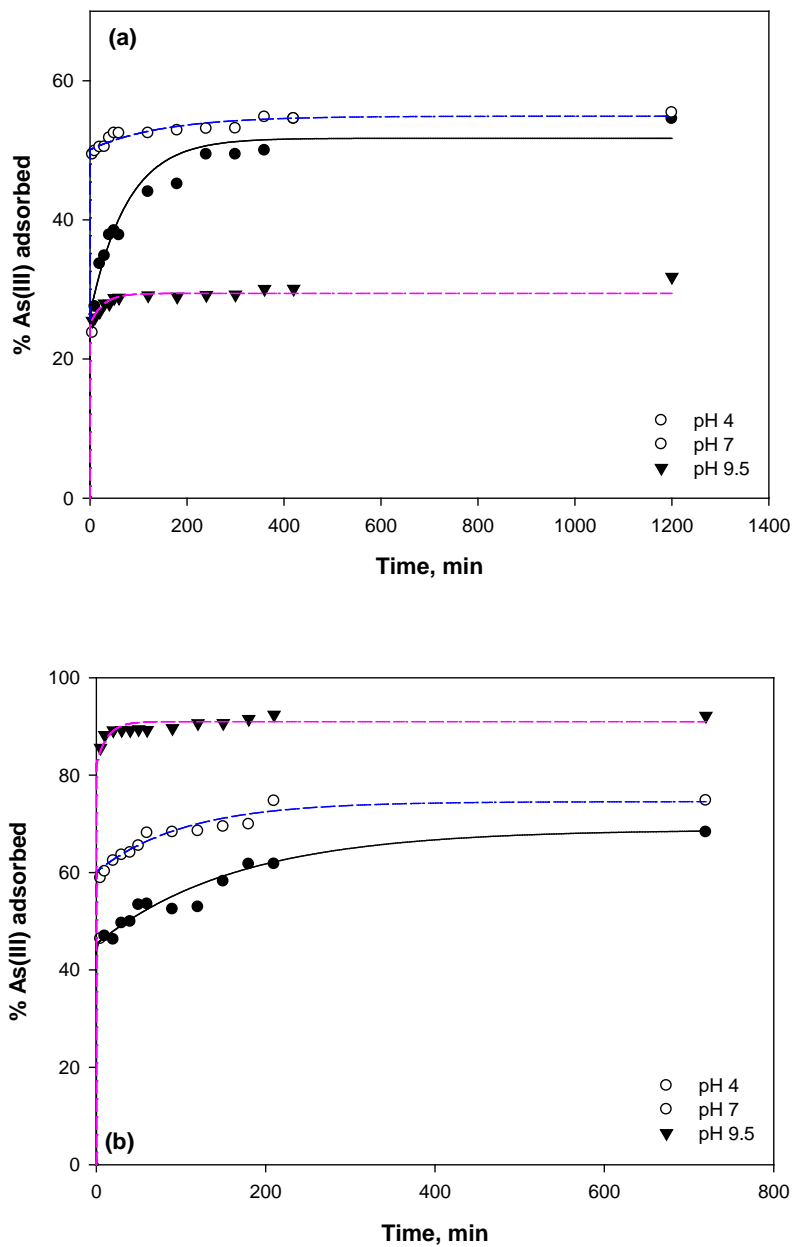


Figure 3.7 Percentage of As(III) adsorbed by (a) Ti₍₂₅₎-SBA-15 and (b) MT as a function of time at different pH values with predictions of kinetic model.

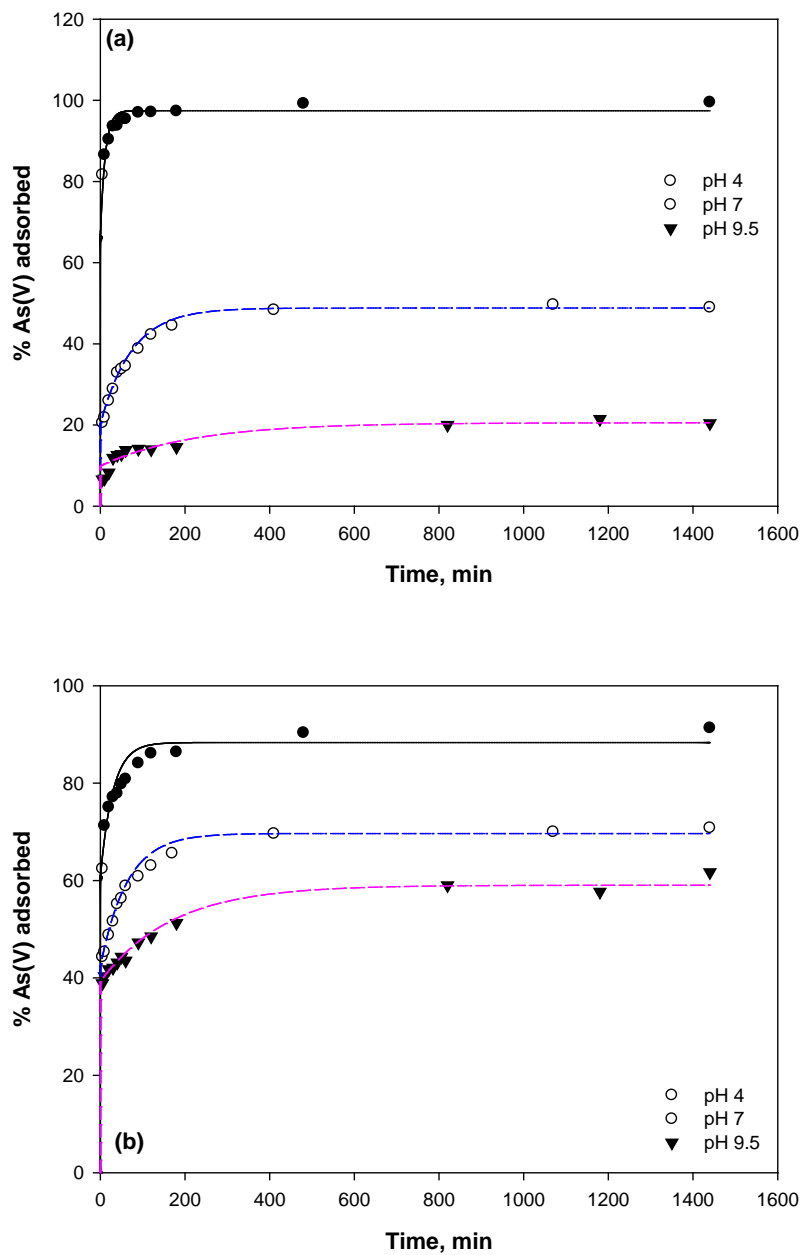


Figure 3.8 Percentage of As(V) adsorbed by (a) $\text{Ti}_{(25)}\text{-SBA-15}$ and (b) MT as a function of time at different pH values with predictions of kinetic model.

Table 3.1 Calculated parameters of the adsorption kinetic model for arsenic (As(III,V)) uptake by NTAs, as affected by initial pH values (pH 4, 7, 9.5).

| Arsenic species | Adsorbents | pH | Parameters | | | | |
|-----------------|----------------------------|-----|--|------------------|-----------------|-----------------|------|
| | | | k_f | k_s | $q_{max,f}$ | $q_{max,s}$ | GFP |
| As(III) | Ti ₍₂₅₎ -SBA-15 | 4 | $1.6 \times 10^5 \pm 4.0 \times 10^4$ | 0.02 ± 0.01 | 2.64 ± 0.53 | 2.99 ± 0.79 | 0.06 |
| | | 7 | $1.0 \times 10^5 \pm 2.4 \times 10^5$ | 0.05 ± 0.34 | 5.01 ± 0.97 | 0.92 ± 1.24 | 0.02 |
| | | 9.5 | $2.1 \times 10^8 \pm 4.3 \times 10^8$ | 0.06 ± 0.28 | 2.51 ± 0.50 | 0.73 ± 0.63 | 0.03 |
| | MT | 4 | $6.8 \times 10^6 \pm 6.6 \times 10^{10}$ | 0.006 ± 0.01 | 6.55 ± 1.05 | 3.45 ± 4.78 | 0.08 |
| | | 7 | $4.9 \times 10^3 \pm 4.1 \times 10^3$ | 0.02 ± 0.08 | 8.24 ± 1.66 | 2.31 ± 3.27 | 0.02 |
| | | 9.5 | $5.5 \times 10^6 \pm 1.1 \times 10^8$ | 0.03 ± 0.46 | 12.5 ± 2.83 | 0.79 ± 4.06 | 0.01 |
| As(V) | Ti ₍₂₅₎ -SBA-15 | 4 | $4.6 \times 10^5 \pm 1.1 \times 10^8$ | 0.07 ± 0.42 | 13.1 ± 2.2 | 4.44 ± 0.41 | 0.02 |
| | | 7 | $2.6 \times 10^6 \pm 1.1 \times 10^8$ | 0.01 ± 0.02 | 3.05 ± 0.68 | 4.96 ± 1.23 | 0.04 |
| | | 9.5 | $3.1 \times 10^7 \pm 2.6 \times 10^{10}$ | 0.01 ± 0.01 | 1.05 ± 0.27 | 2.19 ± 0.51 | 0.12 |
| | MT | 4 | $3.3 \times 10^9 \pm 7.9 \times 10^{11}$ | 0.07 ± 0.18 | 9.12 ± 2.45 | 6.34 ± 3.26 | 0.05 |
| | | 7 | 465 ± 200 | 0.01 ± 0.03 | 7.04 ± 1.44 | 4.43 ± 2.63 | 0.02 |
| | | 9.5 | $1.2 \times 10^4 \pm 8.0 \times 10^3$ | 0.01 ± 0.02 | 6.07 ± 1.21 | 3.48 ± 2.42 | 0.03 |

3.3.2.2 Effect of Arsenic Concentrations

The effect of three different initial As(III,V) concentrations (5.3, 9.3, 13.3 $\mu\text{mol/L}$) on arsenic sorption kinetics by Ti₍₂₅₎-SBA-15 and MT were investigated in a batch system at pH 7. These experiments used a solids concentration of 1 g/L and an ionic strength of 0.01 M achieved by addition of NaCl. Figures 3.9(a) and (b) show that adsorption rates of As(III) and (V) by Ti₍₂₅₎-SBA-15 decrease over time. More than 30 % arsenic removal occurs in the first 30 minutes (except As(V)=13.3 μM) followed by an additional 30% removal, or less, over more than 1,000 minutes. The NTAs used in this research have substantial internal porosity, so the decrease in adsorption rate with time might be due to intraparticle diffusion. After a longer period of time, the fractions of As(V) removed were nearly as high as those of As(III).

Figures 3.10(a) and (b) show that adsorption of As(III) and As(V) by MT at all concentrations of arsenic added follow similar patterns to those observed for Ti₍₂₅₎-SBA-15. More than half of the ultimate removal occurred in the first 5 minutes and less than 50% additional removal is observed in the following 1400 minutes. The ultimate amounts of As(V) removed were nearly as high as those of As(III). Comparing Figures 3.9 and 3.10 shows that ultimate removals of arsenic (As(III) and As(V)) by MT are much higher than those by Ti₍₂₅₎-SBA-15.

Table 3.2 shows the parameters of the kinetic model for arsenic adsorption on NTAs at pH 7 as affected by initial arsenic concentration. The kinetic model provides good fits to experimental data as shown by the low values of goodness of fit parameter (GFP). The maximum amount of arsenic adsorbed on fast-reacting sites ($q_{f, \max}$) and on slow-reacting sites ($q_{s, \max}$) are generally seen to increase as total arsenic concentration increases except in a few cases. There was a weak correlation of rate constants with maximum adsorbed concentration (k_f and $q_{f, \max}$, k_s and $q_{s, \max}$) in which faster sorption rates tend to occur with greater ultimate sorption levels.

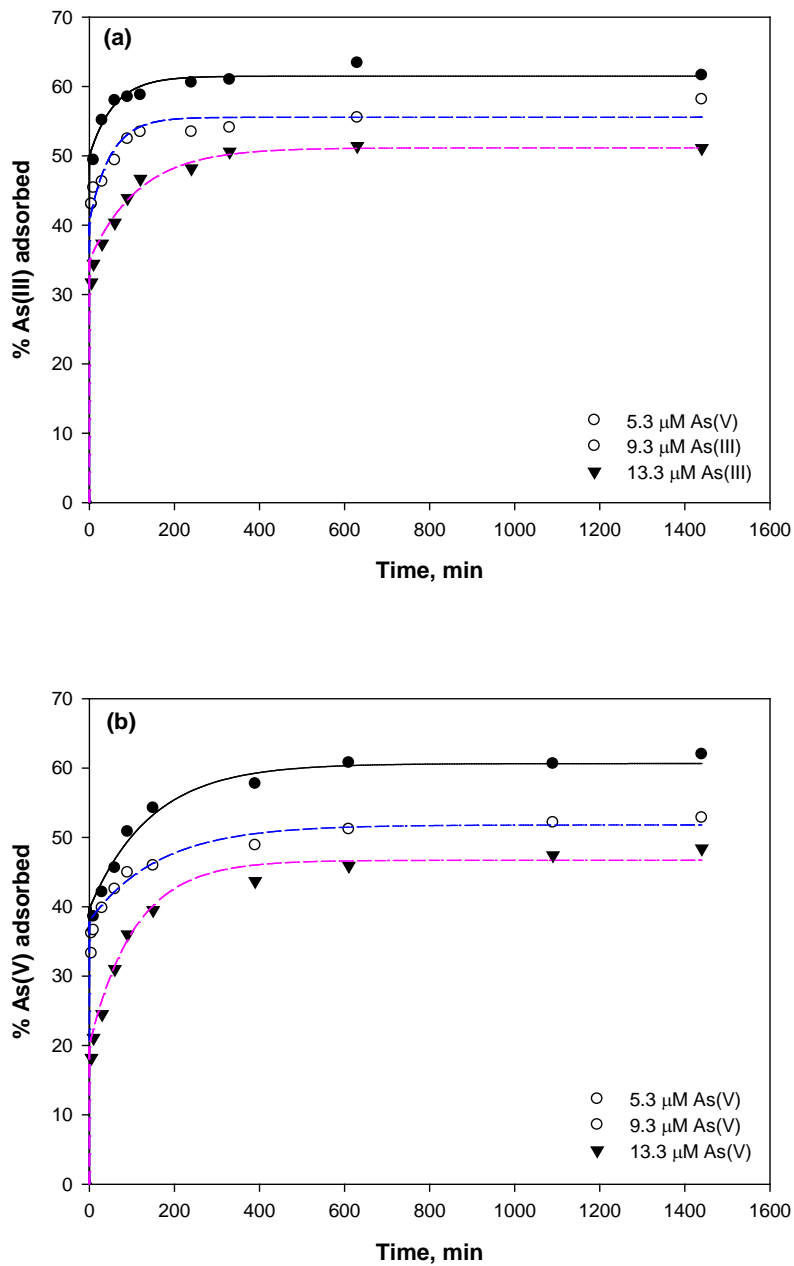


Figure 3.9 Percentage of (a) As(III) and (b) As(V) adsorbed by $Ti_{(25)}\text{-SBA-15}$ at pH 7 as affected by initial arsenic concentration with model predictions.

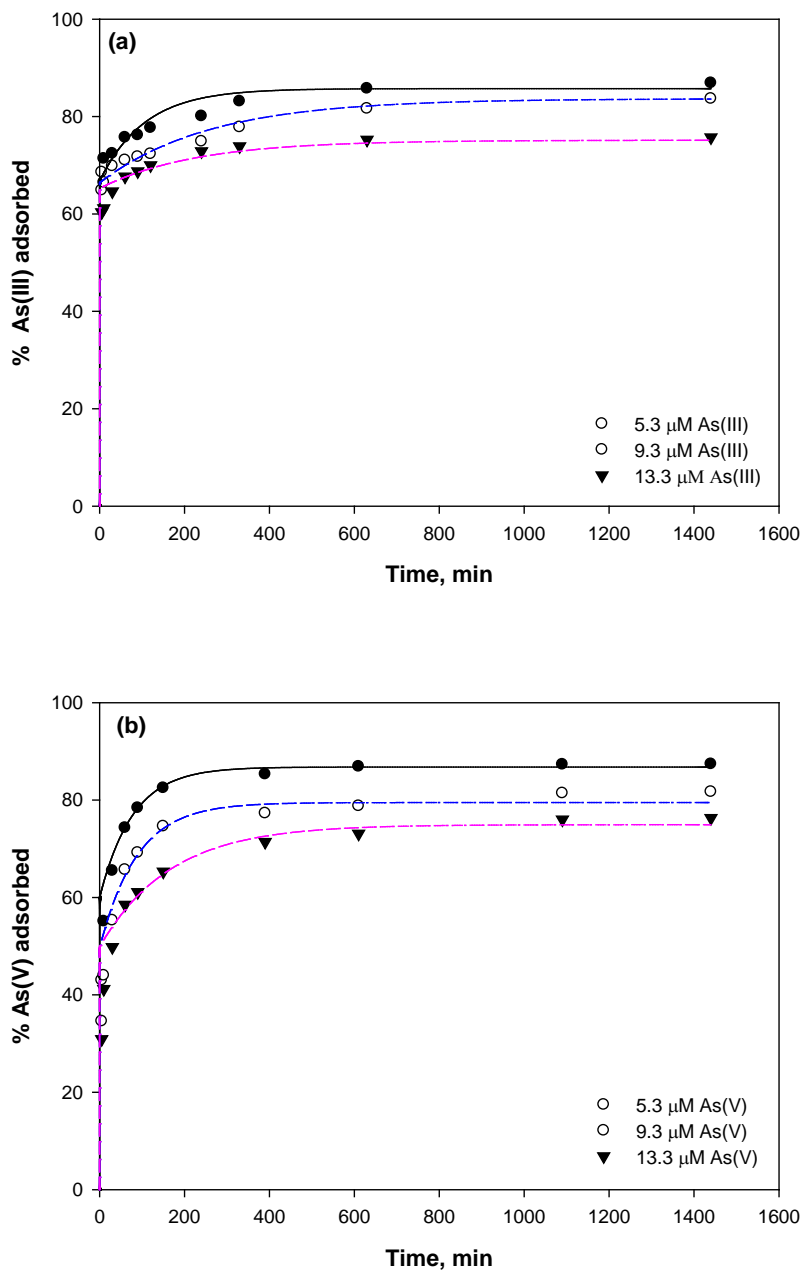


Figure 3.10 Percentage of (a) As(III) and (b) As(V) adsorbed by MT at pH 7 as affected by initial arsenic concentration with model predictions.

Table 3.2 Calculated parameters of the adsorption kinetic model for arsenic (As(III,V)) uptake by NTAs, as affected by initial As(III, V) concentrations (5.3, 9.3, 13.3 μM).

| Arsenic species | Adsorbents | C_0 | Parameters | | | | |
|-----------------|----------------------------|-------|---|-------------------|-----------------|-----------------|------|
| | | | k_f | k_s | q_{f_max} | $q_{s,e}$ | GFP |
| As(III) | Ti ₍₂₅₎ -SBA-15 | 5.3 | $3.2 \times 10^5 \pm 2.9 \times 10^9$ | 0.048 ± 0.02 | 2.3 ± 0.65 | 0.93 ± 0.77 | 0.03 |
| | | 9.3 | $9.8 \times 10^3 \pm 7.2 \times 10^3$ | 0.01 ± 0.07 | 4.01 ± 1.10 | 1.19 ± 1.78 | 0.02 |
| | | 13.3 | $7.1 \times 10^8 \pm 1.7 \times 10^{10}$ | 0.01 ± 0.03 | 4.04 ± 0.62 | 2.77 ± 1.89 | 0.02 |
| | MT | 5.3 | $1.4 \times 10^{10} \pm 9.6 \times 10^{10}$ | 0.007 ± 0.05 | 3.6 ± 1.0 | 0.96 ± 1.9 | 0.02 |
| | | 9.3 | $1.9 \times 10^3 \pm 4.6 \times 10^3$ | 0.005 ± 0.31 | 6.06 ± 1.65 | 1.70 ± 3.85 | 0.02 |
| | | 13.3 | $3.0 \times 10^3 \pm 2.5 \times 10^5$ | 0.03 ± 0.12 | 7.06 ± 2.18 | 2.81 ± 3.09 | 0.04 |
| As(V) | Ti ₍₂₅₎ -SBA-15 | 5.3 | $5.3 \times 10^4 \pm 3.6 \times 10^8$ | 0.01 ± 0.02 | 1.91 ± 0.55 | 1.33 ± 0.82 | 0.02 |
| | | 9.3 | $7.1 \times 10^7 \pm 5.9 \times 10^7$ | 0.01 ± 0.04 | 3.04 ± 0.86 | 1.76 ± 1.27 | 0.04 |
| | | 13.3 | $9.1 \times 10^5 \pm 1.2 \times 10^9$ | 0.02 ± 0.01 | 2.42 ± 0.68 | 3.80 ± 1.04 | 0.04 |
| | MT | 5.3 | $9.1 \times 10^6 \pm 4.9 \times 10^6$ | 0.02 ± 0.03 | 2.98 ± 0.63 | 1.63 ± 0.92 | 0.07 |
| | | 9.3 | $1.2 \times 10^4 \pm 8.0 \times 10^3$ | 0.007 ± 0.013 | 6.08 ± 1.20 | 3.48 ± 2.42 | 0.08 |
| | | 13.3 | $2.2 \times 10^5 \pm 5.1 \times 10^9$ | 0.02 ± 0.03 | 4.13 ± 1.24 | 5.75 ± 1.70 | 0.06 |

3.3.3 Equilibrium Isotherms for Arsenic Adsorption

3.3.3.1 Effect of Ratio of Ti to SBA-15

Figure 3.11(a) and (b) show the Langmuir and Freundlich adsorption isotherms for As(III) on Ti_(15,25,35)-SBA-15 and MT. These isotherms were obtained by nonlinear regression and Table 3.3 shows the values of the isotherm parameters and of the goodness of fit parameter (GFP). These results show that the maximum sorption capacity for As(III) decreases as follows; MT (162 $\mu\text{mol/g}$) > Ti₍₂₅₎-SBA-15 (87 $\mu\text{mol/g}$) > Ti₍₃₅₎-SBA-15 (76 $\mu\text{mol/g}$) > Ti₍₁₅₎-SBA-15 (60 $\mu\text{mol/g}$). The GFP values in Table 3.3 show that the Langmuir isotherm model provided a better fit than the Freundlich isotherm model for both adsorbents. Similar experiments were conducted to determine equilibrium behavior of Ti to SBA-15 and MT with As(V). Figures 3.12(a) and (b) show Langmuir and Freundlich isotherm models fitted to experimental data using nonlinear regression. Table 3.4 lists values for the model parameters and GFP. The values of GFP indicate that the Langmuir isotherm model provides a better fit than the Freundlich isotherm, except for MT. The maximum sorption capacity for As(V) removal decreases as follows; MT (116 $\mu\text{mol/g}$)

> $Ti_{(25)}$ -SBA-15 (72 $\mu\text{mol/g}$) > $Ti_{(35)}$ -SBA-15 (55 $\mu\text{mol/g}$) > $Ti_{(15)}$ -SBA-15 (51 $\mu\text{mol/g}$). These results indicate that the optimal weight ratio of Ti to SBA-15 for As(III) and As(V) adsorption is 25 %. Sorption capacity for arsenic decreased when the incorporation ratio increased from 25% to 35%, possibly due to incorporation of some Ti into the silica framework. Ti that is in the silica framework would not function as reactive sorption sites for arsenic. Similar results have been observed in other studies that investigated $La_{(x)}$ -SBA-15, $Al_{(x)}$ -SBA-15, and $Fe_{(x)}$ -SBA-15(200). In addition, MT had a higher sorption capacity than $Ti_{(25)}$ -SBA-15, by factors of 1.7 and 1.6, for As(III) and As(V), respectively.

Table 3.3 Comparison of isotherm parameters \pm 95% confidence levels for As(III) adsorption.

| | <u>$Ti_{(15)}$-SBA-15</u> | <u>$Ti_{(25)}$-SBA-15</u> | <u>$Ti_{(35)}$-SBA-15</u> | <u>MT</u> |
|---|---|---|---|---|
| Langmuir | | | | |
| b (L/ μmol) | $1.4 \times 10^{-2} \pm 4 \times 10^{-3}$ | $1.4 \times 10^{-2} \pm 3 \times 10^{-2}$ | $1.3 \times 10^{-2} \pm 3 \times 10^{-3}$ | $8 \times 10^{-3} \pm 2 \times 10^{-3}$ |
| Q_{max} ($\mu\text{mol/g}$) | 60 ± 6 | 87 ± 5 | 76 ± 5 | 162 ± 14 |
| GFP | 0.09 | 0.05 | 0.06 | 0.09 |
| Freundlich | | | | |
| K_f ($\mu\text{mol}^{1-1/n} \cdot \text{L}^{1/n}/\text{g}$) | 8.3 ± 6.4 | 11 ± 6.3 | 8.6 ± 5.5 | 12.7 ± 6.8 |
| n | 3.6 ± 1.7 | 3.4 ± 1.1 | 3.3 ± 1.1 | 2.8 ± 0.6 |
| GFP | 0.30 | 0.23 | 0.25 | 0.21 |

Table 3.4 Comparison of isotherm parameters \pm 95% confidence levels for As(V) adsorption.

| | <u>$Ti_{(15)}$-SBA-15</u> | <u>$Ti_{(25)}$-SBA-15</u> | <u>$Ti_{(35)}$-SBA-15</u> | <u>MT</u> |
|---|---|---|---|---|
| Langmuir | | | | |
| b (L/ μmol) | $1.1 \times 10^{-2} \pm 3 \times 10^{-3}$ | $1.2 \times 10^{-2} \pm 3 \times 10^{-3}$ | $1.3 \times 10^{-2} \pm 3 \times 10^{-3}$ | $8 \times 10^{-3} \pm 2 \times 10^{-3}$ |
| Q_{max} ($\mu\text{mol/g}$) | 51.3 ± 3.71 | 72 ± 7.04 | 55.5 ± 2.16 | 116.3 ± 16.8 |
| GFP | 0.07 | 0.09 | 0.04 | 0.14 |
| Freundlich | | | | |
| K_f ($\mu\text{mol}^{1-1/n} \cdot \text{L}^{1/n}/\text{g}$) | 4.86 ± 3.82 | 6.98 ± 4.83 | 5.85 ± 4.25 | 8.81 ± 2.38 |
| n | 2.93 ± 1.11 | 2.98 ± 1.02 | 3.09 ± 1.13 | 2.74 ± 0.24 |
| GFP | 0.25 | 0.25 | 0.19 | 0.09 |

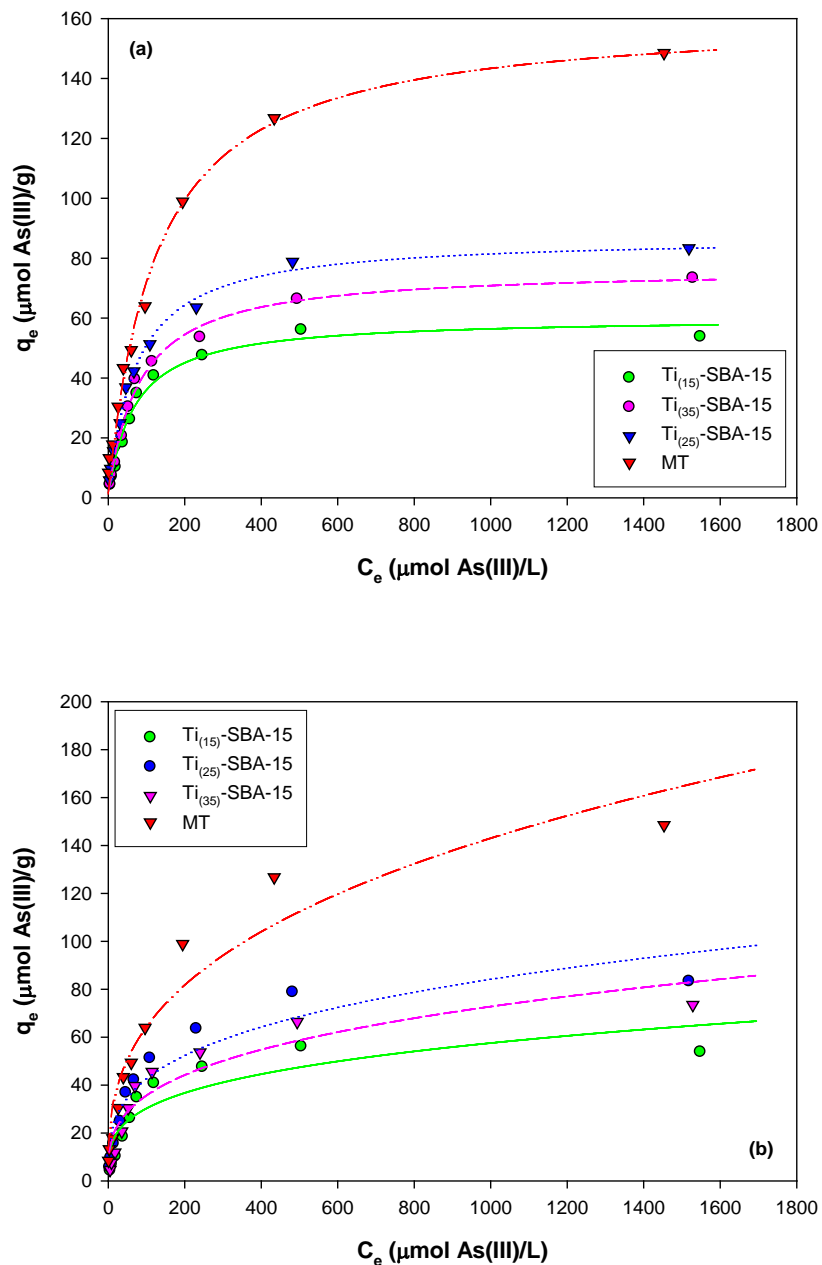


Figure 3.11 Langmuir (a) and Freundlich (b) adsorption isotherms for As(III) on $\text{Ti}_{(15,25,35)}$ -SBA-15 and MT. Solid concentration is 1 g/L. Curves are isotherm models obtained by nonlinear regression.

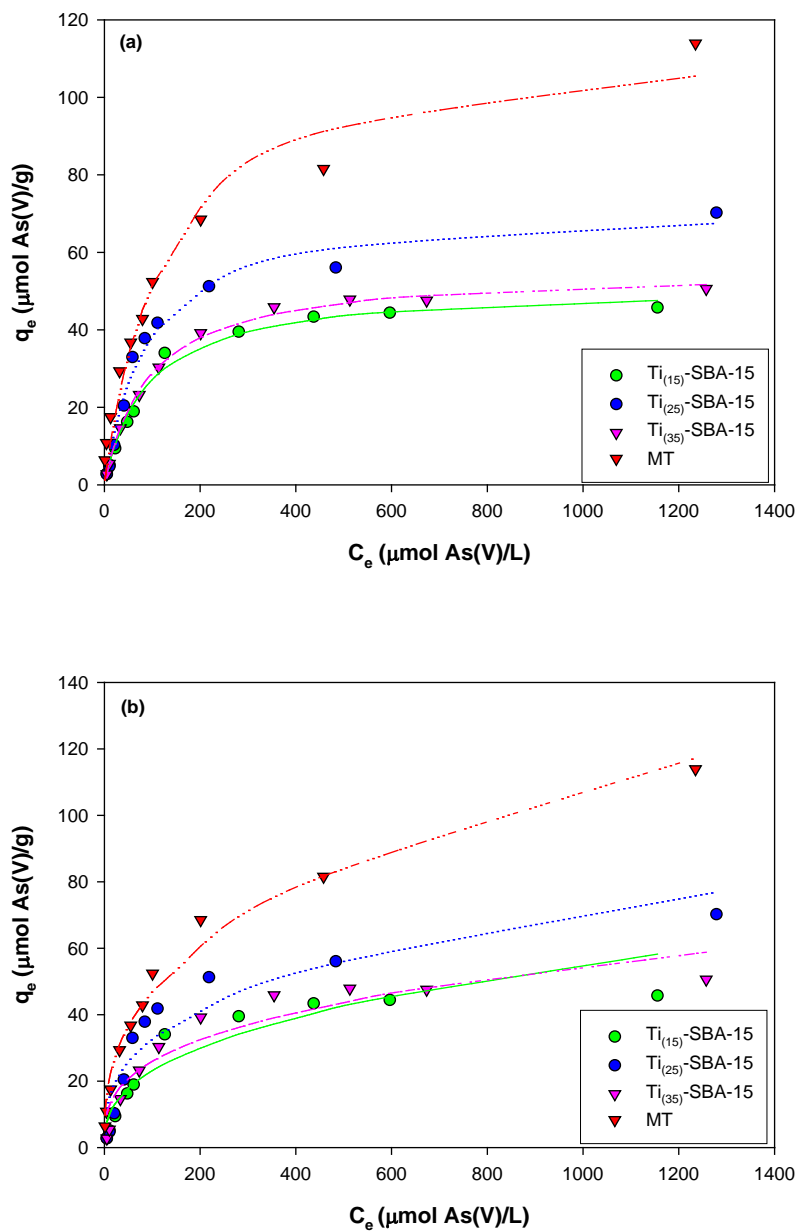


Figure 3.12 Langmuir (a) and Freundlich (b) adsorption isotherms for As(V) on $\text{Ti}_{(15,25,35)}$ -SBA-15 and MT. Solid concentration is 1 g/L. Curves are isotherm models obtained by nonlinear regression.

3.3.3.2 Effect of pH

Experiments were conducted at three pH values (pH 4, 7, 9.5) in order to investigate the effect of pH on equilibrium isotherms for each adsorbent and for both As(III) and As(V). Figures 3.13 and 3.15 show adsorption isotherms fitted by the Langmuir model and the fit of the Freundlich model is presented in Figures 3.14 and 3.16. Adsorption isotherm parameters are summarized in Tables 3.5 and 3.6 for both the Langmuir and Freundlich models. In the case of As(III), the order of maximum sorption capacity is: MT (pH 9.5, 285 $\mu\text{mol/g}$) > MT (pH 7, 162 $\mu\text{mol/g}$) > Ti₍₂₅₎-SBA-15 (pH 4, 121 $\mu\text{mol/g}$) > Ti₍₂₅₎-SBA-15 (pH 7, 87 $\mu\text{mol/g}$) > MT (pH 4, 66 $\mu\text{mol/g}$) > Ti₍₂₅₎-SBA-15 (pH 9.5, 60 $\mu\text{mol/g}$). In addition, at all pH except for pH 9.5, the Langmuir model for As(III) sorption by Ti₍₂₅₎-SBA-15 provided a better fit than the Freundlich model as indicated by lower values of GFP. However, As(III) adsorption by MT is described well by the Freundlich model at all pH values except at pH 4. In contrast to the results for As(III), the order of maximum sorption capacity for As(V) is: Ti₍₂₅₎-SBA-15 (pH 4, 193 $\mu\text{mol/g}$) > MT (pH 4, 173 $\mu\text{mol/g}$) > MT (pH 7, 116 $\mu\text{mol/g}$) > Ti₍₂₅₎-SBA-15 (pH 7, 72 $\mu\text{mol/g}$) > MT (pH 9.5, 56 $\mu\text{mol/g}$) > Ti₍₂₅₎-SBA-15 (pH 9.5, 30 $\mu\text{mol/g}$). The Langmuir model for As(V) adsorption by Ti₍₂₅₎-SBA-15 provides the best fit to experimental data at all pH, whereas the Freundlich model is better for As(V) adsorption by MT at all pH except pH 4.

Table 3.5 Comparison of As(III) adsorption isotherm parameters as a function of pH.

| NTAs | pH | <u>Langmuir</u> | | | <u>Freundlich</u> | | |
|----------------------------|-----|---|---|------|--|----------------|------|
| | | b (L/ μmol) | q_{max} ($\mu\text{mol/g}$) | GFP | k_f ($\mu\text{mol}^{1-1/n} \cdot \text{L}^{1/n}/\text{g}$) | n | GFP |
| MT | 4 | $1 \times 10^{-2} \pm 4 \times 10^{-3}$ | 66 ± 11 | 0.12 | 4.7 ± 2.9 | 2.5 ± 0.7 | 0.18 |
| | 7 | $8 \times 10^{-3} \pm 2 \times 10^{-3}$ | 162 ± 14 | 0.12 | 12.7 ± 6.8 | 2.8 ± 0.6 | 0.09 |
| | 9.5 | $1.5 \times 10^{-2} \pm 8 \times 10^{-3}$ | 285 ± 52 | 0.17 | 22.4 ± 7.8 | 2.48 ± 0.4 | 0.13 |
| Ti ₍₂₅₎ -SBA-15 | 4 | $9 \times 10^{-3} \pm 2.7 \times 10^{-3}$ | 121 ± 14 | 0.23 | 6.8 ± 5.3 | 2.3 ± 0.7 | 0.24 |
| | 7 | $1.4 \times 10^{-2} \pm 3 \times 10^{-3}$ | 87 ± 5 | 0.06 | 11 ± 6.3 | 3.4 ± 1.1 | 0.14 |
| | 9.5 | $8.3 \times 10^{-3} \pm 3 \times 10^{-3}$ | 60 ± 9 | 0.11 | 3.6 ± 1.4 | 2.4 ± 0.4 | 0.10 |

Table 3.6 Comparison of As(V) adsorption isotherm parameters as a function of pH.

| NTAs | pH | <u>Langmuir</u> | | | <u>Freundlich</u> | | |
|----------------------------|-----|---|---|------|--|-----------------|------|
| | | b (L/ μmol) | q_{max} ($\mu\text{mol/g}$) | GFP | k_f ($\mu\text{mol}^{1-1/n} \cdot \text{L}^{1/n}/\text{g}$) | n | GFP |
| MT | 4 | $1.3 \times 10^{-2} \pm 3.8 \times 10^{-3}$ | 173 ± 16 | 0.11 | 17.8 ± 6.9 | 3.03 ± 0.59 | 0.15 |
| | 7 | $8 \times 10^{-3} \pm 3 \times 10^{-3}$ | 116 ± 17 | 0.14 | 8.8 ± 2.4 | 2.75 ± 0.33 | 0.09 |
| | 9.5 | $7.8 \times 10^{-3} \pm 4 \times 10^{-3}$ | 56 ± 11 | 0.18 | 5.1 ± 1.1 | 2.99 ± 0.31 | 0.07 |
| Ti ₍₂₅₎ -SBA-15 | 4 | $8.1 \times 10^{-3} \pm 4.9 \times 10^{-3}$ | 193 ± 17 | 0.09 | 20.5 ± 9.1 | 3.08 ± 0.71 | 0.18 |
| | 7 | $3.1 \times 10^{-3} \pm 1.7 \times 10^{-3}$ | 72 ± 7.0 | 0.09 | 6.9 ± 4.7 | 2.98 ± 1.02 | 0.25 |
| | 9.5 | $4.1 \times 10^{-3} \pm 1.3 \times 10^{-3}$ | 30 ± 4.0 | 0.11 | 1.85 ± 1.27 | 2.62 ± 0.76 | 0.22 |

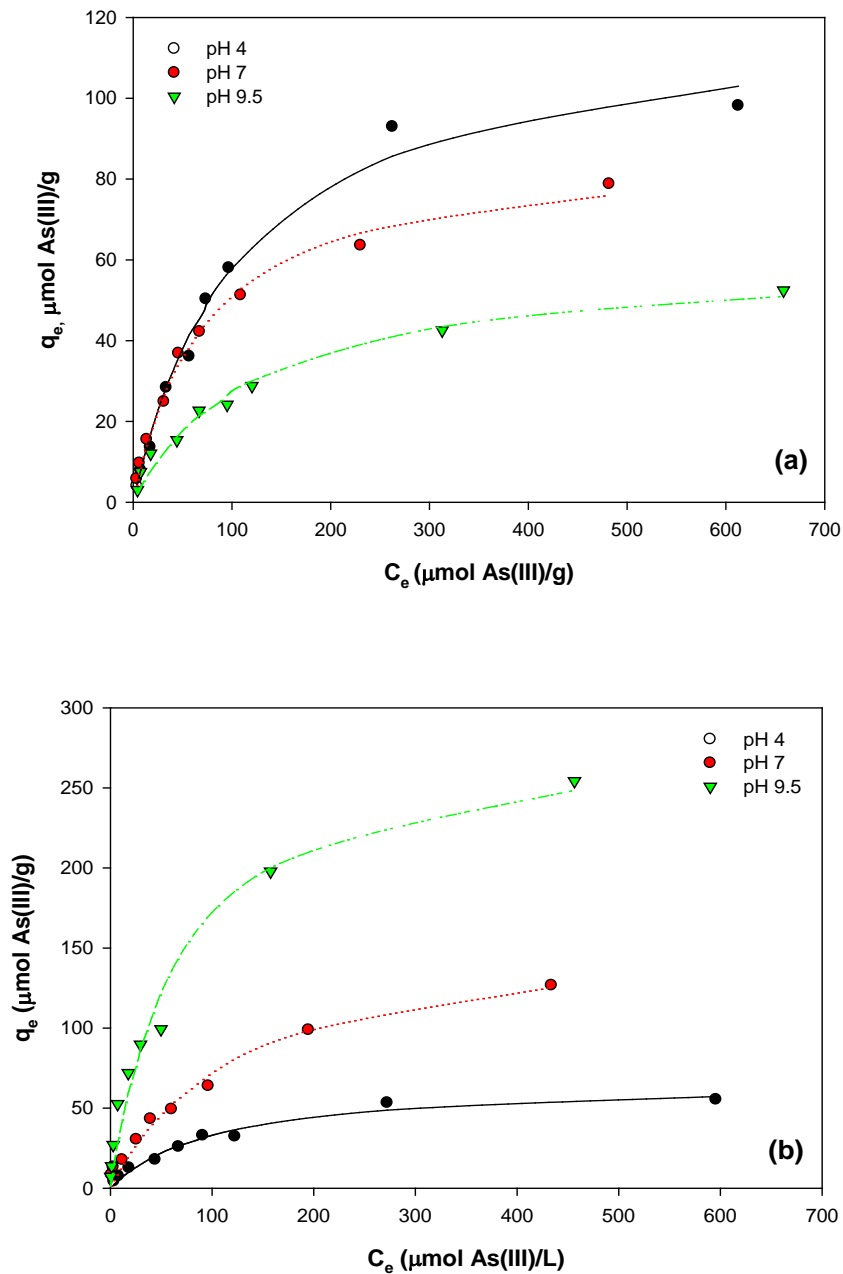


Figure 3.13 Langmuir adsorption isotherms for As(III) on (a) $\text{Ti}_{(25)}\text{-SBA-15}$ and (b) MT as affected by pH. Curves are isotherm models obtained by nonlinear regression.

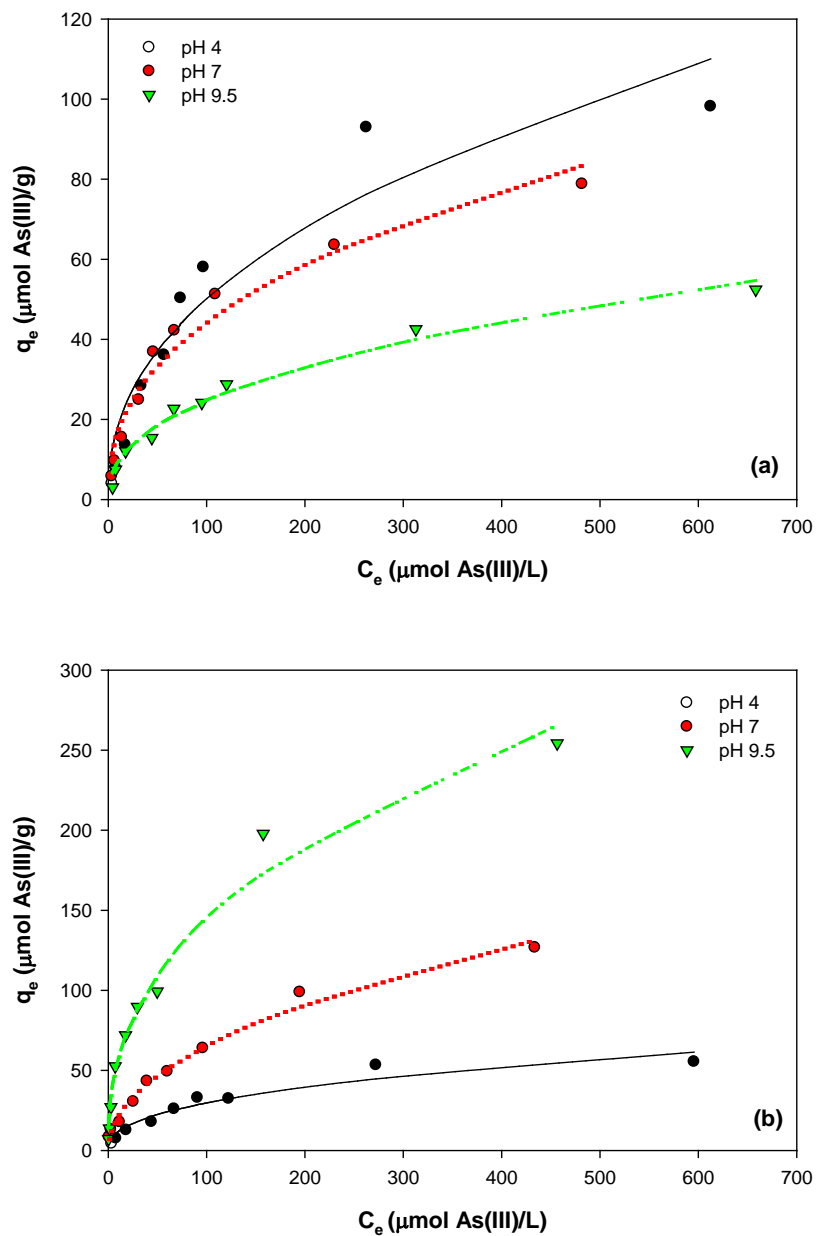


Figure 3.14 Freundlich adsorption isotherms for As(III) on (a) $\text{Ti}_{(25)}\text{-SBA-15}$ and (b) MT as affected by pH. Curves are isotherm models obtained by nonlinear regression.

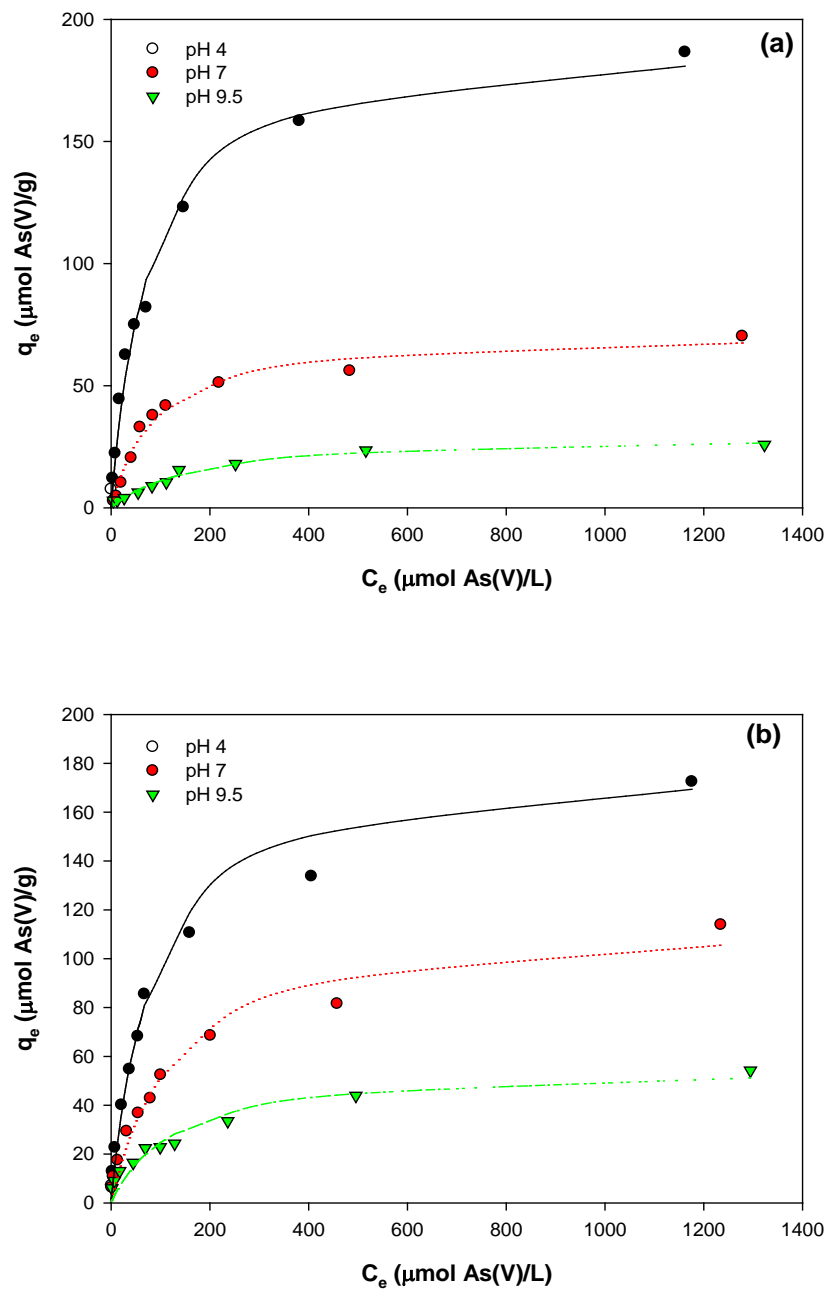


Figure 3.15 Langmuir adsorption isotherms for As(V) on (a) $\text{Ti}_{(25)}\text{-SBA-15}$ and (b) MT as affected by pH. Curves are isotherm models obtained by nonlinear regression.

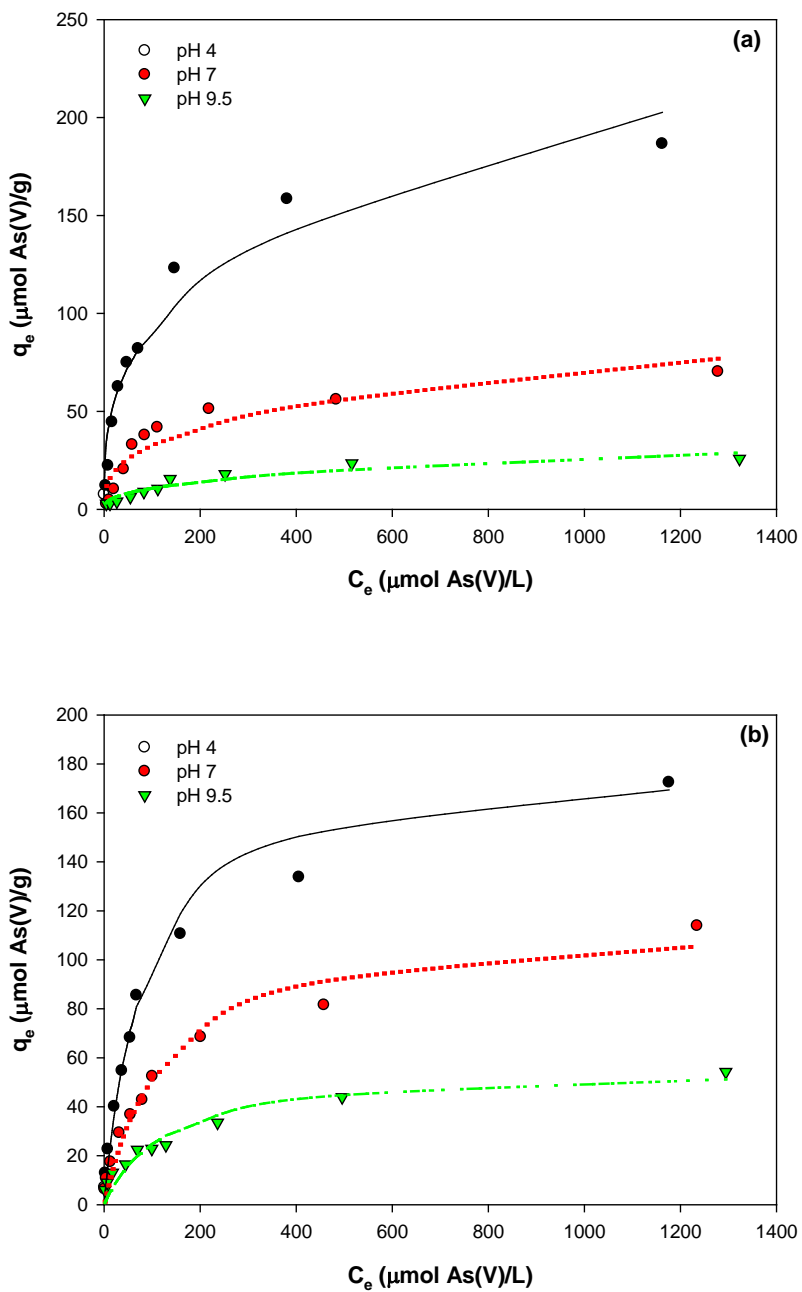


Figure 3.16 Freundlich adsorption isotherms for As(V) on Ti₍₂₅₎-SBA-15 and MT as affected by pH. Curves are isotherm models obtained by nonlinear regression.

4. MODELING ON ADSORPTION OF ARSENIC(III) AND ARSENIC(V) ONTO NANOPOROUS TITANIA ADSORBENTS (NTAs)

Nanoporous titania adsorbents (NTAs) were synthesized and applied to remove As(III) as well as As(V). Here, a surface complexation model (SCM) based on the diffuse layer model (DLM) was used to predict arsenic adsorption envelopes by NTAs under various environmental conditions. The extent of arsenic adsorption onto the two NTAs studied (Ti₍₂₅₎-SBA-15, MT) showed a regular pattern with pH. This pattern was not affected by total arsenic concentration or solid concentration. Optimal pH ranges for As(III) removal were between pH 4 and pH 7 for Ti₍₂₅₎-SBA-15 and between pH 8 and 11 for MT. Maximum removal efficiencies for As(V) by Ti₍₂₅₎-SBA-15 was observed to be near pH 4 and the maximum for MT was in the pH range between pH 4 and pH 7. However, at environmental pH (near pH 7 to pH 8) the extent of removal of As(III) and As(V) by MT was relatively greater than that by Ti₍₂₅₎-SBA-15. Surface complexation modeling for As(III,V) adsorption by NTAs demonstrated the role of mono- and bidentate surface complexes in arsenic adsorption. For As(III) sorption on Ti₍₂₅₎-SBA-15, monodentate surface complexes were more important than bidentate ones over the entire pH range investigated, but bidentate complexes played a role near pH 8. When As(III) was being sorbed onto MT, the model predicted that monodentate complexes dominate arsenic removal, except at below pH 6 when the higher initial concentration was used. For As(V) adsorption, monodentate surface complexes are apparently responsible for As(V) removal over the entire pH range at both initial As(V) concentrations. At higher solid concentration of Ti₍₂₅₎-SBA-15, the patterns of surface speciation that were observed for both As(III) and As(V) adsorption were the same as was observed at lower solid concentration (i.e., monodentate surface complexes dominate over entire pH, with small contribution of bidentate surface complexes below pH 8). This behavior was also true for As(III) adsorbed to MT. For As(V) adsorption onto MT, however,

the contribution of bidentate surface complexes at low pH became more intense than observed for lower solid concentration with the same initial As(V) concentration.

4. 1 Introduction

Arsenic contamination in surface or subsurface water has occurred widely and can be caused by naturally occurring weathering of rocks or by anthropogenic sources. Exposure to arsenic in drinking water can seriously affect the health of human beings. Recently, the United States Environmental Protection Agency set the maximum contaminant level (MCL) for arsenic in drinking water to 10 ppb, which required many treatment facilities to be applied to remove arsenic.

Mobility and toxicity of arsenic are strongly affected by oxidation state, so redox conditions can be very important in determining the behavior of arsenic. Under reducing conditions, arsenite (As(III)) is mainly present, whereas arsenate (As(V)) dominates in oxidizing environments. At circumneutral pH, neutral As(III) species (H_3AsO_3) and negatively charged As(V) species (H_2AsO_4^- or HAsO_4^{2-}) dominate. Thus, the fact that As(III) is uncharged at environmental pH makes it more mobile than As(V) in subsurface environments. Moreover, toxicity is much higher for As(III) than As(V). Adsorption technology has been widely used to remove various inorganic contaminants, including toxic metals, oxyanions and radionuclides. The advantages of adsorption include easier set-up, easier regeneration or disposal of adsorbents, and high removal efficiency. Up to now, various adsorbents such as iron oxides (goethite, lepidocrocite, hematite, magnetite), alumina, titania, and metal sulfides have been employed to remove arsenic from water (201-205). However, the structural limitations of conventional adsorbents limit their ability to lower arsenic concentrations to levels below the maximum contaminant level (MCL). These structural limitations include irregular pore structure and low specific surface area. Results presented in Section 3 demonstrated that two synthesized

nanoporous titania adsorbents, Ti₍₂₅₎-SBA-15 and MT, had higher specific surface areas and higher sorption capacity for As(III,V) at pH 7 than other NTAs studied. However, specific adsorption mechanisms for As(III,V) removal by NTAs have not been established.

Surface complexation models (SCM) have been widely used to describe adsorption of various inorganic contaminants on solids and several tools (e.g., FITEQL, MINEQL+, CD-MUSIC, PHREEQC) have been developed based on mass actions laws to solve equilibrium problems that include adsorption. Moreover, numerous different SCMs have been developed or modified to provide more precise quantitative interpretations for adsorption data, because these models are sensitive to solution composition. So far, SCMs based on assuming an inner-sphere complex mechanism and a single type of adsorption site has been widely used to describe sorption behavior. However, a two-site approach based on assuming a mixture of monodentate and bidentate complexes has not been extensively studied. Zeng et al. (2008) modeled the individual and competitive adsorption of arsenate and phosphate to iron oxide-based sorbent (Fe/Mn-hydroxide) using the DLM with eight complexation reactions based on including monodentate and bidentate surface complexes (206). They reported that in a non-competitive model, the relative importance of each surface complexes is strongly dependent on pH and total As loading. When pH is low, bidentate surface complexes dominate, but when pH is high or when arsenic loadings are low, monodentate complexes are dominate.

Adsorption mechanisms have been established with the help of surface analysis techniques, including X-ray absorption spectroscopy (XAS), wide-angle X-ray scattering (WAXS), and Fourier transform infrared spectrometry (FT-IR) (35, 39, 40, 205, 207-211). Several spectroscopic studies indicated that arsenate forms binuclear bridging complexes on iron oxides (goethite and ferrihydrite) or amorphous mineral-type solids (allophane). These are inner-sphere complexes that are formed via a ligand exchange mechanism between As(V) and surface-

coordinated water molecules or hydroxyl ions (212-214). However, the local coordination environment of arsenic adsorbed on solids appears to be dominated by the level of surface coverage (215). At low surface coverage, monodentate surface complexes are dominant, while bidentate mononuclear or binuclear surface complexes dominate at high surface loading (215). Therefore, this shows that the mechanism of arsenic adsorption can differ according to environmental conditions. Thus, it is expected that a SCM that considers both mono- and bidentate surface complexes will be able to better predict sorption behavior of arsenic under various conditions.

The purposes of this study are to characterize surface acid-base properties of NTAs using a diffuse layer model (DLM), to evaluate the sorption envelopes of As(III,V) by NTAs over a wide range of pH as affected by various solution compositions (arsenic concentrations and solid concentrations), to obtain surface complexation constants using DLM with a few surface reactions including both monodentate and bidentate surface complexes, and to evaluate the speciation of the surface complexes.

4.2 Materials and Methods

4.2.1 Materials

All chemicals used in this study were reagent grade or better and DIW (deionized water) was prepared using a Barnstead Nanopure filter system. The arsenic stock solution was prepared at a concentration of 1000 mg/L by dissolving NaAsO₂ (Sigma-Aldrich) or Na₂HAsO₄·7H₂O (Sigma-Aldrich) into deionized water. The specified arsenic concentration was obtained by diluting the arsenic stock solution with DIW. NaCl (Sigma-Aldrich) was used at a concentration of 0.01 or 0.10 M to maintain ionic strength. Zero-graded air and atomic grade acetylene were used as fuel gases during arsenic analysis by atomic adsorption spectrometry (AAS) and ultra high purity grade argon gas was the carrier gas in the hydride generation system. The NTAs

were synthesized and used in batch experiments to determine arsenic adsorption envelopes. The synthesis methods for the NTAs are described in Section 3.

4.2.2 Equilibrium Adsorption Experiments

All adsorption experiments were conducted in batch reactors. Prior to conducting experiments to determine arsenic adsorption envelopes, the required suspensions of NTAs were prepared by adding specified amounts to 1-L polyethylene bottles containing solutions of 0.1 M NaCl. The suspensions were equilibrated for 3 hours while mixing with a magnetic stirrer. Then, the initial pH of the solid suspension was adjusted by dropwise addition of 0.1 M HCl or 0.1 M NaOH to give values that were separated by 1.0 ± 0.05 . A 20-mL sample of the solid suspension was transferred to 25-mL polypropylene bottles, followed by addition of stock solution of As(III) or As(V) into each bottle to provide the desired initial arsenic concentration (7.82, 14.4, 45.6 μM). The samples were allowed to equilibrate over a 24 hour period while being mixed by a shaker operated at 200 rpm. After equilibration, the equilibrium pH of each aliquot was immediately measured at room temperature and the samples were filtered with 0.02 μm Whatman cellulose nitrate membranes. Measurements of pH were made with an Orion glass pH electrode calibrated using commercial buffers at pH 4.0, 7.0 and 10.0. The percent of arsenic adsorbed on the solid was calculated by Equation 4.1.

$$\% \text{ As(III or V) adsorbed} = \frac{([\text{As(III or V)}]_o - [\text{As(tot)}]_{\text{eq}})}{[\text{As(III or V)}]_o} \times 100 \quad (4.1)$$

where $[\text{As(III, V)}]_o$ is the initial concentration of arsenic and $[\text{As(tot)}]_{\text{eq}}$ is total As concentration (As(III) + As(V)) at equilibrium. A similar set of experiments was conducted to evaluate the effect of solid concentration (1, 2, 3 g/L) on As(III,V) adsorption envelopes.

4.2.3 Analytical Methods

Measurement of arsenic was conducted using a model Solar M6 atomic absorption spectrometer equipped with a model V90 continuous hydride generator (Thermo Elemental). Prior to analysis, all samples and standard solutions were prepared in 20-mL polyethylene plastic bottles in order to provide amounts greater than those needed to conduct duplicate experiments. Total arsenic was determined by mixing a sample flow of 7 mL/min with an equal flow of strong acid (6 M HCl) and a 3.5 mL/min flow of sodium borohydride. With these flows and pH conditions, both As(III) and As(V) can be reduced by borohydride to arsine gas (191). The arsine is transferred by argon gas with a 250 mL/min flow to the flame AA, where its absorbance is determined. Measured absorbances were used to calculate arsenic concentrations using a standard calibration curve. The same conditions were used for calibration standards and experimental samples.

4.2.4 Potentiometric Titration

Potentiometric titrations were carried out to determine intrinsic surface acidity constants for protonation of the surface hydroxyl groups. Suspensions with solids concentrations of 10 g/L and with two NaCl concentrations (0.01 M, 0.1 M) were mixed by a magnetic stirrer for 3 hours under inert atmosphere (N₂ purging). Thereafter, the solid suspensions were titrated by adding no more than 0.3 mL of 0.01 or 0.1 M HCl or NaOH to achieve pH values separated by 0.5 unit. Values of pH were measured before addition of acid or base and after an equilibration period of 5 minutes. The effect of atmospheric CO₂ on pH of the solid suspensions was assumed to be negligible, because all titration experiments were conducted in an environment purged by nitrogen gas. The FITEQL 4.0 software program was used to determine optimal values of the surface acidity constants of NTAs by fitting the diffuse layer model (DLM) to titration data (216). Figure 4.1 shows the results of the potentiometric titrations and model

predictions. The apparent acidity constants for surface acidity reactions on NTAs can be expressed in terms of ion activity product multiplied by an exponential term that describes the effects of electrostatic interactions between the charged surface and hydrogen ion (Table 4.1) (217). Values for the surface acidity constants of these solids were calculated using the two equations in Table 4.1 and the corresponding mass action law based on the diprotic surface group model (2-pK model).

Table 4.1 Intrinsic surface acidity constants for Ti₍₂₅₎-SBA-15 and MT using diffuse layer model.

| Reactions | Adsorbent | Ionic strength, M | Log K |
|---|----------------------------|-------------------|-------|
| $\equiv \text{TiOH} + \text{H}^+ \leftrightarrow \equiv \text{TiOH}_2^+$; $\log K_{a1}^{\text{int}}$ $K_{a1}^{\text{int}} = \frac{[\equiv \text{TiOH}_2^+]}{[\equiv \text{TiOH}][\text{H}^+]} \exp\left(\frac{z_1 F \phi_0}{RT}\right)$ | Ti ₍₂₅₎ -SBA-15 | 0.01 | 3.28 |
| | | 0.1 | 2.87 |
| | MT | 0.01 | 4.39 |
| | | 0.1 | 4.12 |
| $\equiv \text{TiOH}_2^+ \leftrightarrow \equiv \text{TiO}^- + \text{H}^+$; $\log K_{a2}^{\text{int}}$ $K_{a2}^{\text{int}} = \frac{[\equiv \text{TiO}^-][\text{H}^+]}{[\equiv \text{TiOH}_2^+]} \exp\left(\frac{z_2 F \phi_0}{RT}\right)$ | Ti ₍₂₅₎ -SBA-15 | 0.01 | -5.03 |
| | | 0.1 | -5.79 |
| | MT | 0.01 | -4.38 |
| | | 0.1 | -4.47 |

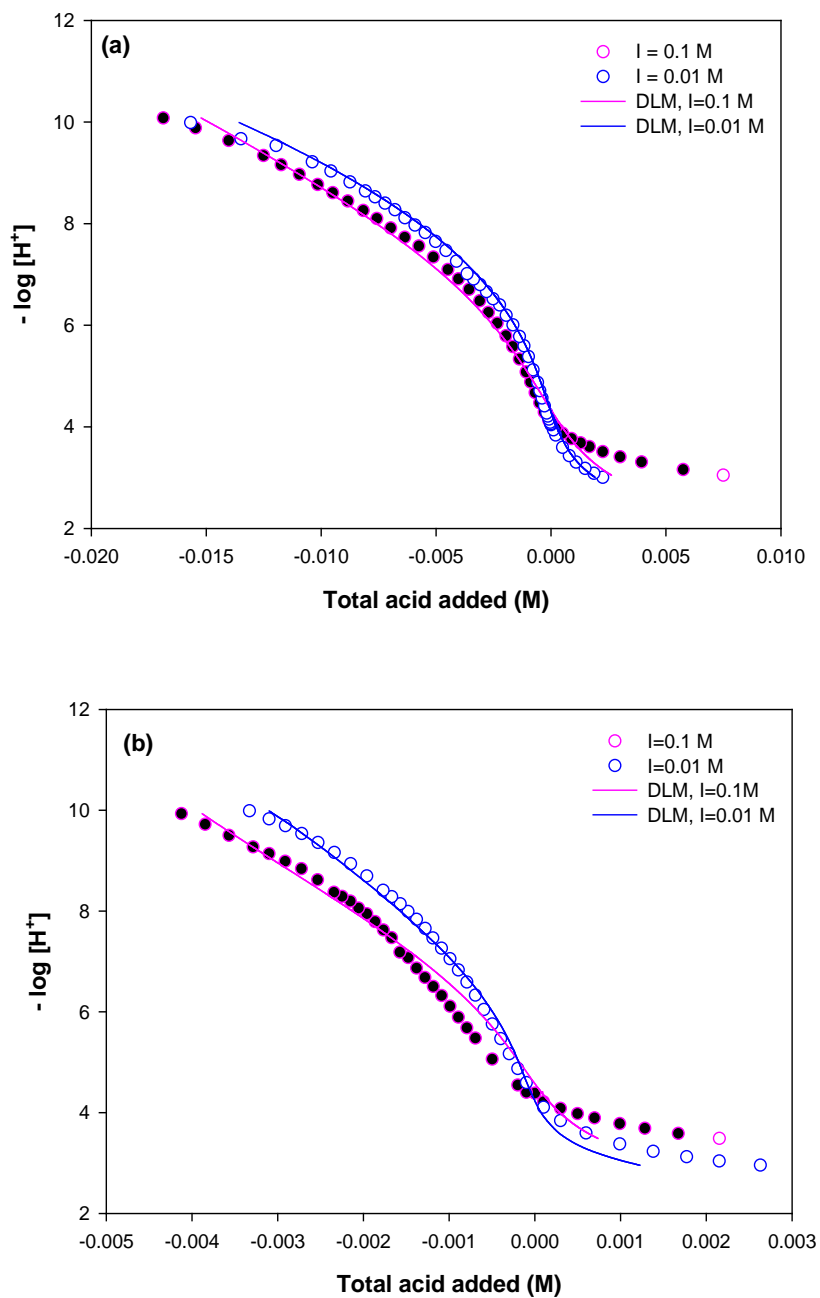


Figure 4.1 Fits of DLM to titration data for (a) $Ti_{(25)}-SBA-15$ and (b) MT in 0.01 and 0.1 M NaCl background electrolyte: The symbols represent experimental data and lines indicate the predictions of the DLM.

4.2.5 Surface Complexation Model

The diffuse layer model (DLM) was used to predict arsenic adsorption envelopes over a wide range of pH by varying total arsenic concentration and solid loadings. In this study, FITEQL was used to fit DLM to adsorption envelope data, so that values of the intrinsic surface complexation constants are chosen using a nonlinear least squares optimization method. To ensure the best fits of each model to experimental sorption data, a goodness-of-fit parameter (V_y) was used. This parameter was defined as the weighted sum of squares of the difference in data points between model simulations and experimental data (WSOS) divided by the degrees of freedom (DF) as shown in Equation 4.2.

$$V_y = WSOS / DF = \frac{\sum (Y_i / s_i)^2}{(n_p n_c) - n_a} \quad (4.2)$$

where Y_i and s_i are the residual and the error estimate for each data point, n_p is the number of data points, n_c is the number of components for which both total and free concentrations are known, and n_a is the number of adjustable parameters. Here, lower values of V_y indicate a better fit of a model to data. When values of V_y are between 0.1 and 20, the model fitting is considered to be reasonably good (216).

In order to provide better fit to sorption data, a two-site approach was applied, where mono- and bidentate binuclear surface complexes were assumed to occur at two separate adsorption sites ($\equiv\text{SOH}$ and $\equiv(\text{SOH})_2$). The related surface reactions between NTAs and As(III,V) and their surface complexation constants are summarized in Table 4.2.

Table 4.2 Arsenic surface reactions and intrinsic surface complexation constants.

| Surface complexation reactions | Log K | |
|--|----------------------------|------|
| For As(III) | Ti ₍₂₅₎ -SBA-15 | MT |
| <u>monodentate complexes</u> | | |
| $\equiv \text{TiOH} + \text{AsO}_3^{3-} + 3\text{H}^+ \leftrightarrow \equiv \text{TiOAsO}_2\text{H}_2 + \text{H}_2\text{O}; \log K_{\text{As}3}^{\text{m},1}$ | 43.1 | 50.3 |
| $\equiv \text{TiOH} + \text{AsO}_3^{3-} + 2\text{H}^+ \leftrightarrow \equiv \text{TiOAsO}_2\text{H}^- + \text{H}_2\text{O}; \log K_{\text{As}3}^{\text{m},2}$ | 34.8 | 46.0 |
| <u>bidentate binuclear complexes</u> | | |
| $\equiv (\text{TiOH})_2 + \text{AsO}_3^{3-} + 3\text{H}^+ \leftrightarrow \equiv (\text{TiO})_2\text{AsOH} + 2\text{H}_2\text{O}; \log K_{\text{As}3}^{\text{b},1}$ | 49.7 | 43.0 |
| $\equiv (\text{TiOH})_2 + \text{AsO}_3^{3-} + 2\text{H}^+ \leftrightarrow \equiv (\text{TiO})_2\text{AsO}^- + 2\text{H}_2\text{O}; \log K_{\text{As}3}^{\text{b},2}$ | 43.9 | 38.1 |
| For As(V) | | |
| <u>monodentate complexes</u> | | |
| $\equiv \text{TiOH} + \text{AsO}_4^{3-} + 3\text{H}^+ \leftrightarrow \equiv \text{TiOAsO}_3\text{H}_2 + \text{H}_2\text{O}; \log K_{\text{As}5}^{\text{m},1}$ | 25.4 | 25.4 |
| $\equiv \text{TiOH} + \text{AsO}_4^{3-} + 2\text{H}^+ \leftrightarrow \equiv \text{TiOAsO}_3\text{H}^- + \text{H}_2\text{O}; \log K_{\text{As}5}^{\text{m},2}$ | 18.2 | 21.1 |
| $\equiv \text{TiOH} + \text{AsO}_4^{3-} + \text{H}^+ \leftrightarrow \equiv \text{TiOAsO}_3^{2-} + \text{H}_2\text{O}; \log K_{\text{As}5}^{\text{m},3}$ | 10.2 | 14.8 |
| <u>bidentate binuclear complexes</u> | | |
| $\equiv (\text{TiOH})_2 + \text{AsO}_4^{3-} + 3\text{H}^+ \leftrightarrow \equiv (\text{TiO})_2\text{AsO}_2\text{H} + 2\text{H}_2\text{O}; \log K_{\text{As}5}^{\text{b},1}$ | 42.4 | 39.5 |
| $\equiv (\text{TiOH})_2 + \text{AsO}_4^{3-} + 2\text{H}^+ \leftrightarrow \equiv (\text{TiO})_2\text{AsO}_2^- + 2\text{H}_2\text{O}; \log K_{\text{As}5}^{\text{b},2}$ | 30.4 | 29.6 |

4.3 Results and Discussion

4.3.1 Arsenic Adsorption Envelopes: Variation of Initial Arsenic Concentration

To investigate the effect of pH and initial As(III) concentration on the extent of adsorption onto NTAs, three different initial As(III) concentrations (7.82, 14.4, and 45.6 μM) were chosen. The diffuse layer model (DLM) with a two-site model approach was used to describe As(III) adsorption envelopes. Figure 4.2(a1) shows that As(III) removal by Ti₍₂₅₎-SBA-15 was somewhat constant over the pH range between pH 4 and 7, but decreased as pH increased from about pH 8.5. This sorption pattern is similar to iron (hydr)oxide (e.g., HFO, goethite) for which maximum As(III) sorption occurs at pH 6-9 and minimum sorption occurs at pH > 9 (218). The reduction in As(III) adsorption at high pH may be caused by increased electrostatic

repulsion between negatively charged sorption sites ($\equiv\text{TiO}^-$) and arsenic species ($[\text{H}_2\text{AsO}_3^-]$). The percentage of As(III) adsorbed decreased with increasing total As(III) concentration. For instance, in the pH range 4-7, the percent As(III) adsorbed at $[\text{As(III)}]_o=45.6 \mu\text{M}$ was two times lower than that at $[\text{As(III)}]_o=7.82 \mu\text{M}$. The DLM model fitted sorption data well, except for some regions where the model mostly underestimated As(III) adsorption. Three such regions were at pH above 9.2 with $[\text{As(III)}]_o=7.32 \mu\text{M}$, at pH above 8.5 with $[\text{As(III)}]_o=14.4 \mu\text{M}$, and at pH above 8 with $[\text{As(III)}]_o=45.6 \mu\text{M}$. However, the model somewhat overestimated removals at pH 4.5-7.5 with $[\text{As(III)}]_o=45.6 \mu\text{M}$. Figures 4.2(a2) and 4.2(a3) indicate the predicted model speciation of As(III) adsorbed on $\text{Ti}_{(25)}\text{-SBA-15}$ at the lowest and highest initial As(III) concentrations. Figure 4.2(a2) shows that the monodentate surface complex ($\equiv\text{TiOAsO}_2\text{H}_2$) was the dominant species until pH approaches pH 9.0. However, the deprotonated mono- and bidentate species ($\equiv\text{TiOAsO}_2\text{H}$ and $\equiv(\text{TiO})_2\text{AsO}^-$) also contributed to As(III) adsorption as pH increased from pH 6.0, but they did not account for more than 20 % As(III) removal. The speciation profiles of adsorbed As(III) with $[\text{As(III)}]_o=45.6 \mu\text{M}$ (Figure 4.2(a3)) were similar to those with $[\text{As(III)}]_o=7.82 \mu\text{M}$ (Figure 4.2(a2)).

Figure 4.2(b1) shows As(III) adsorption on MT as function of pH for various initial As(III) concentrations. As observed on $\text{Ti}_{(25)}\text{-SBA-15}$, the maximum percent removal of As(III) on MT decreases with increasing As(III) concentration over the entire pH range. However, maximum and minimum removals of As(III) were seen around pH 8-11 and at low pH, respectively. At $[\text{As(III)}]_o=45.6 \mu\text{M}$, the percent removal of As(III) at acidic pH (4~6) and at basic pH (8~10) were lower than those at $[\text{As(III)}]_o=7.82 \mu\text{M}$ by a factor of 6.2 and 1.5, respectively. As(III) adsorption envelopes were simulated well by the DLM, except at high pH with $[\text{As(III)}]_o=7.82 \mu\text{M}$ and with $[\text{As(III)}]_o=14.4 \mu\text{M}$, where the model underestimates adsorption, and at pH below pH 6.5 with $[\text{As(III)}]_o=7.82 \mu\text{M}$, where the model overestimates

adsorption. The model fits to As(III) removals shown in Figure 4.2(b1) for initial arsenic concentrations of 7.82 μM and 45.6 μM are reproduced by Figures 4.2(b2) and 4.2(b3) along with surface speciation predicted by the DLM. At the lower initial As(III) concentration, the monodentate surface complexes ($\equiv\text{TiOAsO}_2\text{H}_2$ and $\equiv\text{TiOAsO}_2\text{H}^-$) dominated over the entire pH range, with small contributions of the bidentate surface complexes ($\equiv(\text{TiO})_2\text{AsOH}$ and $\equiv(\text{TiO})_2\text{AsO}^-$) in the pH range between pH 4 and 6.5 (Figure 4.2(b2)). As initial As(III) concentration increased, however, the contribution of the monodentate surface complex to As(III) adsorption at low pH was replaced by the bidentate binuclear surface complex ($\equiv(\text{TiO})_2\text{AsOH}$). As pH approached neutral and increased, the deprotonated monodentate species ($\equiv\text{TiOAsO}_2\text{H}^-$) became dominant. Therefore, it can be concluded that as initial As(III) concentration increases, the bidentate surface complexes become more important. Also, the optimal pH range for removal of As(III) by $\text{Ti}_{(25)}$ -SBA-15 was observed at pH 6-8.5 and up to circumneutral pH for MT.

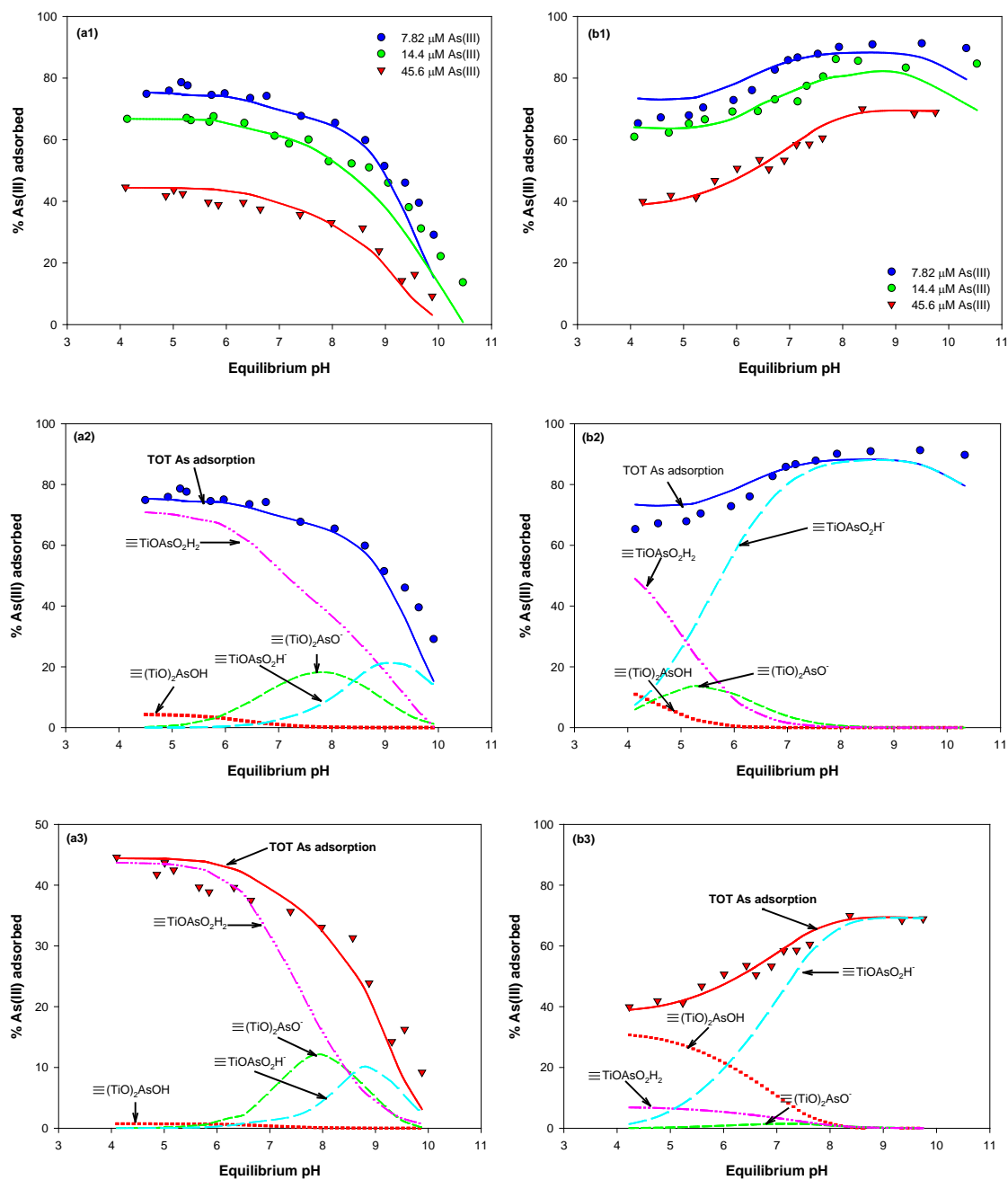


Figure 4.2 Modeling As(III) adsorption on NTAs. Effect of pH at various initial As(III) concentrations on percent adsorption by: (a1) Ti₍₂₅₎-SBA-15 and (b1) MT. Surface speciation predicted by DLM as function of pH for: (a2) Ti₍₂₅₎-SBA-15 + 7.82 μM As(III), (a3) Ti₍₂₅₎-SBA-15 + 45.6 μM As(III), (b2) MT + 7.82 μM As(III), (b3) MT + 45.6 μM As(III).

Figure 4.3 shows the effect of pH and initial As(V) concentration on the extent of adsorption by Ti₍₂₅₎-SBA-15 and MT. Figure 4.3(a1) shows that the effect of pH on As(V) adsorption by Ti₍₂₅₎-SBA-15 is similar to that observed for adsorption on metal (hydr)oxides. With both adsorbents, the highest and lowest removals of As(V) were observed at acidic and basic pH, respectively, with steep decreases in adsorption in the range between pH 5 and pH 8. Since the p*H*_{zpc} of Ti₍₂₅₎-SBA-15 is 4.3, the sorption sites at low pH are expected to be positively charged, which contributes to improved removal of the negatively charged As(V) by electrostatic attraction, whereas the opposite is true at higher pH. In addition, the percent As(V) adsorbed decreased a small amount with increasing As(V) initial concentration with the bigger differences observed at low pH. The percent As(V) adsorbed at [As(V)]_o=39.4 μM was 1.6 times lower than that observed at [As(V)]_o=9.86 μM, when pH < 7. In order to attain over 80 % removal of As(V) by Ti₍₂₅₎-SBA-15, the pH should be below about pH 5.0. As shown in Figure 4.3(a1), the model fits to As(V) adsorption by Ti₍₂₅₎-SBA-15 were simulated well except at pH below 5.0 with [As(V)]_o=19.7 μM and at pH below 6.0 with [As(V)]_o=39.4 μM, where As(V) adsorption was underestimated. Figures 4.3(a2) and 4.3(a3) show the model predictions for speciation of As(V) adsorbed on Ti₍₂₅₎-SBA-15 under lowest and highest initial As(III) concentration. At low pH, the mono- (≡TiOAsO₃H₂) and bidentate binuclear surface complexes (≡(TiO)₂AsO₂⁻) coexist and at circumneutral pH the deprotonated monodentate specie (≡TiOAsO₃H) becomes more important and at higher pH doubly charged monodentate specie (≡TiOAsO₃²⁻) dominates. At the higher initial As(V) concentration, the bidentate binuclear surface complexes (≡(TiO)₂AsO₂⁻) are less important.

Figure 4.3(b1) displays As(V) adsorption envelopes for MT that are similar to those for Ti₍₂₅₎-SBA-15. The effect of pH on As(V) adsorption is similar to that observed for other metal (hydr)oxides with p*H*_{zpc} of 5~7, but the slopes of adsorption edges are not as steep, resulting in

the extension of high As(V) removals to circumneutral pH. In this pH range, the removals of As(V) by MT were higher than those by Ti₍₂₅₎-SBA-15 by a factor of 3.2. In addition, As(V) removals over the entire pH range studied were lower with higher initial As(V) concentration. At pH below 7.0, with [As(V)]_o=9.86 μM the DLM overestimated As(V) adsorption and at pH above 7.0, with [As(V)]_o=19.7 and 39.4 μM, the model highly underestimates As(V) adsorption. Figures 4.3(b2) and (b3) indicate the pH dependence of the speciation of surface complexes with [As(V)]_o=9.86 μM and [As(V)]_o=39.4 μM, respectively. At the lowest initial As(V) concentration, the monodentate surface complexes ($\equiv\text{TiOAsO}_3\text{H}_2$, $\equiv\text{TiOAsO}_3\text{H}$, $\equiv\text{TiOAsO}_3^{2-}$) play the important role in As(V) adsorption over the entire pH range examined with only a small contribution of the bidentate complex ($\equiv(\text{TiO})_2\text{AsO}_2^-$) being observed at low pH (Figure 4.3(b2)). At the higher initial As(V) concentrations, the pattern of surface speciation was similar to that observed at the lower concentration. As observed with Ti₍₂₅₎-SBA-15, the fully protonated monodentate species ($\equiv\text{TiOAsO}_3\text{H}_2$) contributed strongly to As(V) adsorption up to circumneutral pH. Therefore, it can be concluded for As(V) adsorption on NTAs that the monodentate surface complexes play a more important role in adsorption than do the bidentate binuclear surface complexes for all initial As(V) concentrations studied.

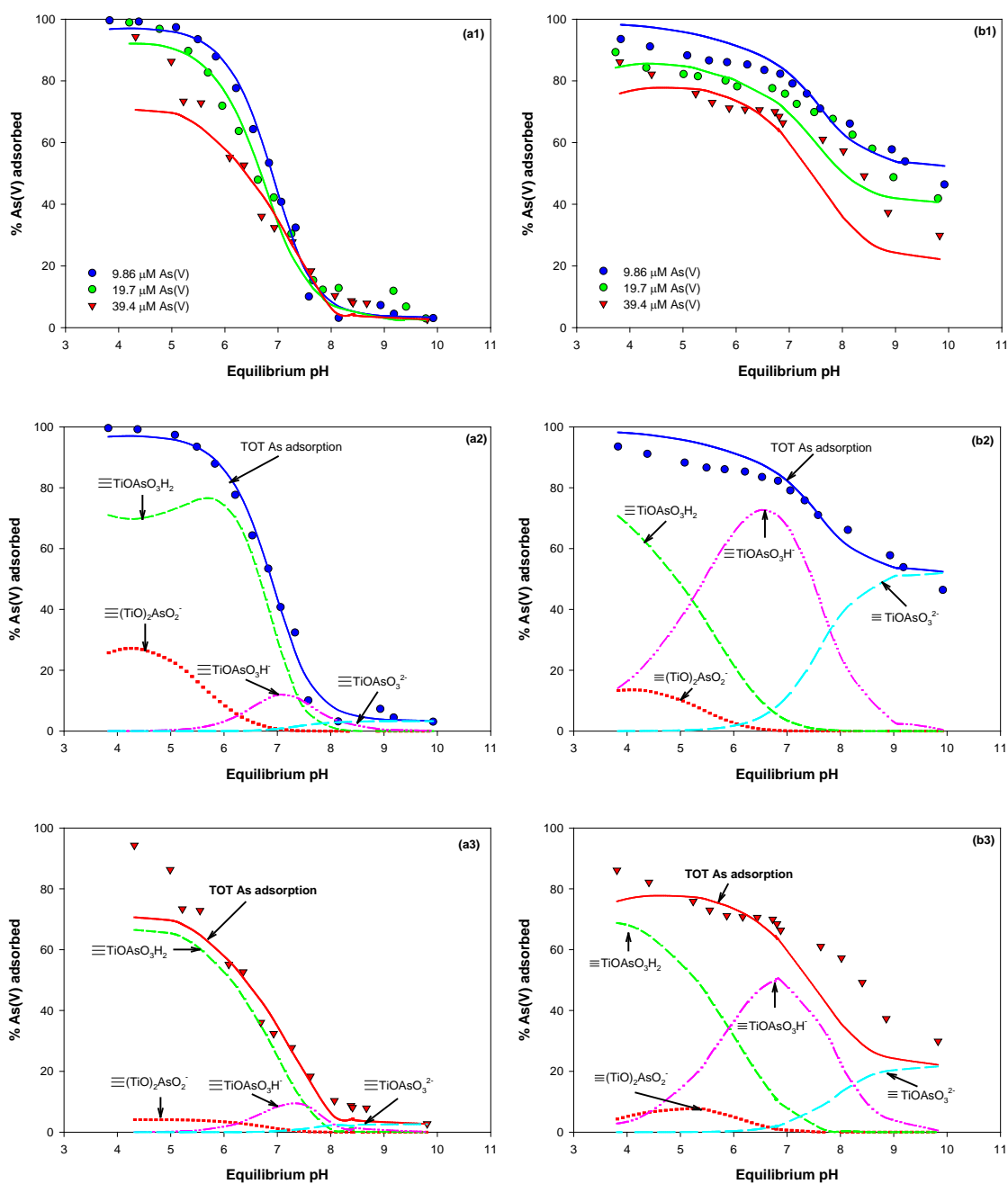


Figure 4.3 Modeling As(V) adsorption on NTAs. Effect of pH at various initial As(V) concentrations on percent adsorption by: (a1) $\text{Ti}_{(25)}$ -SBA-15, (b1) MT; Surface speciation predicted by DLM as function of pH for: (a2) $\text{Ti}_{(25)}$ -SBA-15 + 9.86 μM As(V), (a3) $\text{Ti}_{(25)}$ -SBA-15 + 39.4 μM As(V), (b2) MT + 9.86 μM As(V), (b3) MT + 39.4 μM As(V).

4.3.2 Modeling Arsenic Adsorption Envelopes: Various Solid-To-Liquid Ratios

Adsorption of As(III) and As(V) on $\text{Ti}_{(25)}$ -SBA-15 and MT was investigated by varying solid loadings (i.e., 1, 2, 3 g/L). Figure 4.4 shows that As(III) adsorption on $\text{Ti}_{(25)}$ -SBA-15 and MT was highly dependent on solid concentration as well as solution pH. Figure 4.4(a1) shows that for 1 g/L of $\text{Ti}_{(25)}$ -SBA-15, high removal was observed in the pH range 4-6, but higher solid concentrations cause As(III) adsorption edges to be shifted toward basic pH, so that the plateau showing high As(III) removal becomes more extended. For solid concentration of 2 and 3 g/L, the DLM underestimated adsorption of As(III) on $\text{Ti}_{(25)}$ -SBA-15 over basic pH ranges. Figures 4.4(a2) and 4.4(a3) show predictions of the model for surface speciation on $\text{Ti}_{(25)}$ -SBA-15 at concentrations of 1 g/L and 3 g/L. Figure 4.4(a2) shows that the monodentate surface complexes ($\equiv\text{TiOAsO}_2\text{H}_2$, $\equiv\text{TiOAsO}_2\text{H}$) are predominant at low and high pH, but the negatively charged bidentate surface complex ($\equiv(\text{TiO})_2\text{AsO}^-$) dominates near pH 8. Figure 4.4(a3) shows that the monodentate surface complexes ($\equiv\text{TiOAsO}_2\text{H}_2$, $\equiv\text{TiOAsO}_2\text{H}$) are predominant over all pH ranges, but bidentate surface complexes ($\equiv(\text{TiO})_2\text{AsOH}$, $\equiv(\text{TiO})_2\text{AsO}^-$) are responsible for up to 23 % removal of As(III).

Figure 4.4(b1) shows that the extent of As(III) adsorption by MT varies according to solid concentration. Removals of 64%, 76%, and 88% at pH 4 and 80%, 85%, and 92% at pH 10 were observed at solid concentrations of 1, 2, and 3 g/L, respectively. At a solid concentration of 3 g/L, the percent of As(III) adsorbed was above 88 % over the entire pH range investigated. Good agreement between the model fits and the experimental data were obtained at pH above neutral, regardless of the solid concentration. However, at lower pH, As(III) removals with solid loadings of 2 g/L and 3 g/L were underestimated and removals at a loading of 1 g/L was underestimated. Figure 4.4(b2) and 4.4(b3) show the predicted speciation of As(III) adsorbed on 1 g/L and 3 g/L of MT, respectively. Figure 4.4(b2) shows that the monodentate surface

complexes are predicted to account for most of the sorbed As(III), with $\equiv\text{TiOAsO}_2\text{H}_2$ being predominant below pH 5.3 and $\equiv\text{TiOAsO}_2\text{H}$ dominating at higher pH. Below pH 7, however, up to 15 % As(III) removal was associated with bidentate surface complexes ($\equiv(\text{TiO})_2\text{AsO}^-$ or $\equiv(\text{TiO})_2\text{AsOH}$). As the higher solid concentration, there were no important changes in the pattern of surface speciation compared to that observed at solid concentration of 1 g/L (Figure 4.4(b2)). Consequently, it can be concluded that As(III) adsorption on NTAs was predominantly due to formation of monodentate surface complexes at all solid concentrations and over the entire pH range examined.

Figure 4.5 shows the effect of solid loading (1, 2, 3 g/L) on As(V) adsorption by $\text{Ti}_{(25)}$ -SBA-15 and MT. As(V) adsorption by $\text{Ti}_{(25)}$ -SBA-15 was strongly dependent on solution pH but little affected by solid loading (Figure 4.5(a1)). The model shows relatively good fits to the experimental data, except in the case of solid loadings of 2 g/L and 3 g/L, where data was underpredicted below pH 5.5 and overpredicted between pH 5.5 and near pH 7. Figures 4.5(a2) and 4.5(a3) show the distribution of surface complex species calculated by the DLM using the two-sites approach at solids loadings of 1 g/L and 3 g/L, respectively. At 1 g/L, the monodentate surface complexes are predicted to be predominant, with $\equiv\text{TiOAsO}_3\text{H}_2$ dominating at pH below neutral. Other monodentate species contribute to As(V) adsorption below pH 6 ($\equiv\text{TiOAsO}_3^{2-}$) and between pH 6 and pH 8 ($\equiv\text{TiOAsO}_3\text{H}$). For 3 g/L, the pattern of the predicted model speciation of As(V) is similar to that observed for 1 g/L, but the increased As(V) adsorption at low pH is due to the growth of the bidentate surface complex ($\equiv\text{TiOAsO}_3^2$) rather than the monodentate surface complexes ($\equiv\text{TiOAsO}_3\text{H}_2$). The effect of solid concentration (1, 2, 3 g/L) on As(V) adsorption by MT was also investigated and the DLM model was fit to experimental data (Figure 4.5(b1)). The percentage of As(V) removed by 1 g/L MT was only a little lower than that removed by loadings of 2 g/L and 3 g/L.

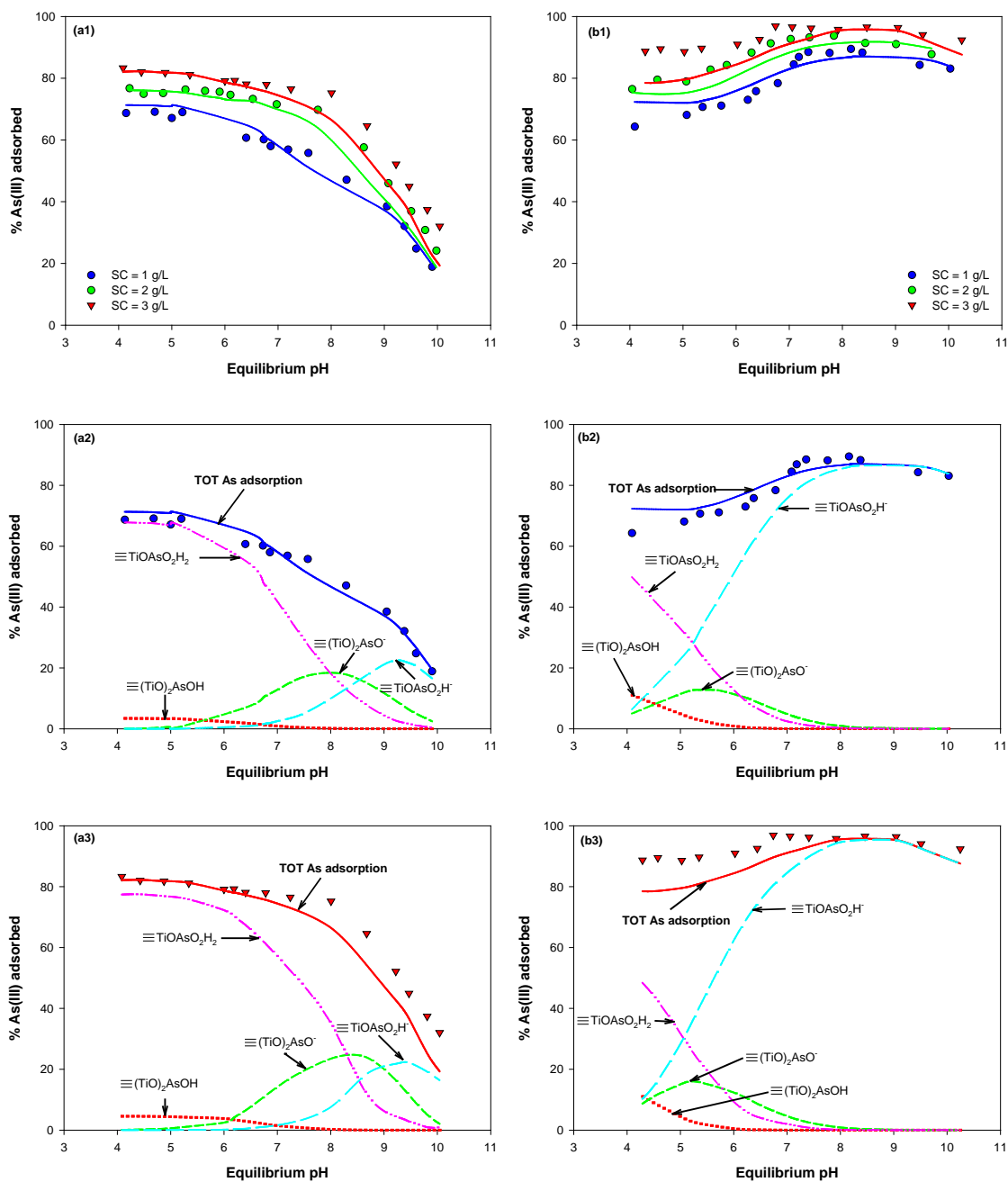


Figure 4.4 Modeling As(III) adsorption on NTAs. Effect of pH at various solid concentrations on adsorption of As(III) by: (a1) Ti₍₂₅₎-SBA-15 and (b1) MT. Surface speciation predicted by DLM as function of pH for: (a2) 1 g/L Ti₍₂₅₎-SBA-15, (a3) 3 g/L Ti₍₂₅₎-SBA-15, (b2) 1 g/L MT, (b3) 3 g/L MT.

The model predictions for removal of As(V) on MT were generally in good agreement with experimental data. However, the models slightly overpredicted As(V) removal between pH 6 and pH 7.5 for a loading of 1 g/L and underestimated removals above pH 9 for a loading of 3 g/L. Figures 4.5(b2) and 4.5(b3) display the predicted speciation of As(III) complexes on the surface of MT at solid concentrations of 1 g/L and 3 g/L. For a loading of 1 g/L (Figure 4.5(b2)), the bidentate ($\equiv(\text{TiO})_2\text{AsO}_2^-$) species dominates at the lowest pH. As pH is raised, the predominant species shifts to monodentate surface complexes: $\equiv\text{TiOAsO}_3\text{H}_2$ becomes dominant at pH 5.5; $\equiv\text{TiOAsO}_3\text{H}$ becomes dominant at pH 6.5; and $\equiv\text{TiOAsO}_3^{2-}$ becomes dominant at pH 8.5. At a loading of 3 g/L, only the bidentate complex ($\equiv(\text{TiO})_2\text{AsO}_2^-$) is important to As(V) adsorption below pH 6. As pH increases, the deprotonated monodentate species ($\equiv\text{TiOAsO}_3\text{H}$ and $\equiv\text{TiOAsO}_3^{2-}$) dominate. Therefore, it appears that higher solid concentrations of MT favor formation of bidentate surface complexes of As(V) at lower pH and deprotonated monodentate surface complexes at higher pH 6.0.

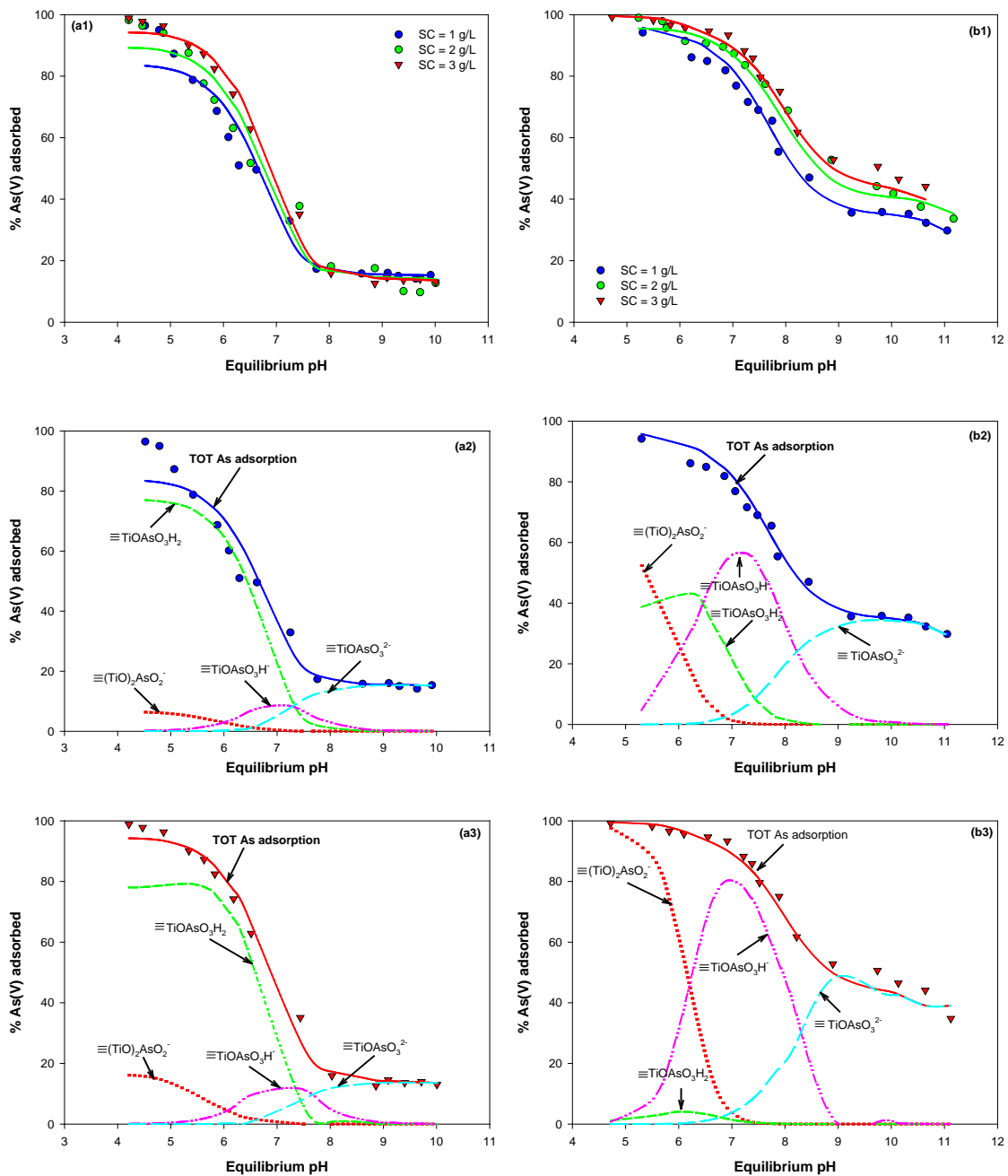


Figure 4.5 Modeling As(V) adsorption on NTAs. Effect of pH at various solid concentration on adsorption of As(V) by: (a1) $\text{Ti}_{(25)}\text{-SBA-15}$ and (b1) MT. Surface speciation predicted by the DLM as a function of pH for: (a2) 1 g/L $\text{Ti}_{(25)}\text{-SBA-15}$, (a3) 3 g/L $\text{Ti}_{(25)}\text{-SBA-15}$, (b2) 1 g/L MT, (b3) 3 g/L MT.

5. SORPTION OF SELENIUM(IV) AND SELENIUM(VI) TO SYNTHETIC PYRITE (FeS₂): 1. MICROSCOPIC AND SPECTROSCOPIC ANALYSES

In this study, pyrite (FeS₂) was synthesized and used to remove Se(IV) and Se(VI) selectively from solution, because selenium has a strong affinity to iron surface sites. Transport of selenium in water could be limited by the formation of precipitates such as FeSe or FeSe₂ via its adsorption onto pyrite and subsequent reactions. Surface properties of pyrite were characterized by surface analysis techniques, including XRD, TEM, SEM and AFM. These analyses showed that synthetic pyrite was identical to the mineral and was crystalline with a highly regular rectangular morphology. After pyrite was contacted with Se(IV), binding energies of peaks in the XPS Se 3d spectra were observed to increase with time which indicates that Se(IV) reacts with the pyrite surface. The XPS Fe 2p spectra showed small increases in Fe(III)-S and Fe(III)-O which indicates that surface Fe(II) was oxidized by Se(IV) or other compounds. Evidence was found for the presence of additional sulfur species, such as sulfide and sulfate. This indicates that sulfur at the surface of pyrite (S₂²⁻) can be both oxidized and reduced after contact with Se(IV). XPS analysis of pyrite at different times after contact with Se(VI) indicated no changes in Se 3d spectra. Also, no substantial changes in the iron and sulfur XPS spectra were observed. Additional evidence for the formation of precipitates on pyrite after contact with Se(IV) was seen in SEM images that showed rod-like particles. In contrast, no important changes in the pyrite surface were observed after contact with Se(VI) during a period of 30 days. AFM analysis indicated that pyrite contacted with Se(IV) has a topography image with much higher peaks and phase image with higher voltage compared to pyrite contacted with Se(VI). This is probably due to formation of precipitates or surface complexes on the pyrite surface that leads to bending deformation.

5.1 Introduction

One of the environmental issues regarding selenium (Se) is related to a very narrow concentration range between its nutritional deficiency and toxicity (219). Therefore, its mobility, fate, and concentration in the environment have important implications for human health and the growth of animals and plants (220). Selenium is released from natural and anthropogenic sources and coal-fired power stations are one of the largest anthropogenic sources. Selenium is present in coal at small concentrations of several parts per million and most of that is associated with organic matter, but 5-10 % appears to be associated with pyrite or other mineral sulfides (3, 57). Selenium in all phases can be released to the environment if not managed continuously. Recently, selenium (^{79}Se , $t_{1/2}=1.0\times 10^6$ years) has been found in radioactive wastes resulting from processing spent fuel and in releases from operating nuclear reactors and fuel reprocessing plants (62).

Selenium is an analogue of sulfur, so it is expected that its mechanisms of surface complexation are quite similar. Selenium can exist in four oxidation states (-II, 0, IV, and VI), depending on aqueous redox status. Under more reducing conditions, selenide (Se(-II)) is the dominant valence state and it can form metal selenide minerals or gaseous hydrogen selenide (H_2Se). Zero-valent selenium (Se(0)) can also exist under reducing conditions and it forms crystalline or amorphous solids that have low solubility in water (220). Selenate (Se(VI)) is a weakly basic group IV oxyanion, which is fully oxidized and exists as a tetrahedral oxyanion. It will exist as biselenate (HSeO_4^-) or selenate (SeO_4^{2-}) depending on whether pH is below or above the pK_a of 1.7 (58, 221). Another important form of selenium is selenite (Se(IV)), which can exist as selenious acid, a weak diprotic acid with pK_a values of 2.64 and 8.4. Thus, selenite is can be found as H_2SeO_3 , HSeO_3^- , and SeO_3^{2-} depending on aqueous pH (222). Therefore, at natural environmental pH, the primary species will be SeO_4^{2-} and HSeO_3^- . Many studies have

proven that selenite (SeO_3^{2-}) forms stronger complexes than selenate (SeO_4^{2-}), due to its higher affinity for sorption sites (220, 223). Consequently, changes in those species can affect the transport and solubility of selenium.

One treatment technology for selenium is bioremediation, which uses microbial reduction to reduce the oxidized selenium compounds (Se(VI) and Se(IV)) to elemental selenium (Se(0)) that is relatively insoluble (224). However, the high cost of chemical nutrients (e.g., acetate, lactate, and glucose) makes bioremediation expensive for treating selenium under field conditions. However, adsorption processes have been intensively employed to remove selenium oxyanions, because of the ease of set-up, ease of phase-separation, and increased safety. Moreover, adsorption of selenium onto iron oxy-hydroxides has been adopted as the Best Demonstrated Available Technology (BDAT) by the EPA (225).

When hydrous metal oxides containing selenium are disposed to landfills, however, the residuals may be unstable due to reductive dissolution of the iron oxy-hydroxides under the anoxic conditions. In addition, removal of selenium by adsorption onto iron oxy-hydroxides can be inhibited by competing anions such as phosphate or sulfate in a way that is similar to that observed during arsenic treatment. Since selenide is often found in subsurface environments as a component of metal sulfides, metal selenides (FeSe , FeSe_2) are expected to be stable (62). Until now, little information has been provided on the stability of pyrites reacted with selenium.

Therefore, an ultimate goal of this study is to stabilize the pyrite residuals after contact with selenium under various solution conditions. This Section focuses on evaluating both surface properties of synthetic pyrite and surface reactions between the pyrite and selenium using surface analyses techniques including scanning electron microscopy (SEM), transmission electron microscopy (TEM), X-ray photoelectron spectroscopy (XPS) and atomic force microscopy (AFM).

5.2 Materials and Method

5.2.1 Materials

All chemicals used in this study were of analytical-grade quality. To provide deionized and deoxygenated water for sorption experiment, nanopure water (resistance > 18.3 M Ω) produced by a Milli-Q water purification system was first purged with N₂ gas (ultra high purity grade) for at least 2 hours and subsequently equilibrated overnight with the gas (5% H₂/95% N₂) in an anaerobic chamber. Selenite (Se(IV)) and selenate (Se(VI)) stock solutions (1000 ppm) were prepared by dissolving Na₂SeO₃ and Na₂SeO₄ (Sigma-Aldrich), respectively. Prior to initiating sorption experiments, all glassware and plasticware was uncapped and placed into an anaerobic chamber for at least 1 day to remove all oxygen sorbed on wall. Oxygen was scavenged in the anaerobic chamber (Coy Laboratory Products Inc.) by reaction with 5% H₂, promoted by a palladium catalyst.

5.2.2 Synthesis of Nanoparticulate Pyrite

Pyrite was synthesized by the modified Wei's method which uses FeCl₃ and NaHS as sources of Fe(III) and sulfide (134). A Fe/S molar ratio of 0.5 was obtained by mixing equal volumes of 0.1 M FeCl₃ and 0.2 M NaHS stock solutions in an anaerobic chamber with 5% H₂/95% N₂ atmosphere. As soon as the two stock solutions were mixed in a 1-L volumetric flask, the pH of solid suspension was adjusted to 4.5 \pm 0.1 using 1 N HCl or 1N NaOH. To facilitate the formation of nuclei, the heat was applied to achieve a temperature of approximately 60 °C for 1 day of aging. The final solid products were then filtered with a 0.25 μ m anodisc filter using a vacuum pump and washed several times with acetone and carbon disulfide to remove residual sulfur completely from the surface of the solids. Finally, the synthesized pyrite solids were dried in the anaerobic chamber.

5.2.3 Sorption/Reaction Experiments

All sorption experiments were conducted using batch systems at ambient temperature in an anaerobic chamber. These experiments were designed to produce solids for surface analysis using X-ray photoelectron spectroscopy (XPS), scanning electron microscopy (SEM), atomic force microscopy (AFM). To acquire solid samples, 1 g/L pyrite suspension was reacted with Se(IV) or Se(VI) at a concentration of 3.1 mM and at pH 8. At sampling times of 1, 15, and 30 days, the solid suspensions were filtered using 0.02- μ m anodisc membrane filters (Whatmann). The filter disk including the wet solids was directly dried and stored in the anaerobic chamber until analyses by spectroscopic techniques.

5.2.4 Spectroscopic Analyses

X-ray diffraction analysis was carried out by a Rigaku automated diffractometer using Cu K α radiation with 0.03° step size and 3s step time over range 2° < 2 θ < 65°. Before XRD analysis, all solid samples were washed with acetone (99%, Sigma-Aldrich) and then dried in anaerobic chamber to avoid oxidation of solid samples. The measured XRD data were compared to library spectra.

Transmission electron microscopy (TEM) was performed using a JEOL 2010 microscope with a lanthanum hexaboride filament and an excitation voltage of 200 kV. The solid samples were suspended in ethanol (99.99%, Aldrich), and then placed on a 400-mesh copper grid, followed by dispersion of solid using sonication.

The XPS spectra for pyrite combined with selenium were obtained using a Kratos Axis Ultra Imaging X-ray photoelectron spectrometer with a monochromatized Al K α (1253.6 eV) source. The pressure in analytical chamber was below 10⁻⁷ Pa. The survey scans were recorded with pass energy of 80 eV and the narrow scans used 40 eV or 20 eV for higher resolution. In order to obtain the oxidation status of surface sorption sites and target contaminants, narrow scan

spectra for Fe 2p, S 2p, O 1s, and Se 3d were acquired. Since pyrite is a conducting solid, it would be expected that charge effects could occur, resulting in the shifts of spectra. To calibrate this region shift, the spectra peak of C 1s at 284.5 ± 0.1 eV was used as reference. The narrow scan spectra of Fe 2p_{3/2}, S 2p, O 1s, and Se 3d were fitted using a XPSPEAK41 fitting program with Gaussian Lorentzian function through background-subtraction corrections using a Shirley-type optimization.

The surface morphology and chemical composition of pyrite after contact with Se(IV) or Se(VI) was characterized by scanning electron microscopy (SEM) using energy dispersive spectrometer (EDS) analysis. A JEOL JSM 6400 equipped with a PGT EDS system was used. Prior to inserting a sample onto the specimen holder, the surface of the sample was coated with Pd and Au by a sputtering instrument in order to reduce its surface electric charge. The secondary SEM images were collected at a working distance of 39 or 15 mm under an acceleration voltage of 15 kV and a magnification range of 10 to 300,000 \times . Elements that were analyzed by EDS were Fe, S, O, Se, Pd, Au and C.

The topographic information of pyrite after contact with Se(IV) or Se(VI) was obtained by atomic force microscopy (Nano-R, Pacific Nanotechnology Inc., USA). An anodisc filter containing the solid sample was directly moved to the specimen holder. Two types of AFM images such as height and phase were obtained by a tapping mode (or close contact mode) that collects changes of cantilever oscillation as the tip of the cantilever assembly travels on the solid sample, and then transforms their signals to images through software (NanoRule+ Ver. 2.5, Pacific Nanotechnology Inc.). The tip assembly was composed of single-crystal silicon probe and the scan rate was set at 0.5 Hz over a selected area in the dimension of $3.22 \mu\text{m} \times 3.22 \mu\text{m}$ for pyrite, $4 \mu\text{m} \times 4 \mu\text{m}$ for Se(IV) -contacted pyrite, and $1.46 \mu\text{m} \times 1.46 \mu\text{m}$ for Se(VI) -contacted pyrite.

5.2.5 Measurement of Aqueous Concentrations

Selenate was analyzed by a hydride generation atomic absorption spectrometry (HGAAS) method using a Thermo Elemental Solar M6 AA and a VP90 continuous hydride generator. Selenate was first reduced to selenite by acid digestion (5 mL sample, 5 mL concentrated HCl in 40 mL borosilicate glass vial placed in boiling water bath for 10 minutes). The following parameters were used for these analyses: wavelength of 196.0 nm, band pass of 0.5 nm, lamp current of 75%, measurement number of 4, measurement time of 4 s, background correction is on, stabilization time of 30 s, baseline delay time of 40 s, carrier gas flow rate of 240 mL/min. The average recovery (accuracy) and relative standard deviation (precision) were 103.0 % and 1.8 % for Se(IV), and 101.8 % and 1.62 % for Se(VI). The average method detection limit (MDL) for Se(IV) and Se(VI) were 0.75 $\mu\text{g/L}$ and 0.75 $\mu\text{g/L}$, respectively.

5.3 Results and Discussion

5.3.1 Surface Characterization of Synthetic Pyrite

Figure 5.1 shows results of microscopic and spectroscopic analysis that were conducted by XRD, TEM and SEM, in order to characterize synthetic pyrite and confirm its identity. The X-ray diffractogram shown in Figure 5.1(a) was analyzed by a library simulation search/match program which confirmed that pyrite crystals were being produced by the synthesis method employed. Figure 5.1(b) shows that synthetic pyrite has a highly regular rectangular morphology with particle sizes between 100 and 1000 nm. The right-hand side of the picture shows the diffraction pattern that identified crystalline pyrite. Figure 5.1(c) shows the SEM image and EDS analysis for pyrite, supporting results of the TEM.

Figure 5.2 depicts the three-dimensional height images and phase image of synthesized pyrite before contact with selenium. Figure 5.2(a) indicates a 3D height image in the range of 0

to 944 nm. The height profile for the cross-sectional region was in the range of about 200 to 800 nm. Figure 5.2(b) exhibits the phase image of pyrite that was obtained simultaneously with the height image. The phase image is often used to characterize the local changes in physical and mechanical properties of materials, based on the phase lag between the oscillation amplitude of cantilever and driver as the probe taps the surface (226, 227). The phase lag is affected by the extent of the interactions between the scanning tip and the sample surface (227). Since the initial frequency of the cantilever was set to constant value, exterior power was added to the cantilever in order to maintain initial frequency whenever a phase lag occurs. Thus, the y-axis scale in the phase image or phase profile is expressed in terms of voltage (mV). When a solid surface consists of regions of different composition, a phase shift in the phase image will be presented by both dark-colored and bright-colored regions with different levels of voltage, which is due to bending deformation. The phase image (Figure 5.2(b)) shows small regions with surface heterogeneity on pyrite, but it indicates that the synthetic pyrite has a mostly homogeneous surface.

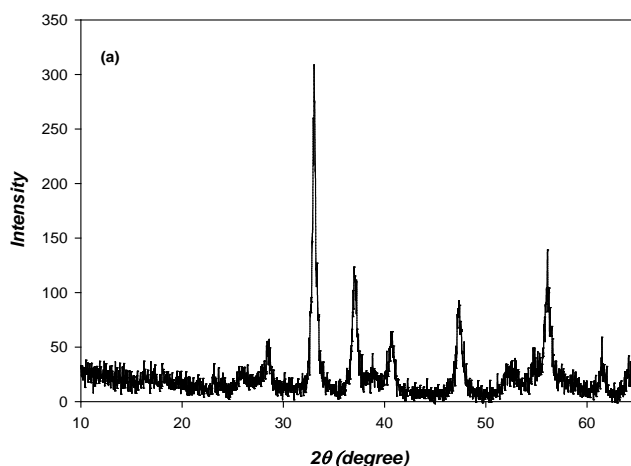
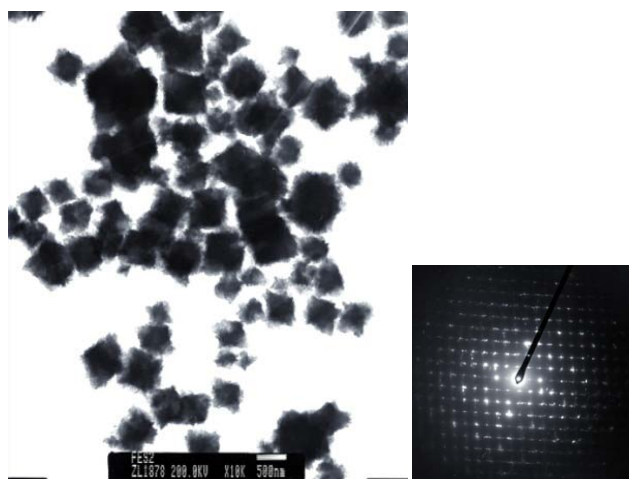
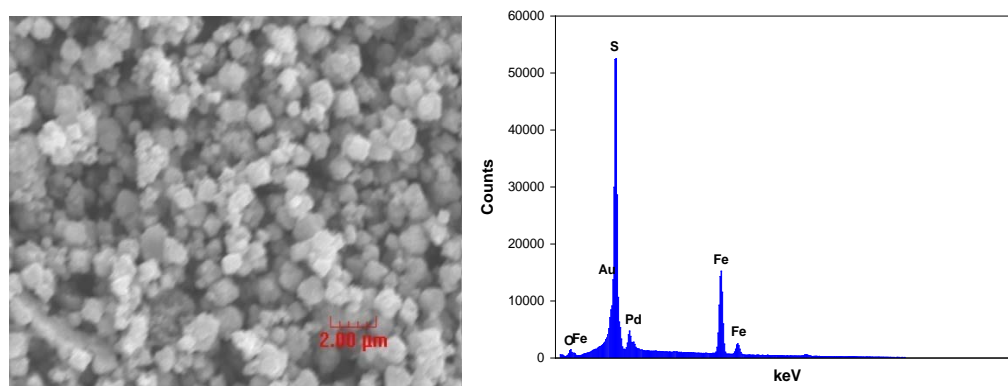


Figure 5.1 Surface characterization of synthetic pyrite using (a) XRD, (b) TEM, (c) SEM-EDS.

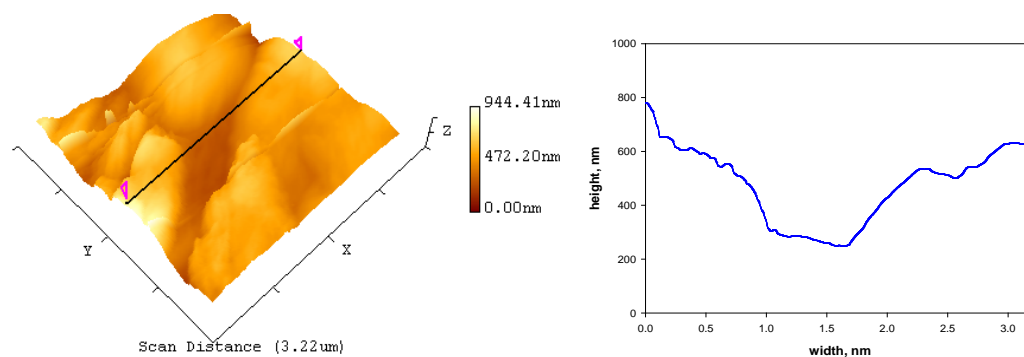


(b)

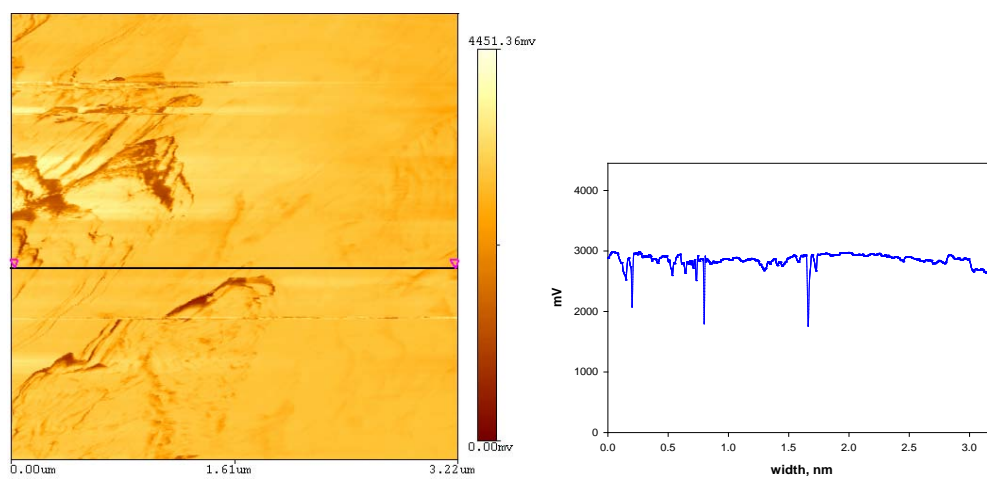


(c)

Figure 5.1 Continued.



(a)



(b)

Figure 5.2 AFM images of synthetic pyrite before contact with selenium: (a) $3.22 \mu\text{m} \times 3.22 \mu\text{m}$ 3D topography image (left) and height profile for cross-sectional region (right), (b) 2D phase image (left) and phase profile for cross-sectional region (right).

5.3.2 XPS Investigations for Se-Contacted Pyrites

Tables 5.1-5.3 provide information about the Fe $2p_{3/2}$, S 2p and O 1s XPS spectra of pyrite contacted with Se(IV) and Se(VI) over contact time. This information includes binding energies (BE), full width at half maximum (FWHM), percentages of peak area.

Figure 5.3 presents the Se 3d XPS spectra of pyrite before and at various times after it was contacted with Se(IV) or Se(VI). Pyrite displays a peak in the the Se 3d spectra at binding energy in the range of 50-65 eV that is due to iron (8). Figure 3(a) shows that important shifts in binding energies for this peak occur at different times after contact with solutions of Se(IV). The most important change is the shift in binding energy from 54.2 eV to 55.2 eV. This shift could be caused by Se(IV) being sorbed to the surface of pyrite and subsequently being reduced by surface reactions to form a variety of reduced species of selenium (Se(0), Se(-I), Se(-II)). Reduced species of selenium produce spectra with peaks in the range of 53.7~56.3 eV, which is the range where peaks are observed in Figure 5.3(a). In addition, it was also observed that the binding energy of the main peak in Se 3d spectra in Figure 5.3(a) did not shift substantially at contact times larger than one day. This is unlike the case of Se(IV) where the Se 3d spectra (Figure 5.3(b)) does not show shifts in location of any important peaks. This result could be due to low amounts of Se(VI) being sorbed onto pyrite or to the resistance of sorbed Se(VI) to being reduced by surface reactions. However, after 30 days of contact, the peak begins to widen, probably due to Se(VI) reduction to reduced species.

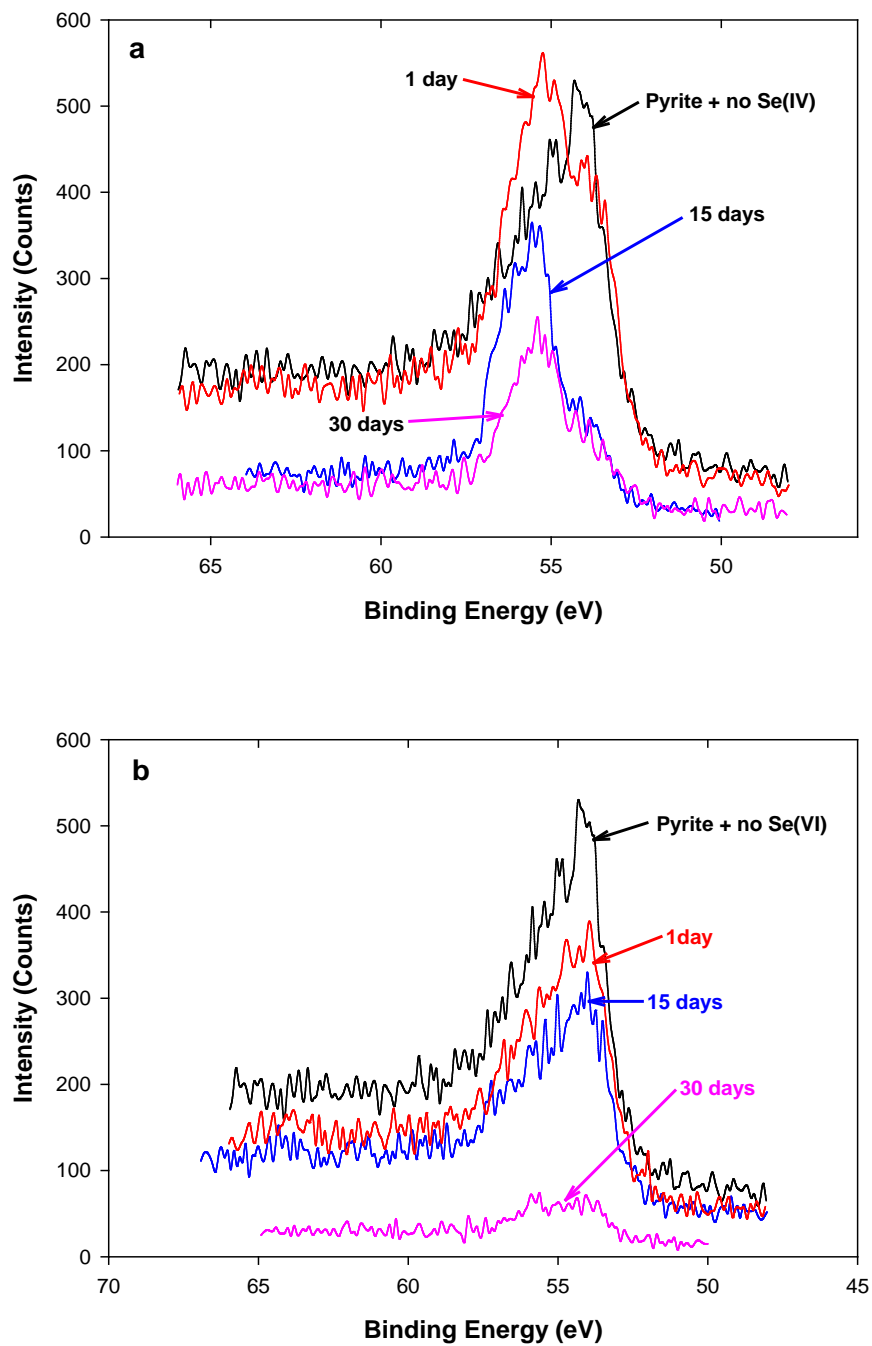


Figure 5.3 High resolution Se 3d XPS spectra of synthetic pyrite (1 g/L) reacted with (a) 3.1 mM Se(IV) and (b) 3.1 mM Se(VI) at pH 8 and various contact times.

Figures 5.4 and 5.5 show high resolution Fe $2p_{3/2}$ XPS spectra for pyrite reacted with Se(IV) and Se(VI), respectively. Three major Fe $2p_{3/2}$ peaks are seen at 706.7~706.8 eV, 708.4~709.1 eV, and 710.2~711.5 eV, which correspond to Fe(II)-S, Fe(III)-S, and Fe(III)-O, respectively. These peaks are observed in all spectra, regardless of the type of selenium and contact time. However, the 30 day sample for Se(IV) and the 1 day sample for Se(VI) exhibited another peak at 707.4 eV and 707.3 eV, indicative of an Fe(II)-O specie. However, the peak associated with this specie is added by the fitting program when the major Fe(II)-S peak is observed to be wider. This peak width could be the result of other things, besides formation of Fe(II)-O species. In the case of pyrite reacted with Se(IV), the relative areas for the Fe(III)-S and Fe(III)-O peaks tend to increase with increasing contact time (Table 5.1), but not substantially. In the case of pyrite contacted with Se(VI), the relative areas for the Fe(III)-S and Fe(III)-O peaks decrease slightly with increasing contact time (Table 5.1), but the changes are not substantial. Therefore, it is difficult to conclude that iron in pyrite is strongly associated with the reduction of Se(IV) or Se(VI).

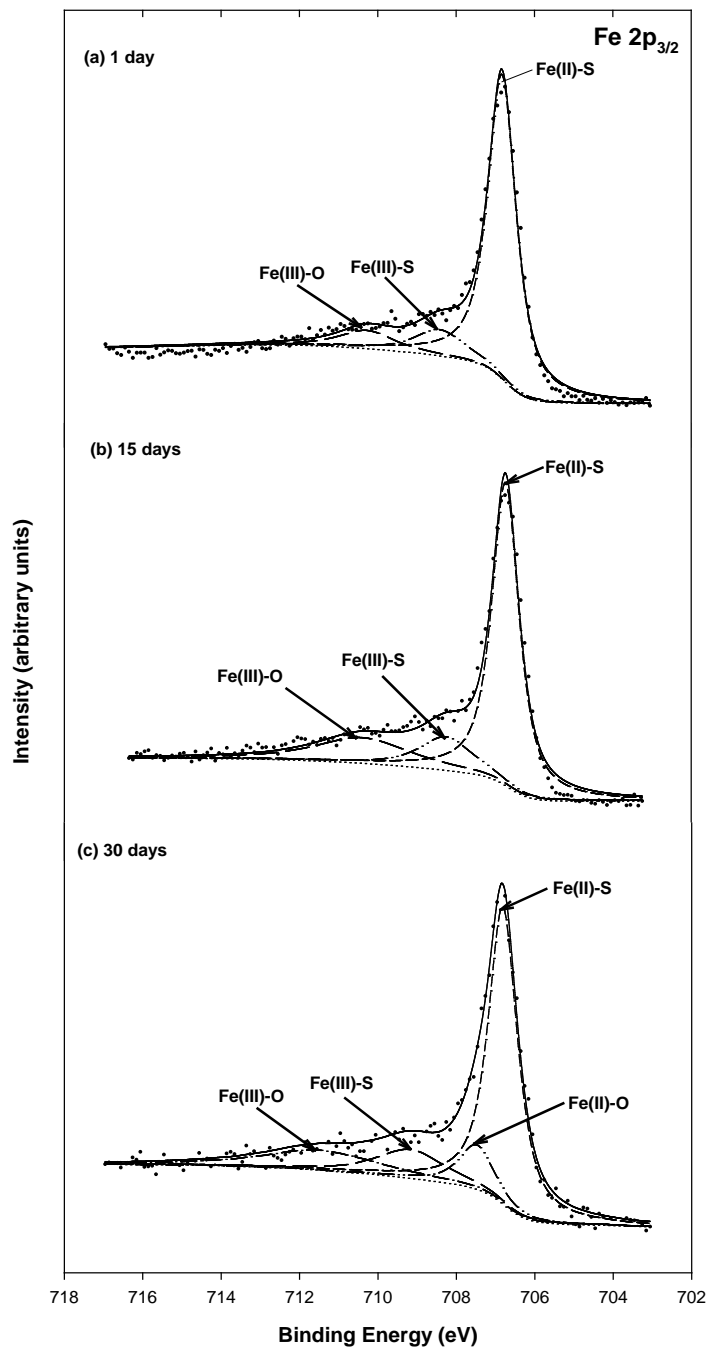


Figure 5.4 High resolution Fe 2p_{3/2} XPS spectra of synthetic pyrite (1 g/L) reacted with 3.1mM Se(IV) at pH 8 for various times: (a) 1 day, (b) 15 days, (c) 30 days.

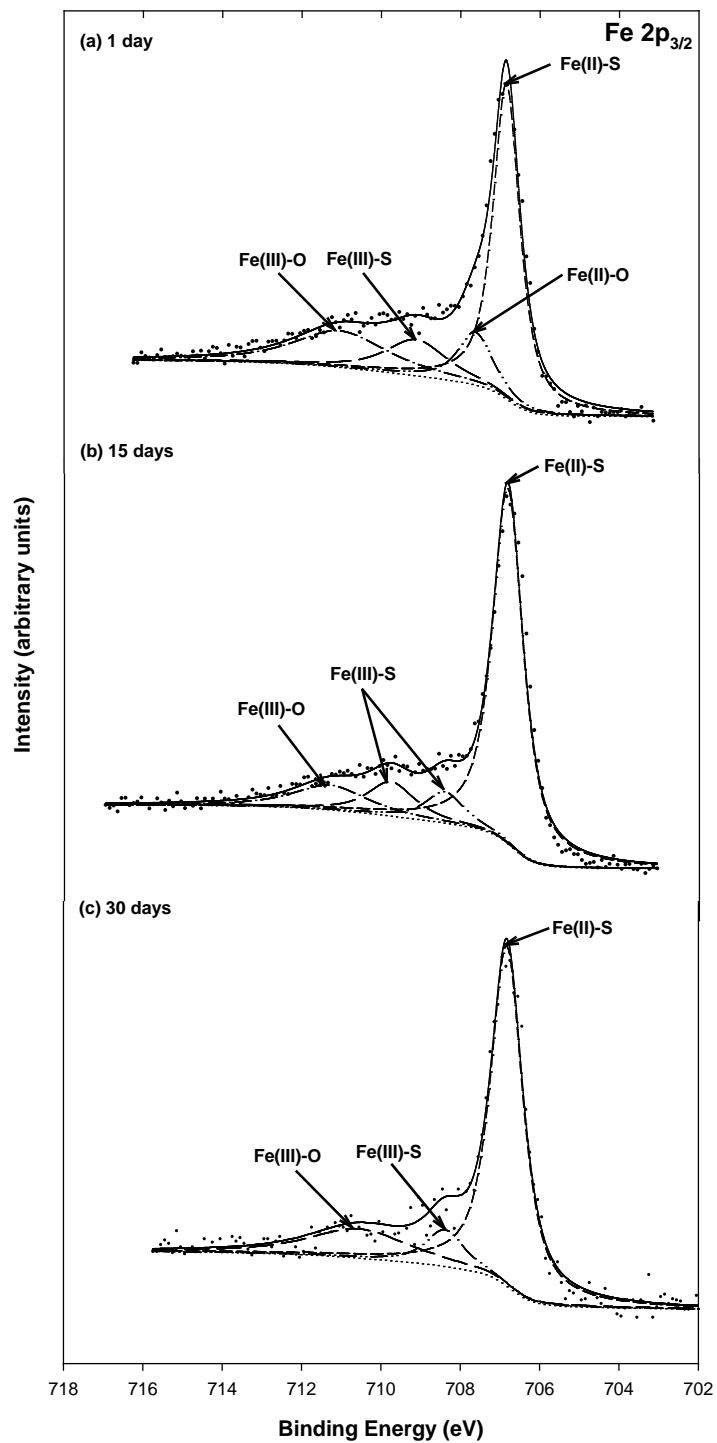
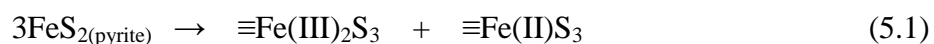


Figure 5.5 High resolution Fe 2p_{3/2} XPS spectra of synthetic pyrite (1 g/L) reacted with 3.1mM Se(VI) at pH 8 for various times: (a) 1 day, (b) 15 days, (c) 30 days.

Figures 5.6 and 5.7 show the S 2p spectra for pyrites reacted with Se(IV) and Se(VI), respectively. These spectra are fitted with doublets to characterize the spin-orbit splitting of the S $2p_{1/2}$ and S $2p_{3/2}$ peaks assigned to S_2^{2-} species. Unlike the S 2p peak distribution for pyrite that had not contacted selenium, pyrites reacted with Se(IV) appear to have spectra indicating that sulfur is present in other forms, presumably due to surface disproportionation. There is evidence for S^{2-} species at about 161.5 eV and SO_4^{2-} species at the higher binding energy in the range of 167.2-167.5 eV. This observation indicates that the sulfur in pyrite undergoes both oxidation and reduction reactions when Se(IV) sorbs to the surface. Based on these observations, reduction of Se(IV) by pyrite coupled with production of sulfate (SO_4^{2-}) could occur through several reaction pathways. One possible way is that pyrite reacted with Se(IV) could produce thiosulfate ($S_2O_3^{2-}$) and tetrathionate ($S_4O_6^{2-}$) via sequential redox reactions. Similar reactions have been observed in Cr(V) reduction by pyrite (228). When thiosulfate ions are produced, they tend to disproportionate into elemental sulfur and tetrathionate. Finally, tetrathionate can be oxidized to sulfate as Se(IV) is reduced. However, the presence of intermediate species of sulfur was not observed for all samples and peaks associated with sulfate species did not appear until 15 days of contact time. An alternative explanation for the occurrence of sulfate, especially in the 15 days sample, is that it could be produced when the surface-bound sulfur is oxidized by Fe(III)-oxyhydroxide surface species. The presence of these species is indicated by development of a broad Fe(III) peaks in the Fe 2p spectra. This was particularly evident in the 15 day sample, which showed the sum of relative peak areas for Fe(III)-S and Fe(III)-O to be 34%, compared to 21 % for the 1 day sample. However, the evidence for sulfate on the pyrite surface may also be the result of aqueous sulfate sorbing to the surface, because the pyrite solids were not washed before analysis (228). In addition, reduction of Se(IV) by pyrite coupled with oxidation of surface-bound Fe can be associated with production of monosulfide (S^{2-}) and sulfate (SO_4^{2-}) to

fulfill charge balance. Nesbitt et al. showed that the presence of the three S species such as monosulfide (S^{2-}), disulfide (S_2^{2-}) and polysulfide (S_n^{2-}) on the vacuum-fractured pyrite could be explained by charge compensation for ferric iron, resulting in disproportionation of disulfide to monosulfide and polysulfide, as follows (229).



where "≡" indicates a surface species. Nesbitt et al. emphasized the uncertainty of the origin of the high energy tail of Fe 2p spectrum and suggested that more detailed studies of the oxidation states of Fe and S are required to clarify relationships among Fe(III), S^{2-} , and S_n^{2-} (229). Based on our results, Se(IV) reduction by pyrite may be responsible for oxidation of Fe(II) that leads to formation of monosulfide bonded to Fe(III) ($\equiv\text{Fe(III)}_2\text{S}_3$) and polysulfide (S_3^{2-}) bonded to Fe(II) ($\equiv\text{Fe(II)}\text{S}_3$). Subsequently, polysulfide bonded to Fe(II) can be continuously oxidized to sulfate by reduction of Se(IV). Relative peak areas for monosulfide and sulfate were observed to increase with reaction time (Table 5.2). However, in the case of Se(VI)-contacted pyrite, important changes in S 2p spectra were not observed. This could be caused by the fact that lower amounts of Se(VI) compared to Se(IV) were sorbed onto pyrite, or that Se(VI) was less prone to undergo redox reactions on the surface.

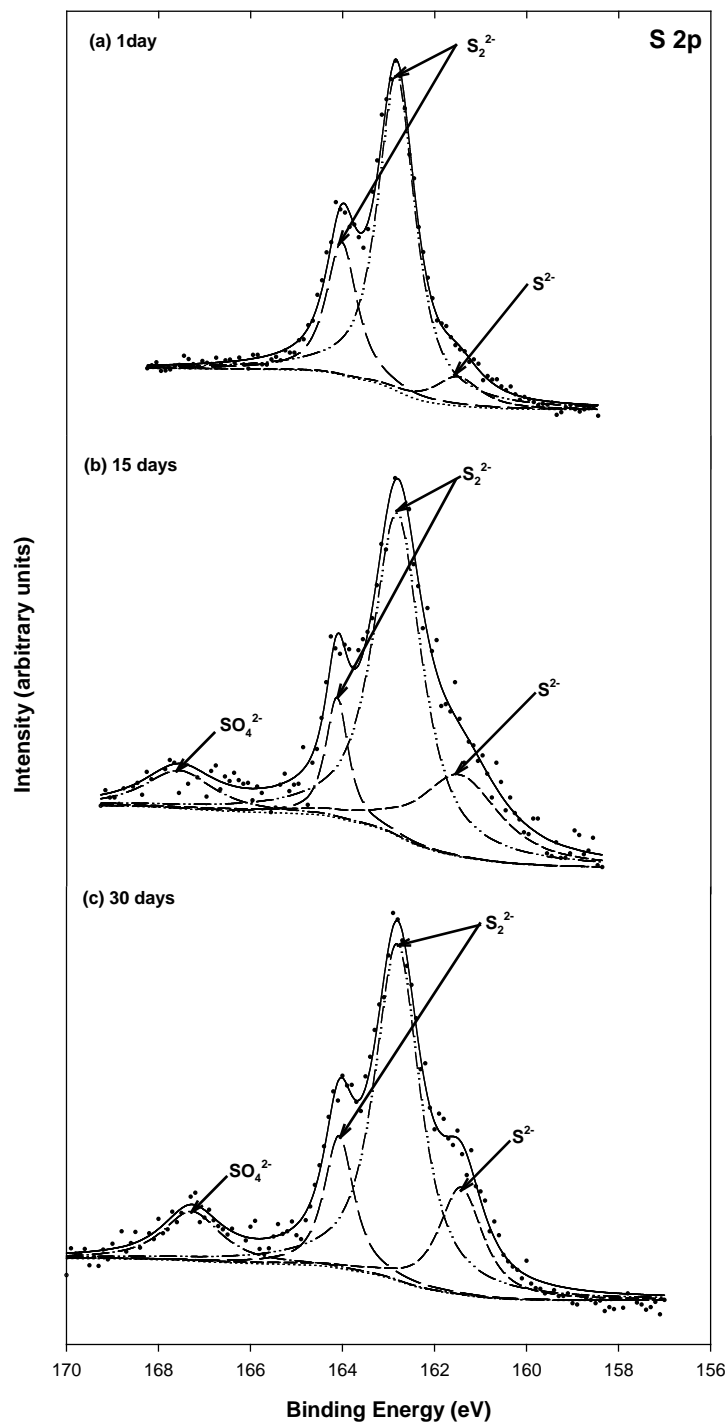


Figure 5.6 High resolution S 2p XPS spectra of synthetic pyrite (1 g/L) reacted with 3.1 mM Se(IV) at pH 8 for various times: (a) 1 day, (b) 15 days, (c) 30 days.

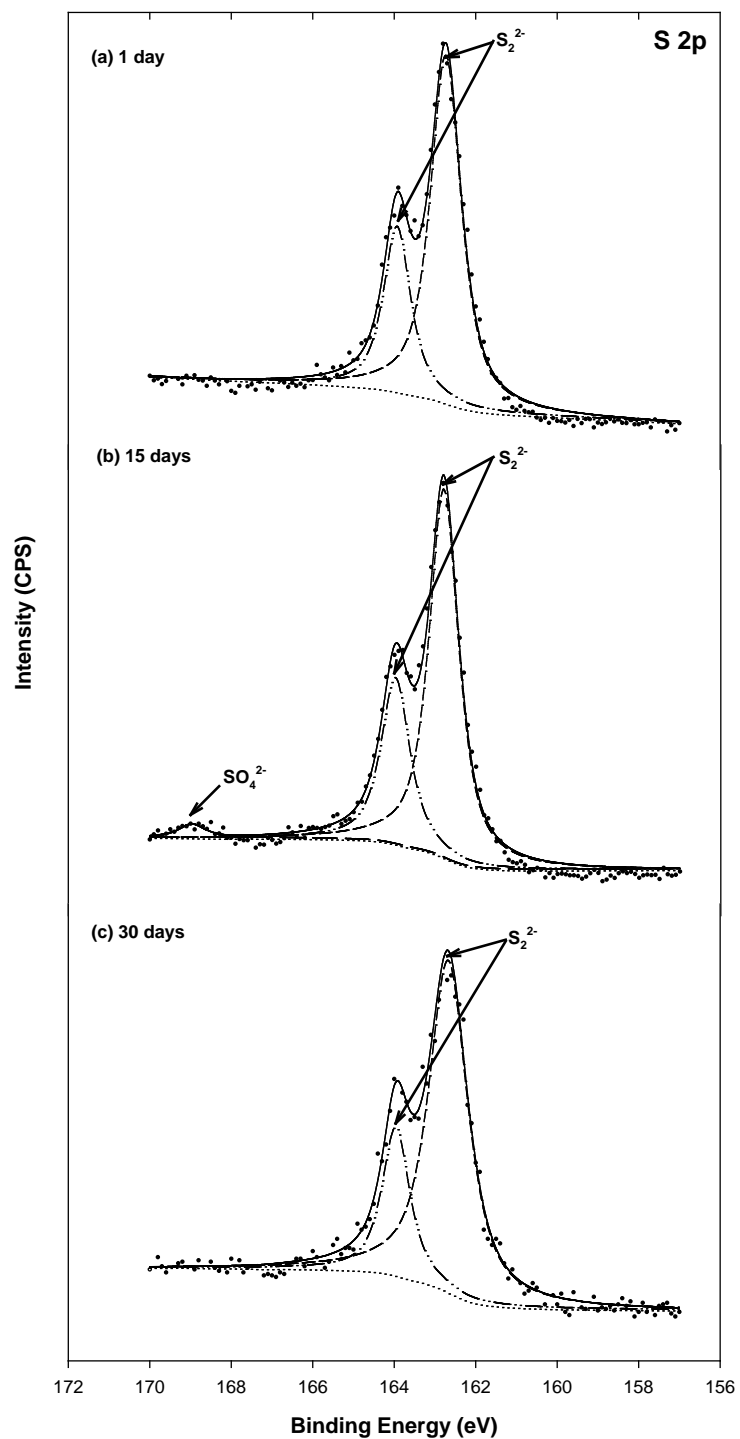


Figure 5.7 High resolution S 2p XPS spectra of synthetic pyrite (1 g/L) reacted with 3.1 mM Se(VI) at pH 8 for various times: (a) 1 day, (b) 15 days, (c) 30 days.

Figures 5.8 and 5.9 exhibit O 1s XPS spectra that discriminate oxygen types (O^{2-} , OH^- , H_2O molecule) on the surface. Three major components of all samples are located at 529.3~530 eV, 530.1~531.1 eV, and 531.3~532.4 eV, which are associated with O^{2-} ions of oxides, OH^- of structural hydroxide, and H_2O of attached water molecules, respectively. Figure 5.8 indicates that the OH^- peak and O^{2-} peak increase over time, while the H_2O peak decreases. Roberts and Nesbitt demonstrated that both OH^- and O^{2-} are formed by reaction of O_2 with pyrite (229, 230). If Fe(III) is produced by oxidation by O_2 or by Se(IV), then Fe(III)-oxyhydroxide surface species could be formed that include both OH^- and O^{2-} . However, oxidation by Se(IV) is more likely, because all experiments were conducted in an anaerobic chamber that excluded O_2 . Oxidation by O_2 cannot be ruled out completely, because the amount of Fe(II) that was oxidized was small, and it is possible that sufficient oxygen could have contacted the surface after transfer from the chamber and before analysis. This is supported by the growth in peaks for OH^- and O^{2-} , the decrease in the peak for H_2O , and the appearance of peaks for Fe(III)-O. However, the increased peak for OH^- could also be related to the production sulfate observed in the S 3p spectra, because the sulfate peak is very close to the OH^- peak (229, 231). In the case of Se(VI)-contacted pyrites (Figure 5.9), the O 1s spectra showed an increase in OH^- and a decrease in H_2O , as observed for Se(IV)-contacted pyrite. However, appreciable changes in the O^{2-} peak areas were not observed.

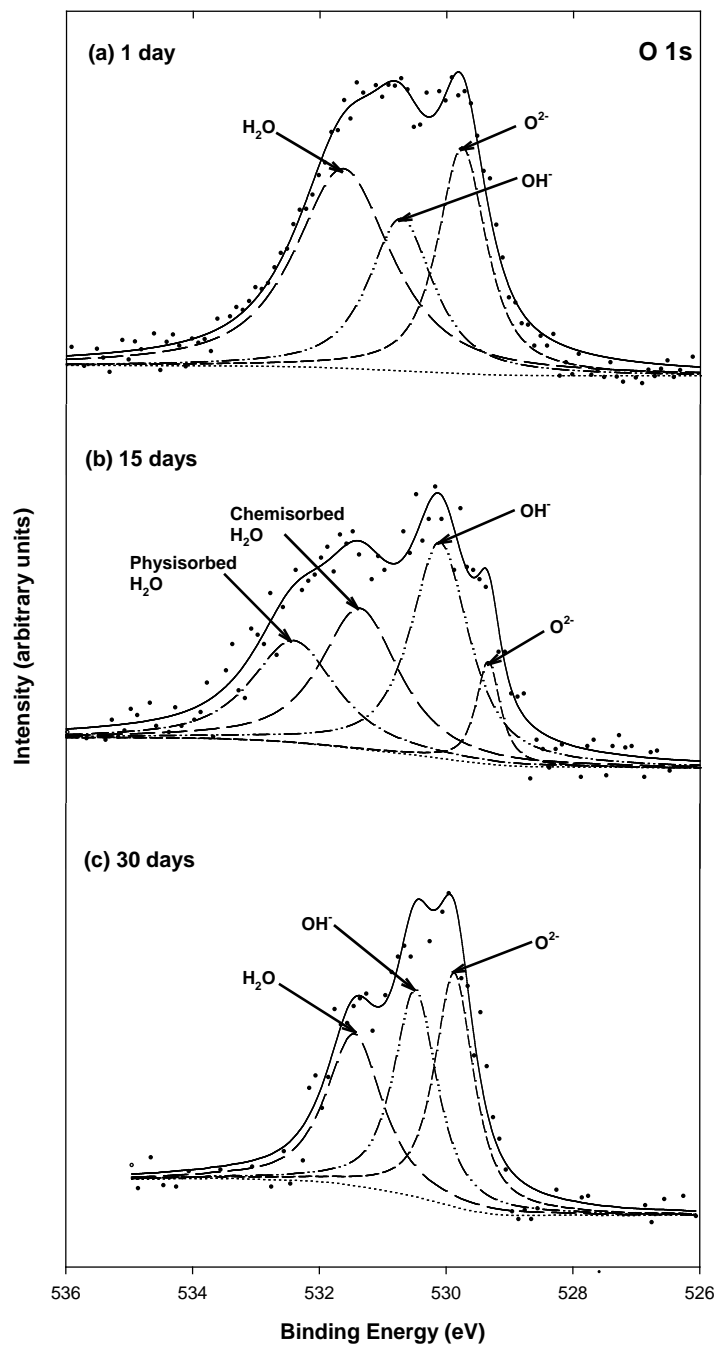


Figure 5.8 High resolution of O 1s XPS spectra for synthetic pyrite (1 g/L) reacted with 3.1 mM Se(IV) at pH 8 for various times: (a) 1 day, (b) 15 days, (c) 30 days.

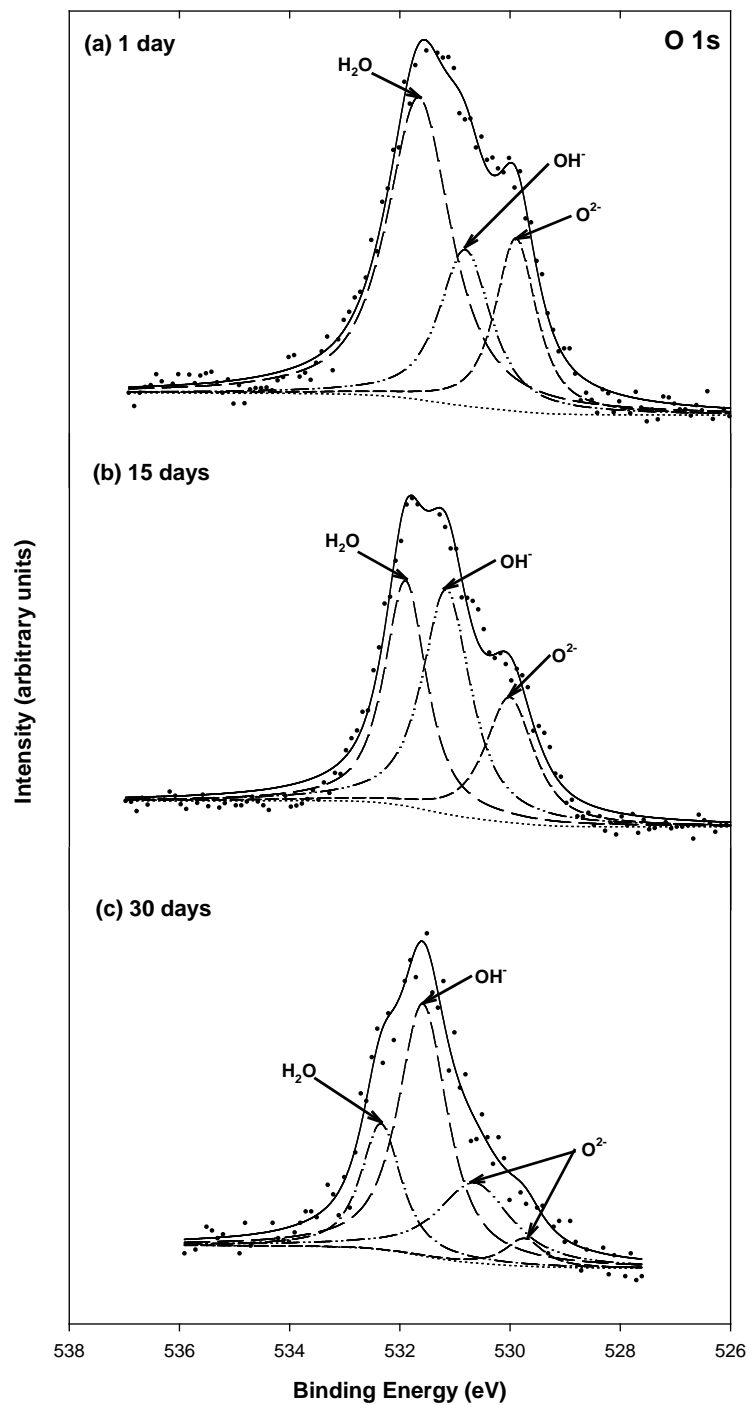


Figure 5.9 High resolution of O 1s XPS spectra for synthetic pyrite (1 g/L) reacted with 3.1 mM Se(VI) at pH 8 for various times: (a) 1 day, (b) 15 days, (c) 30 days.

Table 5.1 Binding energies (BE), full width at half maximum (FWHM), and area percentage for peaks in the Fe 2p_{3/2} XPS spectra of pyrite contacted with Se(IV) and Se(VI) for various times.

| Sample | Contact time (days) | BE (eV) | FWHM (eV) | Area (%) | Chemical states |
|---------------|---------------------|---------|-----------|-----------|-----------------|
| Pyrite | 0 | 706.8 | 0.86 | 72.4 | Fe(II)-S |
| | | 708.3 | 1.66 | 14.2 | Fe(III)-S |
| | | 710.4 | 2.09 | 13.4 | Fe(III)-O |
| Pyrite+Se(IV) | 1 | 706.8 | 0.86 | 78.5 | Fe(II)-S |
| | | 708.4 | 1.54 | 12.2 | Fe(III)-S |
| | | 710.2 | 1.69 | 9.3 | Fe(III)-O |
| | 15 | 706.7 | 0.83 | 65.9 | Fe(II)-S |
| | | 708.2 | 1.64 | 14.5 | Fe(III)-S |
| | | 710.3 | 2.89 | 19.5 | Fe(III)-O |
| | 30 | 706.8 | 0.89 | 59.7 | Fe(II)-S |
| | | 707.4 | 1.07 | 10.6 | Fe(II)-O |
| | | 709.1 | 2.1 | 13.7 | Fe(III)-S |
| | 711.5 | 3.57 | 15.9 | Fe(III)-O | |
| Pyrite+Se(VI) | 1 | 706.8 | 0.75 | 45.3 | Fe(II)-S |
| | | 707.3 | 0.73 | 13.6 | Fe(II)-O |
| | | 708.6 | 1.86 | 16.0 | Fe(III)-S |
| | | 710.8 | 2.96 | 25.1 | Fe(III)-O |
| | 15 | 706.7 | 0.86 | 65.3 | Fe(II)-S |
| | | 708.0 | 1.52 | 11.6 | Fe(III)-S |
| | | 709.7 | 1.68 | 13.2 | Fe(III)-S |
| | | 711.4 | 2.12 | 9.8 | Fe(III)-O |
| | 30 | 706.8 | 0.93 | 72.7 | Fe(II)-S |
| | | 708.3 | 1.32 | 11.9 | Fe(III)-S |
| | | 710.6 | 2.41 | 15.3 | Fe(III)-O |

Table 5.2 Binding energies (BE), full width at half maximum (FWHM), and area percentage for peaks in the S 2p XPS spectra of pyrite contacted with Se(IV) and Se(VI) for various times.

| Sample | Contact time (days) | BE (eV) | FWHM (eV) | Area (%) | Chemical states |
|---------------|---------------------|---------|-----------|-------------------------------|-------------------------------|
| Pyrite | 0 | 162.8 | 0.87 | 64.7 | S ₂ ²⁻ |
| | | 164.0 | 0.95 | 33.5 | S ₂ ²⁻ |
| Pyrite+Se(IV) | 1 | 161.5 | 1.17 | 7.7 | S ²⁻ |
| | | 162.8 | 0.97 | 68.7 | S ₂ ²⁻ |
| | | 164.0 | 0.79 | 23.6 | S ₂ ²⁻ |
| | 15 | 161.4 | 2.08 | 23.8 | S ²⁻ |
| | | 162.8 | 1.27 | 57.1 | S ₂ ²⁻ |
| | | 164.1 | 0.58 | 9.7 | S ₂ ²⁻ |
| | 30 | 167.5 | 1.77 | 9.4 | SO ₄ ²⁻ |
| | | 161.4 | 1.13 | 17.6 | S ²⁻ |
| | | 162.8 | 1.17 | 57.1 | S ₂ ²⁻ |
| | 164.0 | 0.77 | 14.7 | S ₂ ²⁻ | |
| | 167.2 | 1.49 | | SO ₄ ²⁻ | |
| Pyrite+Se(VI) | 1 | 162.7 | 0.91 | 70.6 | S ₂ ²⁻ |
| | | 163.9 | 0.80 | 29.4 | S ₂ ²⁻ |
| | 15 | 162.7 | 0.87 | 69.7 | S ₂ ²⁻ |
| | | 163.9 | 0.84 | 30.3 | S ₂ ²⁻ |
| | 30 | 162.7 | 1.15 | 76.1 | S ₂ ²⁻ |
| | | 163.9 | 0.81 | 23.9 | S ₂ ²⁻ |

Table 5.3 Binding energies (BE), full width at half maximum (FWHM), and area percentage for peaks in the O 1s XPS spectra of pyrite contacted with Se(IV) and Se(VI) for various times.

| Sample | Contact time (days) | BE (eV) | FWHM (eV) | Area (%) | Chemical states |
|---------------|---------------------|---------|-----------|----------|------------------|
| Pyrite | 0 | 530.0 | 1.01 | 25.5 | O ²⁻ |
| | | 531.1 | 1.10 | 38.0 | OH ⁻ |
| | | 531.8 | 1.17 | 36.4 | H ₂ O |
| Pyrite+Se(IV) | 1 | 529.7 | 0.91 | 27.5 | O ²⁻ |
| | | 530.7 | 1.21 | 24.6 | OH ⁻ |
| | | 531.6 | 1.80 | 47.9 | H ₂ O |
| | 15 | 529.3 | 0.45 | 7.07 | O ²⁻ |
| | | 530.1 | 1.09 | 36.2 | OH ⁻ |
| | | 531.3 | 1.47 | 31.6 | H ₂ O |
| | 30 | 532.4 | 1.59 | 25.1 | H ₂ O |
| | | 529.8 | 0.73 | 34.2 | O ²⁻ |
| | | 530.4 | 0.81 | 33.6 | OH ⁻ |
| Pyrite+Se(VI) | 1 | 529.8 | 0.89 | 20.7 | O ²⁻ |
| | | 530.8 | 1.12 | 23.5 | OH ⁻ |
| | | 531.6 | 1.38 | 55.8 | H ₂ O |
| | 15 | 530.0 | 1.05 | 23.1 | O ²⁻ |
| | | 531.1 | 1.04 | 40.9 | OH ⁻ |
| | | 531.9 | 0.91 | 35.9 | H ₂ O |
| | 30 | 529.7 | 0.81 | 4.30 | O ²⁻ |
| | | 530.6 | 1.59 | 24.2 | OH ⁻ |
| | | 531.5 | 1.06 | 50.7 | H ₂ O |
| | | 532.3 | 0.87 | 20.8 | H ₂ O |

5.3.3 SEM Investigation for Se-Contacted Pyrites

Figure 5.10 shows the secondary SEM images for selenium-contacted pyrites with contact times of 1, 15, and 30 days. For Se(IV)-contacted pyrites (Figures 5.10(a), 5.10(b), 5.10(c)), rod-shaped particles were present in 15 day samples and appeared to increase in size in the 30 day samples. This observation may be due to the formation of precipitates through Se(IV) reduction to Se(-I) or Se(-II), which was suggested by the XPS results previously discussed. The Se(VI)-contacted pyrites (Figures 5.10(d), 5.10(e), 5.10(f)), on the other hand, did not show any obvious changes and kept the rectangular morphology of pyrite. This supports the belief that Se(VI) was not reduced, which was also supported by the Se 3d spectra.

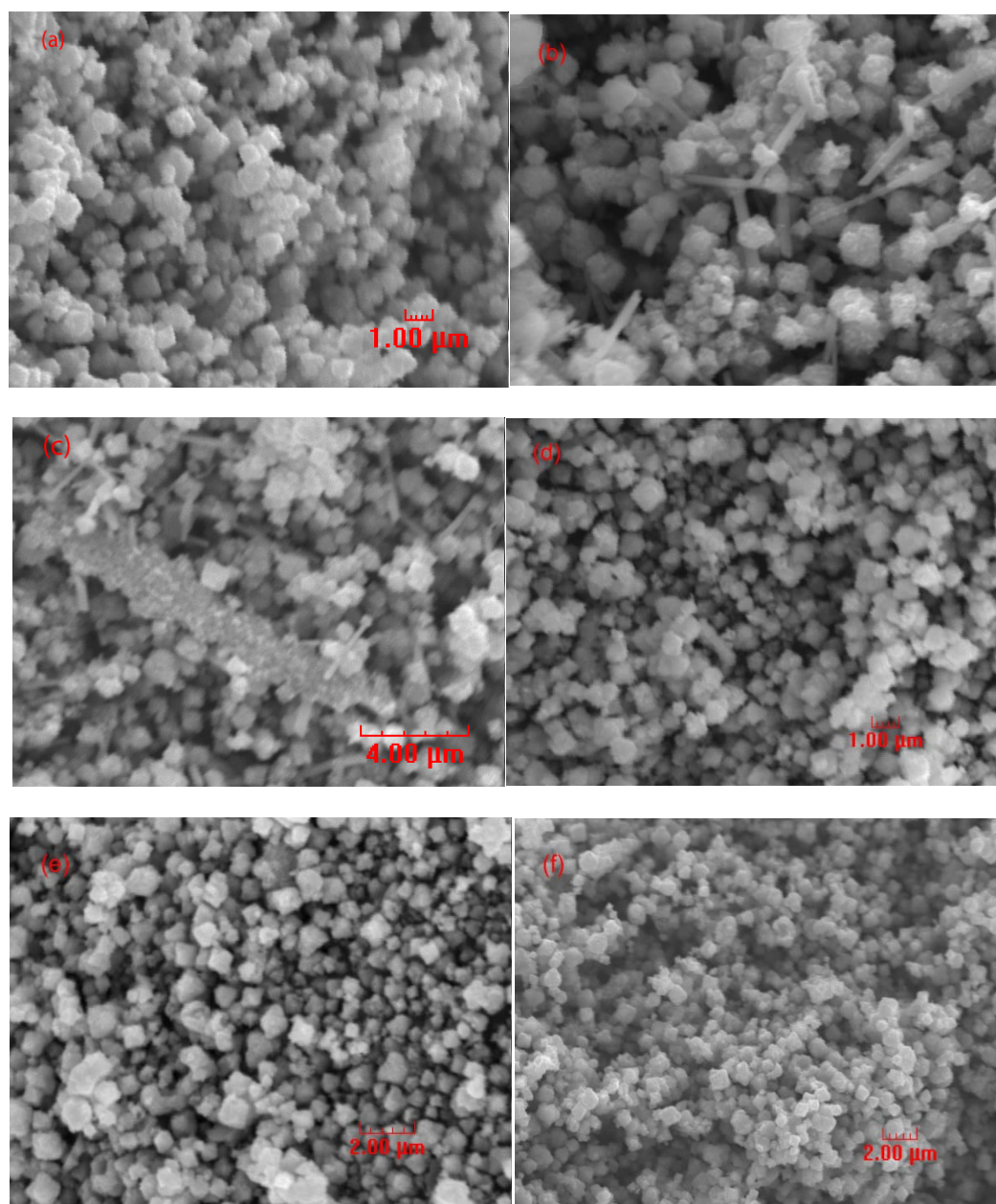
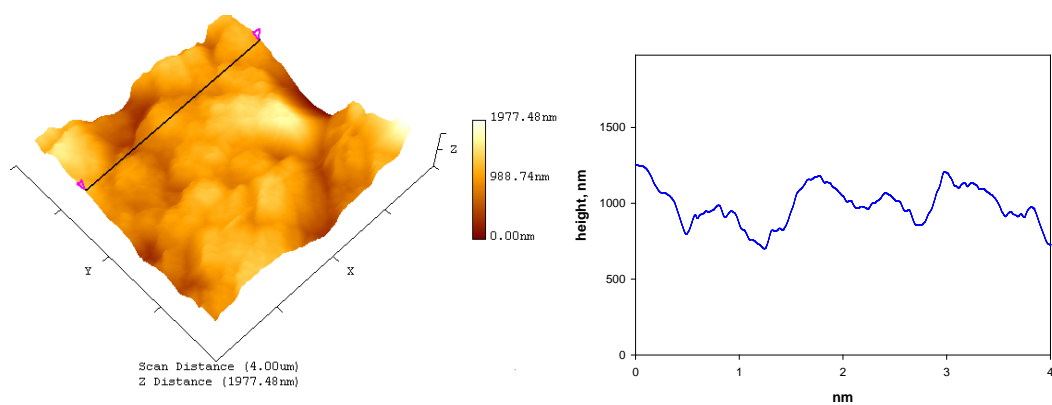


Figure 5.10 Secondary images of SEM analysis for Se(IV)- and Se(VI)-contacted pyrites: (a) 1 day, (b) 15 days, (c) 30 days of contact times for Se(IV) (3.1 mM, pH 8), and (d) 1 day, (e) 15 days, (f) 30 days of contact times for Se(VI) (3.1 mM, pH 8).

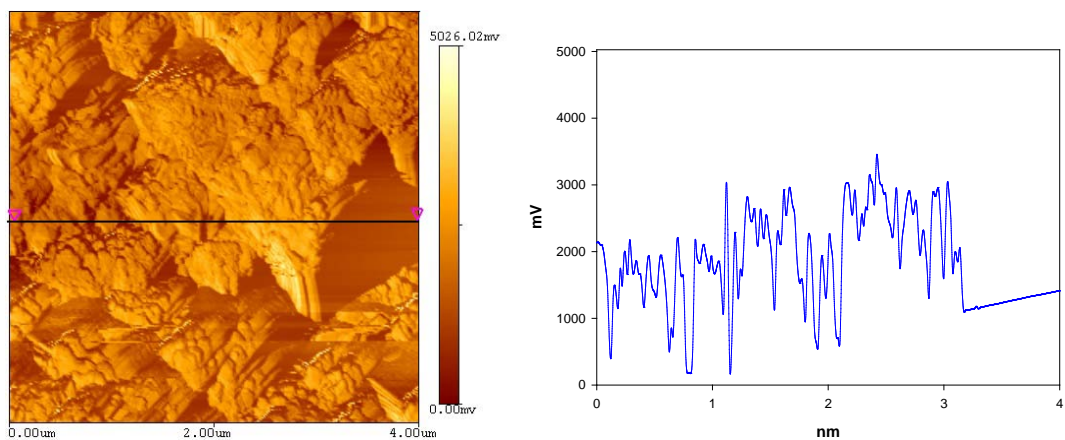
5.3.4 AFM Investigations for Se-Contacted Pyrites

Figures 5.11 and 5.12 show the AFM results for pyrites contacted with Se(IV) and Se(VI). As shown in Figure 5.11(a), the highest peak in the scanning area ($4.0\ \mu\text{m} \times 4.0\ \mu\text{m}$) for Se(IV)-contacted pyrite was 1977 nm, which is higher by a factor of 2.0 than observed for pyrite that had not contacted selenium. The increase might be caused by the formation of precipitates or attachment of other particles on the pyrite surface, which was observed by SEM (Figure 5.10). The height profile for the cross-sectional region, (right side of Figure 5.11(a)) indicates that heights are in the range of 700 to 1300 nm. The left side of Figure 5.11(b) shows that the phase image has at least two different morphological patterns, which are the mountains or lake-like morphological features in the voltage range of 0 to 5026 mV. This heterogeneous surface causes the levels of voltage to be broad, resulted from the phase lag. The phase profile for the cross-sectional region presents severe fluctuation of voltage levels.

For Se(VI)-contacted pyrite, the topography image exhibited that the highest peak in the scanning area ($1.46\ \mu\text{m} \times 1.46\ \mu\text{m}$) was 977 nm and the height profile for the cross-sectional region was in the range of about 20 to 900 nm (Figure 5.12(a)). The range of height is not as different as that of pure pyrite (Figure 5.2(a)). However, the phase image shows different morphological patterns, exhibiting dark and bright-colored regions with a variety of voltage levels (0 to 2981 mV), but the extent of surface heterogeneity is not greater than for Se(IV)-contacted pyrite. From these results, it appears that the Se(IV)-contacted pyrite has higher height and phase profiles than Se(VI)-contacted pyrite. Consequently, the results of analyses by AFM, XPS, and SEM provide evidence of formation of precipitates or other complexes on pyrite surfaces contacted with selenium.

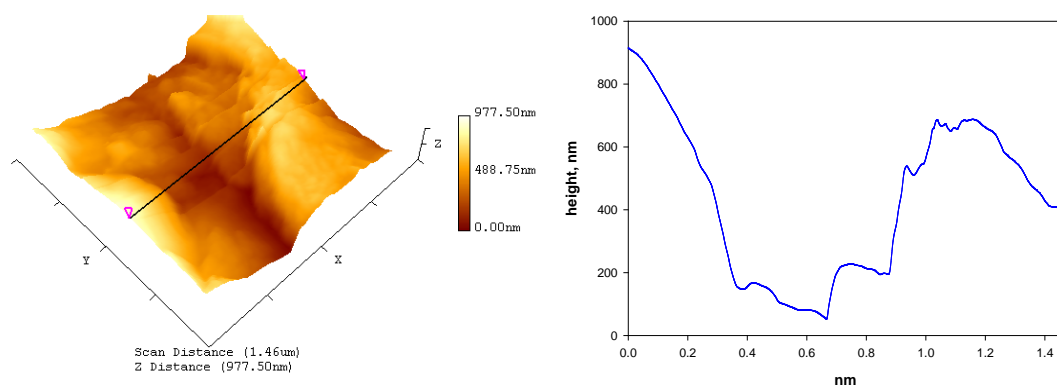


(a)

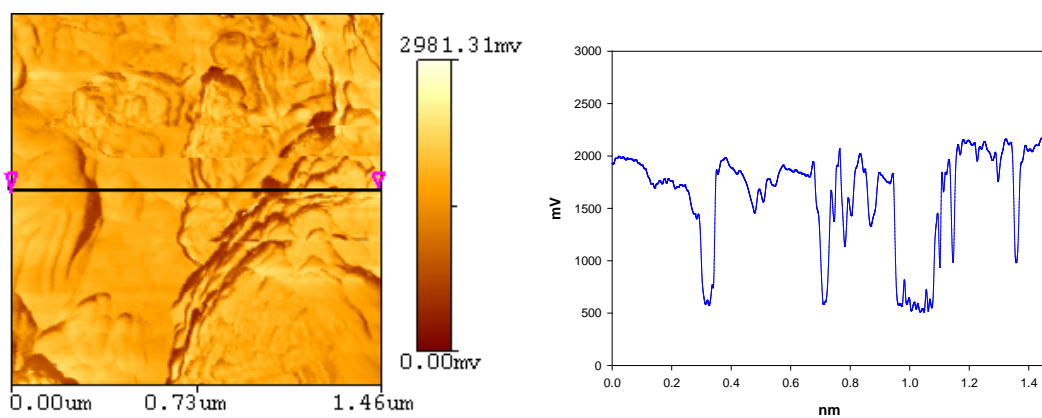


(b)

Figure 5.11 AFM images of synthetic pyrite contacted with Se(IV) (3.1 mM, pH 8) for 15 days: (a) 4.0 $\mu\text{m} \times 4.0 \mu\text{m}$ 3D topography image (left) and height profile for cross-sectional region (right), (b) 2D phase image (left) and phase profile for cross-sectional region (right).



(a)



(b)

Figure 5.12 AFM images of synthetic pyrite contacted with Se(VI) (3.1 mM, pH 8) for 15 days: (a) 1.46 μm × 1.46 μm 3D topography image (left) and height profile for cross-sectional region (right), (b) 2D phase image (left) and phase profile for cross-sectional region (right).

6. SORPTION OF SELENIUM(IV) AND SELENIUM(VI) TO SYNTHETIC PYRITE (FeS₂): KINETICS, EXTENT OF REMOVAL, STABILITY

Batch experiments were conducted to evaluate kinetics of removal of Se(IV) and Se(VI) by synthesized pyrite, the effects of pH and sulfate concentration on removals, and the stability with changing pH of pyrite contacted with Se(IV, VI). These experiments were conducted in a way that is similar to that for systems in which adsorption equilibrium is believed to occur, but that was not the case in these experiments. Removal of Se(IV) by pyrite was slow, with half-lives of about 25 and 55 hours at pH 7 and pH 10, respectively. The slower removal kinetics indicates that surface reactions control the rates of removal rather than external mass transport kinetics. For Se(VI), rapid removal was observed at lower initial concentrations. The effect of pH on removal of Se(IV) by pyrite was small with slightly more removal at lower pH, possibly due to the faster removal kinetics. In the case of Se(VI), however, pH affected the amounts removed at higher initial concentrations, with greater removals observed in the order pH 7 > pH 8 ~ pH 9 > pH 10. Sulfate inhibited removal of Se(IV) and Se(VI) by pyrite at higher concentrations of selenium, but the effect was smaller, or non-existent, at lower concentrations. Stability tests for mixtures of Se(IV) and pyrite showed them to be stable. Nearly complete removal was observed as pH was lowered from an initial high value and no release of Se(IV) back to solution was seen after pH was subsequently raised. Analyses by XPS indicated that the high level of stability could be due to reduction of Se(IV) to more stable forms. Stability tests with mixtures of Se(VI) and pyrite showed higher removals at extreme pH with little stability observed.

6.1 Introduction

Selenium is an increasingly important environmental issue because of its toxicity, in spite of the fact that it is an essential micronutrient for plants, animal and humans (232). Most selenium contamination is the result of releases from anthropogenic sources such as agriculture activities (233, 234) or coal-fired power plants (235, 236). Coal or lignite can contain selenium and can be concentrated in fly ashes or bottom ashes produced during combustion. It can also be transferred to the atmosphere because it is one of the most volatile trace elements (55, 235, 237, 238). Furthermore, coal-fired power plants can discharge wastewaters that contain trace levels of toxic elements such as mercury (Hg), arsenic (As), and selenium (Se) (236). Thus, ashes are not the only by-product of coal combustion that can contain selenium, as well as high concentrations of other toxic compounds, as well as calcium and sulfur. It was reported that approximately 45 % of fly ash in landfills is from coal-fire power plants (55, 239). When disposal of fly ash and wastewaters from power plants is not properly managed, release of selenium to the environment can be a serious concern.

Selenium exists in four different oxidation states (-II, 0, IV, VI) with different fates under various environmental conditions. Under anaerobic conditions, the primary forms are Se(-II) and Se(0) and they exist as low solubility solid phases (elemental selenium and metal selenides). FeSe_2 or FeSe have been proposed to be the solids that control solubility in reduced sediments contaminated with selenium (64). The soluble concentration of Se in equilibrium with FeSe at pH 7 can be calculated as being less than 1 $\mu\text{g/L}$ using the chemical equilibrium program VMINTEQ (65). Metal selenides are known to be stable, as shown by the fact that selenium is often found in nature as the selenide substituting for sulfide in metal sulfide solids with low solubility (9, 60, 66, 240). On the other hand, the oxidized forms of selenium (Se(IV) and Se(VI)), typically exist in water released from power plants (9). Transport and bioavailability of

Se(VI) are observed to be greater than for Se(IV), because Se(VI) is less strongly adsorbed. Many reports in the literatures have demonstrated that Se(IV) and Se(VI) can be adsorbed and subsequently reduced by a variety of reactive solids such as metal sulfides (e.g., mackinawite (61, 67), troilite (241), pyrrhotite (9), pyrite (9, 62)), Fe(II)/Fe(III) mixtures (e.g., green rust (54, 61, 242)) or other Fe(II)-bearing solids (e.g., magnetite (61, 67, 243), siderite (61, 67)), and zero-valent iron (243). Therefore, the Fe(II)-containing sorbents are promising materials for removing Se(IV) and Se(VI) from solution, because they are capable of facilitating reduction on the surface followed by precipitation of FeSe or FeSe₂.

In the present study, Se(IV) and Se(VI) are considered the primary target compounds to be removed using synthesized pyrite. There is little information about macroscopic interaction mechanisms between Se oxyanions and pyrite under various solution conditions, although some earlier studies have elucidated the solid-phase reaction products using X-ray absorption spectroscopy (XAS). Therefore, the goals of this work are to determine the effect of time on removals of Se oxyanions; to evaluate removal behavior of selenium under a variety of pH with and without presence of sulfate as a competing ion that exists in wastewater from coal-fired power plants; to investigate the stability of pyrites combined with Se oxyanions over a range of pH; and to evaluate the solid phases that are produced in order to better understand the chemical changes that occur and that can improve stability. If solid residuals are sufficiently stable, they can be disposed to the environment without concern for subsequent release and environment contamination.

6.2 Material and Methods

6.2.1 Materials

All reagents used in this study are of analytical grade or higher. All solutions are prepared using deoxygenated and deionized water (Milli-Q, 18.2 $\text{M}\Omega^{-1}$). Stock solutions of Se(IV) and Se(VI) at a concentration of 1000 mg/L were prepared by dissolving Na_2SeO_3 or Na_2SeO_4 (Sigma-Aldrich) into distilled deionized water. A series of standard solutions of specified initial concentrations was prepared for batch sorption experiment by diluting the stock solution. Synthesized pyrite was used as an adsorbent/reactant to remove selenium from solution and to form stable surface compounds. The method of pyrite synthesis was described detail in Section 5. Before sorption experiments were initiated, all reaction vessels, glassware, and other experimental supplies were equilibrated with the gas (95% N_2 / 5% H_2) in an anaerobic chamber for 6 hours. Oxygen concentration was maintained a low levels by a Pd catalyst that removed residual oxygen by reaction with hydrogen gas. All procedures during these experiments were performed in an anaerobic chamber.

6.2.2 Sorption/Reaction Experiments

Batch experiments were conducted to evaluate the ability of pyrite to remove selenium. Initial kinetic experiments were conducted at pH 7 and pH 10 with an initial concentration of 100 μM Se(IV) and a pyrite dose of 1 g/L. Initial kinetic experiments for Se(VI) were conducted at pH 8 with 1 g/L pyrite and different initial selenium concentrations (6.3, 12.7 and 38 μM). Experiments were initiated by spiking the suspensions with stock solution of Se(IV) or Se(VI) and adjusting pH and then mixing the reaction vessels with a reciprocal rotator. Samples were taken at times up to about 200 hours and were immediately filtered with 0.02- μm Whatman anodisk membrane filters. Filtrates were stored in an anaerobic chamber until they were analyzed

for Se(IV) and Se(VI) by HGAAS. The kinetic data were expressed in terms of “% Se sorbed” over reaction time. The percentage of Se(IV) sorbed was calculated by the following equation.

$$\% \text{ Se sorbed} = \frac{(\text{Se}_{\text{initial}} - \text{Se}_{\text{specific time}})}{\text{Se}_{\text{initial}}} \times 100 \quad (6.1)$$

where $\text{Se}_{\text{initial}}$ and $\text{Se}_{\text{specific time}}$ are concentration of selenium at initial and sampling time. The effect of pH (7, 8, 9, 10) on Se(IV) or Se(VI) removal by pyrite (1 g/L) was evaluated in a series of batch experiments conducted with variable initial concentrations (25 to 1000 μM for Se(IV); 6.5 to 1395 μM for Se(VI)). Suspensions were allowed to react for 24 hours before sampling and analysis of Se(IV, VI) in the solution. The effect of sulfate concentration (0, 1, 10 mM) on Se(IV, VI) removal was evaluated in a series of batch experiments conducted at pH 7 for Se(IV) and pH 8 for Se(VI).

6.2.3 Stability of Se-Contacted Pyrites

The experimental method described by Bostick and Fendorf (39) was followed to investigate the stability of Se(IV) and Se(VI) on pyrite. This method measures the effect of pH on removal of Se(IV) and Se(VI) by decreasing and increasing pH with 1 or 2 M solutions of HCl or NaOH. A 1-g/L pyrite suspension was adjusted to about pH 10 for Se(IV) and about pH 4 for Se(VI). Then, the Se oxyanion was added to achieve a selenium concentration of 16.5 μM in the aqueous phase. Then, pH was adjusted sequentially to different values and the system was allowed to react for 30 minutes at each pH before sampling. During sampling, the suspensions were filtered using 0.02- μm Whatman anodisc membrane filters. This procedure was repeated until the pH reached the highest or lowest point desired. Herein, samples will be identified with the following nomenclature to simplify the discussion. For Se(IV)-contacted pyrite, the initial sample at pH 10 will be named the “pH 10_(i)” sample and the sample at pH 4 after acid titration will be named the “pH 4_(a.a.t)” sample. Another stability test was conducted for the Se(VI) in a

similar way, but the initial pH was pH 4. Thus the initial sample at pH 4 will be named the “pH 4_(i)” sample and the samples at the pH 7 and 10 after base titration will be named the “pH 7_(a,b,t)” and “pH 10_(a,b,t)”, respectively. The filtered solution samples and the solids on the filters were stored before spectroscopic analysis and AAS measurement in an anaerobic chamber to prevent any change in the oxidation state of selenium. The chamber contained an atmosphere of 5% H₂ and 95% N₂.

6.2.4 Spectroscopic Analyses

Microscopic and spectroscopic analyses to characterize pyrites reacted with selenium were conducted using similar procedures as described in Section 5. Scanning electron microscopy (SEM) was conducted using JEOL JSM-6400 equipped with an energy dispersive spectrometer (EDS). X-ray photoelectron spectroscopy (XPS) was conducted with a Kratos Axis Ultra Imaging X-ray photoelectron spectrometer with a monochromatized Al K α (1253.6 eV) source. The pressure in the analytical chamber was below 10⁻⁷ Pa. The survey scans were recorded with a pass energy of 80 eV and the narrow scans used pass energies of 40 eV or 20 eV. In order to obtain oxidation states of elements on the pyrite surface, narrow scan spectra of the Fe 2p, S 2p, O 1s, C 1s, and Se 3d were acquired. The narrow scan spectra were fitted using a XPSPEAK fitting program with Gaussian Lorentzian function through background-subtraction corrections using a Shirley-type optimization.

6.2.5 Measurements of Aqueous Concentrations

Selenium as Se(IV) or Se(VI) was analyzed by the hydride generation atomic absorption spectrometry method using a Thermo Elemental Solar M6 AA with a VP90 continuous hydride generator. Detailed procedures for this measurement are described in Section 5. In short, the reduction of selenate (Se(VI)) was performed by acid digestion (5 mL sample, 5

mL concentrated HCl in 40 mL borosilicate glass vial placed in boiling water bath for 20 minutes). The samples were analyzed by the hydride method that uses borohydride (0.75% NaBH₄ in 0.25% NaOH) as the reducing agent and detected by flame AA after purging. The measurement of Se(IV) followed similar procedures except no acid digestion occurred. A preliminary experiment showed that recoveries of Se(VI) and Se(IV) were the same from equivalent concentrations, which indicated that Se(VI) was completely reduced to Se(IV) during the procedure.

6.3 Results and Discussion

6.3.1 Kinetics

Results of the initial kinetic experiment for Se(IV, VI) at 100 μ M are shown in Figure 6.1. Figure 6.1 indicates that removal of Se(IV) is relatively slow, with half-lives of approximately 25 hr and 55 hr at pH 7 and pH 10, respectively. The slow removal is consistent with removal being controlled by slower surface reactions, rather than transport to the surface. The effect of pH on removal kinetics could be related to the effect of pH on the surface reaction, with more rapid reactions at pH 7 than at pH 10. Removal kinetics of Se(IV) by hematite has been reported to depend on pH (244). Lowering pH was reported to result in more rapid uptake of Se(IV) during the first 100 minutes, but after that time all of the Se(IV) was removed from solution, regardless of initial pH (244). However, the much slower removal kinetics observed in the pyrite/Se(IV) system indicates that there is a different mechanism, probably sorption followed by surface reaction, rather than just sorption.

Figure 6.2 shows the results of the effect of time on removal of Se(VI) by pyrite at pH 8 at different initial concentrations (6.3, 12.7, 38 μ M). Nearly complete removal was observed within 1 hour in experiments with the lower initial concentrations (6.3, 12.7 μ M). At a higher initial concentration (38 μ M), removal was slower and occurred in two steps. A plateau in

removal was observed from 12 hours to almost 40 hours, and then removals increased during the rest of the experiment and finally reached 95 %. The slower removal kinetics may be due to limitations due to surface reactions rather than external mass transfer kinetics.

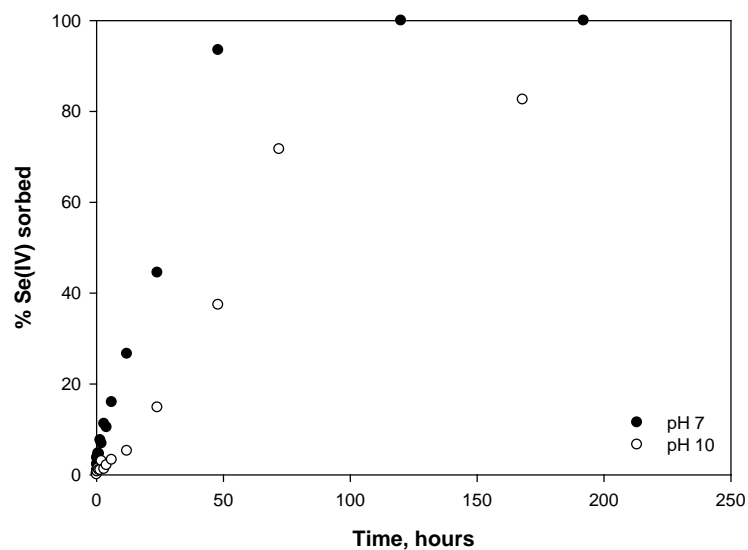


Figure 6.1 Effect of time on removal of Se(IV) ($100 \mu\text{M}$) in the presence of pyrite (1 g/L) at pH 7 and 10.

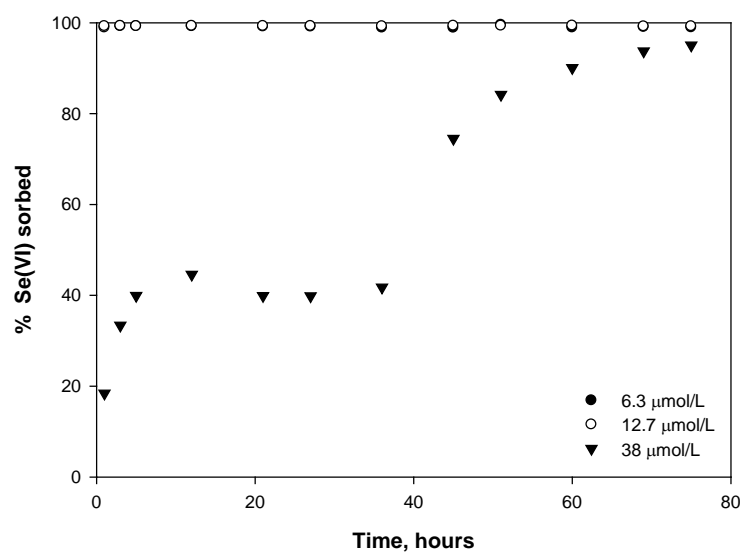


Figure 6.2 Effect of time on removal of Se(VI) in the presence of pyrite (1 g/L) at pH 8.

6.3.2 Nonlinear Removal Patterns

6.3.2.1 Effect of pH

The effect of pH on removal of Se(IV) by pyrite after 24 hours of reaction is shown in Figure 6.3. The data obtained from this experiment is plotted as the solid-phase concentration of Se(IV) as a function of the aqueous phase concentration, which is the way that results of sorption experiments are typically reported. However, conditions in this experiment are not at equilibrium and adsorption is not the only process occurring. Figure 6.3 shows that the solid-phase concentration of Se(IV), which is proportional to the amount removed, increases as pH decreases. This could be the result of faster removal kinetics at lower pH (Figure 6.1). Faster removal kinetics would give higher solid phase concentrations in experiments with constant reaction times. If longer times were allowed for reaction of Se(IV) with the pyrite surface, greater removal and higher solid-phase concentrations would be expected. However, the effect of pH is not large. At pH 7 and pH 8, the solid phase concentration does not approach zero as liquid-phase concentration approaches zero. This indicates that Se(IV) is being very effectively removed when sufficient time is provided to allow surface reactions to proceed.

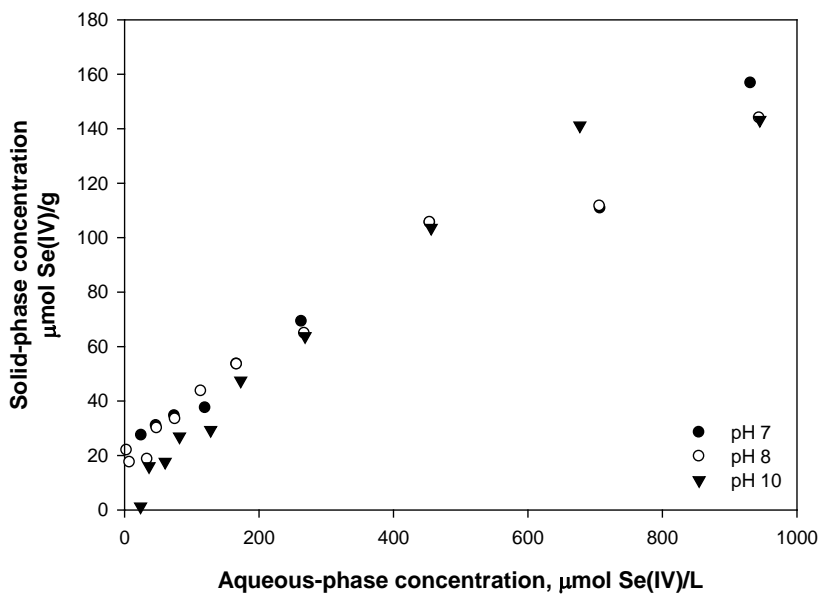


Figure 6.3 Amounts of Se(IV) removed per mass of solid (pyrite) as functions of concentration of Se(VI) in water for various pH.

The effect of pH on removal of Se(VI) by pyrite after 24 hours of reaction is shown in Figure 6.4. The solid-phase concentrations of Se(VI) were not strongly affected by pH at low concentrations. This is shown Figure 6.5, which is a selection of the low concentration data from Figure 6.4. However, at higher concentrations, removal of Se(VI) was observed to increase as pH decreased, with highest removals observed at pH 7, although the surface concentrations did not exceed 90 μmol Se(VI)/g. Removals of Se(VI) were lower than that of Se(IV), so the affinity of Se(IV) for pyrite is stronger than that of Se(VI).

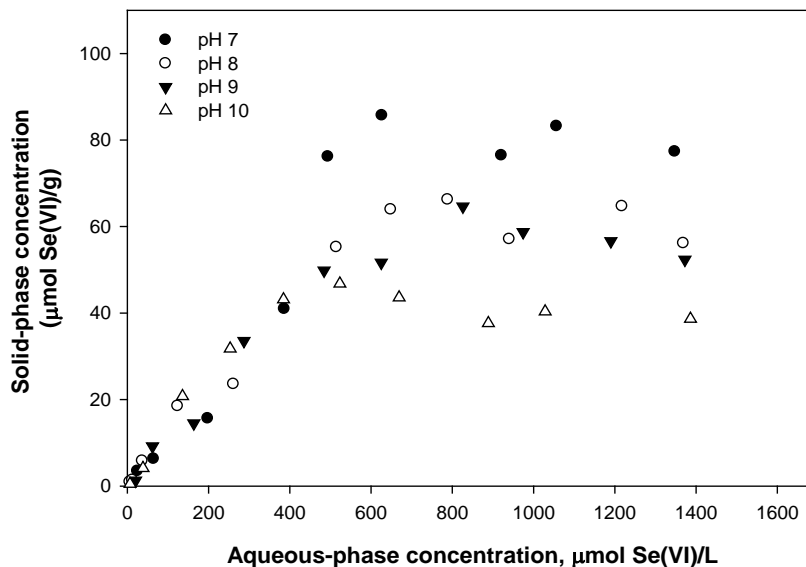


Figure 6.4 Amounts of Se(VI) removed per mass of solid (pyrite) as functions of concentration of Se(VI) in water for various pH.

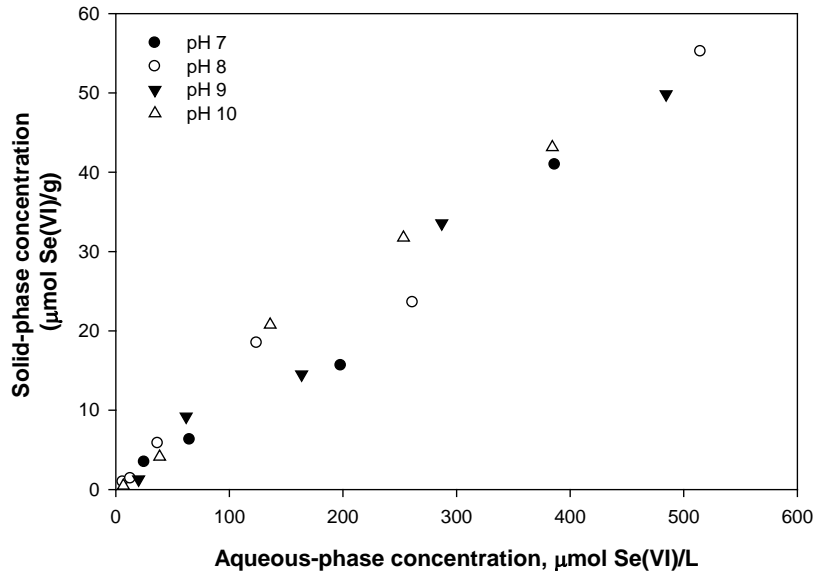


Figure 6.5 Amounts of Se(VI) removed per mass of solid (pyrite) as functions of concentration of Se(VI) in water for various pH, using only data at lower concentrations.

6.3.2.2 Effect of Sulfate Concentration

Figure 6.6 shows the effect of sulfate on the solid phase concentrations of Se(IV) after contact with 1 g/L pyrite for 24 hours at pH 8. Higher concentrations of sulfate are seen to result in lower solid-phase concentrations of Se(IV) when the concentrations of selenium are high. However, there is little effect of sulfate at lower selenium concentrations. This behavior can be explained by sulfate competition with Se(IV) for surface sites on pyrite. The presence of sulfate will initially reduce the concentration of Se(IV) adsorbed to the surface of pyrite.

Figure 6.7 show results of experiments to investigate the effect of sulfate concentration (1 and 10 mM) on Se(VI) removal by pyrite. These experiments used a solid concentration of 1 g/L pyrite, 24 hours of contact time and pH 8. Figure 6.7 shows that there is little effect of sulfate on the amount of Se(VI) removed at low selenium concentrations. At higher concentrations, however, Se(VI) removals were affected by presence of sulfate, but the extent of the effect was the same for both sulfate concentrations that were investigated.

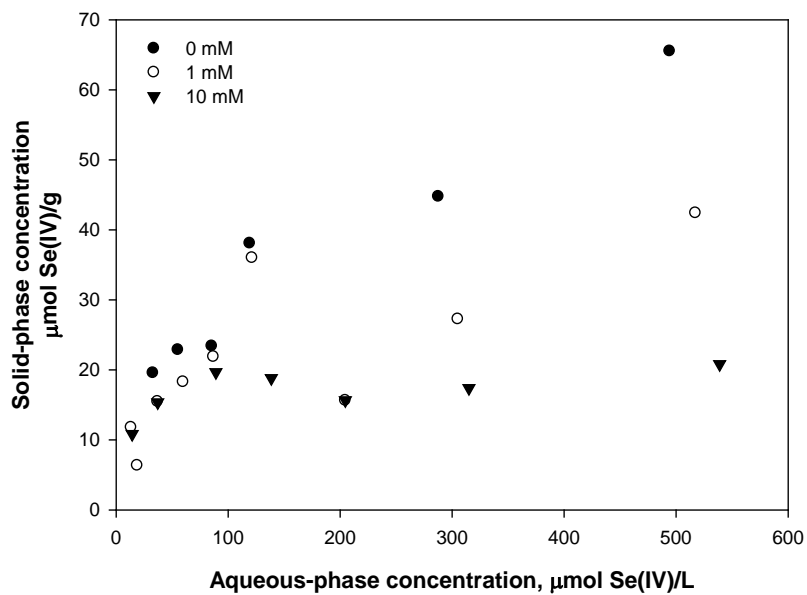


Figure 6.6 Effect of Sulfate on Solid-phase Concentration of Se(IV) on Pyrite.

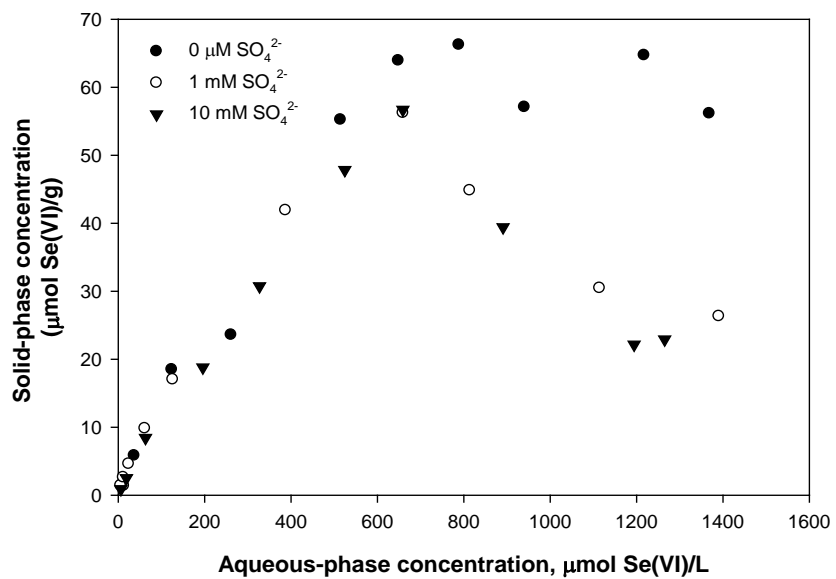


Figure 6.7 Effect of sulfate on solid-phase concentration of Se(VI) on pyrite.

6.3.3 Stability of Se-Contacted Pyrite

6.3.3.1 XPS Investigation of Pure Pyrite

To better understand sorption behavior of selenium by pyrite, the surface of pure pyrite before contact with selenium was characterized by XPS analysis. Figures 6.8 and 6.9 show the Fe 2p_{3/2} and S 2p XPS spectra, respectively, of pure pyrite at pH 4, 8, and 10. Figure 6.8 shows that greater changes in Fe 2p_{3/2} spectra were observed at pH 10 compared to those at pH 4 and pH 8. The most apparent change was the increase in intensity of peaks associated with Fe(III)-S and Fe(III)-O components and decrease in intensity of the peak associated with Fe(II)-S. This might be caused by oxidative dissolution of surface Fe at higher pH. Additional evidence for surface oxidation is shown in Figure 6.9. The S 2p XPS spectra at pH 10 show substantial changes relative to those for pH 4 and pH 8. The major changes are increases in the intensities of peaks associated with polysulfide and sulfate. Therefore, at basic pH, the surface-bound Fe and S species underwent oxidation. The O 1s spectra (Figure 6.10) also support this hypothesis by showing increased intensity of the O²⁻ peak with increasing pH. This peak is associated with structural oxygen of Fe(III)-oxyhydroxides. Table 6.1 summarizes all fitting parameters of the Fe 2p, S 2p, and O 1s spectra for samples of pyrite in suspensions at pH 4, pH 8, and pH 10. The data presented includes binding energy (eV), full width at half maximum (FWHM), and relative area (%) for peaks associated with various chemical states.

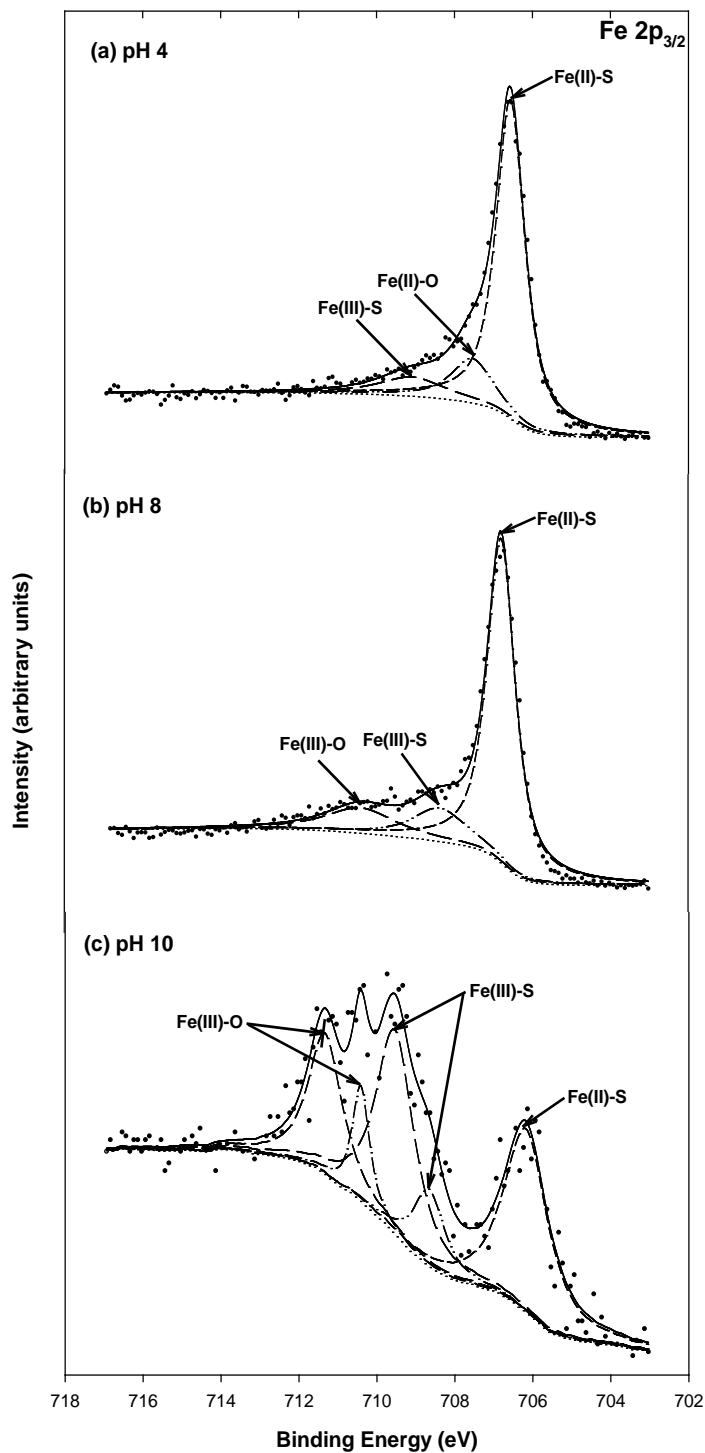


Figure 6.8 High resolution Fe $2p_{3/2}$ XPS spectra of pyrite (1 g/L) before contact with selenium at various pH (4, 8, 10).

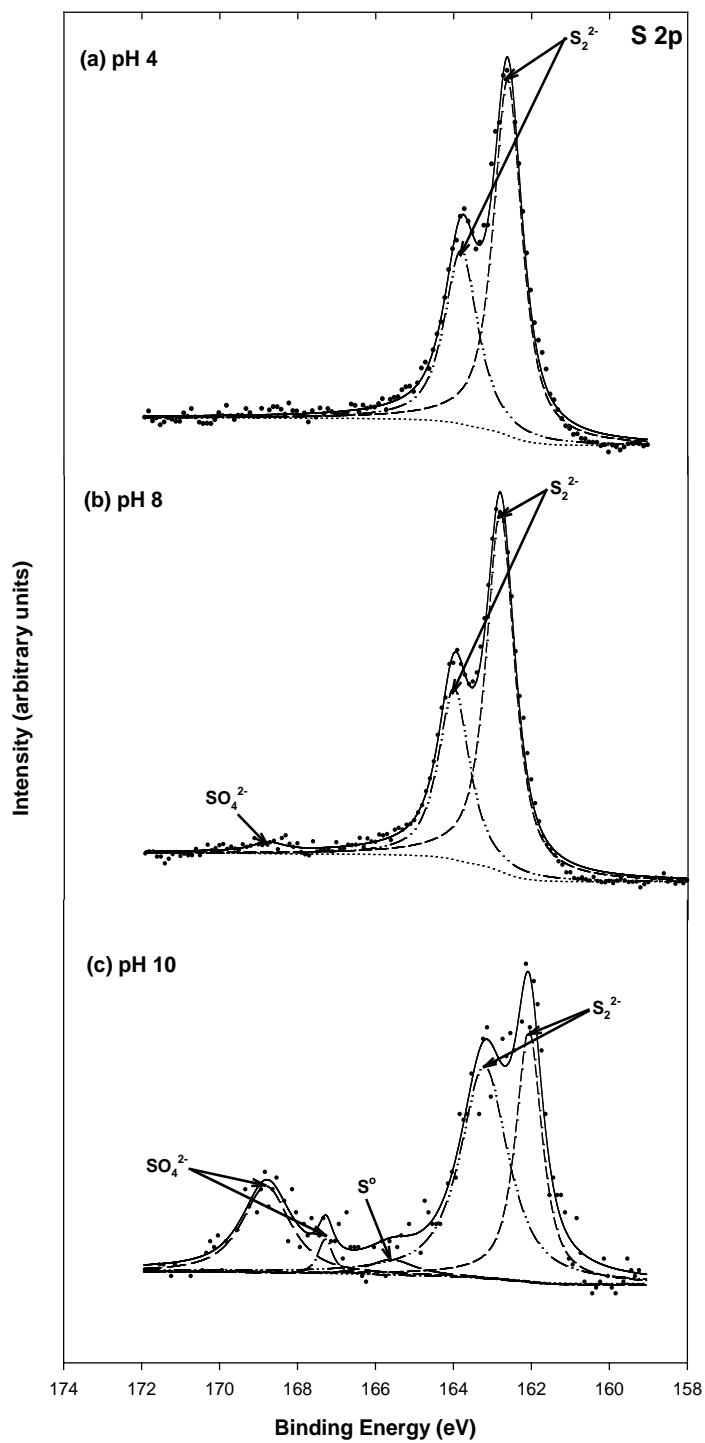


Figure 6.9 High resolution S 2p XPS spectra of pyrite (1 g/L) before contact with selenium at various pH (4, 8, 10).

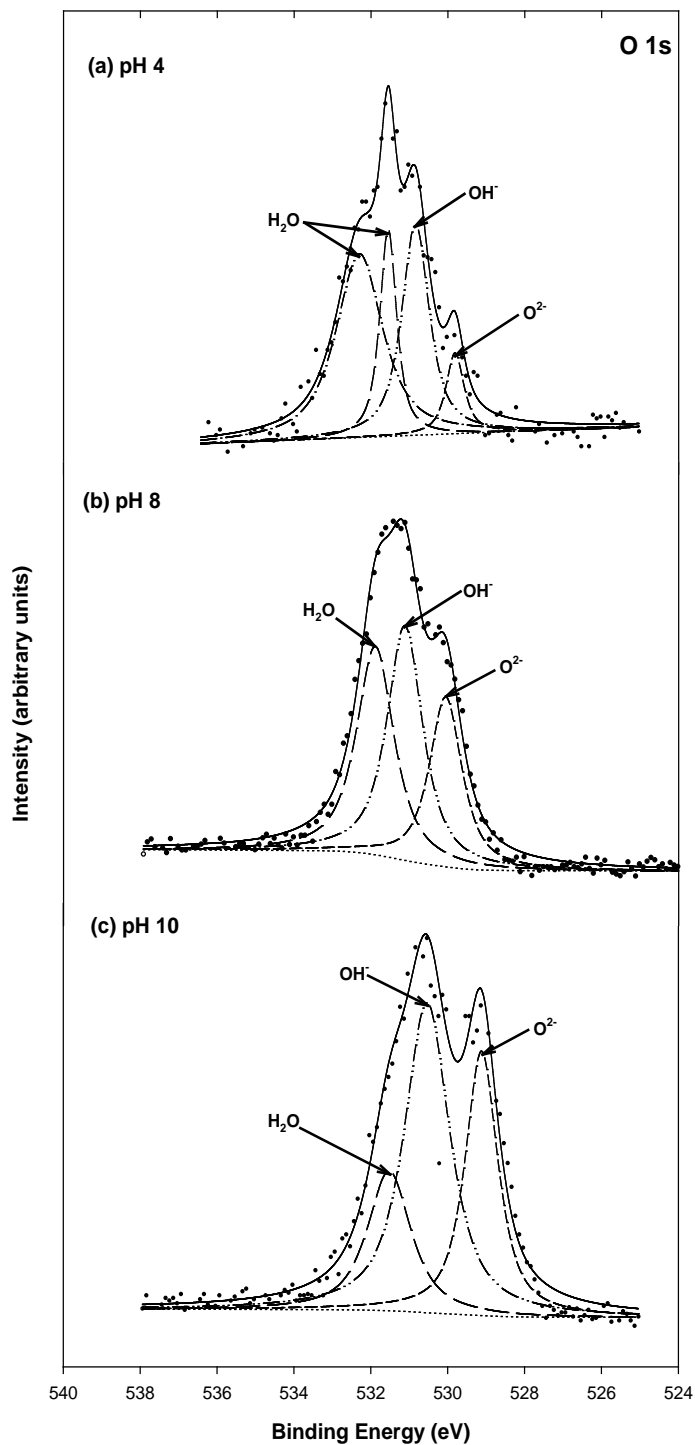


Figure 6.10 High resolution O 1s XPS spectra of pyrite (1 g/L) before contact with selenium at various pH (4, 8, 10).

Table 6.1 Binding energies (BE), full width at half maximum (FWHM), and area percentage for peaks in the Fe 2p_{3/2}, S 2p, and O 1s XPS spectra of synthetic pyrite before contact with selenium at various pH (4, 8, 10).

| Samples | BE (eV) | FWHM (eV) | Area (%) | Chemical states |
|----------------------------|---------|-----------|----------|-------------------------------|
| Fe 2p_{3/2} | | | | |
| pH 4 | 706.5 | 0.88 | 75.5 | Fe(II)-S |
| | 707.5 | 1.25 | 14.9 | Fe(II)-O |
| | 709.1 | 1.96 | 9.62 | Fe(III)-S |
| pH 8 | 706.8 | 0.86 | 72.4 | Fe(II)-S |
| | 708.3 | 1.66 | 14.2 | Fe(III)-S |
| | 710.4 | 2.09 | 13.4 | Fe(III)-O |
| pH 10 | 706.1 | 1.35 | 32.4 | Fe(II)-S |
| | 708.6 | 0.95 | 9.3 | Fe(III)-S |
| | 709.5 | 1.17 | 31.3 | Fe(III)-S |
| | 710.4 | 0.53 | 7.9 | Fe(III)-O |
| | 711.3 | 1.04 | 18.9 | Fe(III)-O |
| S 2p | | | | |
| pH 4 | 162.6 | 0.88 | 63.7 | S ₂ ²⁻ |
| | 163.8 | 1.02 | 36.3 | S ₂ ²⁻ |
| pH 8 | 162.8 | 0.87 | 64.7 | S ₂ ²⁻ |
| | 164.0 | 0.95 | 33.5 | S ₂ ²⁻ |
| | 168.7 | 0.99 | 1.7 | SO ₄ ²⁻ |
| pH 10 | 162.0 | 0.81 | 29.8 | S ₂ ²⁻ |
| | 163.2 | 1.45 | 45.6 | S ₂ ²⁻ |
| | 165.6 | 1.41 | 3.2 | S ⁰ |
| | 167.2 | 0.45 | 2.4 | SO ₄ ²⁻ |
| | 168.7 | 1.47 | 18.7 | SO ₄ ²⁻ |
| O 1s | | | | |
| pH 4 | 529.8 | 0.56 | 7.3 | O ²⁻ |
| | 530.8 | 0.85 | 29.9 | OH ⁻ |
| | 531.5 | 0.52 | 18.2 | H ₂ O |
| | 532.3 | 1.45 | 44.5 | H ₂ O |
| pH 8 | 530.0 | 1.01 | 25.5 | O ²⁻ |
| | 531.1 | 1.10 | 38.0 | OH ⁻ |
| | 531.8 | 1.17 | 36.4 | H ₂ O |
| pH 10 | 529.1 | 1.02 | 30.1 | O ²⁻ |
| | 530.5 | 1.41 | 48.8 | OH ⁻ |
| | 531.5 | 1.35 | 21.1 | H ₂ O |

6.3.3.2 Se(IV)-Contacted Pyrite

Figure 6.11 shows experimental results for the effect of pH change on the stability of Se(IV)-contacted pyrite. The experiments were conducted by adjusting pH initially to near pH 10 and then decreasing pH to near pH 4 and then increasing pH back to near pH 10. When pH was decreased, removal of Se(IV) was observed to increase over the range between pH 9 and pH 10 and to become nearly complete below pH 9. When pH was subsequently increased, no selenium was released from the pyrite. This indicates that strong bonds were formed between Se(IV) and the pyrite surface at lower pH. Previous XPS results indicated that Se(IV) on the surface of

pyrite at pH 8 was reduced to species with a range of oxidation states (Se(0), Se(-I), Se(-II)) (Section 5). Thus, it appears that the formation of FeSe or FeSe₂ leads to stable solid-phase products with low tendencies to be released to solution when pH is changed.

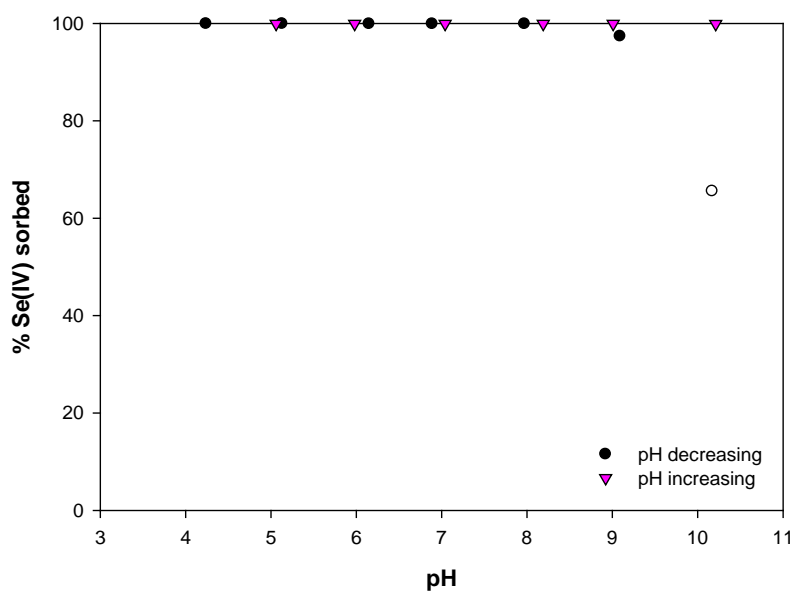


Figure 6.11 Effect of pH on removal of Se(IV) (16.5 μ M) by pyrite (1 g/L) as pH was decreased from near pH 10 and subsequently was increased.

Figure 6.12 shows SEM images for Se(IV)-contacted pyrites at extremes of pH (pH 10, pH 4). As shown in Figure 6.12(a), the morphology of solids in the pH 10 sample was mixed with both regular and irregular particle shapes, presumably due to either oxidative dissolution of pyrite or to formation of other precipitates on the pyrite surface. However, Figure 6.12(b) indicates that particles in the pH 4 sample had regular shapes without fractured pyrites, in spite of the fact that the pH 4 sample was initially at pH 10. This might be caused by irregular particles dissolving at low pH.

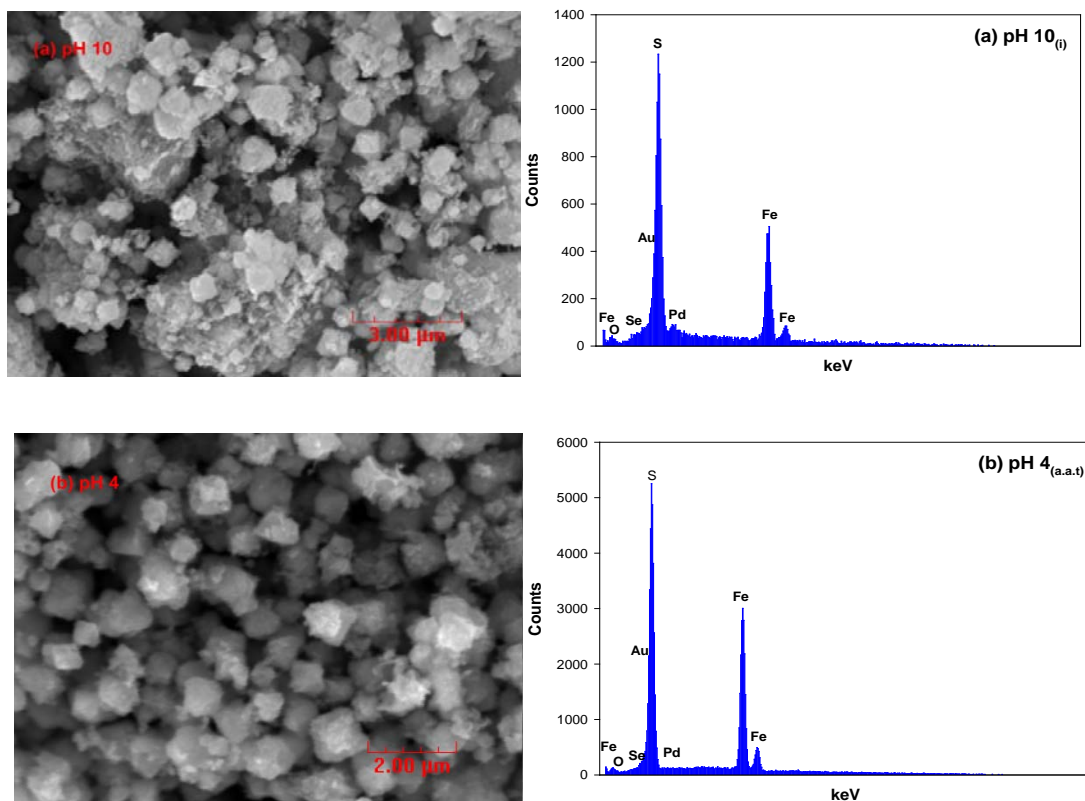


Figure 6.12 Secondary images of SEM analysis for pyrite (1 g/L) reacted with Se(IV) (16.5 μM) at (a) pH 10_(i) and (b) pH 4_(a.a.t.).

The oxidation states of the surface Fe and S, as well as solid-phase Se(IV), were evaluated by XPS analysis to investigate reaction mechanisms between the solid-phase Se(IV) and the pyrite surface. Figure 6.13 shows the Se 3d XPS spectra of pyrite contacted with Se(IV) at pH 10_(i) and pH 4_(a.a.t.). Examination of any Se 3d spectra taken in the presence of Fe should consider the peak with binding energies in the range of 50-65 eV that is caused by Fe and overlaps Se peaks in the Se 3d spectra (8). Similar interference in S 2p spectra is observed in the presence of Se, because the Se 3p spectra has binding energies in the range 157.5-167.5 eV, which is included in the range of binding energies in the Se 3p spectra (155-170 eV) (245). Therefore, investigation of other Fe or S spectra together with Se 3d spectra can help to

indirectly interpret chemical change of solid-phase Se and predict surface reactions on pyrite. As compared to Se 3d spectra of pure pyrite before contact with Se(IV), the Se 3d spectra of both pH 10_(i) and pH 4_(a.a.t) samples shows a shift of binding energy of the main peaks from 53.5 eV to 56.2 eV. This shift could be affected either by sorption of Se(IV) itself or by reduction of Se(IV) to a variety of reduced species (Se(0), Se(-I), Se(-II)). Based on results shown previously (Section 5), the shift is believed to be caused by reduction of Se(IV).

Figures 6.14 and 6.15 show Fe 2p_{3/2} and S 2p spectra for pH 10_(i) and pH 4_(a.a.t) samples. Results of XPS analysis indicates that important changes in Fe 2p_{3/2} and S 2p spectra compared to that for pure pyrite were observed for only the pH 4_(a.a.t) sample. In the case of the Fe 2p_{3/2} spectra of the pH 4_(a.a.t) sample, the intensity of peaks associated with oxidized Fe species (Fe(III)-S, Fe(III)-O) increased, while the intensity of the peak associated with the reduced Fe specie (Fe(II)-S) was relatively weak. The more oxidized surface of pyrite observed in the pH 4_(a.a.t) sample could be caused either by an oxidized patch of pyrite that was originally present, or by reduction of solid-phase Se(IV) coupled with oxidation of surface Fe species. However, the latter explanation is more likely to be correct, because the Se 3d spectra of the pH 4_(a.a.t) sample showed reduction of Se(IV). A similar shift to more oxidized species at pH 4 was observed in the S 2p XPS spectra (Figure 6.15), although some oxidized sulfur, such as sulfate (SO₄²⁻), was detected at both pH values. The presence of sulfate can be attributed to the oxidation of sulfur in pyrite caused by the reduction of Se(IV). This is similar to the behavior of Fe as shown by changes in Fe 2p XPS spectra.

Figure 6.16 displays the O 1s XPS spectra of pH 10_(i) and pH 4_(a.a.t) samples that are fitted to three peaks associated with O²⁻, OH⁻, and H₂O. The peaks are similar, except for the peak associated with OH⁻ in the pH 4_(a.a.t) sample, which has a slightly greater intensity. Moreover, the lack of any changes in peaks associated with oxide oxygen (O²⁻) is consistent with

the lack of changes in the peak associated with Fe(III)-O in the Fe 2p spectra. Table 6.2 summarizes data for binding energies (BE), peak full width at half maximum (FWHM), and relative peak area for Fe 2p_{3/2}, S 2p, O 1s photoelectron spectra of pyrite contacted with Se(IV) for different pH (10, 4).

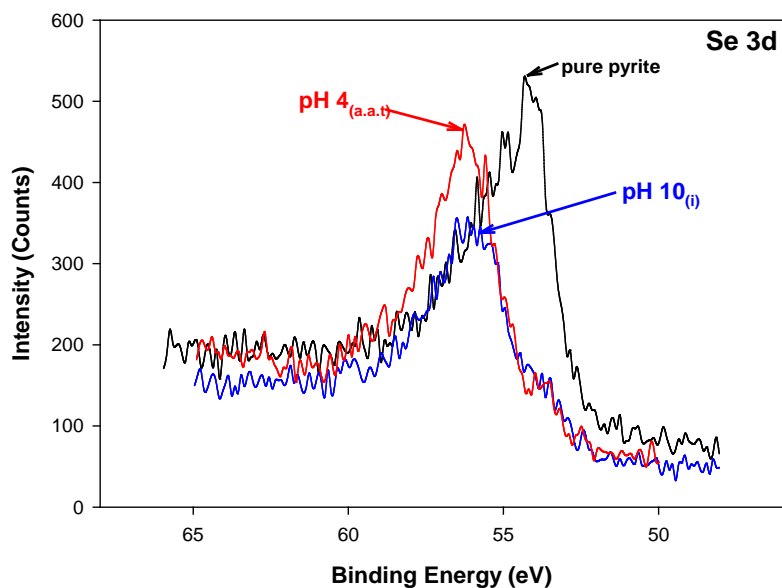


Figure 6.13 High resolution Se 3d XPS spectra for pyrite (1 g/L) after contact with Se(IV) (16.5 μM) at (a) pH 10_(i) and (b) pH 4_(a.a.t).

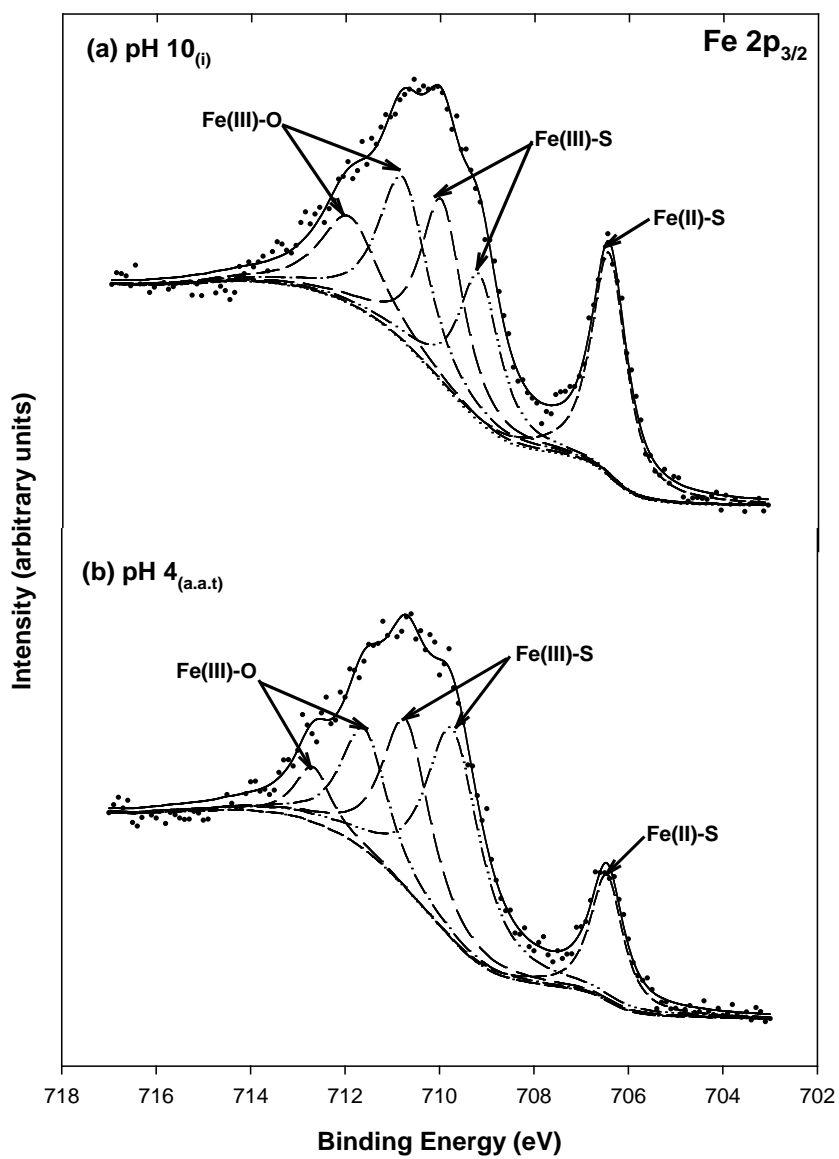


Figure 6.14 High resolution Fe 2p_{3/2} XPS spectra for pyrite (1 g/L) reacted with Se(IV) (16.5 μM) at (a) pH 10_(i) and (b) pH 4_(a.a.t).

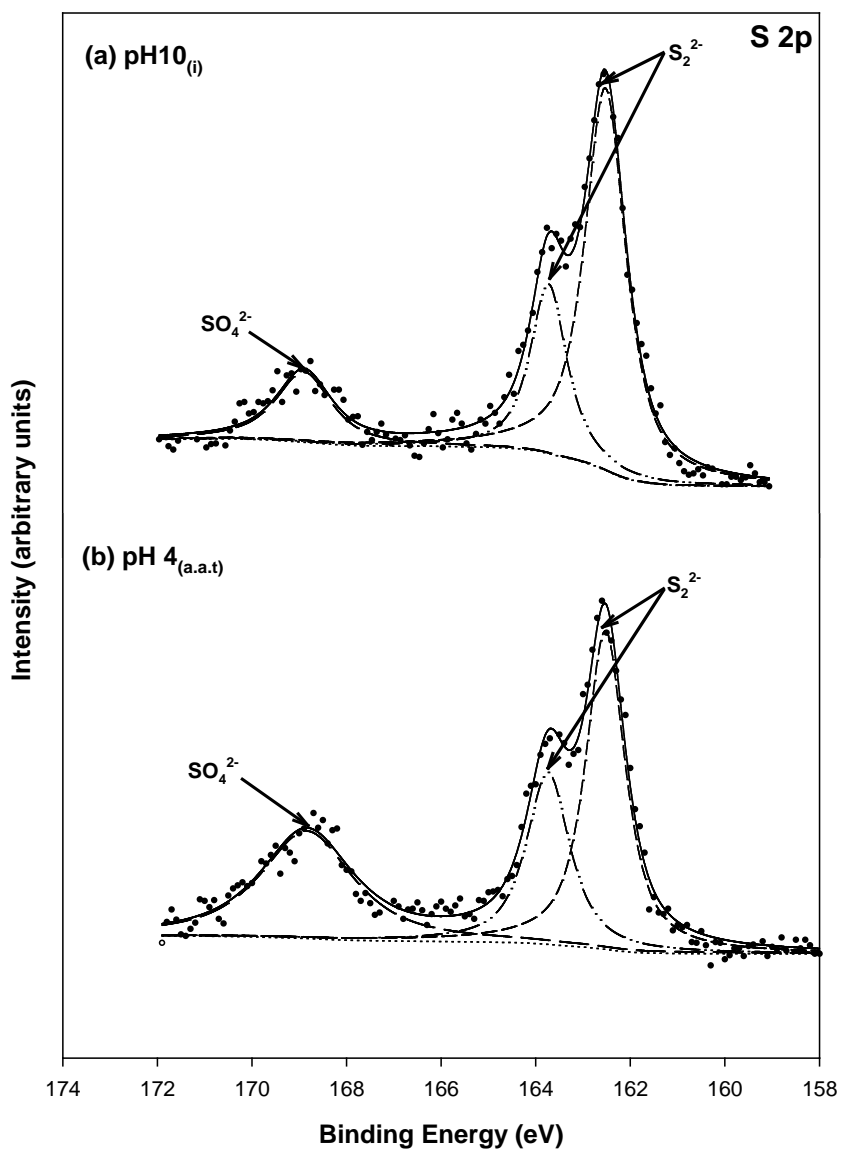


Figure 6.15 High resolution S 2p XPS spectra for pyrite (1 g/L) reacted with Se(IV) (16.5 μM) at (a) pH 10_(i) and (b) pH 4_(a.a.t).

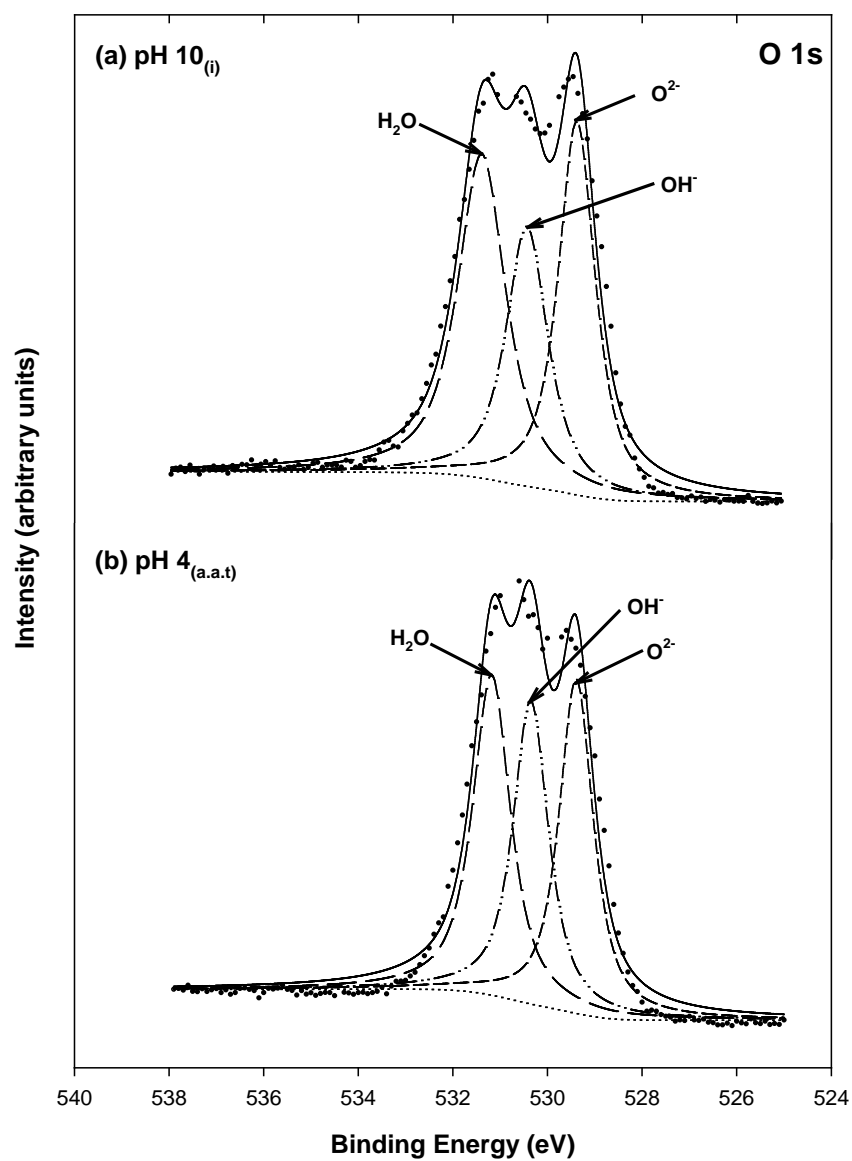


Figure 6.16 High resolution O 1s XPS spectra for pyrite (1 g/L) reacted with Se(IV) (16.5 μ M) at (a) pH 10_(i) and (b) pH 4_(a.a.t).

Table 6.2 Binding energies (BE), full width at half maximum (FWHM), and relative areas for peaks in the Fe 2p_{3/2}, S 2p, O 1s XPS spectra of synthetic pyrite contacted with Se(IV) at pH 10_(i) and pH 4_(a.a.t).

| Samples | BE (eV) | FWHM (eV) | Area (%) | Chemical states |
|-------------------------|---------|-----------|----------|-------------------------------|
| Fe 2p | | | | |
| pH 4 _(a.a.t) | 706.4 | 0.82 | 13.1 | Fe(II)-S |
| | 709.7 | 1.38 | 36.9 | Fe(III)-S |
| | 710.7 | 1.19 | 25.6 | Fe(III)-S |
| | 711.6 | 1.18 | 18.1 | Fe(III)-O |
| | 712.6 | 0.89 | 6.3 | Fe(III)-O |
| pH 10 _(i) | 706.4 | 0.87 | 22.2 | Fe(II)-S |
| | 709.1 | 1.04 | 17.5 | Fe(III)-S |
| | 709.9 | 1.06 | 22.2 | Fe(III)-S |
| | 710.7 | 1.24 | 23.2 | Fe(III)-O |
| | 711.9 | 1.47 | 14.7 | Fe(III)-O |
| S 2p | | | | |
| pH 4 _(a.a.t) | 162.5 | 0.99 | 42.1 | S ₂ ²⁻ |
| | 163.7 | 1.09 | 24.8 | S ₂ ²⁻ |
| | 168.8 | 2.31 | 32.9 | SO ₄ ²⁻ |
| pH 10 _(i) | 162.5 | 1.04 | 61.0 | S ₂ ²⁻ |
| | 163.7 | 0.92 | 23.9 | S ₂ ²⁻ |
| | 168.8 | 1.39 | 15.1 | SO ₄ ²⁻ |
| O 1s | | | | |
| pH 4 _(a.a.t) | 529.4 | 0.86 | 33.4 | O ²⁻ |
| | 530.3 | 0.89 | 31.3 | OH ⁻ |
| | 531.1 | 0.95 | 35.2 | H ₂ O |
| pH 10 _(i) | 529.3 | 0.93 | 30.2 | O ²⁻ |
| | 530.4 | 1.06 | 23.7 | OH ⁻ |
| | 531.3 | 1.22 | 34.2 | H ₂ O |

6.3.3.3 Se(VI)-Contacted Pyrite

Figure 6.17 shows experimental results for the effect of pH change on the stability of Se(VI)-contacted pyrite. The suspension was initially adjusted to near pH 4 and then the pH was raised in increments to near pH 10. It was then decreased in increments back to near pH 4. The highest removals of Se(VI) were observed at the extremes of pH (pH 4, pH 10), with lowest removals in the pH range between pH 6 and pH 8. As pH was decreased to moderate levels, some evidence of stability was observed in that more selenium remained on the pyrite at the same pH values, but when pH was being raised. However, when pH decreased to near initial pH values, less Se(VI) remained on the pyrite than was observed initially. This indicates that the physical/chemical status of the pyrite or Se(IV) may have changed at basic pH in a way that made the selenium more soluble at low pH. To clarify such surface reactions in detail, surface

morphology and oxidation states of Se(VI)-contacted pyrite at pH 4, 7 and 10 were investigated by SEM-EDS and XPS.

Figure 6.18 shows SEM images of pyrite contacted with Se(VI) at pH 4_(i), 7_(a,b,t), 10_(a,b,t). Figure 6.18(a) homogeneous surface morphology of pyrites at pH 4_(i), whereas at pH 7_(a,b,t), some different types of particles appear (Figure 6.18(b)). Furthermore, Figure 6.18(c) shows the presence of thin bundles of thread-like particles. Some parts of these particles could be precipitates that are formed by surface reactions between reduced forms of Se(VI) and pyrite, but their formation is reversible as indicated by release of selenium when pH was decreased (Figure 6.17).

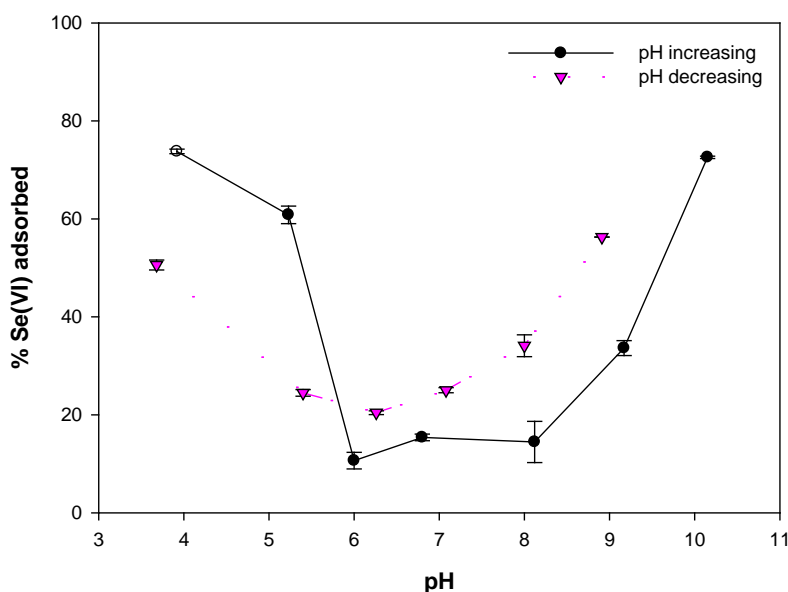


Figure 6.17 Effect of pH on removal of Se(VI) (16.5 μ M) by pyrite (1 g/L) as pH was increased from near pH 4 and subsequently was decreased.

Figure 6.19 shows the Se 3d XPS spectra of Se(VI)-contacted pyrite formed at pH 4_(i), 7_(a,b,t) and 10_(a,b,t) as pH was increased. Except for the pH 4_(i) sample, the observed results are similar to previous spectra, in which the center of the main peak is shifted to higher binding

energies (Figure 6.13). This indicates that oxidation status of Se(VI) at pH 7_(a,b,t) and pH 10_(a,b,t) has changed. This supports the hypothesis that above circumneutral pH, Se(VI) is being reduced by reaction with the pyrite surface.

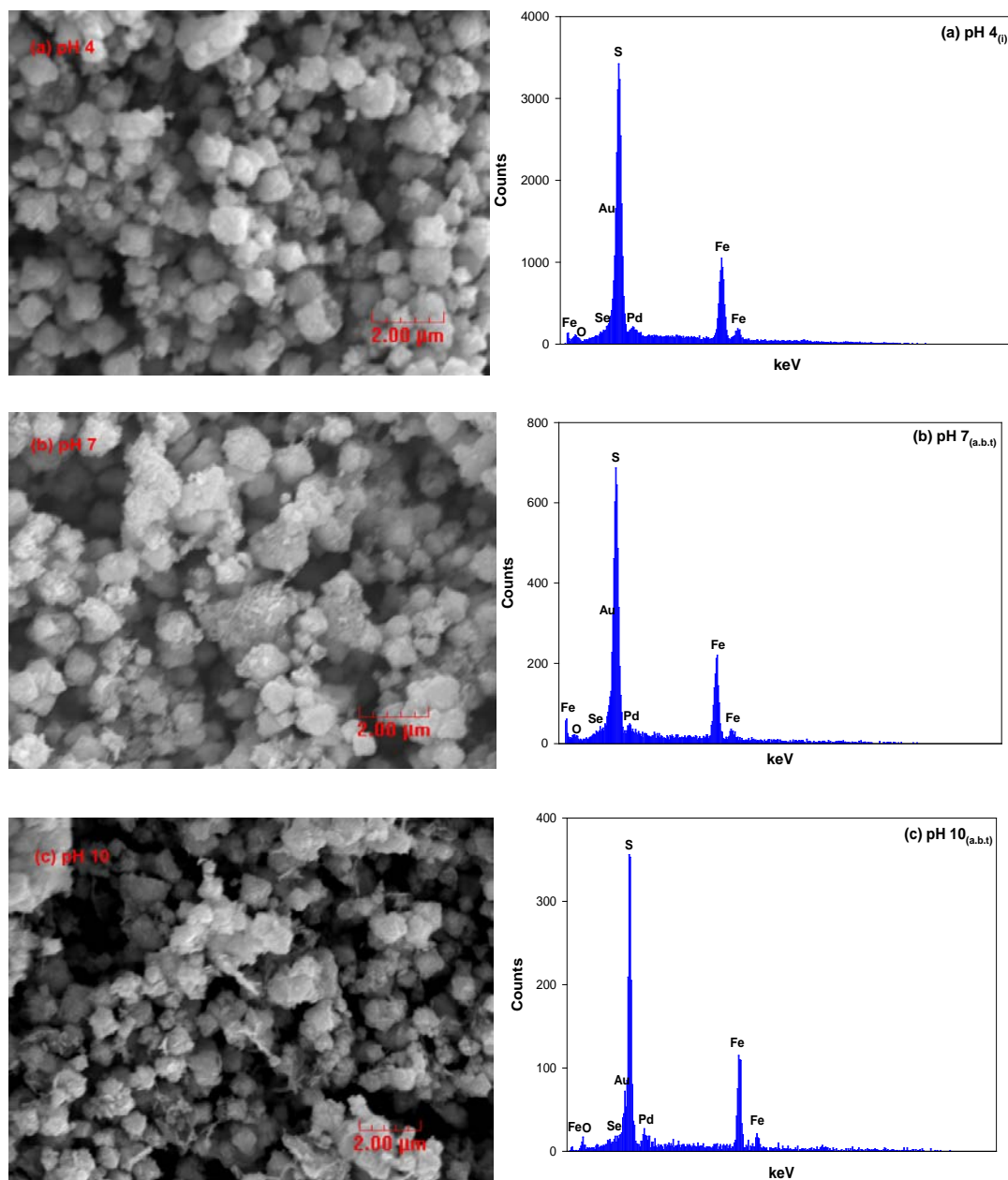


Figure 6.18 Secondary images of SEM analysis for pyrite (1 g/L) reacted with Se(VI) (16.5 μM) at (a) pH 4_(i) and (b) pH 7_(a,b,t) and (c) pH 10_(a,b,t) as pH was increased.

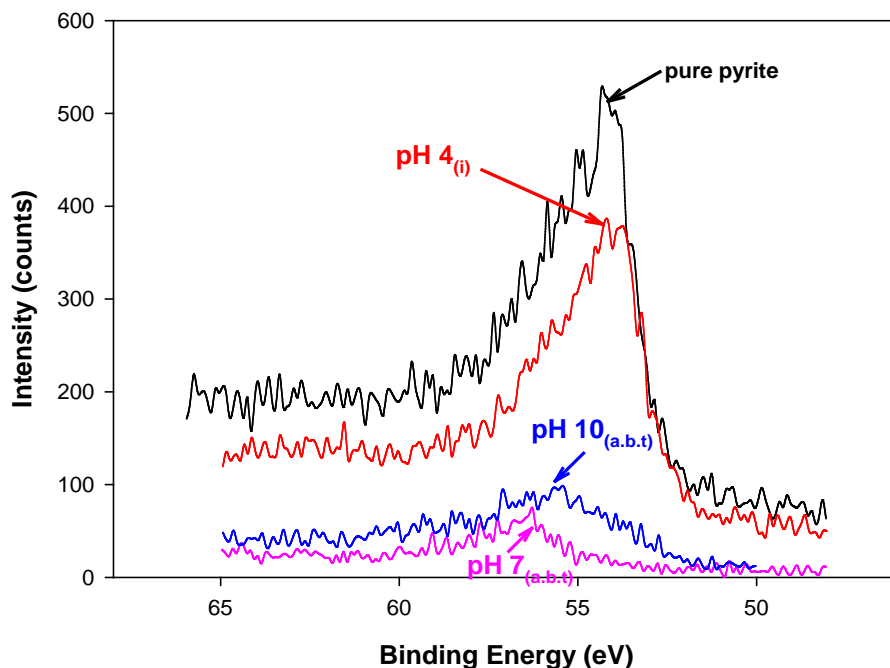


Figure 6.19 High resolution Se 3d XPS spectra for pyrite after contact with Se(VI) (16.5 μM) at pH 4_(i), 7_(a.b.t), 10_(a.b.t) as pH was increased.

The Fe 2p_{3/2} and S 2p spectra for Se(IV)-contacted pyrite were also investigated to further evaluate the hypothesis that above neutral pH, Se(IV) undergoes reduction. Figure 6.20 shows that as pH increased, several oxidized components (Fe(III)-S and Fe(III)-O) are formed at the expense of Fe(II)-S component. In particular, the surface-bound Fe in the pH 10_(a.b.t) sample was more oxidized, compared to that of pure pyrite at pH 10, presumably due to a redox reaction with sorbed Se(VI). Figure 6.21 shows that the S 2p spectra of the pH 4_(i) sample shows small amounts of sulfate, but the higher pH samples show more oxidized forms of sulfur, including elemental sulfur (S⁰) and sulfate (SO₄²⁻).

These results suggest that above circumneutral pH, sorption of Se(VI) and subsequent reduction leads to formation of low-solubility species. The reduction of Se(VI) causes the oxidation of surface Fe and S. However, higher removal of Se(VI) that was observed at pH 4_(i) compared to neutral pH, is not likely to be related to the chemical redox reactions between Se(VI) and the pyrite surface because no evidence of reduction of Se(VI) and only small indications of oxidation of the surface Fe and S were observed in the XPS results.

Figure 6.22 shows the O1s XPS spectra of pH 4_(i), 7_(a,b,t), and 10_(a,b,t) samples. The remarkable difference in the O 1s spectra is the increase in intensity of the peak associated with oxide oxygen peak (O²⁻) in samples at pH 7_(a,b,t) and 10_(a,b,t) compared to the pH 4_(i) sample. Since the intensity of the O²⁻ peak is proportional to growth of Fe(III) hydroxide, this is further evidence of the extent of oxidation of Fe(II) surface species by as pH is raised. These results support the hypothesis that higher removal of Se(VI) above pH 7 is attributed to sorption of Se(VI) followed by its reduction by reaction with the pyrite surface.

Table 6.3 summarizes data for peak binding energies (BE), full width at half maximum (FWHM), relative area for Fe 2p_{3/2}, S 2p, O 1s photoelectron spectra of pyrite contacted with Se(VI) for different pH (4, 7, 10).

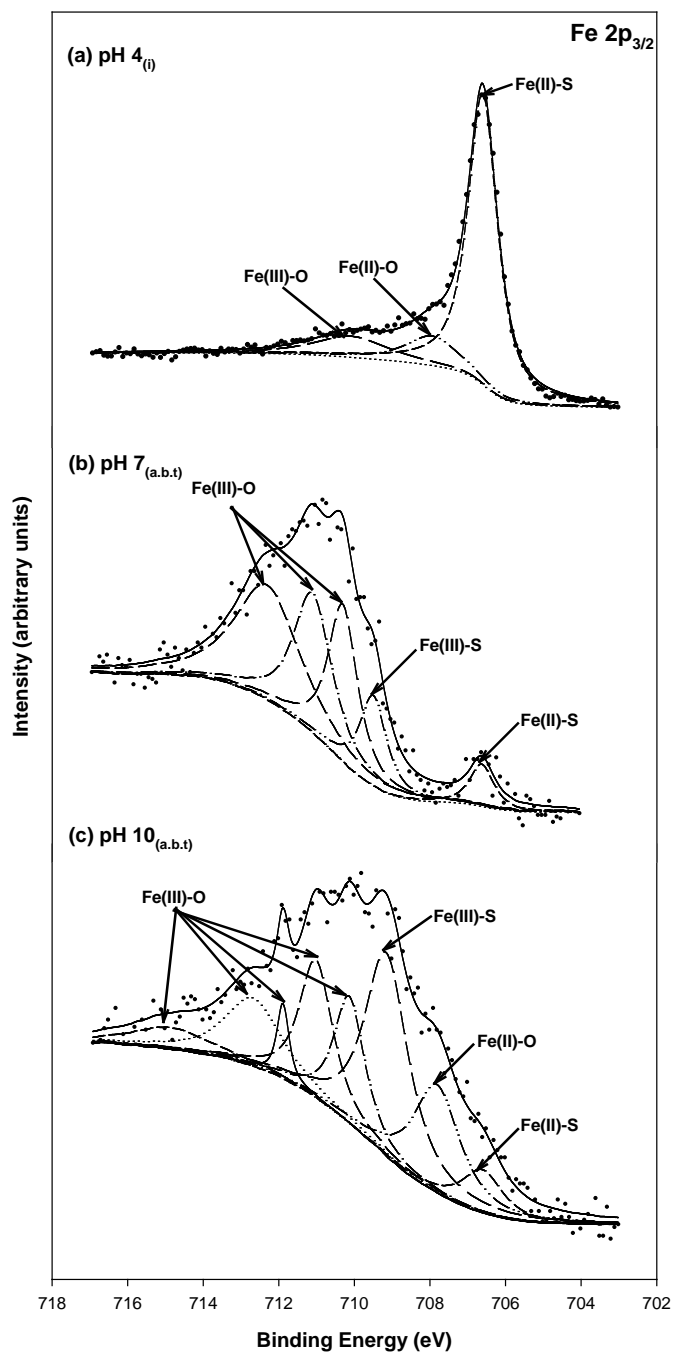


Figure 6.20 High resolution Fe $2p_{3/2}$ XPS spectra for pyrite (1 g/L) reacted with Se(VI) (16.5 μ M) at (a) pH 4_(i) and (b) pH 7_(a,b,t) and (c) pH 10_(a,b,t) as pH increased.

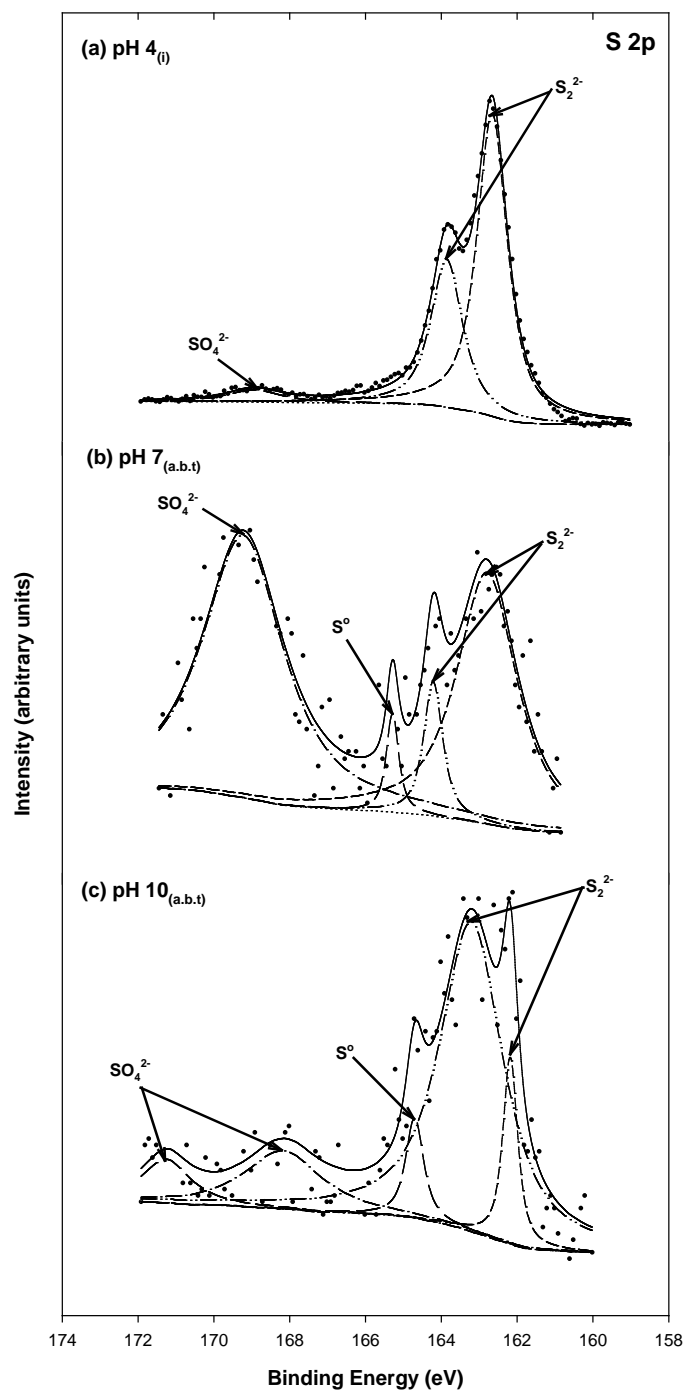


Figure 6.21 High resolution S 2p XPS spectra for pyrite (1 g/L) reacted with Se(VI) (16.5 μ M) at (a) pH 4_(i) and (b) pH 7_(a,b,t) and (c) pH 10_(a,b,t) as pH increased.

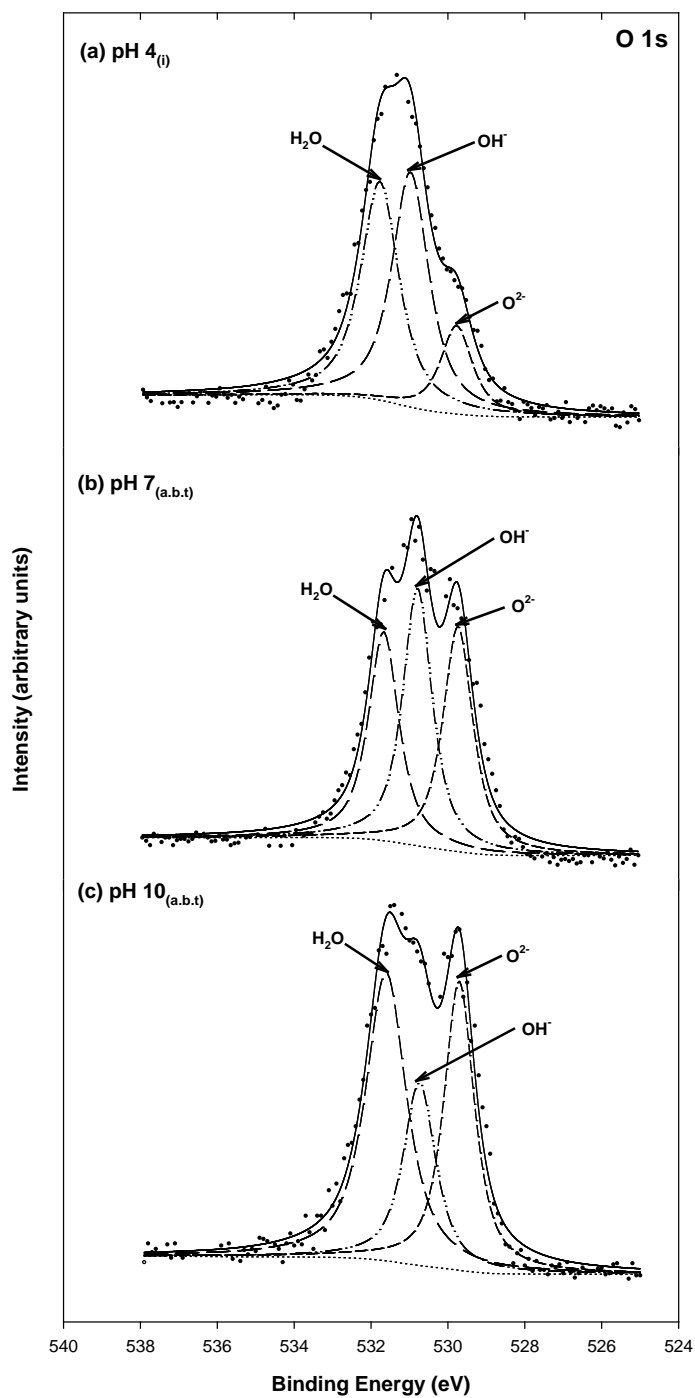


Figure 6.22 High resolution O 1s XPS spectra for pyrite (1 g/L) reacted with Se(VI) (16.5 μ M) at (a) pH 4_(i) and (b) pH 7_(a,b,t) and (c) pH 10_(a,b,t) as pH increased.

Table 6.3 Binding energies (BE), full width at half maximum (FWHM), and relative area for peaks in the Fe 2p_{3/2}, S 2p, and O 1s XPS spectra of synthetic pyrite contacted with Se(VI) at pH 4_(i), 7_(a,b,t), 10_(a,b,t).

| Samples | BE (eV) | FWHM (eV) | Area (%) | Chemical states |
|--------------------------|---------|-----------|----------|-------------------------------|
| Fe 2p | | | | |
| pH 4 _(i) | 706.6 | 0.93 | 73.3 | Fe(II)-S |
| | 707.9 | 1.68 | 13.4 | Fe(II)-O |
| | 710.1 | 2.32 | 13.2 | Fe(III)-S |
| pH 7 _(a,b,t) | 706.6 | 0.77 | 4.84 | Fe(II)-S |
| | 709.5 | 0.85 | 11.6 | Fe(III)-S |
| | 710.3 | 0.93 | 22.2 | Fe(III)-O |
| | 711.1 | 1.22 | 25.7 | Fe(III)-O |
| | 712.3 | 2.05 | 35.5 | Fe(III)-O |
| pH 10 _(a,b,t) | 706.6 | 1.28 | 5.6 | Fe(II)-S |
| | 707.8 | 1.45 | 16.1 | Fe(II)-O |
| | 709.1 | 1.38 | 28.8 | Fe(III)-S |
| | 710.1 | 0.99 | 12.9 | Fe(III)-O |
| | 711.0 | 1.07 | 15.1 | Fe(III)-O |
| | 711.9 | 0.39 | 2.94 | Fe(III)-O |
| | 712.7 | 1.79 | 12.6 | Fe(III)-O |
| | 714.8 | 2.56 | 5.69 | Fe(III)-O |
| S 2p | | | | |
| pH 4 _(i) | 162.6 | 0.96 | 63.4 | S ₂ ²⁻ |
| | 163.8 | 0.99 | 32.1 | S ₂ ²⁻ |
| | 168.9 | 1.69 | 4.50 | SO ₄ ²⁻ |
| pH 7 _(a,b,t) | 162.8 | 1.90 | 37.7 | S ₂ ²⁻ |
| | 164.2 | 0.60 | 6.4 | S ₂ ²⁻ |
| | 165.2 | 0.39 | 3.1 | S ⁰ |
| | 169.2 | 2.54 | 52.8 | SO ₄ ²⁻ |
| pH 10 _(a,b,t) | 162.1 | 0.46 | 8.9 | S ₂ ²⁻ |
| | 163.2 | 1.99 | 63.5 | S ₂ ²⁻ |
| | 164.7 | 0.56 | 5.91 | S ⁰ |
| | 168.1 | 2.44 | 14.7 | SO ₄ ²⁻ |
| | 171.3 | 1.55 | 6.9 | SO ₄ ²⁻ |
| O 1s | | | | |
| pH 4 _(i) | 529.7 | 0.99 | 14.2 | O ²⁻ |
| | 530.9 | 1.15 | 43.8 | OH ⁻ |
| | 531.7 | 1.18 | 42.0 | H ₂ O |
| pH 7 _(a,b,t) | 529.7 | 0.93 | 32.6 | O ²⁻ |
| | 530.7 | 0.92 | 36.6 | OH ⁻ |
| | 531.6 | 0.95 | 30.7 | H ₂ O |
| pH 10 _(a,b,t) | 529.7 | 0.94 | 33.2 | O ²⁻ |
| | 530.7 | 1.01 | 22.5 | OH ⁻ |
| | 531.6 | 1.26 | 44.2 | H ₂ O |

7. SORPTION OF SELENIUM(IV) AND SELENIUM(VI) TO MACKINAWITE (FeS): SPECTROSCOPIC ANALYSES

The surface of mackinawite (FeS) was characterized before and after contact with selenium (IV,VI). Results of XRD analysis of solids before contact with selenium confirmed that the form of iron sulfide being produced was mackinawite with a particle size less than 100 nm and that the diffraction pattern of TEM supports the observation that the solid phase is mostly amorphous. XPS analysis of mackinawite after contact with Se(IV) showed evidence of continuous oxidation of surface Fe(II). S 2p spectra showed some evidence of oxidation of surface S(-II) resulting in formation of polysulfides, elemental sulfur, and possibly sulfate. Se 3d spectra showed evidence of reduction of Se(IV) by contact with the mackinawite surface. These observations support the conclusion that Se(IV) sorbs to the surface of mackinawite and oxidizes surface species of iron and sulfur. XPS analysis of mackinawite after contact with Se(VI) also showed some evidence of oxidation of surface Fe(II), but not to the extent observed with Se(IV). There was little evidence for oxidation of surface sulfur, so it appears that Se(VI) is a weaker oxidant for the surface of mackinawite, either because it sorbs less strongly or that it reacts less strongly after sorption. There was little evidence of reduction of Se(VI) after contact with mackinawite.

7.1 Introduction

In the environment, trace elements are often present that are beneficial to humans, animals, and wildlife, but if they are accumulated to a sufficient degree, they can become toxic. Among them, selenium is known to be essential nutrient for plants and humans, but it can easily become hazardous, due to a very narrow margin between doses that are so low to cause nutrient deficiency and doses that cause toxicity. The U.S. Environmental Protection Agency has set the

maximum contaminant level (MCL) for selenium to be 50 $\mu\text{g/L}$ (0.633 $\mu\text{mol/L}$).

Selenium can exist in most aqueous environments in both organic and inorganic states. Organic moieties contain direct Se-C bonds, and inorganic forms are dominated by selenite (H_2SeO_3 , $\text{pK}_a=2.46, 7.31$) and selenate (HSeO_4^- , $\text{pK}_a=1.7$). Selenite is predominant under reducing to mildly oxidizing conditions and circumneutral pH, whereas selenate prevails under more strongly oxidizing conditions at higher pH (246). The toxicity of selenium depends on its oxidation state, with Se(IV) being more toxic than Se(VI).

Transport of selenium in aquatic environments is controlled by adsorption at solid-water interface. Numerous adsorbents have been utilized to remove selenium from water including goethite (53, 247), hematite (232), magnetite (243, 248), mackinawite (8), pyrite (62), aluminum oxide (222, 249), bentonite (250), zero-valent iron (251, 252), and Fe(II)/Fe(III) oxide (green rust)(242). The affinity of Se(IV) to surfaces of iron or aluminum oxides is known to be stronger than of Se(VI), resulting in higher mobility and bioavailability of Se(VI) (253). Iron sulfide (mackinawite, FeS) is a promising adsorbent for immobilizing and stabilizing selenium, because of its potential capability to reduce Se(VI) or Se(IV) to a form that could produce surface precipitates (FeSe or FeSe_2). However, reduction of selenium (IV,VI) to more electron-rich species (Se(-II), Se(0)) could proceed so slowly that various oxidation states of selenium might coexist on the solid surface (64). How selenium species are transformed on the surface of mackinawite, as well as how surface Fe and S sites change as a function of time have important implications for the extent of stabilization of selenium sorbed to mackinawite.

The purposes of this study are to demonstrate the reduction of selenium adsorbed on mackinawite and to characterize surface reactions by investigating changes in the surface Fe and S sites of mackinawite before contact with selenium(IV,VI) and for a period of 30 days after contact.

7.2 Materials and Method

7.2.1 Materials

All chemicals and solutions used in this study were prepared with analytical grade chemicals (or better) and prepared using deionized/deoxygenated (DI/DO) water. Sodium selenite (Na_2SeO_3), sodium selenate (Na_2SeO_4), sodium sulfide (Na_2S), and ferrous chloride (FeCl_2) were purchased from Sigma-Aldrich. A 1000 mg/L selenium(IV) or selenium(VI) stock solution was prepared by dissolving Na_2SeO_3 or Na_2SeO_4 , respectively. Solutions for sorption experiments at various concentrations were made by diluting a calculated amount of stock solution. All glassware and plasticware were allowed to equilibrate inside the anaerobic chamber for at least one day in order to remove all oxygen sorbed on wall. All sorption experiments were conducted in an anaerobic chamber (Coy Laboratory Products Inc.) with atmosphere of 5% H_2 and 95 % N_2 .

7.2.2 Synthesis of FeS

FeS was synthesized by a modified method of the Hayes research group, which uses FeCl_2 and Na_2S as sources of Fe(II) and sulfide (112, 254). Five hundred mL of 0.1 M Na_2S solution was added to 500 mL of 0.1 M FeCl_2 solution. Black, fine particles were formed as soon as the two solutions were mixed and they were aged for 3 days. Thereafter, the supernatant was decanted, DI/DO water was added, and particles were allowed to settle for 30 minutes. This procedure was repeated until the FeS particles did not settle. The pH of the FeS suspension was adjusted to be around pH 6 to pH 7. In order to determine solid concentration, FeS suspensions of 1 mL were transferred to five plastic bottles of known mass and the final masses of each of the bottles were measured. The solid concentration (SC) was calculated using Equations 8.1 and 8.2.

$$\bar{W}_s = \frac{\sum(W_a - W_b)}{n} \quad (7.1)$$

$$SC = \bar{W}_s \text{ g/ml} = \bar{W}_s \times 10^{-3} \text{ g/l} \quad (7.2)$$

where W_b (g) and W_a (g) are the mass of bottle before and after FeS suspension of 1 mL, n is the number of sample bottles, and \bar{W}_s (g) is the averaged mass of FeS suspension.

7.2.3 Sorption/Reaction Experiments

All sorption experiments were conducted in an anaerobic chamber. The experimental procedure was designed to produce solid samples for surface analysis using X-ray photoelectron spectroscopy (XPS) that had been in contact with Se for various reaction times. The experimental condition was that 1 g/L of FeS was reacted with 3.1 mM Se(IV) or Se(VI) at pH 8 for a period of up to 30 days. All samples were mixed by an end-over-end rotary mixer until specified sampling time (1, 15, 30 day), when the sample was filtered using 0.02- μ m anodisc membrane filter (Whatmann). The filter disk including the wet solids was moved to a labeled petri-dish, which was dried and stored in the anaerobic chamber until XPS analysis.

7.2.4 Spectroscopic Analyses

The XPS spectra for mackinawite in the presence of selenium were obtained using a Kratos Axis Ultra Imaging X-ray photoelectron spectrometer with a monochromatized Al K α (1253.6 eV) source. Before analysis, anodisc membrane filters holding Se-contacted mackinawite were attached to a copper adhesive on a sample bar, which were then loaded to the sample treatment chamber (STC) which was evacuated to a pressure that was less than 5×10^{-7} torr. Spectra were collected with a take-off angle close to 90°. The survey scans were obtained at pass energy of 80 eV to determine chemical elements and the most characteristic spectra were

recorded by the narrow scans with pass energy of 20 or 40 eV to determine oxidation states and bonding type of element (228). The charge effect was corrected using C 1s ($E_b=284.5$ eV) to calibrate the binding energy scale. The XPS spectra (Fe 2p, S 2p, O 1s, Se 3d) that were obtained were fitted using a curve-fitting program (XPSPEAK) with Gaussian Lorentzian function through background-subtraction corrections using a Shirley-type optimization.

7.2.5 Measurements of Selenium Concentration

Concentrations of selenium (IV, VI) were measured by a Perkin-Elmer atomic absorption spectrophotometer with continuous flow hydride generator. Selenite (SeO_3^{2-}) was measured without acid pretreatment, while selenate (SeO_4^{2-}) was first reduced to selenite by acid digestion (5 mL sample, 5 mL concentrated HCl in 40 mL borosilicate glass vial placed in boiling water bath for 10 minutes). The following parameters were used for these analyses: wavelength of 196.0 nm, band pass of 0.5 nm, lamp current of 75%, measurement number of 4, measurement time of 4 s, background correction is on, stabilization time of 30 s, baseline delay time of 40 s, carrier gas flow rate of 240 mL/min.

7.3 Results and Discussion

7.3.1 Surface Characterization of Synthetic Mackinawite

Figures 7.1-7.3 show results of analyses of mackinawite that were conducted by XRD, TEM, and SEM-EDS, in order to characterize surface properties and confirm its identity. The X-ray diffractogram was identified by a library search/match program which confirms that the solid phase that was synthesized is mackinawite (Figure 7.1). The XRD scan indicates that synthesized mackinawite has small particle sizes and is amorphous, because the diffraction peaks are broad and weak (*119*, *255*). There are no peaks that indicate the presence of iron oxides. Figure 7.2

shows TEM image (left-hand side) and the electron diffraction pattern for a selected area on mackinawite (right-hand side). The TEM results show particle sizes generally below about 100 nm and that mackinawite is composed of a mixture of poorly-crystalline and well-crystalline particles. The mixture is indicated by regions without rings and regions with diffuse and weak rings, including distinct spots. The SEM results shown in Figure 7.3 (left-hand side) confirm the TEM results that particles have sizes below 100 nm. Results of EDS analysis shown in Figure 7.3 (right-hand side) indicate that there is more sulfur present than iron.

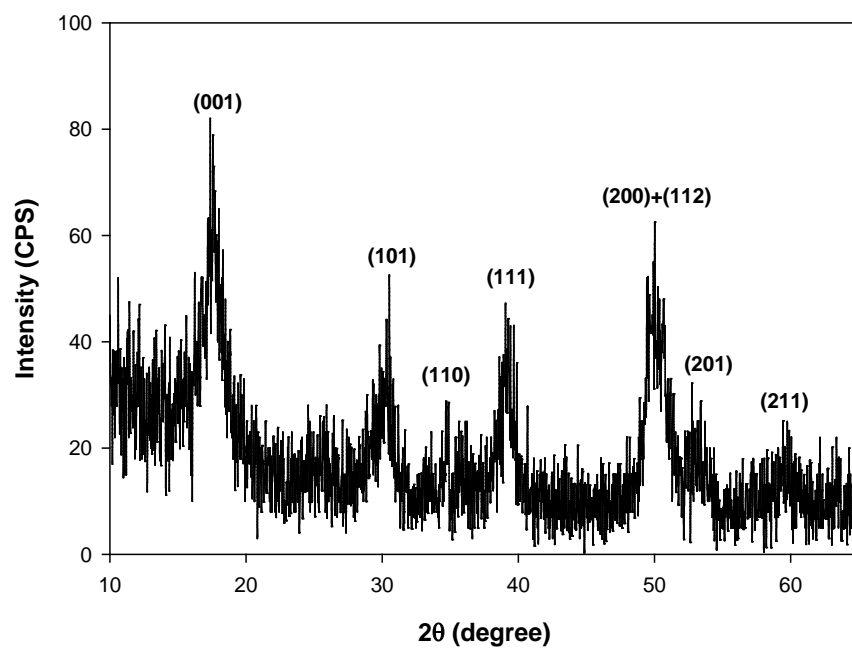


Figure 7.1 X-ray diffraction patterns of synthetic FeS.

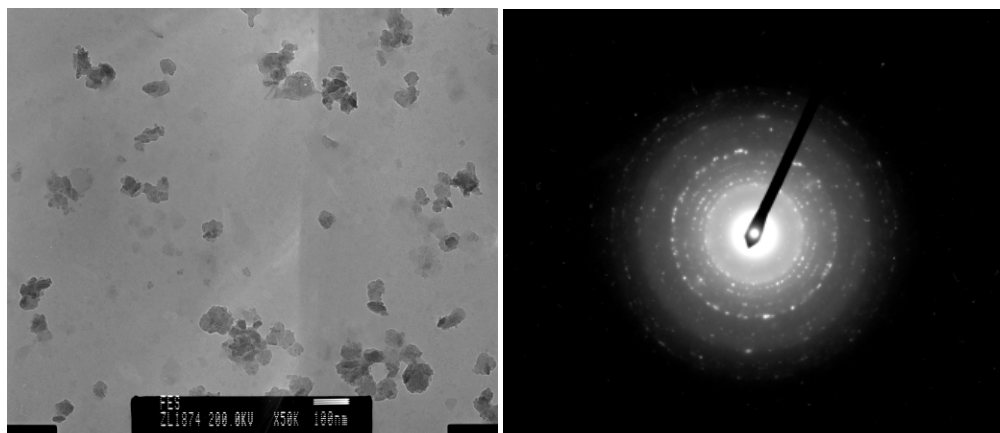


Figure 7.2 Transmission electron microscope (TEM) image (left) and selected area electron diffraction (SAED) pattern (right) of synthetic FeS.

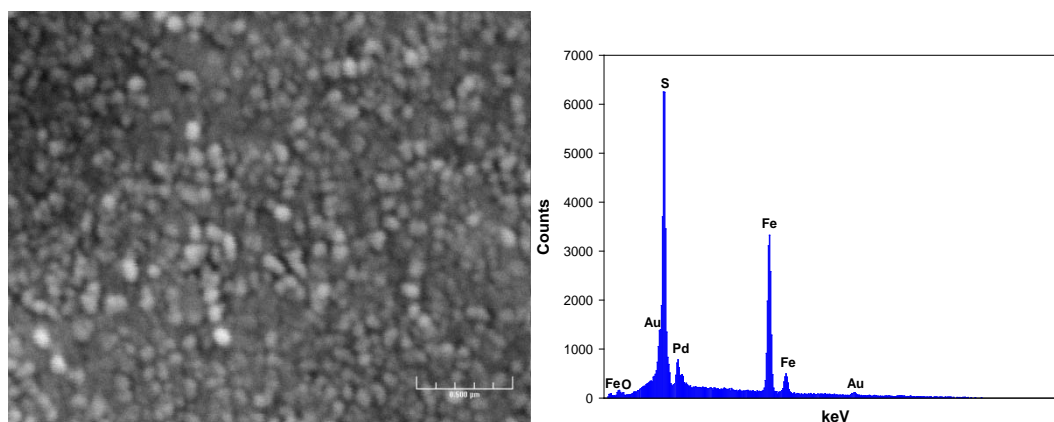


Figure 7.3 Secondary image of scanning electron microscope (SEM) (left) and analysis of energy dispersive spectroscopy (EDS) (right) of synthetic mackinawite.

7.3.2 Spectroscopic Investigation of Se-Contacted Mackinawite

Figure 7.4 shows the Se 3d XPS spectra of mackinawite before and after contact with Se(IV) or Se(VI) for various times. Before contact with Se, the Se 3d spectra for mackinawite show a peak, because of interference by the Fe 3p spectra at binding energies in the range of 50-65 eV. Figure 7.4(a) shows that major changes occur in the Se 3d spectra after contact with Se(IV) and that the changes continue over 30 days. The binding energy of the main peak shifts from 53.5 eV to around 55.6 eV and the area of the peak increases. These results can be

attributed to sorption of Se(IV) to the surface of mackinawite and subsequent reduction via surface reaction to form species such as Se(0), Se(-I), or Se(-II). The main peaks of these reduced selenium species occur with binding energies in the range of 53.7~56.3 eV, which is range where peaks are observed in Figure 7.4(a). Figure 7.4(b) indicates that there are no important changes in Se 3d spectra for mackinawite after contact with Se(VI). The lack of major changes could be caused by low amounts of Se(VI) being sorbed and small fractions of sorbed Se(VI) being reduced.

Tables 7.1-7.3 provide information about the Fe $2p_{3/2}$, S 2p and O 1s XPS spectra of mackinawite reacted with Se(IV) and Se(VI) for different times. This information includes binding energy (BE), full width at half maximum (FWHM) and percentage of peak area. Figures 7.5 and 7.6 show Fe $2p_{3/2}$ XPS spectra for mackinawite reacted for various times with a solutions of Se(IV) and Se(VI), respectively. Figure 7.5 shows four major peaks at 705.9~707.2, 707.4~707.8, 708.7~709.6, and 709.8~712.2 eV, corresponding to Fe(II)-S, Fe(II)-O, Fe(III)-S, Fe(III)-O, respectively. As contact time increases, the relative areas of the peaks associated with Fe(III)-S and Fe(III)-O increase and the relative peak areas associated with Fe(II)-S, Fe(II)-O decrease, indicating an oxidation of the iron on the pyrite surface. This could be the result of surface iron species reducing adsorbed Se(IV).

Figure 7.6 shows the Fe $2p_{3/2}$ XPS spectra for pyrite contacted with a solution of Se(VI) for various times. As contact time increases, the relative area of the peak associated with Fe(III)-O increases, but the magnitude of the change is not as great as was observed for Se(IV). These results indicate that Fe(II) on the pyrite surface undergoes a redox reaction with Se(IV) and Se(VI) resulting in formation of Fe(III) and reduced selenium species (Se(IV), Se(0), Se(-I), Se(-II)). However, the extent of oxidation of Fe(II) by Se(IV) is greater than by Se(VI).

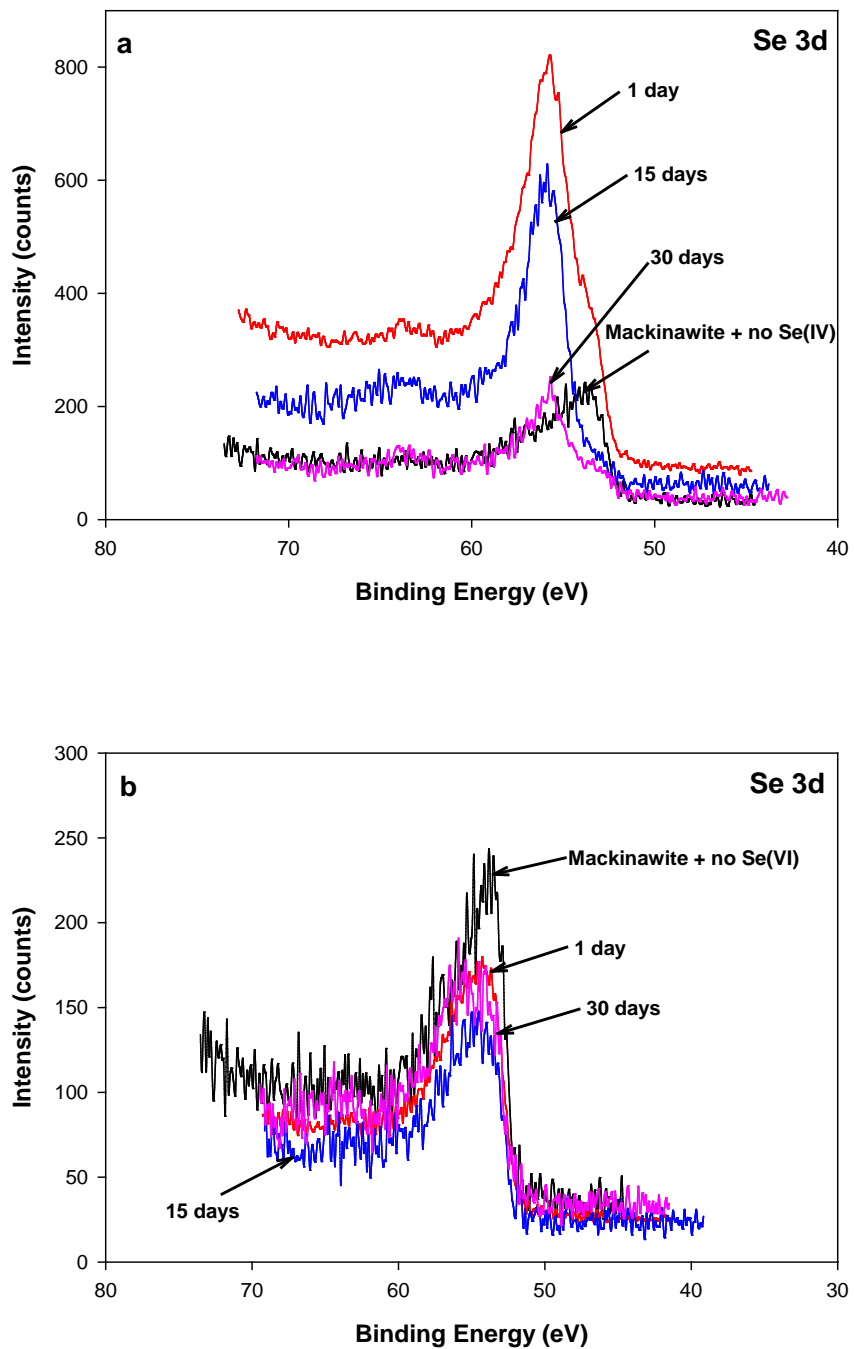


Figure 7.4 High resolution Se 3d spectra of synthetic mackinawite (1 g/L) at pH 8 before and at various times after contact with (a) 3.1 mM Se(IV) and (b) 3.1 mM Se(VI).

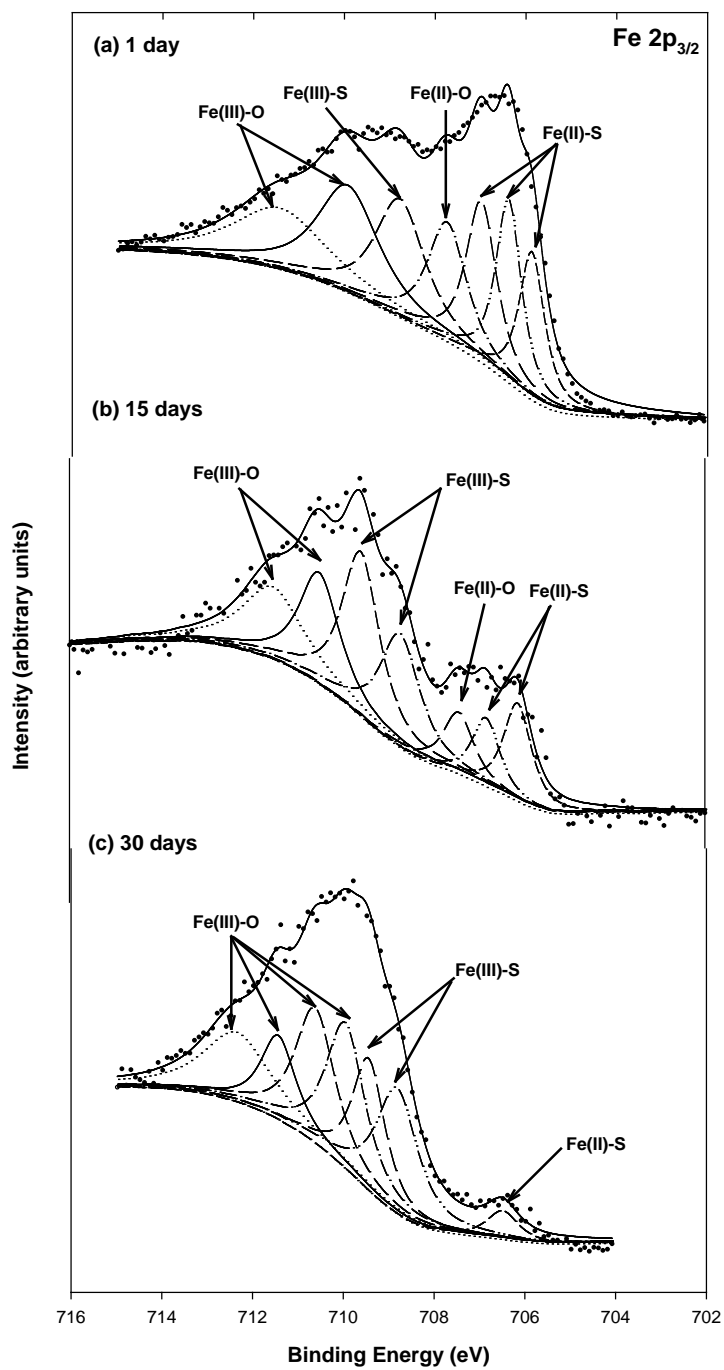


Figure 7.5 High resolution Fe $2p_{3/2}$ XPS spectra of synthetic mackinawite (1 g/L) reacted with 3.1 mM Se(IV) at pH 8 for various times: (a) 1 day, (b) 15 days, (c) 30 days.

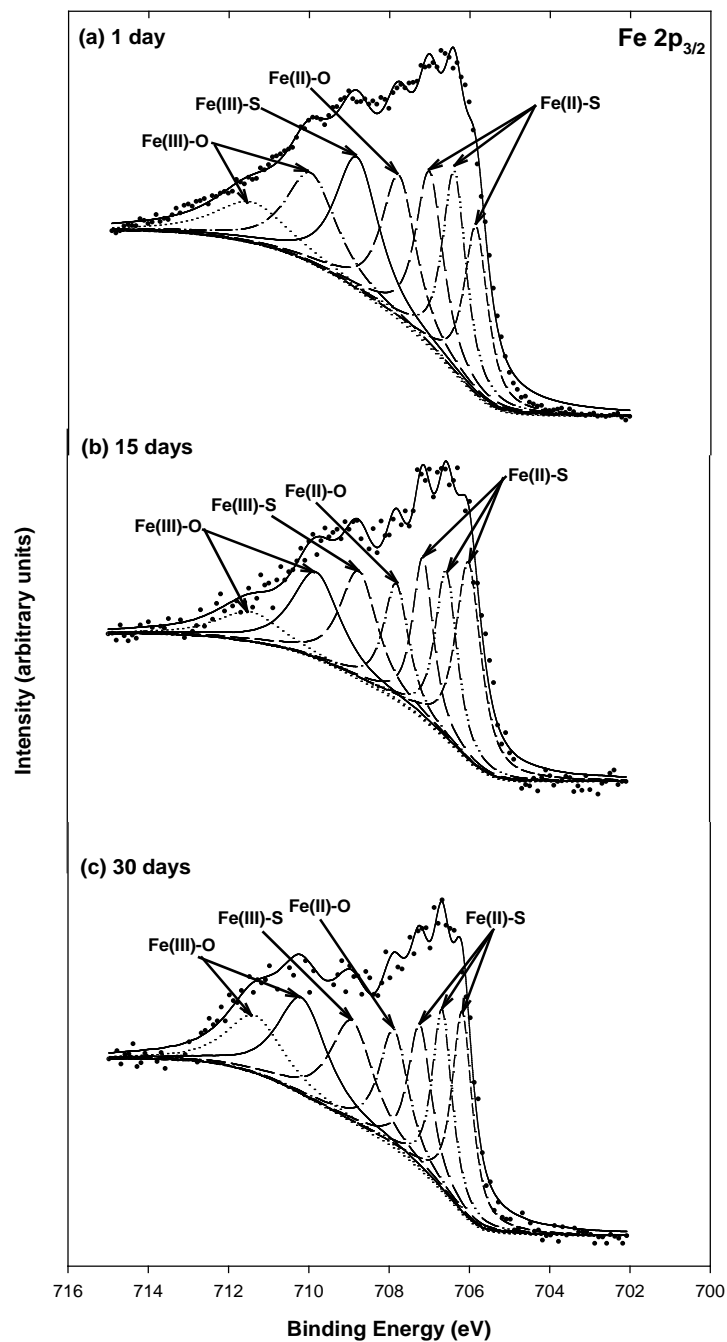


Figure 7.6 High resolution Fe $2p_{3/2}$ XPS spectra of synthetic mackinawite (1 g/L) reacted with 3.1 mM Se(VI) at pH 8 for various times: (a) 1 day, (b) 15 days, (c) 30 days.

Table 7.1 Binding energies (BE), full width at half maximum (FWHM), and area percentage for peaks in the Fe 2p_{3/2} XPS spectra of mackinawite contacted with Se(IV) and Se(VI) for various times.

| Sample | Contact time (days) | BE (eV) | FWHM (eV) | Area (%) | Chemical states |
|--------------------|---------------------|---------|-----------|----------|-----------------|
| Mackinawite | 0 | 706.0 | 0.49 | 10.4 | Fe(II)-S |
| | | 706.4 | 0.55 | 14.6 | Fe(II)-S |
| | | 706.9 | 0.71 | 17.8 | Fe(II)-S |
| | | 707.7 | 0.98 | 18.7 | Fe(II)-O |
| | | 708.8 | 1.26 | 14.6 | Fe(III)-S |
| | | 710.1 | 1.67 | 14.9 | Fe(III)-O |
| | | 711.8 | 2.51 | 9.0 | Fe(III)-O |
| Mackinawite+Se(IV) | 1 | 705.9 | 0.68 | 10.7 | Fe(II)-S |
| | | 706.4 | 0.68 | 13.2 | Fe(II)-S |
| | | 707.0 | 0.81 | 13.9 | Fe(II)-S |
| | | 707.7 | 1.03 | 13.0 | Fe(II)-O |
| | | 708.8 | 1.30 | 16.2 | Fe(III)-S |
| | | 709.9 | 1.61 | 18.0 | Fe(III)-O |
| | | 711.5 | 2.39 | 15.0 | Fe(III)-O |
| | 15 | 706.1 | 0.75 | 10.9 | Fe(II)-S |
| | | 706.8 | 0.72 | 7.3 | Fe(II)-S |
| | | 707.4 | 0.82 | 7.2 | Fe(III)-O |
| | | 708.7 | 1.05 | 17.5 | Fe(III)-S |
| | | 709.6 | 0.98 | 23.8 | Fe(III)-S |
| | | 710.5 | 1.06 | 17.1 | Fe(III)-O |
| | | 711.6 | 1.56 | 16.3 | Fe(III)-O |
| | 30 | 706.5 | 0.82 | 3.1 | Fe(II)-S |
| | | 708.9 | 1.17 | 22.6 | Fe(III)-S |
| | | 709.5 | 0.79 | 13.9 | Fe(III)-S |
| | | 710.1 | 1.02 | 21.4 | Fe(III)-O |
| | | 710.7 | 0.89 | 13.7 | Fe(III)-O |
| | | 711.4 | 0.65 | 6.4 | Fe(III)-O |
| 712.2 | 1.82 | 19.0 | Fe(III)-O | | |
| Mackinawite+Se(VI) | 1 | 705.8 | 0.70 | 12.5 | Fe(II)-S |
| | | 706.4 | 0.71 | 14.9 | Fe(II)-S |
| | | 707.0 | 0.82 | 15.1 | Fe(II)-S |
| | | 707.7 | 1.03 | 15.7 | Fe(II)-O |
| | | 708.8 | 1.30 | 18.1 | Fe(III)-S |
| | | 709.9 | 1.50 | 14.2 | Fe(III)-O |
| | | 711.4 | 2.21 | 9.5 | Fe(III)-O |
| | 15 | 706.0 | 0.76 | 20.1 | Fe(II)-S |
| | | 706.5 | 0.65 | 14.6 | Fe(II)-S |
| | | 707.1 | 0.62 | 13.4 | Fe(II)-S |
| | | 707.8 | 0.75 | 11.6 | Fe(II)-O |
| | | 708.7 | 1.11 | 16.1 | Fe(III)-S |
| | | 709.8 | 1.43 | 16.5 | Fe(III)-O |
| | | 711.4 | 1.91 | 7.6 | Fe(III)-O |
| | 30 | 706.1 | 0.59 | 15.2 | Fe(II)-S |
| | | 706.6 | 0.59 | 13.4 | Fe(II)-S |
| | | 707.2 | 0.70 | 12.7 | Fe(II)-S |
| | | 707.8 | 0.87 | 12.9 | Fe(II)-O |
| | | 708.9 | 1.27 | 16.1 | Fe(III)-S |
| | | 710.1 | 1.47 | 17.7 | Fe(III)-O |
| 711.3 | 1.66 | 12.0 | Fe(III)-O | | |

Figures 7.7 and 7.8 show the S 2p XPS spectra for mackinawite reacted with Se(IV) and Se(VI), respectively. In order to fit the asymmetric peak centered near 161.8 eV and the high

energy tail, polysulfides (S_n^{2-}) and elemental sulfur (S^0) were considered as surface species. Some oxidation of mackinawite surface could occur during the transfer of samples for XPS analysis. In the case of Se(IV) (Figure 7.7), peaks associated with the sulfate ion (SO_4^{2-}) were observed after 15 days of contact, whereas there were no sulfate peaks in the S 2p spectra after contact with Se(VI) (Figure 7.8). These results support the hypothesis that sulfur on the surface of mackinawite reduces Se(IV) and Se(VI), but that it has a greater affinity for Se(IV).

Table 7.2 Binding energies (BE), full width at half maximum (FWHM), area percentage for peaks in the S 2p XPS spectra of mackinawite contacted with Se(IV) and Se(VI) for various times.

| Sample | Contact time (days) | BE (eV) | FWHM (eV) | Area (%) | Chemical states |
|--------------------|---------------------|---------|-----------|------------|-----------------|
| Mackinawite | 0 | 161.3 | 0.55 | 14.0 | S^{2-} |
| | | 161.8 | 0.62 | 22.0 | S^{2-} |
| | | 162.3 | 0.68 | 26.3 | S^{2-} |
| | | 163.1 | 1.03 | 35.0 | S_n^{2-} |
| | | 164.5 | 0.88 | 2.6 | S^0 |
| Mackinawite+Se(IV) | 1 | 161.7 | 0.44 | 12.8 | S^{2-} |
| | | 162.0 | 0.44 | 15.8 | S^{2-} |
| | | 162.5 | 0.62 | 16.2 | S^{2-} |
| | | 163.2 | 0.99 | 32.6 | S_n^{2-} |
| | | 164.1 | 1.73 | 22.5 | S^0 |
| | 15 | 161.6 | 0.50 | 10.1 | S^{2-} |
| | | 162.0 | 0.46 | 18.9 | S^{2-} |
| | | 162.7 | 0.73 | 21.0 | S^{2-} |
| | | 163.2 | 0.67 | 13.8 | S_n^{2-} |
| | | 164.0 | 1.25 | 20.8 | S^0 |
| | 30 | 168.4 | 1.99 | 15.4 | SO_4^{2-} |
| | | 161.4 | 0.45 | 12.4 | S^{2-} |
| | | 162.0 | 0.81 | 25.3 | S^{2-} |
| | | 162.8 | 1.18 | 23.0 | S^{2-} |
| Mackinawite+Se(VI) | 1 | 161.8 | 0.53 | 21.0 | S^{2-} |
| | | 162.2 | 0.51 | 18.4 | S^{2-} |
| | | 162.7 | 0.71 | 24.8 | S^{2-} |
| | | 163.4 | 1.03 | 31.7 | S_n^{2-} |
| | | 164.6 | 1.13 | 4.2 | S^0 |
| | 15 | 161.5 | 0.50 | 11.0 | S^{2-} |
| | | 162.0 | 0.48 | 27.2 | S^{2-} |
| | | 162.7 | 0.76 | 31.6 | S^{2-} |
| | | 163.5 | 0.91 | 26.0 | S_n^{2-} |
| | | 164.5 | 1.24 | 4.3 | S^0 |
| 30 | 161.5 | 0.50 | 8.9 | S^{2-} | |
| | 162.0 | 0.48 | 21.3 | S^{2-} | |
| | 162.5 | 0.69 | 27.1 | S^{2-} | |
| | 163.4 | 0.96 | 32.3 | S_n^{2-} | |
| | 164.7 | 1.63 | 10.4 | S^0 | |

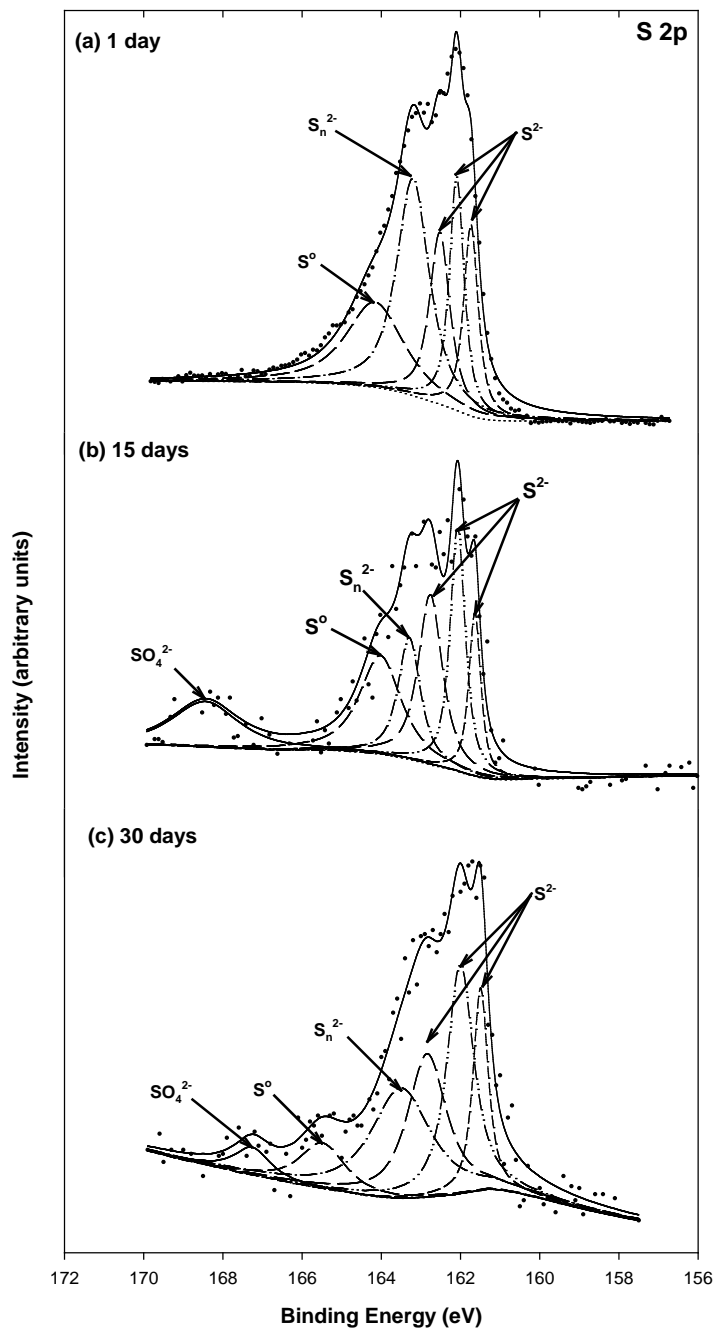


Figure 7.7 High resolution S 2p spectra of synthetic mackinawite (1 g/L) reacted with 3.1 mM Se(IV) at pH 8 for various times: (a) 1 day, (b) 15 days, (c) 30 days.

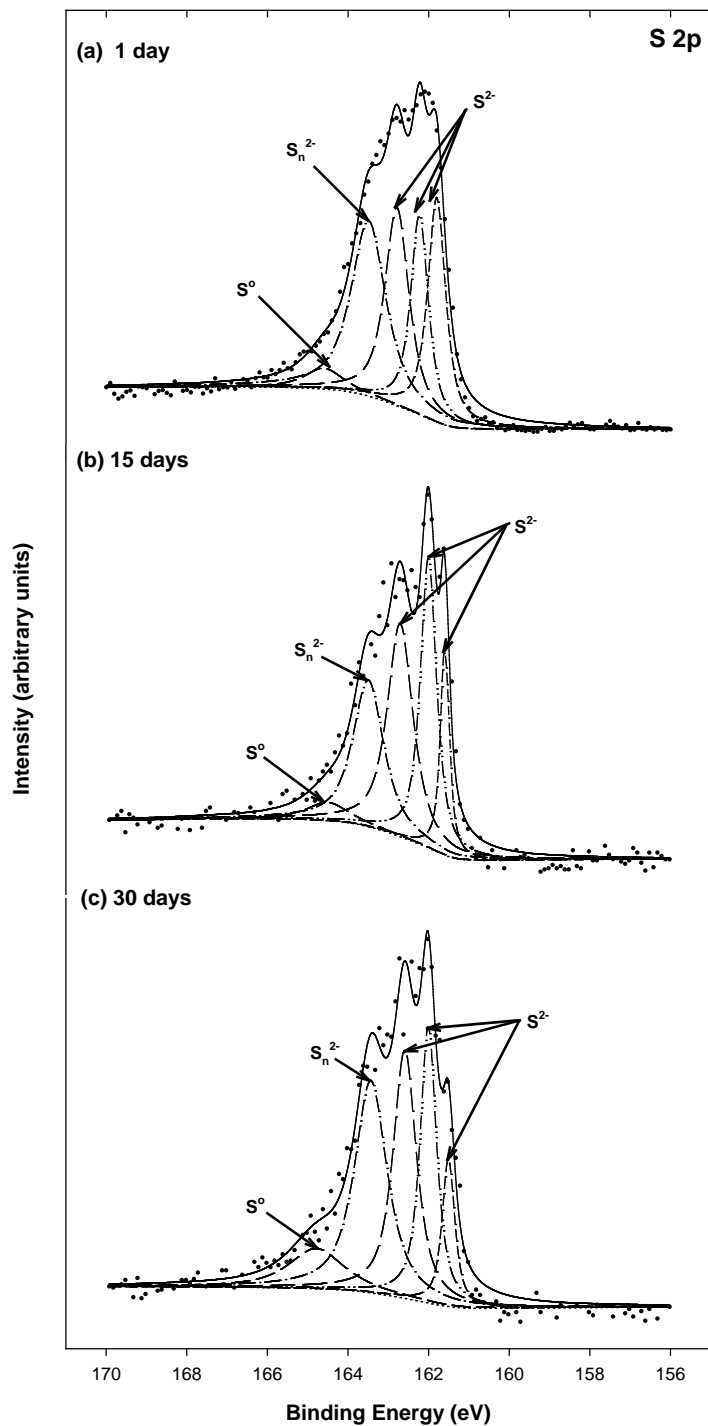


Figure 7.8 High resolution S 2p spectra of synthetic mackinawite (1 g/L) reacted with 3.1mM Se(VI) at pH 8 for various times: (a) 1 day, (b) 15 days, (c) 30 days.

Figures 7.9 and 7.10 show O 1s XPS spectra of mackinawite reacted with Se(IV) and Se(VI) for 1, 15 and 30 days. The O 1s spectra were fitted with three components at 529.0~529.7 eV, 530.2~530.7 eV, and 531.1~531.7 eV, corresponding to oxide oxygen (O^{2-}), structural hydroxide (OH^-), and adsorbed water molecule (H_2O), respectively. The occurrence of oxygen species on the surface of mackinawite may be related to several mechanisms. The structural hydroxide originates from dissociation of sorbed water molecules and, if atmospheric O_2 is present, from the combination of the second a proton (H^+) and O^{2-} , which is produced by reduction of O_2 (229). Although experiments were conducted in an anaerobic chamber, the presence of atmospheric O_2 on the surface cannot be totally ruled out, because the solid samples were exposed to air when transferred for XPS analysis. Figure 7.9 shows that the OH^- peak increases over time, while the H_2O peak decreases from day 1 to day 15, but increases at day 30 back to a value (34.4 %) that is close to the value observed at day 1 (36.1 %) (Table 7.3). The additional OH^- can be incorporated into Fe(III)-oxyhydroxide surface species. At 30 days, an appreciable decrease in the peak for O^{2-} coincides with growth of the OH^- peak, which could be caused by combination of a proton (H^+) and O^{2-} on the surface. In the case of mackinawite contacted with Se(VI) (Figure 7.10), the relationship between H_2O and OH^- that was seen by the Se(IV)-contacted mackinawite was observed at day 15 and day 30. As compared to day 15, the percentage of area for the H_2O peak at 30 days decreased from 54.8 to 45.2 %, while the relative area of the OH^- peak increased from 23.9 % to 29.9 %. The growth of Fe(III)-oxyhydroxide surface species coincide with the increase of OH^- peak, as was observed for mackinawite contacted with Se(IV).

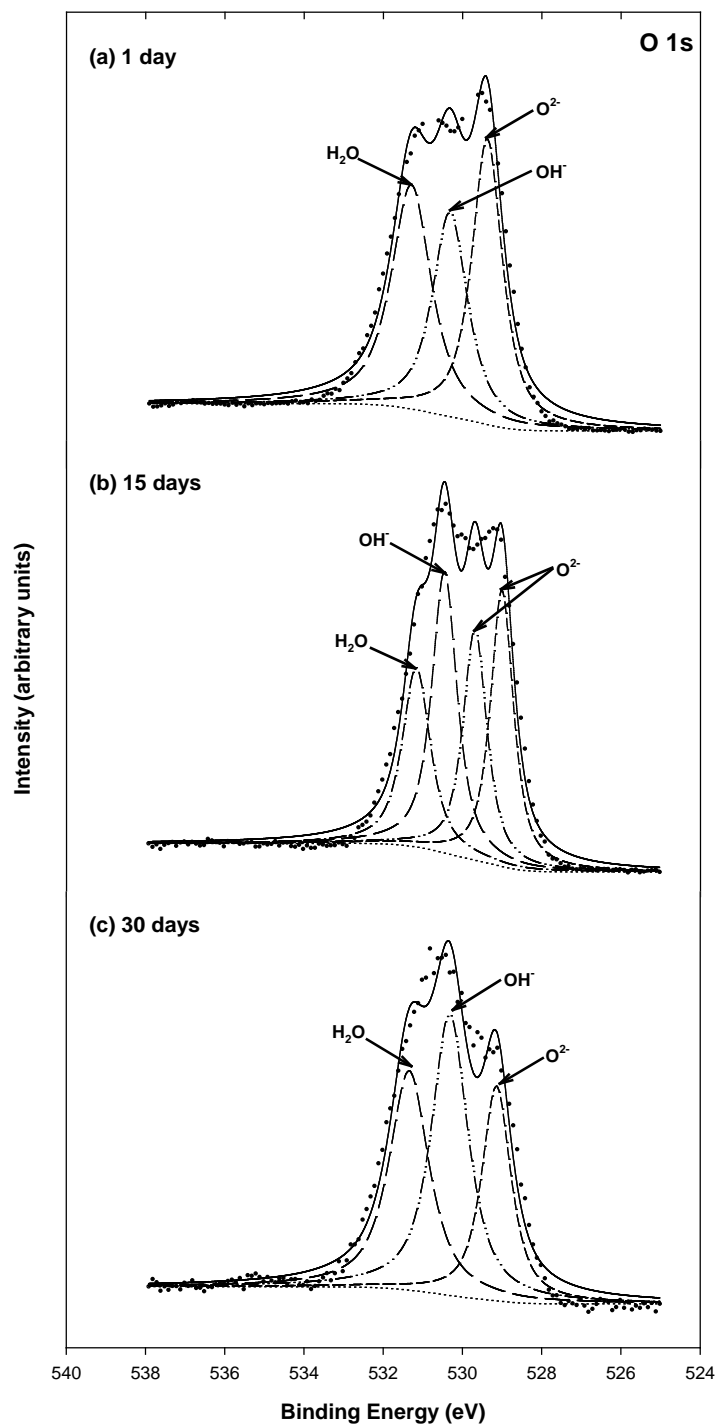


Figure 7.9 High resolution of O 1s XPS spectra for synthetic mackinawite (1 g/L) reacted with 3.1 mM Se(IV) at pH 8 for various times: (a) 1 day, (b) 15 days, (c) 30 days.

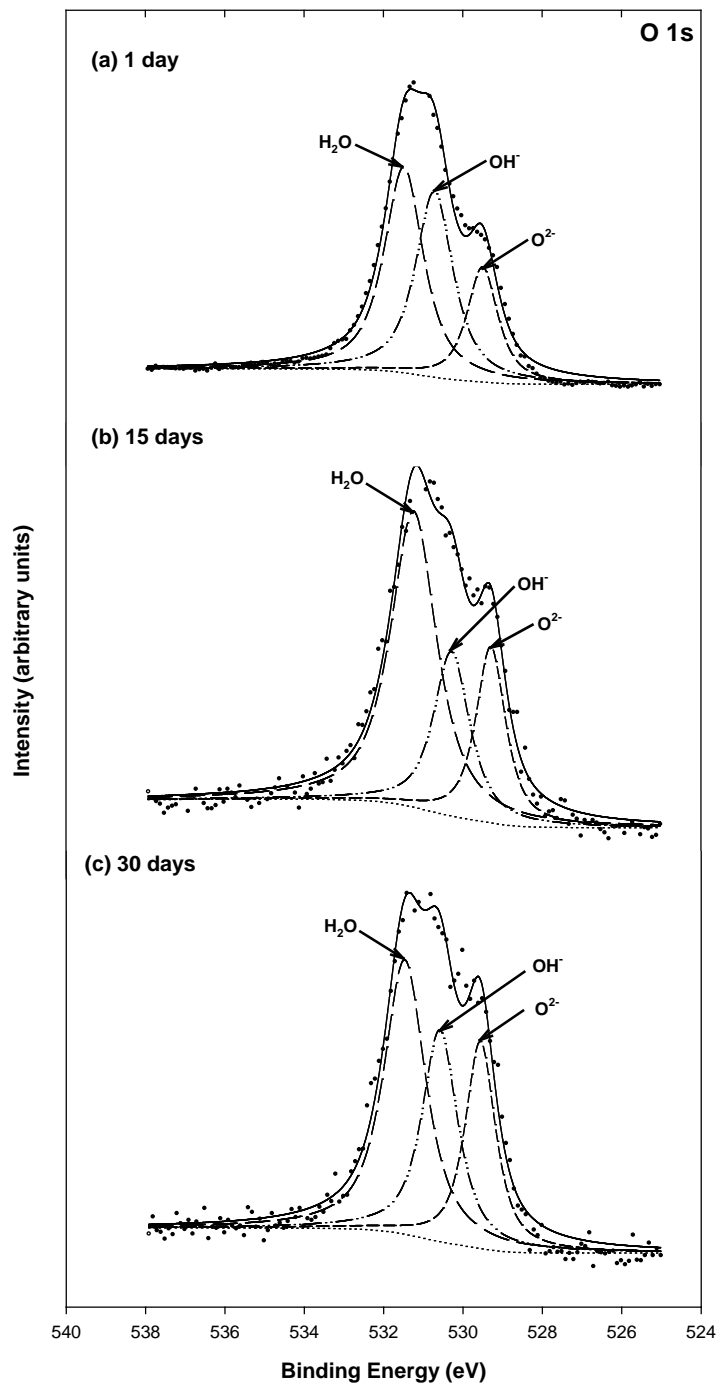


Figure 7.10 High resolution of O 1s XPS spectra for synthetic mackinawite (1 g/L) reacted with 3.1 mM Se(VI) at pH 8 for various times: (a) 1 day, (b) 15 days, (c) 30 days.

Table 7.3 Binding energies (BE), full width at half maximum (FWHM), and area percentage for peaks in the O 1s XPS spectra of mackinawite contacted with Se(IV) and Se(VI) for various times.

| Sample | Contact time (days) | BE(eV) | FWHM (eV) | Area (%) | Chemical states |
|--------------------|---------------------|--------|-----------|----------|------------------|
| Mackinawite | 0 | 529.2 | 0.95 | 23.4 | O ²⁻ |
| | | 530.5 | 1.41 | 48.4 | OH ⁻ |
| | | 531.7 | 1.56 | 28.2 | H ₂ O |
| Mackinawite+Se(IV) | 1 | 529.3 | 0.92 | 35.0 | O ²⁻ |
| | | 530.3 | 1.06 | 28.9 | OH ⁻ |
| | | 531.3 | 1.21 | 36.1 | H ₂ O |
| | 15 | 529.0 | 0.69 | 26.5 | O ²⁻ |
| | | 529.7 | 0.72 | 23.0 | O ²⁻ |
| | | 530.4 | 0.76 | 29.6 | OH ⁻ |
| | 30 | 531.1 | 0.84 | 20.9 | H ₂ O |
| | | 529.1 | 0.88 | 24.8 | O ²⁻ |
| | | 530.3 | 1.10 | 40.8 | OH ⁻ |
| | | 531.3 | 1.19 | 34.4 | H ₂ O |
| Mackinawite+Se(VI) | 1 | 529.4 | 0.93 | 19.1 | O ²⁻ |
| | | 530.7 | 1.13 | 37.6 | OH ⁻ |
| | | 531.4 | 1.18 | 43.3 | H ₂ O |
| | 15 | 529.2 | 0.89 | 21.2 | O ²⁻ |
| | | 530.2 | 1.09 | 23.9 | OH ⁻ |
| | | 531.2 | 1.38 | 54.8 | H ₂ O |
| | 30 | 529.5 | 0.92 | 24.9 | O ²⁻ |
| | | 530.5 | 1.08 | 29.9 | OH ⁻ |
| | | 531.4 | 1.25 | 45.2 | H ₂ O |

8. SORPTION OF SELENIUM(IV) AND SELENIUM(VI) TO MACKINAWITE (FeS): KINETICS, EXTENT OF REMOVAL, STABILITY

Batch experiments were conducted to evaluate kinetics of removal of two oxidation states of selenium (Se(IV), Se(VI)) and to evaluate the effects of pH and sulfate concentration on removals. These experiments were conducted in a way that is similar to those used to measure adsorption equilibrium, although true equilibrium was not observed for selenium removals in this work. Se(IV) was removed very rapidly by FeS with complete removal of low concentration of Se(IV) (6.3, 12.7, 38 μM) by 1.0 g/L FeS being achieved within 30 minutes. Higher concentrations (127, 253 μM) were completely removed by 0.5 g/L FeS within 120 minutes. Removal patterns for Se(IV) by FeS depend on pH. Removal patterns at pH 7 and pH 8 were best described by BET models, while removal patterns at pH 9 and 10 were best described by Langmuir models. Sulfate at 1 and 10 mM had negligible effect on removal of Se(IV) by FeS. Removal of Se(VI) by FeS was less extensive than removal of Se(IV). Only 10 % of the Se(VI) was removed by 1 g/L FeS within 1 hour. At the highest initial concentration examined (126 μM), removals were somewhat steady after several hours contact, but increased at contact times beyond 25 hours. This indicated that surface reactions may have been initiated that promoted removal of additional Se(VI). The removal patterns for Se(VI) on FeS depended on pH. The BET model best described removal patterns at low pH (pH 7, pH 8), but the Langmuir model best described removal patterns at higher pH (pH 9, pH 10). The BET-like pattern indicates that surface reactions are promoted at higher surface concentrations. Similar behavior might also be observed at higher pH if longer reaction times were investigated. Sulfate (1, 10 mM) had little effect on removal of Se(VI) by FeS, but there was some indication that sulfate promoted removal of Se(VI) at intermediate concentrations. Stability tests for mixtures of Se(IV) and FeS showed nearly complete removal at all but the high initial pH and high stability. For mixtures of Se(VI),

moderate removal at low pH, a minimum removal near pH 6 and nearly complete removal at high pH. Very high stability was observed with negligible release as pH decreased. SEM analysis indicated that thin rod-like solids were formed and XPS indicated that Se(IV) was reduced on the surface of FeS.

8.1 Introduction

Selenium is known to be an essential nutrient for animals and humans, although it is not essential for plant growth (53). According to the level of Se in vegetation, however, it can be toxic to animals (53). For instance, leaching of Se-rich soils by agricultural drainage in the San Joaquin valley was found to result in extremely harmful levels, with concentrations in drainage water approaching 140 to 1400 $\mu\text{g/L}$, which is high enough to cause carcinogenic and teratogenic effects (54). In addition, chronic exposure to low levels of Se can cause developmental abnormalities and reproductive disorders. The difference in Se concentrations that cause nutrient deficiency and toxicity is smaller than that noted for other USEPA priority or non-priority pollutant (55, 56).

Selenium is an analogue of sulfur, so they are similar in aquatic chemistry (58). The primary selenium species in oxidized water are selenate ($\text{Se}^{\text{VI}}\text{O}_4^{2-}$), selenite ($\text{Se}^{\text{IV}}\text{O}_3^{2-}$) and their protonated forms. The pK_a values for selenic acid (H_2SeO_4) are <1 and 1.7, and those for selenious acid (H_2SeO_3) are 2.75 and 8.5 (58). Therefore, at pH 7, the primary species will be SeO_4^{2-} and HSeO_3^- . Under more reducing conditions, zero-valent selenium and hydrogen selenide (H_2Se) are found. The pK_a values for hydrogen selenide are 3.89 and 15, so HSe^- will be the primary Se(-II) species observed in the pH range of most natural waters. Se(IV) and Se(VI) are the most mobile forms of selenium, while Se(0) and Se(-II) are relatively immobile because of the low solubility of their solid phases. Se(IV) is more toxic than other forms and that is why Se(IV) removal is extensively studied (59).

A variety of treatment technologies, including reverse osmosis, ion exchange, coagulation, adsorption, and biological treatment, have been applied in order to remove selenium from water (256-258). Among them, adsorption using Fe-, Mn-, or Al-oxyhydroxides has been extensively studied because adsorption of aqueous Se species onto such mineral surfaces plays an important role in determining the mobility and bioavailability of selenium (220, 244, 259). Although these treatment methods can lower selenium to below 5 $\mu\text{g/L}$, they are not suitable for wastewaters originating at coal-fired power plants or mining activities containing high concentration of sulfate (246). Very little information is now available about selenium removal in sulfate-rich environments. Furthermore, removal of selenium by adsorption onto iron oxyhydroxides will not produce stable residuals under the anoxic conditions found in landfills.

Reduction of Se(IV) and Se(VI) to Se(0) or Se(-II) is required to form solid phases with low solubility and therefore, low mobility in the environment. Zero-valent selenium and HSe^- in subsurface environments can form less soluble solid phases such as metal sulfide ores that include Fe, Cu, and Pb (60-62). Recent studies demonstrate that selenite can be reduced to insoluble Se(0) after contact with Fe(II)-bearing minerals such as mackinawite and magnetite with the final product being two iron selenides (Fe_7Se_8 and FeSe) (67).

Previous research has demonstrated that mackinawite (FeS) can be a good reactant/adsorbent to remove selenium from water. However, more detailed studies are needed to evaluate the capability of mackinawite for removal of Se(IV, VI) under a range of various solution conditions. To do so, this study aims to investigate the effect of time on Se(IV,VI) removal by mackinawite, to measure the effect of pH on the extent of removal with and without the presence of a competing ion (sulfate), and to determine the stability of Se-contacted mackinawite when pH changes. To better understand chemical changes that affect stability of mackinawite reacted with Se(IV,VI), X-ray photoelectron spectroscopy will be used to characterize chemical species

on the surface of the solid-phases.

8.2 Materials and Method

8.2.1 Materials

All of the chemicals used in this study were analytical grade or better and all solutions were prepared using deionized/deoxygenated (DI/DO) water ($>18 \text{ M}\Omega^{-1}$ resistivity). The water was deoxygenated by purging with purity nitrogen for more than 2 hours and contacting it with the atmosphere in an anaerobic chamber for at least one day. Sodium selenite (Na_2SeO_3) and sodium selenate (Na_2SeO_4) were purchased from Sigma-Aldrich. Mackinawite (FeS) was synthesized according to method described in Section 7. Se(IV) and Se(VI) stock solutions (1000 mg/L) were prepared by dissolving Na_2SeO_3 and Na_2SeO_4 in DI/DO water. All sorption experiments were performed in an anaerobic chamber (95% N_2 /5 % H_2) with palladium catalyst that maintained O_2 concentrations near zero.

8.2.2 Sorption/Reaction Experiments

Initial kinetic experiments were conducted at pH 8 to evaluate removal of Se(IV) and Se(VI) by suspensions of 1 g/L FeS with different initial concentrations of selenium (6.3, 12.7, 38, 127, 253 μM Se(IV); 12.7, 38, 127 μM Se(VI)). Reactions were initiated by adding Se(IV) or Se(VI) stock solution to a suspension of FeS and then mixing by reciprocal rotator. A 10-mL aliquot was sampled from the suspensions containing Se(IV) at reaction times of 0.5, 1, 2, 3, 6, 9, 18, 30, 43.7 hours. Similar samples were taken from the suspensions containing Se(VI) after reaction times of 1, 3, 7, 10, 19, 25, 32, 44, 49, 57, 68, 100 hours. The samples were immediately filtered using 0.02- μm anodisc membrane filters and the filtrates were stored in an anaerobic chamber until measurement using HGAAS. Experiments to evaluate removal of Se(IV) and Se(VI) by suspensions of FeS were conducted with a similar way to those previously

conducted to evaluate removal of Se(IV) by suspensions of pyrite (Section 6). The effect of pH (7, 8, 9, 10) on removal of Se(IV) and Se(VI) by FeS was evaluated in a series of batch experiments. The initial aqueous-phase concentrations of Se(IV) ranged from 63.3 to 2508 μM and the initial concentrations of Se(VI) ranged from 6.5 to 1395 μM . A constant concentration of FeS of 1.0 g/L was used and the mineral form of FeS was mackinawite. The pH of the suspensions was adjusted by 0.5 M HCl or 0.5 M NaOH. Samples were taken after 24 hours of reaction and analyzed for Se(IV) or Se(VI). Experiments to determine the effect of sulfate on selenium removal were conducted similarly at pH 8 and at three sulfate concentrations (0, 1, 10 mM).

8.2.3 Stability Test of Se(IV)/Se(VI)-Contacted FeS

These experiments were conducted using the same procedure that was followed for examining behavior of Se(IV) and Se(VI) with suspensions of pyrite (Section 6), except that the suspensions contained mackinawite (FeS). To investigate the stability of Se(IV)- and Se(VI)-contacted FeS, the experimental method used by Bostick and Fendorf (2003) was modified (39). This method measures removal of selenium as a function of pH, which is adjusted by addition of 1 or 2 M of HCl or NaOH (39). The experiments were initiated by adjusting pH near pH 10 (for Se(IV)) or pH 4.0 (for Se(VI)) and then selenium was added to obtain a concentration of 16.5 μM . An initial sample was taken after 30 minutes and then pH was adjusted to desired values. Samples of 10 mL were taken after 30 minutes reaction at each pH and they were filtered with 0.02- μm pore sized anodisc membrane filters. Herein, samples will be identified with the following nomenclature to simplify the discussion. For Se(IV)-contacted mackinawite, the initial sample at pH 10 will be named the “pH 10_(i)” sample and the sample at pH 4 after acid titration will be named the “pH 4_(a.a.t)” sample. Another stability test was conducted for the Se(VI) in a similar way, but the initial pH was pH 4. Thus the initial sample at pH 4 will be named the “pH

4_(i)” sample and the samples at the pH 6 and 10 after base titration will be named the “pH 6_(a.b.t)” and “pH 10_(a.b.t)”, respectively. The filtered samples were stored in an anaerobic chamber until selenium analysis by AAS in order to prevent changes in the redox states of selenium.

8.2.4 Spectroscopic Analyses

XPS spectra were obtained using a KRATOS Axis Ultra Imaging X-ray photoelectron spectrometer with a monochromatized Al K α (1253.6 eV) source. The detailed analysis procedure was described in Sections 5-7. Briefly, a filter disk containing solid samples were attached to a copper adhesive on a sample bar, which was then loaded to the sample treatment chamber (STC) that was evacuated to a pressure less than 5×10^{-7} torr. Thereafter, the sample bar was transferred to the sample analysis chamber (SAC) where spectra were collected with a take-off angle close to 90. The survey scans were obtained at a pass energy of 80 eV to determine chemical elements and the most characteristic spectra were recorded by the narrow scans with fixed pass energy of 20 or 40 eV to determine oxidation states and bonding type of element (228). The charge effect was corrected using C 1s ($E_b=284.5$ eV) to calibrate the binding energy scale. The XPS spectra (Fe 2p, S 2p, O 1s, Se 3d) were fitted using a program (XPSPEAK) that uses a Gaussian Lorentzian function and background-subtraction corrections using a Shirley-type optimization. The surface species with various oxidation states were identified by comparison of their binding energies with literature values.

8.2.5 Measurements

Selenium (IV, VI) was measured by a Perkin-Elmer atomic absorption spectrophotometer with a continuous flow, hydride generator. Selenite (SeO_3^{2-}) was measured without acid pretreatment, while selenate (SeO_4^{2-}) was first reduced to selenite by acid digestion (5 mL sample, 5 mL concentrated HCl in 40 mL borosilicate glass vial placed in boiling water bath for

10 minutes). The following parameters were used for these analyses: wavelength of 196.0 nm, band pass of 0.5 nm, lamp current of 75%, measurement number of 4, measurement time of 4 s, background correction is on, stabilization time of 30 s, baseline delay time of 40 s, carrier gas flow rate of 240 mL/min.

8.3 Results and Discussion

8.3.1 Kinetics

Results of the kinetic experiment with Se(IV) and FeS are shown in Figures 8.1(a) and 8.1(b). Figure 8.1(a) shows that removal of Se(IV) by 1 g/L of FeS is so fast that Se(IV) can be completely removed within 30 minutes at all initial concentrations studied (6.3, 12.7, 38 μM). No release of Se(IV) was observed during the period of the experiment. Since 1 g/L of FeS was sufficient to remove Se(IV) completely, kinetic experiments were also conducted at higher Se(IV)/FeS ratios. These experiments were conducted with a FeS dose of 0.5 g/L and initial concentrations of Se(IV) of 127 and 253 μM and the results are shown in Figure 8.1(b). Se(IV) was completely removed by 0.5 g/L of FeS within 120 minutes when the initial concentration was 127 μM , while complete removal of Se(IV) dosed at 253 μM occurs after 480 minutes. Also, no release of Se(IV) was observed at times longer than needed for complete removal.

Results of the initial kinetic experiment to evaluate removal of Se(VI) by FeS are shown in Figure 8.2. These experiments were conducted with 1 g/L FeS at pH 8 and various initial concentrations of Se(VI) (12.7, 38, 127 μM). Figure 8.2 shows that an initial stage of removal of Se(VI) occurs in the first hour of contact, where about 10 % of Se(VI) is removed. After one hour, the removal continues at a slow rate with lower initial concentrations of Se(VI), but at more rapid rate with the highest initial concentration. The slower rate of uptake of Se(VI) compared to that of Se(IV) may be due to a lower affinity of Se(VI) for the FeS surface.

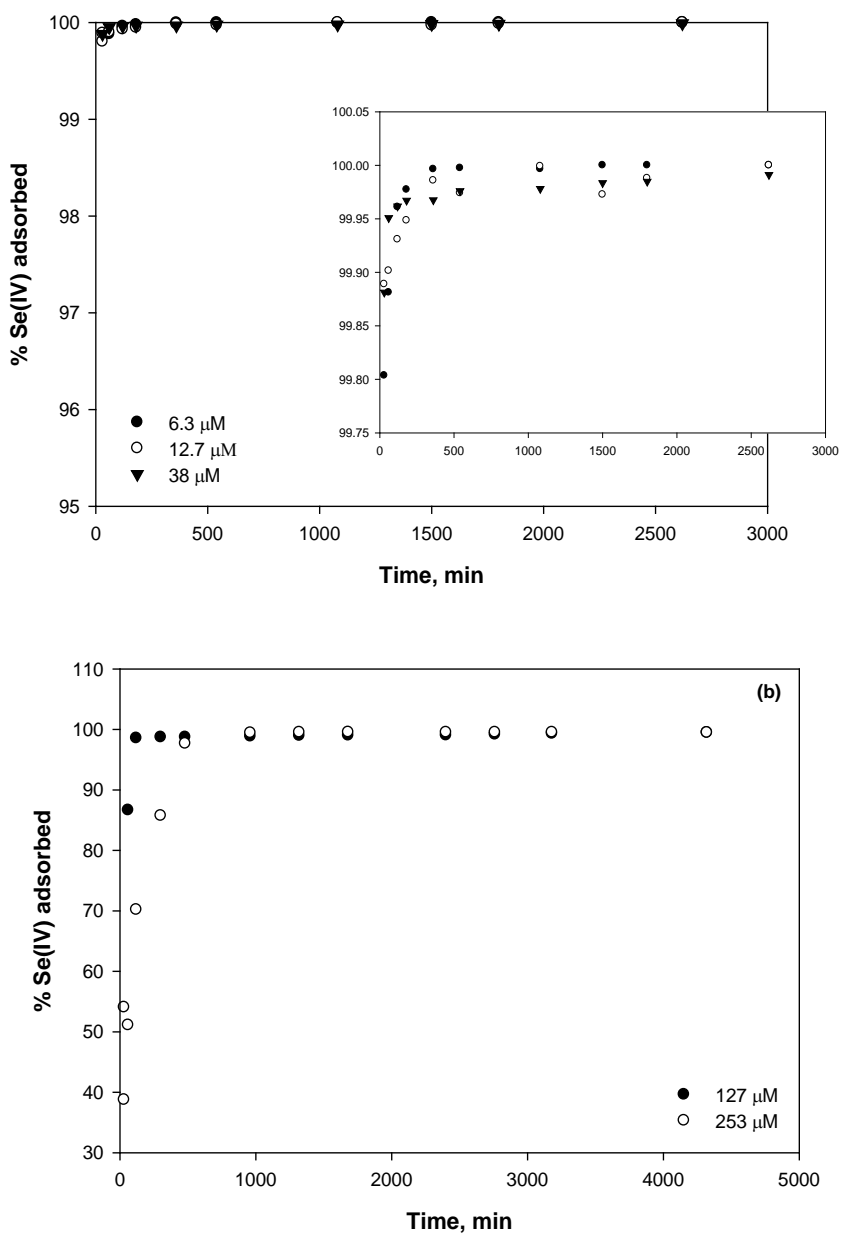


Figure 8.1 Kinetics of Se(IV) uptake by FeS at pH 8 as affected by initial concentrations of FeS and Se(IV): (a) FeS = 1 g/L and Se(IV) = 6.3, 12.7, 38 μM ; (b) FeS = 0.5 g/L and Se(IV) = 127 and 253 μM .

This would occur if the surface was negatively charged at pH 8. Se(VI) would be present as an anion with two negative charges at pH 8, compared to Se(IV) which would be present mostly as an anion with one negative charge. Figure 8.2 also shows that increasing initial concentration results in higher amounts removed.

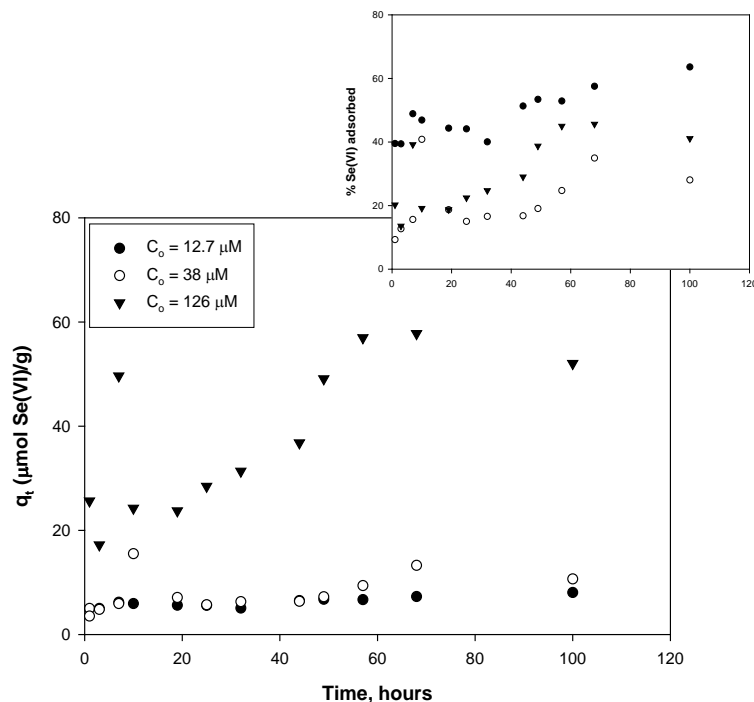


Figure 8.2 Effect of time on concentrations of Se(VI) in presence of 1 g/L FeS at pH 8.

8.3.2 Nonlinear Removal Patterns

8.3.2.1 Effect of pH

Figure 8.3 shows the results of experiments describing removal of Se(IV) by FeS at four different pH values. These experiments were conducted with a concentration of FeS of 0.5 g/L and a contact time of 24 hours. The symbols represent the measured data and the lines represent predictions of different models. The models used to correlate the data were equations (Langmuir, Freundlich, and BET) that are typically used to describe data from equilibrium

adsorption experiments. However, they are being used here without implication that the experimental systems had reached equilibrium or that adsorption was the only mechanism affecting results. Table 8.1 shows the parameters of the different models that were obtained by nonlinear regression. This procedure chooses parameters to minimize the sum of squared residuals (SSR). A goodness of fit parameter (GFP) was calculated using SSR in order to numerically compare the fits to different data sets. It is the ratio of the standard deviation of the points about regression line divided by the average value of the data. As such, it represents the ratio of an average error to the average value. Smaller values represent better fits of the model to the data.

$$GFP = \frac{\sqrt{\frac{SSR}{n-2}}}{\bar{q}} \quad (8.1)$$

Figure 8.3 shows that different patterns of removal were observed at different pH values. Results from experiments conducted at pH 7 and 8 are described best by the BET isotherm model and results at other pH values are described best by the Langmuir isotherm. These comparisons are made using the goodness of fit parameter. Since Se(IV) removal at pH 7 and 8 is well described by the BET isotherm, it can be inferred that some surface reactions were occurring. For example, Se(IV) could be reduced to Se(-II) and precipitate as FeSe. The results shown in Figure 8 also indicate that greater amounts of Se(IV) were removed at lower pH where BET-like behavior was observed.

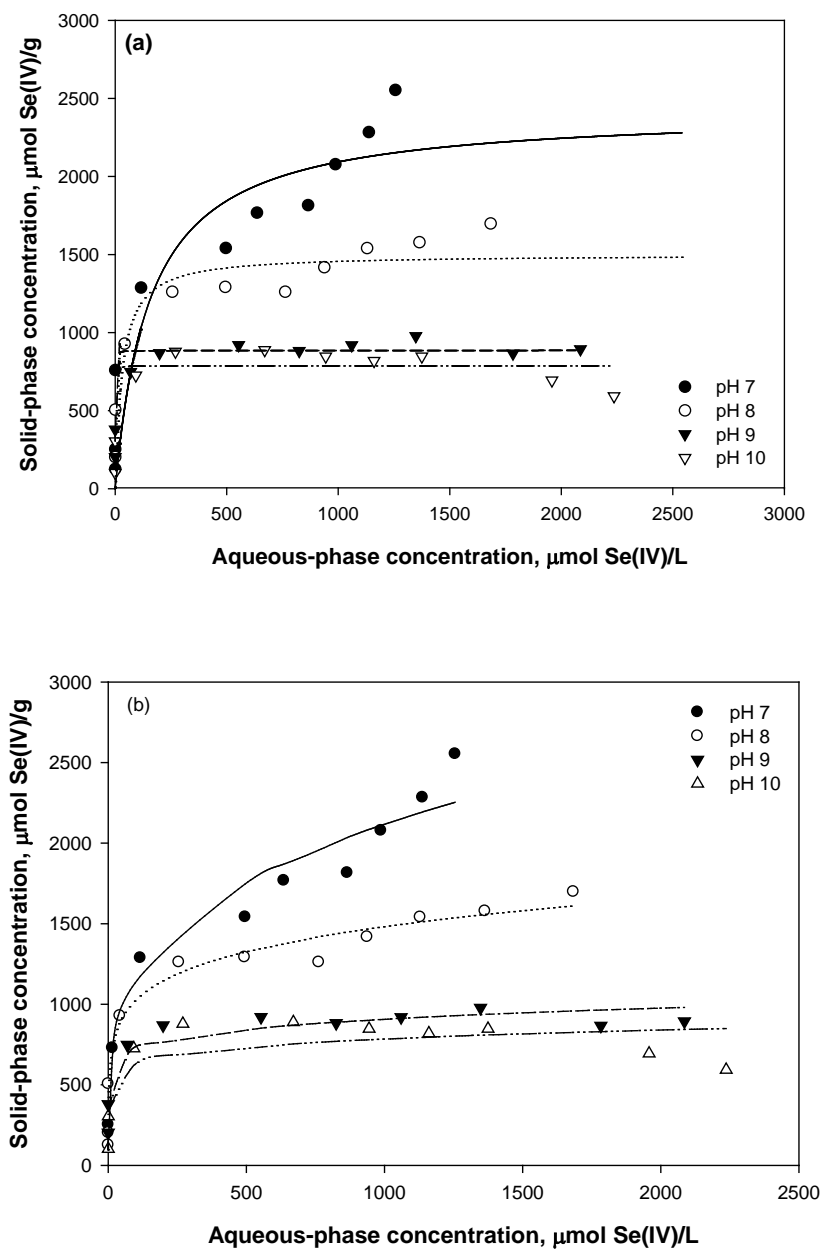


Figure 8.3 Measured concentrations of Se(IV) on FeS (symbols) as functions of concentration in water with (a) Langmuir, (b) Freundlich, and (c) BET model predictions (lines) at various pH.

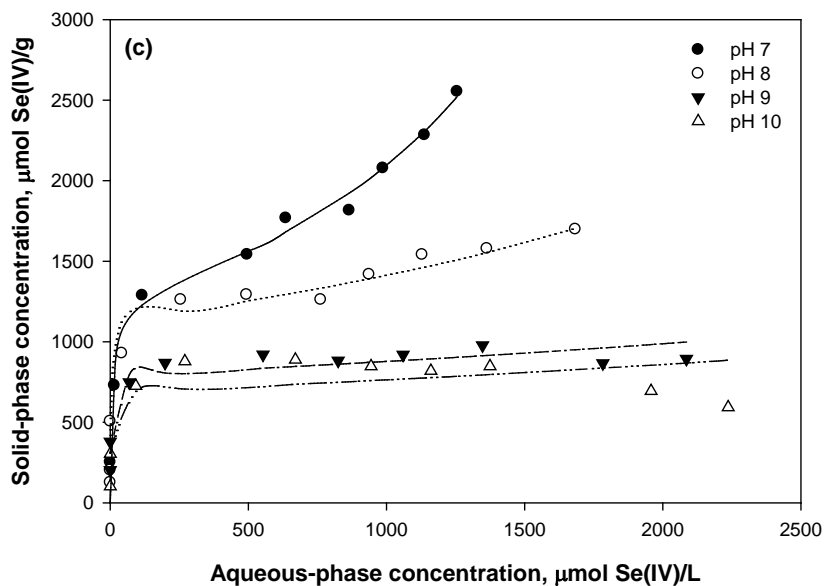


Figure 8.3 Continued.

Table 8.1 Summary of model parameters for Se(IV) removal by FeS.

| Models | Solution pH | | | |
|---|-----------------|---------------------------------------|---------------------------------------|---------------------------------------|
| | pH 7 | pH 8 | pH 9 | pH 10 |
| Langmuir | | | | |
| q_{\max} ($\mu\text{mol/g}$) | 2206 ± 438 | 1377 ± 184 | 886 ± 56.6 | 787 ± 80 |
| b ($\text{L}/\mu\text{mol}$) | 0.00 ± 0.00 | 2.4 ± 3.3 | 3.67 ± 2.15 | 3.46 ± 3.94 |
| GFP | 0.281 | 0.209 | 0.092 | 0.147 |
| Freundlich | | | | |
| k_f ($\mu\text{mol}^{1-1/n} \cdot \text{L}^{1/n} / \text{g}$) | 319 ± 191 | 492 ± 136 | 436 ± 120 | 395 ± 215 |
| n | 3.65 ± 1.19 | 6.26 ± 1.62 | 9.43 ± 3.65 | 10.1 ± 8.2 |
| GFP | 0.116 | 0.085 | 0.114 | 0.231 |
| BET | | | | |
| A | 234 ± 193 | $1.6 \times 10^4 \pm 1.0 \times 10^4$ | $4.4 \times 10^4 \pm 3.1 \times 10^4$ | $4.4 \times 10^4 \pm 8.2 \times 10^4$ |
| q_{\max} ($\mu\text{mol/g}$) | 1276 ± 67 | 1130 ± 62 | 790 ± 57 | 687 ± 107 |
| GFP | 0.077 | 0.080 | 0.102 | 0.223 |

Figure 8.4 shows the results of experiments for removal of Se(VI) by FeS at four different pH values (i.e., 7, 8, 9, 10), but the same concentration of FeS (1.0 g/L) and the same contact time (24 hours). Table 8.2 shows the parameters of the Langmuir, Freundlich, and BET models that were obtained by nonlinear regression. Figure 8.4 shows that the solid-phase

concentrations of Se(VI) are below 140 $\mu\text{mol Se/g}$ in all experiments, indicating that the sorption capacity of FeS for Se(VI) is much lower than for Se(IV). Maximum solid phase concentrations (q_{max}) of Se(IV) on FeS were observed to be in the range 800~1200 $\mu\text{mol/g}$. This range is similar to what was observed for removal of Se(IV) by pyrite (Section 6). At pH 7 and 8, solid-phase concentration increases rapidly at higher aqueous concentration, indicating that Se(VI) may be undergoing surface reactions. The BET model fits this data best, as indicated by the GFP in Table 8.2. Results of experiments conducted at pH 9 and pH 10 shows a pattern of removal that is better described by the Langmuir model (Table 8.2). A pattern of removal that is more like that observed for experiments at lower pH might be observed at higher pH, if higher concentrations were investigated or more time was allowed for surface reactions to occur.

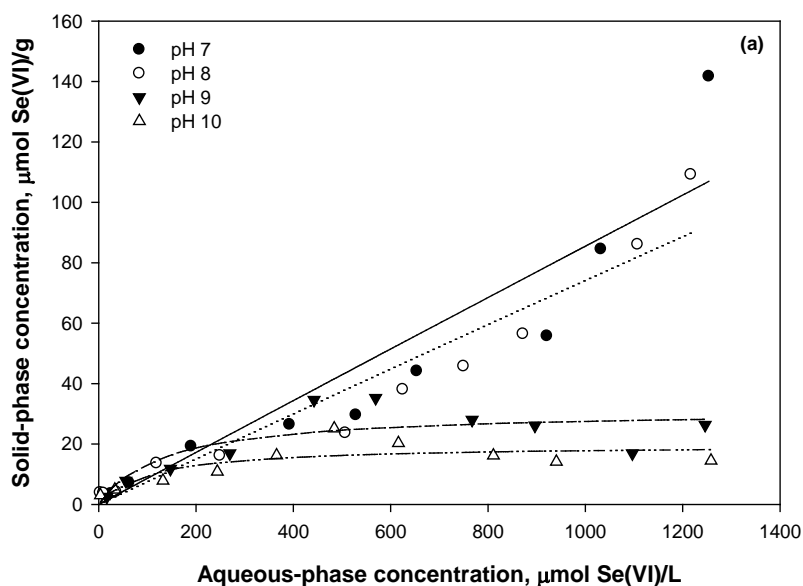


Figure 8.4 Measured concentrations of Se(VI) on FeS (symbols) as functions of concentration in water with (a) Langmuir, (b) Freundlich, and (c) BET model predictions (lines) at various pH.

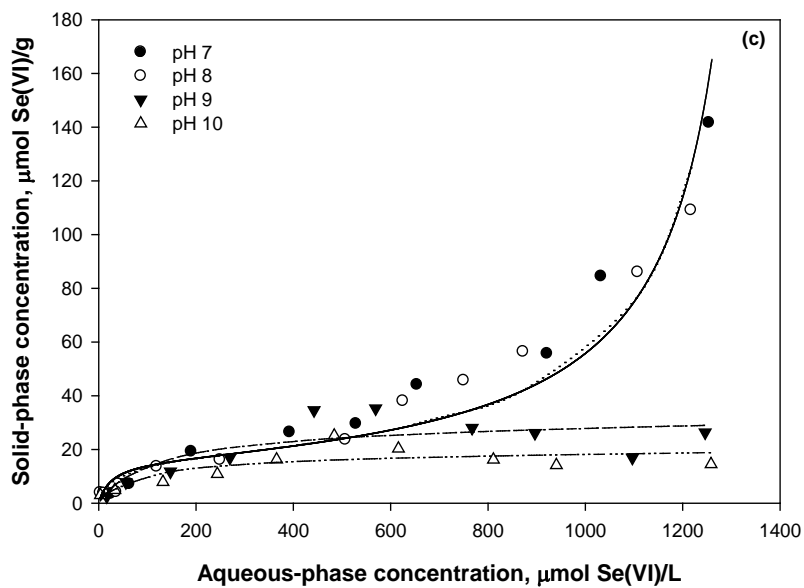
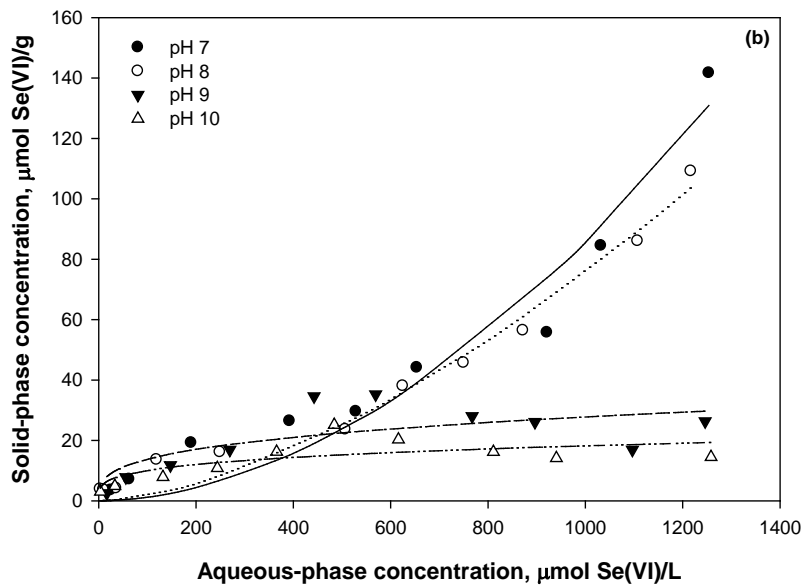


Figure 8.4 Continued.

Table 8.2 Summary of model parameters for Se(VI) removal by FeS.

| Models | Solution pH | | | |
|---|---|---|--|--|
| | pH 7 | pH 8 | pH 9 | pH 10 |
| Langmuir | | | | |
| q_{\max} ($\mu\text{mol/g}$) | $3.94 \times 10^4 \pm 1.29 \times 10^7$ | $1.67 \times 10^5 \pm 2.17 \times 10^8$ | 31.2 ± 12.9 | 19.7 ± 7.95 |
| b ($\text{L}/\mu\text{mol}$) | $2.16 \times 10^{-6} \pm 8.12 \times 10^{-4}$ | $4.45 \times 10^{-7} \pm 5.89 \times 10^{-4}$ | $7.4 \times 10^{-3} \pm 1.34 \times 10^{-2}$ | $9.25 \times 10^{-3} \pm 1.8 \times 10^{-2}$ |
| GFP | 0.40 | 0.26 | 0.33 | 0.32 |
| Freundlich | | | | |
| k_f ($\mu\text{mol}^{1-1/n} \cdot \text{L}^{1/n}/\text{g}$) | $2.3 \times 10^{-4} \pm 1.0 \times 10^{-3}$ | $1.32 \times 10^{-3} \pm 4.4 \times 10^{-2}$ | 3.39 ± 7.24 | 3.01 ± 2.8 |
| n | 0.54 ± 0.19 | 0.63 ± 0.14 | 3.28 ± 3.55 | 3.85 ± 4.02 |
| GFP | 0.26 | 0.15 | 0.39 | 0.36 |
| BET | | | | |
| A | 15.8 ± 2.5 | 15.8 ± 2.4 | 28.3 ± 11.2 | 17.9 ± 6.86 |
| q_{\max} ($\mu\text{mol/g}$) | 55.2 ± 279 | 44.1 ± 175 | $1.21 \times 10^2 \pm 237$ | $1.56 \times 10^2 \pm 3.24 \times 10^2$ |
| GFP | 0.30 | 0.25 | 0.34 | 0.33 |

8.3.2.2 Effect of Sulfate Concentration

Experiments were conducted to investigate the effect of sulfate concentration on selenium removal by FeS. Initial concentrations of 1 and 10 mM of sulfate were added to batch reactors containing 1 g/L of FeS at pH 8. Figure 8.5(a) shows the amounts of Se(IV) removed per mass of FeS as a function of Se(IV) concentration in the liquid as affected by total sulfate concentration and a Langmuir model is fitted to the data. Figure 8.5(b) presents the same data but it is fitted with the Freundlich model. These figures show that sulfate concentration of 1 and 10 mM had a negligible effect on removal of Se(IV) on FeS. Table 8.3 shows the model parameters that were obtained by nonlinear least square regression. The goodness of fit parameters (GFP) shows that the Langmuir model provides the better fit than does the Freundlich model. The BET model was not fitted to this data, because there was no indication in the data that BET-like behavior was occurring.

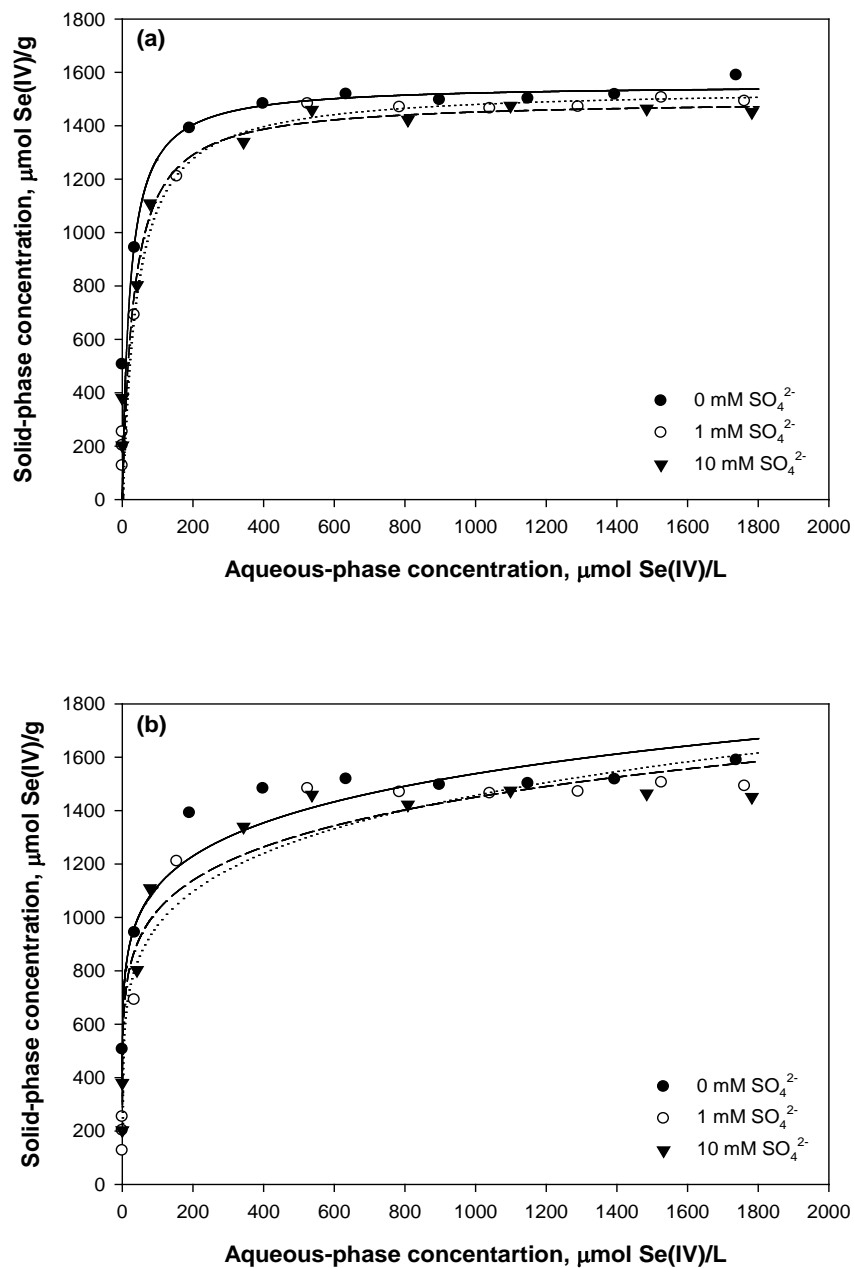
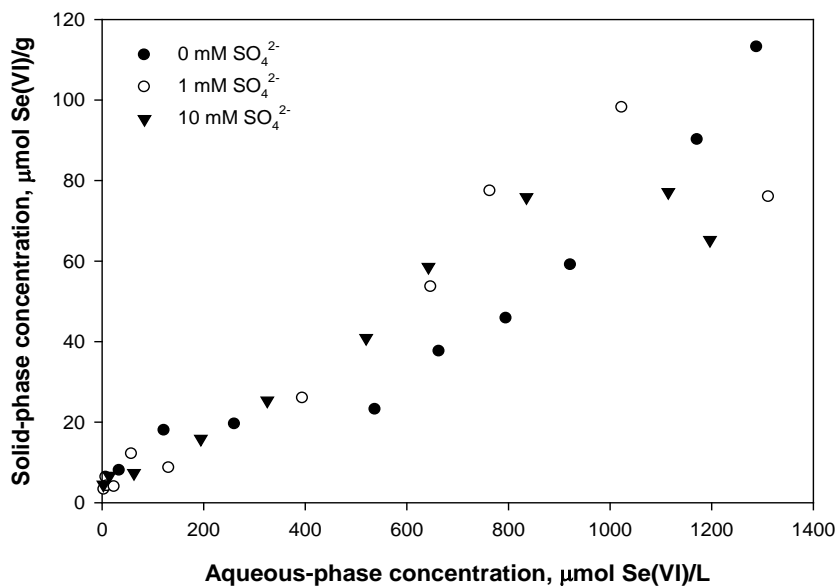


Figure 8.5 Effect of sulfate on solid-phase concentration of Se(IV) on FeS with (a) the Langmuir and (b) Freundlich models (lines) fitted to data (symbols).

Table 8.3 Summary of model parameters for Se(IV) removal as affected by sulfate.

| SO ₄ ²⁻ (mM) | <i>Langmuir</i> | | | | <i>Freundlich</i> | | | |
|---------------------------------------|-----------------|------------------------------|---------------------|------|--|-----------|---------------------|------|
| | b (L/mol) | q _{max} (μmol/g) | SSR | GFP | K _f (μmol ^{1-1/n} ·L ^{1/n} /g) | n | SSR | GFP |
| 0 | 0.046±0.058 | 1555±198 | 2.8±10 ⁵ | 0.16 | 588±162 | 7.19±2.16 | 5.1±10 ⁵ | 0.17 |
| 1 | 0.024±0.014 | 1541±114 | 8.1±10 ⁴ | 0.09 | 432±157 | 5.68±1.73 | 1.0±10 ⁵ | 0.11 |
| 10 | 0.031±0.026 | 1498±173 | 1.8±10 ⁵ | 0.13 | 495±147 | 6.43±1.87 | 9.0±10 ⁵ | 0.19 |

Figure 8.6 shows that there is little effect of sulfate on the amount of Se(VI) removed, although there is some indication that the higher level of sulfate resulted in increased Se(VI) removal when the concentrations of Se(VI) in solution were at intermediate levels.

**Figure 8.6 Effect of sulfate on solid-phase concentration of Se(VI) on FeS.**

8.3.2 Stability of Selenium-Contacted Mackinawite

8.3.2.1 XPS Investigation of Pure Mackinawite

Surface characterization by XPS was conducted for mackinawite in suspensions with a range of pH (pH 4, 8, 10) before contact with selenium(IV, VI). Table 8.4 summarizes the fitting parameters of the Fe 2p_{3/2}, S 2p, and O 1s spectra that were obtained. Figures 8.7, 8.8 and 8.9 show the Fe 2p_{3/2}, S 2p, and O 1s XPS spectra, respectively, of pure mackinawite at pH 4, 8, and 10. Figure 8.7 shows that Fe 2p_{3/2} spectra for all pH samples had a long left tail, which indicates the presence of additional species beyond Fe(II)-S, such as Fe(II)-O, Fe(III)-S, and Fe(III)-O. The presence of Fe(II)-O could be the result of surface hydroxylation (228). The presence of some Fe(III)-O species could originate from oxidation of Fe(II) by exposure to air during sample transfer prior to XPS analysis. Figure 8.8 shows the S 2p spectra, which indicates the existence of polysulfides in addition to sulfide and there is no substantial difference in their intensities. The O 1s spectra (Figure 8.9) shows an increase in intensity of the peak associated with H₂O and a decrease in the intensity of the peak associated with OH⁻ as pH increases. This is probably the result of dissociation of H₂O that is observed at lower pH. A similar pattern was seen for the peak associated with O²⁻, which also decreased with increasing pH. Although this peak is associated with the structural oxygen of Fe(III)-oxyhydroxides, there is no substantial change observed in the intensities of Fe(III)-O peak in the Fe 2p XPS spectra.

Table 8.4. Binding energies (BE), full width at half maximum (FWHM), and area percentage for peaks in the Fe 2p_{3/2}, S 2p, and O 1s XPS spectra of mackinawite before contact with selenium at various pH (4, 8, 10).

| Samples | BE (eV) | FWHM (eV) | Area (%) | Chemical states |
|-----------------------------------|---------|-----------|----------|------------------------------|
| <u>Fe 2p_{3/2}</u> | | | | |
| pH 4 | 706.1 | 0.69 | 12.5 | Fe(II)-S |
| | 706.8 | 0.82 | 21.3 | Fe(II)-S |
| | 707.6 | 0.96 | 20.6 | Fe(II)-O |
| | 708.5 | 0.94 | 10.4 | Fe(III)-S |
| | 709.5 | 1.16 | 16.3 | Fe(III)-S |
| | 711.0 | 1.77 | 18.9 | Fe(III)-O |
| pH 8 | 706.0 | 0.46 | 9.07 | Fe(II)-S |
| | 706.4 | 0.52 | 13.8 | Fe(II)-S |
| | 706.9 | 0.72 | 18.7 | Fe(II)-S |
| | 707.7 | 1.02 | 19.8 | Fe(II)-O |
| | 708.9 | 1.29 | 15.0 | Fe(III)-S |
| | 710.1 | 1.71 | 15.2 | Fe(III)-O |
| | 711.9 | 2.44 | 8.23 | Fe(III)-O |
| pH 10 | 705.9 | 0.67 | 13.2 | Fe(II)-S |
| | 706.5 | 0.86 | 20.6 | Fe(II)-S |
| | 707.4 | 1.16 | 22.4 | Fe(II)-O |
| | 708.6 | 1.28 | 15.2 | Fe(III)-S |
| | 709.7 | 1.30 | 13.1 | Fe(III)-S |
| | 710.8 | 1.51 | 10.9 | Fe(III)-O |
| | 712.4 | 1.66 | 4.62 | Fe(III)-O |
| <u>S 2p</u> | | | | |
| pH 4 | 161.2 | 0.72 | 25.4 | S ²⁻ |
| | 161.7 | 0.63 | 22.8 | S ²⁻ |
| | 162.2 | 0.49 | 12.9 | S ²⁻ |
| | 162.6 | 0.51 | 12.1 | S _n ²⁻ |
| | 163.2 | 1.26 | 26.8 | S _n ²⁻ |
| pH 8 | 161.4 | 0.63 | 18.1 | S ²⁻ |
| | 162.1 | 0.85 | 42.6 | S ²⁻ |
| | 163.1 | 1.19 | 39.3 | S _n ²⁻ |
| pH 10 | 160.9 | 0.53 | 17.7 | S ²⁻ |
| | 161.4 | 0.53 | 19.9 | S ²⁻ |
| | 161.9 | 0.64 | 23.2 | S ²⁻ |
| | 162.5 | 0.79 | 20.8 | S _n ²⁻ |
| | 163.1 | 1.14 | 18.4 | S _n ²⁻ |
| <u>O 1s</u> | | | | |
| pH 4 | 529.5 | 1.03 | 25.7 | O ²⁻ |
| | 530.9 | 1.51 | 48.6 | OH ⁻ |
| | 532.1 | 1.57 | 25.7 | H ₂ O |
| pH 8 | 529.6 | 0.94 | 21.9 | O ²⁻ |
| | 531.1 | 1.46 | 47.1 | OH ⁻ |
| | 532.2 | 1.75 | 31.0 | H ₂ O |
| pH 10 | 529.3 | 0.86 | 19.5 | O ²⁻ |
| | 530.4 | 1.11 | 27.8 | OH ⁻ |
| | 531.3 | 1.48 | 52.7 | H ₂ O |

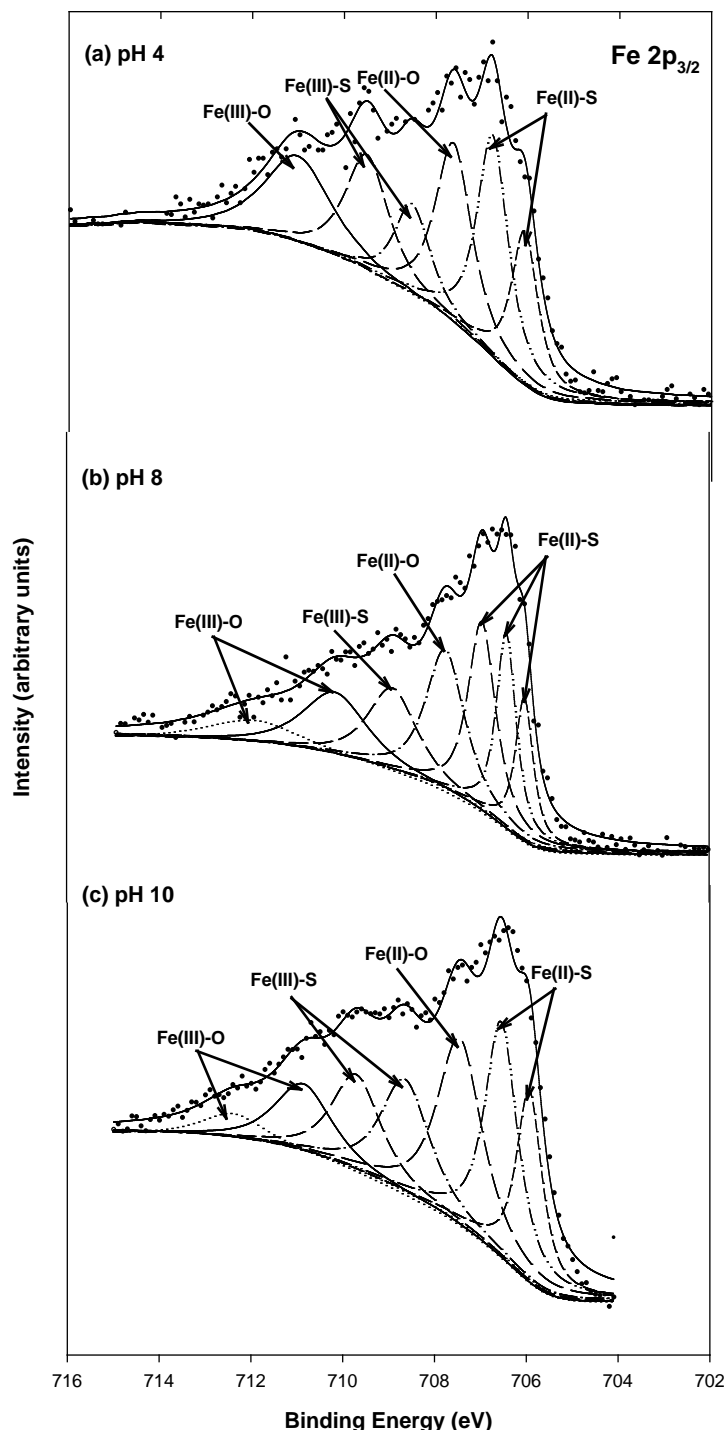


Figure 8.7 High resolution Fe 2p_{3/2} XPS spectra for mackinawite (1 g/L) before contact with selenium at various pH (4, 8, 10).

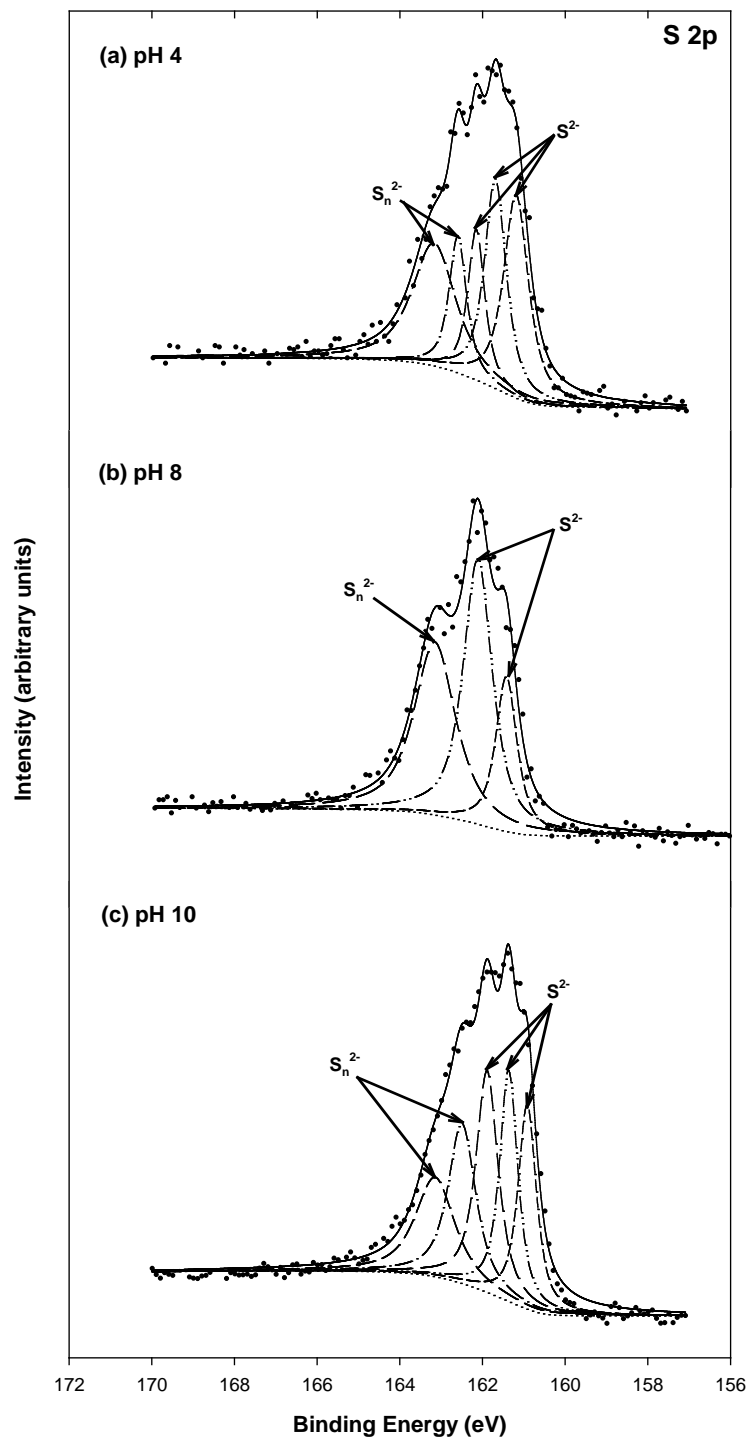


Figure 8.8 High resolution S 2p XPS spectra of mackinawite (1 g/L) before contact with selenium at various pH (4, 8, 10).

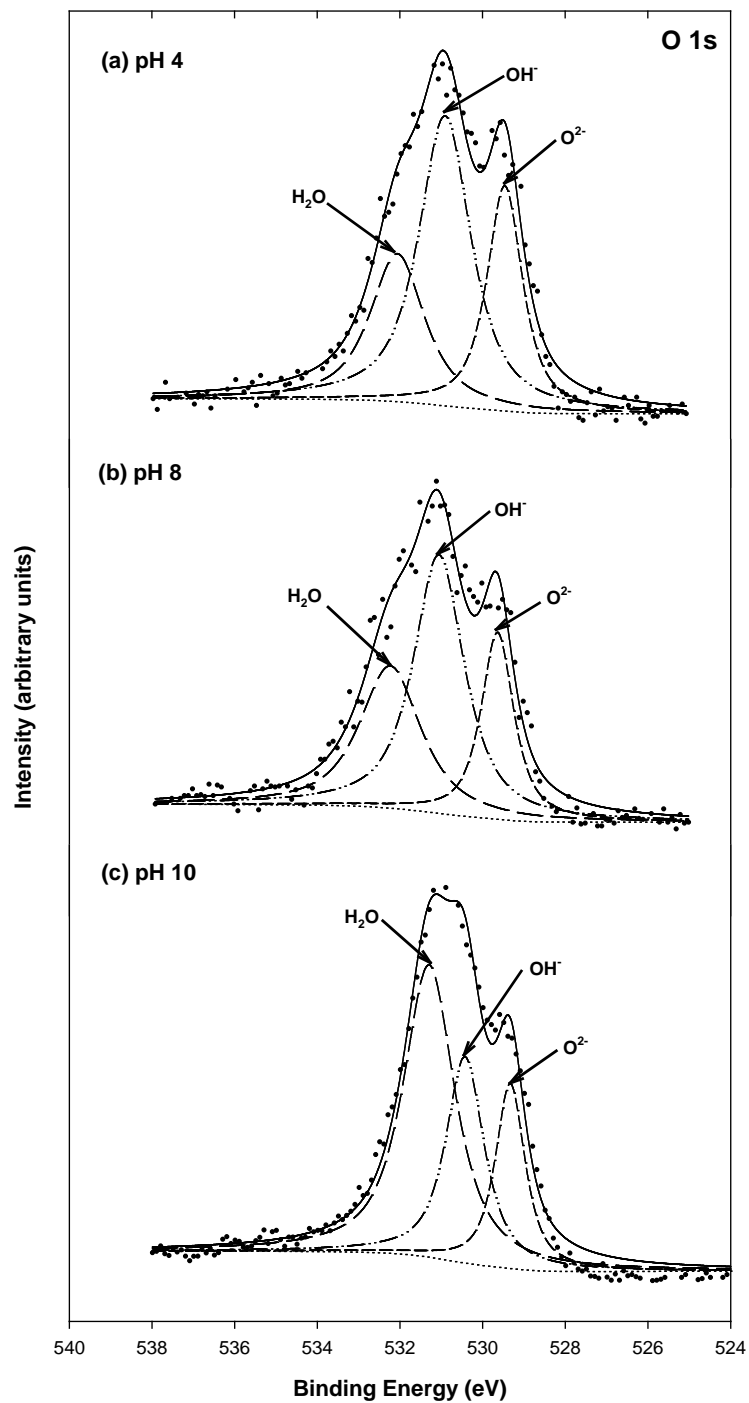


Figure 8.9 High resolution O 1s XPS spectra of mackinawite (1 g/L) before contact with selenium at various pH (4, 8, 10).

8.3.2.2 *Se(IV)-Contacted FeS*

Figure 8.10 shows results of experiments on the stability of Se(IV)-contacted FeS over a range of pH. The pH was initially adjusted to near pH 10 and then lowered in a series of steps. Nearly complete removal was observed for all pH values below about pH 9. As pH was raised, there was no release of Se(IV), even near pH 10. Retention of Se(IV) after pH was raised to near pH 10 indicates that stronger bonds between Se(IV) and mackinawite were formed at the lower pH. However, it is also possible that the time of the experiments resulted in formation of stronger bonds, rather than the effects of lower pH.

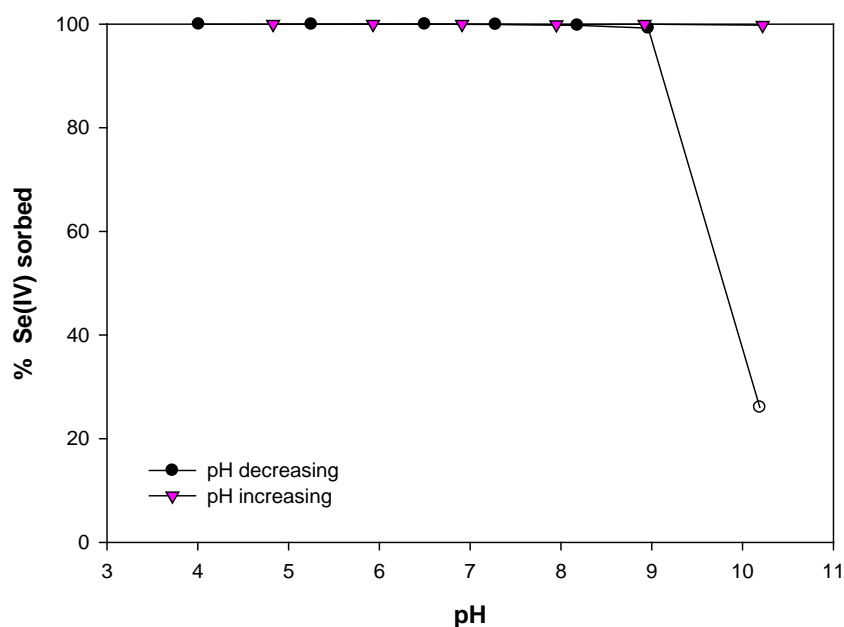


Figure 8.10 Effect of pH on removal of Se(IV) (16.6 μ M) by FeS (1 g/L) as pH was decreased from pH 10 and subsequently was increased.

The possible mechanisms of surface reactions between Se(IV) and FeS were elucidated using XPS analysis on the samples of FeS before contact with selenium and after contact at pH 10_(i) and pH 4_(a.a.t.). When selenium sorbs to a surface that does not contain iron, the width and

intensity of the selenium peak in the Se 3d spectra depends on the extent of sorption and the redox state of selenium. However, when selenium sorbs to a surface that contains iron, the Se 3d spectra can be affected by interference caused by the Fe 3d spectra. For the pH 4_(a.a.t) sample shown in Figure 8.11, the center of the Se 3d peak was located at a higher bonding energy than the pH 10_(i) sample, which is evidence that the pH 4_(a.a.t) sample was more reduced. Such a shift was shown in Section 7, where the Se 3d peak of Se(IV)-contacted mackinawite was located at higher bonding energy after undergoing reduction. Thus, reduction of Se(IV) is more likely to have occurred on the pH 4_(a.a.t) sample than on the pH 10_(i) sample.

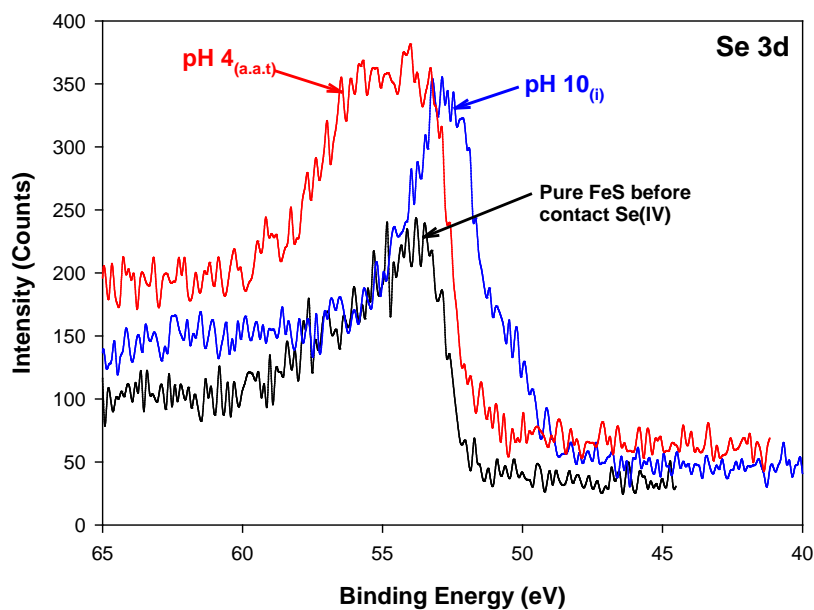


Figure 8.11 High resolution Se 3d XPS spectra for FeS before and after contact with Se(IV) (16.6 μM) at pH 10_(i) and pH 4_(a.a.t).

Figure 8.12 shows the Fe $2p_{3/2}$ spectra for samples collected at pH 10_(i) and pH 4_(a.a.t). The increase in the intensity of the Fe(III)-O peak at pH 4_(a.a.t) compared to pH 10_(i) is evidence that more iron is oxidized at pH 4, which is consistent with increased Se(IV) reduction at the lower pH. As shown in Figure 8.13, oxidation of surface S species was observed in samples at both pH, as indicated by the occurrence of elemental sulfur (S⁰), which suggests that both Fe and S can reduce Se(IV). However, this peak is much larger in the pH 4_(a.a.t) sample, suggesting that more reduction of Se(IV) occurred at lower pH. Therefore, at low pH, the surface-bound Fe and S can act effectively as sorbents/reactants, resulting in reduction of Se(IV) to electron-rich chemical forms that could subsequently react with the surface of mackinawite to form strong bonds between reduced species of Se(IV) and the surface, or surface precipitates such as FeSe or FeSe₂. This hypothesis is indirectly supported by the observation that surface Se(IV) was not released to solution at any pH, after the sample was adjusted to pH 4 (Figure 8.10).

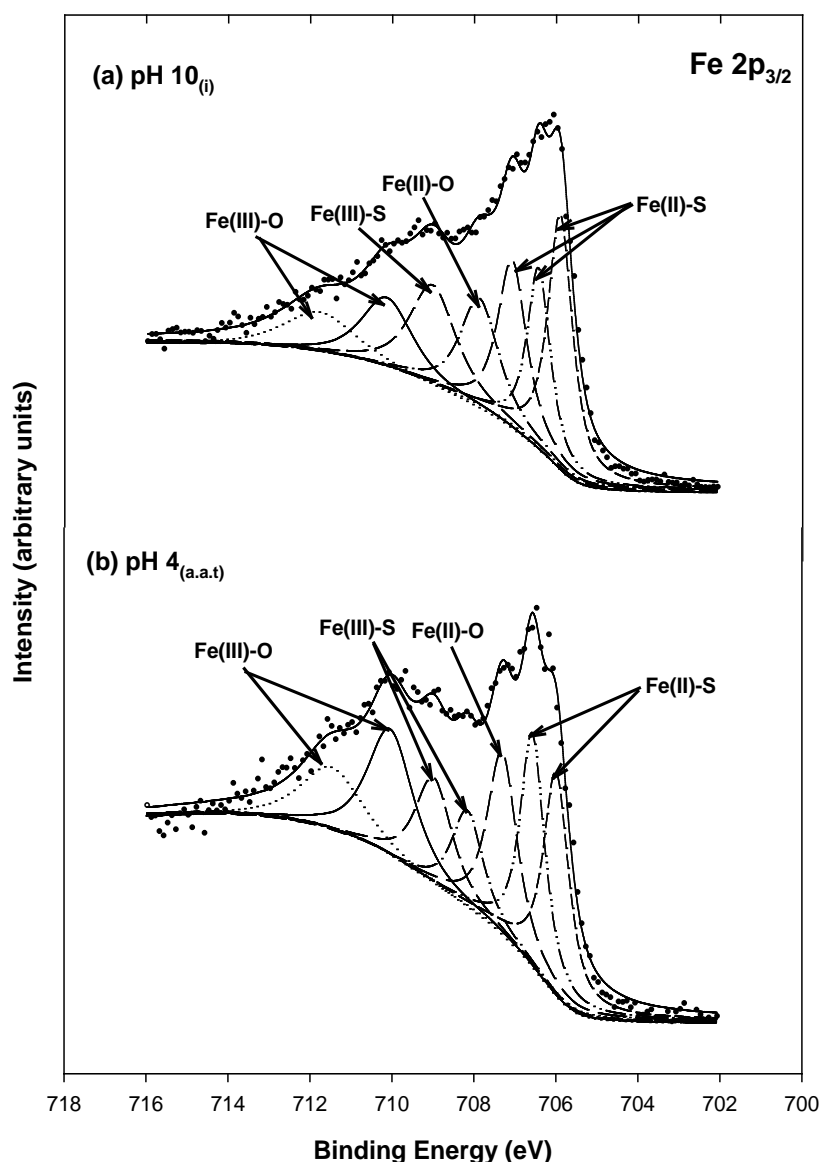


Figure 8.12 High resolution Fe $2p_{3/2}$ XPS spectra for FeS reacted with Se(IV) (15.2 μM) at (a) pH 10_(i) and (b) pH 4_(a.a.t).

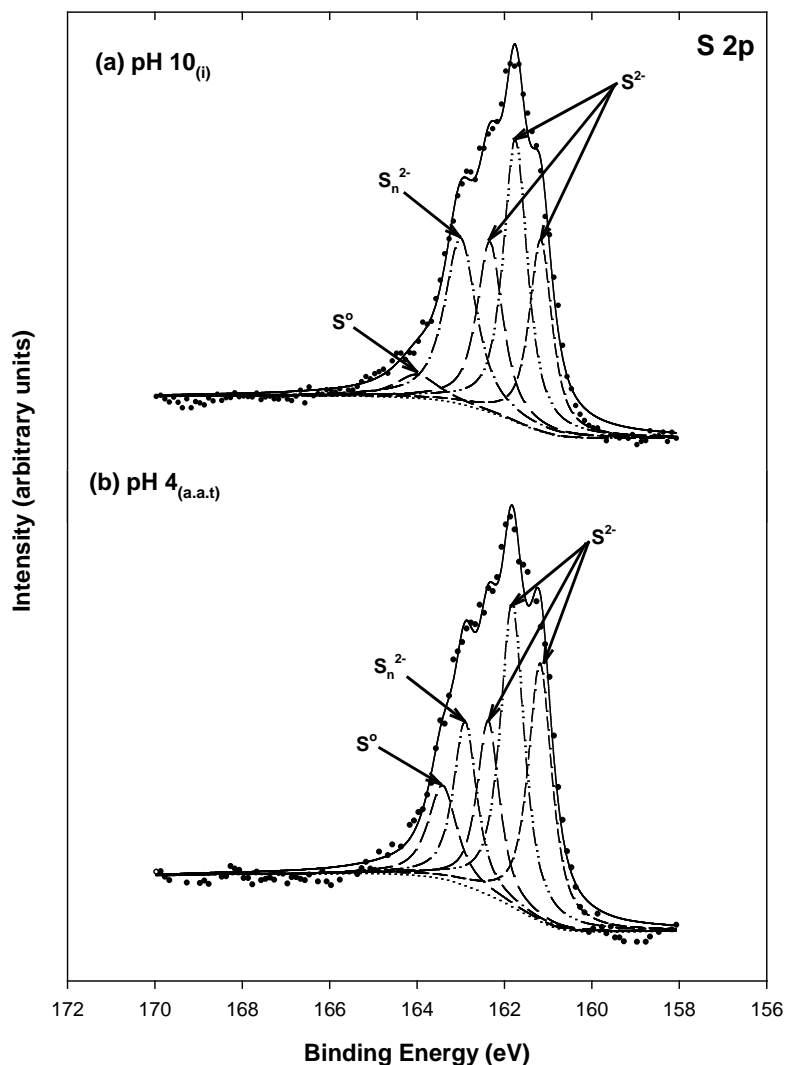


Figure 8.13 High resolution S 2p XPS spectra for FeS reacted with Se(IV) (15.2 μ M) at (a) pH 10_(i) and (b) pH 4_(a.a.t).

8.3.2.3 Se(VI)-Contacted FeS

Figure 8.14 shows results of experiments on the stability of Se(VI)-contacted FeS. For these experiments, pH was initially adjusted to near pH 4, raised in a series of steps, and then decreased in a series of steps to near pH 4. Removal of Se(VI) decreased as pH increased with a minimum near pH 6. Removals increased above pH 6 with nearly complete removal observed

near pH 8 and above. No Se(VI) was released when pH was decreased. This indicates that strong bonds were formed by reaction between selenium and the FeS, possibly including redox reactions. Such reactions were observed in mixtures of Se(VI) and pyrite (Section 6). Both Se(IV) and Se(VI) are stable after contact with FeS when pH is optimal and sufficient time is allowed for surface reactions.

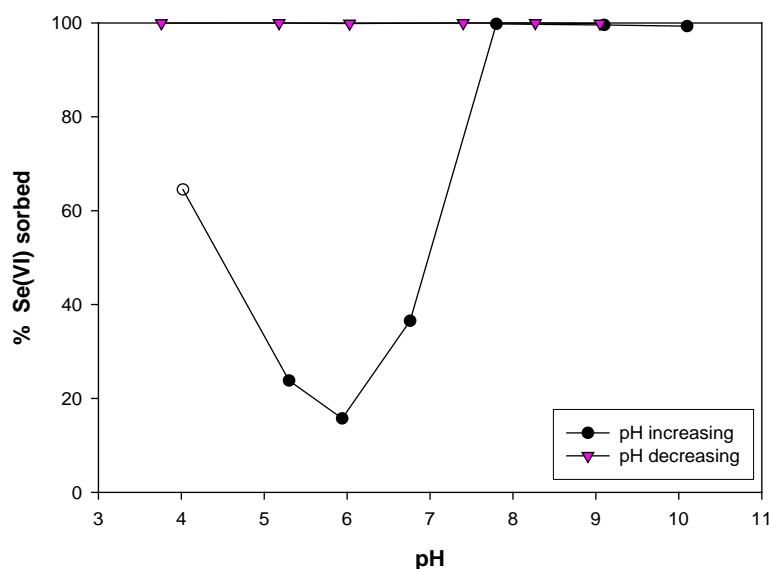


Figure 8.14 Effect of pH on removal of Se(VI) (16.6 μM) by FeS (1 g/L) as pH was increased from near pH 4 and subsequently was decreased.

Figure 8.15 shows the Se 3d XPS spectra for FeS before and after contact with Se(VI). The pH 10_(a,b,t) sample shows shift of the main peak to higher binding energy, compared to FeS that had not contacted Se(VI). This indicates that Se(VI) was reduced to forms such as Se(IV), Se(0), Se(-I), or Se(-II) by reaction with the FeS surface. These more reduced species may be more tightly bound to the surface or may form insoluble solid phases distinct from FeS. Such transformations would explain the behavior observed in the stability experiments. Unlike the pH 10_(a,b,t) sample, the Se 3d spectra of pH 4_(i) and 6_(a,b,t) samples looks similar to that of pure FeS,

which indicates that there was negligible reduction of Se(VI). This behavior is in contrast to what was observed for mixtures of Se(IV) and FeS at pH 4_(i), although comparable high removals are observed.

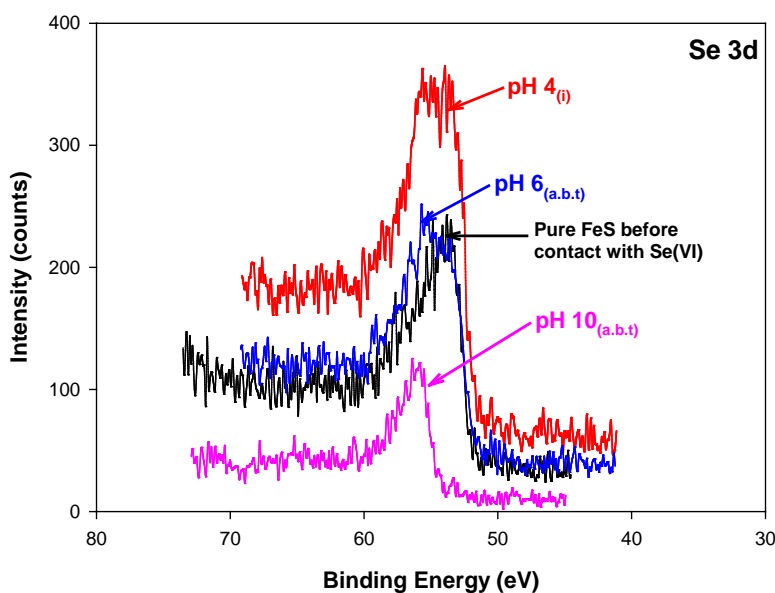


Figure 8.15 High resolution Se 3d XPS spectra for FeS before and after contact with Se(VI) (16.6 μM) at pH 4_(i), 6_(a,b,t), and 10_(a,b,t).

Figure 8.16 shows that a little more oxidation of the surface Fe species was observed in pH 10_(a,b,t) samples than other pH samples, presumably associated with reduction of Se(VI). In accordance with results of Fe 2p_{3/2} spectra, the surface S species at pH 10_(a,b,t) underwent more oxidation, with increased intensity of polysulfides species (Figure 8.17). Therefore, Se(VI) reduction occurs mostly at pH 10_(a,b,t) and is coupled with the oxidation of the surface Fe and S species.

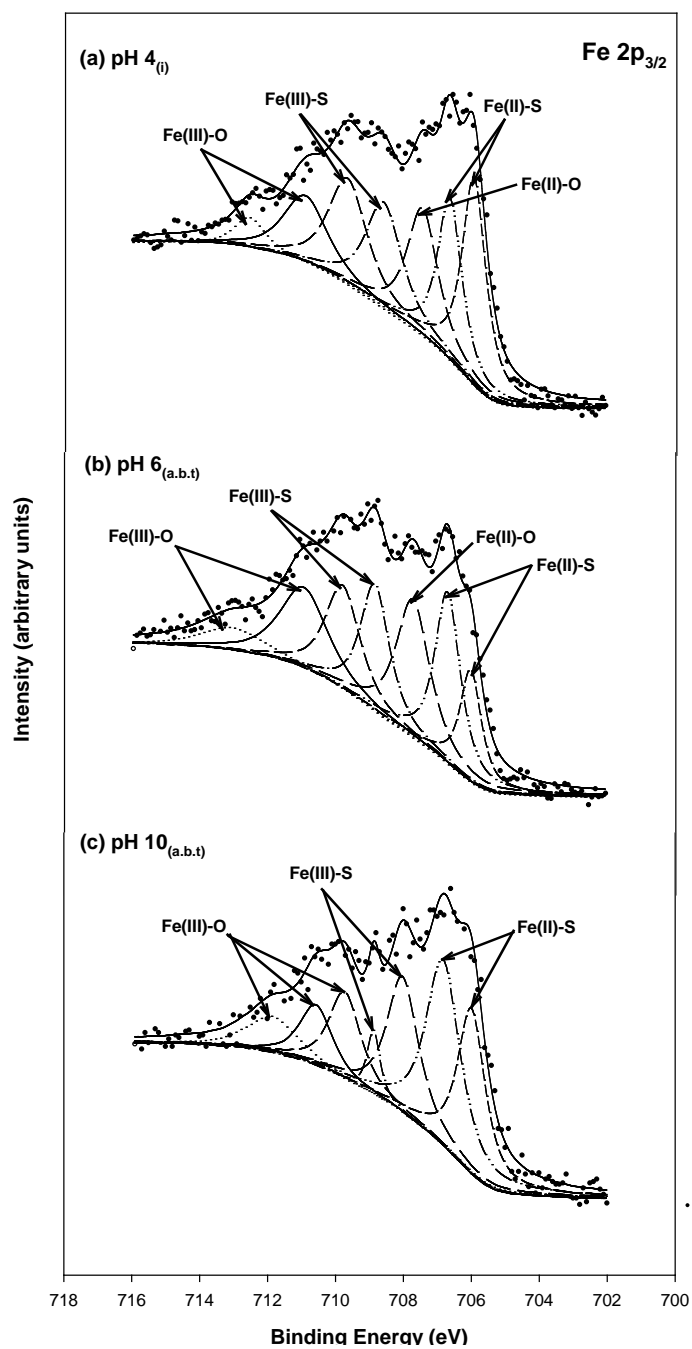


Figure 8.16 High resolution Fe 2p_{3/2} XPS spectra for FeS reacted with Se(VI) (15.2 μM) at (a) pH 4_(i) and (b) pH 6_(a,b,t) and (c) pH 10_(a,b,t) as pH increased for sorption.

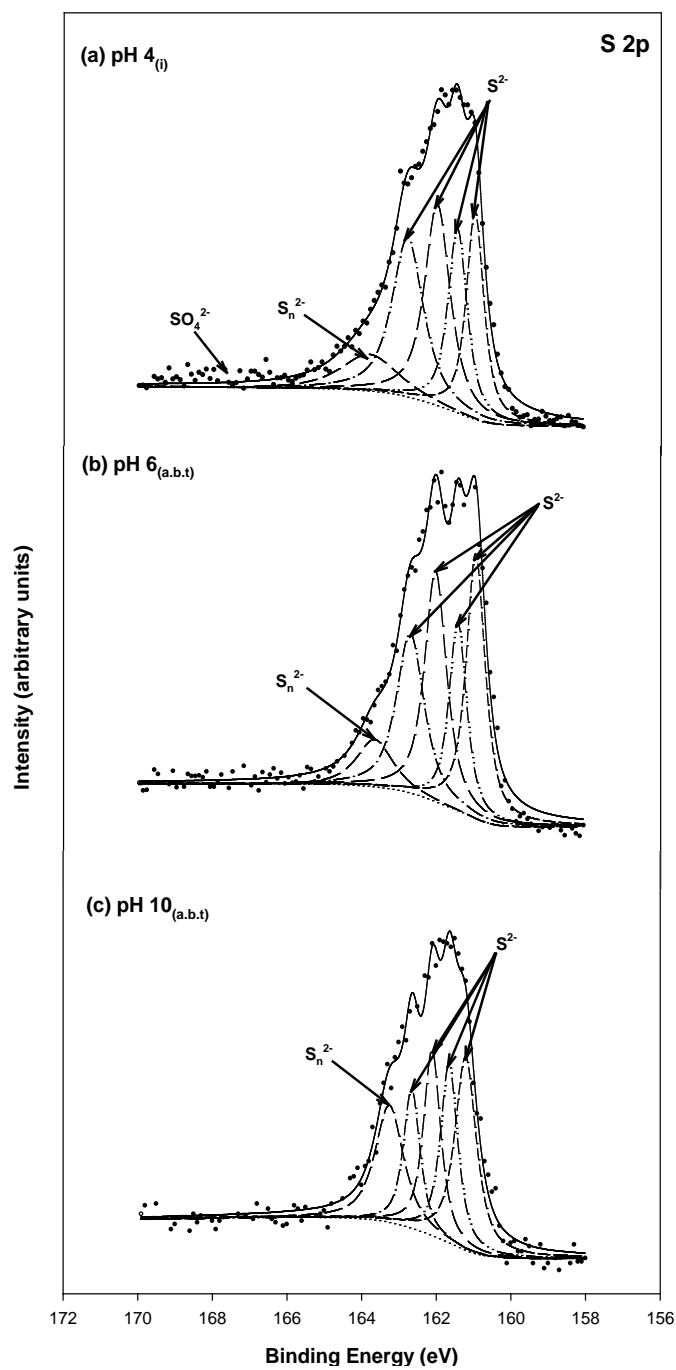


Figure 8.17 High resolution S 2p XPS spectra for FeS reacted with Se(VI) (15.2 μ M) at (a) pH 4_(t) and (b) pH 6_(a,b,t) and (c) pH 10_(a,b,t) as pH increased for sorption.

9. SORPTION OF ARSENIC(III) AND ARSENIC(V) TO SYNTHETIC PYRITE (FeS₂) AND MACKINAWITE (FeS): SPECTROSCOPIC INVESTIGATIONS

XPS analysis of pyrite after contact with arsenic(III,V) showed evidence of reduction of arsenic accompanied by oxidation of surface Fe and S. Various oxidation states of arsenic (i.e., As(V), As(III), As(II), As(I) for As(III)-contacted pyrite, As(III) and As(V) for As(V)-contacted pyrite) were observed in the As 3d_{5/2} spectra for pyrite reacted with As(III, V), which indicates reaction of As(III) and As(V) on the pyrite surface. Simultaneously, the surface Fe and S species were oxidized over contact time, but the extent of oxidation of surface Fe were larger than surface S. The O 1s spectra for pyrite after contact with As(III) and As(V) indicated that there were no important changes in O 1s peaks, but a new peak with a longer tail at higher binding energies near 540 eV was observed only for As(III)-contacted pyrite. Similarly to pyrite, mackinawite contacted with As(III) and As(V) showed evidence of reduction of arsenic in the As 3d_{5/2} spectra. Various oxidation states such as As(V), As(III), As(II), As(I) were observed for As(III)-contacted mackinawite, but only As(V) and As(III) were observed for As(V)-contacted mackinawite. This reduction reaction resulted in oxidation of the surface Fe and S species. The O 1s spectra of mackinawite reacted with As(III) and As(V) showed the relationship between the H₂O peak and the OH⁻ peak, where the peak for OH⁻ increased by dissociation of H₂O over time.

9.1 Introduction

Arsenic concentrations in drinking water have been regulated for protection of public health in the U.S. since 1942. The standard of 50 µg/L was the maximum contaminant level (MCL) for total arsenic in drinking water for over 50 years. Epidemiological evidence of arsenic carcinogenicity was taken as evidence that this standard might not be sufficiently protective of human health. The cancer risk from arsenic in drinking water at the 50-µg/L level is estimated to

be 200 times the acceptable level of 10^{-4} specified by EPA (15). Therefore, EPA promulgated a new health-based enforceable MCL of 10 $\mu\text{g/L}$ and a non-enforceable maximum contaminant level goal (MCLG) of 0.0 $\mu\text{g/L}$ (16). However, this standard might also need to be revised by regulatory agencies, because significant biological effects of As at less than the current EPA MCL of 10 ppb on the innate immune system has recently been observed in a mouse model of exposure (17). It has also been suggested that those who have a weakened immune system can be easily infected by the H1N1 flu that has recently been found in Mexico (18).

The two primary oxidation states of arsenic that are of importance in natural waters are the +V oxidation state (arsenate or arsenic acid) and the +III oxidation state (arsenite or arsenious acid) (19, 20). Arsenic acid has pK_a values at 2.20, 6.97 and 11.53 while arsenous acid has pK_a values of 9.22, 12.13, and 13.40. Therefore, at pH 7, As(V) will exist primarily as negatively charged species and As(III) will exist primarily as an uncharged specie. Under oxidizing conditions, arsenate is predicted to be the stable form, while under reducing conditions, arsenite becomes the stable form. At pH 7, H_3AsO_3 and HAsO_4^{2-} will have equal activities at $\text{pe} = 0.22$ (equilibrium data from Vink (1996)) (21). Co-precipitation and sorption methods have been widely used to remove arsenic from water. For instance, arsenic readily precipitates as a sulfide (22) or co-precipitates with metal sulfides (19). The available thermodynamic data indicate that the presence of sulfide should result in the effective precipitation and removal of arsenic. Kim et al. (2000) reported that both As(V) and As(III) are quickly converted to insoluble arsenic sulfide precipitate when sulfides are present (23). Packed beds of ferrous sulfide and the addition of hydrogen sulfide or sodium sulfide have been used in removal processes (24, 25). Blakey (1984) investigated the behavior and attenuation of arsenical waste co-disposed with domestic solid wastes (26). Results of this study indicated that under strongly reducing conditions in the presence of hydrogen sulfide, the iron present in the solution precipitates as

iron sulfide. The arsenic present is either co-precipitated with iron sulfide or is reduced to the arsenic sulfide directly, particularly at about pH 7. Attenuation of arsenic by a factor of 10 was obtained. However, under mildly reducing conditions, where hydrogen sulfide is absent, the presence of soluble ferrous iron had little effect on the mobility of the more toxic reduced As(III) ion.

One of the least soluble arsenic solids is arsenopyrite (FeAsS). This is the primary mineral form of arsenic and it is believed to have been formed geologically under conditions of high temperature and pressure (30). However, arsenopyrite has also been reported to be formed in natural sediments and water treatment sludges under less extreme conditions (31-33). Vlassopoulos et al. (1999) reported that arsenic was immobilized in a tidal marsh groundwater by coprecipitation with iron sulfide and formation of arsenopyrite (31). Rittle (1995) reported formation of arsenopyrite from As(III) in sediment microorganisms in which sulfide was formed by microbial sulfate reduction (32). Heinrich and Eadington (1986) describe a pathway for formation of arsenopyrite at low temperatures by reaction of As(III) and Fe(II) with Sn^{2+} (33). Even if formation of arsenopyrite is difficult, it may be possible to form arsenian pyrite ($\text{Fe}(\text{S},\text{As})_2$) (30), which may approach the low solubility of arsenopyrite.

An attractive sorption method for arsenic is to apply iron sulfides (i.e., pyrite (FeS_2) and mackinawite (FeS)) as reactants/adsorbents. Recent research has demonstrated that pyrite can adsorb arsenic and produce new solid phases such as arsenian pyrite ($\text{Fe}(\text{S},\text{As})_2$) and arsenopyrite (FeAsS) (30, 39, 40, 260). Zouboulis et al. (1993) observed that arsenic (As(III,V)) can be successfully adsorbed to pyrite and that optimal pH ranges for arsenic removal were 7-10 for As(III) and 3-9 for As(V) (34). Equilibrium was observed to occur within 10 minutes. Farquhar et al. (2002) evaluated As(III,V) sorption onto ground natural pyrite (size < 32 μm) and FeS (mackinawite) and investigated surface complex structures using As K-edge X-ray

absorption spectroscopy (XAS) (35). They observed that at low As(III,V) concentration, outer-sphere surface complex structures were observed, whereas at high As(III,V) concentration, arsenic sulfide precipitates were formed. Bostick et al. (2004) investigated As(III) sorption to FeS and FeS₂ in slightly sulfidic solution (39). Surface analysis by XANES showed that increased residence time led to the formation of both a bidentate arsenite complex and stable arsenic sulfide complexes such as arsenopyrite (FeAsS). They interpreted their results as the formation of an insoluble solid phase by surface reactions that continue to remove arsenic to lower levels. Therefore, the interaction of arsenic with iron sulfides may regulate arsenic solution concentration in reducing environments and should be considered an adsorption/reaction process, not solely an adsorption process.

The purpose of this study is to evaluate surface reactions between arsenic(III,V) and iron sulfides (pyrite and mackinawite) by identifying chemical states of As(III) and As(V) on the surface, as well as identifying the surface Fe and S species. These results can provide important information on mechanisms of arsenic removal by iron sulfides that can help attain the final goal of producing stable final solid products that can be safely disposed to a landfill.

9.2 Materials and Methods

9.2.1 Materials

All reagents were prepared using reagent grade chemicals or better and synthetic water samples were prepared by dissolving chemicals into deionized/deoxygenated (DI/DO) water. In order to produce DI/DO water, nanopure water (resistance > 18.3 MΩ) was first acquired by a Barnstead Nanopure filter system and then purged with N₂ gas (purity > 99.99 %) for at least 2 hours in the laboratory. Finally, the purged water was equilibrated overnight with the gas (5% H₂ and 95% N₂) in an anaerobic chamber. NaAsO₂ (Sigma-Aldrich) and Na₂HAsO₄·7H₂O (Sigma-Aldrich) were used for As(III) and As(V) sorption experiments. Pyrite (FeS₂) and mackinawite

(FeS) were used as adsorbent/reactants for arsenic removal and stabilization. Methods for synthesis of pyrite and mackinawite were described in Sections 5 and 7, respectively. All parts of the sorption/reaction experiments were conducted in an anaerobic chamber, except for solid surface analyses.

9.2.2 Sorption/Reaction Experiments

All sorption/reaction experiments were performed using batch systems at ambient temperature in an anaerobic chamber. All reactor vessels (20 mL) contained 1 g/L of solid suspension and 3.3 mM As(III) or As(V) solution at pH 8. They were mixed using an end-over-end rotary mixer until specified sampling time (1, 15, 30 day), when the sample was filtered using 0.02- μ m anodisc membrane filter (Whatmann). In order to analyze the solid surface, the disc containing the wet solid sample was moved to a labeled petri-dish, which was dried and stored in an anaerobic chamber until XPS and SEM-EDS analyses.

9.2.3 Spectroscopic Analyses

The surfaces of solid samples contacted with As(III) and As(V) for various times were analyzed using spectroscopic techniques such as X-ray photoelectron spectroscopy (XPS) and scanning electron microscopy (SEM) with energy dispersive spectrometry (EDS). The XPS spectra for oxidation states of the surface Fe and S species and solid-phase As(III) or As(V) were obtained using a Kratos Axis Ultra Imaging X-ray photoelectron spectrometer with a monochromatized Al K α (1253.6 eV) source operated at 200 W. Survey scans were recorded with pass energy of 80 eV, while high resolution spectra of Fe 2p, O 1s, S 2p, and As 3d levels used 20 eV. To calibrate charge effect, the spectra peak of C 1s at 284.5 ± 0.1 eV was used as reference. The high resolution spectra of Fe 2p, O 1s, S 2p, and As 3d were fitted using a program (XPSPEAK41) with Gaussian Lorentzian function through background-subtraction

corrections using a Shirley-type optimization.

The secondary SEM images and EDS analysis for solid samples were obtained using a JEOL JSM 6400 equipped with a PGT EDS system. The pretreatment method and analysis procedure were described in detail in Section 5.

9.3 Results and Discussion

9.3.1 Spectroscopic Investigation of As-Contacted Pyrite

Figures 9.1 and 9.2 show the As 3d XPS spectra of pyrite after contact with As(III) and As(V), respectively. For As(III)-contacted pyrite, there are peaks for four different As oxidation states, including As(I)-O, As(II)-O, As(III)-O, and As(V)-O at binding energies of 43.6~43.9, 44.0~44.3, 44.4~44.8, and 45.0~45.7 eV, respectively (Figure 9.1). The surprising observation is that species that are more reduced and more oxidized than As(III) are observed on the same samples. Peaks associated with more oxidized forms (As(V)-O) increased with increasing contact times. After contact with As(V), pyrite displayed peaks associated two different oxidation states of arsenic. Peaks associated with As(V)-O were observed at binding energy of 44.1~44.9 and peaks associated with As(III)-O were observed at 45.2~46.6 eV. The peak associated with As(III) at day 30 was higher than at day 1 by a factor of 1.5, although there was a decrease in peak height at 15 day. These results suggest that As(V) was being reduced to As(III) during the 30-day period of reaction. Some evidence exists that may help identify some of surface species and surface reactions.

There are conflicting results reported in the literature regarding sorption of As(III) or As(V) on pyrite. For instance, Farquhar et al. (2002) demonstrated with As K-edge EXAFS spectroscopy that the interaction of As(III) or As(V) with pyrite at pH 5.5-6.5 resulted in arsenic being coordinated to four oxygen atoms (As-O: 0.169-0.176 nm) in the first coordination shell, and coordinated with two sulfur (~0.31 nm) and three iron atoms (0.34-0.35 nm) in the second

shell. This suggests interactions via outer-sphere complexation, because the distances for the As-S and As-Fe bonds are longer than for As-O (35). In contrast, Bostick et al. (2003) identified other products of surface reaction between As(III) and pyrite at pH 4 (39). They used EXAFS to conclude that arsenopyrite (FeAsS) or a similar compound was present. This was based on measurements of As-Fe and As-S bond lengths of about 0.24 nm, which is similar to those found in arsenopyrite. They also reported that As-O bonds were not detected, which was taken to indicate that the arsenic compounds had oxidized the surface and had formed reduced arsenic compounds that did not contain oxygen. Since they had insufficient high-quality data to characterize the As-S and As-Fe features, the presence and identity of surface precipitates could not be determined (39). Table 9.1 summarizes the fitting parameters of As 3d_{5/2} XPS spectra for pyrites reacted with As(III) and As(V) at pH 8 as a function of reaction times.

Table 9.1 Binding energies (BE), full width at half maximum (FWHM), and area percentage for peaks in the As 3d_{5/2} XPS spectra of pyrite contacted with As(III) and As(V) for various times.

| Sample | Contact time (days) | BE (eV) | FWHM (eV) | Area (%) | Chemical states |
|----------------|---------------------|---------|-----------|----------|-----------------|
| Pyrite+As(III) | 1 | 43.6 | 0.52 | 8.3 | As(I)-O |
| | | 44.0 | 0.44 | 19.6 | As(II)-O |
| | | 44.4 | 0.46 | 25.8 | As(III)-O |
| | | 44.8 | 0.42 | 21.1 | As(III)-O |
| | | 45.2 | 0.44 | 16.7 | As(V)-O |
| | 15 | 45.6 | 0.53 | 8.6 | As(V)-O |
| | | 43.6 | 0.49 | 9.6 | As(I)-O |
| | | 44.0 | 0.51 | 19.5 | As(II)-O |
| | | 44.5 | 0.57 | 26.9 | As(III)-O |
| | | 45.0 | 0.72 | 28.3 | As(V)-O |
| | 30 | 45.7 | 0.95 | 15.6 | As(V)-O |
| | | 43.9 | 0.59 | 10.5 | As(I)-O |
| | | 44.3 | 0.47 | 19.4 | As(II)-O |
| | | 44.7 | 0.47 | 20.7 | As(III)-O |
| | | 45.1 | 0.67 | 34.1 | As(V)-O |
| Pyrite+As(V) | 1 | 44.7 | 1.09 | 19.0 | As(III)-O |
| | | 45.2 | 0.50 | 9.7 | As(V)-O |
| | | 45.9 | 0.91 | 39.5 | As(V)-O |
| | | 46.5 | 0.95 | 31.7 | As(V)-O |
| | | 44.5 | 1.03 | 16.7 | As(III)-O |
| | 15 | 45.3 | 0.72 | 28.2 | As(V)-O |
| | | 46.0 | 0.98 | 55.1 | As(V)-O |
| | | 44.1 | 0.83 | 11.5 | As(III)-O |
| | | 44.9 | 0.67 | 17.4 | As(III)-O |
| | | 45.6 | 0.74 | 34.3 | As(V)-O |
| | 30 | 46.1 | 0.63 | 23.8 | As(V)-O |
| | | 46.6 | 0.59 | 12.8 | As(V)-O |

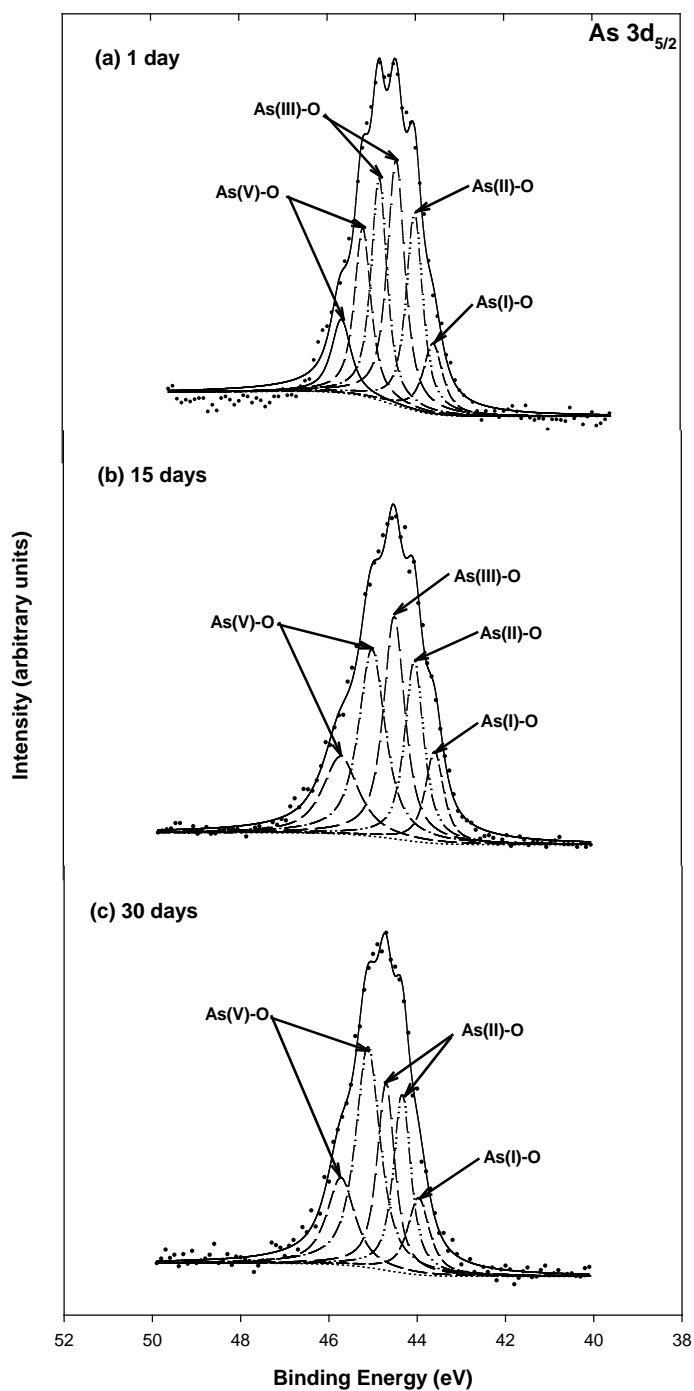


Figure 9.1 High resolution $\text{As } 3d_{5/2}$ XPS spectra of synthetic pyrite (1 g/L) reacted with 3.3 mM As(III) at pH 8 for various times: (a) 1 day, (b) 15 days, (c) 30 days.

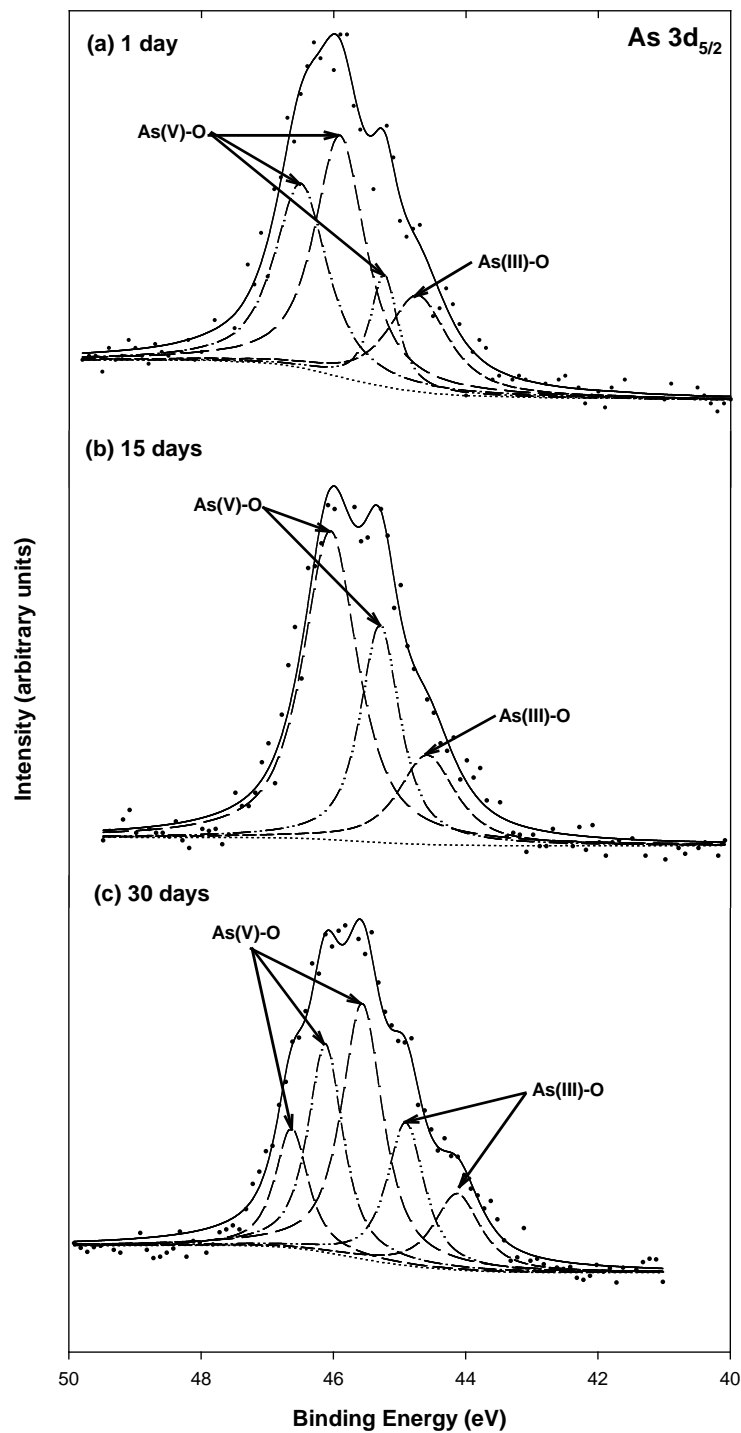


Figure 9.2 High resolution As 3d_{5/2} XPS spectra of synthetic pyrite (1 g/L) reacted with 3.3 mM As(V) at pH 8 for various times: (a) 1 day, (b) 15 days, (c) 30 days.

Figures 9.3 and 9.4 show the Fe 2p_{3/2} XPS spectra of pyrite after contact with As(III) and As(V), respectively. The spectra for synthetic pyrite before contact with As (Figure 6.7 in Section 6) shows three major peaks that are centered at 706.8, 708.3 and 710.4 eV and these peaks are assigned to Fe(II)-S, Fe(III)-S and Fe(III)-O, respectively. Since there is limited oxidation of pyrite before contact with arsenic, the Fe(II)-S peak is much higher than the others. However, after contact with As(III) and As(V) the spectra changes. Peaks associated with Fe(III)-S and Fe(III)-O increase in intensity and are found at higher bonding energy, which indicates that surface-bound iron species were oxidized. Therefore, it appears that the reduction of As(III) and As(V) is associated with the oxidation of Fe(II). Figures 9.5 and 9.6 show the S 2p XPS spectra of pyrite after contact with As(III) and As(V), respectively. Prior to contact with arsenic, the S 2p_{3/2} and S 2p_{1/2} spectra contained two main peaks, which were centered at 162.8 and 164 eV with 1.2 eV energy separation (Figure 6.9 in Section 6). These peaks were assigned to S₂²⁻ species, although a minor peak associated with SO₄²⁻ was observed at higher binding energy. After contact with As(III), there were no important changes in the S 2p spectra. However, after contact with As(V), the spectra developed a long tail at binding energy near 169 eV. This indicated that a small amount of SO₄²⁻ was present, which is evidence that sulfur on the surface may be oxidized in connection with reduction of As(V).

Analysis of the O 1s spectra can provide important information about the types of oxide phases that develop on pyrite surfaces after reaction with inorganic contaminants (261). In general, O 1s peaks associated with metal oxides and other components such as oxide, hydroxyl, and surface water are expected to have binding energies in the range from 529.5 to 533 eV (262). Figures 9.7 and 9.8 show the O 1s spectra for pyrite contacted with As(III) and As(V), respectively. There are no important changes in O 1s peaks before and after contact with As(III) or As(V). However, Figure 9.9 shows the O 1s spectra over a wider range of binding energy and

indicates that a new peak is being formed with a binding energy near 540 eV. This peak is observed only for As(III)-contacted pyrite. There are no peaks for oxygen in any other solids that have been reported at this binding energy, nor is it assigned to the main peak of another element (262). Knipe et al. (1995) said that the anomalous peak near 540 eV might be caused by adsorption of electrically isolated water clusters through hydrogen bonding (262). Bonnissel-Gissinger et al. (1998) reported that extra peaks in the O 1s spectra were observed at 535 ± 0.1 eV or 537.6 ± 0.1 eV as pyrite was oxidized by oxygen and formed islands of iron (hydr)oxides on the pyrite surface (263).

Table 9.2 Binding energies (BE), full width at half maximum (FWHM), and area percentage for peaks in the Fe 2p_{3/2} XPS spectra of pyrite contacted with As(III) and As(V) for various times.

| Sample | Contact time (days) | BE (eV) | FWHM (eV) | Area (%) | Chemical states |
|----------------|---------------------|---------|-----------|-----------|-----------------|
| Pyrite | 0 | 706.8 | 0.86 | 72.4 | Fe(II)-S |
| | | 708.3 | 1.66 | 14.2 | Fe(III)-S |
| | | 710.4 | 2.09 | 13.4 | Fe(III)-O |
| Pyrite+As(III) | 1 | 706.9 | 0.94 | 31.6 | Fe(II)-S |
| | | 708.4 | 1.51 | 6.41 | Fe(III)-S |
| | | 710.0 | 1.79 | 25.8 | Fe(III)-O |
| | | 711.2 | 1.90 | 28.9 | Fe(III)-O |
| | 15 | 712.8 | 1.50 | 7.22 | Fe(III)-O |
| | | 706.8 | 1.01 | 28.0 | Fe(II)-S |
| | | 708.3 | 1.16 | 2.64 | Fe(III)-S |
| | | 710.2 | 1.54 | 38.0 | Fe(III)-O |
| | 30 | 711.3 | 1.05 | 17.7 | Fe(III)-O |
| | | 712.4 | 1.42 | 13.6 | Fe(III)-O |
| | | 706.8 | 0.95 | 29.6 | Fe(II)-S |
| | | 709.3 | 2.29 | 20.3 | Fe(III)-S |
| Pyrite+As(V) | 1 | 710.5 | 1.56 | 27.1 | Fe(III)-O |
| | | 711.6 | 1.44 | 13.7 | Fe(III)-O |
| | | 713.2 | 1.85 | 9.21 | Fe(III)-O |
| | | 706.8 | 0.95 | 53.6 | Fe(II)-S |
| | 15 | 708.3 | 1.45 | 10.6 | Fe(III)-S |
| | | 709.9 | 1.69 | 21.1 | Fe(III)-O |
| | | 711.4 | 2.10 | 14.7 | Fe(III)-O |
| | | 706.6 | 1.09 | 44.1 | Fe(II)-S |
| | 30 | 709.1 | 1.84 | 15.8 | Fe(III)-S |
| | | 710.3 | 1.27 | 17.3 | Fe(III)-O |
| | | 711.4 | 1.71 | 16.5 | Fe(III)-O |
| | | 713.0 | 1.79 | 6.07 | Fe(III)-O |
| 30 | 706.5 | 0.90 | 48.2 | Fe(II)-S | |
| | 708.4 | 1.95 | 16.8 | Fe(III)-S | |
| | 710.1 | 2.08 | 25.5 | Fe(III)-O | |
| | 712.3 | 2.74 | 9.41 | Fe(III)-O | |

Table 9.3 Binding energies (BE), full width at half maximum (FWHM), and area percentage for peaks in the S 2p XPS spectra of pyrite contacted with As(III) and As(V) for various times.

| Sample | Contact time (days) | BE (eV) | FWHM (eV) | Area (%) | Chemical states |
|----------------|---------------------|---------|-----------|----------|-------------------------------|
| Pyrite | 0 | 162.8 | 0.87 | 64.7 | S ₂ ²⁻ |
| | | 164.0 | 0.95 | 33.5 | S ₂ ²⁻ |
| Pyrite+As(III) | 1 | 162.9 | 0.91 | 65.4 | S ²⁻ |
| | | 164.1 | 1.00 | 32.7 | S ₂ ²⁻ |
| | | 168.9 | 0.85 | 1.83 | SO ₄ ²⁻ |
| | 15 | 162.7 | 0.91 | 55.3 | S ²⁻ |
| | | 163.9 | 1.25 | 40.0 | S ₂ ²⁻ |
| | | 169.0 | 1.76 | 4.59 | SO ₄ ²⁻ |
| | 30 | 162.8 | 1.05 | 60.4 | S ²⁻ |
| | | 164.0 | 1.23 | 36.8 | S ₂ ²⁻ |
| | | 169.4 | 0.73 | 2.77 | SO ₄ ²⁻ |
| Pyrite+As(V) | 1 | 162.8 | 0.91 | 42.1 | S ₂ ²⁻ |
| | | 164.1 | 1.37 | 41.3 | S ₂ ²⁻ |
| | | 169.1 | 1.80 | 16.6 | SO ₄ ²⁻ |
| | 15 | 162.8 | 0.90 | 68.1 | S ₂ ²⁻ |
| | | 164.0 | 0.95 | 31.9 | S ₂ ²⁻ |
| | | 162.7 | 0.91 | 61.5 | S ₂ ²⁻ |
| | 30 | 163.9 | 1.09 | 34.7 | S ₂ ²⁻ |
| | | 169.1 | 1.25 | 3.75 | SO ₄ ²⁻ |

Table 9.4 Binding energies (BE), full width at half maximum (FWHM), and area percentage for peaks in the O 1s XPS spectra of pyrite contacted with As(III) and As(V) for various times.

| Sample | Contact time (days) | BE (eV) | FWHM (eV) | Area (%) | Chemical states |
|----------------|---------------------|---------|-----------|----------|------------------|
| Pyrite | 0 | 530.0 | 1.01 | 25.5 | O ²⁻ |
| | | 531.1 | 1.10 | 38.0 | OH ⁻ |
| | | 531.8 | 1.17 | 36.4 | H ₂ O |
| Pyrite+As(III) | 1 | 530.0 | 0.75 | 23.7 | O ²⁻ |
| | | 530.6 | 0.81 | 39.8 | OH ⁻ |
| | | 531.3 | 1.05 | 36.4 | H ₂ O |
| | 15 | 530.0 | 0.92 | 26.3 | O ²⁻ |
| | | 530.9 | 0.99 | 36.7 | OH ⁻ |
| | | 531.7 | 1.29 | 36.8 | H ₂ O |
| | 30 | 529.9 | 0.86 | 32.4 | O ²⁻ |
| | | 530.6 | 0.80 | 40.8 | OH ⁻ |
| | | 531.3 | 0.92 | 26.7 | H ₂ O |
| Pyrite+As(V) | 1 | 529.6 | 1.07 | 25.9 | O ²⁻ |
| | | 530.6 | 1.04 | 46.1 | OH ⁻ |
| | | 531.4 | 1.01 | 28.0 | H ₂ O |
| | 15 | 530.0 | 0.82 | 40.9 | O ²⁻ |
| | | 530.6 | 0.73 | 35.4 | OH ⁻ |
| | | 531.2 | 0.82 | 23.7 | H ₂ O |
| | 30 | 529.8 | 0.84 | 23.2 | O ²⁻ |
| | | 530.6 | 0.89 | 36.3 | OH ⁻ |
| | | 531.5 | 1.16 | 40.4 | H ₂ O |

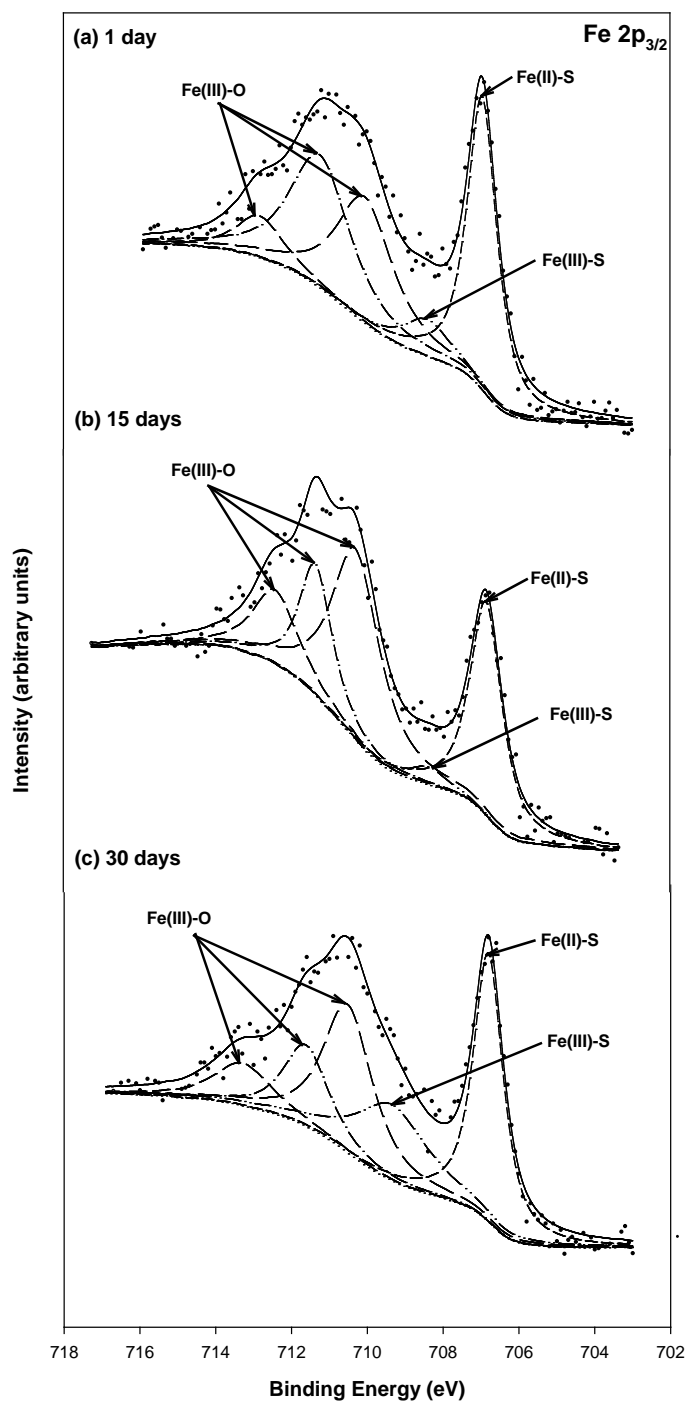


Figure 9.3 High resolution Fe 2p_{3/2} XPS spectra for synthetic pyrite (1 g/L) reacted with 3.3 mM As(III) at pH 8 for various times: (a) 1 day, (b) 15 days, (c) 30 days.

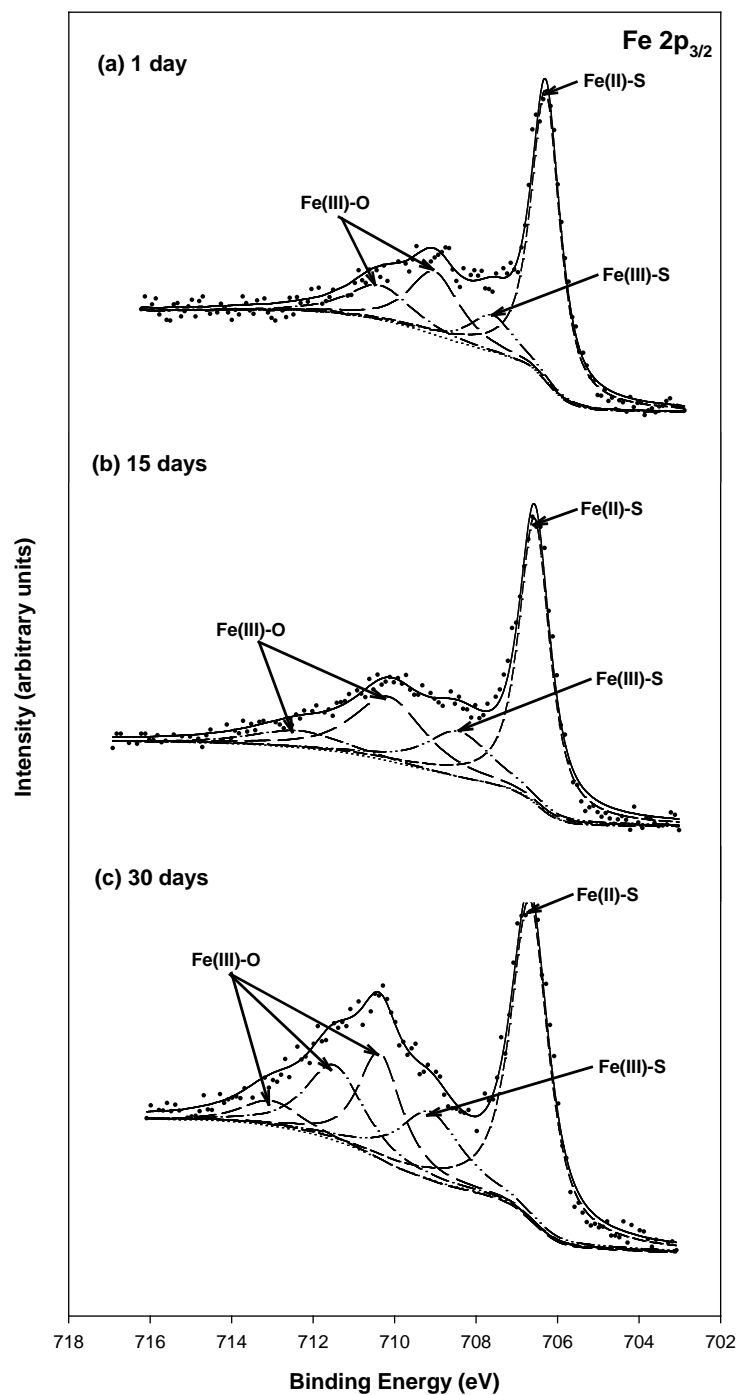


Figure 9.4 High resolution Fe $2p_{3/2}$ XPS spectra for synthetic pyrite (1 g/L) reacted with 3.3 mM As(V) at pH 8 for various times: (a) 1 day, (b) 15 days, (c) 30 days.

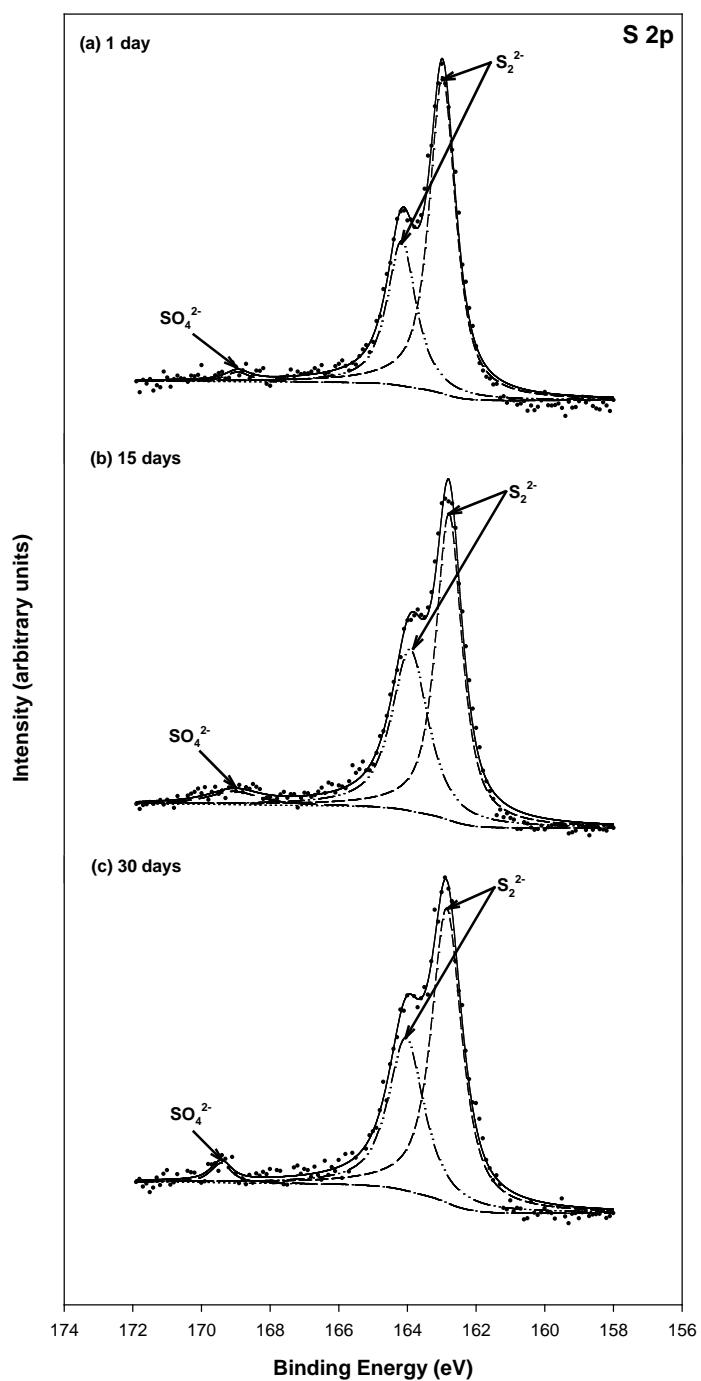


Figure 9.5 High resolution S 2p XPS spectra for synthetic pyrite (1 g/L) reacted with 3.3 mM As(III) at pH 8 for various times: (a) 1 day, (b) 15 days, (c) 30 days.

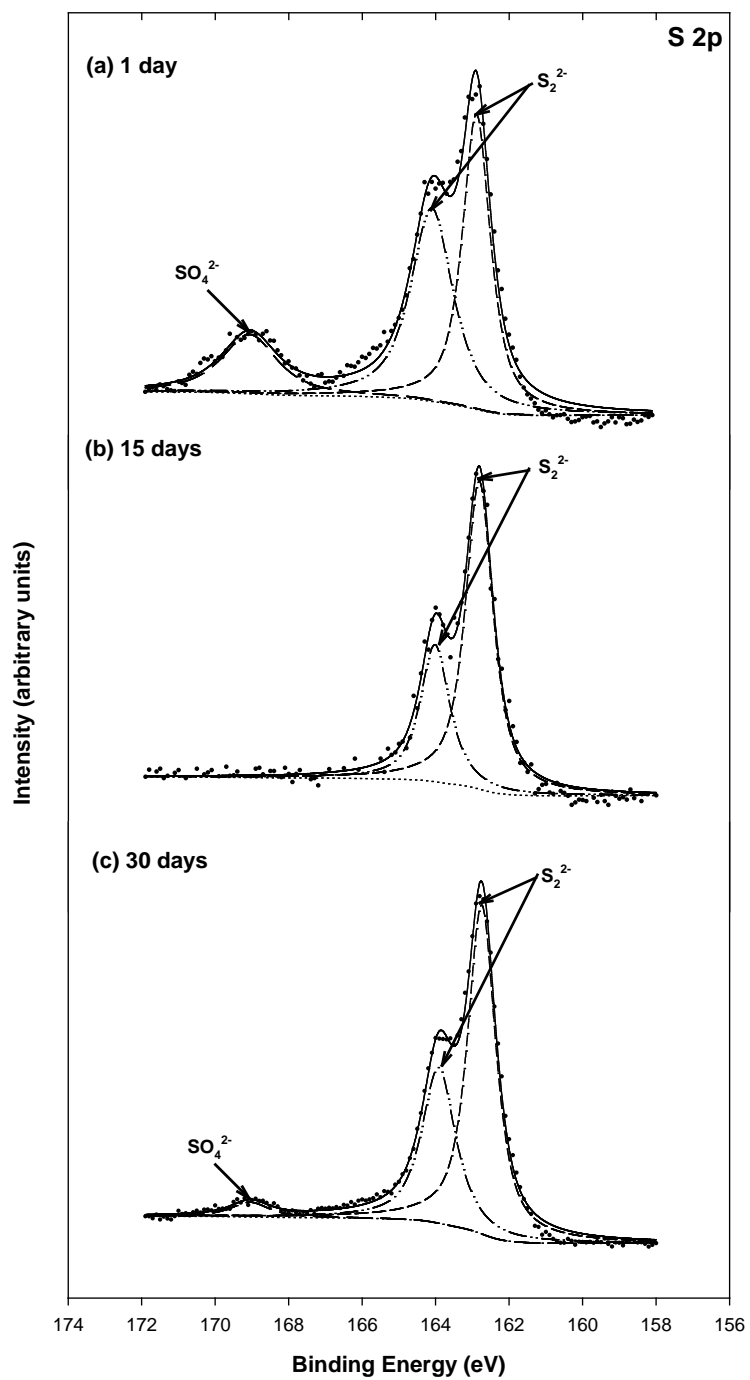


Figure 9.6 High resolution S 2p XPS spectra for synthetic pyrite (1 g/L) reacted with 3.3 mM As(V) at pH 8 for various times: (a) 1 day, (b) 15 days, (c) 30 days.

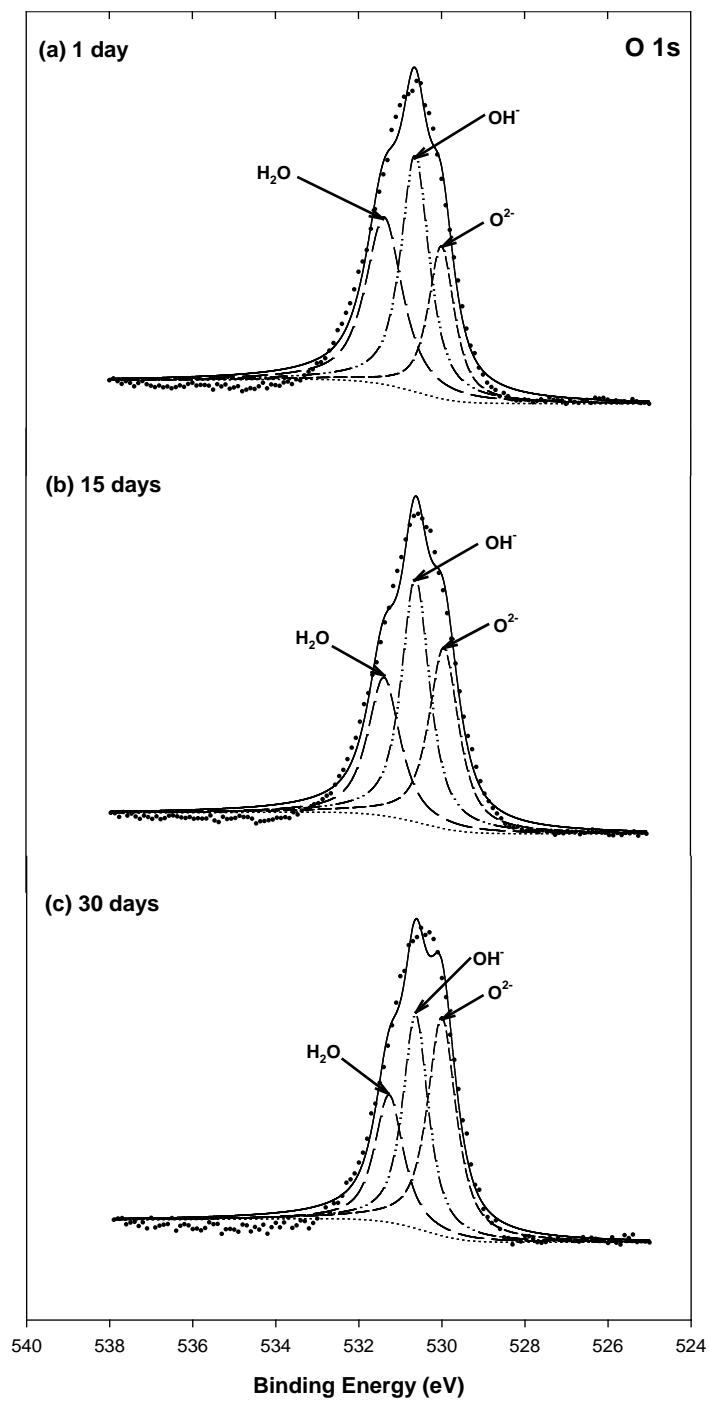


Figure 9.7 High resolution O 1s XPS spectra for pyrite reacted with 3.3 mM As(III) at pH 8 for various times: (a) 1 day, (b) 15 days, (c) 30 days.

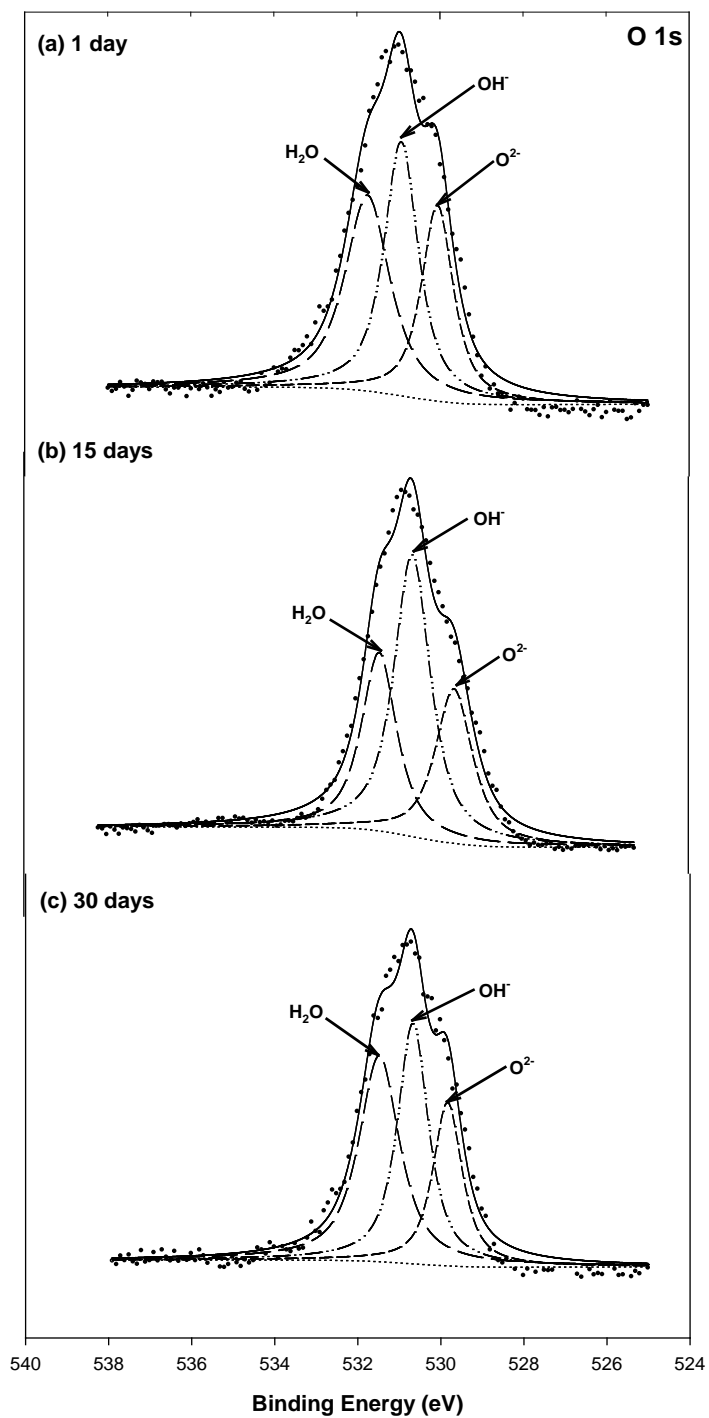


Figure 9.8 High resolution O 1s XPS spectra for pyrite reacted with 3.3 mM As(V) at pH 8 for various times: (a) 1 day, (b) 15 days, (c) 30 days.

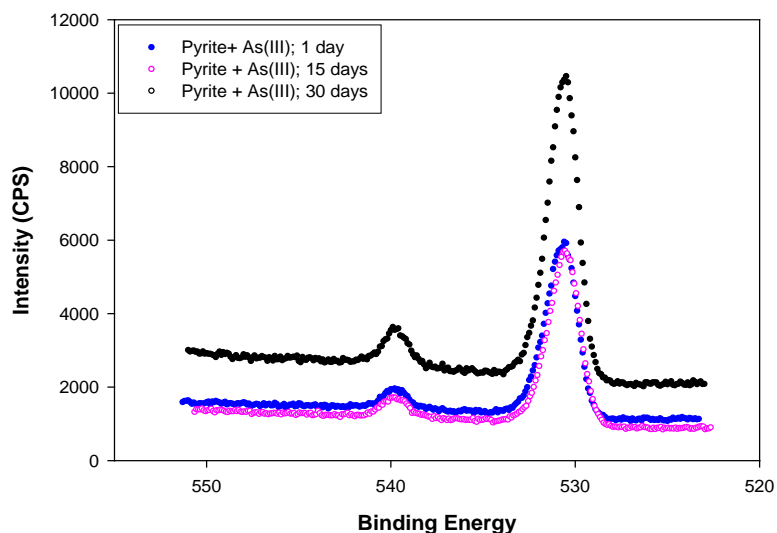


Figure 9.9 The O 1s XPS spectra for pyrite reacted with As(III) (3.3 mM) at pH 8 and various reaction times (1, 15, 30 days).

9.3.2 SEM-EDS Investigation for As-Contacted Pyrites

Figures 9.10 and 9.11 show the secondary SEM images and EDS results for pyrites contacted with arsenic for 1, 15, and 30 days. Pyrite showed a changed morphology after contact with As(III) for 15 days, where earthworm-like thin particles covered the pyrite surface (Figure 9.10(b)). The changed morphology was kept in the 30-day sample (Figure 9.10(c)), but the changes were not as severe as in the 15-day sample. This suggests that surface reactions between As(III) and pyrite may change the morphology of pyrite. However, EDS analysis indicated that there were no substantial changes in elemental composition. For As(V)-contacted pyrites (Figures 9.11(a), 9.11(b), 9.11(c)), a bundle of thin particles were present after 1 day and sheet-like thin plates developed on the pyrite surface at longer contact times. The occurrence of different particles may be also related to surface reactions between As(V) and the pyrite surface. EDS analysis indicated that there were no considerable changes in elemental composition of the surface.

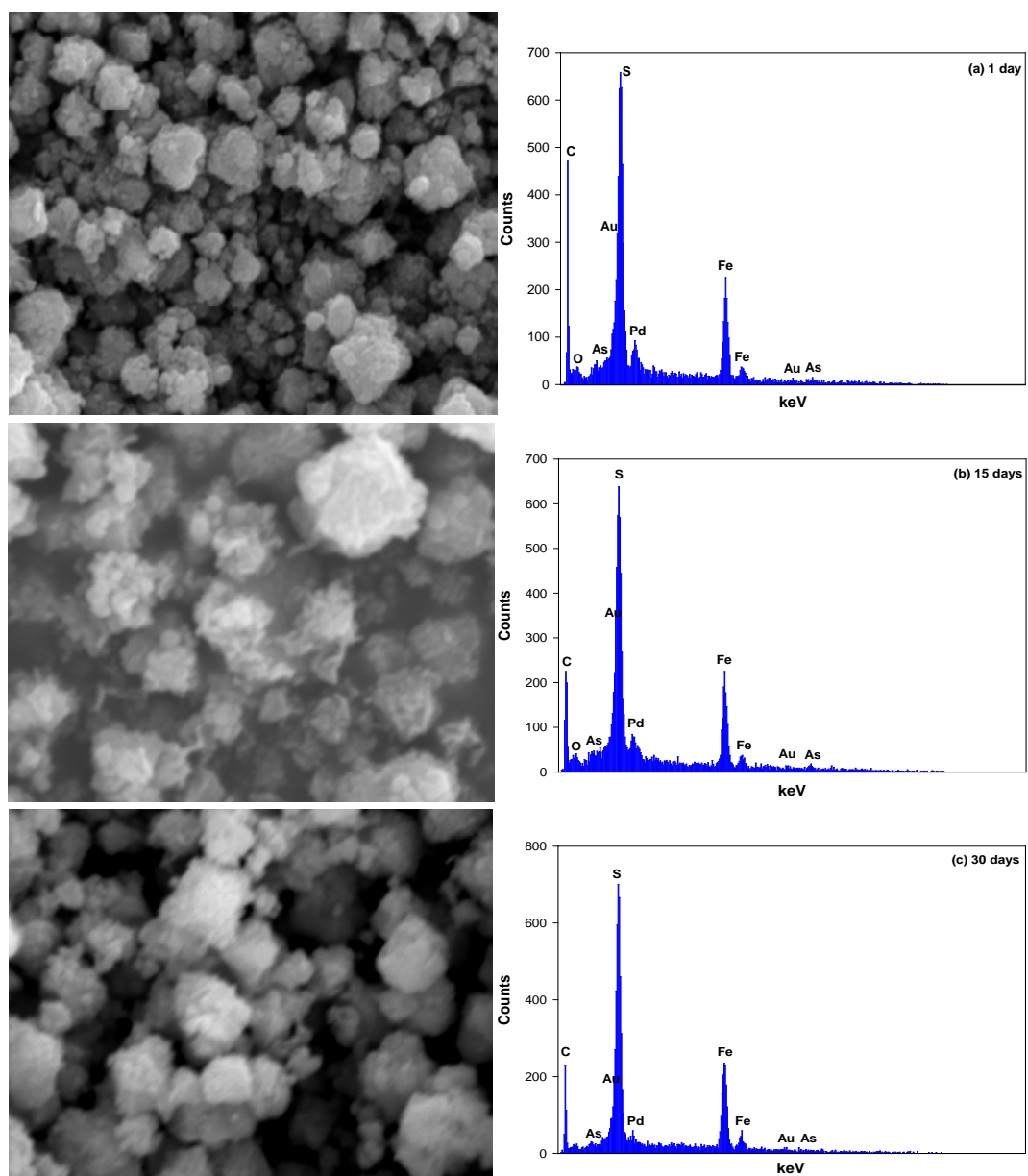


Figure 9.10 Secondary SEM images and EDS analysis of pyrites after contact with As(III) (3.3 mM) as a function of reaction times: (a) 1 day, (b) 15 day, (c) 30 days.

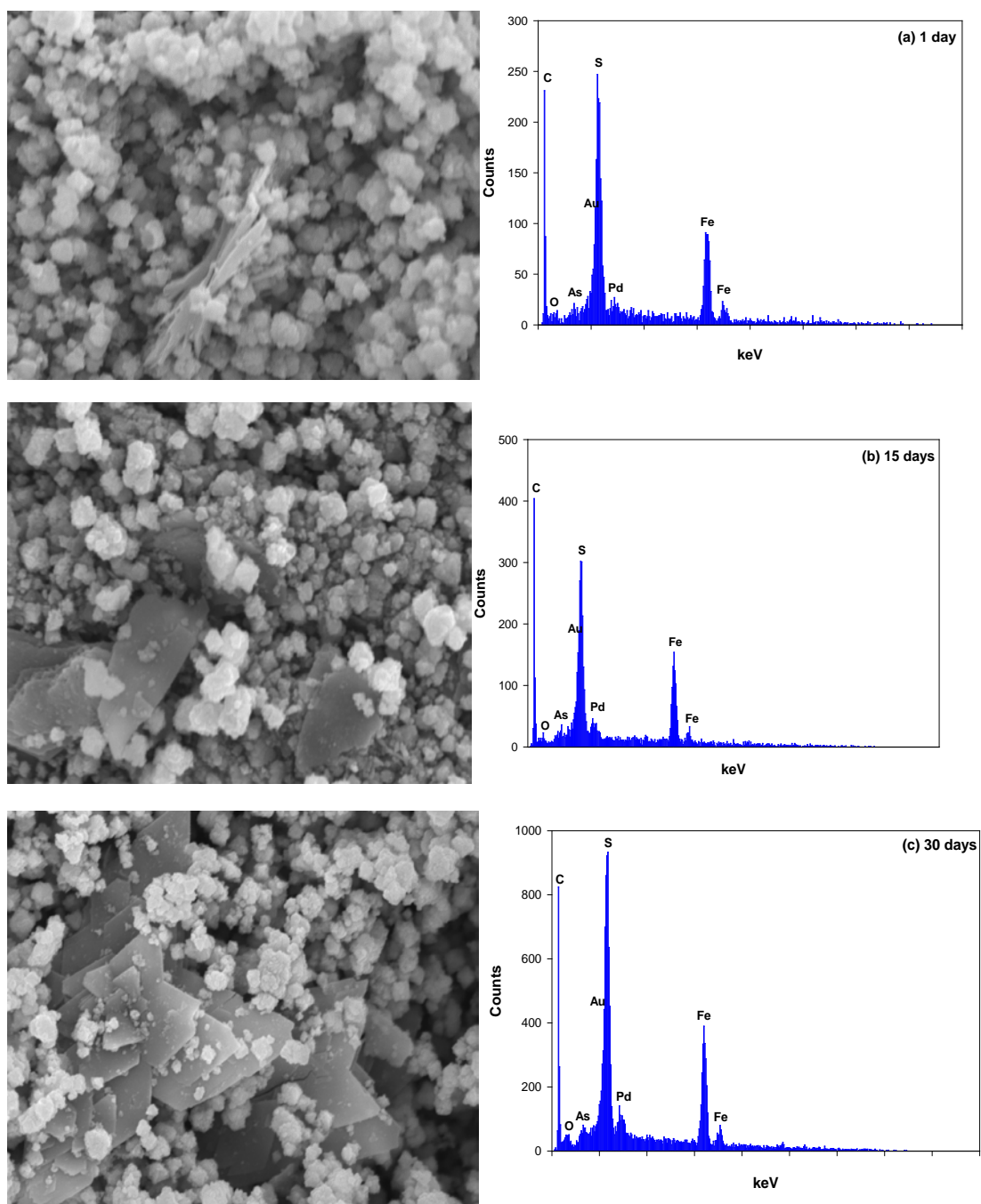


Figure 9.11 Secondary SEM images and EDS analysis of pyrites after contact with As(V) (3.3mM) as a function of reaction times: (a) 1 day, (b) 15 day, (c) 30 days.

9.3.3 Spectroscopic Analyses of As-Contacted FeS

Figures 9.12 and 9.13 show the As $3d_{5/2}$ XPS spectra of mackinawite reacted with As(III) or As(V) for various times. For As(III)-contacted mackinawite (Figure 9.12), the As $3d_{5/2}$ spectra include peaks associated with various oxidation states of arsenic such as As(I), As(II), As(III), and As(V). The relative peak areas for a reduced specie (As(II)) increased by a factor of 1.7 in the 30-day sample compared to the 1-day sample, while the peaks associated with an oxidized specie (As(V)) increased by a factor of 2.4. The relative peak area for As(III) increased over the same time period by a factor of 2.8 (Table 9.5). These results indicate that As(III) was undergoing simultaneous oxidation and reduction reactions on the pyrite surface, but there was a trend to production of more reduced species over time.

For As(V)-contacted mackinawite, peaks associated with As(V) and As(III) are the major components of the As $3d_{5/2}$ spectra. As(V) sorbed on mackinawite represented 35.1 %, 21.4 %, and 25.9% of surface arsenic after contact for 1, 15 and 30 days, respectively. However, the relative peak area for As(III) in the 15-day sample decreased somewhat compared to that for the 1-day sample, but increased again in the 30-day sample. This might be associated with chemical changes in the surface-bound Fe and S species. Consequently, the results discussed above suggest that there are surface reactions between As(III, V) and the mackinawite surface.

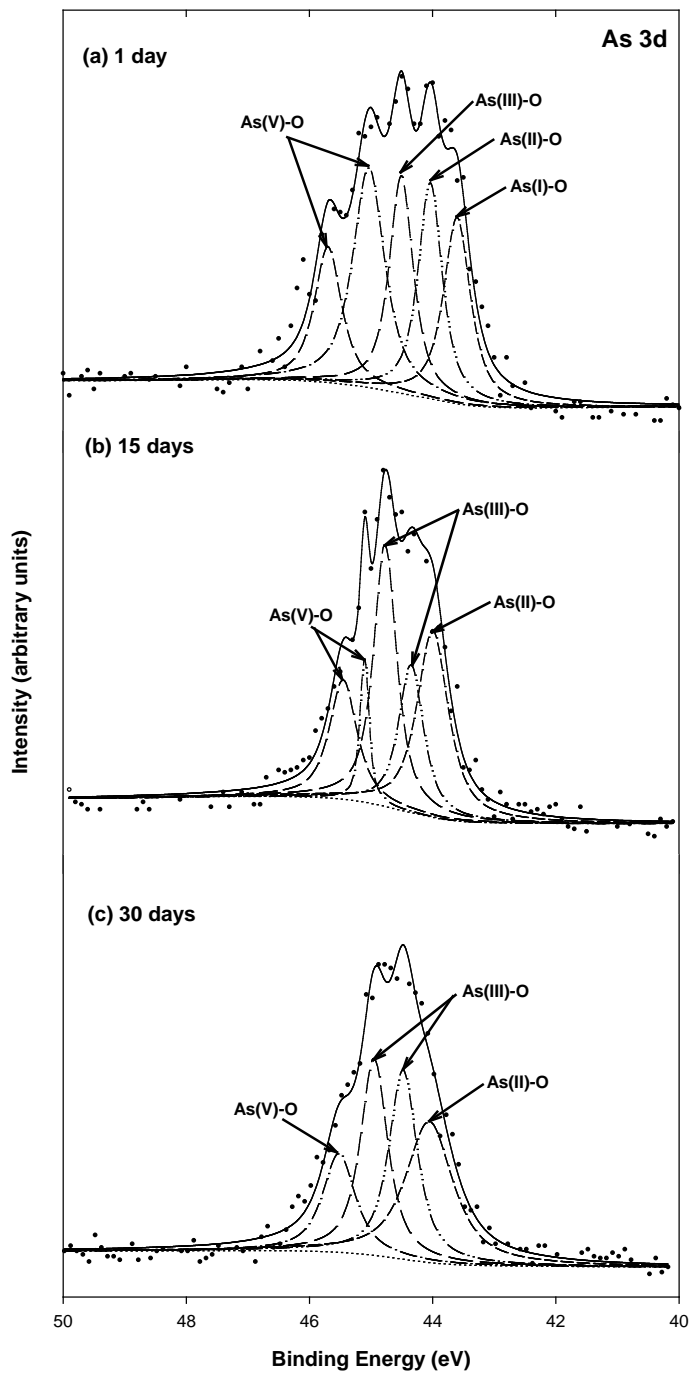


Figure 9.12 High resolution As 3d_{5/2} XPS spectra of synthetic pyrite (1 g/L) reacted with 3.3 mM As(III) at pH 8 for various times: (a) 1 day, (b) 15 days, (c) 30 days.

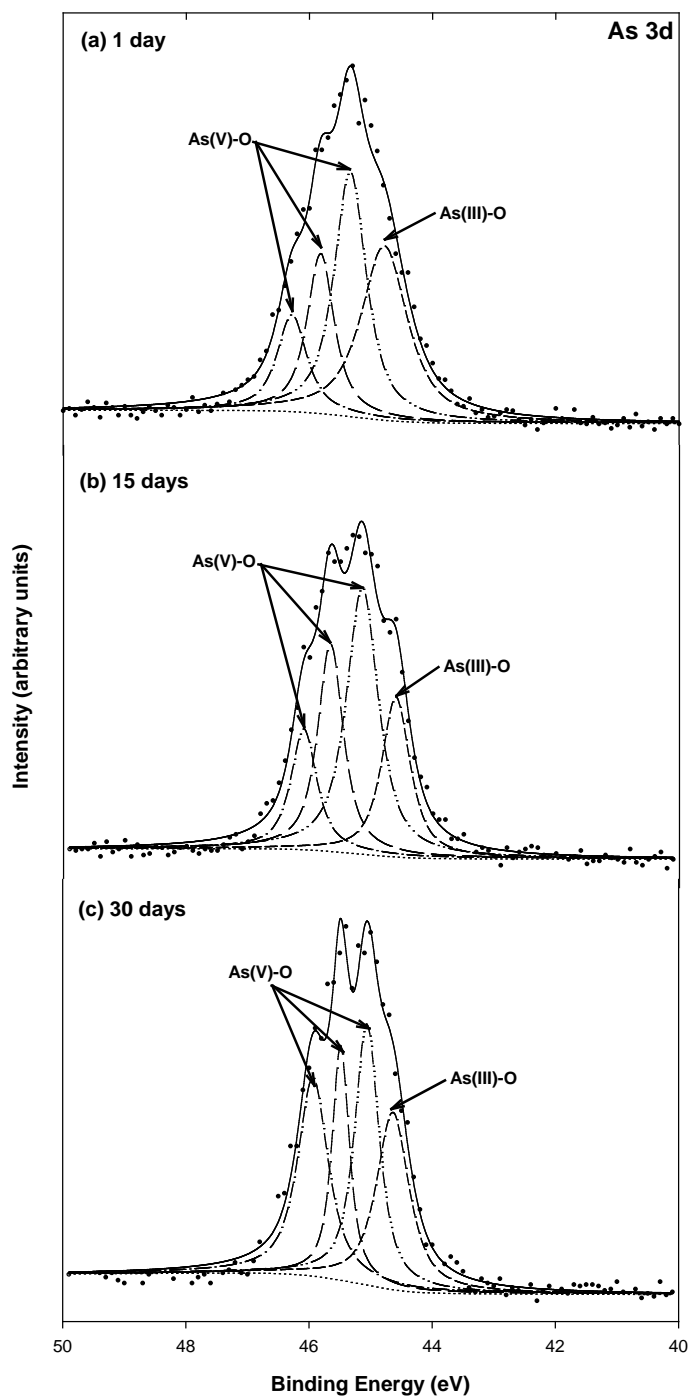


Figure 9.13 High resolution As 3d_{5/2} XPS spectra of synthetic pyrite (1 g/L) reacted with 3.3 mM As(V) at pH 8 for various times: (a) 1 day, (b) 15 days, (c) 30 days.

Table 9.5 Binding energies (BE), full width at half maximum (FWHM), and area percentage for peaks in the As 3d_{5/2} XPS spectra of mackinawite contacted with As(III) and As(V) for various times.

| Sample | Contact time (days) | BE (eV) | FWHM (eV) | Area (%) | Chemical states |
|-------------|---------------------|---------|-----------|----------|-----------------|
| FeS+As(III) | 1 | 43.6 | 0.52 | 19.1 | As(I)-O |
| | | 44.0 | 0.46 | 18.6 | As(II)-O |
| | | 44.5 | 0.46 | 18.5 | As(III)-O |
| | | 45.0 | 0.62 | 24.9 | As(V)-O |
| | | 45.7 | 0.53 | 13.0 | As(V)-O |
| | 15 | 44.0 | 0.61 | 29.0 | As(II)-O |
| | | 44.3 | 0.48 | 18.4 | As(III)-O |
| | | 44.7 | 0.45 | 29.9 | As(III)-O |
| | | 45.1 | 0.17 | 16.2 | As(V)-O |
| | | 45.4 | 0.53 | 16.2 | As(V)-O |
| | 30 | 44.0 | 0.92 | 32.4 | As(II)-O |
| | | 44.5 | 0.55 | 26.1 | As(III)-O |
| | | 44.9 | 0.53 | 26.1 | As(III)-O |
| | | 45.5 | 0.63 | 15.5 | As(V)-O |
| | FeS+As(V) | 1 | 44.8 | 0.89 | 35.1 |
| 45.3 | | | 0.62 | 34.1 | As(V)-O |
| 45.8 | | | 0.52 | 18.5 | As(V)-O |
| 46.3 | | | 0.57 | 12.3 | As(V)-O |
| 15 | | 44.6 | 0.55 | 21.4 | As(III)-O |
| | | 45.1 | 0.62 | 39.8 | As(V)-O |
| | | 45.7 | 0.49 | 24.5 | As(V)-O |
| | | 46.1 | 0.49 | 14.3 | As(V)-O |
| 30 | | 44.6 | 0.63 | 25.9 | As(III)-O |
| | | 45.1 | 0.47 | 28.7 | As(V)-O |
| | | 45.5 | 0.33 | 18.2 | As(V)-O |
| | | 45.9 | 0.59 | 27.1 | As(V)-O |

Figure 9.14 shows the Fe 2p_{3/2} XPS spectra of mackinawite after contact with As(III) for various times. There are four major peaks for Fe(II)-S, Fe(II)-O, Fe(III)-S, Fe(III)-O at 706.0~706.9, 707.1~707.8, 708.0~709.7, 709.8~713.3 eV, respectively. The relative peak area for Fe(III)-S and Fe(III)-O species increased with time, while the relative peak area related to Fe(II)-S and Fe(II)-O species decreased indicating the oxidation of iron surface sites. Also, Figure 9.15 shows the Fe 2p_{3/2} XPS spectra for As(V) contacted with mackinawite for various times. The spectra for As(V)-contacted mackinawite present four major peaks, which are similar to those observed for As(III)-contacted mackinawite. Longer contact times resulted in larger peaks for Fe(III)-S and Fe(III)-O. In particular, the Fe(III)-O peaks at 710.3~712.3 eV are

attributed to Fe(III) hydr(oxides) and the peak at 713.3 eV may be due to an Fe(III) multiplet structure (263).

Figure 9.16 shows the S 2p XPS spectra for mackinawite reacted with As(III) for various times. The major component of the S 2p spectra is located at ~161.9 eV and this peak is assigned to sulfide (S^{2-}) in mackinawite. However, more components are required to fit the high energy tail, so polysulfides (S_n^{2-}) and elemental sulfur (S^0) are included as sulfur species. A peak for SO_4^{2-} in the S 2p spectra is observed at 168.4 eV in samples that had reacted for 30 days. Figure 9.17 shows the S 2p XPS spectra for mackinawite reacted with As(V) for various times. For mackinawite reacted with As(V) for 1 and 15 days, the S 2p spectra are decomposed by four multiplets associated with S^{2-} and singlet or doublet associated with S_n^{2-} . The spectra for mackinawite reacted for 30 days differs in that it includes peaks associated with elemental sulfur (S^0), which is needed to fit the high energy tail. Therefore, the oxidations of surface Fe and S species are associated with reductions of As(III) and As(V). Tables 9.6 and 9.7 summarize binding energies (BE), peak full width at half maximum (FWHM), peak area percentage for Fe $2p_{3/2}$ and S 2p photoelectron spectra of mackinawite contacted with As(III) and As(V) for various times.

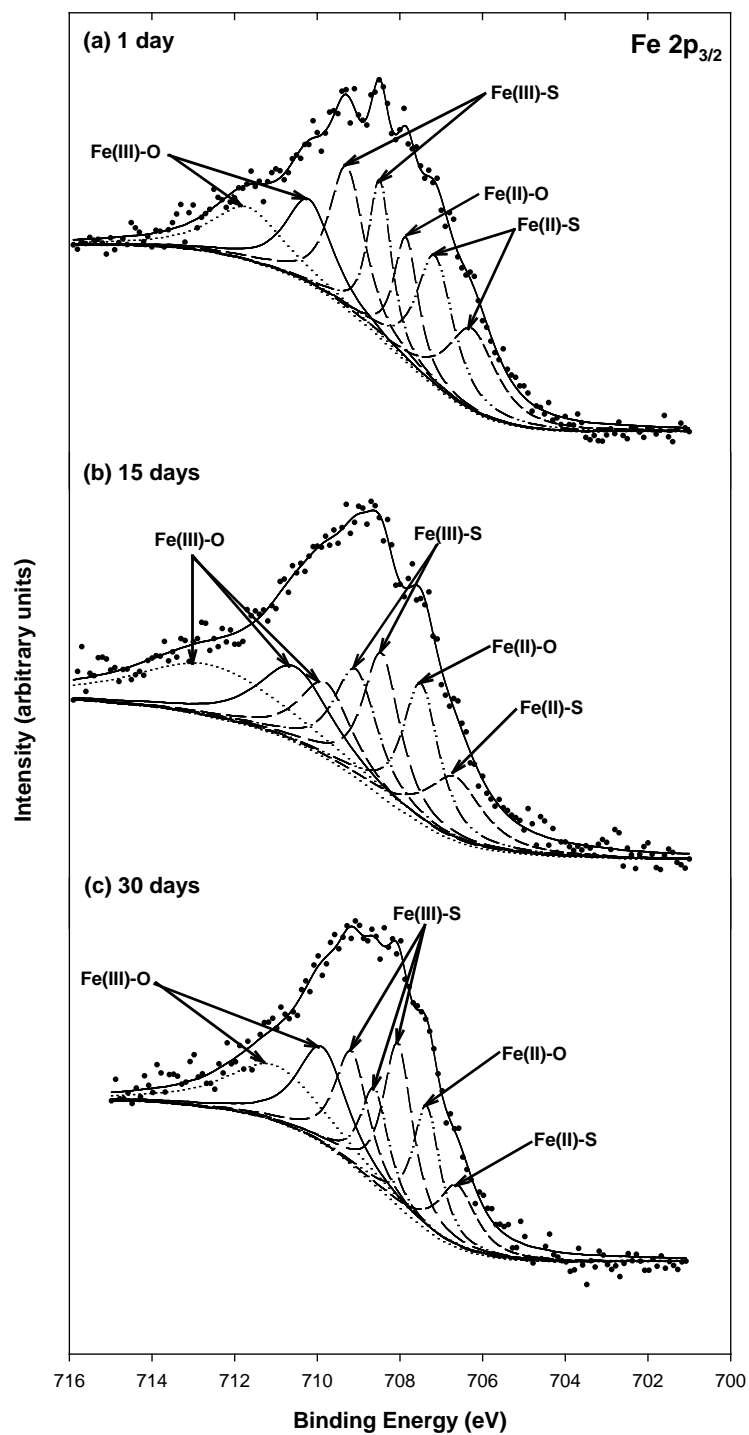


Figure 9.14 High resolution Fe 2p_{3/2} XPS spectra of synthetic mackinawite (1 g/L) reacted with 3.3 mM As(III) at pH 8 for various times: (a) 1 day, (b) 15 days, (c) 30 days.

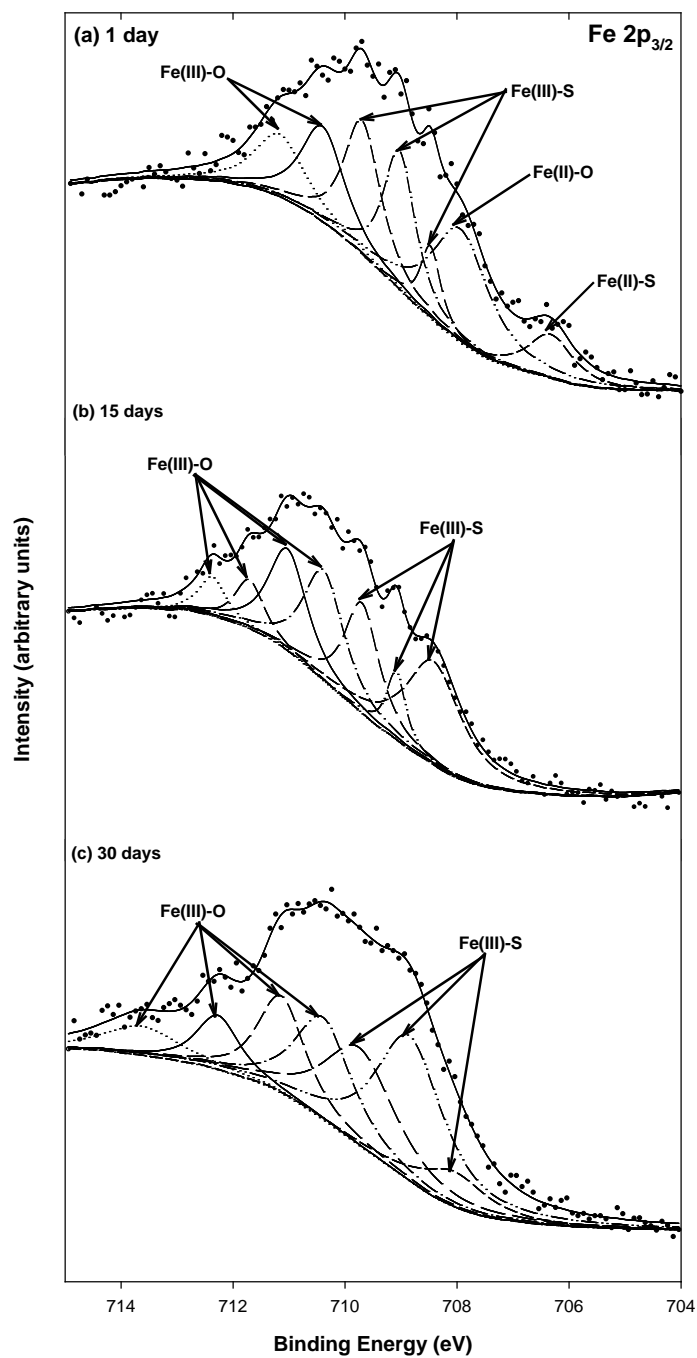


Figure 9.15 High resolution Fe $2p_{3/2}$ XPS spectra of synthetic mackinawite (1 g/L) reacted with 3.3 mM As(V) at pH 8 for various times: (a) 1 day, (b) 15 days, (c) 30 days.

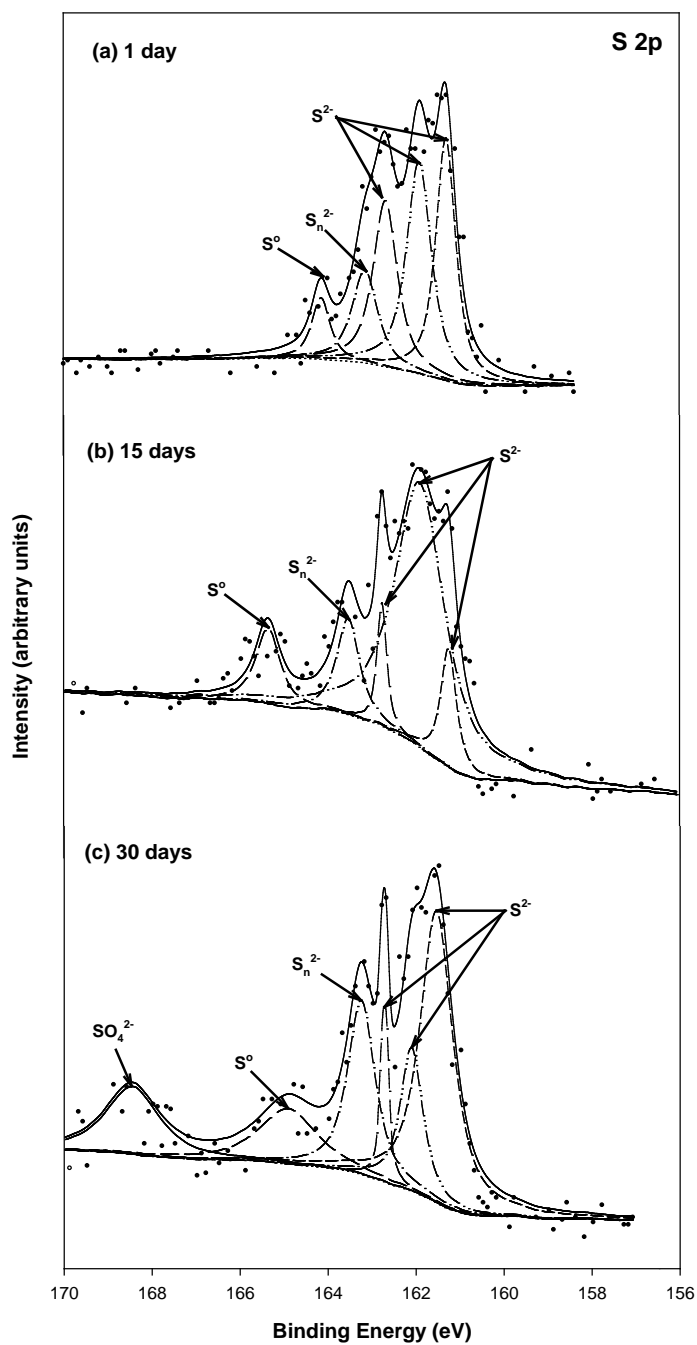


Figure 9.16 High resolution S 2p XPS spectra of synthetic mackinawite (1 g/L) reacted with 3.3 mM As(III) at pH 8 for various times: (a) 1 day, (b) 15 days, (c) 30 days.

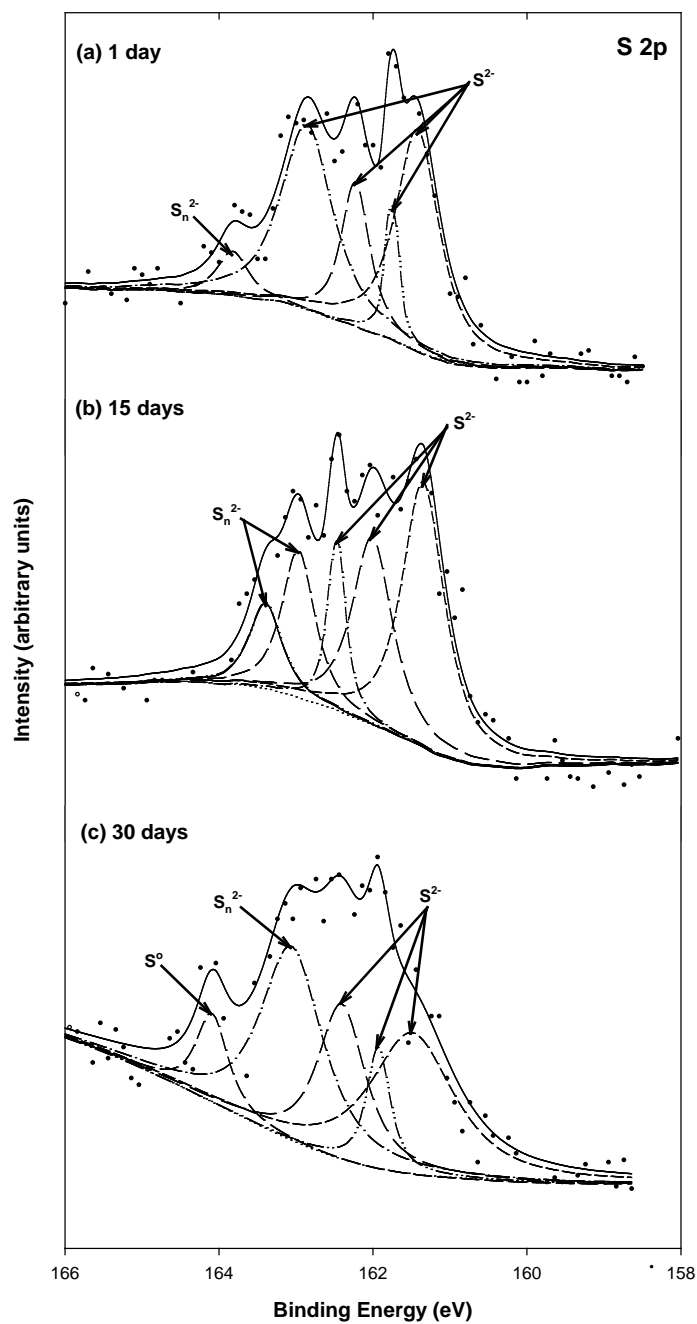


Figure 9.17 High resolution S 2p XPS spectra of synthetic mackinawite (1g/L) reacted with 3.3 mM As(V) at pH 8 for various times: (a) 1 day, (b) 15 days, (c) 30 days.

Table 9.6 Binding energies (BE), peak full width at half maximum (FWHM), peak area percentage for Fe 2p_{3/2} photoelectron spectra of mackinawite contacted with As(III) and As(V) for various times.

| Sample | Time | χ^2 | BE (eV) | FWHM (eV) | Area (%) | Chemical states |
|---------------------|------|----------|-----------|-----------|-----------|-----------------|
| Mackinawite | 0 | 0.49 | 706.0 | 0.46 | 9.07 | Fe(II)-S |
| | | | 706.4 | 0.52 | 13.8 | Fe(II)-S |
| | | | 706.9 | 0.72 | 18.7 | Fe(II)-S |
| | | | 707.7 | 1.02 | 19.8 | Fe(II)-O |
| | | | 708.9 | 1.29 | 15.0 | Fe(III)-S |
| | | | 710.1 | 1.71 | 15.2 | Fe(III)-O |
| | | | 711.9 | 2.44 | 8.23 | Fe(III)-O |
| Mackinawite+As(III) | 1 | 0.63 | 706.2 | 1.43 | 14.3 | Fe(II)-S |
| | | | 707.1 | 1.07 | 16.9 | Fe(II)-O |
| | | | 707.8 | 0.72 | 10.8 | Fe(II)-O |
| | | | 708.4 | 0.67 | 12.8 | Fe(III)-S |
| | | | 709.2 | 1.03 | 17.7 | Fe(III)-S |
| | | | 710.2 | 1.36 | 13.9 | Fe(III)-O |
| | | | 711.7 | 2.08 | 13.3 | Fe(III)-O |
| | 15 | 0.56 | 706.6 | 1.63 | 9.9 | Fe(II)-S |
| | | | 707.5 | 1.05 | 14.1 | Fe(II)-O |
| | | | 708.4 | 1.06 | 14.6 | Fe(III)-S |
| | | | 709.1 | 1.28 | 13.2 | Fe(III)-S |
| | | | 709.8 | 1.53 | 11.1 | Fe(III)-O |
| | | | 710.5 | 2.12 | 15.3 | Fe(III)-O |
| | 30 | 0.75 | 712.6 | 4.35 | 21.6 | Fe(III)-O |
| | | | 706.6 | 1.11 | 8.8 | Fe(II)-S |
| | | | 707.3 | 0.78 | 12.3 | Fe(II)-O |
| | | | 708.0 | 0.84 | 17.4 | Fe(III)-S |
| 708.6 | | | 0.81 | 9.8 | Fe(III)-S | |
| 709.1 | | | 0.98 | 14.0 | Fe(III)-S | |
| 709.8 | | | 1.45 | 17.7 | Fe(III)-O | |
| 711.0 | 2.82 | 19.9 | Fe(III)-O | | | |
| Mackinawite+As(V) | 1 | 0.72 | 706.3 | 0.98 | 7.6 | Fe(II)-S |
| | | | 707.9 | 1.22 | 24.3 | Fe(III)-S |
| | | | 708.4 | 0.44 | 5.6 | Fe(III)-S |
| | | | 709.0 | 0.69 | 16.8 | Fe(III)-S |
| | | | 709.6 | 0.78 | 18.4 | Fe(III)-S |
| | | | 710.4 | 0.93 | 15.6 | Fe(III)-O |
| | | | 711.1 | 1.07 | 11.8 | Fe(III)-O |
| | 15 | 1.03 | 708.4 | 1.19 | 26.4 | Fe(III)-S |
| | | | 709.0 | 0.41 | 6.03 | Fe(III)-S |
| | | | 709.6 | 0.74 | 17.5 | Fe(III)-S |
| | | | 710.3 | 0.87 | 20.6 | Fe(III)-O |
| | | | 711.0 | 0.84 | 18.2 | Fe(III)-O |
| | | | 711.7 | 0.62 | 6.5 | Fe(III)-O |
| | 30 | 0.47 | 712.3 | 0.58 | 4.8 | Fe(III)-O |
| | | | 708.0 | 1.41 | 6.83 | Fe(III)-S |
| | | | 708.8 | 1.45 | 28.6 | Fe(III)-S |
| | | | 709.7 | 1.52 | 20.3 | Fe(III)-S |
| | | | 710.3 | 1.22 | 17.2 | Fe(III)-O |
| | | | 711.1 | 1.03 | 13.7 | Fe(III)-O |
| | | | 712.2 | 0.93 | 6.9 | Fe(III)-O |
| 713.3 | 1.61 | 6.4 | Fe(III)-O | | | |

Table 9.7 Binding energies (BE), peak full width at half maximum (FWHM), peak area percentage for S 2p photoelectron spectra of mackinawite contacted with As(III) and As(V) for various times.

| Sample | Contact time (days) | χ^2 | BE (eV) | FWHM (eV) | Area (%) | Chemical states |
|---------------------|------------------------|----------|---------|-----------|----------|-------------------------------|
| Mackinawite | 0 | 0.46 | 161.4 | 0.63 | 18.1 | S ²⁻ |
| | | | 162.1 | 0.85 | 42.6 | S ²⁻ |
| | | | 163.1 | 1.19 | 39.3 | S _n ²⁻ |
| Mackinawite+As(III) | 1 | 0.78 | 161.3 | 0.54 | 27.7 | S ²⁻ |
| | | | 161.9 | 0.67 | 30.0 | S ²⁻ |
| | | | 162.6 | 0.65 | 22.7 | S ²⁻ |
| | | | 163.1 | 0.69 | 13.2 | S _n ²⁻ |
| | | | 164.1 | 0.44 | 6.40 | S ⁰ |
| | 15 | 0.64 | 161.2 | 0.43 | 9.20 | S ²⁻ |
| | | | 161.9 | 1.34 | 65.0 | S ²⁻ |
| | | | 162.7 | 0.26 | 5.80 | S ²⁻ |
| | | | 163.5 | 0.62 | 10.7 | S _n ²⁻ |
| | 30 | 0.47 | 165.3 | 0.66 | 9.20 | S ⁰ |
| | | | 161.5 | 0.89 | 36.9 | S ²⁻ |
| | | | 162.1 | 0.61 | 12.6 | S ²⁻ |
| | | | 162.7 | 0.20 | 5.70 | S ²⁻ |
| | | | 163.2 | 0.74 | 18.3 | S _n ²⁻ |
| | | | 164.9 | 1.56 | 12.4 | S ⁰ |
| | | | 168.4 | 1.46 | 14.0 | SO ₄ ²⁻ |
| | | | | | | |
| Mackinawite+As(V) | 1 | 0.60 | 161.4 | 0.68 | 36.3 | S ²⁻ |
| | | | 161.7 | 0.21 | 7.30 | S ²⁻ |
| | | | 162.2 | 0.45 | 15.5 | S ²⁻ |
| | | | 162.8 | 0.80 | 35.8 | S ²⁻ |
| | | | 163.8 | 0.50 | 5.20 | S _n ²⁻ |
| | 15 | 0.74 | 161.3 | 0.67 | 37.9 | S ²⁻ |
| | | | 162.0 | 0.63 | 25.6 | S ²⁻ |
| | | | 162.4 | 0.28 | 10.6 | S ²⁻ |
| | | | 163.0 | 0.52 | 16.5 | S _n ²⁻ |
| | 30 | 0.87 | 163.4 | 0.51 | 9.40 | S _n ²⁻ |
| | | | 161.5 | 1.30 | 31.9 | S ²⁻ |
| | | | 161.9 | 0.37 | 7.90 | S ²⁻ |
| | | | 162.4 | 0.74 | 19.9 | S ²⁻ |
| | | | 163.0 | 0.96 | 32.7 | S _n ²⁻ |
| | | | 164.1 | 0.50 | 7.60 | S ⁰ |

Figures 9.18 and 9.19 display O 1s XPS spectra of mackinawite reacted with As(III) and As(V) for various times. All spectra were fitted to three peaks, associated with oxide oxygen (O^{2-}), structural hydroxide (OH^-), and attached water (H_2O) at 529.5~529.8, 530.1~530.9, and 531.1~531.9 eV, respectively. The O 1s spectra of mackinawite reacted with As(III) shows that the peaks for H_2O decrease over time, while the OH^- peak and O^{2-} peak increase (Figure 9.18). The increase of the OH^- peak over time may be due to dissociation of the adsorbed water and combination of protons (H^+) produced by disassociation of H_2O and O^{2-} that was produced by reduction of O_2 by mackinawite when O_2 is present (229, 230). When the Fe(II) surface species are oxidized by O_2 or As(III), the Fe(III) surface species that are formed can develop into Fe(III) oxyhydroxides that include both OH^- and O^{2-} . The growth of Fe(III)-oxyhydroxide surface species coincided with the increase of peaks for OH^- and O^{2-} . For mackinawite reacted with As(V), the O 1s XPS spectra indicate that the peak area for H_2O increases somewhat from day 1 to day 15, but decreases at 30 day by a factor of 6.6 compared to day 15. The peak for OH^- increases gradually over time and the peak for O^{2-} decreases from day 1 to day 15, but increases at 30 day back to a value (18.7 %) that is close to the value observed at day 1 (19.0 %). The O 1s spectra is consistent with the Fe $2p_{3/2}$ spectra of mackinawite with As(V) (Figure 9.15), in that both indicate the reduction of As(V) to As(III) by the surface Fe(II) sites that results in the formation of Fe(III) hydroxide surface species that include both OH^- and O^{2-} .

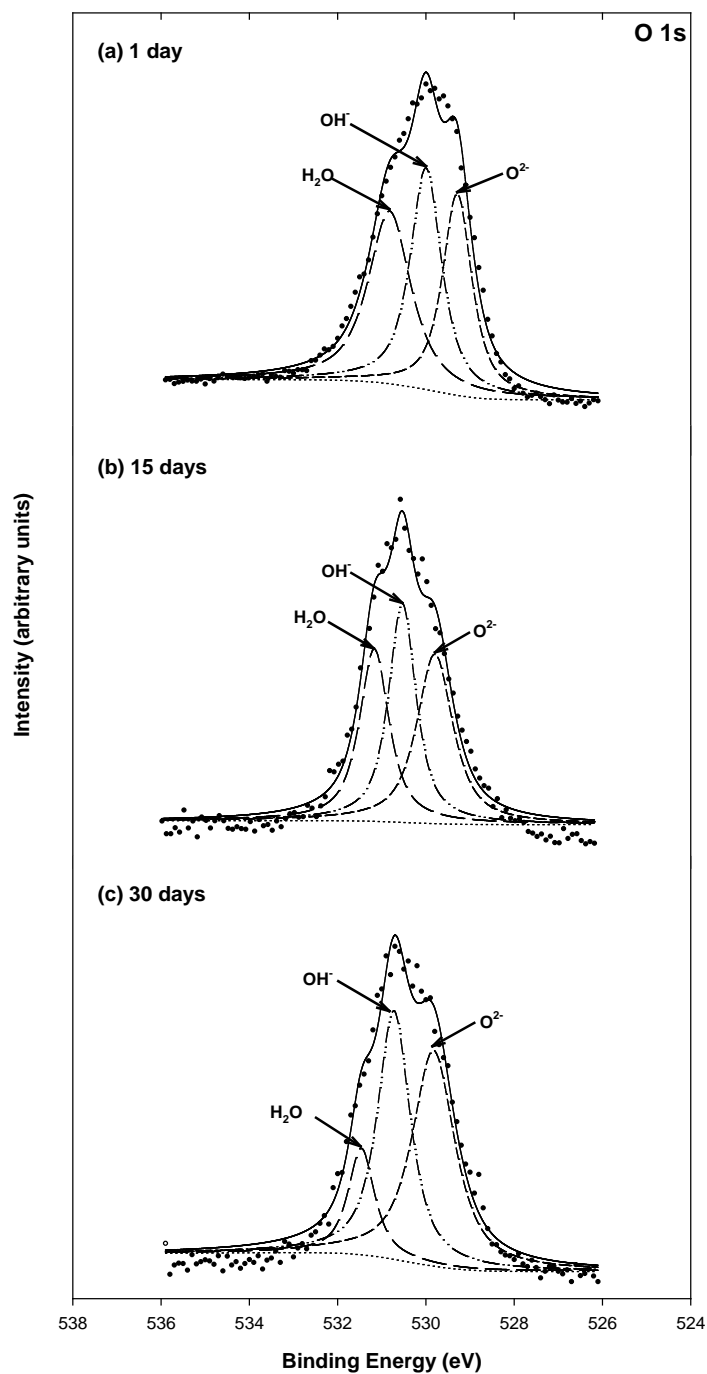


Figure 9.18 High resolution O 1s XPS spectra for pyrite reacted with 3.3 mM As(III) at pH 8 for various times: (a) 1 day, (b) 15 days, (c) 30 days.

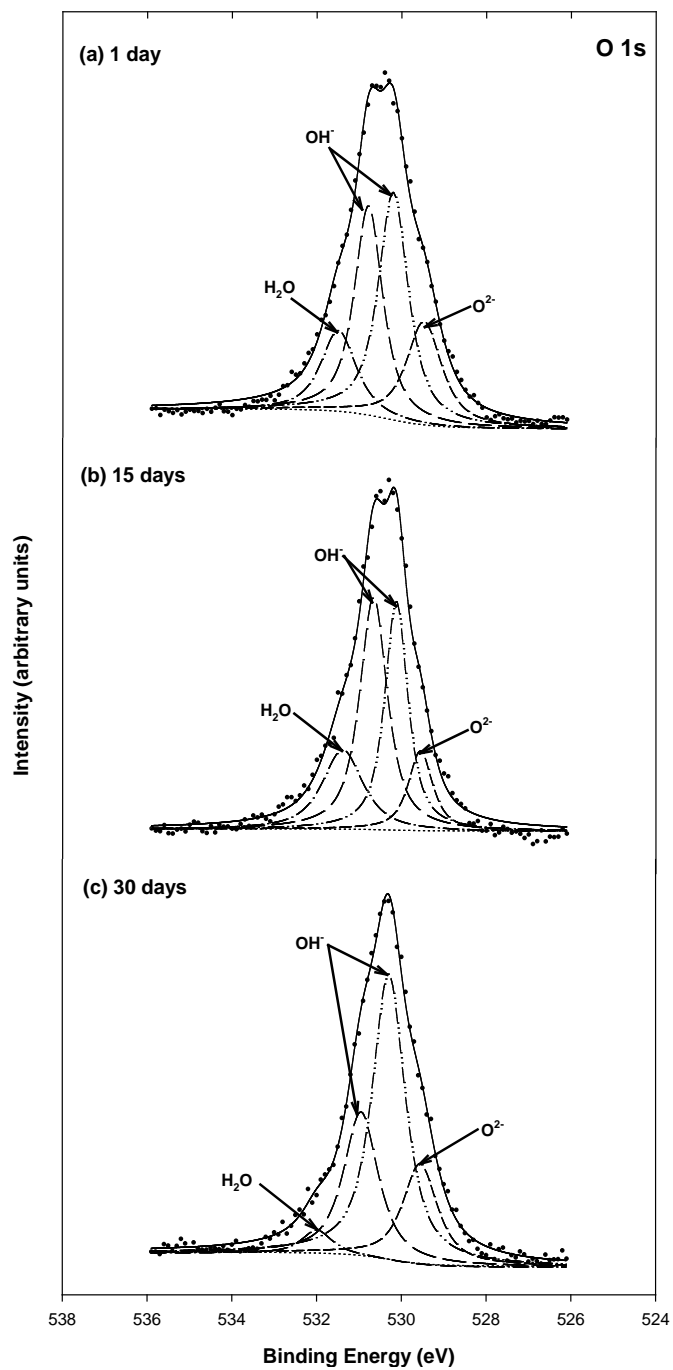


Figure 9.19 High resolution O 1s XPS spectra for pyrite reacted with 3.3 mM As(V) at pH 8 for various times: (a) 1 day, (b) 15 days, (c) 30 days.

Table 9.8 Binding energies (BE), peak fill width at half maximum (FWHM), peak area percentage for O 1s photoelectron spectra of mackinawite contacted with As(III) and As(V) over contact time.

| Sample | Contact time | BE (eV) | FWHM (eV) | Area (%) | Chemical states |
|---------------------|--------------|---------|-----------|----------|------------------|
| Mackinawite | 0 | 529.6 | 0.94 | 21.9 | O ²⁻ |
| | | 531.1 | 1.46 | 47.1 | OH ⁻ |
| | | 532.2 | 1.75 | 31.0 | H ₂ O |
| Mackinawite+As(III) | 1 | 529.8 | 0.85 | 30.6 | O ²⁻ |
| | | 530.5 | 0.88 | 34.3 | OH ⁻ |
| | | 531.3 | 1.17 | 35.1 | H ₂ O |
| | 15 | 529.8 | 0.97 | 35.6 | O ²⁻ |
| | | 530.5 | 0.74 | 34.9 | OH ⁻ |
| | | 531.1 | 0.79 | 29.5 | H ₂ O |
| | 30 | 529.8 | 1.15 | 45.7 | O ²⁻ |
| | | 530.7 | 0.88 | 40.4 | OH ⁻ |
| | | 531.4 | 0.71 | 13.8 | H ₂ O |
| Mackinawite+As(V) | 1 | 529.5 | 0.99 | 19.0 | O ²⁻ |
| | | 530.2 | 0.85 | 35.4 | OH ⁻ |
| | | 530.7 | 0.80 | 30.8 | OH ⁻ |
| | | 531.5 | 0.99 | 14.8 | H ₂ O |
| | 15 | 529.5 | 0.68 | 11.4 | O ²⁻ |
| | | 530.1 | 0.65 | 31.2 | OH ⁻ |
| | | 530.6 | 0.78 | 38.1 | OH ⁻ |
| | | 531.4 | 1.14 | 19.2 | H ₂ O |
| | 30 | 529.5 | 0.98 | 18.7 | O ²⁻ |
| | | 530.3 | 0.93 | 50.8 | OH ⁻ |
| | | 530.9 | 0.97 | 26.7 | OH ⁻ |
| | | 531.9 | 0.86 | 3.90 | H ₂ O |

10. SORPTION OF ARSENIC(III) AND ARSENIC(V) TO PYRITE (FeS₂): KINETICS, EXTENT OF REMOVAL, STABILITY

Experiments on arsenic removal by pyrite showed that removal of As(V) from solution was faster than removal of As(III). This indicates that As(III) and As(V) are interacting differently with the pyrite surface. The extent of removal of both As(III) and As(V) were more accurately described by the Langmuir adsorption model than the Freundlich adsorption model. This supports the hypothesis that all surface sites on pyrite have similar affinities for arsenic species and that there is a maximum removal capacity. Removal of As(III) was observed to increase as pH increased across the range investigated (pH 7 – pH 10). However, an optimum pH in the range between pH 8 and pH 9 was observed for removal of As(V). Sulfate had little effect on removal of As(III) or As(V) at the concentrations investigated (0, 1, 10 mM). There were small decreases in the amount of arsenic removed at the highest concentration of sulfate and the effect was more apparent with As(V) than with As(III). Stability tests for mixtures of As(III) and pyrite showed low removal at low pH, increasing removal as pH was increased and moderate stability, i.e. moderate levels of release as pH was decreased, but the concentrations did not return to levels observed initially in the experiment. Stability of mixtures of As(V) and pyrite showed similar behavior except low removals were observed initially at high pH, removals increased as pH decreased and moderate to high levels of stability were observed as pH was raised back to the initial values.

10.1 Introduction

The most common adsorbent for removing arsenic from water is iron oxy-hydroxide. However, when it is disposed to an anoxic landfill, ferric iron can be reduced to ferrous iron, thereby destroying the solid phase that had been retaining the arsenic compounds, which results

in their release to solution. In addition, ripening of iron oxy-hydroxide solids from high surface area amorphous solid phases to lower surface area crystalline phases could also result in releasing arsenic because arsenic removal is via surface adsorption and not by formation of precipitated arsenic-containing solid phase (43). Furthermore, As(V) can be reduced to As(III), which is less strongly bound to the remaining iron hydroxide sites. Since these residuals are not always stable, some type of treatment should be developed before disposal. Barnett (1992) reported that the behavior of arsenic in engineered systems such as landfills and water distribution systems is probably influenced by many factors operative in natural systems (46). Conceptually, the mobility of arsenic below a landfill would be controlled by the redox condition of the groundwater in a manner analogous to natural waters (44). Arsenic would be expected to be immobile in the oxic zone because of adsorption onto ferric (oxy)hydroxides. However, it could become mobile upon the onset of moderately reducing conditions which would result in reductive dissolution of ferric oxy-hydroxides. It could become immobile again, if more strongly reducing conditions developed and sulfide solid phases were generated. In laboratory leaching tests with concentrated arsenic wastes (concentrations from <1 to 121 g/wet kg), arsenic was most mobile at neutral pH under mildly reducing conditions and least mobile under neutral pH and strongly reducing conditions, possibly the result of sulfide precipitation (26).

Thus, the solubility and mobility of arsenic is significantly increased under reducing conditions found in landfills. White and Sevee (1999) reported that landfills in southern New Hampshire contribute to the mobilization of arsenic by generating soluble total organic carbon, which creates and sustains the reductive dissolution mechanism responsible for the release of arsenic to the groundwater (47). Welch (1999) indicated that synthetic organic compounds can lead to reductive dissolution of iron oxide and arsenic release (48). Laboratory experiments by Ahmann (1997) showed that significant arsenic mobilization from contaminated sediments by

microbial arsenic reduction (45). Moore et al. (1998) reported that total interstitial arsenic in sediments increased from less than 20 mg/kg of soil in the oxidized zone to > 550 mg/kg in the reduced zone, indicative of the dissolution of iron and manganese (oxy)hydroxides (49).

An attractive treatment method for arsenic removal is to apply pyrites (FeS_2) as a reactant/adsorbent. Zouboulis et al. (1993) investigated the application of pyrite as a sorbent for arsenic (34). The pyrite that was used was a byproduct/solid waste from an industrial process and had a median diameter of 11 μM and a specific surface area of 4.7 m^2/g . Removal of As(V) was optimal at pH 3-9, while removal of As(III) was optimal at pH 7-10. Equilibrium was observed to occur within 10 minutes. Using the data presented in that paper, linear partition coefficients can be calculated that are in the range between 100 – 200 L/kg. Farquhar et al. (2002) investigated sorption of arsenic onto ground natural pyrite (size < 32 μm) and FeS (mackinawite) (35). The data presented could be used to calculate linear sorption coefficients of 32 and 41 L/kg for As(III) and As(V), respectively, on pyrite and 1340 and 420 L/kg for As(III) and As(V), respectively, on FeS. Differences in partition coefficients between Farquhar et al. (2002) and Zouboulis et al. (1993) could be due to differences in pyrite size (34). Others have reported successful removal of arsenic by adsorption/reaction with FeS (36, 37). Pyrite (FeS_2) is a naturally occurring mineral that often contains impurities such as arsenic(38). The fact that these minerals have existed for geologic time periods attests to their stability.

The objectives of this study are 1) to investigate the surface reactions between As(III)/As(V) and pyrite as a function of contact time and 2) to determine the stability of As(III)/As(V)-contacted pyrites as pH is changed. This motivated by need to better understand arsenic immobilization in order to prevent its release to the environment under reducing conditions. Thus, this study can be expected to contribute to the design of stabilization processes for residuals from treatment systems that remove arsenic from water.

10.2 Materials and Method

10.2.1 Sorption/Reaction Experiments

Kinetic experiments for removal of As(III) or As(V) were performed at pH 8 in 20-mL reaction vessels. To start a kinetic test, the pyrite slurry and arsenic stock solution were added to the reaction vessels to reach concentrations of 1 g/L pyrite and 13.3 μ M As. Acid (0.5 M HCl) or base (0.5 M NaOH) were added to adjust the pH. The reaction vessels were mixed by an end-over-end rotary mixer until specified sampling time (10, 30, 60, 120, 180, 240, 420, 660, 1000, 1440 minutes). Approximately ten milliliters of suspension were sampled and filtered using 0.02- μ m anodisc membrane filters. All samples were stored until AAS analysis in an anaerobic chamber, in order to avoid arsenic oxidation and pH change.

Removal tests at pH 7, 8, 9, and 10 were conducted to evaluate the ability of pyrite to remove As(III) and As(V). A suspension of pyrite was mixed with a sufficient amount of 2000-mg/L arsenic stock solution to provide the desired initial arsenic concentration and a pyrite concentration of 1 g/L. The desired pH was adjusted using 0.5 M HCl or 0.5 M NaOH. The procedures of mixing and filtration followed the methods used in the kinetic experiments. Experiments to determine the effect of sulfate on arsenic removal were conducted similarly at pH 8 and at three sulfate concentrations (0, 1, 10 mM). In order to describe nonlinear removal patterns, two adsorption models (Langmuir and Freundlich) were applied to the experimental data. The Langmuir model, is shown in Equation 11.1.

$$q = \frac{q_{\max} bC}{1 + bC} \quad (10.1)$$

where q is the concentration of arsenic on the solid (μ mol/g), q_{\max} is maximum concentration of arsenic on the solid (i.e., maximum sorption capacity, μ mol/g), b is the Langmuir parameter (L/ μ mol). The Freundlich model is shown in Equation 10.2.

$$q = k_f C^{1/n} \quad (10.2)$$

where k_f ($\mu\text{mol}^{1-1/n} \cdot \text{L}^{1/n}/\text{g}$) and n are parameters in the Freundlich model. Coefficients in the Langmuir and Freundlich equations were determined by non-linear least-squares regression using MATLAB[®] with its embedded function “nlinfit”

10.2.2 Stability of As-Contacted Pyrites

To investigate the stability of As(III) and As(V) sorbed on pyrite, the experimental method described by Bostick and Fendorf (2003) was followed (39). This method measures the effect of pH on stability of solid-phase As(III) and As(V) by decreasing and increasing pH with 1 or 2 M solutions of HCl or NaOH. A 1-g/L pyrite suspension was adjusted to about pH 4 for As(III) and to about pH 10 for As(V). Then, the target compound (As(III) or As(V)) was added to achieve an arsenic concentration of 15.2 μM in the aqueous phase. Then, pH was adjusted to series of different values and the system was allowed to react for 30 minutes at each pH before sampling. Samples will be identified with the following nomenclature to simplify the discussion. For As(III), “pH 4_(i)” will stand for the initial sample at pH 4 and the sample at pH 10 after base titration pH will be named the “pH 10_(a.b.t)” sample. For As(V), the initial sample at pH 10 and the sample at pH 4 after acid titration will be named “pH 10_(i)” and “pH 4_(a.a.t)”. The sample at pH 7 after base titration that had previously been in contact with a solution at pH 4 will be named “pH 7_(a.b.t)”. While being sampling, the suspensions were filtered using 0.02- μm anodisc membrane filters. This procedure was repeated until the pH reached the highest or lowest point desired. The filtered samples were stored before AAS analysis in an anaerobic chamber to prevent any change in the oxidation state of arsenic. The chamber contained an atmosphere of 5% H_2 and 95% N_2 .

10.2.3 Measurements

The technique for arsenic analysis was based on Standard Method 3114C, which is a continuous hydride generation/atomic absorption spectrometer (HGAAS) method (264). It was modified to be conducted with a model Solar M6 atomic absorption spectrometer with model V90 continuous hydride generator manufactured by Thermo Elemental. It was also modified to speciate arsenic between As(III) and total arsenic (As(III) + As(V)) based on the relative reactivities of As(III) and As(V) with borohydride at different pH (191). At low pH, both As(III) and As(V) can be reduced by sodium borohydride to arsine gas. However, at moderate pH, only As(III) is reduced. Therefore, As(III) was measured by mixing a sample flow of 7 mL/min with an equal flow of phosphate buffer (0.2 M NaH_2HPO_4) and a 3.5 mL/min flow of sodium borohydride. The arsine gas was removed from the solution by purging with a 250 mL/min flow of argon and it was transferred to the flame AA where its concentration was determined by comparison with standard responses. Total arsenic was determined by a similar procedure, but the buffer flow was replaced with a flow of strong acid (5 M HCl). The concentration of As(V) was determined as the difference between the total arsenic concentration and the As(III) concentration.

10.3 Results and Discussion

10.3.1 Kinetics

Figure 10.1 shows the results of kinetic experiments on removal of As(III) and As(V) by pyrite at pH 8. The rates of As(III) and As(V) uptake were different with As(V) being nearly completely removed within 30 minutes, while 95 % of As(III) was removed after 180 minutes. However, after 600 minutes, As(III) was nearly completely removed. In order to evaluate kinetic effects (how rapidly q increased) separately from equilibrium effects (how high q would become

after a sufficiently long time), a general kinetic model for sorption was used. Equation 10.3 combines the rate equation for this model with the material balance for a batch reactor.

$$\frac{dq}{dt} = k(q_{max} - q) \quad (10.3)$$

where q ($\mu\text{mol/g}$) is the amount sorbed, t (min) is time, q_{max} is the maximum value of q that would occur if a sufficiently long react time were allowed, and k (min^{-1}) is the rate constant for sorption. However, true chemical equilibrium was not achieved during these experiments, because surface reactions between target contaminants and the pyrite surface were probably continuing to occur throughout the removal experiments. Equation 10.3 can be modified to describe experimental data in which two different removal process appear to occur at different rates. Equations 10.4 and 10.5 describe the biphasic model that was introduced in Section 3.

$$\frac{dq_f}{dt} = k_f(q_{f,max} - q_f) \quad (10.4)$$

$$\frac{dq_s}{dt} = k_s(q_{s,max} - q_s) \quad (10.5)$$

where q_f , q_s , k_f , k_s , $q_{f,max}$, $q_{s,max}$ are concentrations of adsorbate on the solid, removal rate coefficients, maximum concentration on the solid for fast-reacting sites and for slow-reacting sites, respectively. All coefficients were obtained by nonlinear regression using MATLAB[®] with its embedded functions “nlinfit and ode23s”. The structure of models with fast and slow processes that are described by similar equations and coefficients would make it difficult for a normal regression routine to determine both sets of coefficients at the same time. Therefore, a sequential approach was used in which coefficients for the “slow” process were obtained and then they were used in another regression to determine values for “fast” coefficients. This process continued until a satisfactory fit was obtained.

Table 10.1 shows the parameters of the kinetic model for As(III) and As(V) sorption on

pyrite at pH 8 that were obtained by nonlinear regression. The kinetic model provides good fits to experimental data as shown by the low values of the goodness of fit parameter (GFP). The sorption rate constants (k_f) for fast-reacting sites were higher for As(III) than for As(V), but they have very large confidence limits, which are often larger than the value of parameter. This is caused by the fact that there are few data points during the early stages of the reaction, where the fast-reacting sites would be filled, so it is very difficult to determine the exact value of the coefficients. The rate constant (k_s) for slow-reacting sites for As(III) was lower than for As(V) by a factor of 13.5. This difference is due to differences in rates of reaction with the surface.

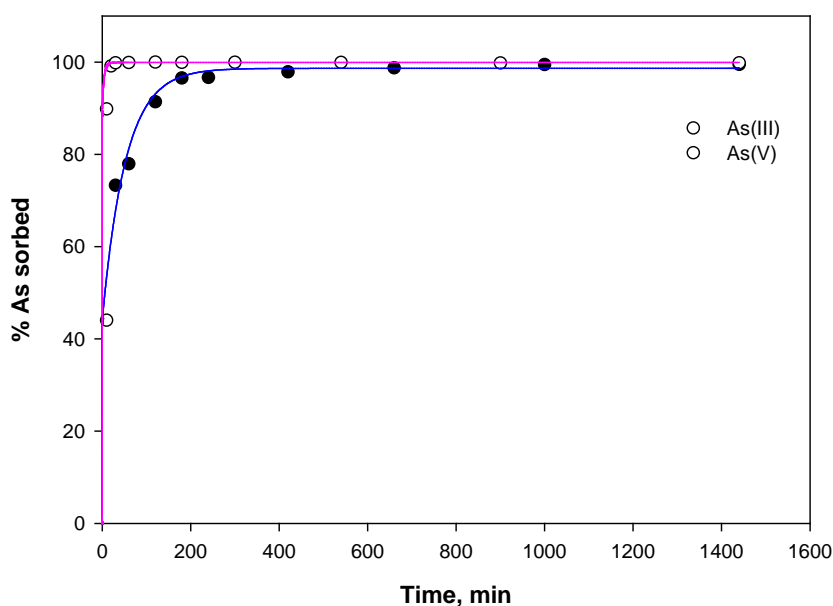


Figure 10.1 Removal of As(III) and As(V) by pyrite as a function of time at pH 8. Initial concentrations of As(III) and As(V) were 13.6 and 20.9 μM , respectively.

Table 10.1 Calculated parameters of the sorption kinetic model for As(III) and As(V) uptake by pyrite at pH 8.

| Arsenic species | <u>Parameters</u> | | | | |
|-----------------|------------------------|------------------------|------------------------|------------------------|------|
| | $k_f(\text{min}^{-1})$ | $k_s(\text{min}^{-1})$ | $q_f(\mu\text{mol/g})$ | $q_s(\mu\text{mol/g})$ | *GFP |
| As(III) | 145 ± 80.4 | 0.02 ± 0.03 | 6.0 ± 1.7 | 7.4 ± 2.2 | 0.05 |
| As(V) | 120 ± 461 | 0.27 ± 7.9 | 18 ± 5.7 | 2.9 ± 5.5 | 0.03 |

* Goodness of fit parameter (GFP) = $\sqrt{SSR / (n - 2)} / \bar{q}$ where SSR is sum of squared residual, n is the number of data points, \bar{q} is average value of the concentration of As on pyrite

10.3.2 Nonlinear Removal Patterns

10.3.2.1 Effect of pH

Figures 10.2 and 10.3 show the results of experiments using pyrite at four different pH values to remove As(III) or As(V), respectively. The symbols represent the measured data and the lines represent the Langmuir (Figures 10.2(a) and 10.3(a)) and Freundlich (Figures 10.2(b) and 10.3(b)) models fitted to the data. Tables 10.2 and 10.3 show the parameters of the Langmuir and Freundlich models obtained by non-linear regression. This procedure chooses parameters to minimize the goodness of fit parameters (GFP) and this parameter can be used to compare how well each model fits the data. The Langmuir model generally provided the best fit to the data for As(III) removal, as indicated by it having the lowest GFP for three out of four data sets (Table 10.2). Maximum sorption capacities (q_{max}) and Langmuir parameters (b) generally increased with higher pH. This result was in good agreement with those reported by Bostick et al. (39). The Langmuir model was generally better able to fit the data for As(V) removal, with a lower GFP for three of the four data sets (Table 10.3). The maximum adsorption capacity (q_{max}) tended toward a maximum around pH 8 to pH 9. There was no evidence of a relationship like a BET model, which would indicate the existence of surface reactions such as surface precipitation. However, these experiments were conducted with only 24 hours of contact time. If longer contact time were allowed, BET-like behavior might occur.

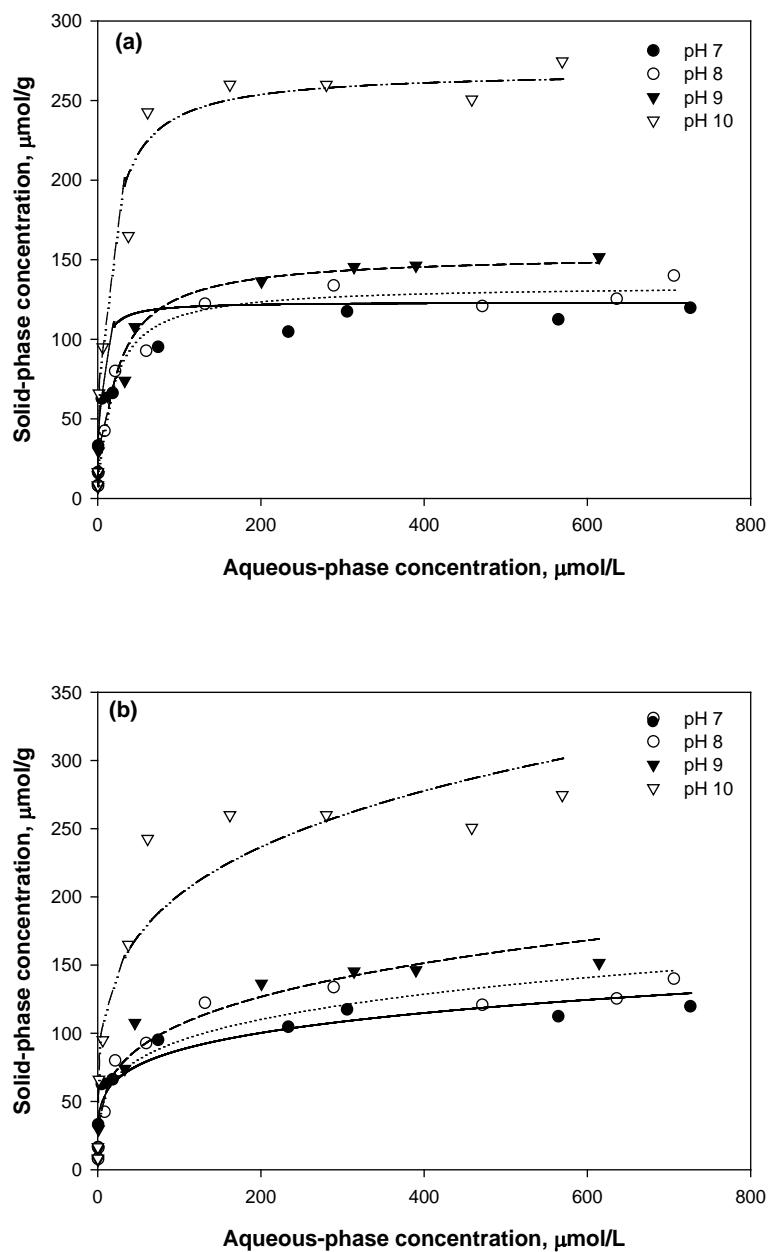


Figure 10.2 Measured concentrations of As(III) on pyrite (symbols) as function of concentration in water with (a) Langmuir and (b) Freundlich models (lines) fitted to data at various pH.

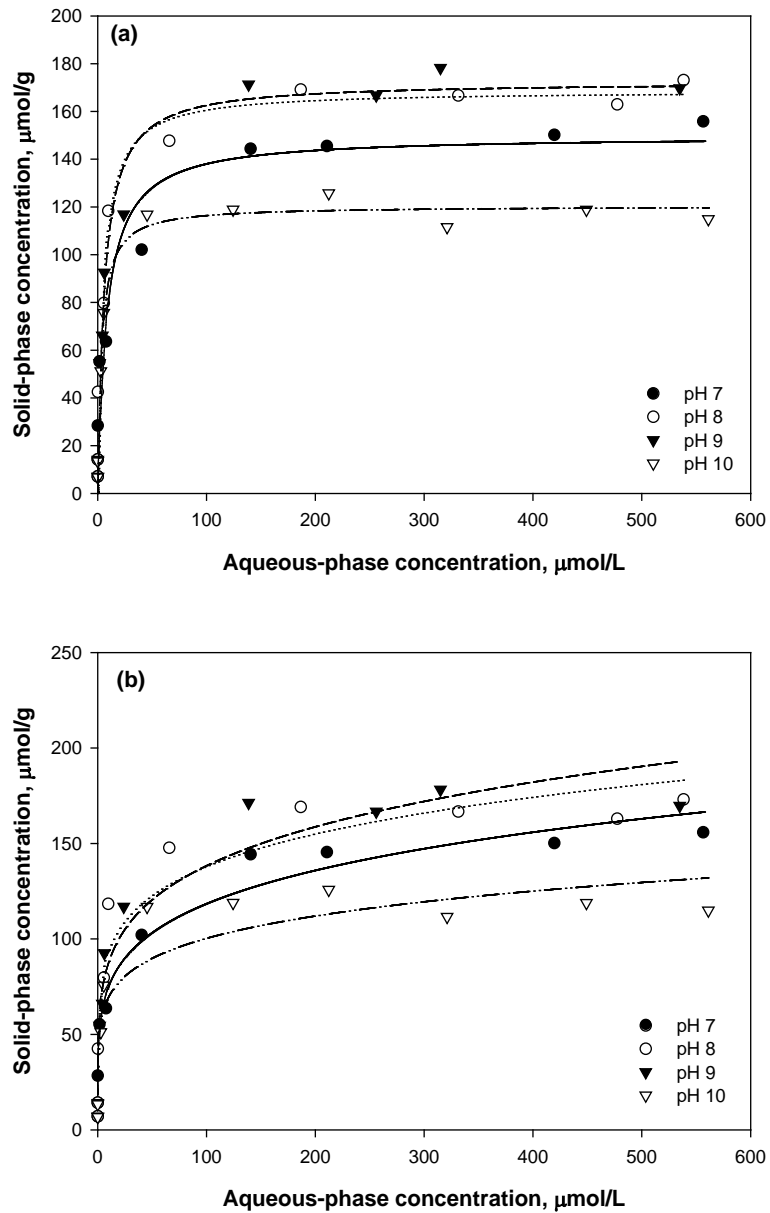


Figure 10.3 Measured concentrations of As(V) on pyrite (symbols) as function of concentration in water with Langmuir model (lines) fitted to data at various pH.

Table 10.2 As(III) adsorption model parameters.

| pH | <i>Langmuir</i> | | | <i>Freundlich</i> | | |
|----|---------------------|------------------------------------|------|--|-----------|------|
| | b (L/ μ mol) | q _{max} (μ mol/g) | GFP | K _f (μ mol ^{1-1/n} ·L ^{1/n} /g) | n | GFP |
| 7 | 0.24 ± 0.22 | 107 ± 13.7 | 0.17 | 36.3 ± 12.0 | 5.2 ± 1.6 | 0.16 |
| 8 | 0.059 ± 0.026 | 133 ± 9.9 | 0.09 | 32.9 ± 17.1 | 4.4 ± 1.7 | 0.19 |
| 9 | 0.046 ± 0.026 | 153 ± 17.3 | 0.13 | 31.8 ± 12.5 | 3.9 ± 1.1 | 0.15 |
| 10 | 0.084 ± 0.056 | 268 ± 27.4 | 0.12 | 68.5 ± 35.4 | 4.3 ± 1.8 | 0.22 |

Table 10.3 As(V) adsorption model parameters.

| pH | <i>Langmuir</i> | | | <i>Freundlich</i> | | |
|----|---------------------|------------------------------------|------|--|-----------|------|
| | b (L/ μ mol) | q _{max} (μ mol/g) | GFP | K _f (μ mol ^{1-1/n} ·L ^{1/n} /g) | n | GFP |
| 7 | 0.12 ± 0.11 | 149 ± 22.5 | 0.21 | 47.4 ± 10.6 | 5.0 ± 1.0 | 0.11 |
| 8 | 0.20 ± 0.14 | 168 ± 17.7 | 0.14 | 63.6 ± 19.1 | 5.9 ± 1.9 | 0.16 |
| 9 | 0.16 ± 0.07 | 172 ± 14.1 | 0.11 | 55.6 ± 16.3 | 5.0 ± 1.4 | 0.15 |
| 10 | 0.29 ± 0.11 | 120 ± 6.56 | 0.07 | 48.5 ± 20.2 | 6.3 ± 3.1 | 0.21 |

10.3.2.2 Effect of Sulfate Concentration

Figures 10.4 and 10.5 show results of experiments to determine the effect of a competing ion (sulfate) on removal by pyrite of As(III) or As(V), respectively. Tables 10.4 and 10.5 present values of model parameters fitted to the data. The Langmuir model provided a much better fit to experimental data than the Freundlich model as shown by lower values of GFP for all data sets. Sulfate at 1 mM concentration had a negligible effect on removal of As(III) or As(V) by pyrite and it had a small effect at 10 mM with the effect being more apparent with As(V) than with As(III).

Table 10.4 As(III) adsorption model parameters as affected by sulfate.

| SO ₄ ²⁻ (mM) | <i>Langmuir</i> | | | <i>Freundlich</i> | | |
|---------------------------------------|---------------------|------------------------------------|------|--|-----------|------|
| | b (L/ μ mol) | q _{max} (μ mol/g) | GFP | K _f (μ mol ^{1-1/n} ·L ^{1/n} /g) | n | GFP |
| 0 | 0.059 ± 0.026 | 133 ± 9.9 | 0.09 | 32.9 ± 17.1 | 4.4 ± 1.7 | 0.19 |
| 1 | 0.067 ± 0.022 | 133 ± 9.3 | 0.08 | 26.9 ± 12.4 | 3.6 ± 1.1 | 0.18 |
| 10 | 0.038 ± 0.014 | 129 ± 9.2 | 0.07 | 24.9 ± 14.3 | 3.6 ± 1.4 | 0.15 |

Table 10.5 As(V) adsorption model parameters as affected by sulfate.

| SO ₄ ²⁻ (mM) | <i>Langmuir</i> | | | <i>Freundlich</i> | | |
|---------------------------------------|---------------------|------------------------------------|------|--|-----------|------|
| | b (L/ μ mol) | q _{max} (μ mol/g) | GFP | K _f (μ mol ^{1-1/n} ·L ^{1/n} /g) | n | GFP |
| 0 | 0.20 ± 0.14 | 168 ± 17.7 | 0.14 | 63.6 ± 19.1 | 5.9 ± 1.9 | 0.16 |
| 1 | 0.19 ± 0.13 | 160 ± 15.7 | 0.13 | 61.3 ± 17.2 | 6.1 ± 1.9 | 0.16 |
| 10 | 0.30 ± 0.12 | 146 ± 6.20 | 0.06 | 48.8 ± 20.4 | 5.3 ± 2.0 | 0.15 |

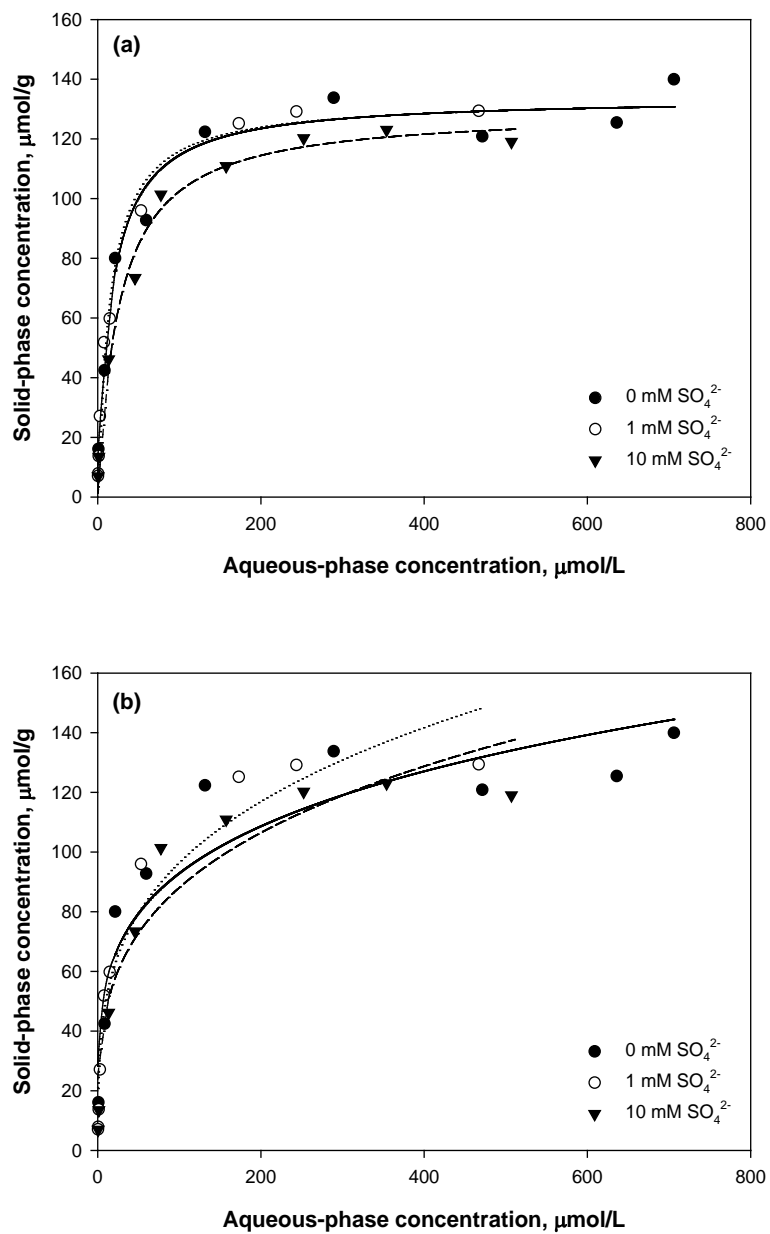


Figure 10.4 Measured concentrations of As(III) on pyrite (symbols) as function of concentration in water in water with (a) Langmuir and (b) Freundlich models (lines) fitted to data at various concentrations of sulfate.

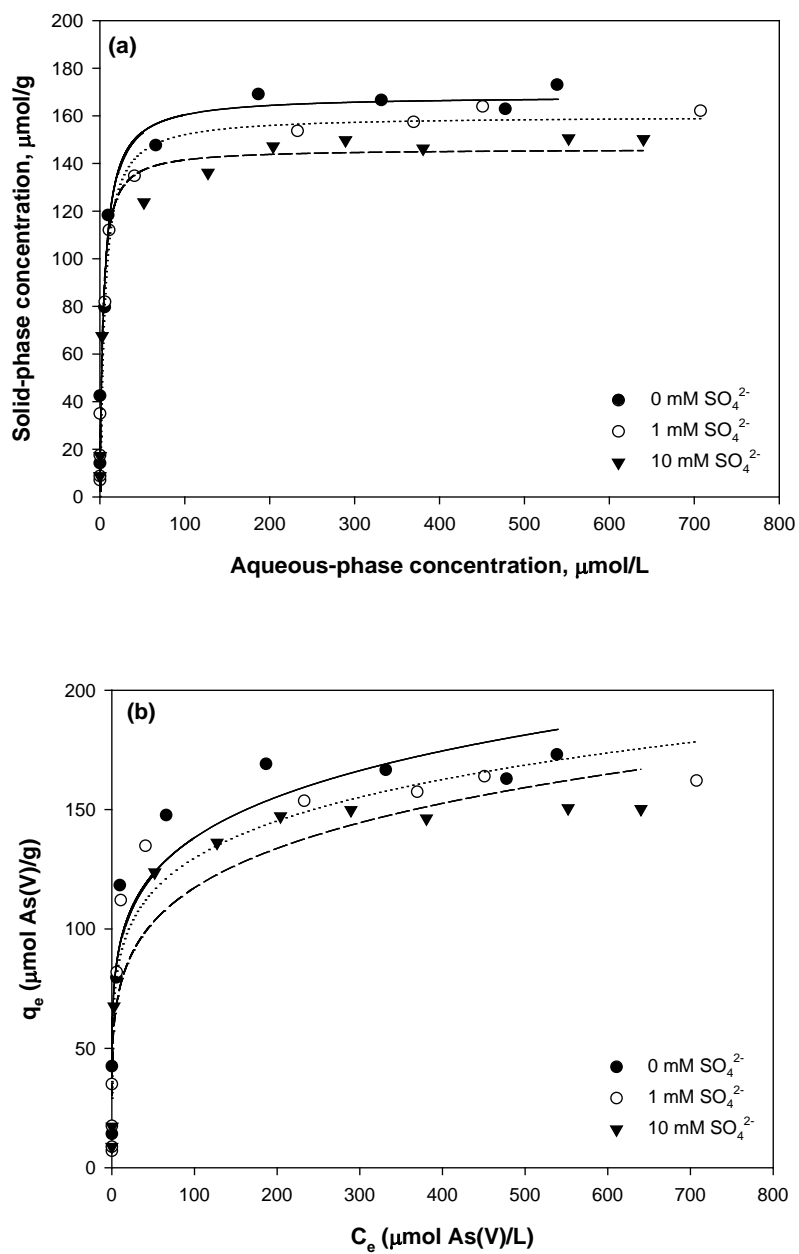


Figure 10.5 Measured concentration of As(V) on pyrite (symbols) as function of concentration in water with (a) Langmuir and (b) Freundlich models (lines) fitted to data at various concentrations of sulfate.

10.3.3 Stability of As-Contacted Pyrites

10.3.3.1 As(III)-Contacted Pyrite

Figure 10.6 shows that as pH is raised from pH 4, sorption of As(III) increases with a steep sorption edge in the pH range between 6 and 8. At high pH, nearly 100% removal of As(III) is achieved, while at acidic pH values (pH 4 – pH 6) only 20% removal is observed. Hysteresis was observed, which indicates that strong bonds are formed between As(III) and the pyrite surface at high pH that are not easily broken when pH is reduced. Therefore, stabilization of As(III) sorbed on pyrite could be expected at high pH. These results are well in agreement with those studied by Bostick et al. (2003) (39).

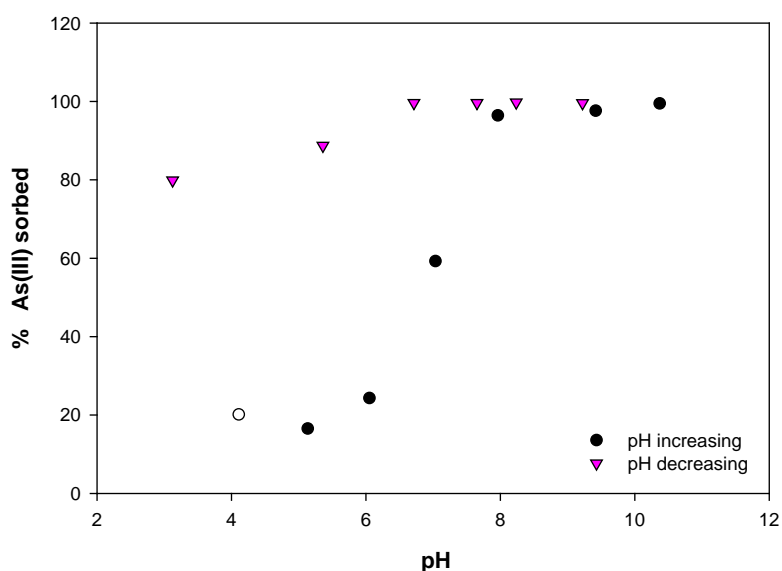


Figure 10.6 Effect of pH on removal of As(III) (15.2 μM) by pyrite (1 g/L) as pH was increased from pH 4 to pH 10 and subsequently was decreased.

Figure 10.7 shows SEM images of pyrites reacted with As(III) at initial pH 4 (pH 4_(i)) and pH 10 after base titration (pH 10_(a,b,t)). As compared to pyrite after synthesis, particles of pyrite at pH 4 are relatively intact, but at pH 10 large parts of the particles appear to be broken,

possibly due to oxidative dissolution that can occur at basic pH. However, the EDS results indicate that there are little differences in elemental composition.

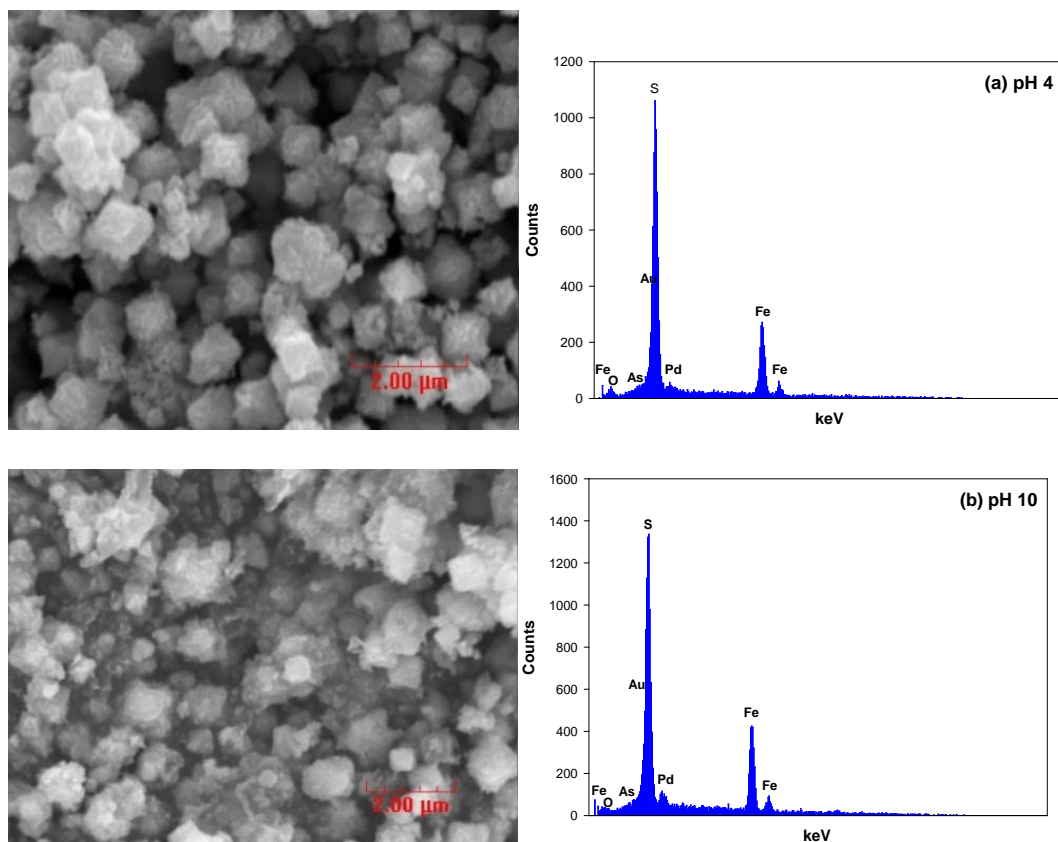


Figure 10.7 Secondary SEM images and EDS results for pyrite after contact with 15.2 μM As(III) at (a) pH 4_(i) and (b) pH 10_(a,b,t).

Oxidation states of As(III) on pyrite as well as the surface Fe and S species were evaluated by a XPS study. Figure 10.8 shows the As 3d XPS spectra of pH 4_(i) and pH 10_(a,b,t). The initial As(III) concentration (15.2 μM) was low, so the XPS spectra included only small peaks associated with As(III) near 44.4 eV for both pH samples. Peaks associated with Fe species also appear in Figure 10.8 near 52~55 eV and they are much higher than the peaks associated with As due to the much larger concentration of Fe on the surface compared to As.

There is no significant change in Fe 2p_{3/2} (Figure 10.9) and S 2p spectra (Figure 10.10), compared to pure pyrite contacted at same pH (Section 6). Samples before and after contact with As(III) showed more oxidation at pH 10 than at pH 4. However, results of experiments to measure stability (Figure 10.6), indicated that strong bonds between As(III) and the pyrite surface could be expected to form at high pH. However, there is no clear evidence of the surface reactions leading to formation of surface precipitates. As shown in Figure 10.11, the peaks for H₂O and O²⁻ in the O 1s XPS spectra increased as pH increased from 4 and 10, while the relative OH⁻ peak decreased. Table 10.6 summarizes all fitting parameters of the Fe 2p, S 2p, O 1s spectra for pH 4_(i) and pH 10_(a,b,t). The data presented includes binding energy (eV), full width at half maximum (FWHM), and relative area (%) for various peaks.

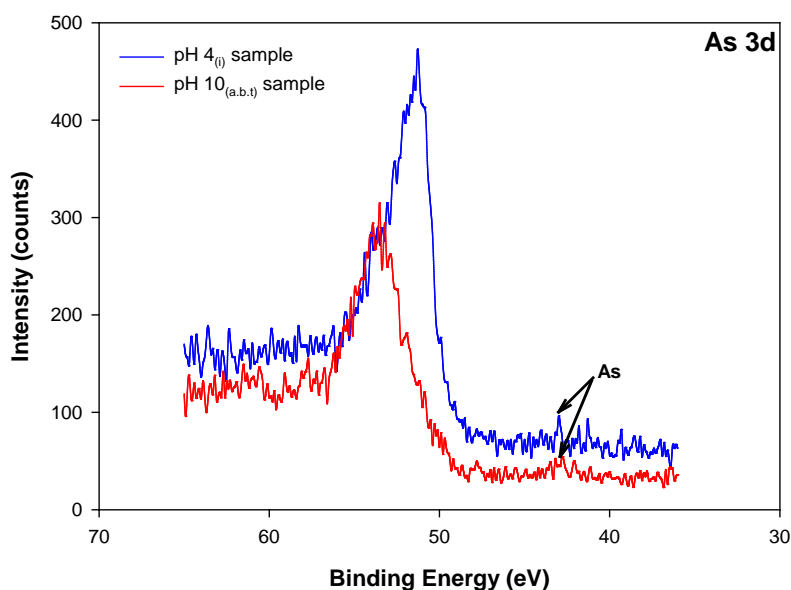


Figure 10.8 High resolution As 3d XPS spectra for pyrite after contact with As(III) (15.2 μM) at (a) pH 4_(i) and (b) pH 10_(a,b,t).

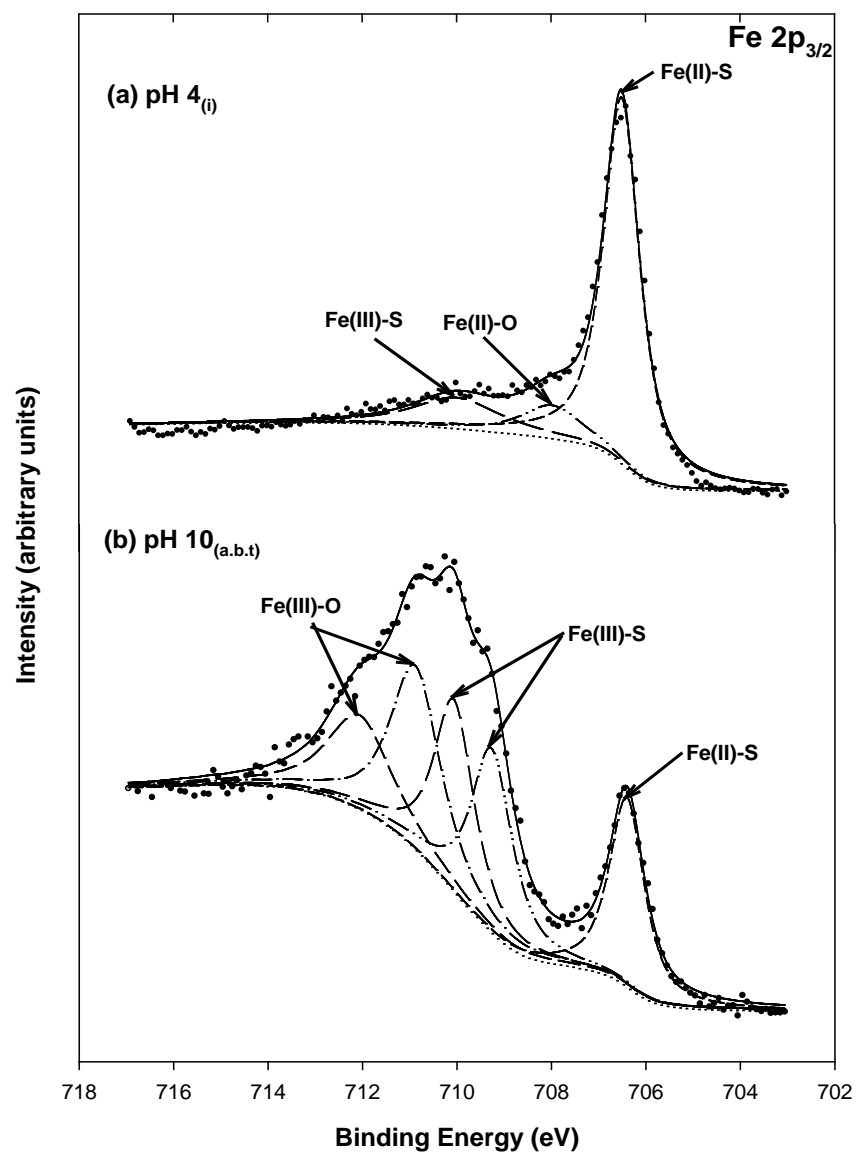


Figure 10.9 High resolution Fe 2p_{3/2} XPS spectra for pyrite after contact with As(III) (15.2 μM) at (a) pH 4_(i) and (b) pH 10_(a,b,t).

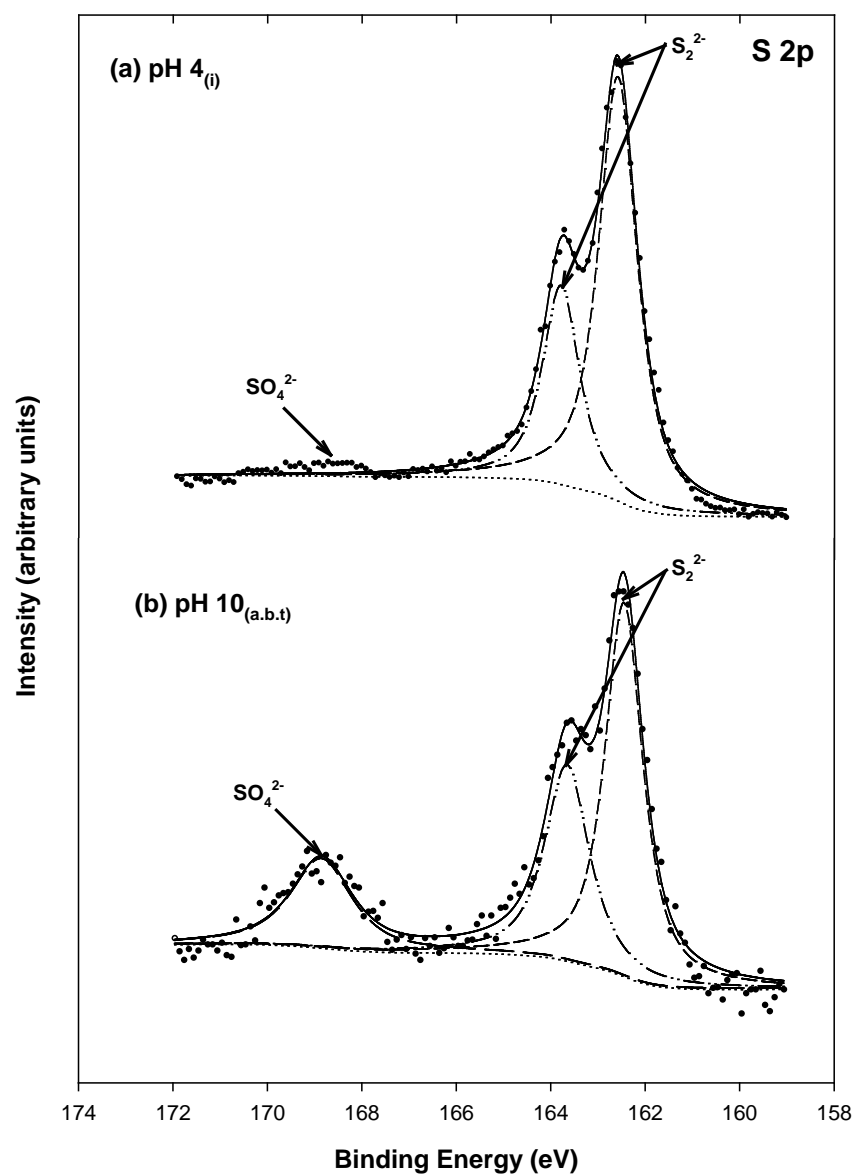


Figure 10.10 High resolution S 2p XPS spectra for pyrite after contact with As(III) (15.2 μM) at (a) pH 4_(i) and (b) pH 10_(a.b.t).

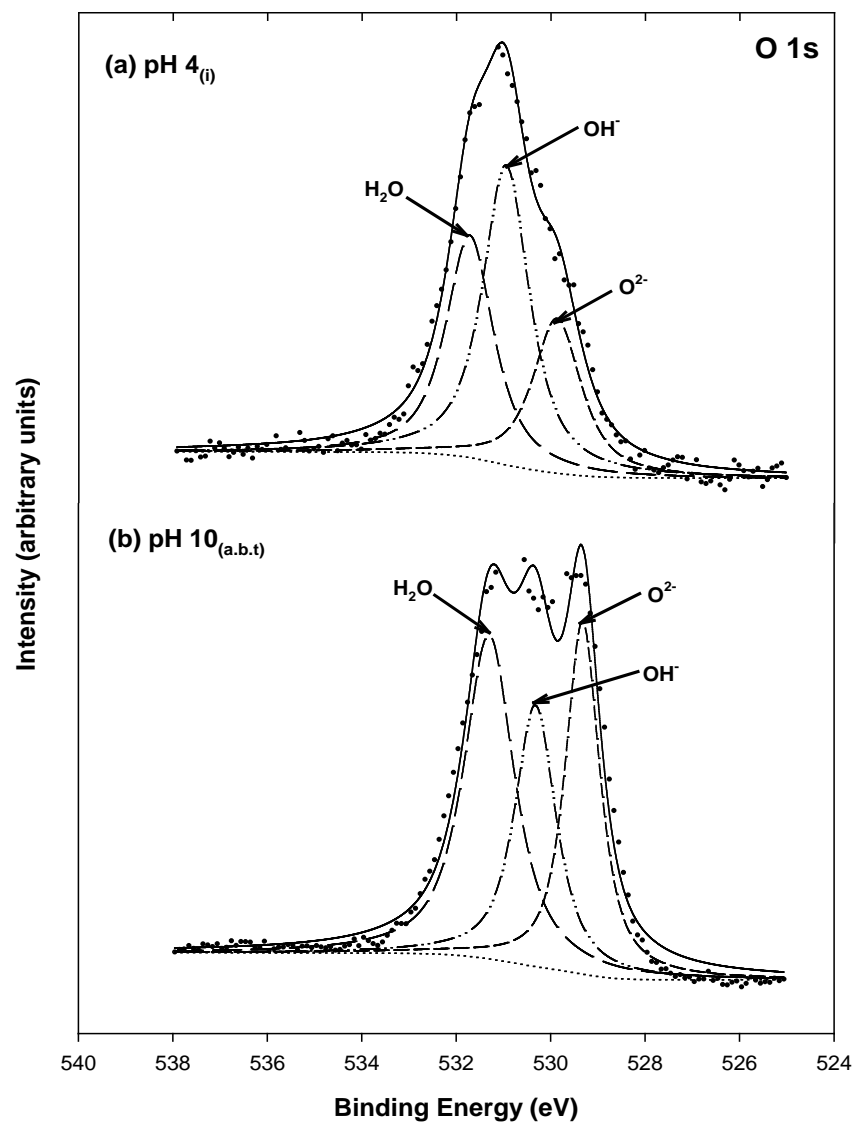


Figure 10.11 High resolution O 1s XPS spectra for pyrite after contact with As(III) (15.2 μM) at (a) pH 4_(i) and (b) pH 10_(a,b,t).

Table 10.6 Binding energies (BE), full width at half maximum (FWHM), and area percentage for peaks in the Fe 2p_{3/2}, S 2p, and O 1s XPS spectra of pyrite after contact with As(III) (15.2 μM) at pH 4_(i) and pH 10_(a,b,t).

| Samples | BE (eV) | FWHM (eV) | Area (%) | Chemical states |
|----------------------------|---------|-----------|----------|-------------------------------|
| Fe 2p_{3/2} | | | | |
| pH 4 _(i) | 706.5 | 0.91 | 74.4 | Fe(II)-S |
| | 707.9 | 1.53 | 11.1 | Fe(II)-O |
| | 710.0 | 2.16 | 14.5 | Fe(III)-S |
| pH 10 _(a,b,t) | 706.4 | 0.89 | 17.9 | Fe(II)-S |
| | 709.3 | 1.05 | 20.5 | Fe(III)-S |
| | 710.1 | 1.01 | 20.7 | Fe(III)-O |
| | 710.9 | 1.28 | 24.9 | Fe(III)-O |
| | 712.1 | 1.60 | 15.9 | Fe(III)-O |
| S 2p | | | | |
| pH 4 _(i) | 162.6 | 0.98 | 68.9 | S ₂ ²⁻ |
| | 163.8 | 0.94 | 31.1 | S ₂ ²⁻ |
| pH 10 _(a,b,t) | 162.4 | 0.96 | 50.2 | S ₂ ²⁻ |
| | 163.6 | 1.12 | 30.6 | S ₂ ²⁻ |
| | 168.8 | 1.54 | 19.1 | SO ₄ ²⁻ |
| O 1s | | | | |
| pH 4 _(i) | 529.8 | 1.23 | 23.3 | O ²⁻ |
| | 530.9 | 1.19 | 45.3 | OH ⁻ |
| | 531.7 | 1.19 | 31.4 | H ₂ O |
| pH 10 _(a,b,t) | 529.3 | 0.87 | 30.9 | O ²⁻ |
| | 530.3 | 1.05 | 27.7 | OH ⁻ |
| | 531.3 | 1.27 | 41.4 | H ₂ O |

10.3.3.2 As(V)-Contacted Pyrite

In order to investigate the stability of As(V) sorbed on pyrite, a 1-g/L suspension of pyrite containing 15.2 μM As(V) was adjusted to approximately pH 10 and then the pH was adjusted down and then back up. Results of arsenic analyses at each step of the experiment are shown in Figure 10.12. Near pH 10, removal of As(V) was the lowest observed (30%), but as pH decreased, removals gradually increased. However, a small decrease in removal was observed near pH 4. The trends of the As(V) removal curves were similar to those observed for As(V) on iron (hydr)oxides or pyrite (34, 217). As pH increased to near pH 10, some As(V) was released, but the amount retained on the pyrite was much greater than the amount removed initially at pH 10. The hysteresis in these curves indicates that strong bonds are formed between As(V) and the pyrite surface at lower pH and that they are not easily reversed when pH is raised. The formation of these strong bond is responsible for the stability of As(V)-contacted pyrite.

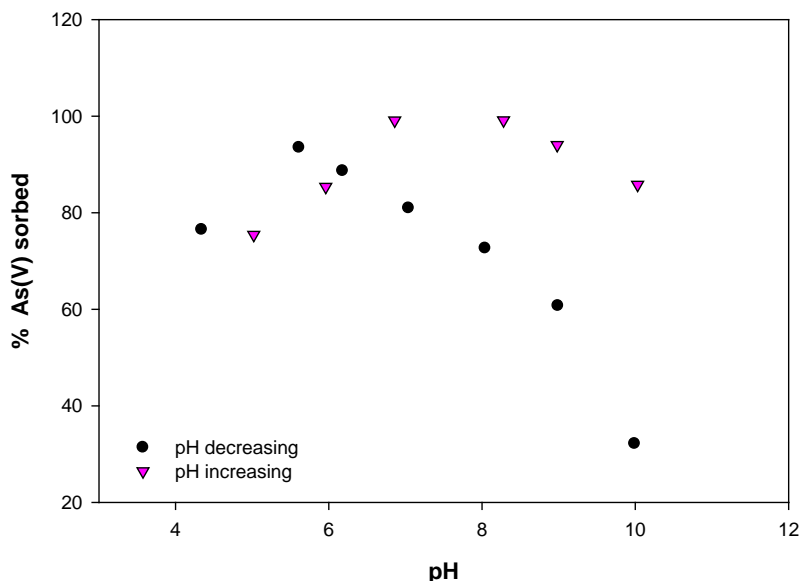


Figure 10.12 Effect of pH on removal of As(V) (15.2 μM) by pyrite (1 g/L) as pH was decreased from pH 10 and subsequently was increased.

To determine more detailed information on surface reaction mechanisms, XPS and SEM-EDS analyses were performed. Figure 10.13 shows SEM images of pyrites reacted with As(V) at pH 10 (pH 10_(i)), at pH 4 (pH 4_(a.a.t)) after pH was decreased from pH 10, and at pH 7 (pH 7_(a.b.t)) after pH had been decreased to pH 4 and then raised to pH 7. Changes in the pyrite surface on the pH 10_(i) sample were observed. Irregularly shaped particles of pyrite were observed, presumably due to oxidative dissolution at high pH. However, the pH 4_(a.a.t) sample had particles that were typically shaped, in spite of the fact that the sample was initially at pH 10. This might be caused by low pH that dissolved irregularly shaped particles. A similar observation was made for pyrites reacted with Se(IV) at pH 10 and 4 (Section 6). As pH was raised back to basic pH, however, the pH 7_(a.b.t) sample begins to present the fractured pyrite. The EDS analysis did not show any difference in elemental composition for As(V)-contacted pyrites at pH 10, 4, and 7.

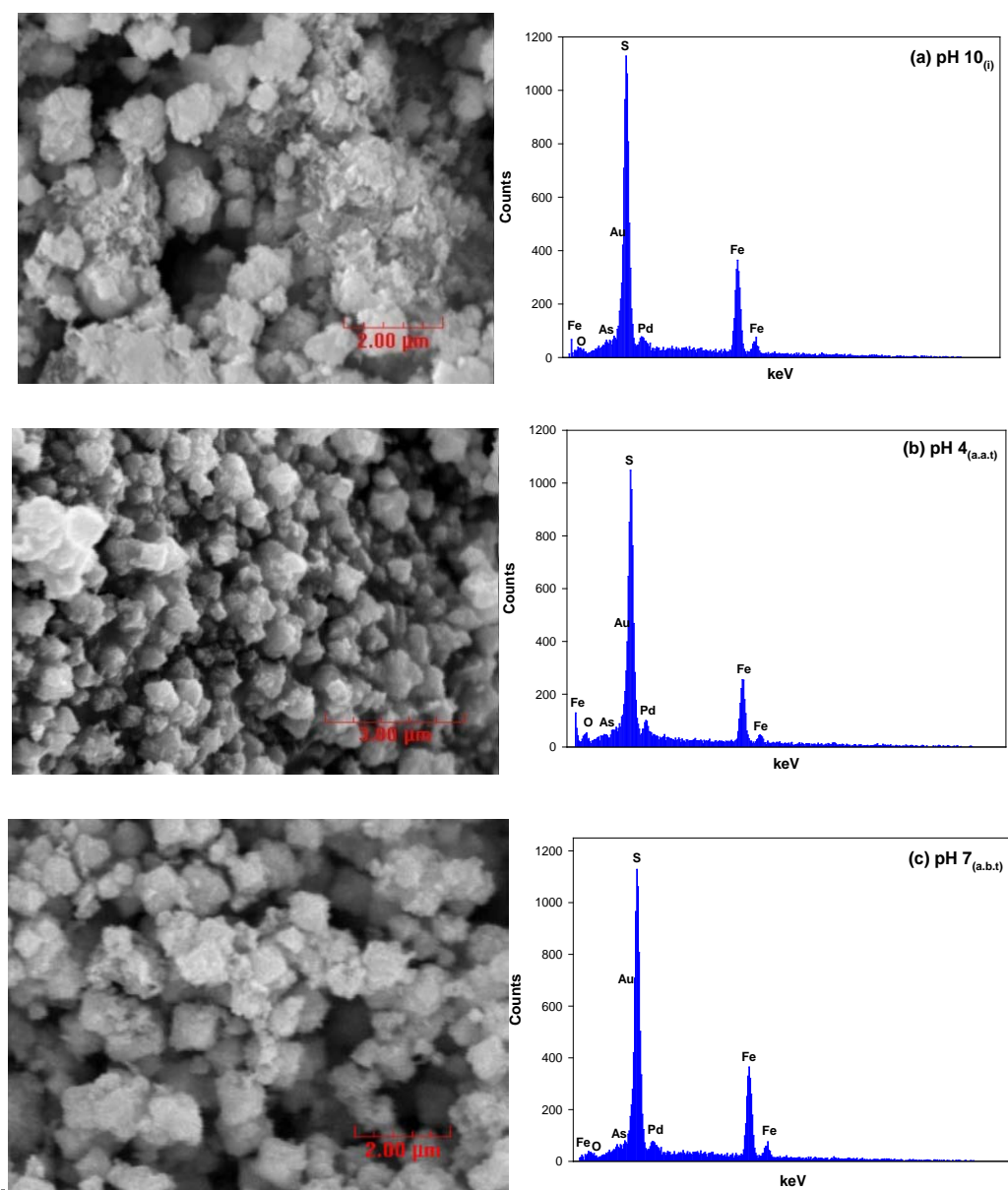


Figure 10.13 Secondary images of SEM and EDS analysis for pyrite after contact with As(V) (15.2 μM) at (a) pH 10_(i) (b) pH 4_(a.a.t), and (c) pH 7_(a.b.t).

To evaluate oxidation states of As(V) on pH 10_(i), pH 4_(a.a.t), and pH 7_(a.b.t) samples, the As 3d XPS spectra were obtained as shown in Figure 10.14. The peaks for As(V) were not obtained clearly due to insufficient concentrations of As(V), so that the identification of different oxidation states of As species is difficult. However, the As 3d peaks for the pH 4_(a.a.t) sample as pH decreased and pH 7_(a.b.t) sample as pH increased show peaks over a broad range of binding energies between 42 and 45 eV (Figure 10.14, expanded view). This is indicative of the presence of reduced As(V) species such as As(III), As(II), and As(I). In addition, the Fe 2p_{3/2} (Figure 10.15) and the S 2p spectra (Figure 10.16) for As(V)-contacted pyrite were similar to those for As(III)-contacted pyrite, although the amounts of As sorbed on pyrite at pH 10 and 4 are different. As pH was raised back to pH 7, both the Fe 2p spectra and S 2p spectra display oxidation of the surface Fe and S species as indicated by increasing peaks associated with Fe(III)-S, Fe(III)-O, S_n²⁻, S⁰, and SO₄²⁻. However, pyrite at pH 8 that was not contacted with arsenic did not present substantial oxidation of the surface Fe and S species (Section 6). This fact suggests that oxidation of surface Fe and S species on pyrite at pH 7 is associated with surface reactions between As(V) and the pyrite surface. These reactions could be associated with additional removals of As(V) at pH 7 (Figure 10.12). Figure 10.17 indicates that as pH decreased from pH 10 to pH 4, the peaks associated with H₂O and O²⁻ decreased, while the peaks associated with OH⁻ increased, presumably due to dissociation of H₂O on the surface and combination of protons (H⁺) with and O²⁻ that is produced by reduction of O₂ by pyrite.

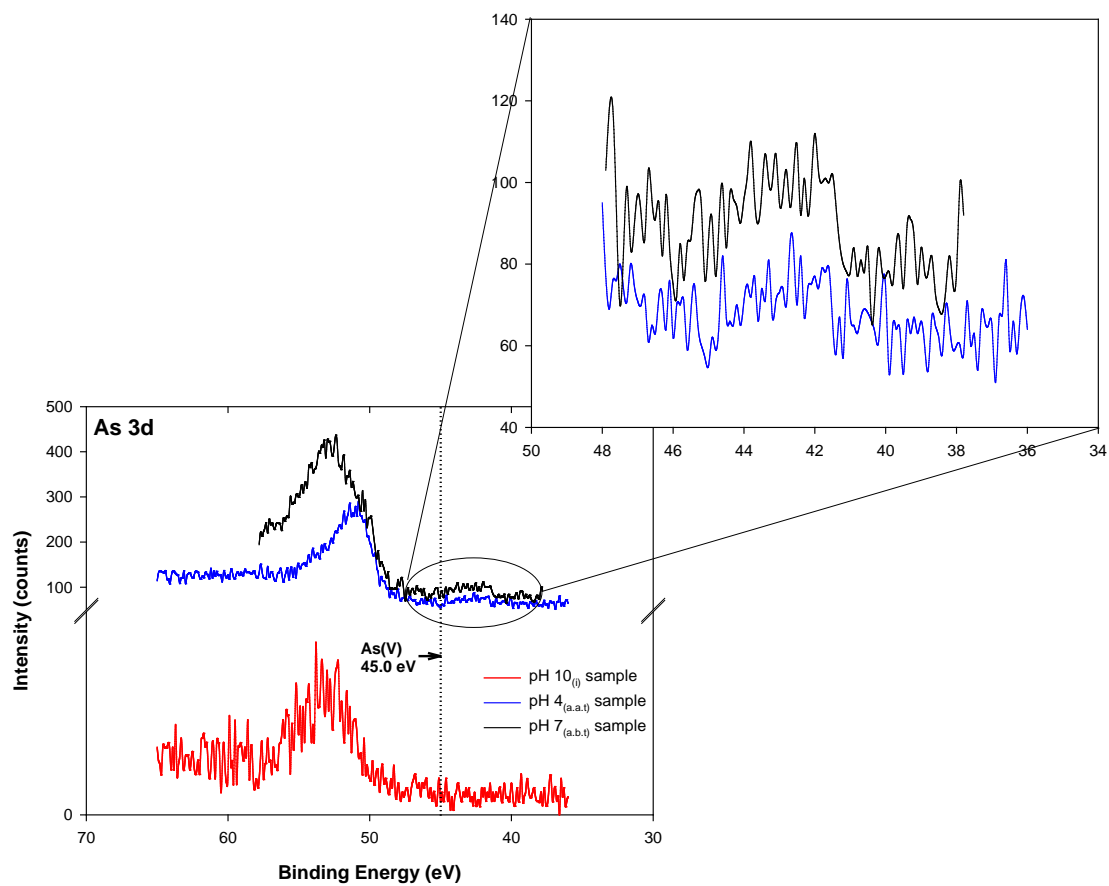


Figure 10.14 High resolution As 3d XPS spectra for pyrite after contact with As(V) (15.2 μM) at (a) pH 10_(i), (b) pH 4_(a.a.t), and (c) pH 7_(a.b.t). Expanded view shows XPS spectra at binding energy between 36 and 48 eV.

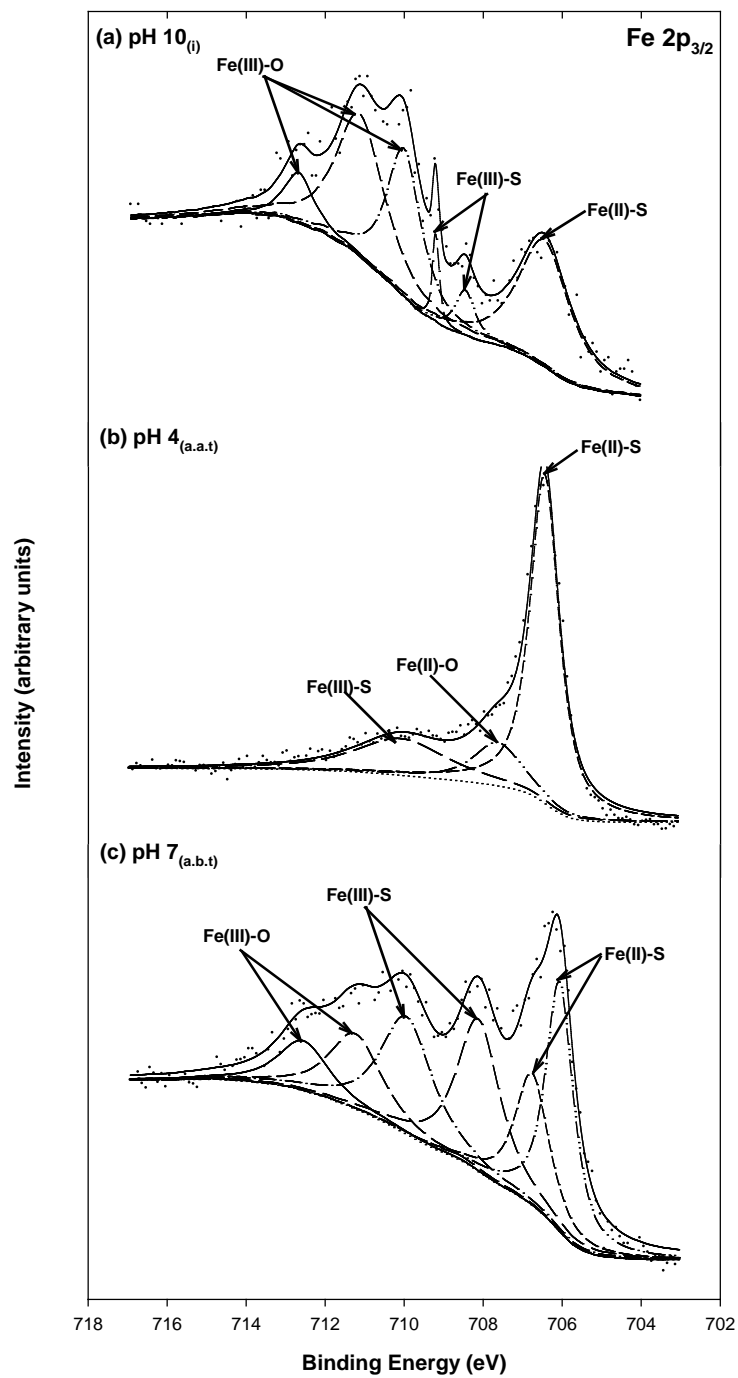


Figure 10.15 High resolution Fe $2p_{3/2}$ XPS spectra for pyrite after contact with As(V) (15.2 μM) at (a) pH 10, (b) pH 4, and (c) pH 7.

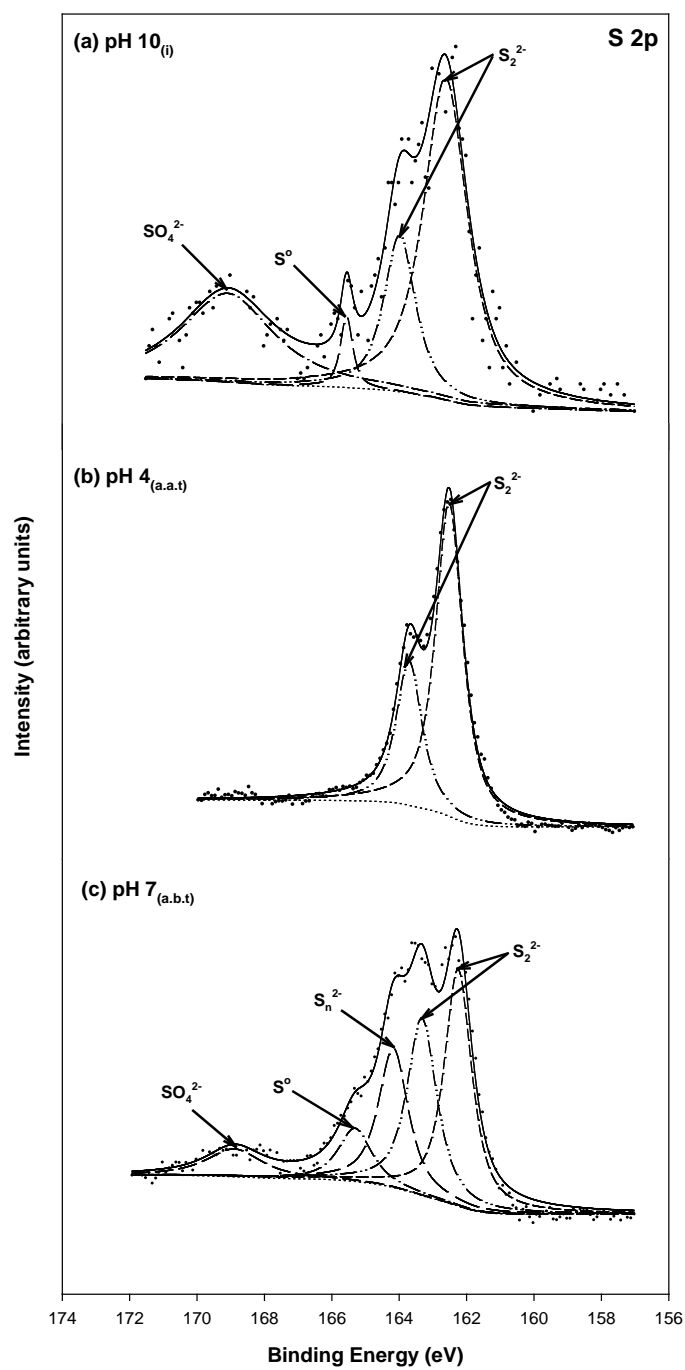


Figure 10.16 High resolution S 2p XPS spectra for pyrite after contact with As(V) (15.2 μM) at (a) pH 10_(i), (b) pH 4_(a.a.t), and (c) pH 7_(a.b.t).

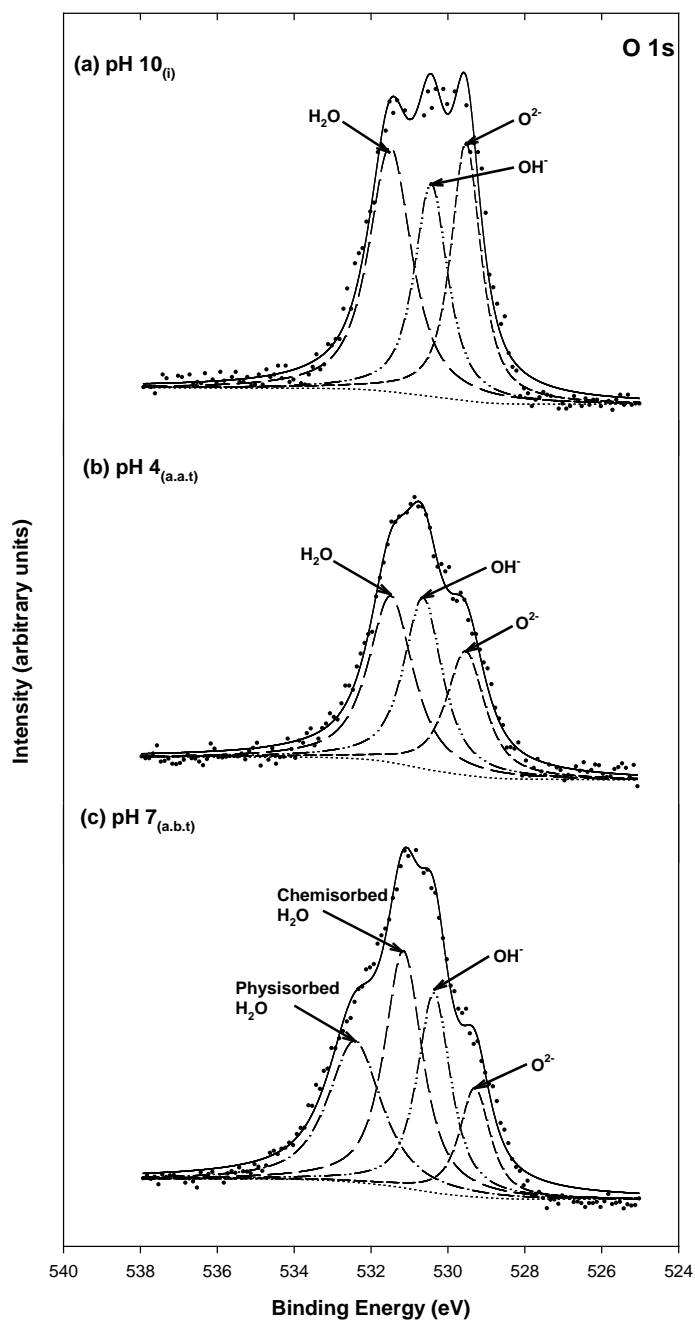


Figure 10.17 High resolution O 1s XPS spectra for pyrite after contact with As(V) (15.2 μ M) at (a) pH 10_(i), (b) pH 4_(a.a.t), and (c) pH 7_(a.b.t).

Table 10.7 Binding energies (BE), full width at half maximum (FWHM), and area percentage for peaks in the Fe 2p_{3/2}, S 2p, and O 1s XPS spectra of pyrite after contact with As(V) (15.2 μM) at (a) pH 10_(i), pH 4_(a.a.t), and pH 7_(a.b.t).

| Samples | BE (eV) | FWHM (eV) | Area (%) | Chemical states |
|----------------------------|---------|-----------|----------|-------------------------------|
| Fe 2p_{3/2} | | | | |
| pH 10 _(i) | 706.4 | 1.55 | 30.3 | Fe(II)-S |
| | 708.4 | 0.62 | 4.2 | Fe(III)-S |
| | 709.2 | 0.19 | 2.7 | Fe(III)-S |
| | 710.0 | 1.04 | 23.8 | Fe(III)-O |
| | 711.1 | 1.47 | 32.1 | Fe(III)-O |
| | 712.7 | 0.89 | 6.8 | Fe(III)-O |
| pH 4 _(a.a.t) | 706.4 | 0.87 | 63.3 | Fe(II)-S |
| | 707.6 | 1.47 | 14.1 | Fe(II)-O |
| | 710.1 | 2.78 | 22.5 | Fe(III)-O |
| pH 7 _(a.b.t) | 706.1 | 0.85 | 22.7 | Fe(II)-S |
| | 706.7 | 1.03 | 14.6 | Fe(II)-S |
| | 708.1 | 1.31 | 21.4 | Fe(III)-S |
| | 709.9 | 1.59 | 20.0 | Fe(III)-S |
| | 711.2 | 1.61 | 13.0 | Fe(III)-O |
| | 712.6 | 1.54 | 8.2 | Fe(III)-O |
| S 2p | | | | |
| pH 10 _(i) | 162.6 | 1.57 | 50.7 | S ²⁻ |
| | 163.9 | 1.12 | 17.5 | S ²⁻ |
| | 165.6 | 0.43 | 3.14 | S ⁰ |
| | 169.1 | 3.23 | 28.7 | SO ₄ ²⁻ |
| pH 4 _(a.a.t) | 162.5 | 0.96 | 69.5 | S ²⁻ |
| | 163.7 | 0.91 | 30.5 | S ²⁻ |
| pH 7 _(a.b.t) | 162.2 | 0.97 | 33.9 | S ²⁻ |
| | 163.3 | 1.05 | 27.3 | S ²⁻ |
| | 164.1 | 1.05 | 21.6 | S _n ²⁻ |
| | 165.3 | 1.17 | 9.14 | S ⁰ |
| | 168.8 | 1.96 | 7.98 | SO ₄ ²⁻ |
| O 1s | | | | |
| pH 10 _(i) | 529.5 | 0.92 | 30.4 | O ²⁻ |
| | 530.4 | 1.03 | 28.1 | OH ⁻ |
| | 531.5 | 1.32 | 41.5 | H ₂ O |
| pH 4 _(a.a.t) | 529.5 | 1.19 | 25.2 | O ²⁻ |
| | 530.6 | 1.20 | 34.8 | OH ⁻ |
| | 531.5 | 1.39 | 40.0 | H ₂ O |
| pH 7 _(a.b.t) | 529.3 | 0.95 | 12.6 | O ²⁻ |
| | 530.4 | 1.03 | 14.9 | OH ⁻ |
| | 531.2 | 1.17 | 33.8 | H ₂ O |
| | 532.4 | 1.65 | 28.6 | H ₂ O |

11. SORPTION OF ARSENIC(III) AND ARSENIC(V) TO MACKINAWITE (FeS): KINETICS, EXTENT OF REMOVAL, STABILITY

Removals of As(III) and As(V) by FeS were fast with half lives that were less than 10 minutes. This indicates that removals of As(III) and As(V) on FeS are probably limited by external transport of the soluble compound to the surface of the solid. Removal of As(V) was faster than that of As(III), with nearly complete removal observed at the first sampling time (10 minutes). The effect of pH on the extent of removal of As(III) by FeS was moderate with highest removals occurring at intermediate pH (pH 8, pH 9). Sulfate inhibited removal of As(III), but there was little difference between the effect of 1 mM and 10 mM sulfate, except at the highest concentrations of As(III). There was a strong effect of pH on removal of As(V), with greater removals observed at lower pH. Sulfate reduced removal of As(V) at higher concentrations of As(V), but showed a smaller effect at lower concentrations. Stability tests with As(III) and FeS showed low removal at high pH, increasing removal as pH was decreased, and nearly complete stability (no contaminant release) as pH was raised back to initial values. Similar behavior was observed for mixtures of As(V) and FeS, but the levels of stability were moderate to high. Surface analysis of mixtures of arsenic and FeS showed some evidence of change in redox state, which indicates that the high levels of stability are due to formation of strong bonds by redox reactions.

11.1 Introduction

Efficient water management at thermo-electric power plants is becoming increasingly important in the U.S. Electric power production is a major user of water in the U.S., accounting for almost 40 % of fresh water withdrawals in 2000 (1). Increases in projected demands for electrical power will tend to increase water use in the future. Much of the projected increase in

demand is expected in areas that are already facing water shortages, so the problem will be additionally difficult to solve. One important area for improved water management at power plants is that of wastewaters from ash and scrubber ponds. These waters can be contaminated with toxic compounds such as arsenic, selenium and mercury as well as high concentrations of calcium and sulfate and must be treated before discharge (3). A variety of techniques can be applied to removing arsenic from ash and scrubber pond waters. Probably the most commonly applied treatment method is adsorption onto iron oxy-hydroxides (5, 6), which is sometimes called coprecipitation. However, the presence of high concentrations of sulfate observed in scrubber waters would substantially reduce removals by adsorption.

A major source of arsenic-contaminated wastes will be residuals from treatment processes that use iron oxy-hydroxides. Robins (1992) questioned the long term stability of the (oxy)hydroxide-arsenic solid material (43). He has demonstrated that arsenic removal is via adsorption and not by formation of a precipitated arsenic-containing solid phase. Therefore, ripening of the (oxy)hydroxide solids after disposal could result in reduced surface area that would cause arsenic to be released. Arsenic could also be released under moderately reducing environments where Fe(III) in the (oxy)hydroxides could be reduced to soluble Fe(II), dissolving the solid phase and releasing the sorbed arsenic. Moderately reducing conditions are found in most landfills due to high concentrations of dissolved organic carbon and bacteria, which often results in reduction of As(V) and release of As(III), which is less strongly bound (26, 44, 45).

Although adsorption can be reasonably used to describe the mechanism of arsenic removal from solution, it does not completely describe the interaction of arsenic with iron sulfide and disulfides. Bostick et al. (2004) have shown that substantial arsenic removal occurs in the first 30 minutes after contact with FeS and FeS₂, but that soluble arsenic concentrations continue to decrease for as long as 100 hours (39). This is much longer than would be needed for

equilibration with the surface of a non-porous solid phase if adsorption were the only reaction occurring. They interpret the slow removal as the result of surface reactions that form a series of more insoluble solid phases that continue to remove arsenic to lower levels. Surface analysis by XANES showed that the initial solid phase was similar to arsenopyrite, which is a very insoluble solid phase and a major form of arsenic in nature (39). Therefore, the interaction of arsenic with iron sulfide and disulfide should be considered to be an adsorption/reaction process, not solely an adsorption process. Wolthers et al. (2005) exhibited that As(III) sorption to disordered mackinawite is explained by a Freundlich isotherm and is not strongly pH-dependent (40). A X-ray absorption spectroscopy (XAS) study showed that both As(III) and As(V) form outer-sphere complexes at the surface of mackinawite (40). This result is in accordance with those reported by Farquhar et al. (2002) and indicates that both As(III) and As(V) at pH 5.5-6.5 coordinate to four oxygen atoms (As-O: 1.69-1.76 Å) in the first coordination shell, and that they coordinate with two sulfur (~3.1 Å) and three iron atoms (3.4-3.5 Å) in the second shell. This suggests interactions via outer-sphere complexation, because the distances for the As-S and As-Fe bonds are longer than that for As-O. (35). However, this result was obtained under experimental conditions of low arsenic concentration and pH in the range 5.5 – 6.5 and when pH was lowered to pH 4.0, arsenic was coprecipitated with mackinawite. The formation of precipitates is affected by arsenic concentration as well as pH. For example, a poorly crystalline arsenic sulfide (As_2S_3) was formed at high As(III) and As(V) concentrations and low pH (35). A similar result was obtained when pyrite reacted with arsenic at acidic pH and As_2S_3 and As_4S_4 -like precipitates were observed to form (41). Gallegos et al. (2008) studied the removal of As(III) using nanoparticulate mackinawite with the help of surface analysis techniques, including XAS and XRD (42). They found that sorption mechanisms of As(III) are very different under different solution conditions, such as initial As(III) concentration or pH. For instance, when mackinawite was

reacted with 5×10^{-4} M As(III) at basic pH (5, 7, 9), a realgar-like solid phase was identified and showed that As(III) was being reduced. This identification was made by XRD and XAS, which indicated arsenic coordination environments in which arsenic was bound to sulfur (As-S: ~ 2.26 Å) and to arsenic (As-As: ~ 2.54 Å). At lower As(III) concentration (5×10^{-5} M), the realgar-like solid phase was observed below pH 5, while only adsorption of As(III) without the occurrence of reduction-mediated precipitation was observed at basic pH. Therefore, it was demonstrated that whether As(III) sorbed to mackinawite or precipitated via surface reactions is strongly affected by environmental conditions. This could be the reason why discrepant results are frequently reported in the literature, even when conditions are similar.

The purposes of this study are to investigate the effect of various conditions (time, pH, competing ion (sulfate)) on removal of arsenic by mackinawite, and to evaluate the stability of mixtures of mackinawite and arsenic as affected by pH change. By doing so, the optimum condition and sorption mechanism are determined to provide crucial information on safe disposal of arsenic-treated solid wastes in landfill.

11.2 Materials and Methods

11.2.1 Sorption/Reaction Experiments

Kinetic experiments on removal of As(III) or As(V) were performed by using 1g/L suspensions of FeS at pH 8 in 20-mL reaction vessels. To start a kinetic test, FeS slurry and arsenic stock solution were added to the reaction vessels to reach concentrations of 1 g/L of solids and 13.3 μ M As. Acid (0.5 M HCl) or base (0.5 M NaOH) were added to adjust the pH. The reaction vessels were mixed on a shaker at 2000 rpm until specified sampling time. Samples of approximately 10 mL were taken and filtered using 0.2- μ m membrane filters after 10, 30, 60, 120, 180, 240, 420, 660, 1000, 1440 minutes of reaction. All samples were stored in an anaerobic chamber to avoid arsenic oxidation until analysis by hydride generation atomic absorption

spectrometry (HGAAS). Removal tests at pH 7, 8, 9, and 10 were conducted to evaluate the ability of FeS to remove As(III) and As(V). A suspension of FeS was mixed with a sufficient amount of 2000 mg/L arsenic stock solution to provide the desired initial arsenic concentration and a FeS concentration of 1 g/L. The desired pH was adjusted using 0.5 M HCl or 0.5 M NaOH. The reaction vessels were mixed at 200 rpm on rotary shaker for 24 hours. All samples were filtered using 0.2- μm membrane filters and were stored in an anaerobic chamber until analysis by HGAAS. Experiments to determine the effect of sulfate on arsenic removal were conducted similarly at pH 8 and at three sulfate concentrations (0, 1, 10 mM). Coefficients in the Langmuir, Freundlich, and BET models were determined by non-linear least-squares regression using MATLAB[®] with its embedded function “nlinfit”

11.2.2 Stability of As-Contacted FeS

A series of experiments to measure the effect of pH on removal of As(III) and As(V) by FeS were conducted using a similar procedure as was used for pyrite suspensions. Suspensions containing 1 g/L of FeS were adjusted to initially to achieve a pH of about pH 10, before adding As(III) or As(V) to create an arsenic concentration of 15.2 μM . Then pH was reduced by addition of 1 or 2 M HCl to achieve a set of desired pH values and then 1.0 M NaOH was added to raise the pH to a number of values with the highest being near pH 10. After each pH adjustment, the system was allowed to react for 30 minutes, before removing 10-mL samples that were filtered through 0.02- μm anodisc membrane filters. Samples will be identified with the following nomenclature to simplify the discussion. The initial sample at pH 10 will be named the “pH 10_(i)” sample, the sample at pH 4 after acid titration will be named the “pH 4_(a.a.t)” sample, and the final sample obtained at pH 10 after the titrations will be named the “pH 10_(f)” sample. The filtered samples and the filter disk including wet solids were stored in the anaerobic chamber until analysis by AAS (solutions) and XPS (solids).

11.3 Results and Discussion

11.3.1 Kinetics

Figure 11.1 shows the results of kinetic experiments and model predictions on removal of As(III) and As(V) by FeS at pH 8. The rates of As(III) and As(V) uptake were different with As(V) being nearly completely removed within 10 minutes, while 96 % of As(III) was removed after 180 minutes. However, after 6.6 hours, As(III) was nearly completely removed. As discussed in Section 10, a general kinetic model (Equation 11.1) was modified to describe rapid and slower removal (Equations 11.2 and 11.3).

$$\frac{dq}{dt} = k(q_{\max} - q) \quad (11.1)$$

$$\frac{dq_f}{dt} = k_f(q_{f,\max} - q_f) \quad (11.2)$$

$$\frac{dq_s}{dt} = k_s(q_{s,\max} - q_s) \quad (11.3)$$

This kinetic model is based on the assumption that there are two types of surface sites that account for biphasic kinetic behavior, i.e. initial fast removal and subsequent slow removal. Table 11.1 displays all of parameters calculated by nonlinear regression using MATLAB[®] with its embedded functions “nlinfit” and ode23s”. A sequential approach was used in determining values of coefficients, in which values for “slow” coefficients were initially obtained and then they were used in subsequent regression to search values for “fast” coefficients. This was continued until a satisfactory fit was obtained. The rate coefficients (k_f and k_s) for As(V) sorption have very large confidence limits because As(V) sorption was so fast that complete removal was reached in minutes which provided very little data to define values of kinetic coefficients. However, the model fit the data well, as indicated by a low value of the goodness-of-fit parameter. Unlike As(V) sorption, when As(III) is removed, the rate coefficient for fast-reacting

sites has a larger confidence interval than for slow-reacting sites. Removal of As(III) shows more biphasic behavior than As(V) as indicated by its larger surface concentration associated with slow-reacting sites ($q_{s,max}$).

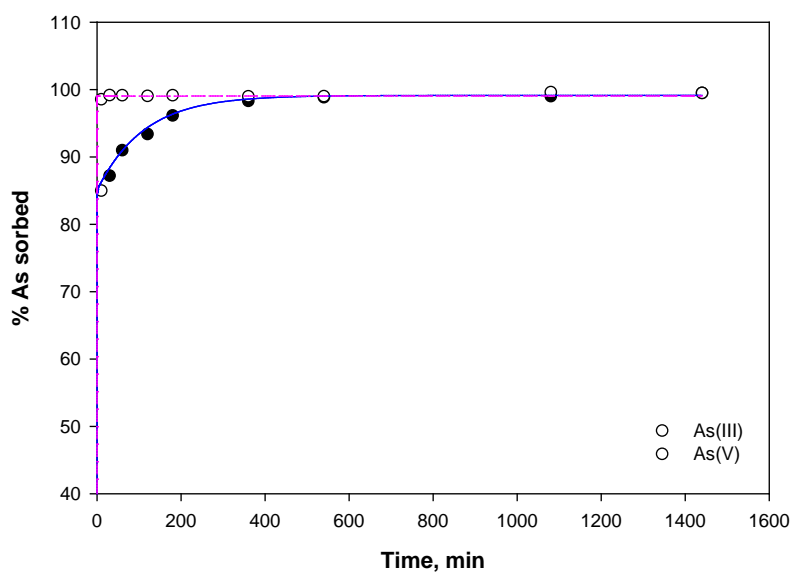


Figure 11.1 Removal of As(III) and As(V) by FeS as a function of time at pH 8. Initial concentrations of As(III) and As(V) were 13.3 μM and dose of FeS was 1 g/L.

Table 11.1 Calculated parameters for kinetic model of As(III) and As(V) uptake by FeS at pH 8.

| Arsenic species | Parameters | | | | |
|-----------------|--|------------------------------|-------------------------|-------------------------|-------|
| | $k_f (\text{min}^{-1})$ | $k_s (\text{min}^{-1})$ | $q_f (\mu\text{mol/g})$ | $q_s (\mu\text{mol/g})$ | *GFP |
| As(III) | $2.8 \times 10^5 \pm 1.3 \times 10^6$ | 0.01 ± 0.1 | 11.3 ± 3.6 | 1.9 ± 5.5 | 0.01 |
| As(V) | $2.1 \times 10^3 \pm 1.8 \times 10^{10}$ | $4.1 \times 10^{-4} \pm 0.6$ | 13.2 ± 4.3 | 0.2 ± 2.3 | 0.002 |

* Goodness of fit parameter (GFP) = $\frac{\sqrt{SSR/(n-2)}}{\bar{q}}$ where SSR is sum of squared residual, n is the number of data points, \bar{q} is average value of the amount of As sorbed per amount of pyrite

11.3.2 Nonlinear Removal Patterns

11.3.2.1 Effect of pH

Figure 11.2 shows the results of removal experiments conducted with As(III) and FeS at four different pH values. The symbols represent the measured data and the lines represent Langmuir, Freundlich, and BET equations that were fitted to the data. Table 11.2 summarizes all parameters calculated by nonlinear regression using MATLAB[®]. The Langmuir and Freundlich equations were presented in Section 10 as Equations 11.1 and 11.2, respectively. Figure 11.2(c) shows lines that are predictions made by the BET equation with coefficients that were fitted to the data. The BET equation is shown in Equation 11.4:

$$q = \frac{q_{\max} AC}{(C_s - C) \left(1 + (A-1) \frac{C}{C_s} \right)} \quad (11.4)$$

where q is the concentration of arsenic on the solid ($\mu\text{mol/g}$); q_{\max} is the concentration of arsenic on the solid at a monolayer coverage, ($\mu\text{mol/g}$); C is the concentration of arsenic in solution ($\mu\text{mol/L}$); A is adsorption energy parameter (A/C_s corresponds to b in the Langmuir model); and C_s is saturation concentration in solution ($\mu\text{mol/L}$). These equations are usually used to describe results of equilibrium adsorption experiments. However, use of this equation to fit the data does not imply that equilibrium was achieved nor that adsorption is the only process occurring during the experiment. Classic isotherm models (Langmuir, Freundlich, BET) were not very effective in correlating data on removal of As(III) because of the irregularly shaped relationships between solid phase concentration and liquid phase concentration. The inability of the models to describe systems in which surface reactions are probably occurring is not surprising. Figure 11.3 shows the experimental data at lower concentrations. There were little differences in the extent of As(III) removal between pH 7 and pH 9, while there were somewhat larger differences between pH 8

and pH 10.

Table 11.2 Parameters of models describing removal of As(III) by FeS as affected by pH.

| Models | pH | | | |
|---|---|---|---|---|
| | pH 7 | pH 8 | pH 9 | pH 10 |
| Langmuir | | | | |
| b (L/ μmol) | $1.4 \times 10^{-3} \pm 1.6 \times 10^{-3}$ | $9.3 \times 10^{-4} \pm 2.3 \times 10^{-3}$ | $4.8 \times 10^{-4} \pm 1.0 \times 10^{-3}$ | $3.3 \times 10^{-6} \pm 1.2 \times 10^{-3}$ |
| q_{max} ($\mu\text{mol/g}$) | $1.1 \times 10^3 \pm 0.78 \times 10^3$ | $2.3 \times 10^3 \pm 5.1 \times 10^3$ | $3.9 \times 10^3 \pm 7.79 \times 10^3$ | $3.1 \times 10^5 \pm 1.2 \times 10^8$ |
| GFP | 0.14 | 0.20 | 0.08 | 0.17 |
| Freundlich | | | | |
| k_f ($\mu\text{mol}^{1-1/n} \cdot \text{L}^{1/n} / \text{g}$) | 3.25 ± 3.0 | 3.10 ± 3.69 | 2.48 ± 1.46 | 0.48 ± 0.64 |
| n | 1.23 ± 0.26 | 1.11 ± 0.28 | 1.07 ± 0.13 | 0.88 ± 0.18 |
| GFP | 0.14 | 0.20 | 0.08 | 0.16 |
| BET | | | | |
| A | 5.9 ± 4.4 | 4.4 ± 5.6 | 3.4 ± 2.4 | 0.45 ± 1.98 |
| q_{max} ($\mu\text{mol/g}$) | 556 ± 242 | $1.0 \times 10^3 \pm 9.0 \times 10^2$ | $1.1 \times 10^3 \pm 0.6 \times 10^2$ | $3.8 \times 10^3 \pm 1.6 \times 10^4$ |
| GFP | 0.13 | 0.20 | 0.08 | 0.15 |

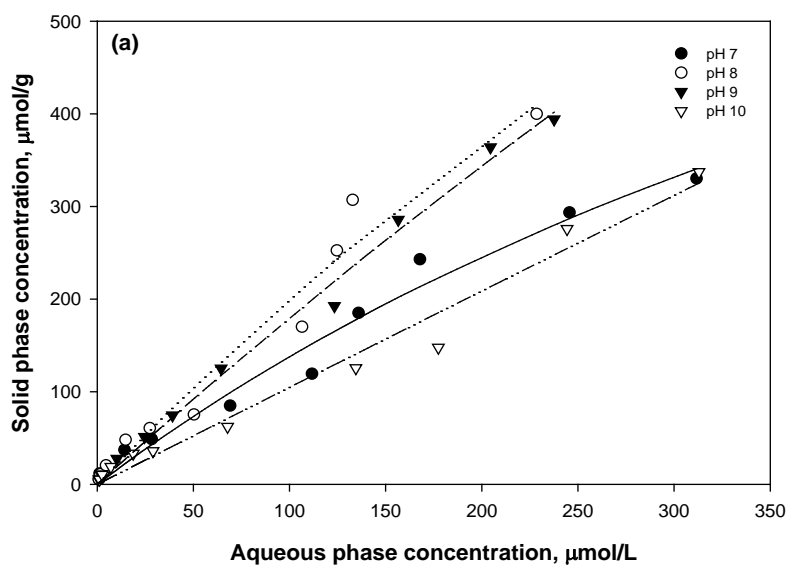


Figure 11.2 Measured concentrations of As(III) on FeS as function of concentration in water with (a) Langmuir, (b) Freundlich, (c) BET equations (lines) fitted to data (symbols) at various pH.

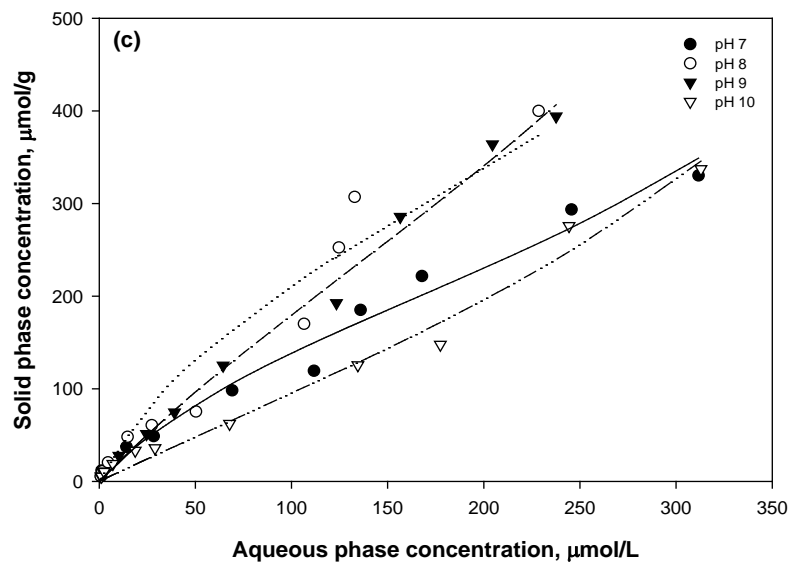
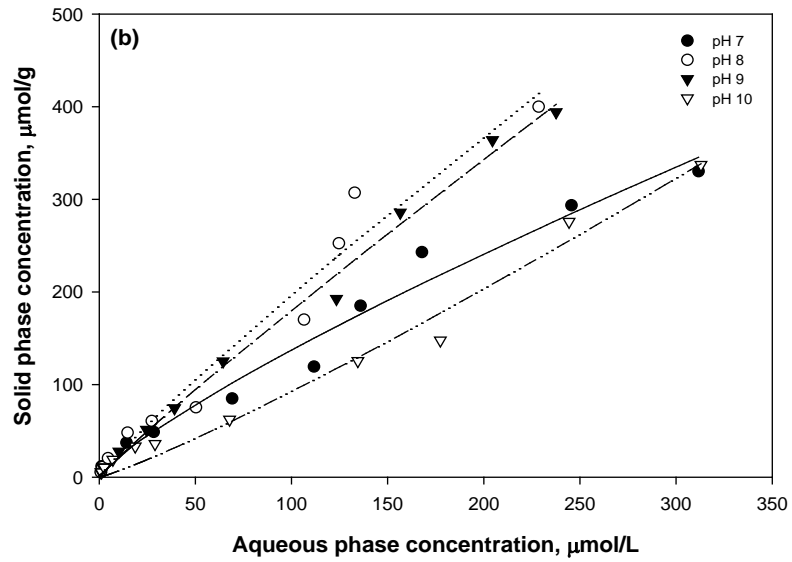


Figure 11.2 Continued.

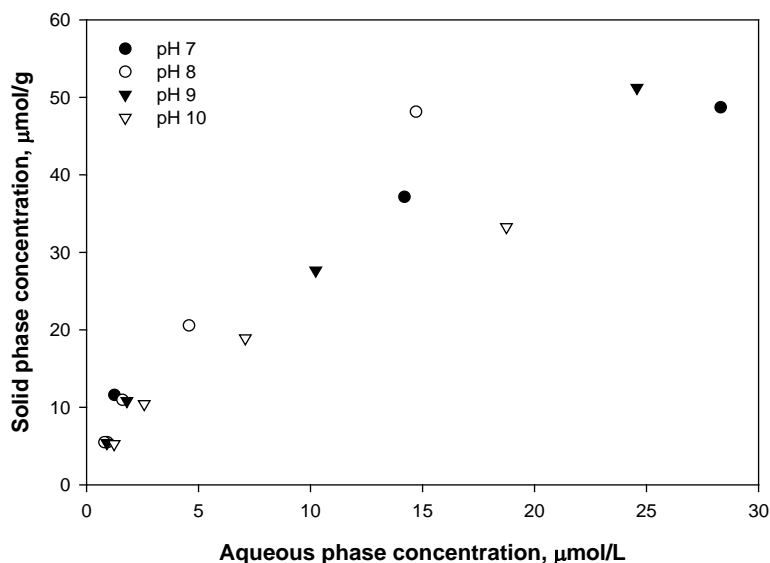


Figure 11.3 Measured concentrations of As(III) on FeS as a function of concentration in water for various pH using data at lower concentrations.

Figure 11.4 show results of removal experiments conducted with As(V) and FeS. Figure 11.4(a) shows a Langmuir equation (line) fitted to the data (symbols) with normal axes and an inset with a logarithmic y-axis used to better display low values. Figure 11.4(b) shows the fit of the Freundlich equation and Figure 11.4(c) shows the fit of the BET equation. Table 11.3 shows the values of model parameters that were calculated by non-linear regression and used to generate the lines in Figure 11.4. The Freundlich model was generally better able to fit the data as shown by its lower GFP. The maximum solid-phase concentration for As(V) on FeS tended to increase with lower pH. Models were not very effective in correlating data of solid-phase concentration as a function of liquid phase concentration, because the data did not show behavior that is typical of systems that have achieved adsorption equilibrium.

Table 11.3 Parameters of models describing removal of As(V) by FeS as affected by pH.

| Models | pH | | | |
|---|--|---|-------------------|--|
| | pH 7 | pH 8 | pH 9 | pH 10 |
| <i>Langmuir</i> | | | | |
| b (L/ μmol) | $2.4 \times 10^{-5} \pm 0.12$ | $2.5 \times 10^{-6} \pm 2.4 \times 10^{-3}$ | 0.002 ± 0.003 | $4.3 \times 10^{-5} \pm 7.8 \times 10^4$ |
| q_{max} ($\mu\text{mol/g}$) | $2.2 \times 10^6 \pm 1.1 \times 10^{10}$ | $8.0 \times 10^5 \pm 8.0 \times 10^8$ | 75.5 ± 46.5 | $1.1 \times 10^3 \pm 1.9 \times 10^4$ |
| GFP | 0.56 | 0.23 | 0.20 | 0.19 |
| <i>Freundlich</i> | | | | |
| k_f ($\mu\text{mol}^{1-1/n} \cdot \text{L}^{1/n}/\text{g}$) | 11.6 ± 13.9 | 0.52 ± 0.84 | 0.98 ± 0.76 | 0.04 ± 0.06 |
| n | 0.56 ± 0.18 | 0.79 ± 0.99 | 1.68 ± 0.37 | 0.97 ± 0.26 |
| GFP | 0.32 | 0.18 | 0.14 | 0.19 |
| <i>BET</i> | | | | |
| A | 0.36 ± 237.6 | 0.04 ± 3.91 | 13.1 ± 9.8 | 2.7 ± 2.8 |
| q_{max} ($\mu\text{mol/g}$) | $2.8 \times 10^6 \pm 1.7 \times 10^8$ | $7.6 \times 10^4 \pm 6.7 \times 10^6$ | 36.2 ± 8.2 | 36.2 ± 21.4 |
| GFP | 0.55 | 0.20 | 0.17 | 0.19 |

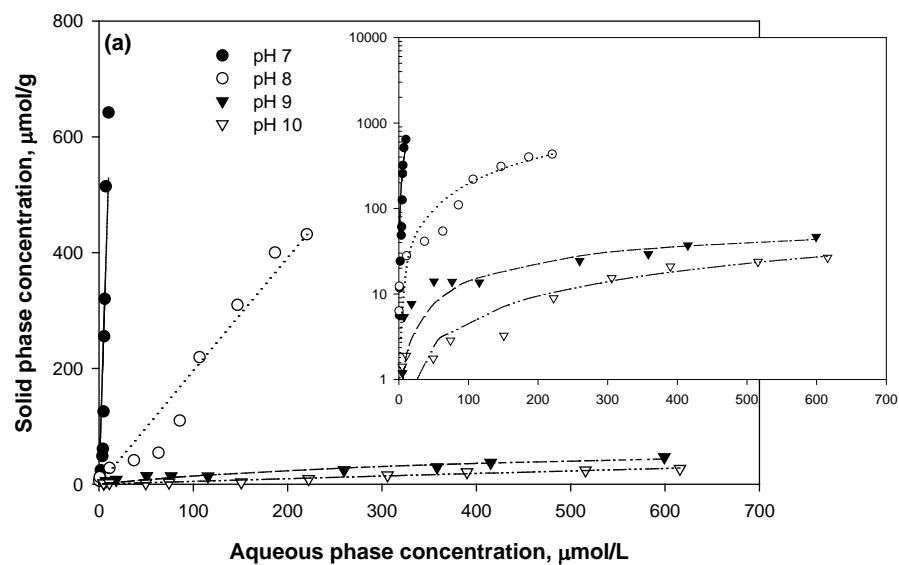


Figure 11.4 Measured concentrations of As(V) on FeS as function of concentration in water with (a) Langmuir, (b) Freundlich, (c) BET equations (lines) fitted to data (symbols) at various pH.

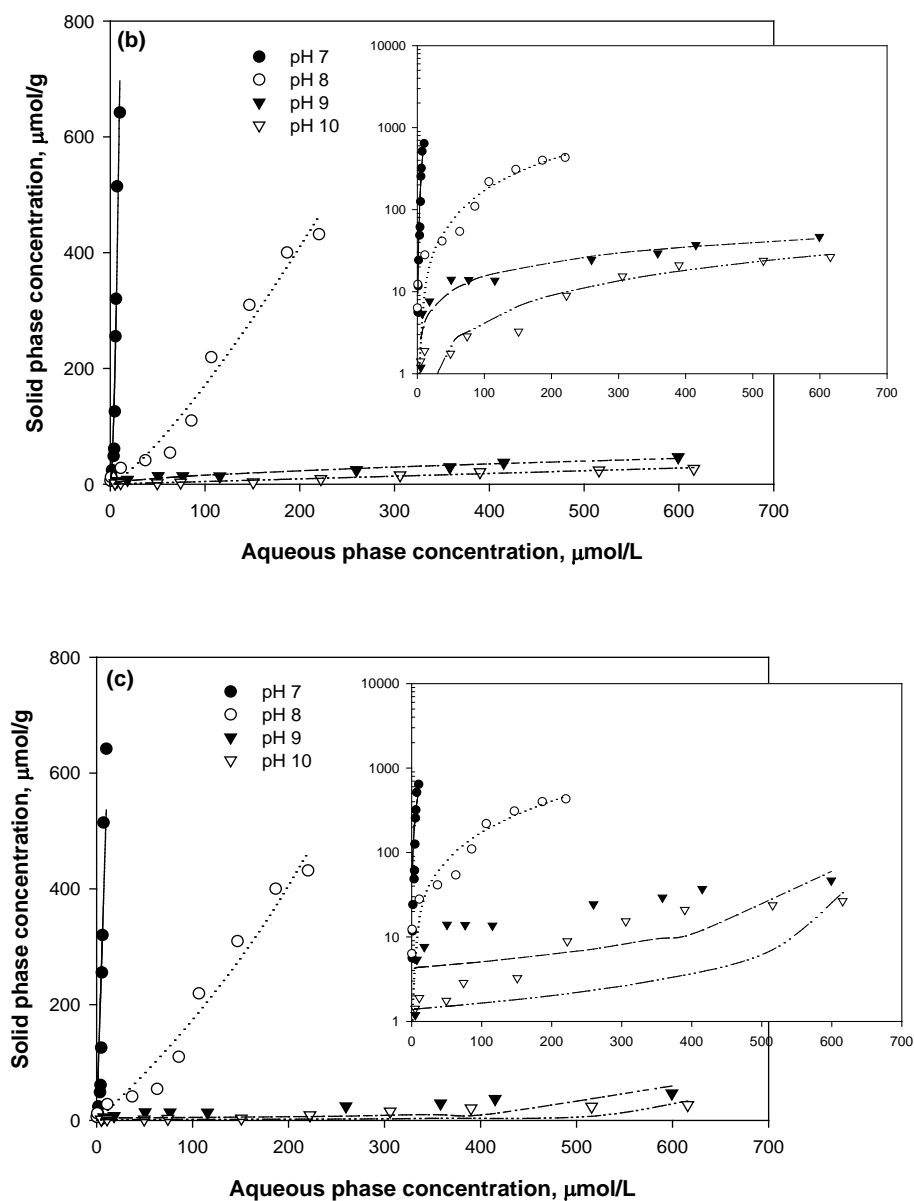


Figure 11.4 Continued.

11.3.2.2 Effect of Sulfate Concentration

Figure 11.5 show results of experiments to determine the effect of a competing ion (sulfate) on removal of As(III) by FeS. Figures 11.5(a), 11.5(b), and 11.5(c) show Langmuir, Freundlich, and BET equations fitted to the data, respectively. Table 11.3 presents values of

model parameters fitted to the data. When 1 or 10 mM of sulfate concentration was added, the amount of As(III) removal by FeS decreased.

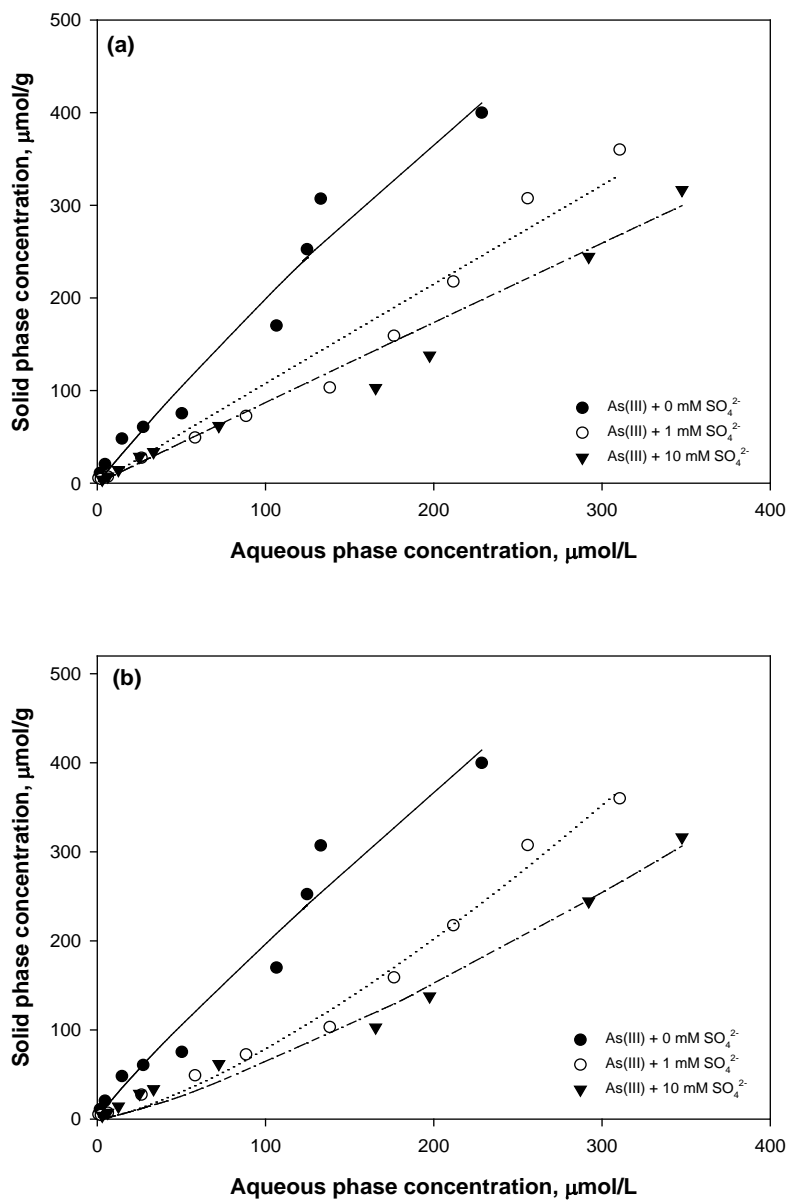


Figure 11.5 Measured concentrations of As(III) on FeS as function of concentration in water with (a) Langmuir, (b) Freundlich, and (c) BET equations (lines) fitted to data (symbols) at various concentrations of sulfate.

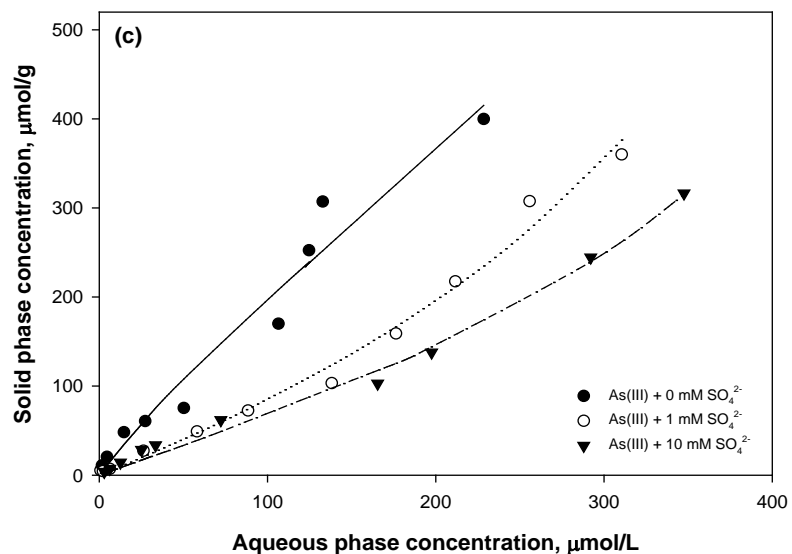


Figure 11.5 Continued.

Figure 11.6 show results of experiments to determine the effect of a competing ion (sulfate) on removal of As(V) by FeS. Figures 11.6(a), 11.6(b), and 11.6(c) show Langmuir, Freundlich, and BET equations fitted to the data, respectively. Table 11.4 presents values of model parameters fitted to the data. Better fits to the data were obtained with the Langmuir equation, as shown by lower values of GFP. Lower amounts of As(V) were removed when sulfate was present at 1 or 10 mM.

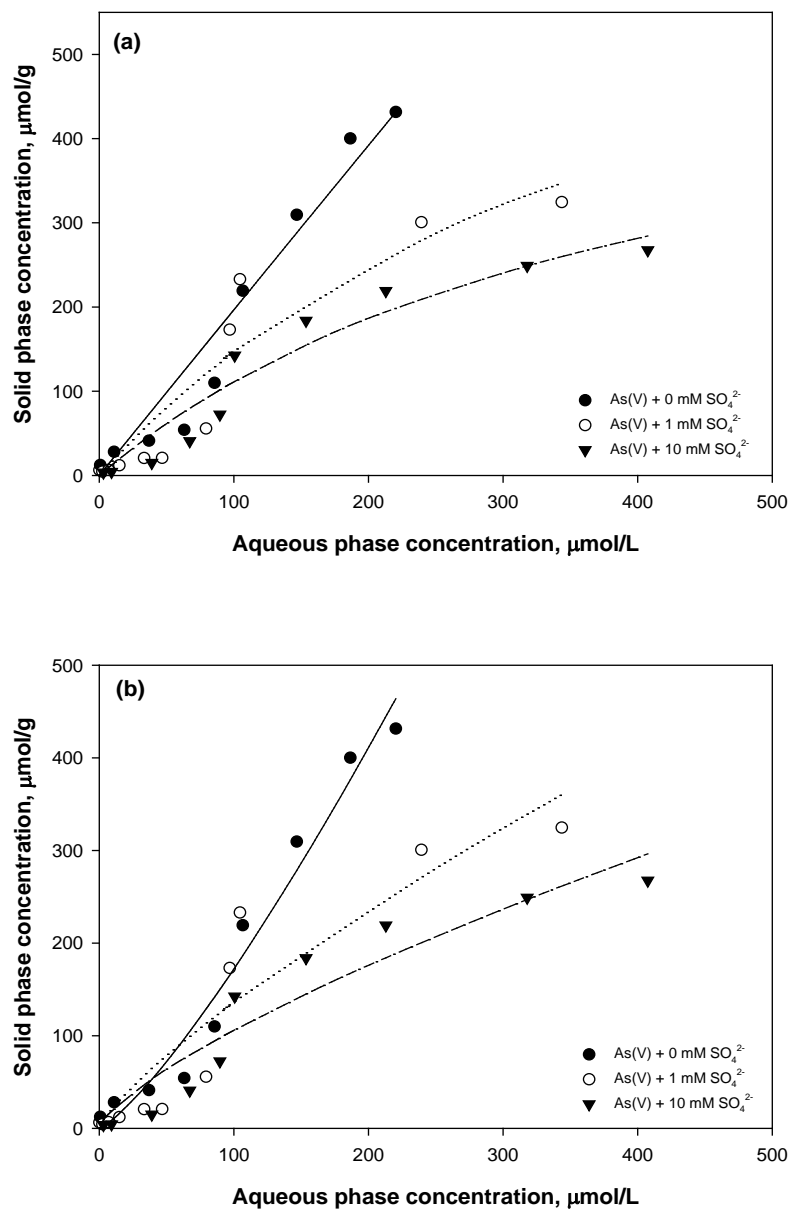


Figure 11.6 Measured concentrations of As(V) on FeS as function of concentration in water with (a) Langmuir, (b) Freundlich, and (c) BET equations (lines) fitted to data (symbols) at various concentrations of sulfate.

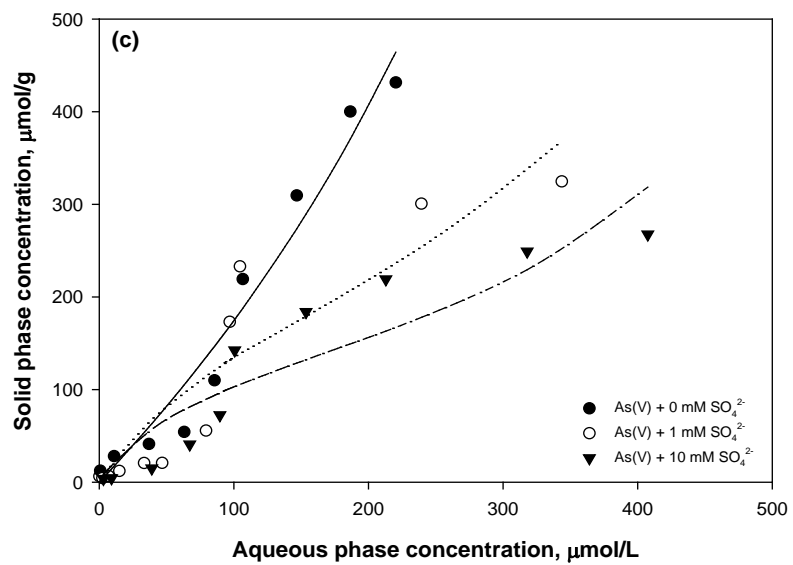


Figure 11.6 Continued.

Table 11.4 Parameters of models describing removal of As(III) by FeS as affected by sulfate concentration.

| SO ₄ ²⁻ (mM) | <i>Langmuir</i> | | | <i>Freundlich</i> | | | <i>BET</i> | | |
|---------------------------------------|--|--|------|---|-------------|------|--|----------|------|
| | b (L/μmol) | q _{max} (μmol/g) | GFP | K _f (μ ^{mol-1/n} ·L ^{1/n} /g) | n | GFP | q _{max} (μmol/g) | a | GFP |
| 0 | 9.3×10 ⁻⁴ ±2.3×10 ⁻³ | 2.3×10 ³ ±5.1×10 ³ | 0.20 | 3.10±3.69 | 1.11±0.28 | 0.20 | 1.0×10 ³ ±9.0×10 ² | 4.4±5.6 | 0.20 |
| 1 | 1.3×10 ⁻⁶ ±1.6×10 ⁻³ | 8.4×10 ⁵ ±9.9×10 ⁸ | 0.20 | 0.15 ± 0.17 | 0.73 ± 0.11 | 0.10 | 5.3×10 ³ ±2.7×10 ⁶ | 0.03±1.1 | 0.12 |
| 10 | 2.4×10 ⁻⁶ ±1.3×10 ⁻³ | 3.5×10 ⁵ ±1.9×10 ⁸ | 0.19 | 0.19 ± 0.28 | 0.79 ± 0.16 | 0.15 | 3.3×10 ⁴ ±1.2×10 ⁶ | 0.04±1.4 | 0.12 |

Table 11.5 Parameters for models describing removal of As(V) by FeS as affected by sulfate concentration.

| SO ₄ ²⁻ (mM) | <i>Langmuir</i> | | | <i>Freundlich</i> | | | <i>BET</i> | | |
|---------------------------------------|--|--|------|---|-------------|------|--|-------------|------|
| | b (L/μmol) | q _{max} (μmol/g) | GFP | K _f (μ ^{mol-1/n} ·L ^{1/n} /g) | n | GFP | q _{max} (μmol/g) | a | GFP |
| 0 | 2.5×10 ⁻⁶ ±2.4×10 ⁻³ | 8.0×10 ⁵ ±8.0×10 ⁸ | 0.23 | 0.52 ± 0.84 | 0.79 ± 0.99 | 0.18 | 7.6×10 ⁴ ±6.7×10 ⁶ | 0.04±3.91 | 0.20 |
| 1 | 0.002±0.007 | 787±960 | 0.41 | 3.61 ± 7.26 | 1.27 ± 0.59 | 0.44 | 457 ± 356 | 7.93 ± 11.4 | 0.41 |
| 10 | 0.002±0.005 | 577± 423 | 0.24 | 3.62 ± 5.59 | 1.36 ± 0.52 | 0.28 | 334 ± 152 | 8.86 ± 8.34 | 0.25 |

11.3.3 Stability of As-Contacted FeS

11.3.3.1 As(III)-Contacted FeS

Stability experiments were conducted by first contacting FeS with solutions of As(III)/As(V) and providing time for reactions to occur between arsenic and the solid surface. Then the solution pH was changed in a series of steps and the concentration of As(III)/As(V) was measured in the aqueous phase after 30 minutes reaction. The extent of release of As(III)/As(V) as pH changed was used as a measure of the stability of the combination of arsenic and FeS. The initial pH was chosen as the value where the best removal of As(III) or As(V) had been observed, so that high loadings would be obtained initially. Figure 11.7 shows that as pH decreased from an initial value near pH 10, As(III) removal by mackinawite (FeS) increased as pH was decreased from pH 10 with nearly complete removal observed for pH less than about pH 6.5. This result is in contrast to what has been reported for As(III) removal by troilite (FeS), where higher removals occurred above pH 5 and very little As(III) was removed below pH 5 (39). However, experiments on As(III) sorption by synthetic mackinawite (FeS) that were performed by Gallegos (2007), showed a comparable sorption trend with our results (42). The difference in As(III) sorption edges may be caused by higher solubility of synthetic mackinawite than troilite (42). At low pH, the dissolved sulfide from mackinawite can react with soluble As(III) to form As-S precipitates, resulting in higher As(III) removal. Hysteresis was observed in the sorption/desorption curves when pH was raised from pH 4. Little arsenic was released as pH was raised, indicating that strong bonds were formed between As(III) and the surface at low pH that were not broken when pH was raised.

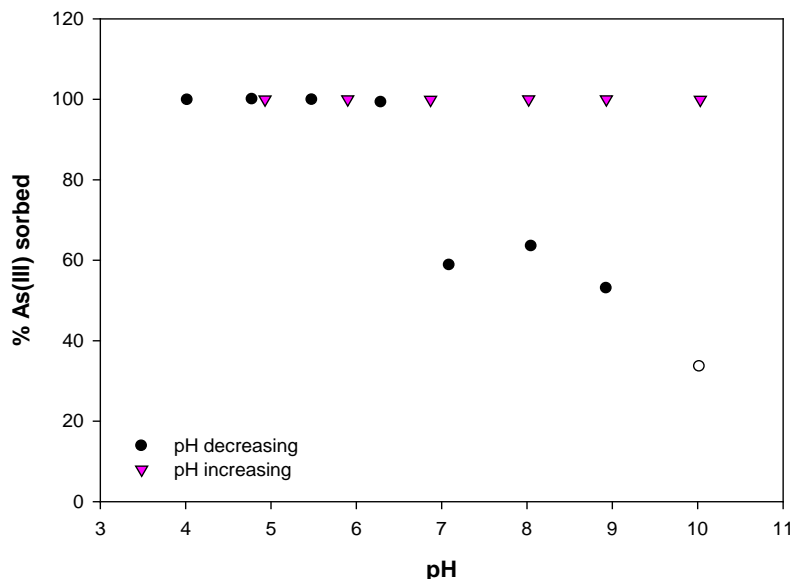


Figure 11.7 Effect of pH on removal of As(III) (15.2 μM) by FeS (1 g/L) as pH was decreased from pH 10 to pH 4 and then increased back to pH 10.

To investigate reaction mechanisms affecting the stability of As(III)-contacted FeS, the oxidation states of the surface-bound Fe and S were analyzed through Fe 2p_{3/2} and S 2p spectra obtained by XPS. Figure 11.8 shows the As 3d XPS spectra of FeS after contact with As(III) at pH 10_(i) and pH 4_(a.a.t). The As 3d spectra was not useful in determining oxidation state of As, because the solid-phase As concentration was too low. Nonetheless, a minimal arsenic peak was centered at the binding energy near 44.3 eV, which is representative of As(III). In addition, a large peak associated with Fe 3p was observed near 55 eV.

The Fe 2p_{3/2} XPS spectra (Figure 11.9) shows that more oxidation of the surface-bound Fe was observed in the pH 4_(a.a.t) sample than in the pH 10_(i) sample as shown by the peak area for Fe(III)-O being larger by a factor of 2.4. Analogous to the XPS results for the Fe 2p_{3/2} spectra, the S 2p spectra of the pH 4_(a.a.t) sample exhibited evidence for more oxidation of the surface S species, as indicated by the presence of a peak associated with elemental sulfur (S⁰) that was not

observed in the spectra for the pH 10_(i) sample (Figure 11.10). Based on the results of XPS analysis and the stability test (Figure 11.3), high removal of As(III) at pH 4 may be the result of redox reaction in which surface species are oxidized and As(III) is reduced, leading to formation of strongly bound surface species that are not easily released to solution as pH is changed.

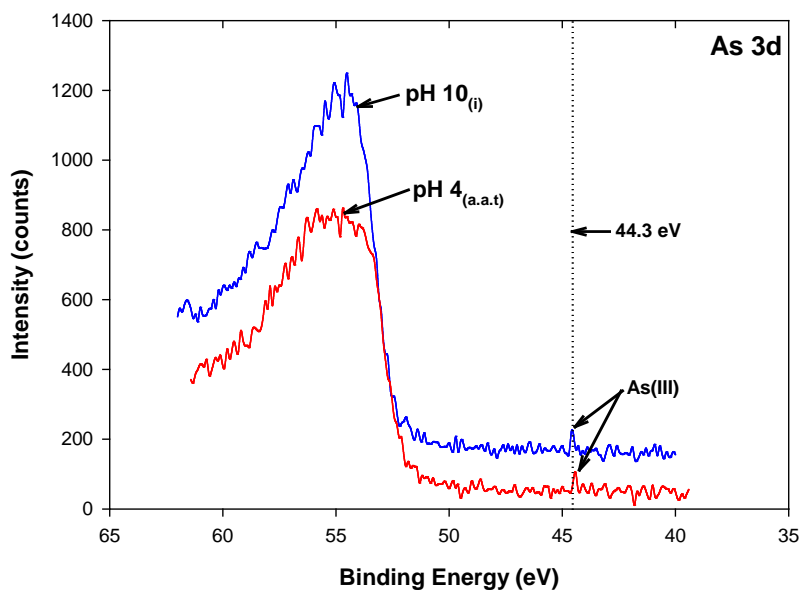


Figure 11.8 High resolution As 3d XPS spectra for FeS after contact with As(III)(15.2 μ M) at (a) pH 10_(i) and (b) pH 4_(a.a.t).

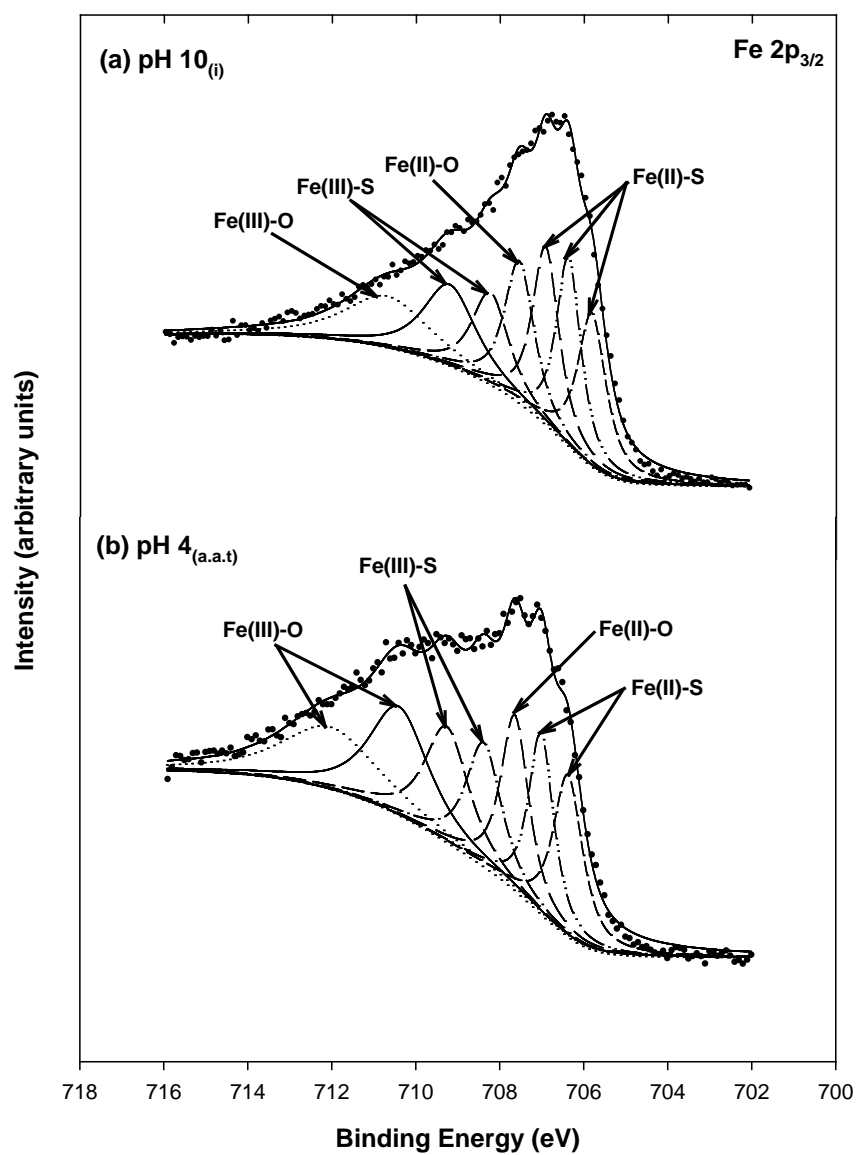


Figure 11.9 High resolution Fe $2p_{3/2}$ XPS spectra for FeS reacted with As(III) (15.2 μM) at (a) pH 10_(i) and (b) pH 4_(a.a.t).

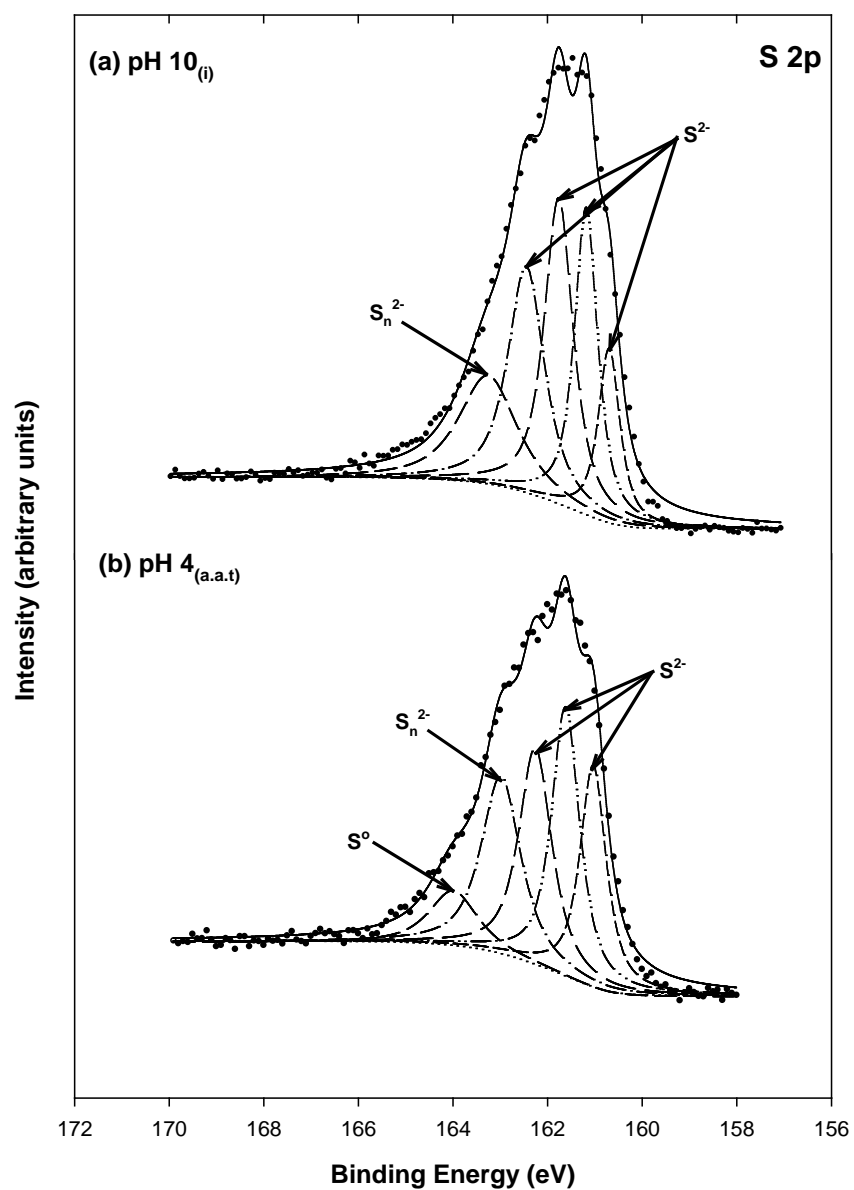


Figure 11.10 High resolution S 2p XPS spectra for FeS reacted with As(III) (15.2 μ M) at (a) pH 10_(i) and (b) pH 4_(a.a.t).

Table 11.6 Binding energies (BE), full width at half maximum (FWHM), and area percentage for peaks in the Fe 2p_{3/2} and S 2p XPS spectra of FeS after contact with As(III) at pH 10_(i) and pH 4_(a.a.t).

| Samples | BE (eV) | FWHM (eV) | Area (%) | Chemical states |
|----------------------------|---------|-----------|----------|------------------------------|
| Fe 2p_{3/2} | | | | |
| pH 10 _(i) | 705.8 | 0.81 | 14.5 | Fe(II)-S |
| | 706.4 | 0.71 | 15.5 | Fe(II)-S |
| | 706.9 | 0.76 | 15.8 | Fe(II)-S |
| | 707.5 | 0.85 | 14.1 | Fe(II)-O |
| | 708.2 | 1.06 | 11.4 | Fe(III)-S |
| | 709.2 | 1.50 | 14.3 | Fe(III)-S |
| | 710.7 | 2.41 | 14.4 | Fe(III)-O |
| pH 4 _(a.a.t) | 706.3 | 0.84 | 13.1 | Fe(II)-S |
| | 707.0 | 0.72 | 12.6 | Fe(II)-S |
| | 707.6 | 0.80 | 13.5 | Fe(II)-O |
| | 708.3 | 1.01 | 12.1 | Fe(III)-S |
| | 709.2 | 1.27 | 14.1 | Fe(III)-S |
| | 710.4 | 1.71 | 17.9 | Fe(III)-O |
| | 712.0 | 2.75 | 16.5 | Fe(III)-O |
| S 2p | | | | |
| pH 10 _(i) | 160.7 | 0.55 | 10.9 | S ²⁻ |
| | 161.2 | 0.59 | 20.7 | S ²⁻ |
| | 161.7 | 0.73 | 25.6 | S ²⁻ |
| | 162.4 | 0.93 | 24.1 | S ²⁻ |
| | 163.2 | 1.48 | 18.6 | S _n ²⁻ |
| pH 4 _(a.a.t) | 161.0 | 0.66 | 19.1 | S ²⁻ |
| | 161.6 | 0.72 | 25.0 | S ²⁻ |
| | 162.2 | 0.84 | 23.6 | S ²⁻ |
| | 162.9 | 1.00 | 23.3 | S ²⁻ |
| | 163.9 | 1.23 | 8.9 | S _n ²⁻ |

11.3.3.2 As(V)-contacted FeS

A 1 g/L of suspension of FeS containing 15.2 μM As(V) was initially adjusted to near pH 10 and then titrated with acid to near pH 4 and then with base to above pH 10. Figure 11.11 shows that removal of As(V) initially was low (20%) at pH 10, but as pH decreased, the removals gradually increased to about 80% near pH 4. This could be caused by formation of strongly bound surface species as pH decreased. The trend of As(V) removal shown in Figure 11.11 for decreasing pH was similar to that observed for As(V) on iron (hydr)oxides or pyrite (34, 217). As pH was increased back to the initial pH, arsenic was released to the solution between pH 5 and pH 7 and then additional removal occurred above pH 7. It is difficult to explain this behavior simply, but it is possible that surface reactions occurred that produced new compounds that determined arsenic binding as pH was increased. For example, at low pH, As(V) might be

reduced to As(III) by FeS along with oxidation of Fe or S, resulting in the formation of SO_4^{2-} and Fe(III). Formation of Fe(III) could lead to formation of sulfate green rust (GR- SO_4) or other oxidized products. If this occurred, interaction of arsenic with the GR- SO_4 surface could be important in determining soluble arsenic concentrations. Surface characterization using XPS might be able to provide evidence to evaluate this hypothesis.

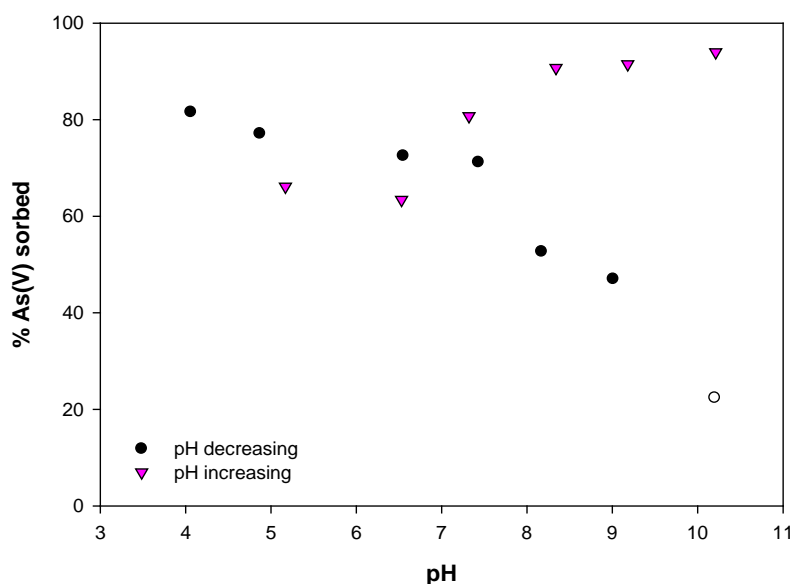


Figure 11.11 Effect of pH on removal of As(V) (15.2 μM) by FeS (1 g/L) as pH was decreased from pH 10 to pH 4 and then increased back to pH 10.

The solids in samples at pH 10_(i) and pH 4_(a.a.t) were analyzed using XPS. Figure 11.12 shows the As 3d XPS spectra of FeS reacted with As(V) at pH 4_(a.a.t), pH 10_(i), and pH 10_(f). As shown in the As 3d spectra of As(III)-contacted FeS (Figure 11.8), the spectra for As(V)-contacted FeS also exhibited a relatively large Fe 3p peaks near 55 eV. All of the peaks in the As 3d XPS spectra are of low intensity relative to Fe 3p peaks, because the As loading on solids was low, so determination of arsenic species on the surface is difficult. However, we can recognize that the main peaks of the As 3d spectra for the pH 10_(i) and pH 4_(a.a.t) are located near 46 eV,

which is representative of As(V), although there is a minor shift of As(V) peak to lower binding energy in the pH 4_(a.a.t) sample. In the case of pH 10_(t) sample, the occurrence of species that are more reduced than As(V) could not be totally ruled out, because a weak peak was observed at 43.77 eV, which is assigned to As(III). The additional removal of As(V) as pH increased could be explained by sorption of As(V) onto newly formed surface species or onto patches of oxidized products of FeS, such as GR-SO₄ or iron (hydro)oxides. To confirm this hypothesis, the Fe 2p_{3/2} and S 2p XPS spectra were obtained and evaluated.

Figure 11.13 indicated that surface Fe species on the three samples had not undergone appreciable surface oxidation, compared to pure FeS at pH 4 and 10. In contrast to the Fe 2p_{3/2} spectra, the S 2p spectra shows that the surface S species had experienced surface oxidation whenever pH was changed (Figure 11.14). Although removal of As(V) was initially low at pH 10, a peak associated with elemental sulfur (S⁰) was present and is evidence of surface oxidation. This suggests that surface S species are acting as sorbent/reactant for As(V), rather than the surface Fe species. Moreover, the extent of the surface S oxidation increased at lower pH, where removal of As(V) increased strongly. In addition to showing increased removal of As(V), the pH 10_(t) sample exhibited more oxidation of surface-bound S, as indicated by peaks associated with polysulfides (S_n²⁻) and elemental sulfur (S⁰) showing higher intensity. These results may be attributed not only to the simple chemical reaction between As(V) and the surface, but to the complicated interactions between As(V) itself or forms of reduced As and the FeS surface. It is possible that removal of As(V) is due at least in part to reaction of arsenic with newly formed surface species containing iron and sulfur.

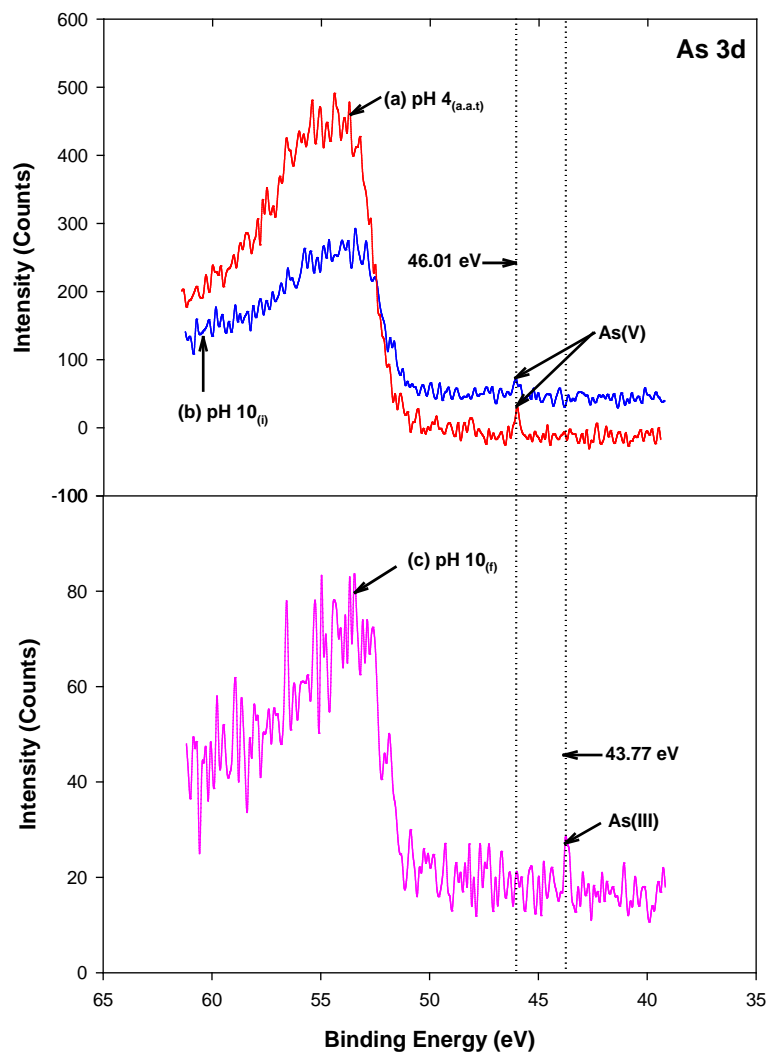


Figure 11.12 High resolution As 3d XPS spectra for pyrite after contact with As(V) (15.2 μM) at (a) pH 4_(a.a.t), (b) pH 10_(i), and (c) pH 10_(f).

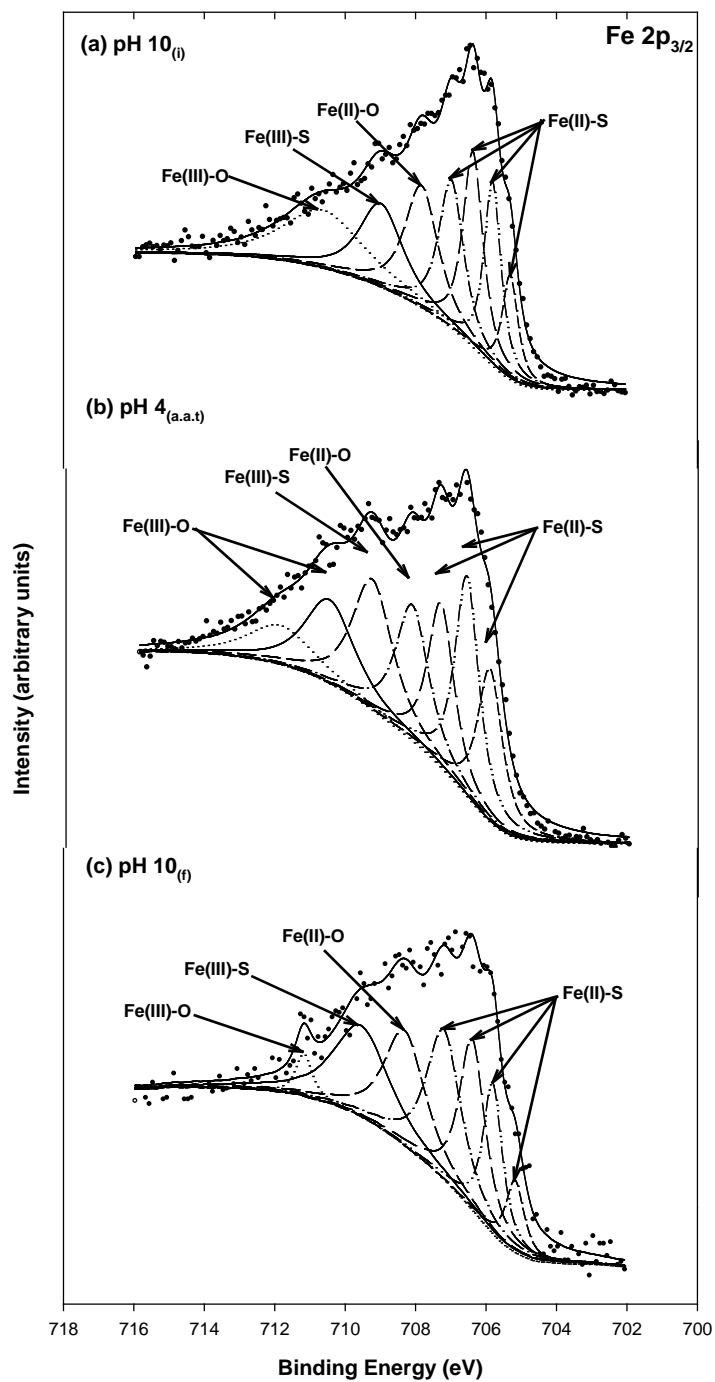


Figure 11.13 High resolution Fe 2p_{3/2} XPS spectra for pyrite after contact with As(V) (15.2 μM) at (a) pH 10_(i), (b) pH 4_(a.a.t), and (c) pH 10_(f).

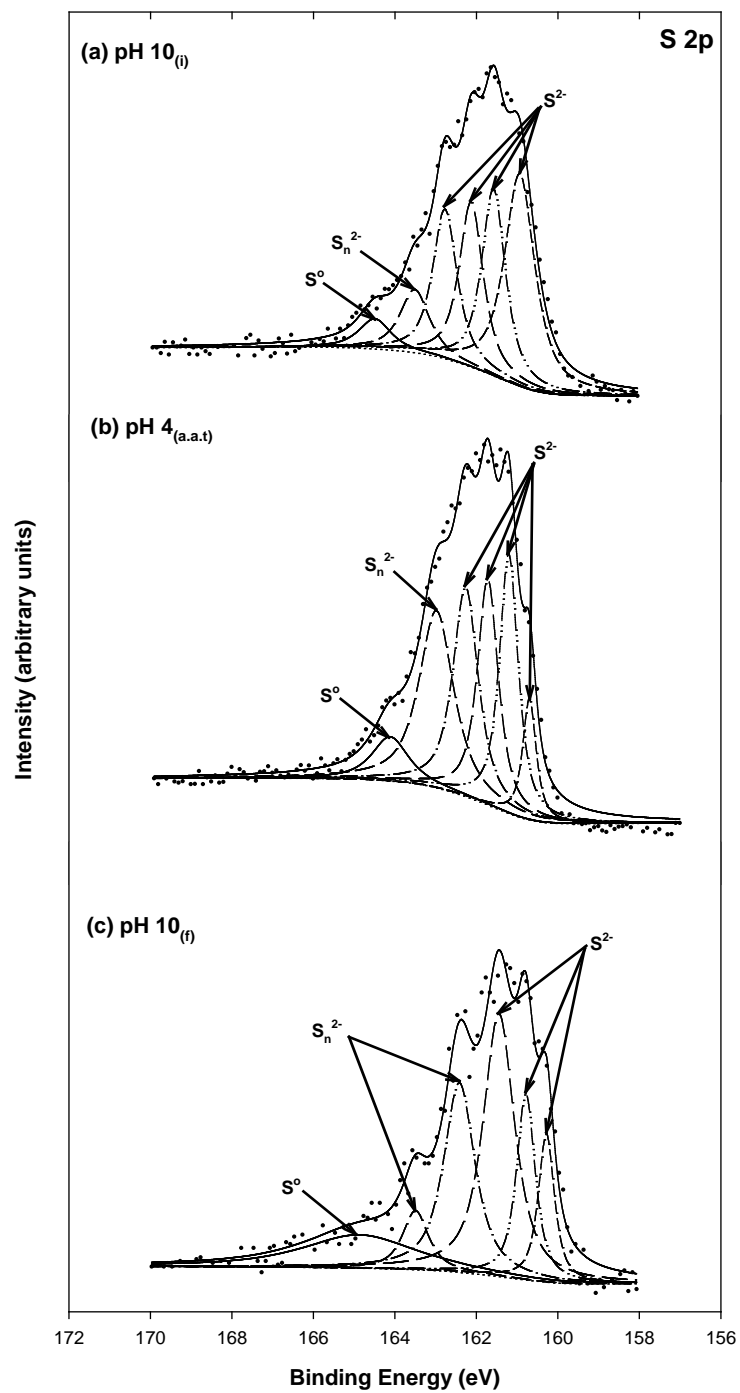


Figure 11.14 High resolution S 2p XPS spectra for pyrite after contact with As(V) (15.2 μ M) at (a) pH 10_(i), (b) pH 4_(a.a.t), and (c) pH 10_(f).

Table 11.7 Binding energies (BE), full width at half maximum (FWHM), and area percentage for peaks in the Fe 2p_{3/2} and S 2p XPS spectra for pyrite after contact with As(V) (15.2 μM) at pH 10_(i), pH 4_(a.a.t), and pH 10_(f).

| Samples | BE (eV) | FWHM (eV) | Area (%) | Chemical states |
|----------------------------|---------|-----------|----------|------------------------------|
| Fe 2p_{3/2} | | | | |
| pH 10 _(i) | 705.3 | 0.54 | 6.7 | Fe(II)-S |
| | 705.8 | 0.58 | 12.7 | Fe(II)-S |
| | 706.3 | 0.69 | 15.9 | Fe(II)-S |
| | 706.9 | 0.85 | 14.9 | Fe(II)-S |
| | 707.8 | 1.14 | 16.5 | Fe(II)-O |
| | 708.9 | 1.48 | 14.7 | Fe(III)-S |
| | 710.6 | 2.71 | 18.6 | Fe(III)-O |
| pH 4 _(a.a.t) | 705.9 | 0.84 | 12.6 | Fe(II)-S |
| | 706.6 | 0.82 | 17.7 | Fe(II)-S |
| | 707.3 | 0.89 | 14.5 | Fe(II)-O |
| | 708.1 | 1.13 | 15.0 | Fe(III)-S |
| | 709.3 | 1.35 | 17.1 | Fe(III)-S |
| | 710.5 | 1.68 | 13.9 | Fe(III)-O |
| | 711.8 | 2.29 | 9.11 | Fe(III)-O |
| pH 10 _(f) | 705.2 | 0.62 | 5.4 | Fe(II)-S |
| | 705.8 | 0.66 | 11.9 | Fe(II)-S |
| | 706.4 | 0.88 | 18.2 | Fe(II)-S |
| | 707.2 | 1.18 | 21.3 | Fe(II)-O |
| | 708.3 | 1.41 | 19.6 | Fe(III)-S |
| | 709.5 | 1.90 | 20.8 | Fe(III)-S |
| | 711.2 | 0.56 | 2.9 | Fe(III)-O |
| S 2p | | | | |
| pH 10 _(i) | 160.9 | 0.89 | 30.3 | S ²⁻ |
| | 161.5 | 0.69 | 20.8 | S ²⁻ |
| | 162.1 | 0.71 | 18.7 | S ²⁻ |
| | 162.7 | 0.71 | 17.1 | S ²⁻ |
| | 163.5 | 0.86 | 8.7 | S _n ²⁻ |
| | 164.5 | 0.93 | 4.5 | S ⁰ |
| pH 4 _(a.a.t) | 160.6 | 0.40 | 6.8 | S ²⁻ |
| | 161.2 | 0.55 | 20.1 | S ²⁻ |
| | 161.7 | 0.61 | 19.5 | S ²⁻ |
| | 162.2 | 0.74 | 21.9 | S ²⁻ |
| | 162.9 | 1.01 | 25.1 | S ²⁻ |
| | 164.1 | 1.07 | 6.6 | S ⁰ |
| pH 10 _(f) | 160.2 | 0.47 | 9.5 | S ²⁻ |
| | 160.7 | 0.55 | 13.8 | S ²⁻ |
| | 161.4 | 0.92 | 32.6 | S ²⁻ |
| | 162.4 | 0.91 | 23.3 | S ²⁻ |
| | 163.5 | 0.75 | 5.8 | S _n ²⁻ |
| | 164.8 | 3.30 | 14.9 | S ⁰ |

12. SORPTION OF MERCURY(II) TO ADSORBENTS/REACTANTS:

1. PYRITE (FeS_2)

Kinetics of removal of mercury was very rapid at lower ratios of mercury/pyrite. Concentrations of mercury in solution were below detection limits within 10 minutes. A mercury/pyrite ratio of 25 was necessary to obtain measurable concentrations. This behavior indicates that the kinetics were similar to what would be expected if external transport controls. Maximum loadings of mercury typically exceeded 6 mmol/g and in some cases exceeded 20 mmol/g. These loading mean that the mass of mercury removed exceeded the mass of pyrite present. The pH of the solution did not appear to have a major effect on the extent of removal. However, there was a substantial amount of variability within the results of experiments at different pH. Exceptionally high removals of mercury could be the result of surface reactions and differences in removal could be the result of how fast these reactions occur at different pH. If experiments were conducted over longer time periods that would allow for initiation of surface reactions in all systems, then these differences would tend to decrease. Sulfate was observed to have little effect on removal of mercury by pyrite over the concentration range that was investigated (0 – 10 mM). XPS analysis of pyrite after contact with Hg(II) after 30 days showed evidence of Hg(II) reduction to Hg(I), coupled with oxidation of surface Fe(II) species, but no evidence of changes in oxidation state of surface sulfur was observed. Stability tests for mixtures of Hg and pyrite were conducted at two initial concentrations of Hg(II). Nearly complete removal (>98%) was observed in all samples when the initial concentration was low. XPS analysis provided some evidence of mercury reduction and iron oxidation on the surface. When the initial concentration was high, low removal was observed at low pH, high removal at pH in the range pH 4 – pH 6, and moderate removal at higher pH. Good stability was observed when pH was reduced. XPS analysis showed evidence of mercury reduction and good evidence of iron

oxidation and formation of sulfur species that support formation of precipitates such as HgS or Hg₂S.

12.1 Introduction

Increased concern is being shown for contamination of mercury in surface water, groundwater, and soils because it is highly toxic, non-biodegradable, and can exist in various forms even at very low concentrations. Exposure to high levels of metallic, inorganic or organic mercury can cause impairment of pulmonary and kidney function, inhibition of enzyme activity and cell damage (72). Furthermore, EPA has determined that mercury is a possible carcinogen. Mercury contamination in water and the atmosphere is usually caused by anthropogenic activity such as discharges from industrial operations such as sulfide ore roasting and manufacture of electrical and electronics materials, paints, fungicides, chlorine, pharmaceuticals, and pulp and paper. Furthermore, mercury release due to the increased use of coal in thermo-electric power plants is becoming a serious problem in the U.S., accounting for approximately 1 % of the total global mercury emissions (44-75 tons/yr) (86, 265, 266). This high level of emission is driving more stringent effluent discharge criteria. Elemental mercury (Hg⁰), oxidized mercury (Hg⁺ or Hg²⁺), and particulate mercury are the three forms of mercury that are usually released from power plants (266). Under anoxic conditions, mercury can be methylated by the mediation of sulfate reducing bacteria (SRB). Methyl mercury (MeHg) can be a serious hazard to fish, because it is poisonous and it accumulates in their tissues. Therefore, to avoid formation of methylated mercury, appropriate pretreatment is required to remove mercury before the discharges are released into the environment. In addition, elemental mercury (Hg(0)) can be formed by biological action, but it is expected to volatilize if it is produced (76, 77). Under reducing conditions, soluble complexes such as Hg(HS)₂, HgS₂H, HgS₂²⁻ are primarily formed, whereas under oxic conditions, Hg(II) tends to form soluble complexes with chloride or

hydroxide, or solid phases such as $\text{HgCl}_{2(s)}$ or $\text{Hg}(\text{OH})_{2(s)}$ (76, 78).

Oxides and hydroxides have been widely used to remove Hg(II) by adsorption (92, 267, 268). However, their sorption capacities are lower than that of iron sulfides. For example, mercury loadings on biogenic FeS particles were found to be as high as 0.66 Hg/g FeS (0.29 mole/mole) and if Hg(II) reacts with iron sulfides, formation of HgS could lead to much lower mercury concentrations in solution (84, 87, 88, 92). According to Pearson's hard and soft acid-base theory, it is generally known that Hg(II) has a high affinity for ligands containing reduced sulfur, because Hg(II) is a soft Lewis acid that will react strongly with a soft Lewis base, such as a thiol functional groups (269). So, the formation of insoluble solid phase (HgS) with sulfide has been the basis for the most common treatment method for removing mercury from industrial wastewaters, such as those at chlor-alkali plants (85, 270). It can typically achieve effluent concentrations in the range between 10 and 100 $\mu\text{g/L}$. X-ray photoelectron spectroscopy (XPS) studies on interactions between Hg(II) and pyrite demonstrated that high sorption is caused by the formation of weakly or strongly bound species including Hg-chloro and Hg-sulphydryl complexes rather than HgS(s) (11, 92-94). Bower et al (2008) conducted experiments on removal of Hg(II) by pyrite in batch and column systems (11). XPS analyses indicated that during aging over two weeks at low pH, an ordered monolayer of mono-dentate Hg-Cl complexes was formed on the pyrite surface. In studies with columns packed with mixtures of pyrite and pure quartz sand, a great retardation of Hg(II) was observed, although the system was exposed to oxygen (11). More recently, mesoporous silica molecular sieves functionalized with thiol/mercaptan or sulfur impregnated activated carbons also have been used to enhance removal of Hg(II) from water (83, 271-273). Moreover, the fact that Hg(II) has a strong affinity towards S, N, and O has driven development of chelating resins with those elements in functional groups (265, 274).

Although many researchers have shown that iron sulfides contacted with Hg(II) can

lead to stable solid phases, they are only focusing on estimation of sorption capacity of the adsorbent for Hg(II) (12, 92-94). In this study, mechanisms for surface reaction based on spectroscopic analysis will be presented to better understand Hg sorption on and reaction with iron sulfides.

12.2 Materials and Method

12.2.1 Materials

All reagents were prepared by dissolving chemicals with analytical-grade quality or better into deionized/deoxygenated (DI/DO) water. HgCl₂ (Sigma-Aldrich) was used to prepare the mercury stock solution and its concentration was below 1.3 mM to avoid HgO_(s) precipitation at basic pH. Prior to conducting experiments, all experimental supplies were equilibrated with the atmosphere in an anaerobic chamber (5 % H₂/95 % N₂). Pyrite was synthesized by mixing equal volumes of two solutions: 0.1 M ferric chloride (FeCl₃·6H₂O) and 0.2 M sodium hydrosulfide (NaHS·xH₂O). The detailed procedure for pyrite synthesis was discussed in Section 5. The pH was measured using a pH meter (Thermo Scientific) calibrated with three pH standard buffer solutions (pH 4, 7, 10). The specified pH was maintained with pH buffers such as MOPS (4-morpholinepropanesulfonic acid), boric acid, and CAPS (3-cyclohexylaminon-1-propane-sulfonic acid).

12.2.2 Kinetics

Three tests were conducted at pH 7 with three different initial concentrations of mercury and doses of pyrite (100 μM Hg with 1 g/L FeS₂; 250 μM Hg with 0.5 g/L FeS₂; 500 μM Hg with 0.2 g/L FeS₂). Pyrite suspensions in 0.02 M MOPS were prepared in the 250 ml reaction vessels. Reactions were initiated by adding Hg(II) standard solution in pyrite suspension. The suspension was mixed by an end-over-end rotary mixer until specified sampling time. A 10-

mL aliquot was sampled from the suspension at reaction times of 2, 5, 10, 15, 20, 30, 40, 60, 90, 120, 180, 240, 360, 720, 1440 min. The samples were immediately filtered using 0.02- μ m anodisc membrane filters and the filtrates were stored in an anaerobic chamber until analysis. The percentage of Hg(II) removed was calculated by the following equation:

$$\% \text{ Hg sorbed} = \frac{(\text{Hg}_{\text{initial}} - \text{Hg}_{\text{specific time}})}{\text{Hg}_{\text{initial}}} \times 100 \quad (12.1)$$

where $\text{Hg}_{\text{initial}}$ and $\text{Hg}_{\text{specific time}}$ are concentrations of mercury initially and at a specific sampling time.

12.2.3 Sorption/Reaction Experiments

Removal tests for mercury removal by pyrite were conducted in a similar manner, but were adjusted with higher Hg/pyrite ratios to account for the high affinity of mercury for the pyrite surface. A pyrite dose of 0.15 g/L was used with five initial concentrations of mercury (50, 100, 250, 500, and 1000 μ M). A 24 hour reaction time was used and pH was maintained by 0.02 M buffer solutions (pH 7 and pH 8 with MOPS; pH 9 with Borate; pH 10 with CAPS). Experiments to determine the effect of sulfate on mercury removal were conducted similarly at pH 8 and at three sulfate concentrations (0, 1, 10 mM).

12.2.4 Stability of Hg(II)-Contacted Pyrite

A series of experiments to evaluate the effect of pH on removal of Hg(II) by pyrite were conducted using similar procedures as used for selenium and arsenic (Sections 6 and 11). Since chloride ion can affect the sorption behavior of Hg(II) by formation of soluble complexes, HNO_3 was used as an acid to adjust pH. A 1-g/L suspension of pyrite was initially adjusted to the initial pH value and was allowed to equilibrate for 30 minutes. Then, Hg(II) stock solution was added to the suspension to create mercury concentrations of either 6.48 μ M (low $[\text{Hg(II)}]/[\text{pyrite}]$) or 1

mM (high [Hg(II)]/[pyrite]). For low [Hg]/[pyrite], pH was initially adjusted to pH 3.4 and the system was allowed to react for 30 minutes before taking samples of the liquid and solid phases. The suspension was then titrated with base in a series of steps until pH 10 was reached. The suspension was then titrated with acid in a series of steps that stopped near pH 3.4. After 30 minutes at each pH, samples were taken and filtered. The filtered solutions were analyzed by AAS for Hg(II) concentration. The filtered wet solids from samples at pH 3.4 (initial sample) and pH 10 were used for surface analysis (SEM, EDS, XPS). Herein, samples will be identified with the following nomenclature to simplify the discussion. The initial sample at pH 3.4 will be named the “pH 3.4_(i)” sample and the sample at pH 10 after base titration will be named the “pH 10_(a.b.t)” sample. Another stability test was conducted at high [Hg(II)]/[pyrite] in a similar way, but the initial pH was pH 2.4. The nomenclature of samples were named by similar pattern at low [Hg(II)]/[pyrite]. All samples were stored before spectroscopic analysis and AAS measurement in an anaerobic chamber to prevent any change in the oxidation state of mercury.

12.2.5 Spectroscopic Analyses

The solid surfaces were characterized by spectroscopic techniques including scanning electron microscopy (SEM) equipped with an energy dispersive spectrometer (EDS) and X-ray photoelectron spectroscopy (XPS). The morphologies of pyrite particles reacted with Hg(II) were analyzed using SEM (JEOL JSM-6400) and the elemental composition of the pyrite surface was determined by SEM-EDS. Prior to SEM analysis, the solid samples were coated with Pd/Au through a vacuum-sputtering technique to reduce surface electrical charge. The secondary SEM images were collected at a working distance 39 or 15 mm under an acceleration voltage of 15 kV and a magnification range of 10 to 300,000 \times . Elements (Fe, S, O, Hg, Pd, Au) were chosen by EDS analysis program (Spirit V.107). The oxidation states of pyrite after contact with Hg(II) as well as surface Hg were investigated using a Kratos Axis Ultra Imaging XPS with a

monochromatic Al K α X-rays. The narrow scans for Fe 2p, O 1s, C 1s, S 2p and Hg 4f were recorded with pass energy of 40 or 20 eV. The charge effect was corrected using the spectra peak of C 1s at 284.5 ± 0.1 eV as reference. All peaks were fitted using a XPSPEAK41 fitting program with Gaussian Lorentzian function through background-subtraction corrections using a Shirley-type optimization.

12.2.6 Measurement of Aqueous Concentration

A Cold Vapor Atomic Absorption Spectrometry method was adopted for use to analyze mercury. It was similar to that used for analysis of arsenic, but the VP90 "T" cell was replaced with a 15 cm quartz cell. Mercury was reduced by borohydride (1% NaBH₄ in 0.05% NaOH) to the elemental form and was removed by purging. The following parameters were used during analysis: wavelength of 253.7 nm, band pass of 0.5 nm, lamp current of 75%, measurement number of 4, measurement time of 4 s, background correction is off, stabilization time of 60 s, baseline delay time of 60 s, carrier gas flow of 240 mL/min. The average recovery (accuracy) was 102.5 % and the relative standard deviation (precision) was 0.56 %. The average method detection limit (MDL) for mercury was 0.002 μ M.

12.3 Results and Discussion

12.3.1 Kinetics

Figure 12.1 shows the effect of contact time on Hg(II) (100, 250, 500 μ M) removal by pyrite (0.2, 0.5, 1 g/L). At low mercury/pyrite ratios (100 μ mol/g, 500 μ mol/g), very fast removals were observed with concentrations below detection limits within 5 minutes whereas at the higher mercury/pyrite ratio (2500 μ mol/g) a biphasic sorption behavior was observed and nearly complete removal occurred after 180 minutes. In addition, the effects of kinetics (how fast

q increased) and equilibrium (how high q would become after a sufficiently long time) were described using a general model that assumed sorption phenomenon occurred at two types of sites (fast-reacting sites and slow-reacting sites). The kinetic model equations and solving routines were described in Sections 10 and 11. Table 12.1 displays all of model parameters that were calculated by nonlinear regression. At all mercury/pyrite ratios, the values of sorption parameters associated with fast-reacting sites (k_f , $q_{f,max}$) were much larger than the coefficients for slow-reacting sites, except the values of $q_{f,max}$ and $q_{s,max}$ at high Hg/pyrite (2500 $\mu\text{mol/g}$) were about the same. This indicates that the biphasic kinetic behavior was more evident at higher mercury/pyrite ratio (2500 $\mu\text{mol/g}$). This behavior can be caused by fast external transport and slow subsequent surface reaction.

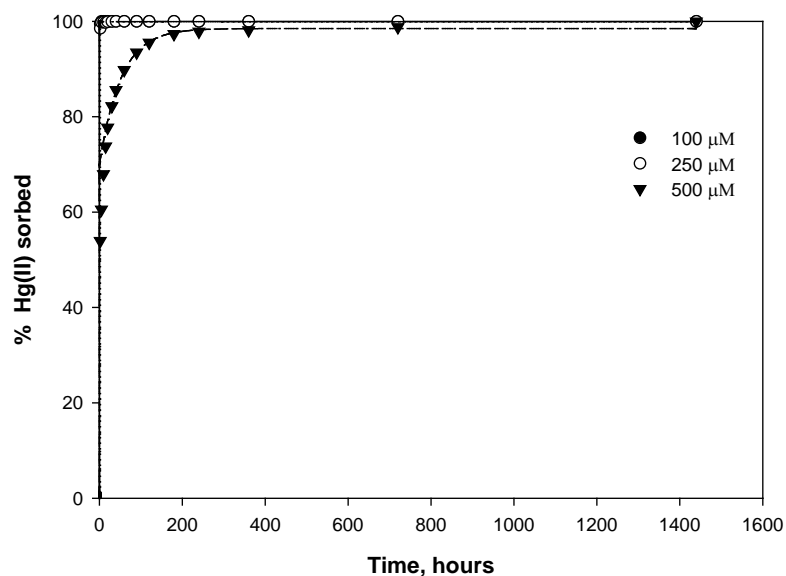


Figure 12.1 Removal of Hg(II) as a function of time at pH 7 (initial concentration = 100, 250, 500 μM , pyrite dose = 1, 0.5, 0.2 g/L).

Table 12.1 Calculated parameters of the kinetic model for Hg(II) uptake by pyrite at pH 7.

| [Hg(II)]/pyrite dose | Parameters | | | | |
|----------------------|--|----------------------------|--|--|-------|
| | k_f (min ⁻¹) | k_s (min ⁻¹) | $q_{f,max}$ (μmol/g) | $q_{s,max}$ (μmol/g) | *GFP |
| 100 μmol/g | 150±1.3×10 ⁷ | 1.79±7.5 ×10 ³ | 497±82 | 3.0±83 | 0.001 |
| 500 μmol/g | 147±5.2×10 ⁴ | 0.15±11.5 | 1.2×10 ³ ±2.0×10 ² | 19.0±232 | 0.002 |
| 2500 μmol/g | 1.0×10 ⁶ ±1.0×10 ⁷ | 0.04±0.05 | 1.4×10 ³ ±5.0×10 ² | 1.1×10 ³ ±3.0×10 ³ | 0.02 |

* Goodness of fit parameter (GFP) = $\frac{\sqrt{SSR/(n-2)}}{\bar{q}}$ where SSR is sum of squared residual, n is the number of data points,

\bar{q} is average value of the concentration of As on pyrite

12.3.2 Nonlinear Removal Patterns

12.3.2.1 Effect of pH

Figure 12.2 shows results of experiments to characterize removal of mercury by pyrite over a range of pH values. Table 12.2 provides all of the parameters for the Langmuir, Freundlich and BET models that were calculated by nonlinear regression. Based on values of GFP (goodness of fit parameters), the BET model provided the best fits to experimental data at pH 9 and 10. The ability of the BET model to fit the data indicates that surface reactions between Hg(II) and the pyrite surface were important in these systems. However, the data at pH 7 and pH 8 was better described by Freundlich isotherm, as indicated by GFP values. Other studies have reported that the maximum sorption capacity of pyrite for Hg(II) varied with solution conditions. For example, Bower (2008) found that sorption maxima were 6.1 μmol/g, 9.9 μmol/g, and 17.4 μmol/g at pH 4.1, 6.4 and 10.4, while Behra (2001) reported a maximum value above 10 μmol/g at pH > 4 (11, 92). However, much greater sorption was observed in this study, by at least two orders of magnitude. In addition, the optimum pH range was observed to differ. Bower (2008) and Behra (2001) found that increased removal occurred at higher pH, while lower pH was to give higher removal in this study (11, 92). This discrepancy regarding sorption capacity and optimum pH range might be caused by the different origin of pyrite. Bower and Behra used

pyrite that was a natural mineral and it could have lower surface area and more impurities.

Natural pyrite has been reported to contain about 3 % impurities, mostly silica (11, 92).

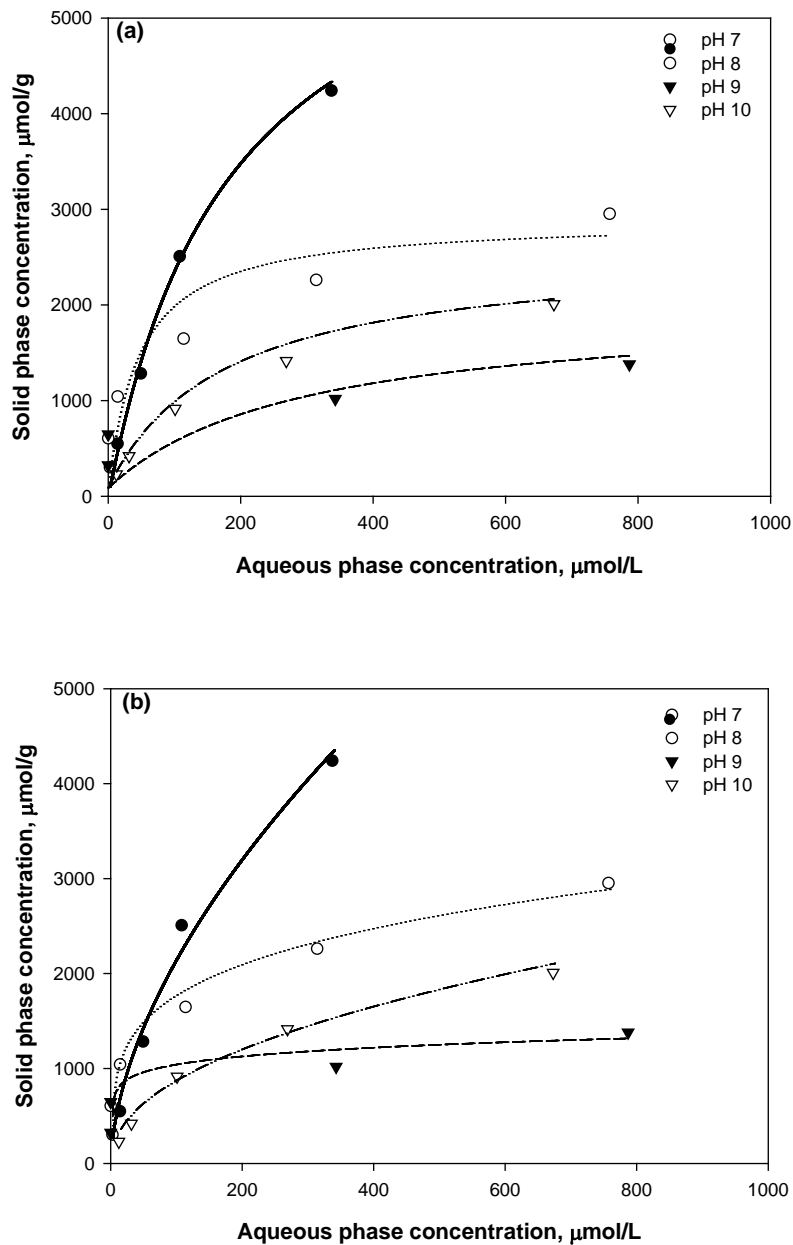


Figure 12.2 Measured concentrations of Hg(II) on pyrite as function of concentration in water with (a) Langmuir, (b) Freundlich, (c) BET models (lines) fitted to data (symbols) at various pH.

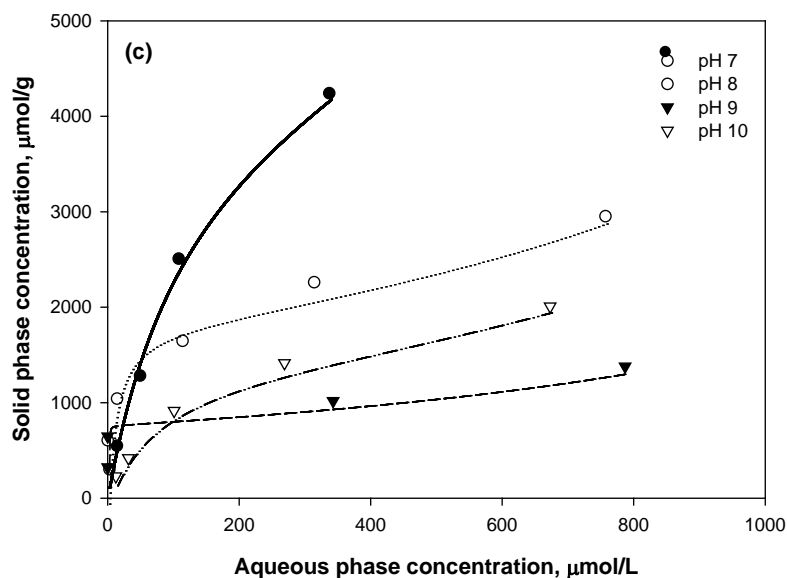


Figure 12.2 Continued.

Table 12.2 Parameters of models describing removal of Hg(II) by pyrite as affected by pH.

| Models | pH | | | |
|--|---------------------------------------|---------------------------------------|---------------------------------------|---|
| | pH 7 | pH 8 | pH 9 | pH 10 |
| Langmuir | | | | |
| b (L/μmol) | 5.6×10^7 | 0.02 ± 0.06 | $3.5 \times 10^{-3} \pm 6.22$ | $5.7 \times 10^{-3} \pm 2.9 \times 10^{-7}$ |
| q_{\max} (μmol/g) | $6.5 \times 10^3 \pm 1.8 \times 10^3$ | $2.8 \times 10^3 \pm 1.7 \times 10^3$ | $1.8 \times 10^3 \pm 9.3 \times 10^2$ | $2.5 \times 10^3 \pm 4.0 \times 10^2$ |
| GFP | 0.48 | 0.28 | 0.64 | 0.23 |
| Freundlich | | | | |
| k_f (μmol $^{1-1/n}$ ·L $^{1/n}$ /g) | 152 ± 133 | 569 ± 365 | 587 ± 513 | 96.1 ± 71.9 |
| n | 1.74 ± 0.49 | 4.12 ± 1.86 | 8.64 ± 11.7 | 2.12 ± 0.57 |
| GFP | 0.26 | 0.11 | 0.21 | 0.18 |
| BET | | | | |
| A | 17.6 ± 10.2 | 172 ± 449 | 844 ± 156 | 28.2 ± 9.2 |
| q_{\max} (μmol/g) | $4.5 \times 10^3 \pm 1.0 \times 10^3$ | $1.9 \times 10^3 \pm 5.0 \times 10^2$ | $1.8 \times 10^4 \pm 2.8 \times 10^4$ | $1.4 \times 10^3 \pm 1.0 \times 10^2$ |
| GFP | 0.38 | 0.21 | 0.17 | 0.07 |

12.3.2.2 Effect of Sulfate Concentrations

Figure 12.3 shows results of experiments to determine the effect of sulfate (1, 10 mM) on removal of mercury by pyrite at pH 8. Sulfate appears to have a little effect on mercury removal at lower aqueous-phase concentrations of mercury. However, the amount of mercury

removed per unit mass of pyrite in the presence of 10 mM sulfate continues to increase with increasing aqueous concentration of Hg. This indicates that the presence of higher concentrations of sulfate promote Hg removal, possibly by forming surface compounds that are mixtures of pyrite, mercury, and sulfate. However, the pyrite surface that reacted with mercury might be heterogeneous, including sulfate green rust ($\text{Fe}_4^{\text{II}}\text{Fe}_2^{\text{III}}(\text{OH})_{12}(\text{SO}_4)$), iron (hydr)oxides, or other surface precipitates. Such species could be formed by redox reactions, but it cannot be assured. To confirm the identity of any solid products formed on the surface, additional surface analyses are required.

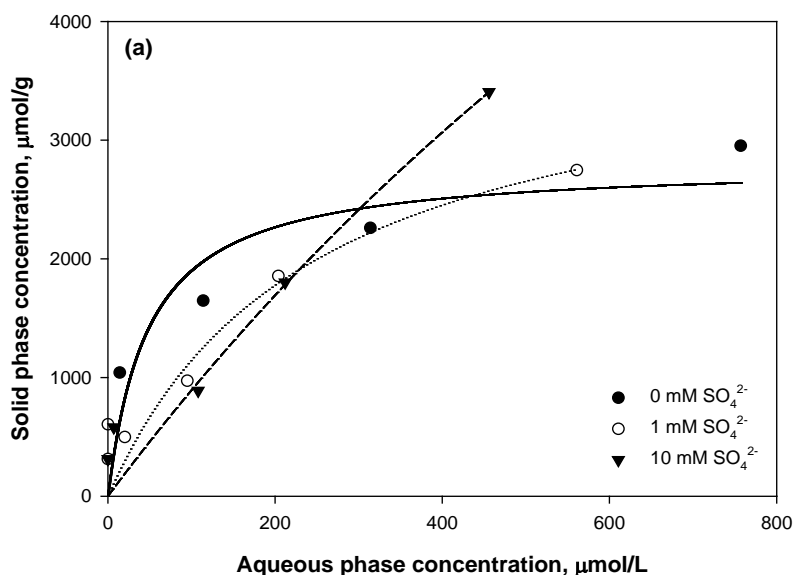


Figure 12.3 Measured concentrations of Hg(II) on pyrite as function of concentration in water with (a) Langmuir, (b) Freundlich, and (c) BET models (lines) fitted to data (symbols) at various concentrations of sulfate.

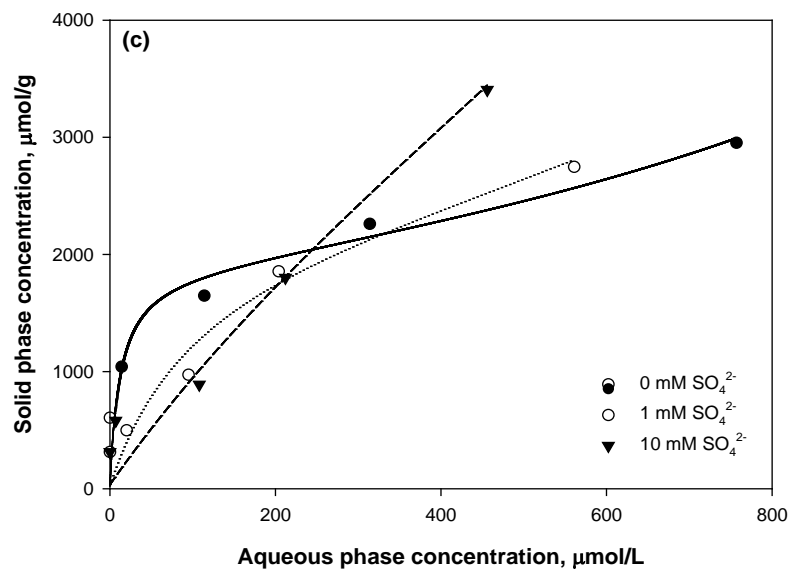
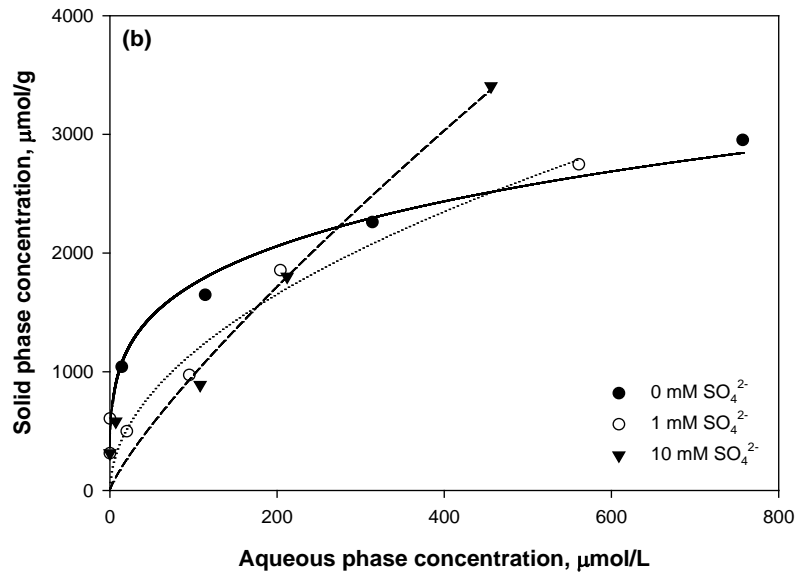


Figure 12.3 Continued.

Table 12.3 Parameters of models describing removal of As(III) by FeS as affected by sulfate concentration.

| SO ₄ ²⁻ (mM) | <i>Langmuir</i> | | | <i>Freundlich</i> | | | <i>BET</i> | | |
|---------------------------------------|--|--|------|--|-------------|------|--|----------|------|
| | b (L/μmol) | q _{max} (μmol/g) | GFP | K _f (μ ^{mol^{1-1/n}·L^{1/n}/g)} | n | GFP | q _{max} (μmol/g) | a | GFP |
| 0 | 0.02±0.06 | 2.8×10 ³ ±1.7×10 ³ | 0.28 | 569±365 | 4.12±1.86 | 0.11 | 1.9×10 ³ ±5.0×10 ² | 172±449 | 0.21 |
| 1 | 4.0×10 ⁻³ ±1.6×10 ⁻³ | 3.9×10 ³ ±2.4×10 ³ | 0.38 | 113 ± 179 | 1.97 ± 1.05 | 0.25 | 2.2×10 ³ ±9.0×10 ² | 18.7±26. | 0.25 |
| 10 | 5.8×10 ⁻⁴ ±3.2×10 ⁻³ | 1.6×10 ⁴ ±7.5×10 ⁴ | 0.26 | 22.1 ± 77.2 | 1.21 ± 0.85 | 0.24 | 4.7×10 ³ ±5.4×10 ³ | 4.27±10. | 0.26 |

12.3.3 Surface Characterization for Hg(II)-Contacted Pyrite

12.3.3.1 XPS Study

Figure 12.4 shows the Hg 4f XPS spectra for pyrite after contacted with Hg(II) for various times. The Hg 4f spectra were fitted with two peaks (Hg 4f_{7/2} and 4f_{5/2}) separated by a spin orbit splitting of 4.0 eV. The binding energy of the Hg 4f_{7/2} peak was observed to be centered in the range from 100.5 to 100.7 eV, which is attributed to the peaks associated with Hg(II) and Hg(I) (92). This can be compared to the binding energy for elemental mercury that is between 99.2 and 99.8 eV. Therefore, it is possible that a conversion occurred, but it is unlikely that it was reduced to Hg(0). In addition, Ehrhardt et al. (2000) reported that the broadening of Hg 4f_{7/2} peaks is associated with the existence of a multiplicity of sorption sites (93). Since Figure 12.4 shows that the 4f_{7/2} peak becomes broader at longer times, this may indicate that different sites are being formed. Ehrhardt et al. (2000) also reported that Hg 4f peaks caused by Fe(III) oxyhydroxides are centered at 103.8 eV (93). However, such peaks are not shown in Figure 12.4, even though the Fe 2p_{3/2} spectra showed the presence of Fe(III)-O peaks after contact with Hg(II) (Figure 12.5).

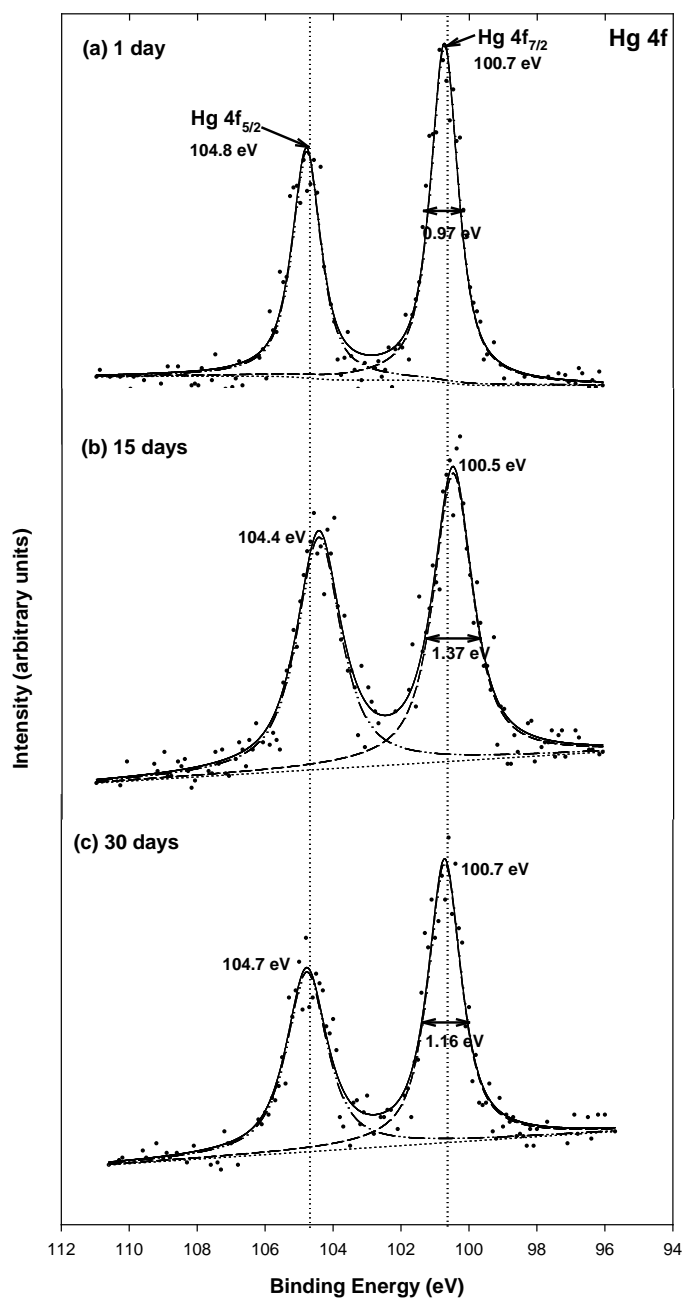


Figure 12.4 High resolution Hg 4f XPS spectra for synthetic pyrite (1 g/L) reacted with 200 μM Hg(II) at pH 8 for various times: (a) 1 day, (b) 15 days, (c) 30 days.

Figure 12.5 shows the Fe $2p_{3/2}$ XPS spectra for pyrite after contact with Hg(II) for various times. After contact with Hg(II), the Fe $2p_{3/2}$ spectra comes to have more peaks at higher binding energies and these peaks represent Fe(III)-S and Fe(III)-O species. In addition, the intensities of those peaks increase with reaction time. The formation of these Fe(III) species is probably caused by reactions between surface Fe(II) and Hg(II) ions that would produce reduced species such as Hg(I). The Hg 4f spectra showed a peak that could include Hg(I) (Figure 12.4). The Fe(III)-O species produced on the surface could exist as Fe(III) oxyhydroxides and differential charge effects could occur due to the formation of heterogeneous surfaces. The confirmation of these charge effects is important, because these Fe(III) species play an important role in catalyzing oxidation processes (references given in Behra et al. 2001) (275). Behra et al. (2001) provided the evidence for existence of charge effects on a pyrite surface after contact with Hg(II) through the investigation of O 1s XPS spectrum (92).

Figure 12.6 shows S 2p spectra of pyrite after contact with Hg(II) for various times. These spectra were fitted with a single doublet (S $2p_{1/2}$ and S $2p_{3/2}$) separated by 1.2 eV that represents an S_2^{2-} species. Contact with Hg(II) does not appear to cause any important changes in oxidation state of sulfur sites on pyrite, which is in agreement with the results obtained by others (94). These results indicate that sulfur on the surface does not participate in redox reactions of Hg(II) sorbed onto pyrite during the 30-day contact time.

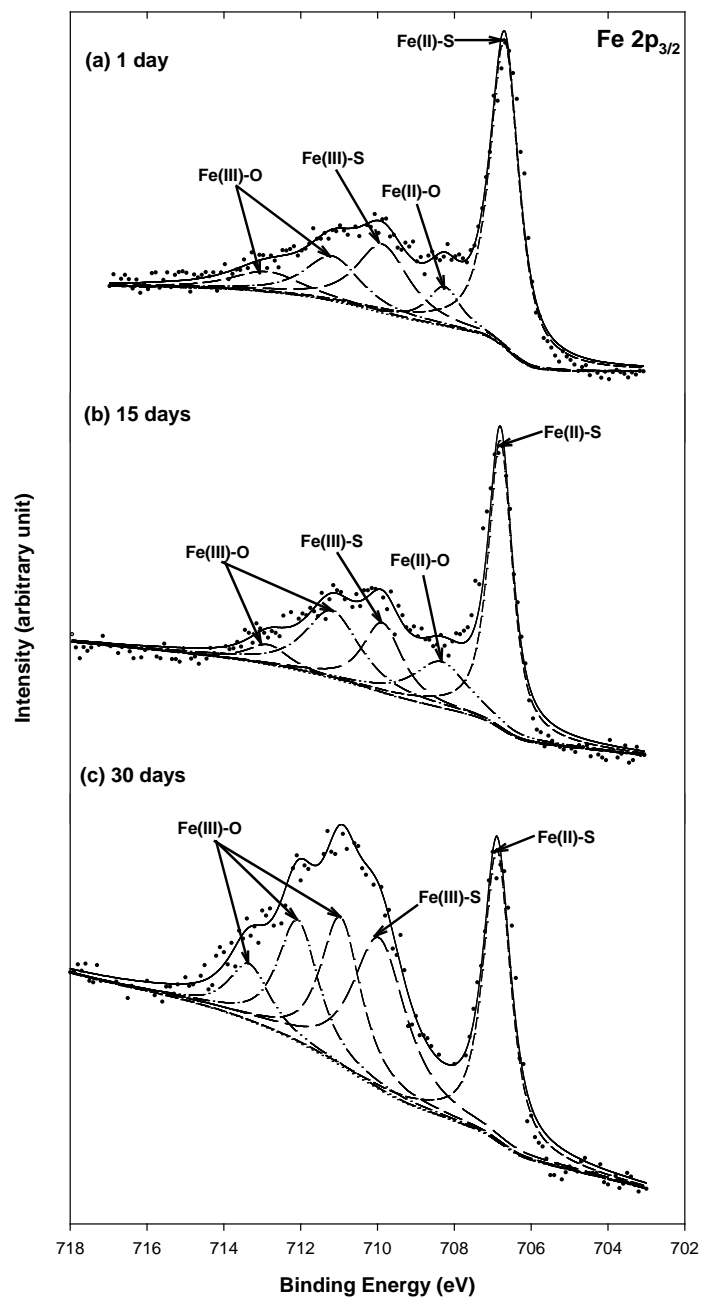


Figure 12.5 High resolution Fe 2p_{3/2} XPS spectra for synthetic pyrite (1 g/L) reacted with 200 μM Hg(II) at pH 8 for various times: (a) 1 day, (b) 15 days, (c) 30 days.

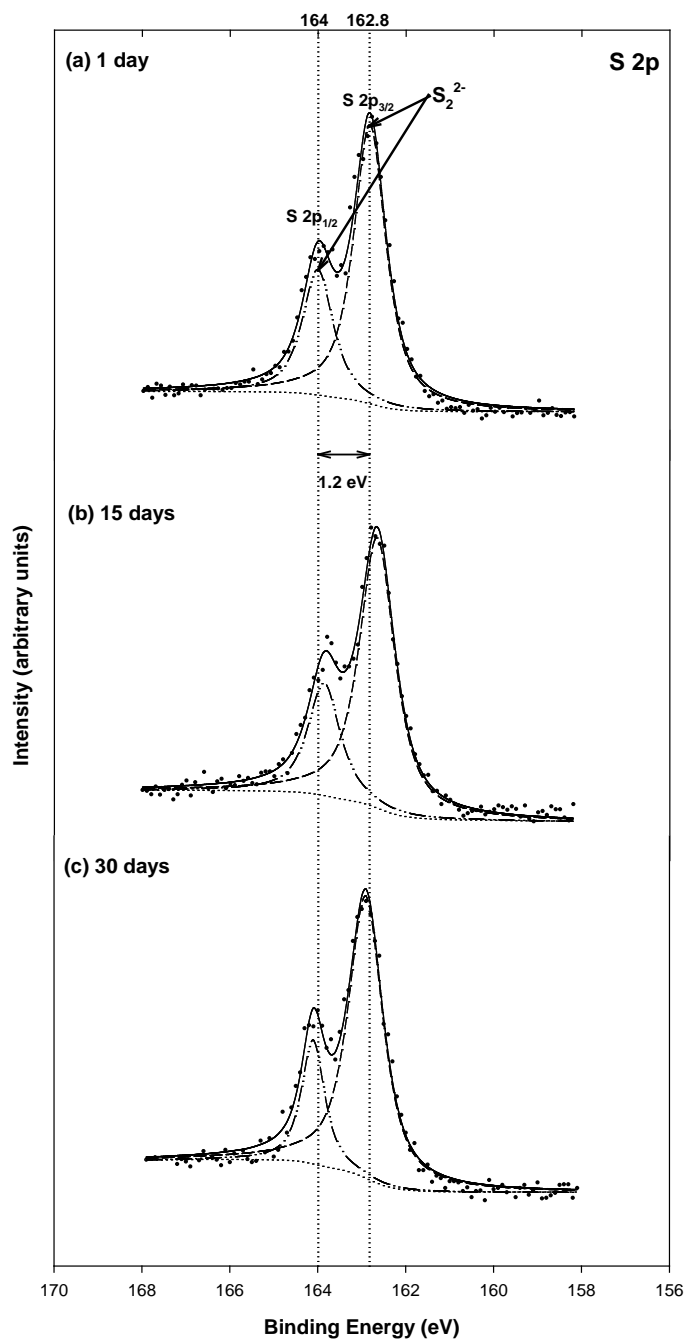


Figure 12.6 High resolution S 2p XPS spectra for synthetic pyrite (1 g/L) reacted with 200 μM Hg(II) at pH 8 for various times: (a) 1 day, (b) 15 days, (c) 30 days.

Figure 12.7 shows the O 1s XPS spectra for pyrite after contact with solutions of Hg(II) for various times. The O 1s spectra display three peaks located at approximately 531.0, 531.5, 532.6 eV, corresponding to O²⁻, OH⁻ and molecular H₂O environments, respectively. Ehrhardt et al. (2000) showed that in addition to the H₂O peak at 532.6 eV, there is an extra peak located near 535.0 eV that is caused by the sorption of water molecules onto isolated islands of Fe(III) oxyhydroxide, which results in a differential charge effect (93). However, Figure 12.6 does not show those peaks at any contact time. These results indicate that even though Fe(III) species are observed, the formation of isolated islands of Fe(III) oxyhydroxide overlayer on the pyrite surface could be neglected. Tables 12.4 – 12.6 show the binding energies (BE), full width at half maximum (FWHM), and relative area for peaks in the Hg 4f_{7/2}, Fe 2p_{3/2} and O 1s XPS spectra of pyrite contacted with Hg(II) for various times.

Table 12.4 Binding energies (BE), peak full width at half maximum (FWHM), peak area percentage for Hg 4f_{7/2} XPS spectra of pyrite contacted with Hg(II) for various times and for reference materials.

| Samples | Contact time (days) | χ^2 | BE (eV) | FWHM (eV) | Chemical states |
|---------------------------------|---------------------|----------|---------------|-----------|-----------------|
| Pyrite+Hg(II) | 1 | 3.90 | 100.7 | 0.97 | Hg(I)/Hg(II) |
| | 15 | 3.90 | 100.5 | 1.37 | Hg(I)/Hg(II) |
| | 30 | 3.91 | 100.7 | 1.16 | Hg(I)/Hg(II) |
| Hg(0) | - | - | 99.2 ~ 99.8 | - | Hg(0)(276, 277) |
| Hg ₂ Cl ₂ | - | - | 100.8 ~ 101.0 | - | Hg(I)(276, 277) |
| HgS | - | - | 100.0 ~ 100.9 | - | Hg(II)(94, 276) |
| HgCl ₂ | - | - | 100.8 ~ 101.6 | - | Hg(II)(276) |

Table 12.5 Binding energies (BE), full width at half maximum (FWHM), and area percentage for peaks in the Fe 2p_{3/2} XPS spectra of pyrite contacted with Hg(II) for various times.

| Sample | Contact time (day) | BE (eV) | FWHM (eV) | Area (%) | Chemical |
|-----------------|--------------------|---------|-----------|----------|-----------|
| Pyrite | 0 | 706.8 | 0.86 | 72.4 | Fe(II)-S |
| | | 708.3 | 1.66 | 14.2 | Fe(III)-S |
| | | 710.4 | 2.09 | 13.4 | Fe(III)-O |
| Pyrite + Hg(II) | 1 | 706.7 | 0.89 | 50.1 | Fe(II)-S |
| | | 708.2 | 1.04 | 7.4 | Fe(II)-O |
| | | 709.8 | 1.62 | 20.2 | Fe(III)-S |
| | | 711.1 | 1.72 | 14.1 | Fe(III)-O |
| | | 712.8 | 2.19 | 8.1 | Fe(III)-O |
| | 15 | 706.8 | 0.74 | 41.2 | Fe(II)-S |
| | | 708.3 | 1.71 | 15.2 | Fe(II)-O |
| | | 709.8 | 1.22 | 16.4 | Fe(III)-S |
| | 30 | 711.1 | 1.70 | 22.3 | Fe(III)-O |
| | | 712.8 | 1.26 | 4.9 | Fe(III)-O |
| | | 706.8 | 0.84 | 26.9 | Fe(II)-S |
| | | 709.9 | 1.66 | 27.5 | Fe(III)-S |
| | | 710.9 | 1.25 | 20.5 | Fe(III)-O |
| | | 712.0 | 1.26 | 16.9 | Fe(III)-O |
| | | 713.3 | 1.26 | 7.92 | Fe(III)-O |

Table 12.6 Binding energies (BE), full width at half maximum (FWHM), and area percentage for peaks in the O 1s spectra of pyrite contacted with Hg(II) for various times.

| Sample | Contact time (day) | BE (eV) | FWHM (eV) | Area (%) | Chemical |
|-----------------|--------------------|---------|-----------|----------|------------------|
| Pyrite | 0 | 530.0 | 1.01 | 25.5 | O ²⁻ |
| | | 531.1 | 1.10 | 38.0 | OH ⁻ |
| | | 531.8 | 1.17 | 36.4 | H ₂ O |
| Pyrite + Hg(II) | 1 | 529.6 | 0.66 | 22.7 | O ²⁻ |
| | | 530.2 | 0.80 | 25.2 | OH ⁻ |
| | | 531.3 | 1.47 | 51.9 | H ₂ O |
| | 15 | 529.3 | 0.65 | 25.1 | O ²⁻ |
| | | 530.0 | 0.85 | 34.8 | OH ⁻ |
| | | 531.1 | 1.35 | 40.0 | H ₂ O |
| | 30 | 529.8 | 0.76 | 33.9 | O ²⁻ |
| | | 530.5 | 0.85 | 30.5 | OH ⁻ |
| | | 531.4 | 1.03 | 35.6 | H ₂ O |

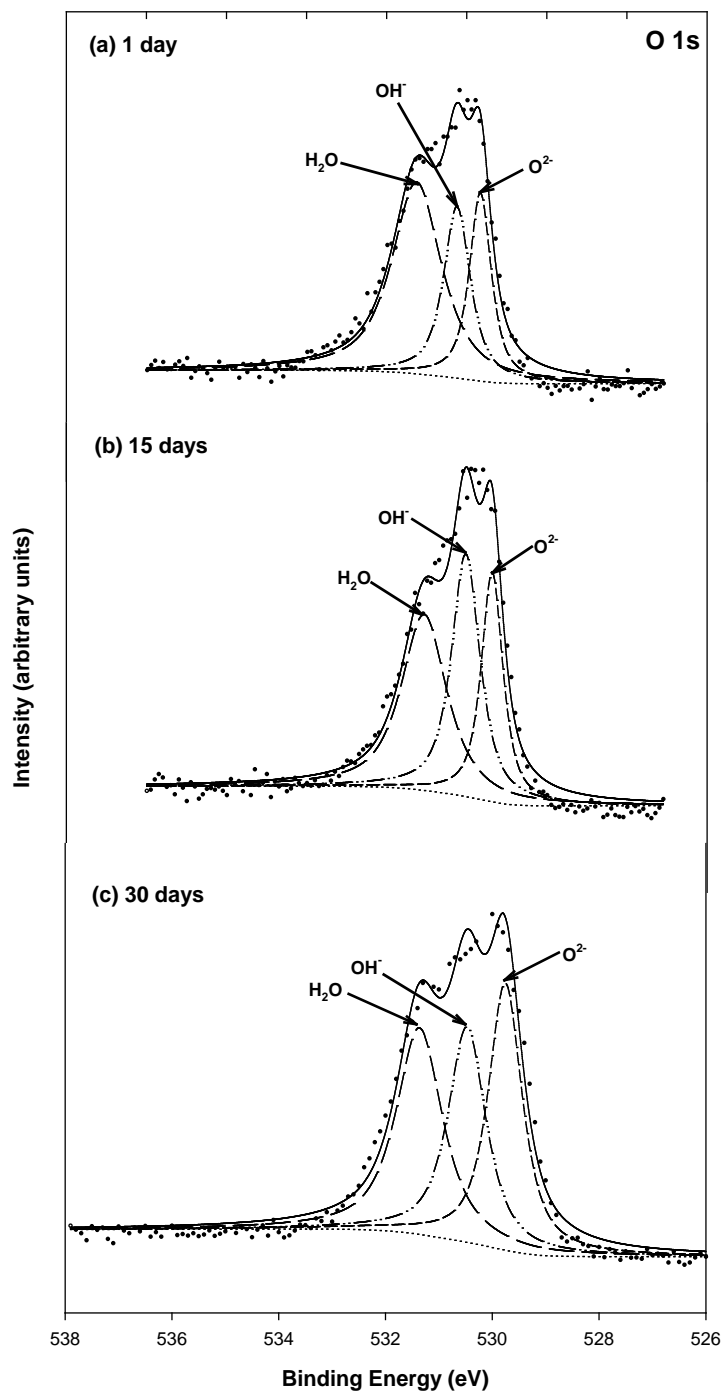


Figure 12.7 High resolution O 1s XPS spectra (Al K α) for synthetic pyrite (1 g/L) reacted with 200 μM Hg(II) at pH 8 for various times: (a) 1 day, (b) 15 days, (c) 30 days.

12.3.3.2 SEM Study

Figure 12.8 shows the secondary SEM images and EDS results for pyrites reacted with Hg(II) for 1, 15, and 30 days. There were not substantial changes in the morphology of pyrite at 1 and 15 days, but at 30 days, agglomerated particles of pyrites were formed and some of particles were observed to be fractured. This could be caused by reactions between Hg(II) and the pyrite surface that lead to formation of other solid phases. The EDS analysis reveals that elemental composition (Fe, S, Hg) of the surface was not changed substantially with contact time.

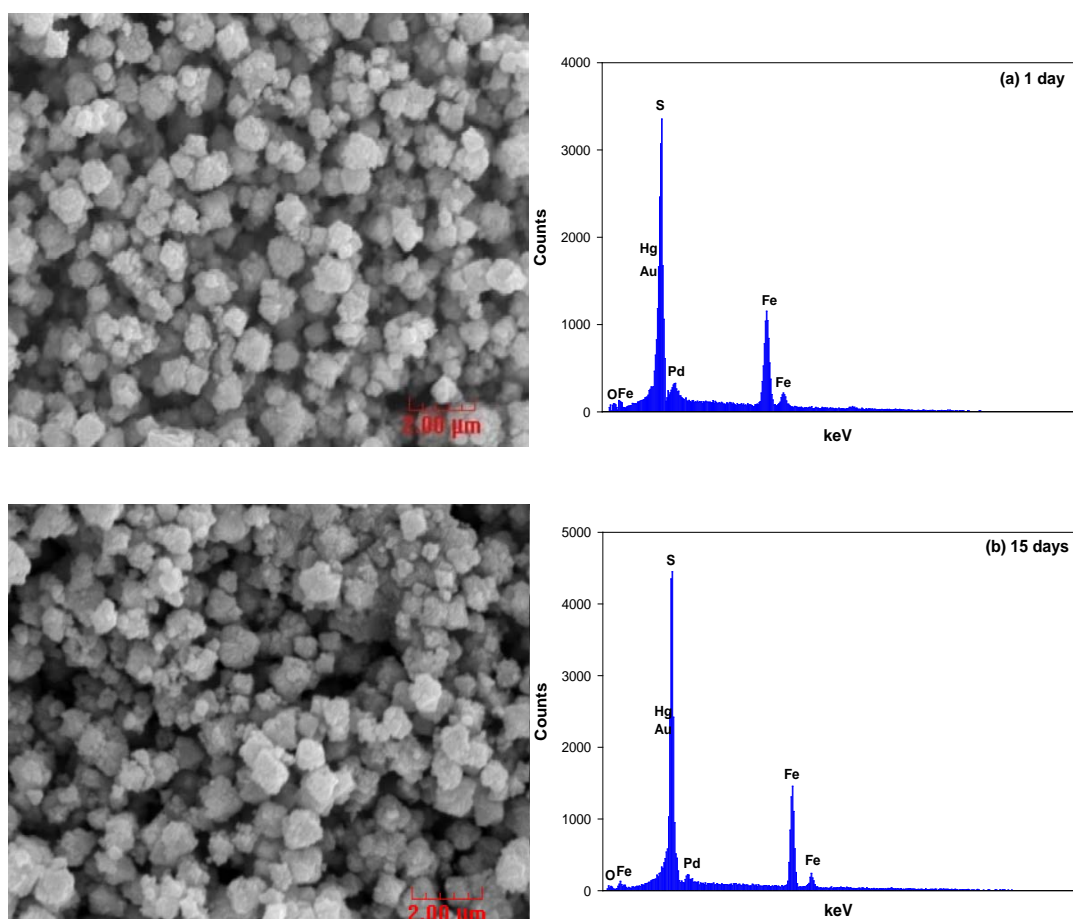


Figure 12.8 Secondary images of SEM and EDS results for pyrites contacted with Hg(II) at various times: (a) 1 day, (b) 15 days, and (c) 30 days.

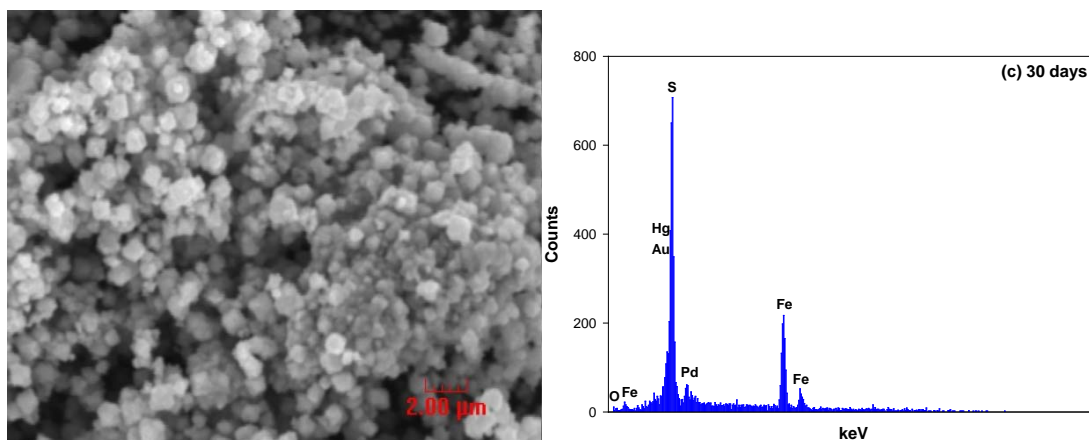
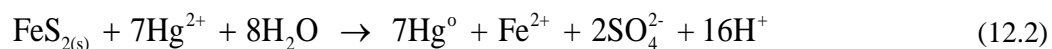


Figure 12.8 Continued.

12.3.4 Stability of Hg(II)-Contacted Pyrite

12.3.4.1 Low Molar Ratio of [Hg(II)]/[FeS₂]

Figure 12.9 shows results of stability experiments for mixtures of Hg(II) and pyrite that were conducted over a range of pH. Hg(II) was nearly completely removed at all pH values tested. As pH decreased back to initial pH value, no release of mercury into solution was observed, probably due to formation of strong bonds between mercury and the pyrite surface or formation of other stable precipitates. Behra et al. (2001) suggested that the following mechanism can lead to formation of elemental mercury and mercury sulfide precipitates in systems with Hg(II) and pyrite (92).



The surface of Hg(II)-contacted pyrites formed at pH 3.4 and pH 10 were analyzed by SEM and XPS to investigate the feasibility of surface precipitation leading to compounds such as HgS_(s) or Hg₂S_(s). Figure 12.10 shows SEM images of Hg(II)-contacted pyrites at pH 3.4 and 10,

respectively. For samples contacted only at pH 3.4, there are no important changes on the surface of Hg(II)-contacted pyrite. However, the pyrite that was exposed to a series of solutions with different pH, ending at pH 10, shows the presence of small, thin particles on the pyrite surface. XPS analysis was conducted on these samples in order to identify the chemical states of mercury in them.

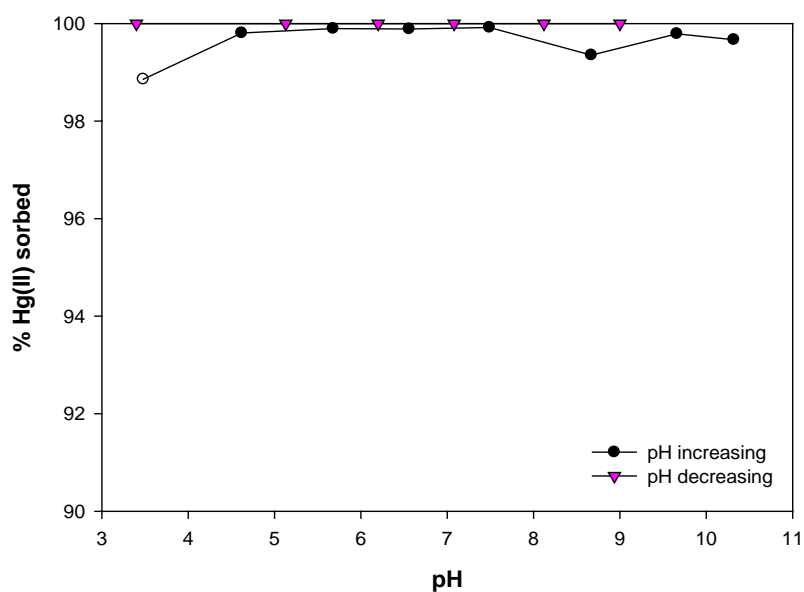


Figure 12.9 Effect of pH change on the stability of Hg(II)-contacted pyrite: $[\text{Hg(II)}]_0 = 6.48 \mu\text{M}$, solid loading = 1 g/L, contact time = 30 minutes, pH was first increased from pH 3.4 to pH 10 and then decreased to pH 3.4.

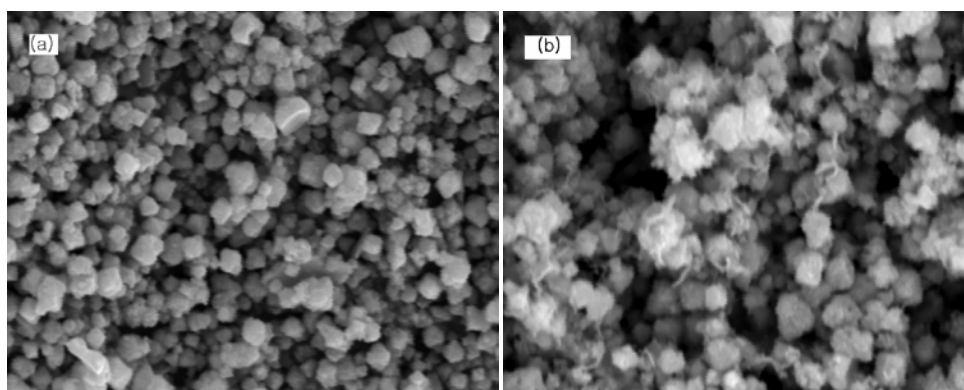


Figure 12.10 Secondary SEM images of synthetic pyrite reacted with Hg(II) (6.48 μM) at (a) pH 3.4_(i) and (b) pH 10_(a,b,t).

Figure 12.11 shows the Hg 4f spectra of Hg(II)-contacted pyrites at pH 3.4_(i) and pH 10_(a,b,t). For Hg(II)-contacted pyrite at pH 3.4, the peaks of Hg 4f_{5/2} and Hg 4f_{7/2} are centered at 104.8 eV and 106.6 eV, respectively, and the value of FWHM (full width at half maximum) for Hg 4f_{7/2} peak is 1.28 eV. Since the Hg 4f_{7/2} peak lies in the range of binding energies between 99.5 eV and 101.8 eV, reduced forms of mercury such as Hg(I) could be present on the surface, because peaks associated with Hg(II) and Hg(I) contribute to the Hg 4f_{7/2} spectra near 100.7 \pm 0.1 eV. This is similar to results obtained previously for Hg(II)-contacted pyrite at pH 8, which also show peaks that could include contributions from (Hg(I)). However, the spectra for pH 10_(a,b,t) sample show a broader (larger FWHM) Hg 4f_{7/2} peak compared to that of the pH 3.4_(i) sample. This broadness could be the result of peaks in the Hg 4f_{7/2} spectra between 99.2 and 100 eV that are caused by the presence of more Hg(0) as well as Hg(I). Therefore, the broader peak supports the possible formation of surface precipitates such as Hg₂S_(s) by Reaction (12.4).

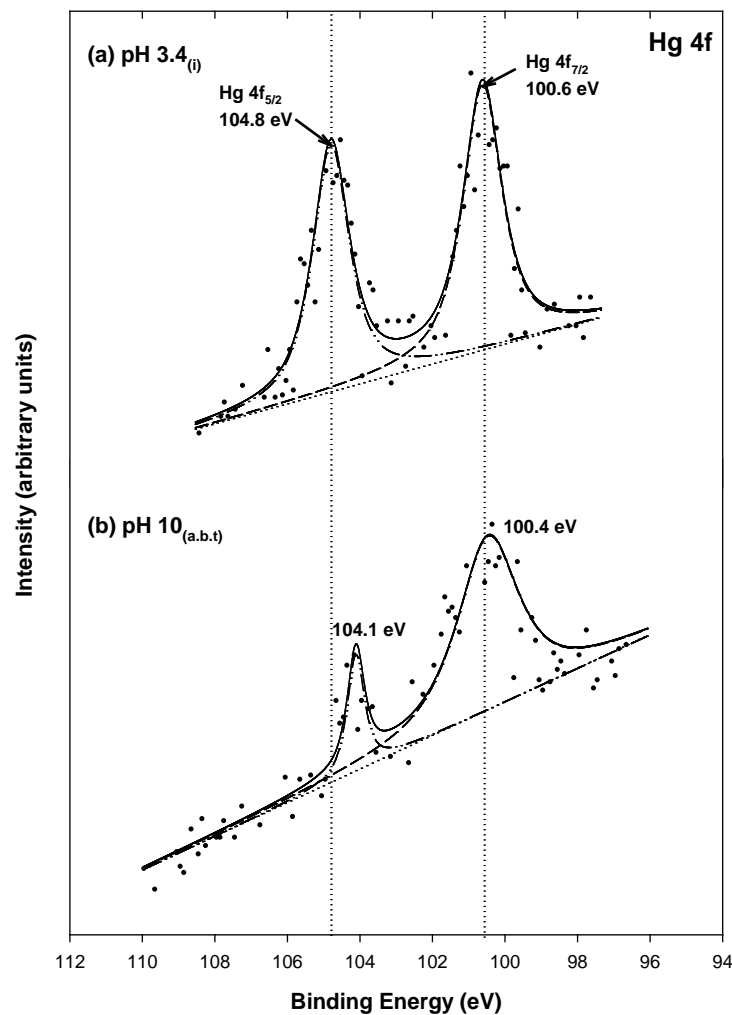


Figure 12.11 High resolution Hg 4f XPS spectra for pyrite after contact with Hg(II) (6.48 μM) at (a) pH 3.4_(i) and (b) pH 10_(a,b,t).

Figure 12.12 shows the Fe 2p_{3/2} spectra of Hg(II)-contacted pyrite at pH 3.4 and pH 10. High levels of oxidation of Fe sorption sites was observed only for pyrite reacted with Hg(II) at pH 10. In this sample, the intensity of the high energy tail increased due to the contributions of the peak associated with Fe(III)-O (Table 12.7). This could be caused by the oxidation of Fe sites that occurs concurrently with the reduction of Hg(II), although Fe could also be oxidized by other compounds.

Figure 12.13 shows the S 2p spectra of the pH 3.4_(i) sample and the pH 10_(a,b,t) sample. There are no major changes in the S 2p_{3/2} and S 2p_{1/2} peaks, compared to S 2p spectra for pure pyrite (Section 6). This suggests that it is unlikely that the surface sulfur sites are involved in redox reactions with Hg(II).

Table 12.7 Binding energies (BE), full width at half maximum (FWHM), and area percentage for peaks in the Fe 2p_{3/2} XPS spectra of the pH 3.4_(i) sample and the pH 10_(a,b,t) sample.

| Spectra | pH | BE (eV) | FWHM (eV) | Area (%) | Chemical |
|----------------------------|-----------------------|---------|-----------|----------|-------------------------------|
| Fe 2p_{3/2} | 3.4 _(i) | 706.8 | 0.85 | 84.8 | Fe(II)-S |
| | | 708.4 | 1.36 | 15.2 | Fe(II)-O |
| | 10 _(a,b,t) | 706.8 | 0.80 | 28.1 | Fe(II)-S |
| | | 708.3 | 1.15 | 10.2 | Fe(III)-S |
| | | 709.9 | 1.18 | 28.8 | Fe(III)-S |
| | | 711.1 | 1.05 | 22.2 | Fe(III)-O |
| | | 712.1 | 1.18 | 10.8 | Fe(III)-O |
| S 2p | 3.4 _(i) | 162.9 | 0.83 | 64.5 | S ₂ ²⁻ |
| | | 164.1 | 0.95 | 35.5 | S ₂ ²⁻ |
| | 10 _(a,b,t) | 162.8 | 1.04 | 66.5 | S ₂ ²⁻ |
| | | 164.1 | 0.97 | 27.4 | S ₂ ²⁻ |
| | | 169.2 | 1.57 | 6.09 | SO ₄ ²⁻ |
| | | | | | |

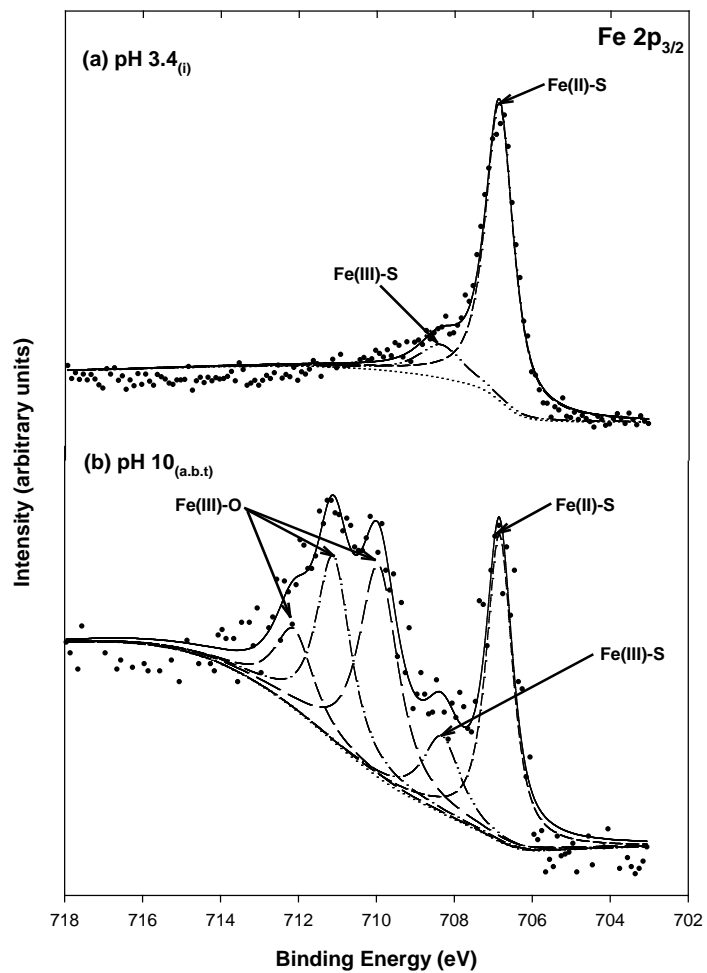


Figure 12.12 High resolution Fe 2p_{3/2} XPS spectra for pyrite after contact with Hg(II) (6.48 μM) at (a) pH 3.4_(i) and (b) pH 10_(a,b,t).

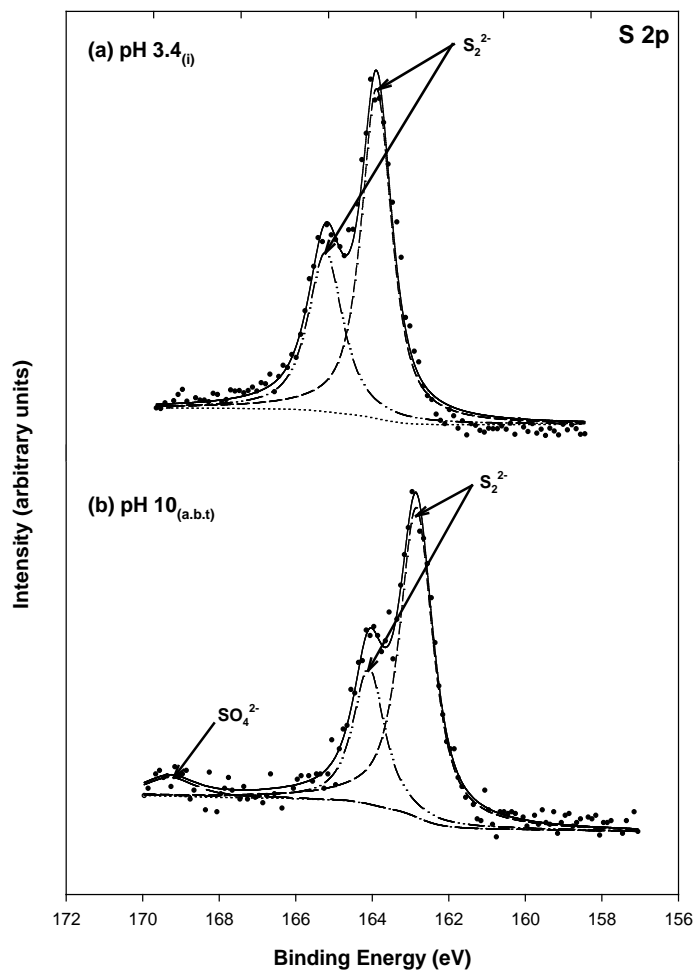


Figure 12.13 High resolution Fe $2p_{3/2}$ XPS spectra for pyrite after contact with Hg(II) (6.48 μM) at (a) pH 3.4_(i) and (b) pH 10_(a,b,t).

12.3.4.2 High Molar Ratio of Hg(II) to Pyrite

Figure 12.14 shows the results of stability experiments conducted with mixtures of Hg(II) and pyrite conducted over a range of pH. These experiments were conducted at higher concentration of Hg(II) (1 mM) than the experiments discussed previously (6.48 μM). The results are similar in the two experiments, but experiments with the higher Hg(II) concentrations show a more pronounced increase in removal when pH was increased above the lowest value.

Furthermore, although removals were high as pH was decreased, they were not near 100%. However, there was no release of mercury as pH was decreased. This suggests that relatively insoluble species were formed by reaction of mercury and pyrite at pH 10. As indicated by Equations 2-4, formation of precipitates such as $\text{HgS}_{(s)}$ or $\text{Hg}_2\text{S}_{(s)}$ could explain the observed behavior. To verify these mechanisms, SEM and XPS analyses were performed. Figure 12.15 shows the results of secondary SEM images for pyrite reacted with Hg(II) at pH 2.4 and pH 10. These images show that there are no specific changes in the morphology of pyrite.

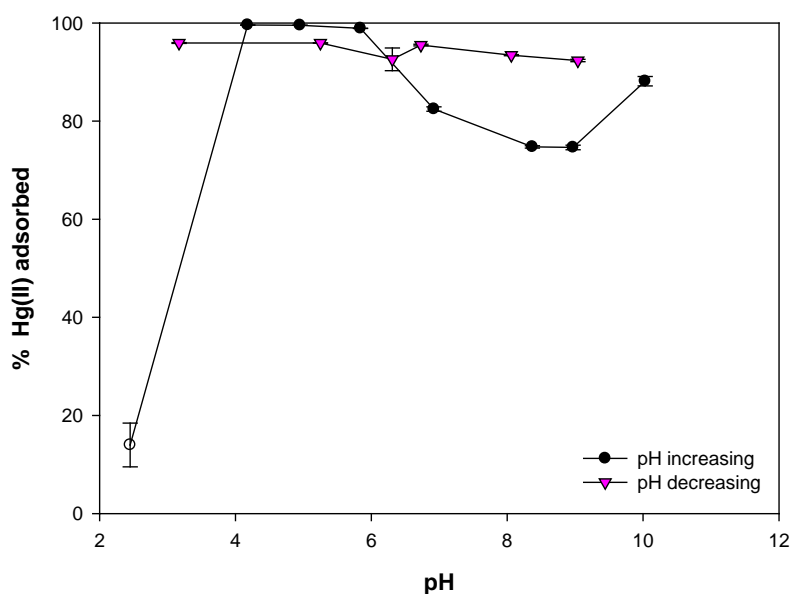


Figure 12.14 Effect of pH change on stability of Hg(II)-contacted pyrite: $[\text{Hg(II)}]_0=1 \text{ mM}$, solid loading = 1 g/L, contact time = 30 minutes, pH was first increased from pH 2.4 to pH 10 and then decreased to pH 3.0.

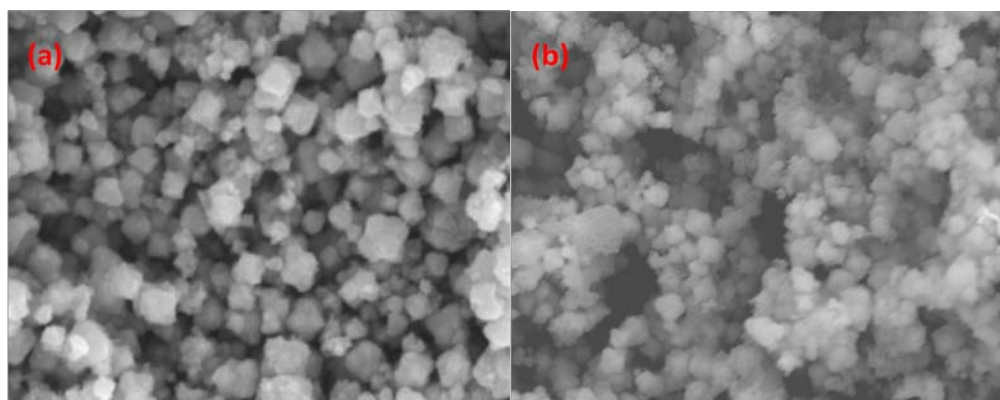


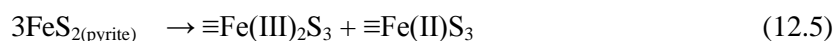
Figure 12.15 Secondary SEM images of pyrite after contact with Hg(II) (1.0 mM) at (a) pH 2.4_(i) and (b) pH 10_(a,b,t).

Figure 12.16 shows the Hg 4f XPS spectra for pyrite after contact with Hg(II) (1 mM) at (a) pH 2.4_(i) and (b) pH 10_(a,b,t). The peaks of Hg 4f_{5/2} and Hg 4f_{7/2} are centered between 104.5 and 104.8 eV and between 100.5 and 100.7 eV, respectively. These values are in good agreement with those reported in the literature (92, 93). Furthermore, the FWHM values of Hg 4f_{7/2} are between 1.02 and 1.08 eV, which are in accordance with the previous results by others. The Hg 4f_{7/2} peaks covered binding energies between 99.5 eV and 101.5 eV, so it is possible that peaks for Hg(I) were present, in addition to peaks for Hg(II).

Figure 12.17 shows the results of Fe 2p_{3/2} XPS spectra for pyrite reacted with Hg(II) (1 mM) at pH 2.4 and pH 10. The pH 2.4_(i) sample has peaks associated with three different Fe species (Fe(II)-S, Fe(III)-S, Fe(III)-O) that are located at 706.7, 709.3, and 710.5 eV, respectively. It also shows the peak associated with Fe(III)-O species at a higher intensity than observed for pure pyrite at pH 4. For the pH 10_(a,b,t) sample, however, only oxidized forms of Fe such as Fe(III)-S and Fe(III)-O are observed, whereas the spectra for pure pyrite at pH 10 has a dominant peak associated with reduced iron, Fe(II)-S (32.4 %), as well as peaks associated with oxidized forms. The difference in the extent of Fe oxidation in the samples at different pH could be caused by different amounts of Hg(II) on the surface that would result in different extents of surface

reaction, or by other reactions that oxidize surface Fe.

Figure 12.18 shows the S 2p XPS spectra for pyrite after contact with Hg(II) at (a) pH 2.4_(i) and (b) pH 10_(a,b,t). The pH 10_(a,b,t) sample had previously contacted solutions at lower pH. For the pH 2.4_(i) sample, there were no important changes in chemical states for surface sulfur species, compared to pure pyrite at pH 4. However, the pH 10_(a,b,t) sample shows the presence of different sulfur species (S(-II), S(-I), S(0), S(+VI)) that could be produced by surface disproportionation reactions of the sulfur surface sites. Similar reactions have been observed pyrite reduces Cr(VI) (228) or Se(IV) (Section 5). If Hg(II) is reduced by pyrite, the surface S(-I) specie could be oxidized to thiosulfate (S₂O₃²⁻) along with the oxidation of the surface Fe(II) to Fe(III). Subsequently, the thiosulfate ions could disproportionate into elemental sulfur (S⁰) and tetrathionate (S₄O₆²⁻). Finally, tetrathionate can be oxidized to sulfate ions when Hg(II) is reduced. Production of monosulfide ions (S(-II)) could be associated with disproportionation of pyrite to monosulfide and polysulfide as shown in Equation (13.5) (229).



where “≡” indicates a surface species, $\equiv\text{Fe(III)}_2\text{S}_3$ and $\equiv\text{Fe(II)}\text{S}_3$ indicate monosulfide bonded to Fe(III) and polysulfide (S₃²⁻) bonded to Fe(II). At higher pH, the presence of thiosulfates, sulfates and sulfites also could be caused by the oxidative dissolution of pyrite (92). However, the occurrence of S(-II) can also be explained by Reactions (12.3) and (12.4), and thereby the presence of S(-II) supports the idea that HgS_(s) or Hg₂S_(s) are being formed. This was also indicated by Hg 4f peaks (Figure 12.16) that show the potential for existence of Hg(I).

In summary, the pyrite reacted with higher concentrations of Hg(II) at pH 10 produces a stable solid that shows no release of Hg(II) as pH was changed. This stability could be the result of formation of precipitates (HgS_(s) or Hg₂S_(s)) as indicate by XPS analysis.

Table 12.8 Binding energies (BE), full width at half maximum (FWHM), and area percentage for peaks in the Fe 2p_{3/2} XPS spectra of pyrite after contact with Hg(II) (1 mM) at pH 2.4_(i) and pH 10_(a,b,t).

| Samples | pH sample | BE (eV) | FWHM (eV) | Area (%) | Chemical |
|----------------------------|-----------------------|---------|-----------|----------|-------------------------------|
| Fe 2p_{3/2} | 2.4 _(i) | 706.7 | 0.91 | 67.4 | Fe(II)-S |
| | | 709.3 | 0.98 | 4.93 | Fe(II)-O |
| | | 710.5 | 1.58 | 27.6 | Fe(III)-O |
| | 10 _(a,b,t) | 708.8 | 0.60 | 8.40 | Fe(III)-S |
| | | 709.5 | 0.99 | 25.4 | Fe(III)-S |
| | | 710.4 | 1.42 | 34.1 | Fe(III)-O |
| | | 711.5 | 2.22 | 32.0 | Fe(III)-O |
| S 2p | 2.4 _(i) | 162.7 | 1.09 | 81.7 | S ₂ ²⁻ |
| | | 163.9 | 0.65 | 18.3 | S ₂ ²⁻ |
| | 10 _(a,b,t) | 161.5 | 0.81 | 18.2 | S ²⁻ |
| | | 162.4 | 1.08 | 52.9 | S ₂ ²⁻ |
| | | 163.5 | 1.22 | 15.9 | S ₂ ²⁻ |
| | | 166.3 | 1.00 | 2.33 | S ⁰ |
| | | 168.4 | 1.64 | 10.6 | SO ₄ ²⁻ |

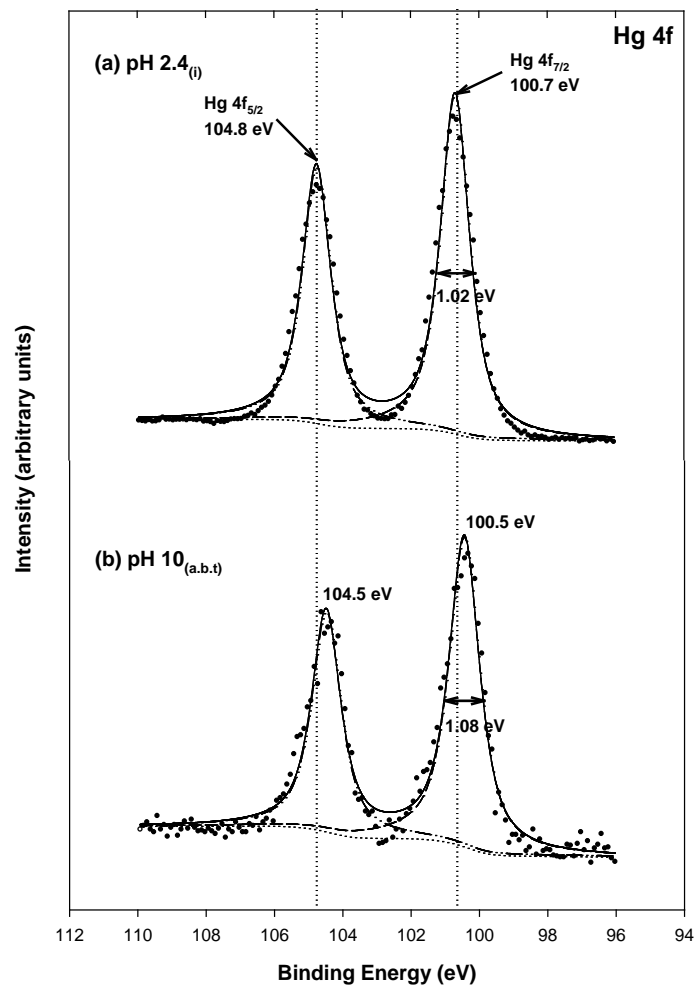


Figure 12.16 High resolution Hg 4f XPS spectra for pyrite after contact with Hg(II) (1 mM) at (a) pH 2.4_(i) and (b) pH 10_(a,b,t).

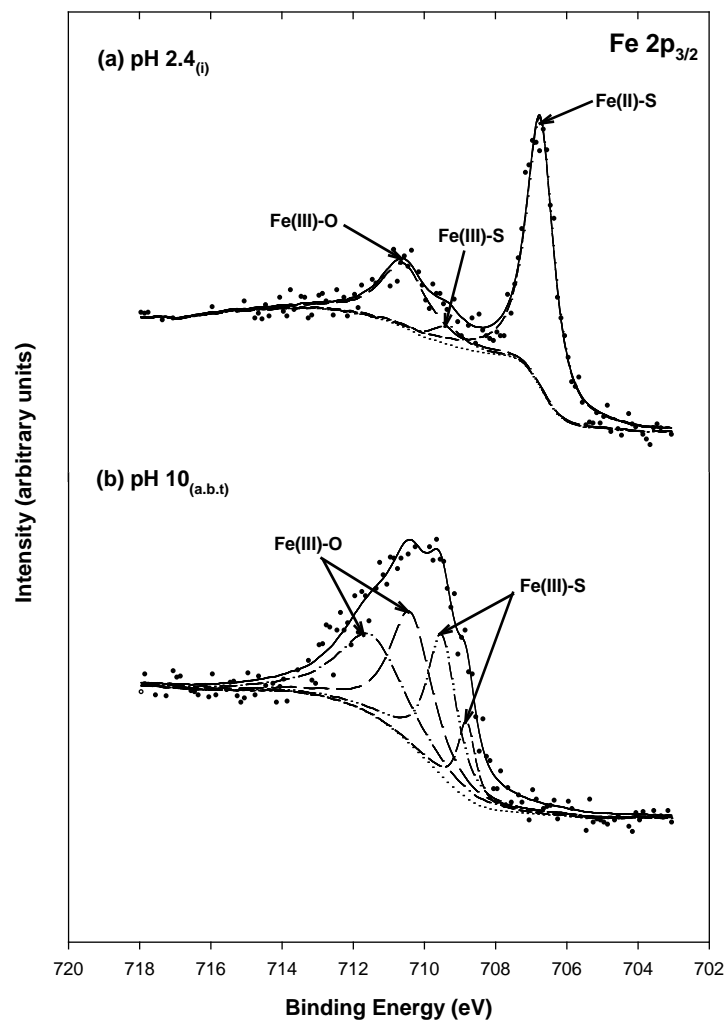


Figure 12.17 High resolution Fe 2p_{3/2} XPS spectra for pyrite after contact with Hg(II) (1 mM) at (a) pH 2.4_(i) and (b) pH 10_(a,b,t).

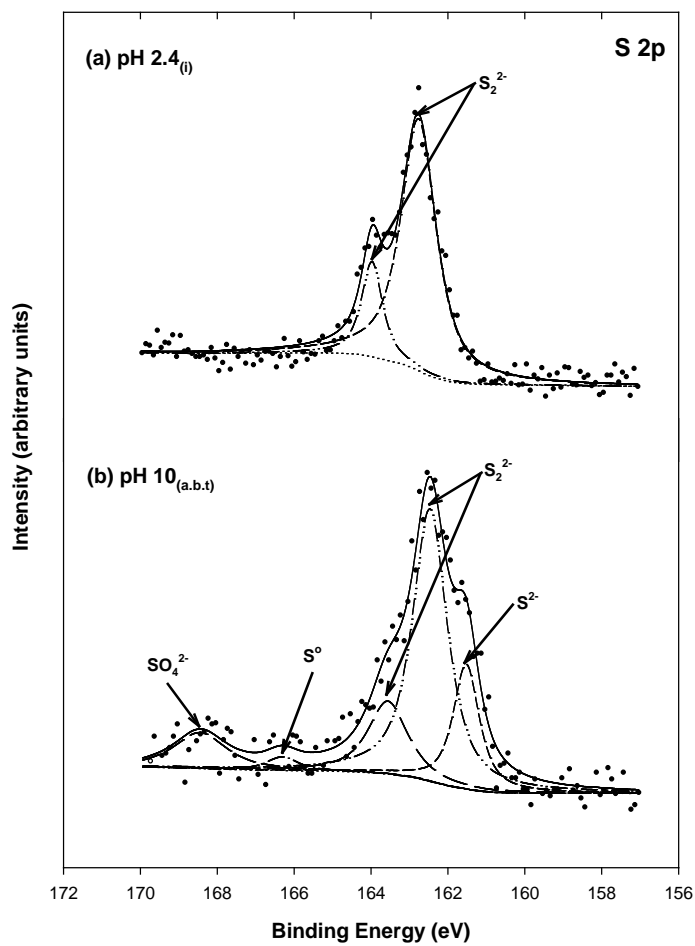


Figure 12.18 High resolution S 2p XPS spectra for pyrite after contact with Hg(II) (1 mM) at (a) pH 2.4_(i) and (b) pH 10_(a,b,t).

13. SORPTION OF MERCURY(II) TO ADSORBENTS/REACTANTS:

2. MACKINAWITE (FeS)

Removal of Hg(II) by FeS was observed to be rapid. At an initial concentration of 500 μM , complete removal occurred within 10 minutes. At higher initial concentrations, more time was required to achieve greater than 99 % removal. Removal experiments were conducted to evaluate the ability of FeS to remove Hg(II) over a period of 24 hours. The amounts of Hg(II) removed per mass FeS were high and were a function of the concentration of Hg(II) in solution at the end of the experiment. Loadings in excess of 50 mmol/g were observed in several experiments. Concentrations of Fe(II) in solution were measured in some experiments to provide information on the mechanism of removal. The concentration of iron released to the solutions remained relatively low, typically below 3 μM . This would present less than 1 % of the Hg(II) removed, so a simple exchange of Hg(II) for Fe(II) in the solid (FeS) does not explain the results. Fe(II) must remain as a solid phase, either by precipitation as a hydroxide or as a mixed Fe-Hg solid phase that contains hydroxide or another anion such as chloride. The removal pattern for Hg(II) by FeS differs depends on pH. Data for the experiments conducted at pH 10 show a relationship for solid phase concentration and liquid phase concentration that is best described by a BET model. This indicates that when concentrations are high enough, Hg(II) on the surface reacts to produce other solids that increase the amount of Hg(II) that can be removed from the liquid phase. The removal patterns at lower pH values were better described by the Langmuir model. However, BET-like behavior might have been observed at lower pH values if longer reaction times were evaluated. Sulfate tended to increase the amounts of Hg(II) removed by FeS, but the effect was not large. This might be caused by sulfate ions being incorporated into mixed Hg-Fe solid phases. Removal of sulfate from solution was observed, but the amounts were much lower than the increased amount of Hg(II) that was removed in the presence of sulfate. The

results of XPS analysis for mackinawites contacted with Hg(II) for a period of 30 days shows the presence of Hg(I) in addition to Hg(II), as well as oxidized iron and sulfur species. Stability tests for mixtures of Hg(II) and FeS were conducted at two initial Hg(II) concentrations. At low initial concentration, results showed good removals were observed for all pH and good stability. XPS showed reduction of Hg(II) to Hg(I) coupled with some evidence of oxidation of the surface Fe and S species. At high initial concentration of Hg(II), high removals were observed under all conditions and high levels of stability were measured. XPS analysis indicated similar patterns in oxidation state of Hg, along with oxidation of Fe and S.

13.1 Introduction

Mercury has been considered to be a global contaminant of significant concern for centuries due to its high toxicity and bioaccumulation via the aquatic food chain, which seriously affects natural ecosystems and the health of humans. Historically, the first mercury-related disaster occurred in the mid 1950s at Minamata, which is a city located in Japan on the coast of the Yatsushiro Sea. More than a few hundred people died as a result of dumping 27 tons of mercury compounds into Minamata Bay (69). Exposure to high levels of mercury can cause inhibition of enzyme activity, cell damage, impairment of pulmonary function and kidney performance, chest pain, and damage to the central nerve system (12, 71). Also, trace quantities of mercury may accumulate in the biosphere, so that many ecologists and health authorities have paid considerable attention to this problem. Mercury contamination occurs due to releases from anthropogenic and natural sources including chloro-alkali plants, mining and smelting activities, coal-fired power plants, electrical and electronic manufacturing plants, and a variety of incinerator facilities (72, 73). Among them, coal-fired power plants and incinerator facilities are the major source, constituting 77 % of anthropogenic Hg emissions in the United States and emitting 120 ton of Hg per year (74). Removal of inorganic Hg from emissions is a crucial

process because in aquatic ecosystems, most inorganic Hg is transformed to methylmercury (MeHg), which leads to highly elevated concentrations in aquatic fish and wildlife (75).

Inorganic mercury exists in the aqueous environment primarily as divalent mercury (Hg(II)), however, the zero-valent state can also exist under some conditions (76, 77). However, formation of Hg(0) is slow without biological action and it is expected to volatilize if it is produced (76, 77). Under reducing conditions, the primary soluble complexes are those formed with sulfide ($\text{Hg}(\text{HS})_2$, HgS_2H^- , HgS_2^{2-}) and insoluble solids are formed depending on various solution conditions (e.g., pH, $[\text{Hg}]/[\text{sulfide}]$). Under oxic conditions, on the other hand, mercury tends to complex with hydroxide (Hg^{2+} , $\text{Hg}(\text{OH})^+$, $\text{Hg}(\text{OH})_{2(\text{aq})}$), chloride ($\text{HgClOH}_{(\text{aq})}$, $\text{HgCl}_{2(\text{aq})}$, HgCl_3^-), and sulfate (HgSO_4) (76, 78, 79). In particular, in oxic seawater, mercury-chloro complexes (HgCl_4^{2-} , HgCl^- , HgCl_2^0 , HgCl^+) are dominant, because chloride ion concentration is much higher than the concentrations of other halide ions, although other mercury-halide complexes are present (80). In such an environment, the concentrations of mercury-hydroxide complexes are not appreciable, because the pH of sea water is about 8. Many earlier studies reported that the maximum adsorption of Hg(II) by a variety of adsorbents (SiO_2 , bentonite, goethite) was observed below pH 5, but in the presence of Cl^- ion, the extent of Hg(II) adsorption is considerably reduced because a larger fraction of mercury is present as HgCl_2 (81).

Hg(II) is a “soft” Lewis acid that is preferentially bonded with “soft” Lewis bases. Since the thiol functional group is a soft base, sulfur-containing chemicals have been widely used to remove mercury (82, 83). For the same reason, mercury forms a very insoluble solid with sulfide (76, 77, 84, 85). However, there are problems associated with controlling the sulfide dose in treatment processes. If excess sulfide is added, then soluble Hg-S complexes are formed and the effluent concentrations of soluble mercury increases (86). In general, the solubility of Hg-sulfide solid phases depends on pH and sulfide concentration. At low pH and low sulfide

concentration, formation of insoluble mercuric sulfide solid phase (HgS) is preferred, whereas soluble Hg-S complexes occur at high pH and high sulfide concentrations (79).

A way of avoiding the problems that occur in precipitation processes that use soluble reagents is to dose with large particles of iron sulfide, which gradually dissolve to produce the needed sulfide (76). If smaller particles are added, the removal mechanism will include sorption and surface reaction. Nano-scale iron sulfide particles have been produced microbially or abiotically and applied to removal of mercury (37, 70, 87, 88). Particle sizes around 2-5 nm and specific surface areas of 280-500 m²/g have been reported (88). Evidence for the production of solid phase products via surface reaction is found in the decrease in soluble mercury concentration with time (1 to 24 hr) that becomes more pronounced as the surface concentration is increased (87). Other metals besides Hg were shown to be removed by biogenic FeS (87, 88). Chemical synthesis of nano-sized FeS has also been reported (89, 90). Others have also reported that iron sulfides are good reagents for removing mercury from solution (10-12, 70, 84, 91-93). For example, Liu et al. (2008) investigated interactions between aqueous Hg(II) and FeS in batch sorption experiments and found that the maximum removal capacity at lower pH was approximately 0.75 mol Hg(II)/mol FeS. They also used X-ray power diffraction (XRPD) to identify the major products as metacinnabar, cinnabar, and mercury iron sulfide (10).

The goals of this work are to investigate the kinetics and extent of removal of Hg(II) by synthetic mackinawite (FeS) as affected by pH and competing ion (sulfate), to determine the stability of mackinawite combined with Hg(II), and to evaluate the solid phases to better understand the chemical changes that occur in order to improve stability. To understand what chemical changes occur when target compounds interact with the surfaces of solids and affect stability, the solid surfaces are characterized with X-ray photoelectron spectroscopy (XPS). XPS provides information on the chemical structures that exist on the surface in terms of oxidation

state of individual elements and the element pairs that are present. If solids are sufficiently stable, they can be disposed to the environment without concern for subsequent release and environmental contamination.

13.2 Materials and Method

13.2.1 Materials

All materials and chemicals applied in this study were used as in experiments on removal of Hg(II) by pyrite that were described in Section 12, except that mackinawite was used instead of pyrite. The method for synthesis of mackinawite was described in Section 7.

13.2.2 Kinetic Experiments

A standard stock solution of mercury was prepared using HgCl₂. Experiments were conducted at pH 8 with three different initial concentrations of mercury (500, 1000, 1250 μM) in the presence of 0.05 g/L FeS. To avoid formation of HgO_(s), the mercury stock solution did not exceed a concentration of 1300 μM. A kinetic test was initiated by mixing a FeS slurry and the mercury stock solution in 20-mL vials to achieve concentrations of 0.05 g/L FeS and 500, 1000, 1250 μM Hg. Acid (0.5 M HNO₃) or base (0.5 M NaOH) were added to adjust the pH. The reaction vessels were mixed with an end-over-end rotator until the specified sampling time (10, 30, 60, 150, 210, 330, 510, 750, 1440 min). Approximately 10 mL of suspension were removed and filtered using 0.02-μm anodisc membrane filters. All samples were stored prior to AAS analysis in an anaerobic chamber filled with 5% H₂/95% N₂ in order to avoid oxidation of mercury and changes in pH.

13.2.3 Sorption/Reaction Experiments

Tests for removal of mercury by suspension of FeS were conducted in a similar manner

as the previous experiments that evaluated removal of Hg(II) by suspensions of pyrite (Section 13). However, the concentration of FeS was adjusted to account for the higher affinity of mercury for the FeS surface. A FeS dose of 0.05 g/L was used with ten initial concentrations of mercury (33 to 826 $\mu\text{mol Hg/L}$) and four values of pH (pH 7, 8, 9, 10). A 24-hour reaction time was used and pH was adjusted by 0.5 M HNO_3 or 0.5 M NaOH. Similar experiments were conducted to determine the effect of sulfate on mercury removal and they were conducted at pH 8 and at three sulfate concentrations (0, 1, 10 mM).

13.2.4 Stability of Hg(II)-Contacted FeS

This experiment was conducted using the same procedure followed for suspensions of pyrite (Section 13), but suspensions of mackinawite (FeS) were used instead. In this system, “stability” is measured by the ability of Hg(II) to resist release into the aqueous phase after removal to the surface of mackinawite. Stability experiments were conducted by first contacting mackinawite with a solution of Hg(II) and allowing the Hg(II) to be removed and to react with the mackinawite surface. Then the solution pH was changed in a series of steps and the concentration of mercury in the aqueous phase measured. The extent of release of mercury as pH was changed is a measure of the stability of the combination of mackinawite and Hg(II). At low molar ratio of mercury to iron sulfide ($[\text{Hg(II)}]/[\text{FeS}]$), the pH of the suspension was initially adjusted to pH 10.5 and then lowered to pH 3.5 in a series of steps, and subsequently raised back to near the initial pH value. Here, samples will be identified with the following nomenclature to simplify the discussion. The initial sample at pH 10.5 will be named the “pH 10_(i)” sample and the sample at pH 3.5 after acid titration will be named the “pH 3.5_(a.a.t)” sample. Another stability test was conducted at high $[\text{Hg(II)}]/[\text{FeS}]$ in a similar way, but the initial pH was pH 10. Also, the pattern of nomenclature for samples at high $[\text{Hg(II)}]/[\text{FeS}]$ is similar to that for samples at low $[\text{Hg(II)}]/[\text{FeS}]$.

13.3 Results and Discussion

13.3.1 Kinetics

Figure 13.1 shows the percentage of Hg(II) removed by FeS as a function of time. The experiments were conducted with a solid concentration of 0.05 g/L and different initial concentrations of Hg(II) (500, 1000, 1250 μM). The experiment conducted with an initial concentration of 500 μM Hg(II) was observed to reach complete removal most rapidly and did so within 10 minutes. Experiments conducted with other initial concentrations required longer reaction times to reach more than 99 % removal. In order to evaluate kinetic effects (how fast q increased) and equilibrium effects (how high q becomes after a sufficiently long time), a general kinetic model was used and its parameters were calculated by nonlinear regression. All of the details of the kinetic model were discussed in Sections 3 and 10-12. The key hypothesis of the kinetic model is that sorption occurs at two types of sites, i.e., fast-reacting sites and slow-reacting sites. This allows the model to better describe a biphasic removal kinetics, which can occur when removal is affected by rapid external mass transfer followed by slower surface reactions. As shown in Table 13.1, the experiment with low initial concentration (500 μM) shows that all kinetic parameters associated with fast-reacting sites have larger values than those for slow-reacting sites, because removal by fast mass transfer to solid surface is predominant. As initial concentration increases, however, a biphasic sorption behavior was apparent, probably due to chemical interactions between mercury and the mackinawite surface. This resulted in lowering the rate coefficient (k_s) for slow-reacting sites by a factor of 2 and 4, compared to those at 500 and 1000 μM initial concentrations, and increasing the maximum solid phase concentration ($q_{s,\text{max}}$) by three orders of magnitude.

To investigate the possibility that FeS dissolved and $\text{HgS}_{(s)}$ precipitated, the concentration of total Fe in solution was measured. Figure 13.1 shows the value of total Fe

concentration measured in samples contacted with Hg(II). The blanks were filtered solutions of 0.05-g/L FeS stock solution that was adjusted to pH 8 but did not receive additions of Hg(II). Figure 13.1 shows that the values of total Fe released are less than about 0.5 % of total amount of Fe added as FeS (569 μM). The amount of Fe released to solution is too small to explain the amounts of mercury removed (500, 1000, 1250 μM), if the removal is due to precipitation of Hg(II) and solubilization of Fe(II). However, Hg(II) could precipitate as HgS and release Fe(II) that reacts to form another solid phase such as $\text{Fe}(\text{OH})_2$ at pH 8. Jeong et al. (12) proposed that resorption of the released Fe(II) by surface complexation at low initial Hg(II) concentration and formation of surface or bulk-precipitation of iron (hydr)oxides by large amounts of the released Fe(II) at high initial Hg(II) concentration could be responsible for decrease of dissolved Fe(II) concentration in solution.

Table 13.1 Calculated parameters of the kinetic model for Hg(II) uptake by FeS at pH 8.

| Initial Hg Concentration (μM) | <u>Parameters</u> | | | | |
|---|---|------------------------|---------------------------------------|---------------------------------------|--------|
| | $k_f(\text{min}^{-1})$ | $k_s(\text{min}^{-1})$ | $q_{f,\text{max}}(\mu\text{mol/g})$ | $q_{s,\text{max}}(\mu\text{mol/g})$ | *GFP |
| 500 | $1.4 \times 10^3 \pm 5.1 \times 10^3$ | 0.02 ± 0.01 | $9.9 \times 10^3 \pm 0.9$ | 7.3 ± 1.3 | 0.0001 |
| 1000 | 81.7 ± 46.3 | 0.01 ± 0.01 | $1.8 \times 10^4 \pm 1.2 \times 10^2$ | $1.9 \times 10^3 \pm 2.2 \times 10^2$ | 0.009 |
| 1250 | $4.3 \times 10^{11} \pm 2.0 \times 10^{11}$ | 0.005 ± 0.004 | $2.3 \times 10^4 \pm 6.0 \times 10^2$ | $1.3 \times 10^3 \pm 2.3 \times 10^2$ | 0.007 |

* Goodness of fit parameter (GFP) = $\sqrt{\text{SSR}/(n-2)}/\bar{q}$ where SSR is sum of squared residual, n is the number of data points,

\bar{q} is average value of the concentration of Hg on pyrite

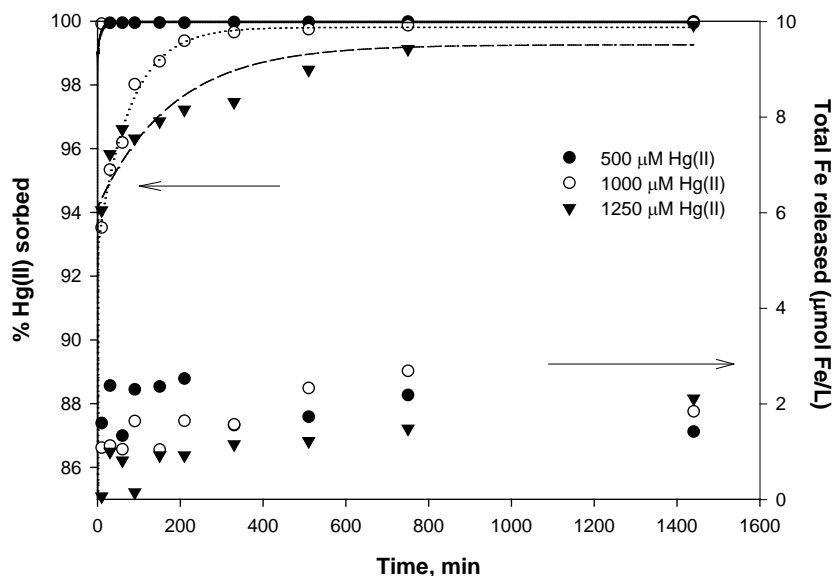


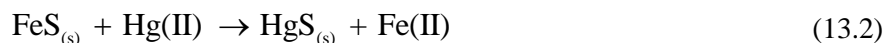
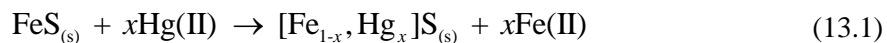
Figure 13.1 Percentage removal of Hg(II) and concentration of total Fe released as a function of time at pH 8 for three initial Hg(II) concentrations.

13.3.2 Nonlinear Removal Patterns

13.3.2.1 Effect of pH

Figure 13.2 shows the solid phase concentration of Hg(II) removed per mass on FeS at pH 7, 8, 9, 10. These experiments were conducted with a concentration of FeS of 0.005 g/L and a contact time of 24 hours. The method of presentation is similar to that used to describe equilibrium sorption isotherms, but in this case there is no intention to imply that equilibrium has been reached. The hard/soft acid/base theory indicates that Hg(II) would be strongly attracted to sulfide and likely to form soluble complexes, surface complexes, surface precipitates such as $(\text{Fe}, \text{Hg})\text{S}_{(s)}$ and separate solid phases, such as cinnabar (HgS) or metacinnabar ($\beta\text{-HgS}$). These forms of HgS would be produced by substitution of Fe(II) in FeS by Hg(II), which is consistent with a soft Lewis acid strongly reacting with soft Lewis base. Jeong et al. (12) suggested several reaction mechanisms leading to strong bonds, including formation of precipitates (Equations

13.1,13.2) or surface complexes (Equation 13.3), when the molar ratio of Hg(II) to FeS_(s) is less than 1.



The tendency of Hg(II) to form surface complexes and solid phases with sulfide could lead to relationships between concentration of Hg(II) on solid phase and concentration of Hg(II) in aqueous phase shown in Figure 13.2 that have the appearance of a BET isotherm. However, the relationships between solid phase concentration and aqueous phase concentration that are presented here are not equilibrium relationships, so they are not isotherms. The results obtained at pH 10, show behavior that is similar to a BET isotherm (Figure 13.2(a)). However, not all results that have been obtained follow the shape of a BET isotherm. At pH 7, 8, and 9, Hg(II) sorption behavior seems to follow a relationship that is similar to a Langmuir isotherm, although there is a decrease in solid phase concentration at higher aqueous phase concentrations that is not consistent with a Langmuir isotherm. The Langmuir-like behavior is also evident in data obtained at lower concentrations, which is shown in Figure 13.2(b).

Other hypotheses are required to explain the observed behavior. Above pH 7, Fe(II) that is released from FeS by exchange with Hg(II) may precipitate as ferrous hydroxide (Fe(OH)₂) and this solid could accumulate on the surface of FeS. This would reduce the area available for removal of Hg(II) from solution. How this mechanism would result in the observed behavior is not clear. The experiment conducted at pH 10 gave results that are similar to those that would be predicted by a BET isotherm (Figure 13.2(a)) and this can be interpreted as the result of adsorption followed by surface precipitation. Behra et al. (92) and Bonnissel-Gissinger et al. (263) observed that the surface of pyrite was oxidized under basic conditions (pH ≥ 10) and was

covered by Fe(III) oxyhydroxides that can also serve sorption sites for Hg(II). Similar behavior was observed on the surface of pure FeS at pH 10 before contact with any contaminant (Section 8). FeS could undergo oxidative dissolution and form Fe(III) oxyhydroxides that provide additional sorption sites for Hg(II) removal. Alternatively, other surface reactions could lead to formation of $\text{HgS}_{(s)}$ and $\text{Fe}(\text{OH})_2$ or mixed solid phases containing Hg(II), Fe(II), S(-II) and other anions such as hydroxide or chloride.

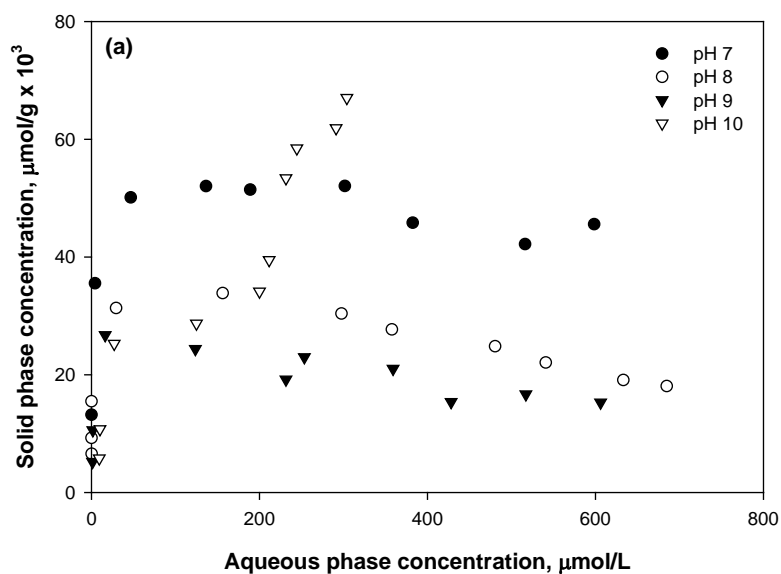


Figure 13.2 Measured concentrations of Hg(II) on FeS as functions of concentration in water for various pH: (a) at all Hg concentrations and (b) at lower Hg concentrations.

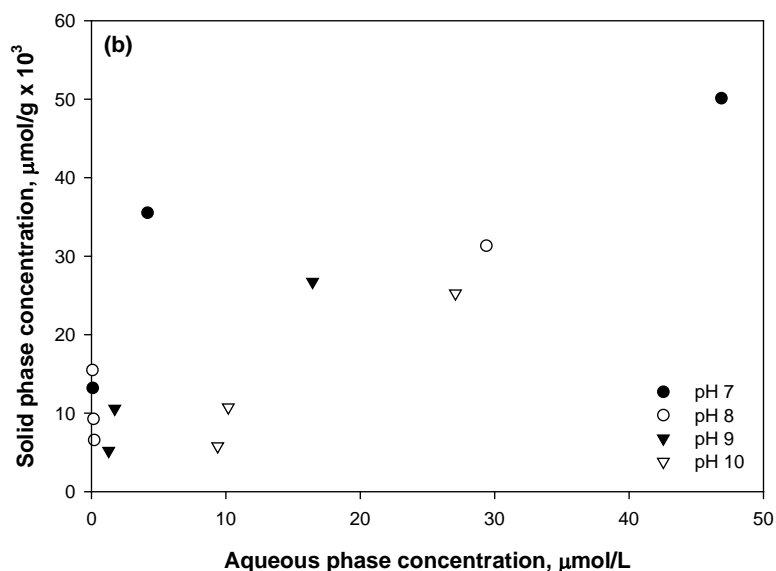


Figure 13.2 Continued.

13.3.2.2 Effect of Sulfate Concentrations

Figure 13.3 shows the effect of sulfate (1, 10 mM) on solid phase concentration of Hg(II) at pH 8. These results were obtained from batch experiments with a solid concentration of 0.005 g/L and 24-hour contact time. The same behavior is shown in the presence of sulfate as in its absence. The solid phase concentrations of Hg(II) increase and then decrease with liquid-phase concentration of Hg(II). The solid-phase concentrations are slightly higher when sulfate is present. One explanation for the positive effect of sulfate, is that mixed solid phases are being formed after removal of Hg(II) from solution. If Hg(II) were the only compound being removed from solution, then the surface would develop a positive charge, which would limit the amount of Hg(II) removed. This could be balanced by release of positive charge by release of Fe(II). However, the amount of iron released was not sufficient to balance charge of the amount of mercury transferred to the solid (Equation 13.1). Another way to balance charge would be for a negatively charged ion to be removed from solution. Sulfate could act as such an anion and could

sorb onto the surface and become incorporated into a mixed mercury-iron-sulfide-sulfate solid phase.

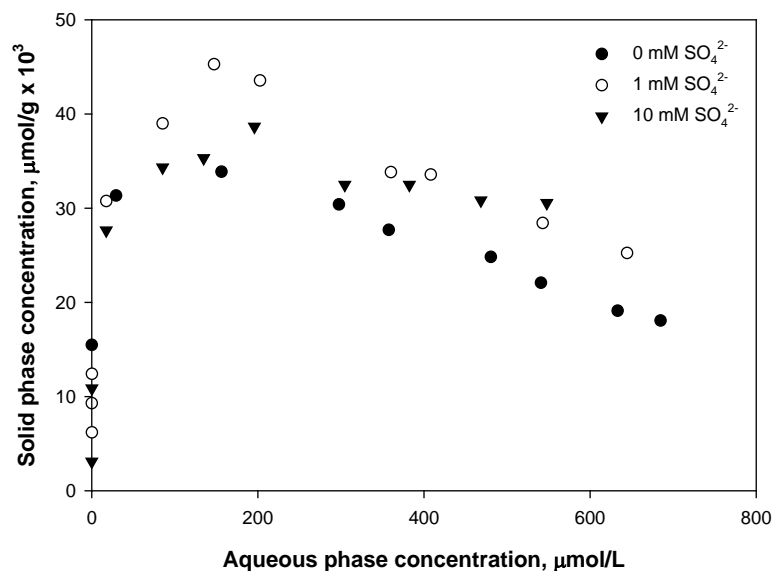


Figure 13.3 Amounts of Hg(II) removed per mass of solid (FeS) as functions of concentration of Hg(II) in water as affected by sulfate concentration (0, 1, and 10 mM) at pH 8.

An alternative mechanism for the positive effect of sulfate is formation of a mixed Fe(II)-Fe(III)-OH-SO₄ solid phases called green rust (Fe₄^{II}Fe₂^{III}(OH)₁₂(SO₄)). This mechanism could be initiated by formation of a Hg-rich sulfide and release of Fe(II) as suggested by Jeong et al. (12) (Reactions 13.1 and 13.2). The next step would be oxidation of Fe(II) to Fe(III) and reduction of Hg(I) or Hg(0). The final step would be formation of green rust (Fe₄^{II}Fe₂^{III}(OH)₁₂(SO₄)). There is evidence available to document the redox reaction that produces Fe(III) by reaction of pyrite with Hg(II) (Section 12).

13.3.3 Spectroscopic Investigations of Hg(II)-Contacted FeS

Figure 13.4 shows the Hg 4f XPS spectra of mackinawite reacted with Hg(II) for different times (1, 15, 30 days). The Hg 4f spectra is composed of two peaks (Hg 4f_{7/2} and Hg 4f_{5/2}) separated by a spin orbit splitting of about 4.0 eV. The Hg 4f_{7/2} peaks are centered at binding energy between 100.4 eV to 100.7 eV, which is where peaks associated with Hg(II) and Hg(I) species would be located (276). Hg(0) species are usually observed at binding energies between 99.2 and 99.8 eV, which is located in the lower energy tail of the Hg 4f_{7/2} spectra (276, 277). Therefore, Figure 13.4 indicates that Hg(II) and Hg(I) species are present, but Hg(0) is not present when mackinawite is allowed to react with Hg(II) for 30 days.

Figure 13.5 shows the Fe 2p_{3/2} XPS spectra of mackinawite reacted with Hg(II) for 1, 15, and 30 days. After 1 day, peaks associated with three different Fe species (Fe(II)-S, Fe(III)-S, Fe(III)-O) were observed. However, the intensity of peaks associated with Fe(III) species increased with reaction time, while those of Fe(II)-S species decreased. This oxidation of iron sorption sites could be related to reduction of Hg(II) to Hg(I) or to reduction of other chemicals.

Figure 13.6 shows the S 2p XPS spectra of mackinawite reacted with Hg(II) for different times. Oxidation of S(-II) species is not observed in the S 2p spectra until 15 days of reaction. At 30 days, peaks associated with products of reaction of S(-II), such as polysulfides (S_n²⁻) appear. Tables 13.2 – 13.4 summarize data for binding energies (BE), peak full width at half maximum (FWHM), peak area percentage for Hg 4f_{7/2}, Fe 2p_{3/2}, and S 2p spectra of FeS contacted with Hg(II) for different times.

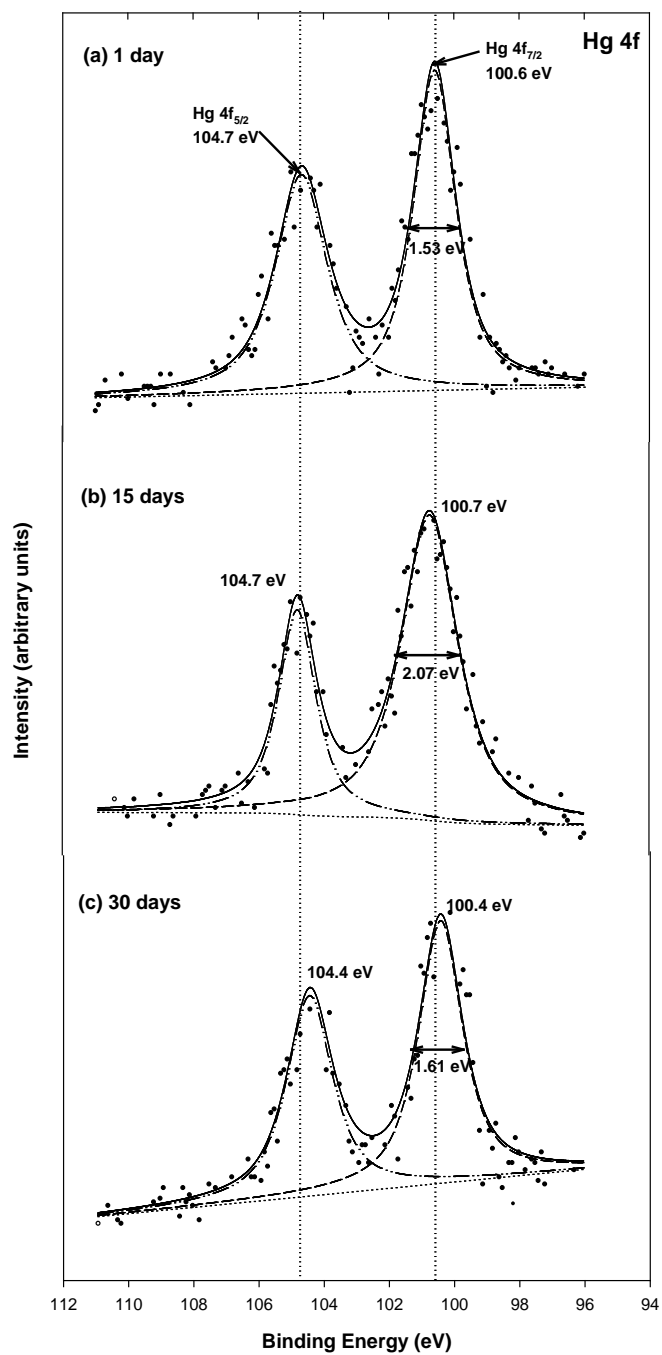


Figure 13.4 High resolution Hg 4f XPS spectra for FeS (1 g/L) reacted with Hg(II) (200 μ M) at pH 8 for various times: (a) 1 day, (b) 15 days, (c) 30 days.

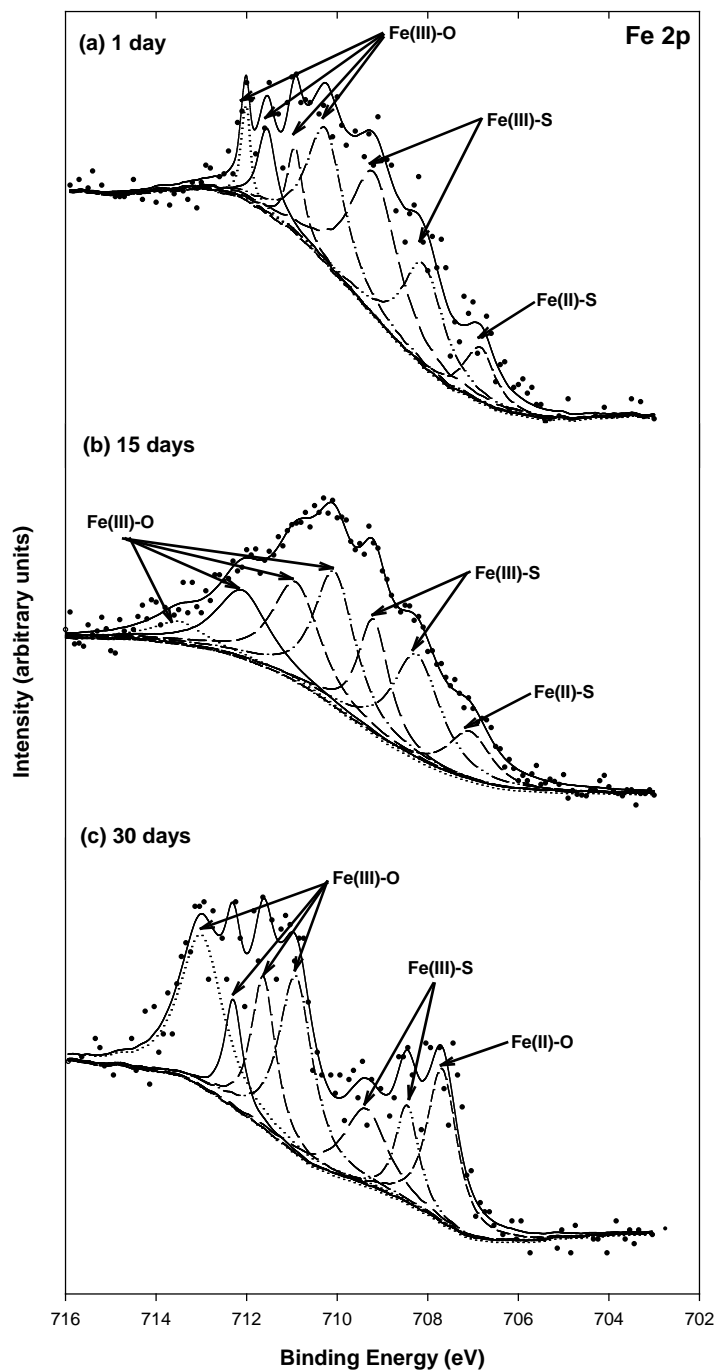


Figure 13.5 High resolution Fe 2p_{3/2} XPS spectra for FeS (1 g/L) reacted with Hg(II) (200 μM) at pH 8 for various times: (a) 1 day, (b) 15 days, (c) 30 days.

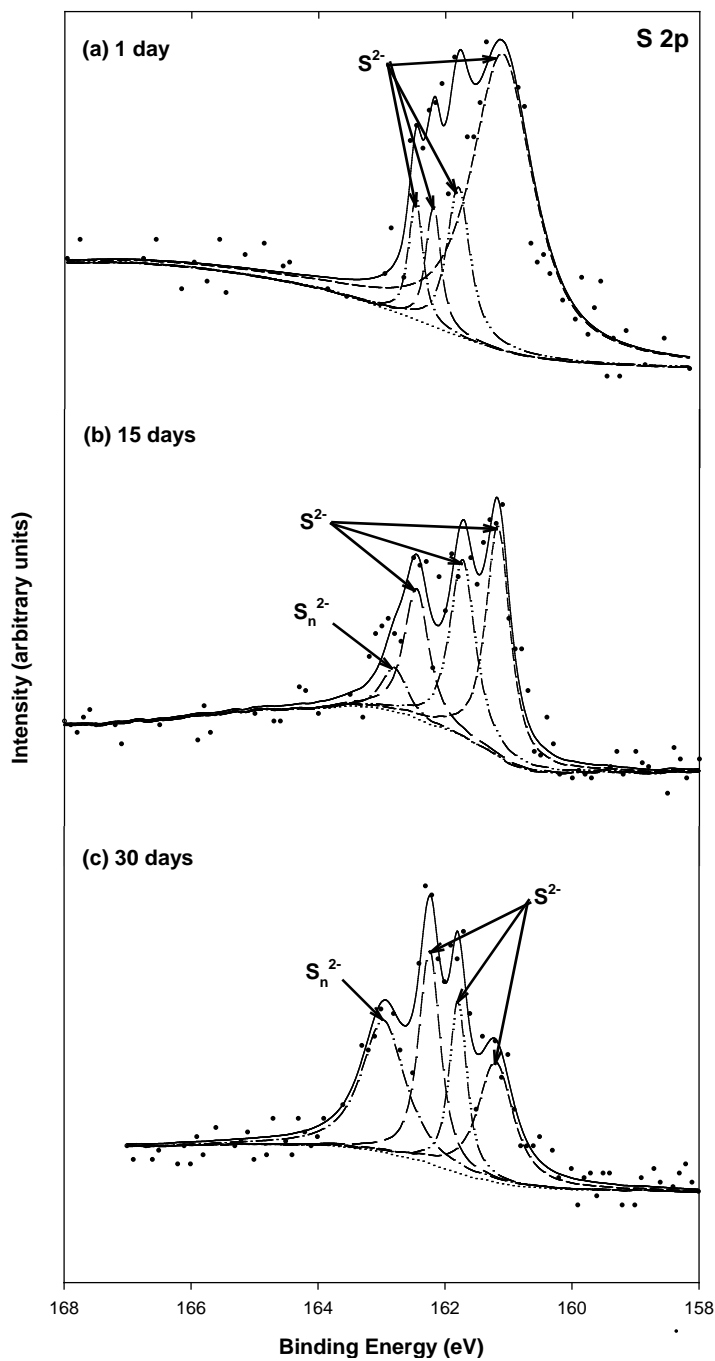


Figure 13.6 High resolution S 2p XPS spectra for FeS (1 g/L) reacted with Hg(II) (200 μ M) at pH 8 for various times: (a) 1 day, (b) 15 days, (c) 30 days.

Table 13.2 Binding energies (BE), peak full width at half maximum (FWHM), peak area percentage for Hg 4f_{7/2} XPS spectra of FeS contacted with Hg(II) for various times and for reference materials.

| Samples | Contact time (days) | χ^2 | BE (eV) | FWHM (eV) | Chemical states |
|---------------------------------|---------------------|----------|---------------|-----------|-----------------|
| Mackinawite+Hg(II) | 1 | 2.57 | 100.6 | 1.53 | Hg(I)/Hg(II) |
| | 15 | 2.57 | 100.7 | 2.07 | Hg(I)/Hg(II) |
| | 30 | 2.58 | 100.4 | 1.61 | Hg(I)/Hg(II) |
| Hg(0) | - | - | 99.2 ~ 99.8 | - | Hg(0) |
| Hg ₂ Cl ₂ | - | - | 100.8 ~ 101.0 | - | Hg(I) |
| HgS | - | - | 100.0 ~ 100.9 | - | Hg(II) |
| HgCl ₂ | - | - | 100.8 ~ 101.6 | - | Hg(II) |

Table 13.3 Binding energies (BE), peak full width at half maximum (FWHM), peak area percentage for Fe 2p_{3/2} XPS spectra of FeS contacted with Hg(II) for various times.

| Sample | Contact time | χ^2 | BE (eV) | FWHM (eV) | Area (%) | Chemical states |
|--------------------|--------------|----------|---------|-----------|----------|-----------------|
| Mackinawite | 0 | 0.49 | 706.0 | 0.46 | 9.07 | Fe(II)-S |
| | | | 706.4 | 0.52 | 13.8 | Fe(II)-S |
| | | | 706.9 | 0.72 | 18.7 | Fe(II)-S |
| | | | 707.7 | 1.02 | 19.8 | Fe(II)-O |
| | | | 708.8 | 1.29 | 15.0 | Fe(III)-S |
| | | | 710.1 | 1.71 | 15.2 | Fe(III)-O |
| | | | 711.8 | 2.44 | 8.23 | Fe(III)-O |
| Mackinawite+Hg(II) | 1 | 0.70 | 706.8 | 0.81 | 7.90 | Fe(II)-S |
| | | | 708.1 | 1.07 | 19.6 | Fe(III)-S |
| | | | 709.2 | 1.24 | 31.6 | Fe(III)-S |
| | | | 710.3 | 0.99 | 23.4 | Fe(III)-O |
| | | | 710.9 | 0.41 | 6.14 | Fe(III)-O |
| | | | 711.6 | 0.48 | 7.10 | Fe(III)-O |
| | | | 712.0 | 0.23 | 3.85 | Fe(III)-O |
| | 15 | 0.54 | 707.1 | 1.14 | 8.51 | Fe(II)-S |
| | | | 708.3 | 1.26 | 19.7 | Fe(III)-S |
| | | | 709.2 | 0.83 | 14.1 | Fe(III)-S |
| | | | 710.1 | 1.08 | 21.8 | Fe(III)-O |
| | | | 710.9 | 1.25 | 18.3 | Fe(III)-O |
| | | | 712.1 | 1.37 | 13.5 | Fe(III)-O |
| | 30 | 1.02 | 713.5 | 1.29 | 3.98 | Fe(III)-O |
| | | | 707.7 | 0.78 | 16.3 | Fe(II)-O |
| | | | 708.5 | 0.62 | 7.95 | Fe(III)-S |
| | | | 709.4 | 1.13 | 11.7 | Fe(III)-S |
| | | | 710.9 | 0.89 | 21.3 | Fe(III)-O |
| | | | 711.6 | 0.64 | 12.9 | Fe(III)-O |
| | | | 712.3 | 0.47 | 6.69 | Fe(III)-O |
| | | | 713.0 | 1.13 | 23.0 | Fe(III)-O |

Table 13.4 Binding energies (BE), peak full width at half maximum (FWHM), peak area percentage for S 2p XPS spectra of FeS contacted with Hg(II) for various times.

| Sample | Contact time | χ^2 | BE (eV) | FWHM (eV) | Area (%) | Chemical states |
|--------------------|--------------|----------|---------|-----------|----------|------------------------------|
| Mackinawite | 0 | 0.46 | 161.4 | 0.63 | 18.1 | S ²⁻ |
| | | | 162.1 | 0.85 | 42.6 | S ²⁻ |
| | | | 163.1 | 1.19 | 39.3 | S _n ²⁻ |
| Mackinawite+Hg(II) | 1 | 0.76 | 161.1 | 1.16 | 72.2 | S ²⁻ |
| | | | 161.8 | 0.43 | 13.6 | S ²⁻ |
| | | | 161.2 | 0.27 | 7.22 | S ²⁻ |
| | | | 162.4 | 0.26 | 6.95 | S ²⁻ |
| | 15 | 0.99 | 161.2 | 0.46 | 38.5 | S ²⁻ |
| | | | 161.7 | 0.48 | 31.2 | S ²⁻ |
| | | | 162.5 | 0.47 | 22.4 | S ²⁻ |
| | | | 162.8 | 0.47 | 7.85 | S _n ²⁻ |
| | 30 | 0.96 | 161.2 | 0.66 | 24.0 | S ²⁻ |
| | | | 161.8 | 0.33 | 17.2 | S ²⁻ |
| | | | 162.2 | 0.41 | 26.3 | S ²⁻ |
| | | | 162.9 | 0.82 | 32.6 | S _n ²⁻ |

13.3.4 Stability of Hg(II)-Contacted Mackinawite

13.3.4.1 Low Molar Ratio of [Hg]/[FeS]

Figure 13.7 shows the results of stability experiments for Hg(II)-contacted mackinawite in which release of Hg was measured over a range of pH. Removal of Hg(II) was high (>98%) but increased as pH decreased from the initial value and resulted in nearly complete removal below pH 7. When pH was raised back to the initial pH value, no release of Hg(II) to the solution was observed, indicating that strong chemical interactions between Hg(II) and the mackinawite surface had occurred. Based on previous XPS results for mackinawite reacted with Hg(II) at various times, the spectra associated with Fe, S and Hg were collected, revealing that a mixture of iron-sulfur-mercury was present on the mackinawite surface. Thus reactions described by Equations (13.1) and (13.3) could be important, but reaction described by Equation (13.2) could not be totally neglected because Fe(II) can resorb on the HgS_(s) surface. Jeong et al. (12) show by XRD analysis that mackinawite after contact with Hg(II) forms metacinnabar (β -HgS). However, greater reductive degradation of hexachloroethane was observed with the metacinnabar phase

formed in the mackinawite suspension than with pure metacinnabar (278). Therefore, whatever the surface reaction pathways, mercury appears to be bound to stable solid phases by strong bonds so that it is not easily released to solution as pH changes.

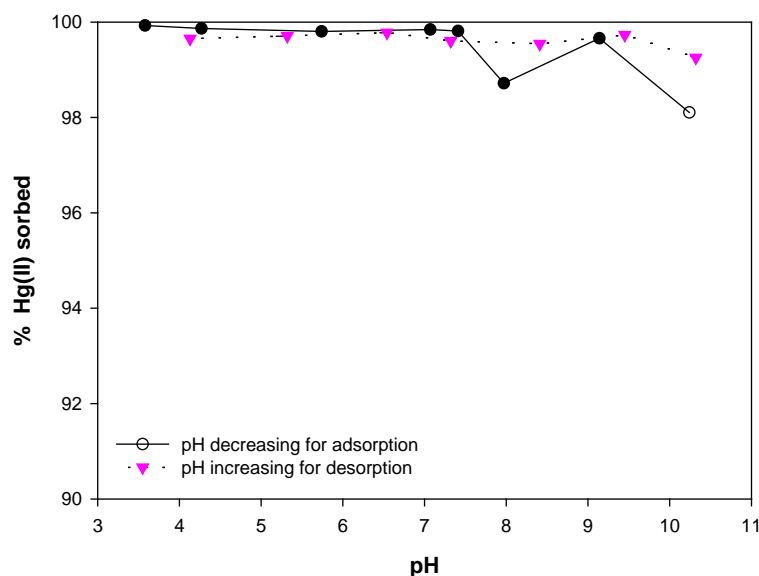


Figure 13.7 Effect of pH on removal of Hg(II) (6.48 μ M) by FeS (1 g/L) as pH was decreased from pH 10.5 and subsequently increased.

Figure 13.8 shows the Hg 4f XPS spectra of pH 10.5_(i) and pH 3.5_(a.a.t). The peaks of the Hg 4f spectra associated with Hg(II) and Hg(I) for both samples were centered at binding energies between 100.2 and 100.5 eV. A peak associated with Hg(0) would appear in the low energy tail of the Hg 4f_{7/2} spectra between 99.2 and 99.8 eV. Therefore, Hg(II) and Hg(I) species, rather than Hg(0), are present on the surface of mackinawite after 30 days of contact time.

Figure 13.9 shows the Fe 2p_{3/2} XPS spectra for pH 10.5_(i) and pH 3.5_(a.a.t) samples. All peaks associated with Fe(II)-S components were small or not present at all, while the relative intensity of peaks associated with oxidized forms of iron (Fe(III)-S and Fe(III)-O) increased, compared to pure mackinawite at pH 10 and pH 4 (Section 8). The oxidation of surface Fe might

be caused by redox reactions with Hg(II) or with other chemicals.

Figure 13.10 shows the S 2p XPS spectra for pH 10.5_(i) and pH 3.5_(a.a.t) samples. Both spectra show the presence of oxidized components of sulfur (S_n^{2-} , S^0 , SO_4^{2-}) as well as S(-II). The oxidation of S(-II) could be caused by oxidative dissolution without reaction with Hg(II), as indicated by the presence of polysulfides (S_n^{2-}) in spectra for pure mackinawite at pH 4 and 10 (Section 8). However, the continued presence of S(-II) indicates the potential to form precipitates such as (Fe,Hg)S or HgS.

Table 13.5 Binding energies (BE), full width at half maximum (FWHM), and area percentage for peaks in the Fe 2p_{3/2} and S 2p XPS spectra of mackinawite at pH 10.5_(i) and pH 3.5_(a.a.t).

| Spectra | pH | BE (eV) | FWHM (eV) | Area (%) | Chemical states |
|----------------------------|------|---------|-----------|----------|-------------------------------|
| Fe 2p_{3/2} | | | | | |
| | 10.5 | 706.5 | 0.45 | 3.62 | Fe(II)-S |
| | | 707.4 | 0.85 | 8.22 | Fe(II)-O |
| | | 708.3 | 1.68 | 37.1 | Fe(III)-S |
| | | 709.5 | 1.46 | 27.6 | Fe(III)-S |
| | | 711.7 | 2.18 | 23.3 | Fe(III)-O |
| | 3.5 | 707.3 | 1.62 | 14.7 | Fe(II)-O |
| | | 708.3 | 1.23 | 34.8 | Fe(III)-S |
| | | 709.2 | 0.91 | 19.6 | Fe(III)-S |
| | | 710.2 | 1.49 | 28.7 | Fe(III)-O |
| | | 711.5 | 0.44 | 2.12 | Fe(III)-O |
| S 2p | | | | | |
| | 10.5 | 160.9 | 1.50 | 42.4 | S ²⁻ |
| | | 161.8 | 0.43 | 16.8 | S ²⁻ |
| | | 162.6 | 0.64 | 12.0 | S ²⁻ |
| | | 163.6 | 0.39 | 5.98 | S _n ²⁻ |
| | | 165.4 | 1.47 | 6.73 | S ⁰ |
| | | 167.4 | 1.05 | 8.55 | SO ₄ ²⁻ |
| | | 168.5 | 1.34 | 7.47 | SO ₄ ²⁻ |
| | 3.5 | 160.4 | 3.17 | 47.3 | S ²⁻ |
| | | 161.3 | 1.52 | 18.6 | S ²⁻ |
| | | 162.5 | 0.87 | 12.5 | S ²⁻ |
| | | 163.6 | 0.72 | 5.77 | S _n ²⁻ |
| | | 167.7 | 3.22 | 15.8 | SO ₄ ²⁻ |

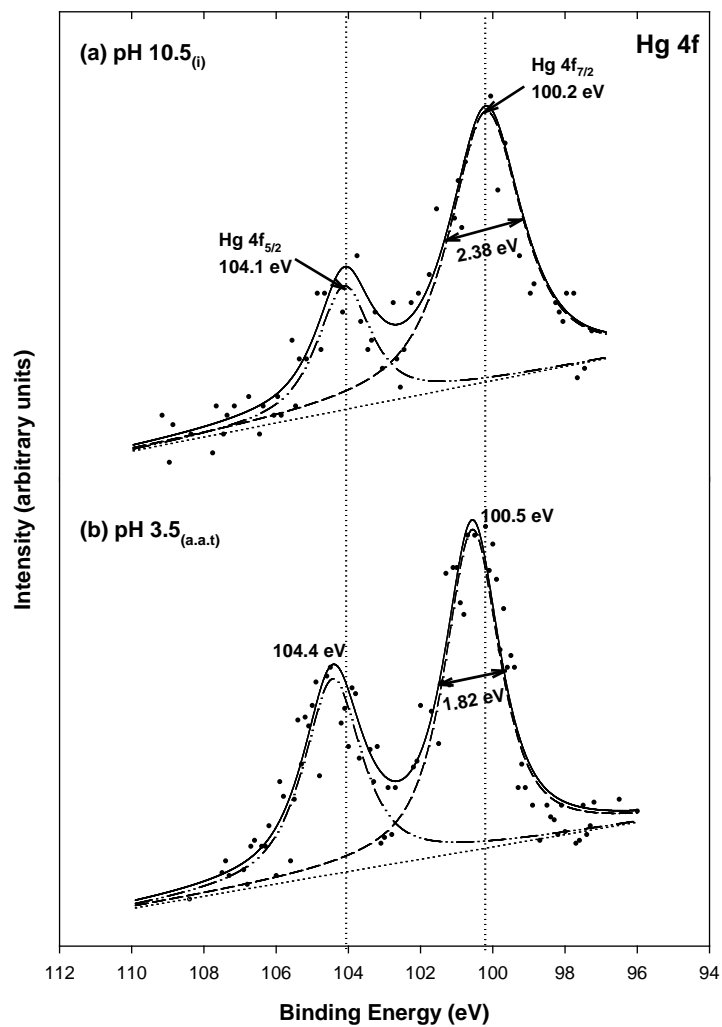


Figure 13.8 High resolution Hg 4f XPS spectra for mackinawite after contact with Hg(II) (6.48 μM) at (a) pH 10.5_(i) and (b) pH 3.5_(a.a.t).

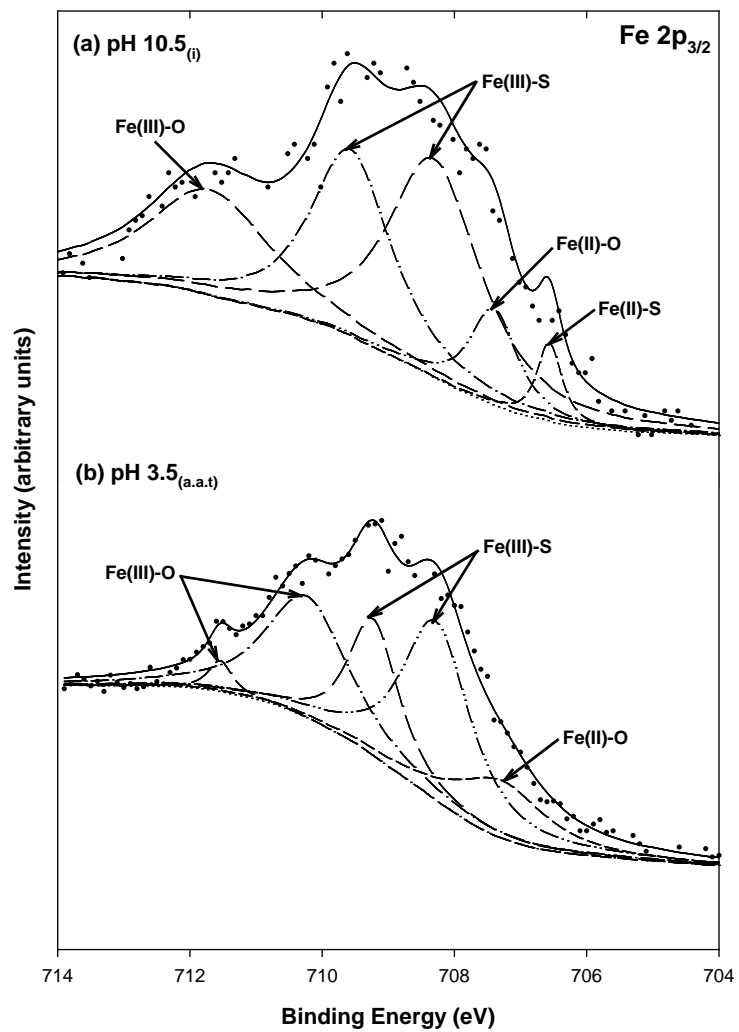


Figure 13.9 High resolution Fe 2p_{3/2} XPS spectra for mackinawite after contact with Hg(II) (6.48 μM) at (a) pH 10.5_(i) and (b) pH 3.5_(a.a.t).

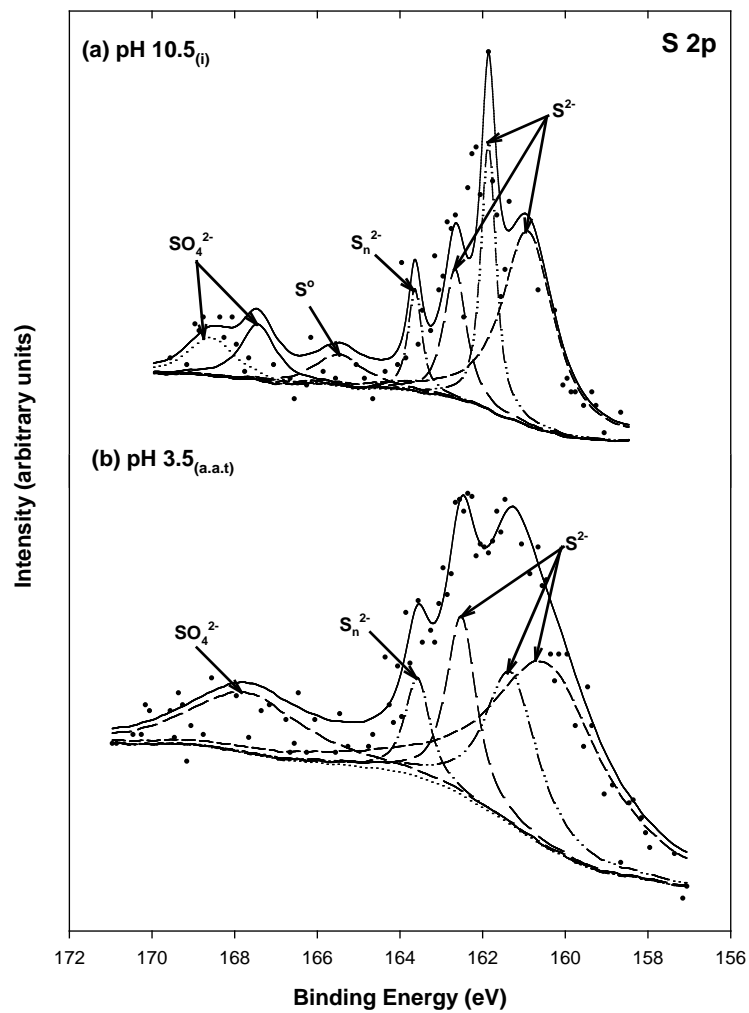


Figure 13.10 High resolution S 2p XPS spectra for mackinawite after contact with Hg(II) (6.48 μM) at (a) pH 10.5_(i) and (b) pH 3.5_(a.a.t).

13.3.4.2 High Molar Ratio of [Hg]/[FeS]

Figure 13.11 shows how pH affects release of Hg(II) from FeS. Additional Hg(II) was removed as pH decreased from the initial value, but good removal of Hg(II) (>99%) was observed for all conditions. Furthermore, as pH increased, there was no release of Hg(II) to solution, indicating that mercury was strongly bound. This could be caused by formation of mixed iron-mercury sulfide precipitates such as $(\text{Fe}, \text{Hg})\text{S}_{(s)}$, or $\text{HgS}_{(s)}$ or strong surface complexes ($\equiv\text{FeS-Hg(II)}$). Formation of such solid-phase products could be responsible for the stability of Hg(II) in contact with FeS.

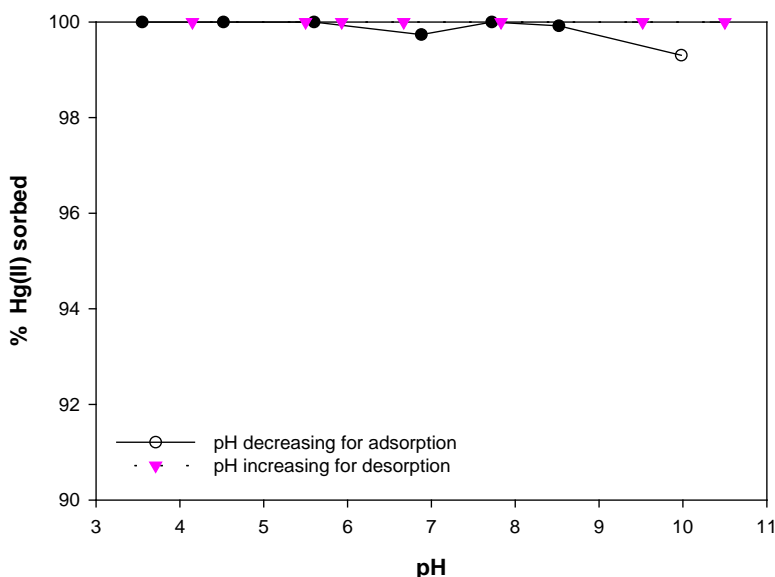


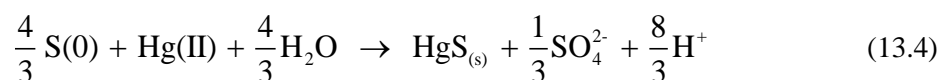
Figure 13.11 Effect of pH on removal of Hg(II) (1.0 mM) by FeS (1 g/L) as pH decreased from pH 10 and subsequently increased.

Figure 13.12 shows the Hg 4f spectra for pH 10_(i) and pH 3.5_(a.a.t) samples. The Hg 4f_{7/2} peaks of both samples are centered at 100.2 eV and FWHM values for their peaks are about 0.98 eV. This indicates the presence of Hg(II) or Hg(I) species. Also, the highly symmetric shape of the Hg 4f_{7/2} peaks indicates that other Hg species (e.g., Hg(0)) are not present, even though low

energy tails of the Hg 4f_{7/2} peaks covers the binding energies (99.2 to 99.8 eV) associated with Hg(0).

Figure 13.13 shows XPS results for Fe 2p_{3/2} spectra of pH 10_(i) and pH 3.5_(a.a.t). Both spectra show that peaks associated with oxidized forms of Fe such as Fe(III)-S and Fe(III)-O are important. Oxidation of surface Fe could occur by redox reactions with Hg(II) or with other chemicals.

Figure 13.14 shows S 2p spectra for Hg(II)-contacted FeS at pH 10 and pH 3.5. Both spectra show the presence of oxidized species such as polysulfides (S_n²⁻) or elemental sulfur (S⁰) in addition to S(-II). However, S(-II) species contribute more to the overall intensity of the S 2p spectra, so it is more likely that they react with Hg(II) to form precipitates or surface complexes. Jeong et al. (12) suggested an alternative theoretical mechanism for the formation of discrete precipitates of HgS(s) through a disproportionation reaction with elemental sulfur.



However, the formation of discrete HgS_(s) by the reaction described by Equation (13.4) could not be substantial, because the relative peaks for S⁰ in spectra of the pH 10 and pH 3.5 samples account for only 8.1 % and 7.8 % of total peak area (Table 13.5).

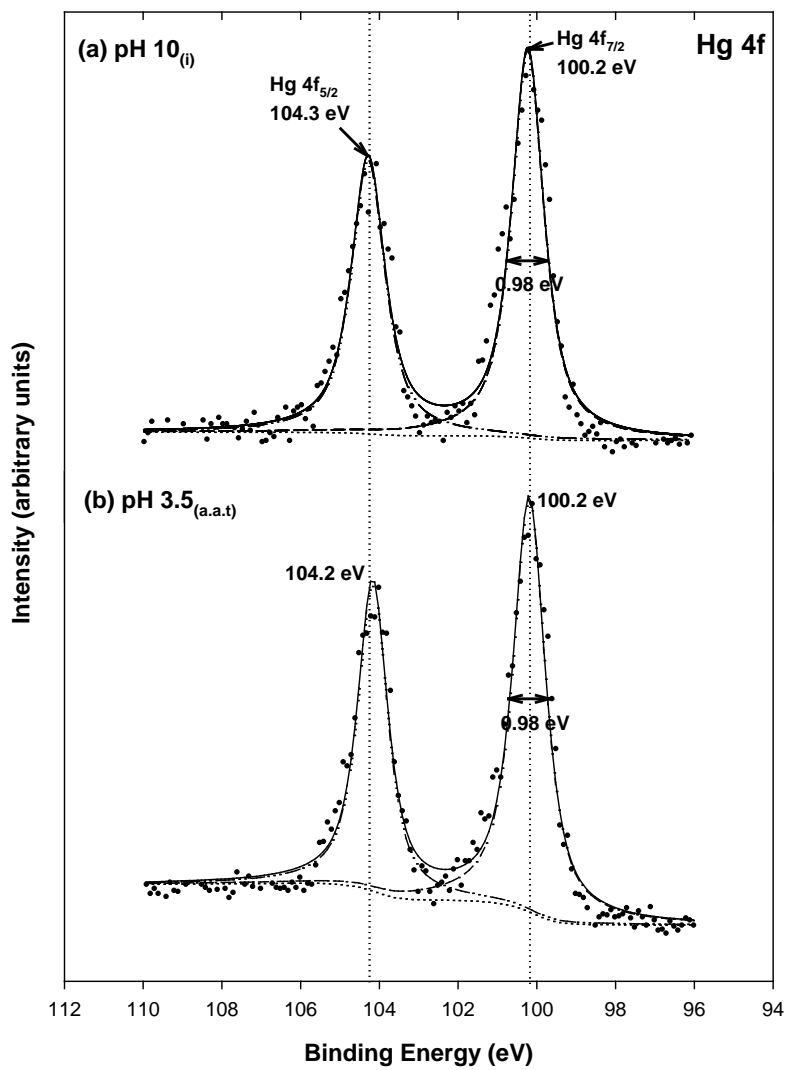


Figure 13.12 High resolution Hg 4f XPS spectra for mackinawite after contact with Hg(II) (1 mM) at (a) pH 10_(i) and (b) pH 3.5_(a.a.t).

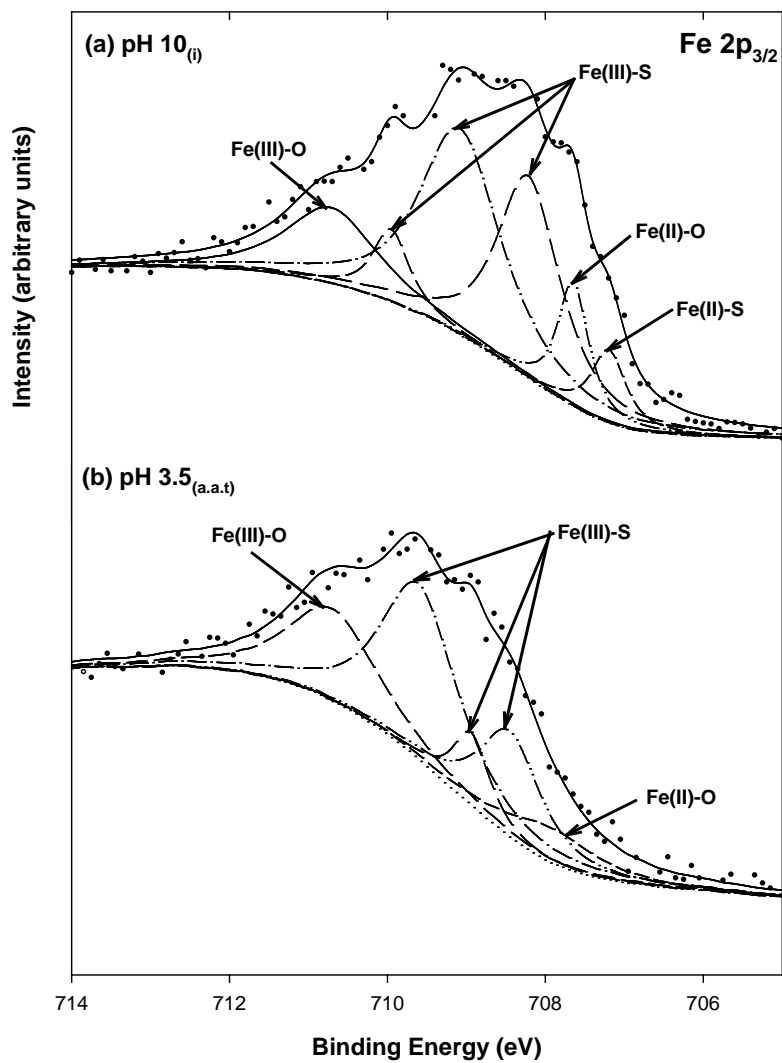


Figure 13.13 High resolution Fe 2p_{3/2} XPS spectra for mackinawite after contact with Hg(II) (1 mM) at (a) pH 10_(i) and (b) pH 3.5_(a.a.t).

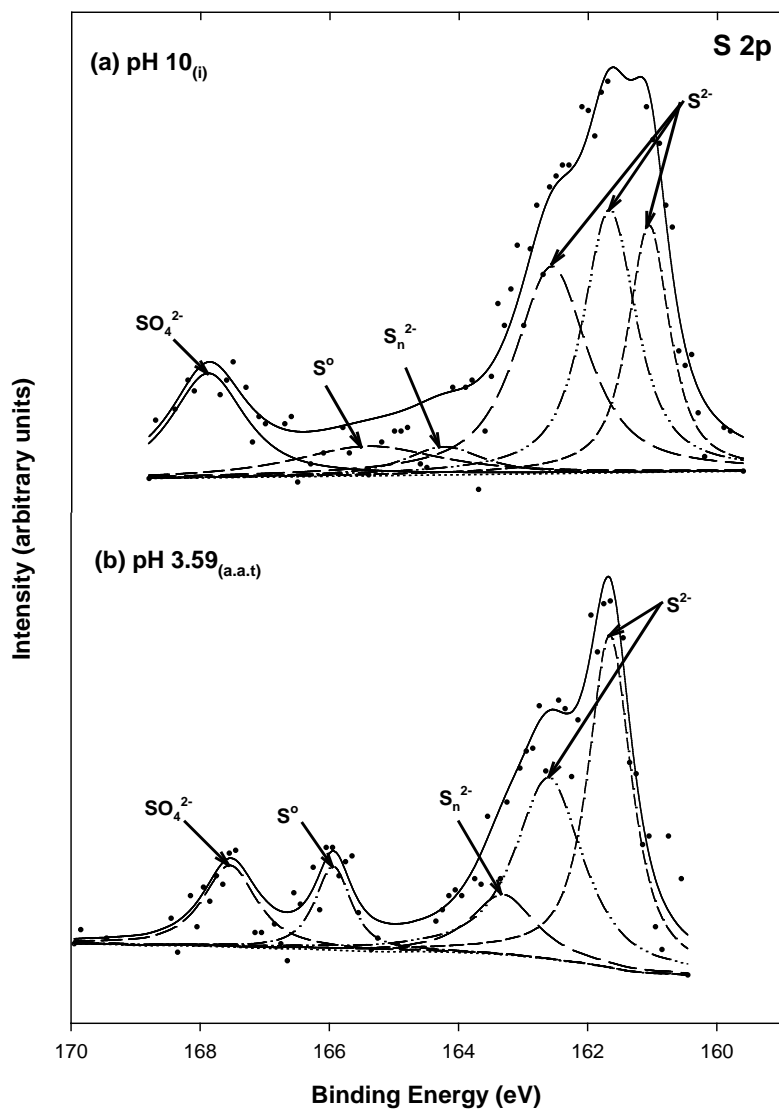


Figure 13.14 High resolution S 2p XPS spectra for mackinawite after contact with Hg(II) (1 mM) at (a) pH 10_(i) and (b) pH 3.5_(a.a.t).

Table 13.6 Binding energies (BE), full width at half maximum (FWHM), and area percentage for peaks in the Fe 2p_{3/2} XPS spectra of mackinawite after contact with Hg(II) at (a) pH 10.5_(i) and (b) pH 3.5_(a.a.t).

| Spectra | pH | BE (eV) | FWHM (eV) | Area (%) | Chemical States |
|----------------------------|-----|---------|-----------|----------|-------------------------------|
| Fe 2p_{3/2} | | | | | |
| | 10 | 707.2 | 0.53 | 5.60 | Fe(II)-S |
| | | 707.6 | 0.47 | 8.53 | Fe(II)-O |
| | | 708.2 | 0.96 | 28.0 | Fe(III)-S |
| | | 709.1 | 1.23 | 36.8 | Fe(III)-S |
| | | 709.9 | 0.56 | 5.85 | Fe(III)-S |
| | | 710.7 | 1.37 | 15.1 | Fe(III)-O |
| | 3.5 | 707.9 | 1.42 | 9.52 | Fe(II)-O |
| | | 708.4 | 0.93 | 18.9 | Fe(III)-S |
| | | 708.9 | 0.56 | 7.71 | Fe(III)-S |
| | | 709.6 | 1.17 | 39.5 | Fe(III)-S |
| | | 710.7 | 1.37 | 24.3 | Fe(III)-O |
| S 2p | | | | | |
| | 10 | 161.1 | 0.76 | 19.2 | S ²⁻ |
| | | 161.6 | 0.98 | 26.3 | S ²⁻ |
| | | 162.5 | 1.34 | 28.0 | S ²⁻ |
| | | 164.2 | 1.42 | 4.04 | S _n ²⁻ |
| | | 165.4 | 2.68 | 8.10 | S ⁰ |
| | | 167.8 | 1.35 | 14.4 | SO ₄ ²⁻ |
| | 3.5 | 161.6 | 0.79 | 38.2 | S ²⁻ |
| | | 162.6 | 1.24 | 32.4 | S ²⁻ |
| | | 163.3 | 1.18 | 10.0 | S _n ²⁻ |
| | | 165.9 | 0.66 | 7.82 | S ⁰ |
| | | 167.5 | 0.99 | 11.4 | SO ₄ ²⁻ |

14. CONCLUSIONS

14.1 Summary and Overall Merits

This study was performed with two types of batch reactor systems. One was for arsenic removal from solution using synthesized nanoporous titania adsorbents (NTAs) and the other one was for removal of As, Hg, Se using synthesized nano-particulate iron sulfides as adsorbent/reactants. For NTAs, the research work was aimed at enhancing adsorption capacity for arsenic compared to conventional adsorbents, and this was believed possible because NTAs have highly regular mesoporosity with high surface areas containing a large number of surface functional groups that more strongly attract arsenic.

In Section 3, a highly ordered mesoporous silica solid phase (SBA-15) that can incorporate reactive titania sorption sites and mesoporous titania (MT) were successfully synthesized. Titania was incorporated into the mesoporous silica at various levels and these NTAs were identified as $Ti_{(x)}$ -SBA-15, where “ x ” represents the mass fraction of titania. $Ti_{(25)}$ -SBA-15 had a greater maximum sorption capacity for As(III) than did $Ti_{(15,35)}$ -SBA-15 as determined by fitting the Langmuir isotherm to obtain q_{max} ($\mu\text{mol/g}$). Arsenic uptake by NTAs was very fast and followed a bi-phasic sorption pattern, where sorption was fast for the first 10 minutes, and then slowed and was almost completed within 200 minutes of contact. Distinct sorption maxima for As(III) removal were observed between pH 8 and pH 11 for MT and between pH 4 and pH 7 for $Ti_{(25)}$ -SBA-15. The amount of As(V) adsorbed generally decreased as pH increased.

In Section 4, a surface complexation model (SCM) based on the diffuse layer model (DLM) was used to predict arsenic adsorption envelopes by NTAs under various environmental conditions. Arsenic adsorption envelopes showed that the optimal pH range for As(III) removal was between pH 4 and pH 7 for $Ti_{(25)}$ -SBA-15 and between pH 8 and 11 for MT. Maximum

removal efficiencies for As(V) by $\text{Ti}_{(25)}$ -SBA-15 was observed to be near pH 4 and the maximum for MT was in the pH range between pH 4 and pH 7. However, at environmental pH (near pH 7 to pH 8) the extent of removal of As(III) and As(V) by MT was relatively greater than that by $\text{Ti}_{(25)}$ -SBA-15. Surface complexation modeling for As(III,V) adsorption by NTAs demonstrated the role of mono- and bidentate surface complexes in arsenic adsorption.

This research work using iron sulfides aimed to provide fundamental information on the behavior of target contaminants (As, Se, Hg) with novel adsorbent/reactants (FeS , FeS_2) as well as to develop techniques to form the adsorbent/reactants as nano-sized particles. These contaminants are important ones in ash and scrubber pond waters. This information will provide the basis for development of treatment processes for ash and scrubber pond effluents that will be effective in removing contaminants and will produce residuals that are stable (low leachability) when disposed to environment. Furthermore, the information will contribute to the knowledge base on the fate and transport of the target contaminants in the natural environment and in engineered environments such as ash and scrubber ponds. Based on the results of this study, information was developed on the effects of important variables (contact time, pH, reagent dose, and competing ion (sulfate)) on the ability of the novel adsorbent/reactants to initially remove target contaminants.

In Sections 5 and 6, pyrite as nano-scale particles (below 500 nm) was successfully synthesized and applied to remove selenium (Se(IV) , Se(VI)) from solution. The sulfur sites on the pyrite were found to play an important role in reducing Se(IV) to a variety of reduced species (Se(0) , Se(-I) , Se(-II)), but this was not true for Se(VI) . The un-oxidized Fe on the pyrite surface was found to react with reduced forms of Se to form surface precipitates (FeSe or FeSe_2) or other strongly bound surface complexes. The extent of removal of selenium (Se(IV) , Se(VI)) by pyrite was affected by sulfate concentration at high concentrations of selenium in the aqueous phase

and at high pH. The mixture of pyrite and Se(IV) was found to be highly stable when pH was changed, but there was little stability observed for Se(VI). Therefore, it can be concluded that pyrite can remove Se(IV) and Se(VI) at intermediate concentrations in the presence of sulfate and that after contact with pyrite, selenium resists release to solution as pH is changed.

In Sections 7 and 8, nanoparticulate mackinawite was successfully synthesized and removed Se(IV) more rapidly from solution than Se(VI). After contact with mackinawite for 30 days, the surface Fe and S sites contributed to reduce Se(IV), but there was little evidence of reduction of Se(VI). Removal of Se(IV) by mackinawite was more extensive than removal of Se(VI) and removal patterns for both depended on pH. Unlike what was observed for pyrite, sulfate (1, 10 mM) had little effect on removals of Se(IV) and Se(VI) by mackinawite, but there was some indication that sulfate promoted removal of Se(VI) at intermediate concentrations. Stability tests for mixtures of Se(IV) and FeS showed nearly complete removal at all but the high initial pH, i.e. high stability. Stability tests for mixtures of Se(VI) and mackinawite showed moderate removal at high pH, a minimum removal near pH 6 and nearly complete removal at high pH. Very high stability was observed with negligible release as pH decreased. Therefore, mackinawite appears to be a good adsorbent/reactant for removal of selenium because it can promote higher removal of selenium even in the presence of sulfate and because it shows high levels of stability when pH changes.

In Section 9, XPS analysis of pyrite and mackinawite after contact with arsenic (As(III), As(V)) for 30 days showed evidence of reduction of arsenic accompanied by oxidation of the surface Fe and S. Regardless of adsorbent type, various oxidation states (i.e., As(V), As(III), As(II), As(I) for As(III)-contacted solids, As(III) and As(V) for As(V)-contacted solids) were observed in the As $3d_{5/2}$ spectra. The results suggest that there are surface reactions between arsenic and the surface of the solids (pyrite, mackinawite).

In Section 10, experiments showed that removal of As(V) from solution by pyrite was faster than removal of As(III), indicating that As(III) and As(V) are interacting differently with the pyrite surface. Removal of As(III) was observed to increase as pH increased across the range investigated (pH 7 – pH 10), whereas an optimum pH in the range between pH 8 and pH 9 was observed for removal of As(V). Sulfate had little effect on removal of As(III) or As(V) at the concentrations investigated (1, 10 mM), but there were small decreases in the amount of arsenic removed at the highest concentration of sulfate and the effect was more apparent with As(V) than with As(III). Stability tests for mixtures of As(III) and pyrite showed low removal at low pH, increasing removal as pH was increased and moderate stability, i.e. moderate levels of release as pH was decreased, but the concentrations did not return to levels observed initially in the experiment. Stability of mixtures of As(V) and pyrite showed similar behavior except low removals were observed initially at high pH, removals increased as pH decreased and moderate to high levels of stability were observed as pH was raised back to the initial values. Therefore, pyrite could be expected to be a moderately effective adsorbent/reactant for removal of arsenic in terms of stability of the product, but inhibition of sulfate was moderate at given experimental conditions.

In Section 11, removals of arsenic (As(III), As(V)) by mackinawite were fast with half lives that were less than 10 minutes, indicating that the removals are probably limited by external transport of the soluble compound to the surface of the solid. However, removal of As(V) was faster than that of As(III). The effect of pH on the extent of removal of As(III) by mackinawite was moderate with highest removals occurring at intermediate pH (pH 8, pH 9), whereas there was strong effect of pH on removal of As(V), with greater removals observed at lower pH. Sulfate inhibited removal of As(III), but there was little difference between the effect of 1 mM and 10 mM sulfate. Removal of As(V) was reduced by sulfate at higher concentrations of As(V),

but showed a smaller effect at lower concentrations. Stability tests with arsenic (As(III), As(V)) and FeS showed nearly complete stability (no contaminant release) for As(III) and moderate to high stability for As(V), probably due to formation of strong bonds by redox reactions.

In Section 12, kinetics of removal of mercury by pyrite was observed to be very rapid and maximum loadings of mercury typically exceeded 6 mmol/g and in some cases exceeded 20 mmol/g. These loadings mean that the mass of mercury removed exceeded the mass of pyrite present. The pH of the solution did not appear to have a major effect on the extent of removal. However, there was a substantial amount of variability within the results of experiments at different pH. Exceptionally high removals of mercury could be the result of surface reactions and differences in removal could be the result of how fast these reactions occur at different pH. Sulfate was observed to have little effect on removal of mercury by pyrite over the concentration range that was investigated (0 – 10 mM). XPS analysis of pyrite after contact with Hg(II) for 30 days showed evidence of Hg(II) reduction to Hg(I), coupled with oxidation of surface Fe(II) species, but no evidence of changes in oxidation state of surface sulfur was observed. Stability tests for mixtures of Hg and pyrite were conducted at two initial concentrations of Hg(II). Nearly complete removal (>98%) was observed in all samples when the initial concentration was low. XPS analysis provided some evidence of mercury reduction and iron oxidation on the surface. When the initial concentration was high, low removal was observed at low pH, high removal at pH in the range pH 4 – pH 6, and moderate removal at higher pH. Good stability was observed when pH was reduced. XPS analysis showed evidence of mercury reduction and good evidence of iron oxidation and formation of sulfur species. These observations support the hypothesis that precipitates such as HgS or Hg₂S were formed. Therefore, pyrite appears to be a good adsorbent/reactant to remove Hg(II) from solution due to its high loading, small pH effect, low level of sulfate inhibition, and good stability.

In Section 13, removal of Hg(II) by FeS was observed to be rapid. At an initial concentration of 500 μM , complete removal occurred within 10 minutes. At higher initial concentrations, more time was required to achieve greater than 99 % removal. The removal pattern for Hg(II) by FeS differs depending on pH. The removal experiment conducted at pH 10 showed a relationship for solid phase concentration and liquid phase concentration that is best described by a BET model. This indicates that when concentrations are high enough, Hg(II) on the surface reacts to produce other solids that increase the amount of Hg(II) that can be removed from the liquid phase. Sulfate tended to increase the amounts of Hg(II) removed by FeS, but the effect was not large. This might be caused by sulfate ions being incorporated into mixed Hg-Fe solid phases. The results of XPS analysis for mackinawites contacted with Hg(II) for a period of 30 days shows the presence of Hg(I) in addition to Hg(II), as well as oxidized iron and sulfur species. Stability tests for mixtures of Hg(II) and FeS were conducted at two initial Hg(II) concentrations. At low initial concentration, results showed good removals were observed for all pH and good stability. XPS showed reduction of Hg(II) to Hg(I) coupled with some evidence of oxidation of the surface Fe and S species. At high initial concentration of Hg(II), high removals were observed under all conditions and high levels of stability were measured. XPS analysis indicated similar patterns in oxidation state of Hg, along with oxidation of Fe and S. Therefore, mackinawite appears to be a good reactant/adsorbent to remove Hg(II) because the mackinawite has high removal, no inhibition by sulfate and good stability.

Consequently, this study provides data on the behavior of the target contaminants (As, Se, Hg) in a novel treatment system that can be employed to control effluents from ash and scrubber pond waters. Development of such technologies will be of benefit to a wide range of power plants where these elements have been identified as contaminants of concern in ash and scrubber waters. The technologies that were evaluated in this study have distinct advantages over

more conventional treatment methods in that they are not expected to be strongly affected by the presence of competing ions such as sulfate and they will produce residuals that will continue to contain the contaminants when disposed in landfills.

14.2 Recommendations

14.2.1 Nanoporous Titania Adsorbents

Arsenic removal by NTAs was satisfactorily characterized using a batch experimental system. However, more extended work is required to evaluate the capacity and applicability of NTAs in natural or engineered systems. First, the highest priority is to enhance the cost and production yield of NTAs through novel synthesis methods (e.g., sonochemistry-based synthesis). Second, the adsorption capacity of NTAs in columns under various experimental conditions should be evaluated. Third, the regenerability of NTAs using various approaches (e.g., NaOH or ultrasonic-assisted desorption) should be evaluated to meet the needs of long-term performance. Finally, models should be developed to describe performance of NTAs in batch and column systems under a variety of environmental factors.

14.2.2 Nano-particulate Iron Sulfides

Nano-particulate iron sulfides (pyrite (FeS_2) and mackinawite (FeS)) were shown to be good adsorbent/reactants for removals of contaminants (As, Se, Hg) found in ash and scrubber pond waters at power plants. However, more extended and detailed studies are required to provide accurate information about sorption behavior and stability of final residuals. However, the first task should be to evaluate a variety of synthesis methods in order to reduce the aging time of particles to a few minutes. The optimized synthesis methods would produce more economical adsorbent/reactants. Based on the results of this study, removals of contaminants (As, Se, Hg) by iron sulfides proceed via surface reactions that lead to formation of stable solid

phases. Therefore, the extent of removal and stability of products should be strongly affected by environmental factors such as contact time, ratio of contaminants/solids, and pH. Thus, as a second task, experiments to determine the extent of removal should be conducted as functions of time and at various ratios of contaminants/solids. Third, as the above tasks are being worked on, application of a variety of reductants such as borohydride or Sn(II) should be evaluated to see if they can promote surface reactions that bring about rapid formation of stable surface precipitates or strong surface complexes. Fourth, the identification of final residuals is needed to provide the accurate reaction pathways by comparing reference solids using surface analysis techniques, including XANES (X-ray absorption near edge structure), EXAFS (Extended X-ray absorption fine structure), or XRD (X-ray diffraction). Finally, additional testing of the stability (or leachability) of the final residuals should be conducted with exposure to the atmosphere. The final residuals would probably be disposed in landfills, so they could come in contact with oxygen, resulting in change of oxidation status of components on the solid surface or structural elements of solids.

LITERATURE CITED

1. Lumia, D. S.; Linsey, K. S.; Barber, N. L.; Geological Survey (U.S.), Estimated use of water in the United States in 2000. In *Fact sheet 2005-3051*, U.S. Dept. of the Interior, U.S. Geological Survey: Reston, VA, 2005.
2. Feeley III, T. J.; Pletcher, S.; Carney, B.; McNemar, A. T. *Department of energy/national energy technological laboratory's power plant-water R&D program*; National Energy Technological Laboratory (NETL), Pittsburgh, PA, 2006.
3. Shah, P.; Strezov, V.; Stevanov, C.; Nelson, P. F., Speciation of arsenic and selenium in coal combustion products. *Energy & Fuels* **2007**, *21*, (2), 506-512.
4. Sandelin, K.; Backman, R., Trace elements in two pulverized coal-fired power stations. *Environ. Sci. Technol.* **2001**, *35*, (5), 826-834.
5. National Risk Management Research Laboratory (U.S.), Aqueous mercury treatment. In *Capsule Report*, National Risk Management Research Laboratory, Office of Research and Development, U.S. Environmental Protection Agency: Cincinnati, OH, 1997.
6. USEPA, Technologies and costs for removal of arsenic from drinking water. EPA 815-R-00-028, Washington, D.C., 2000.
7. O'day, P., Chemistry and mineralogy of arsenic. *Elements* **2006**, *2*, (2), 77-83.
8. Naveau, A.; Monteil-Rivera, F.; Guillon, E.; Dumonceau, J., Interactions of aqueous selenium(-II) and (IV) with metallic sulfide surfaces. *Environ. Sci. Technol.* **2007**, *41*, (15), 5376-5382.
9. deLlano, A. Y.; Bidoglio, G.; Avogadro, A.; Gibson, P. N.; Romero, P. R., Redox reactions and transport of selenium through fractured granite. *Journal of Contaminant Hydrology* **1996**, *21*, (1-4), 129-139.
10. Liu, J. R.; Valsaraj, K. T.; Devai, I.; DeLaune, R. D., Immobilization of aqueous Hg(II) by mackinawite (FeS). *J. Hazard. Mater.* **2008**, *157*, (2-3), 432-440.
11. Bower, J.; Savage, K. S.; Weinman, B.; Barnett, M. O.; Hamilton, W. P.; Harper, W. F., Immobilization of mercury by pyrite (FeS₂). *Environmental Pollution* **2008**, *156*, (2), 504-514.
12. Jeong, H. Y.; Klaue, B.; Blum, J. D.; Hayes, K. F., Sorption of mercuric ion by synthetic nanocrystalline mackinawite (FeS). *Environ. Sci. Technol.* **2007**, *41*, (22), 7699-7705.
13. Wang, L.; Abriola, L. M.; Han, Y. S.; Hayes, K. F.; Demond, A., Modeling As(III) removal by synthesized FeS coated sand in batch and column systems. *Geochim. Cosmochim. Acta* **2008**, *72*, (12), A998-A998.
14. McNeill, L. S., *Field measurement methods for arsenic in drinking water*. AWWA Research Foundation and American Water Works Association: Denver, CO, 2004.

15. Peters, R. W., New research sure to drive arsenic standard down, costs up. *Waterweek* **1992**, *1*, (3), 1.
16. EPA, National primary drinking water regulations: Arsenic and clarifications to compliance and new source contaminants monitoring, **2001**, *66* (14).
17. Kozul, C. D.; Hampton, T. H.; Davey, J. C.; Gosse, J. A.; Nomikos, A. P.; Eisenhauer, P., Chronic exposure to arsenic in the drinking water alters the expression of immune response genes in mouse lung. *Environmental Health Perspectives* **2009**, *In press*.
18. Kozul, C. D.; Ely, K. H.; Enelow, R. I.; Hamilton, J. W., Low dose arsenic compromises the immune response to influenza a infection *in vivo*. *Environmental Health Perspectives* **2009**, *In press*.
19. Ferguson, J. F.; Gavis, J., Review of arsenic cycle in natural waters. *Water Research* **1972**, *6*, (11), 1259-1274.
20. Alloway, B. J., *Heavy metals in soils*. 2nd ed.; Blackie: New York, 1995.
21. Vink, B. W., Stability relations of antimony and arsenic compounds in the light of revised and extended Eh-pH diagrams. *Chem. Geol.* **1996**, *130*, (1-2), 21-30.
22. Eary, L. E., The solubility of amorphous As_2S_3 from 25 to 90 °C. *Geochim. Cosmochim. Acta* **1992**, *56*, (6), 2267-2280.
23. Kim, M. J.; Nriagu, J.; Haack, S., Carbonate ions and arsenic dissolution by groundwater. *Environ. Sci. Technol.* **2000**, *34*, (15), 3094-3100.
24. Rubin, A. J., *Chemistry of water supply, treatment, and distribution*. Ann Arbor Science Publishers: Ann Arbor, MI., 1974.
25. Ghazy, S. E., Removal of cadmium, lead, mercury, tin, antimony, and arsenic from drinking and seawaters by colloid precipitate flotation. *Sep. Sci. Technol.* **1995**, *30*, (6), 933-947.
26. Blakey, N. C., Behavior of arsenical wastes codisposed with domestic solid-wastes. *Journal Water Pollution Control Federation* **1984**, *56*, (1), 69-75.
27. Carbonell-Barrachina, A. A.; Jugsujinda, A.; Burlo, F.; Delaune, R. D.; Patrick, W. H., Arsenic chemistry in municipal sewage sludge as affected by redox potential and pH. *Water Research* **2000**, *34*, (1), 216-224.
28. Carbonell-Barrachina, A.; Jugsujinda, A.; DeLaune, R. D.; Patrick, W. H.; Burlo, F.; Sirisukhodom, S.; Anurakpongsatorn, P., The influence of redox chemistry and pH on chemically active forms of arsenic in sewage sludge-amended soil. *Environ. Int.* **1999**, *25*, (5), 613-618.
29. Robins, R. G., The aqueous chemistry of arsenic in relation to hydrometallurgical processes. *Cim Bulletin* **1985**, *78*, (878), 75-75.

30. Smedley, P. L.; Kinniburgh, D. G., A review of the source, behaviour and distribution of arsenic in natural waters. *Appl. Geochem.* **2002**, *17*, (5), 517-568.
31. Vlassopoulos, D.; Andrews, C. B.; Hennet, R.; Macko, S. A. In *Natural immobilization of arsenic in the shallow groundwater of a tidal marsh, San Francisco bay*, The American Geophysical Union, Boston, Massachusetts, May 31 - June 4, 1999; Boston, Massachusetts, 1999.
32. Rittle, K. A.; Drever, J. I.; Colberg, P. J. S., Precipitation of arsenic during bacterial sulfate reduction. *Geomicrobiology Journal* **1995**, *13*, (1), 1-11.
33. Heinrich, C. A.; Eadington, P. J., Thermodynamic predictions of the hydrothermal chemistry of arsenic, and their significance for the paragenetic sequence of some cassiterite-arsenopyrite-base metal sulfide deposits. *Economic Geology* **1986**, *81*, (3), 511-529.
34. Zouboulis, A. I.; Kydros, K. A.; Matis, K. A., Arsenic(III) and arsenic(V) removal from solutions by pyrite fines. *Sep. Sci. Technol.* **1993**, *28*, (15-16), 2449-2463.
35. Farquhar, M. L.; Charnock, J. M.; Livens, F. R.; Vaughan, D. J., Mechanisms of arsenic uptake from aqueous solution by interaction with goethite, lepidocrocite, mackinawite, and pyrite: An X-ray absorption spectroscopy study. *Environ. Sci. Technol.* **2002**, *36*, (8), 1757-1762.
36. Kuhlmeier, P. D.; Sherwood, S. P., Treatability of inorganic arsenic and organo arsenicals in groundwater. *Water Environment Research* **1996**, *68*, (5), 946-951.
37. Ito, D.; Miura, K.; Ichimura, T.; Ihara, I.; Watanabe, T., Removal of As, Cd, Hg and Pb ions from solution by adsorption with bacterially-produced magnetic iron sulfide particles using high gradient magnetic separation. *IEEE Transactions on Applied Superconductivity* **2004**, *14*, (2), 1551-1553.
38. Morse, J. W.; Millero, F. J.; Cornwell, J. C.; Rickard, D., The chemistry of the hydrogen-sulfide and iron sulfide systems in natural-waters. *Earth-Science Reviews* **1987**, *24*, (1), 1-42.
39. Bostick, B. C.; Fendorf, S., Arsenite sorption on troilite (FeS) and pyrite (FeS₂). *Geochim. Cosmochim. Acta* **2003**, *67*, (5), 909-921.
40. Wolthers, M.; Charlet, L.; Van der Weijden, C. H.; Van der Linde, P. R.; Rickard, D., Arsenic mobility in the ambient sulfidic environment: Sorption of arsenic(V) and arsenic(III) onto disordered mackinawite. *Geochim. Cosmochim. Acta* **2005**, *69*, (14), 3483-3492.
41. Kim, E. J.; Batchelor, B., Macroscopic and X-ray photoelectron spectroscopic investigation of interactions of arsenic with synthesized pyrite. *Environ. Sci. Technol.* **2009**, *43*, (8), 2899-2904.
42. Gallegos, T. J.; Hyun, S. P.; Hayes, K. F., Spectroscopic investigation of the uptake of arsenite from solution by synthetic mackinawite. *Environ. Sci. Technol.* **2007**, *41*, 7781-7786.
43. Robins, R. G. *As chemistry in relation to the disposal and stability of waste* In

Proceedings of Arsenic & Mercury Workshop on Removal, Recovery, Treatment, and Disposal. EPA/600/R-92/105, **1992**, USEPA, Washington, DC.

44. Hounslow, A. W., Groundwater geochemistry - arsenic in landfills. *Ground Water* **1980**, *18*, (4), 331-333.
45. Ahmann, D.; Krumholz, L. R.; Hemond, H. F.; Lovley, D. R.; Morel, F. M. M., Microbial mobilization of arsenic from sediments of the Aberjona Watershed. *Environ. Sci. Technol.* **1997**, *31*, (10), 2923-2930.
46. Barnett, M. O. *Environmental chemistry of arsenic - A literature review*. Department of Environmental Science and Engineering, University of North Carolina at Chapel Hill: 1992.
47. White, C. A.; Sevee, J. E. *Arsenic mobilization mechanisms at a landfill site in Southern New Hampshire and an evaluation of remedial actions on dissolved arsenic concentrations*. American Geophysical Union, **1999**, Spring Meeting, Boston, Massachusetts.
48. Welch, A. H.; Westjohn, D. B.; Helsel, D. R.; Wanty, R. B., Arsenic in ground water of the United States: Occurrence and geochemistry. *Ground Water* **2000**, *38*, (4), 589-604.
49. Moore, J. N.; Ficklin, W. H.; Johns, C., Partitioning of arsenic and metals in reducing sulfidic sediments. *Environ. Sci. Technol.* **1988**, *22*, (4), 432-437.
50. Meng, X. G.; Korfiatis, G. P.; Jing, C. Y.; Christodoulatos, C., Redox transformations of arsenic and iron in water treatment sludge during aging and TCLP extraction. *Environ. Sci. Technol.* **2001**, *35*, (17), 3476-3481.
51. Stollenwerk, K. G.; Colman, J. A. In *Natural remediation of arsenic-contaminated groundwater: Solute-transport model predictions*, American Geophysical Union, **1999** Spring meeting, Boston, Massachusetts.
52. Leist, M.; Casey, R. J.; Caridi, D., The management of arsenic wastes: Problems and prospects. *J. Hazard. Mater.* **2000**, *76*, (1), 125-138.
53. Zhang, P. C.; Sparks, D. L., Kinetics of selenate and selenite adsorption-desorption at the goethite-water interface. *Environ. Sci. Technol.* **1990**, *24*, (12), 1848-1856.
54. Refait, P.; Simon, L.; Genin, J. M. R., Reduction of SeO_4^{2-} anions and anoxic formation of iron(II)-iron(III) hydroxy selenate green rust. *Environ. Sci. Technol.* **2000**, *34*, (5), 819-825.
55. Hyun, S.; Burns, P. E.; Murarka, I.; Lee, L. S., Selenium(IV) and (VI) sorption by soils surrounding fly ash management facilities. *Vadose Zone Journal* **2006**, *5*, (4), 1110-1118.
56. USEPA. *Draft aquatic life water quality criteria for selenium*, USEPA Rep. 822-D-04-001: Washington, DC., 2004.
57. Frankenberger, W. T.; Engberg, R. A., *Environmental chemistry of selenium*. Marcel Dekker: New York, 1998.

58. Bodek, I., *Environmental inorganic chemistry: Properties, processes, and estimation methods*. Pergamon Press: New York, 1988.
59. Peak, D.; Saha, U. K.; Huang, P. M., Selenite adsorption mechanisms on pure and coated montmorillonite: An EXAFS and XANES spectroscopic study. *Soil Sci. Soc. Am. J.* **2006**, *70*, (1), 192-203.
60. Elrashidi, M. A.; Adriano, D. C.; Workman, S. M.; Lindsay, W. L., Chemical equilibria of selenium in soils - A theoretical development. *Soil Science* **1987**, *144*, (2), 141-152.
61. Scheinost, A. C.; Kirsch, R.; Banerjee, D.; Fernandez-Martinez, A.; Zaenker, H.; Funke, H.; Charlet, L., X-ray absorption and photoelectron spectroscopy investigation of selenite reduction by Fe(II)-bearing minerals. *Journal of Contaminant Hydrology* **2008**, *102*, (3-4), 228-245.
62. Bruggeman, C.; Maes, A.; Vancluysen, J.; Vandenmusselle, P., Selenite reduction in Boom clay: Effect of FeS₂, clay minerals and dissolved organic matter. *Environmental Pollution* **2005**, *137*, (2), 209-221.
63. Schecher, W. D.; Mcavoy, D. C., MINEQL+: A chemical equilibrium program for personal computers. *Computers Environment and Urban Systems* **1994**, *16*, (1), 65-76.
64. Masscheleyn, P. H.; Delaune, R. D.; Patrick, W. H., Transformations of selenium as affected by sediment oxidation reduction potential and pH. *Environ. Sci. Technol.* **1990**, *24*, (1), 91-96.
65. Gustafsson, J. P. Visual Minteq ver. 2.61, <http://www.lwr.kth.se/english/OurSoftware/Vminteq>. Nov. 2009
66. Adriano, D. C., *Trace elements in terrestrial environments: Biogeochemistry, bioavailability, and risks of metals*. 2nd ed.; Springer: New York, 2001; p xii, 867 p.
67. Scheinost, A. C.; Charlet, L., Selenite reduction by mackinawite, magnetite and siderite: XAS characterization of nanosized redox products. *Environ. Sci. Technol.* **2008**, *42*, (6), 1984-1989.
68. EPA, *Selenium treatment/removal alternatives demonstration project*, EPA/600/R-01/077, 2001.
69. Eto, K., Minamata disease. *Neuropathology* **2000**, *20*, S14-S19.
70. Jeong, H. Y.; Klaue, B.; Blum, J.; Hayes, K. F., Sorption of mercuric ion by iron sulfide. *Abstracts of Papers of the American Chemical Society* **2004**, *228*, U613-U613.
71. Kaneko, K., Dynamic Hg(II) adsorption characterization of iron oxide-dispersed activated carbon-fibers. *Carbon* **1988**, *26*, (6), 903-905.

72. Vieira, R. S.; Beppu, M. M., Dynamic and static adsorption and desorption of Hg(II) ions on chitosan membranes and spheres. *Water Research* **2006**, *40*, (8), 1726-1734.
73. Weisener, C. G.; Sale, K. S.; Smyth, D. J. A.; Blowes, D. W., Field column study using zerovalent iron for mercury removal from contaminated groundwater. *Environ. Sci. Technol.* **2005**, *39*, (16), 6306-6312.
74. Liu, W.; Vidic, R. D.; Brown, T. D., Optimization of sulfur impregnation protocol for fixed bed application of activated carbon-based sorbents for gas-phase mercury removal. *Environ. Sci. Technol.* **1998**, *32*, (4), 531-538.
75. Skyllberg, U.; Bloom, P. R.; Qian, J.; Lin, C. M.; Bleam, W. F., Complexation of mercury(II) in soil organic matter: EXAFS evidence for linear two-coordination with reduced sulfur groups. *Environ. Sci. Technol.* **2006**, *40*, (13), 4174-4180.
76. Nriagu, J. O., *The Biogeochemistry of mercury in the environment*. Elsevier/North-Holland Biomedical Press; sole distributors for the U.S.A. and Canada, Elsevier/North-Holland: Amsterdam, 1979; p xv, 696 p.
77. Sadiq, M., *Toxic metal chemistry in marine environments*. Marcel Dekker: New York, NY, 1992; p 390 p.
78. Dyrssen, D.; Wedborg, M., The sulfur-mercury(II) system in natural-waters. *Water Air Soil Pollut.* **1991**, *56*, 507-519.
79. Ravichandran, M.; Aiken, G. R.; Ryan, J. N.; Reddy, M. M., Inhibition of precipitation and aggregation of metacinnabar (mercuric sulfide) by dissolved organic matter isolated from the Florida Everglades. *Environ. Sci. Technol.* **1999**, *33*, (9), 1418-1423.
80. Wu, P. Y. Aqueous mercury partition and modeling. Ph.D. Dissertation, University of Utah, 2003.
81. Yin, Y. J.; Allen, H. E.; Huang, C. P.; Sanders, P. F., Adsorption/desorption isotherms of Hg(II) by soil. *Soil Science* **1997**, *162*, (1), 35-45.
82. Chen, C. C.; McKimmy, E. J.; Pinnavaia, T. J.; Hayes, K. F., XAS study of mercury(II) ions trapped in mercaptan - Functionalized mesostructured silicate with a wormhole framework structure. *Environ. Sci. Technol.* **2004**, *38*, (18), 4758-4762.
83. Biester, H.; Zimmer, H., Solubility and changes of mercury binding forms in contaminated soils after immobilization treatment. *Environ. Sci. Technol.* **1998**, *32*, (18), 2755-2762.
84. Brown, J. R.; Bancroft, G. M.; Fyfe, W. S.; Mclean, R. A. N., Mercury removal from water by iron sulfide minerals - Electron-spectroscopy for chemical-analysis (Esca) study. *Environ. Sci. Technol.* **1979**, *13*, (9), 1142-1144.
85. Ebadian, M. A.; Allen, M.; Cai, Y.; McGahan, J. F., Mercury contaminated material

decontamination methods: Investigation and assessment. Department of Energy (DOE), DE-FG21-95EW55094; 2001.

86. EPA. *Capsule report: Aqueous mercury treatment, EPA-815-R-00-018*; 1997.
87. Watson, J. H. P.; Ellwood, D. C.; Deng, Q. X.; Mikhalovsky, S.; Hayter, C. E.; Evans, J., Heavy-metal adsorption on bacterially produced FeS. *Minerals Engineering* **1995**, 8, (10), 1097-1108.
88. Watson, J. H. P.; Croudace, I. W.; Warwick, P. E.; James, P. A. B.; Charnock, J. M.; Ellwood, D. C., Adsorption of radioactive metals by strongly magnetic iron sulfide nanoparticles produced by sulfate-reducing bacteria. *Sep. Sci. Technol.* **2001**, 36, (12), 2571-2607.
89. Martellaro, P. J.; Moore, G. A.; Peterson, E. S.; Abbott, E. H.; Gorenbain, A. E., Environmental application of mineral sulfides for removal of gas-phase Hg(0) and aqueous Hg²⁺. *Sep. Sci. Technol.* **2001**, 36, (5-6), 1183-1196.
90. Butler, E. C.; Hayes, K. F., Effects of solution composition and pH on the reductive dechlorination of hexachloroethane by iron sulfide. *Environ. Sci. Technol.* **1998**, 32, (9), 1276-1284.
91. Jean, G. E.; Bancroft, G. M., Heavy-metal adsorption by sulfide mineral surfaces. *Geochim. Cosmochim. Acta* **1986**, 50, (7), 1455-1463.
92. Behra, P.; Bonnissel-Gissingner, P.; Alnot, M.; Revel, R.; Ehrhardt, J. J., XPS and XAS study of the sorption of Hg(II) onto pyrite. *Langmuir* **2001**, 17, (13), 3970-3979.
93. Ehrhardt, J. J.; Behra, P.; Bonnissel-Gissingner, P.; Alnot, M., XPS study of the sorption of Hg(II) onto pyrite FeS₂. *Surface and Interface Analysis* **2000**, 30, (1), 269-272.
94. Hyland, M. M.; Jean, G. E.; Bancroft, G. M., XPS and AES studies of Hg(II) sorption and desorption reactions on sulfide minerals. *Geochim. Cosmochim. Acta* **1990**, 54, (7), 1957-1967.
95. Ditoro, D. M.; Mahony, J. D.; Hansen, D. J.; Scott, K. J.; Hicks, M. B.; Mayr, S. M.; Redmond, M. S., Toxicity of cadmium in sediments - the role of acid volatile sulfide. *Environmental Toxicology and Chemistry* **1990**, 9, (12), 1487-1502.
96. Posfai, M.; Dunin-Borkowski, R. E., Sulfides in biosystems. *Sulfide Mineralogy and Geochemistry* **2006**, 61, 679-714.
97. Holmes, J., Fate of incorporated metals during mackinawite oxidation in sea water. *Appl. Geochem.* **1999**, 14, (3), 277-281.
98. Morse, J. W.; Arakaki, T., Adsorption and coprecipitation of divalent metals with mackinawite (FeS). *Geochim. Cosmochim. Acta* **1993**, 57, (15), 3635-3640.
99. Arakaki, T.; Morse, J. W., Coprecipitation and adsorption of Mn(II) with mackinawite

(FeS) under conditions similar to those found in anoxic sediments. *Geochim. Cosmochim. Acta* **1993**, *57*, (1), 9-14.

100. Wolthers, M.; Charlet, L.; van der Weijden, C. H., Arsenic sorption onto disordered mackinawite as a control on the mobility of arsenic in the ambient sulphidic environment. *Journal De Physique Iv* **2003**, *107*, 1377-1380.

101. Parkman, R. H.; Charnock, J. M.; Bryan, N. D.; Livens, F. R.; Vaughan, D. J., Reactions of copper and cadmium ions in aqueous solution with goethite, lepidocrocite, mackinawite, and pyrite. *American Mineralogist* **1999**, *84*, (3), 407-419.

102. Widler, A. M.; Seward, T. M., The adsorption of gold(I) hydrosulphide complexes by iron sulphide surfaces. *Geochim. Cosmochim. Acta* **2002**, *66*, (3), 383-402.

103. Rosso, K. M.; Vaughan, D. J., Reactivity of sulfide mineral surfaces. *Sulfide Mineralogy and Geochemistry* **2006**, *61*, 557-607.

104. Moyes, L. N.; Jones, M. J.; Reed, W. A.; Livens, F. R.; Charnock, J. M.; Mosselmans, J. F. W.; Hennig, C.; Vaughan, D. J.; Patrick, R. A. D., An X-ray absorption spectroscopy study of neptunium(V) reactions with mackinawite (FeS). *Environ. Sci. Technol.* **2002**, *36*, (2), 179-183.

105. Livens, F. R.; Jones, M. J.; Hynes, A. J.; Charnock, J. M.; Mosselmans, J. F. W.; Hennig, C.; Steele, H.; Collison, D.; Vaughan, D. J.; Patrick, R. A. D.; Reed, W. A.; Moyes, L. N., X-ray absorption spectroscopy studies of reactions of technetium, uranium and neptunium with mackinawite. *Journal of Environmental Radioactivity* **2004**, *74*, (1-3), 211-219.

106. Wharton, M. J.; Atkins, B.; Charnock, J. M.; Livens, F. R.; Patrick, R. A. D.; Collison, D., An X-ray absorption spectroscopy study of the coprecipitation of Tc and Re with mackinawite (FeS). *Appl. Geochem.* **2000**, *15*, (3), 347-354.

107. Moyes, L. N.; Parkman, R. H.; Charnock, J. M.; Vaughan, D. J.; Livens, F. R.; Hughes, C. R.; Braithwaite, A., Uranium uptake from aqueous solution by interaction with goethite, lepidocrocite, muscovite, and mackinawite: An X-ray absorption spectroscopy study. *Environ. Sci. Technol.* **2000**, *34*, (6), 1062-1068.

108. Hua, B.; Deng, B. L., Reductive immobilization of uranium(VI) by amorphous iron sulfide. *Environ. Sci. Technol.* **2008**, *42*, (23), 8703-8708.

109. Zwank, L.; Elsner, M.; Aeberhard, A.; Schwarzenbach, R. P.; Haderlein, S. B., Carbon isotope fractionation in the reductive dehalogenation of carbon tetrachloride at iron (hydr)oxide and iron sulfide minerals. *Environ. Sci. Technol.* **2005**, *39*, (15), 5634-5641.

110. Diallo, M.; Swaminathan, P.; Balogh, L.; Shi, X. Y.; Johnson, J. H.; Goddard, W. A., Fe(0)/FeS PAMAM dendrimer nanocomposites for reductive dehalogenation of tetrachloroethylene: Synthesis, characterization and evaluation of materials performance. *Abstracts of Papers of the American Chemical Society* **2004**, *227*, U1272-U1272.

111. Choi, J.; Choi, Y.; Lee, W., Effects of transition metal and sulfide on the reductive

dechlorination of carbon tetrachloride and 1,1,1-trichloroethane by FeS. *J. Hazard. Mater.* **2009**, *162*, (2-3), 1151-1158.

112. Jeong, H. Y.; Hayes, K. F., Impact of transition metals on reductive dechlorination rate of hexachloroethane by mackinawite. *Environ. Sci. Technol.* **2003**, *37*, (20), 4650-4655.

113. Jeong, H. Y.; Hayes, K. F., Reductive dechlorination of tetrachloroethylene and trichloroethylene by mackinawite (FeS) in the presence of metals: Reaction rates. *Environ. Sci. Technol.* **2007**, *41*, (18), 6390-6396.

114. Jeong, H. Y.; Kim, H.; Hayes, K. F., Reductive dechlorination pathways of tetrachloroethylene and trichloroethylene and subsequent transformation of their dechlorination products by mackinawite (FeS) in the presence of metals. *Environ. Sci. Technol.* **2007**, *41*, (22), 7736-7743.

115. Butler, E. C.; Hayes, K. F., Factors influencing rates and products in the transformation of trichloroethylene by iron sulfide and iron metal. *Environ. Sci. Technol.* **2001**, *35*, (19), 3884-3891.

116. Butler, E. C.; Hayes, K. F., Kinetics of the transformation of halogenated aliphatic compounds by iron sulfide. *Environ. Sci. Technol.* **2000**, *34*, (3), 422-429.

117. Butler, E. C.; Hayes, K. F., Kinetics of the transformation of trichloroethylene and tetrachloroethylene by iron sulfide. *Environ. Sci. Technol.* **1999**, *33*, (12), 2021-2027.

118. Butler, E. C.; Hayes, K. F., Micellar solubilization of nonaqueous phase liquid contaminants by nonionic surfactant mixtures: Effects of sorption, partitioning and mixing. *Water Research* **1998**, *32*, (5), 1345-1354.

119. Coles, C. A.; Rao, S. R.; Yong, R. N., Lead and cadmium interactions with mackinawite: Retention mechanisms and the role of pH. *Environ. Sci. Technol.* **2000**, *34*, (6), 996-1000.

120. Jeong, H. Y. Removal of heavy metals and reductive dechlorination of chlorinated organic pollutants by nanosized FeS. Ph.D. Dissertation, University of Michigan, 2005.

121. Cooper, D. C. Trace metal diagenesis in anoxic marine sediments. Ph.D. Dissertation, Texas A&M University, College Station, TX, 1998.

122. Rickard, D.; Luther, G. W., Metal sulfide complexes and clusters. *Sulfide Mineralogy and Geochemistry* **2006**, *61*, 421-504.

123. Wolthers, M. Geochemistry and environmental mineralogy of iron-sulphur-arsenic system. Ph.D. Dissertation, Universiteit Utrecht, 2003.

124. Schoonen, M. A. A.; Barnes, H. L., Reactions forming pyrite and marcasite from solution .2. Via FeS precursors below 100 °C. *Geochim. Cosmochim. Acta* **1991**, *55*, (6), 1505-1514.

125. Murphy, R.; Strongin, D. R., Surface reactivity of pyrite and related sulfides. *Surface Science Reports* **2009**, *64*, (1), 1-45.
126. Evangelou, V. P., *Pyrite oxidation and its control : solution chemistry, surface chemistry, acid mine draingae (AMD), molecular oxidation mechanisms, microbial role, kinetics, control, ameliorates and limitations, microencapsulation*. CRC Press: Boca Raton, FL, 1995; p 293 p.
127. Rickard, D. T., Kinetics and mechanism of pyrite formation at low-temperatures. *American Journal of Science* **1975**, *275*, (6), 636-652.
128. Carlson, D. L. Environmental transformations of chloroacetamide herbicides: Hydrolysis and reactions with iron pyrite. Ph.D. dissertation, The Johns Hopkins University, Baltimore, MD, 2004.
129. Schoonen, M. A. A.; Barnes, H. L., Reactions forming pyrite and marcasite from solution .I. Nucleation of FeS₂ Below 100°C. *Geochim. Cosmochim. Acta* **1991**, *55*, (6), 1495-1504.
130. Rickard, D., Kinetics of pyrite formation by the H₂S oxidation of iron (II) monosulfide in aqueous solutions between 25 and 125 °C: The rate equation. *Geochim. Cosmochim. Acta* **1997**, *61*, (1), 115-134.
131. Luther, G. W., Pyrite synthesis via polysulfide compounds. *Geochim. Cosmochim. Acta* **1991**, *55*, (10), 2839-2849.
132. Wilkin, R. T.; Barnes, H. L., Formation processes of framboidal pyrite. *Geochim. Cosmochim. Acta* **1997**, *61*, (2), 323-339.
133. Benning, L. G.; Wilkin, R. T.; Barnes, H. L., Reaction pathways in the Fe-S system below 100 °C. *Chem. Geol.* **2000**, *167*, (1-2), 25-51.
134. Wei, D. W.; OsseoAsare, K., Particulate pyrite formation by the Fe³⁺/HS⁻ reaction in aqueous solutions: Effects of solution composition. *Colloid Surf. A-Physicochem. Eng. Asp.* **1996**, *118*, (1-2), 51-61.
135. Rosso, K. M.; Vaughan, D. J., Sulfide mineral surfaces. *Sulfide Mineralogy and Geochemistry* **2006**, *61*, 505-556.
136. Bednar, A. J.; Garbarino, J. R.; Ranville, J. F.; Wildeman, T. R., Preserving the distribution of inorganic arsenic species in groundwater and acid mine drainage samples. *Environ. Sci. Technol.* **2002**, *36*, (10), 2213-2218.
137. Hacquard, E.; Bessiere, J.; Alnot, M.; Ehrhardt, J. J., Surface spectroscopic study of the adsorption of Ni(II) on pyrite and arsenopyrite at pH 10. *Surface and Interface Analysis* **1999**, *27*, (9), 849-860.
138. Kriegmanking, M. R.; Reinhard, M., Transformation of carbon-tetrachloride by pyrite in aqueous-solution. *Environ. Sci. Technol.* **1994**, *28*, (4), 692-700.

139. Pham, H. T.; Kitsuneduka, M.; Hara, J.; Suto, K.; Inoue, C., Trichloroethylene transformation by natural mineral pyrite: The deciding role of oxygen. *Environ. Sci. Technol.* **2008**, *42*, (19), 7470-7475.
140. Lee, W.; Batchelor, B., Abiotic, reductive dechlorination of chlorinated ethylenes by iron-bearing soil minerals. 2. Green rust. *Environ. Sci. Technol.* **2002**, *36*, (24), 5348-5354.
141. Oh, S. Y.; Chiu, P. C.; Cha, D. K., Reductive transformation of 2,4,6-trinitrotoluene, hexahydro-1,3,5-trinitro-1,3,5-triazine, and nitroglycerin by pyrite and magnetite. *J. Hazard. Mater.* **2008**, *158*, (2-3), 652-655.
142. Mullet, M.; Demoisson, F.; Humbert, B.; Michot, L. J.; Vantelon, D., Aqueous Cr(VI) reduction by pyrite: Speciation and characterisation of the solid phases by X-ray photoelectron, Raman and X-ray absorption spectroscopies. *Geochim. Cosmochim. Acta* **2007**, *71*, (13), 3257-3271.
143. von Oertzen, G. U.; Skinner, W. M.; Nesbitt, H. W.; Pratt, A. R.; Buckley, A. N., Cu adsorption on pyrite (100): Ab initio and spectroscopic studies. *Surface Science* **2007**, *601*, (24), 5794-5799.
144. Naveau, A.; Monteil-Rivera, F.; Dumonceau, J.; Catalette, H.; Simoni, E., Sorption of Sr(II) and Eu(III) onto pyrite under different redox potential conditions. *J. Colloid Interface Sci.* **2006**, *293*, (1), 27-35.
145. Kresge, C. T.; Leonowicz, M. E.; Roth, W. J.; Vartuli, J. C.; Beck, J. S., Ordered mesoporous molecular-sieves synthesized by a liquid-crystal template mechanism. *Nature* **1992**, *359*, (6397), 710-712.
146. Fryxell, G. E.; Cao, G., *Environmental applications of nanomaterials: Synthesis, sorbents and sensors*. Imperial College Press: London, 2007; p xi, 507 p.
147. Isaacs, L. K. Adsorption of lead(II) ions by organosilicate nanoporous materials. Ph.D. Dissertation, Old Dominion University, 2007.
148. Zhao, D. Y.; Feng, J. L.; Huo, Q. S.; Melosh, N.; Fredrickson, G. H.; Chmelka, B. F.; Stucky, G. D., Triblock copolymer syntheses of mesoporous silica with periodic 50 to 300 angstrom pores. *Science* **1998**, *279*, (5350), 548-552.
149. Jang, M. Arsenic removal from water using nano-scale metal oxide incorporated, highly ordered mesoporous silicate media. Ph.D. Dissertation, University of Wisconsin-Madison, 2003.
150. Pinnavaia, T. J.; Thorpe, M. F., *Access in nanoporous materials*. Plenum Press: New York, 1995; p xi, 441 p.
151. Wang, X. C.; Yu, J. C.; Ho, C. M.; Hou, Y. D.; Fu, X. Z., Photocatalytic activity of a hierarchically macro/mesoporous titania. *Langmuir* **2005**, *21*, (6), 2552-2559.

152. Sun, X. Organofunctional silica mesostructures with improved accessibility and applications as heavy metal ion adsorbents Ph.D. Dissertation, Michigan State University, 2008.
153. Soler-illia, G. J. D.; Sanchez, C.; Lebeau, B.; Patarin, J., Chemical strategies to design textured materials: From microporous and mesoporous oxides to nanonetworks and hierarchical structures. *Chemical Reviews* **2002**, *102*, (11), 4093-4138.
154. Jones, J. T. A.; Wood, C. D.; Dickinson, C.; Khimyak, Y. Z., Periodic mesoporous organosilicas with domain functionality: Synthesis and advanced characterization. *Chemistry of Materials* **2008**, *20*, (10), 3385-3397.
155. Sayari, A.; Jaroniec, M., *Nanoporous Materials III : Proceedings of the 3rd International Symposium on Nanoporous Materials, Ottawa, Ontario, Canada, June 12-15, 2002*. Elsevier: Amsterdam ; Boston, 2002; p xvii, 691 p.
156. Wang, X. Functionalized porous titania nanostructures as efficient photocatalysts. Ph.D. Dissertation, Chinese University of Hong Kong, 2005.
157. Luan, Z. H.; Maes, E. M.; van der Heide, P. A. W.; Zhao, D. Y.; Czernuszewicz, R. S.; Kevan, L., Incorporation of titanium into mesoporous silica molecular sieve SBA-15. *Chemistry of Materials* **1999**, *11*, (12), 3680-3686.
158. Aronson, B. J.; Blanford, C. F.; Stein, A., Solution-phase grafting of titanium dioxide onto the pore surface of mesoporous silicates: Synthesis and structural characterization. *Chemistry of Materials* **1997**, *9*, (12), 2842-2851.
159. Fernandez, A.; Lassaletta, G.; Jimenez, V. M.; Justo, A.; GonzalezElipse, A. R.; Herrmann, J. M.; Tahiri, H.; AitIchou, Y., Preparation and characterization of TiO₂ photocatalysts supported on various rigid supports (glass, quartz and stainless steel). Comparative studies of photocatalytic activity in water purification. *Applied Catalysis B-Environmental* **1995**, *7*, (1-2), 49-63.
160. Notari, B., Microporous crystalline titanium silicates. *Advances in Catalysis, Vol 41* **1996**, *41*, 253-334.
161. Prakash, A. M.; Kevan, L.; Zahedi-Niaki, M. H.; Kaliaguine, S., Electron spin resonance and electron spin-echo modulation evidence for the isomorphous substitution of titanium in titanium aluminophosphate molecular sieves. *Journal of Physical Chemistry B* **1999**, *103*, (5), 831-837.
162. Prakash, A. M.; Sung-Suh, H. M.; Kevan, L., Electron spin resonance evidence for isomorphous substitution of titanium into titanasilicate TiMCM-41 mesoporous molecular sieve. *Journal of Physical Chemistry B* **1998**, *102*, (5), 857-864.
163. Chen, Y. Y.; Huang, Y. L.; Xiu, J. H.; Han, X. W.; Bao, X. H., Direct synthesis, characterization and catalytic activity of titanium-substituted SBA-15 mesoporous molecular sieves. *Applied Catalysis a-General* **2004**, *273*, (1-2), 185-191.

164. Prasad Saripalli, K.; McGrail, B. P.; Girvin, D. C., Adsorption of molybdenum on to anatase from dilute aqueous solutions. *Appl. Geochem.* **2002**, *17*, (5), 649-656.
165. Ludwig, C.; Schindler, P. W., Surface complexation on TiO₂: I. Adsorption of H⁺ and Cu²⁺ Ions onto TiO₂ (Anatase). *J. Colloid Interface Sci.* **1995**, *169*, (2), 284-290.
166. Xu, Z.; Meng, X., Size effects of nanocrystalline TiO₂ on As(V) and As(III) adsorption and As(III) photooxidation. **2009** *J. Hazard. Mater. In Press, Corrected Proof*.
167. Tan, X.; Fang, M.; Li, J.; Lu, Y.; Wang, X., Adsorption of Eu(III) onto TiO₂: Effect of pH, concentration, ionic strength and soil fulvic acid. **2009** *J. Hazard. Mater. In Press, Corrected Proof*.
168. Olkhoviyk, O. Environmental applications of ordered mesoporous materials: organosilicas with multifunctional ligands for adsorption of mercury ions. Ph.D. Dissertation, Kent State University, 2007.
169. Kim, Y.; Yi, J., Advances in environmental technologies via the application of mesoporous materials. *Journal of Industrial and Engineering Chemistry* **2004**, *10*, (1), 41-51.
170. Mercier, L.; Pinnavaia, T. J., Access in mesoporous materials: Advantages of a uniform pore structure in the design of a heavy metal ion adsorbent for environmental remediation. *Advanced Materials* **1997**, *9*, (6), 500-&.
171. Evangelista, S. M.; DeOliveira, E.; Castro, G. R.; Zara, L. F.; Prado, A. G. S., Hexagonal mesoporous silica modified with 2-mercaptothiazoline for removing mercury from water solution. *Surface Science* **2007**, *601*, (10), 2194-2202.
172. Antochshuk, V.; Olkhoviyk, O.; Jaroniec, M.; Park, I. S.; Ryoo, R., Benzoylthiourea-modified mesoporous silica for mercury(II) removal. *Langmuir* **2003**, *19*, (7), 3031-3034.
173. Walcarius, A.; Delacote, C., Mercury(II) binding to thiol-functionalized mesoporous silicas: critical effect of pH and sorbent properties on capacity and selectivity. *Analytica Chimica Acta* **2005**, *547*, (1), 3-13.
174. Bibby, A.; Mercier, L., Mercury(II) ion adsorption behavior in thiol-functionalized mesoporous silica microspheres. *Chemistry of Materials* **2002**, *14*, (4), 1591-1597.
175. Silva, A. R.; Wilson, K.; Whitwood, A. C.; Clark, J. H.; Freire, C., Amine-functionalised hexagonal mesoporous silica as support for copper(II) acetylacetonate catalyst. *European Journal of Inorganic Chemistry* **2006**, (6), 1275-1283.
176. Cassiers, K.; Linssen, T.; Mathieu, M.; Bai, Y. Q.; Zhu, H. Y.; Cool, P.; Vansant, E. F., Surfactant-directed synthesis of mesoporous titania with nanocrystalline anatase walls and remarkable thermal stability. *Journal of Physical Chemistry B* **2004**, *108*, (12), 3713-3721.
177. Zhang, Z. B.; Wang, C. C.; Zakaria, R.; Ying, J. Y., Role of particle size in nanocrystalline TiO₂-based photocatalysts. *Journal of Physical Chemistry B* **1998**, *102*, (52),

10871-10878.

178. Yu, J. C.; Yu, J. G.; Zhao, J. C., Enhanced photocatalytic activity of mesoporous and ordinary TiO₂ thin films by sulfuric acid treatment. *Applied Catalysis B-Environmental* **2002**, *36*, (1), 31-43.
179. Dong, J.; Xu, Z. H.; Wang, F., Engineering and characterization of mesoporous silica-coated magnetic particles for mercury removal from industrial effluents. *Appl. Surf. Sci.* **2008**, *254*, (11), 3522-3530.
180. Waltham, C. A.; Eick, M. J., Kinetics of arsenic adsorption on goethite in the presence of sorbed silicic acid. *Soil Sci. Soc. Am. J.* **2002**, *66*, (3), 818-825.
181. DOHHA, CERCLA priority list of hazardous substances that will be the subject of toxicological profiles and support document, ATSDR, 2005; Vol. 44.
182. O'Neil, P. Heavy Metals in Soil. John Wiley & Sons: New York, 1995.
183. Zhang, Y.; Yang, M.; Huang, X., Arsenic(V) removal with a Ce(IV)-doped iron oxide adsorbent. *Chemosphere* **2003**, *51*, (9), 945-952.
184. National Drinking Water Advisory Council, <http://www.epa.gov/safewater/ndwac/novrecs.html>, Nov. 1999
185. Huang, D.; Luo, G. S.; Wang, Y. J., Using phosphoric acid as a catalyst to control the structures of mesoporous titanium dioxide materials. *Microporous and Mesoporous Materials* **2005**, *84*, (1-3), 27-33.
186. Gregg, S. J.; Sing, K. S. W., *Adsorption, surface area and porosity*. 2nd ed.; Academic Press: London ; New York, 1982; p xi, 303 p.
187. Rouquerol, F.; Rouquerol, J.; Sing, K. S. W., *Adsorption by powders and porous solids: Principles, methodology and applications*. Academic Press: San Diego, Calif., 1999; p xvi, 467 p.
188. Barrett, E. P.; Joyner, L. G.; Halenda, P. P., The determination of pore volume and area distributions in porous substances .1. Computations from nitrogen isotherms. *Journal of the American Chemical Society* **1951**, *73*, (1), 373-380.
189. Kruk, M.; Jaroniec, M.; Sayari, A., Application of large pore MCM-41 molecular sieves to improve pore size analysis using nitrogen adsorption measurements. *Langmuir* **1997**, *13*, (23), 6267-6273.
190. APHA; AWWA; WEF; APHA, *Standard methods for examination for water and wastewater*. Washington, DC, 2005.
191. Masscheleyn, P. H.; Delaune, R. D.; Patrick, W. H., A hydride generation atomic-absorption technique for arsenic speciation. *Journal of Environmental Quality* **1991**, *20*, (1), 96-100.

192. Newalkar, B. L.; Olanrewaju, J.; Komarneni, S., Direct synthesis of titanium-substituted mesoporous SBA-15 molecular sieve under microwave-hydrothermal conditions. *Chemistry of Materials* **2001**, *13*, (2), 552-557.
193. Wang, W.; Song, M., Photocatalytic activity of titania-containing mesoporous SBA-15 silica. *Microporous and Mesoporous Materials* **2006**, *96*, (1-3), 255-261.
194. Deboer, J. H.; Linsen, B. G.; Osinga, T. J., Studies on pore systems in catalysts .6. Universal T curve. *Journal of Catalysis* **1965**, *4*, (6), 643-&.
195. Park, S. E., *Nanotechnology in mesostructured materials: Proceedings of the 3rd International Mesostructured Materials Symposium, Jeju, Korea, July 8-11, 2002*. 1st ed.; Elsevier: Amsterdam ; New York, 2003; p xxiii, 823 p.
196. Shin, E. W.; Han, J. S.; Jang, M.; Min, S. H.; Park, J. K.; Rowell, R. M., Phosphate adsorption on aluminum-impregnated mesoporous silicates: Surface structure and behavior of adsorbents. *Environ. Sci. Technol.* **2004**, *38*, (3), 912-917.
197. Yang, J.; Zhang, J.; Zhu, L. W.; Chen, S. Y.; Zhang, Y. M.; Tang, Y.; Zhu, Y. L.; Li, Y. W., Synthesis of nano titania particles embedded in mesoporous SBA-15: Characterization and photocatalytic activity. *J. Hazard. Mater.* **2006**, *137*, (2), 952-958.
198. Sparks, D. L., *Environmental soil chemistry*. 2nd ed.; Academic Press: Amsterdam; Boston, 2003; p xiv, 352 p.
199. Raven, K. P.; Jain, A.; Loeppert, R. H., Arsenite and arsenate adsorption on ferrihydrite: Kinetics, equilibrium, and adsorption envelopes. *Environ. Sci. Technol.* **1998**, *32*, (3), 344-349.
200. Jang, M.; Park, J. K.; Shin, E. W., Lanthanum functionalized highly ordered mesoporous media: Implications of arsenate removal. *Microporous and Mesoporous Materials* **2004**, *75*, (1-2), 159-168.
201. Dixit, S.; Hering, J. G., Sorption of Fe(II) and As(III) on goethite in single- and dual-sorbate systems. *Chem. Geol.* **2006**, *228*, (1-3), 6-15.
202. Ona-Nguema, G.; Morin, G.; Wang, Y. H.; Menguy, N.; Juillot, F.; Olivi, L.; Aquilanti, G.; Abdelmoula, M.; Ruby, C.; Bargar, J. R.; Guyot, F.; Calas, G.; Brown, G. E., Arsenite sequestration at the surface of nano-Fe(OH)₂, ferrous-carbonate hydroxide, and green-rust after bioreduction of arsenic-sorbed lepidocrocite by *Shewanella putrefaciens*. *Geochim. Cosmochim. Acta* **2009**, *73*, (5), 1359-1381.
203. Redman, A. D.; Macalady, D. L.; Ahmann, D., Natural organic matter affects arsenic speciation and sorption onto hematite. *Environ. Sci. Technol.* **2002**, *36*, (13), 2889-2896.
204. Guo, H. M.; Stuben, D.; Berner, Z., Removal of arsenic from aqueous solution by natural siderite and hematite. *Appl. Geochem.* **2007**, *22*, (5), 1039-1051.

205. Gimenez, J.; Martinez, M.; de Pablo, J.; Rovira, M.; Duro, L., Arsenic sorption onto natural hematite, magnetite, and goethite. *J. Hazard. Mater.* **2007**, *141*, (3), 575-580.
206. Zeng, H.; Fisher, B.; Giammar, D. E., Individual and competitive adsorption of arsenate and phosphate to a high-surface-area iron oxide-based sorbent. *Environ. Sci. Technol.* **2008**, *42*, (1), 147-152.
207. Manning, B. A.; Fendorf, S. E.; Goldberg, S., Surface structures and stability of arsenic(III) on goethite: Spectroscopic evidence for inner-sphere complexes. *Environ. Sci. Technol.* **1998**, *32*, (16), 2383-2388.
208. Lafferty, B. J.; Loeppert, R. H., Methyl arsenic adsorption and desorption behavior on iron oxides. *Environ. Sci. Technol.* **2005**, *39*, (7), 2120-2127.
209. Lenoble, V.; Bouras, O.; Deluchat, V.; Serpaud, B.; Bollinger, J. C., Arsenic adsorption onto pillared clays and iron oxides. *J. Colloid Interface Sci.* **2002**, *255*, (1), 52-58.
210. Mishra, D.; Farrell, J., Evaluation of mixed valent iron oxides as reactive adsorbents for arsenic removal. *Environ. Sci. Technol.* **2005**, *39*, (24), 9689-9694.
211. Gallegos, T. J.; Han, Y. S.; Hayes, K. F., Model predictions of realgar precipitation by reaction of As(III) with synthetic mackinawite under anoxic conditions. *Environ. Sci. Technol.* **2008**, *42*, (24), 9338-9343.
212. Waychunas, G. A.; Rea, B. A.; Fuller, C. C.; Davis, J. A., Surface-chemistry of ferrihydrite .1. EXAFS studies of the geometry of coprecipitated and adsorbed arsenate. *Geochim. Cosmochim. Acta* **1993**, *57*, (10), 2251-2269.
213. Fendorf, S.; Eick, M. J.; Grossl, P.; Sparks, D. L., Arsenate and chromate retention mechanisms on goethite .1. Surface structure. *Environ. Sci. Technol.* **1997**, *31*, (2), 315-320.
214. Arai, Y.; Sparks, D. L.; Davis, J. A., Arsenate adsorption mechanisms at the allophane - water interface. *Environ. Sci. Technol.* **2005**, *39*, (8), 2537-2544.
215. O'Reilly, S. E.; Strawn, D. G.; Sparks, D. L., Residence time effects on arsenate adsorption/desorption mechanisms on goethite. *Soil Sci. Soc. Am. J.* **2001**, *65*, (1), 67-77.
216. Herbelin, A. L.; Westall, J. C. *FITEQL-A computer program for determination of chemical equilibrium constants from experimental data*. Oregon State University: 1999.
217. Dzombak, D. A.; Morel, F., *Surface complexation modeling: Hydrous ferric oxide*. Wiley: New York, 1990; p 393 p.
218. Dixit, S.; Hering, J. G., Comparison of arsenic(V) and arsenic(III) sorption onto iron oxide minerals: Implications for arsenic mobility. *Environ. Sci. Technol.* **2003**, *37*, (18), 4182-4189.
219. Chapman, L. A.; Roling, J. A.; Bingham, L. K.; Herald, M. R.; Baldwin, W. S., Construction of a subtractive library from hexavalent chromium treated winter flounder

- (Pseudopleuronectes americanus) reveals alterations in non-selenium glutathione peroxidases. *Aquatic Toxicology* **2004**, 67, (2), 181-194.
220. Balistrieri, L. S.; Chao, T. T., Adsorption of selenium by amorphous iron oxyhydroxide and manganese-dioxide. *Geochim. Cosmochim. Acta* **1990**, 54, (3), 739-751.
221. Peak, D.; Sparks, D. L., Mechanisms of selenate adsorption on iron oxides and hydroxides. *Environ. Sci. Technol.* **2002**, 36, (7), 1460-1466.
222. Peak, D., Adsorption mechanisms of selenium oxyanions at the aluminum oxide/water interface. *J. Colloid Interface Sci.* **2006**, 303, (2), 337-345.
223. Baryosef, B.; Meek, D., Selenium sorption by kaolinite and montmorillonite. *Soil Science* **1987**, 144, (1), 11-19.
224. Zhang, Y. Q.; Zahir, Z. A.; Frankenberger, W. T., Factors affecting reduction of selenate to elemental selenium in agricultural drainage water by *Enterobacter taylorae*. *Journal of Agricultural and Food Chemistry* **2003**, 51, (24), 7073-7078.
225. EPA, Selenium treatment/removal alternatives demonstration project. **2001**, EPA/600/R-01/077.
226. Wang, K.; Lee, H.; Cooper, R.; Liang, H., Time-resolved, stress-induced, and anisotropic phase transformation of a piezoelectric polymer. *Applied Physics a-Materials Science & Processing* **2009**, 95, (2), 435-441.
227. Dong, R.; Yu, L. Y. E., Investigation of surface changes of nanoparticles using TM-AFM phase imaging. *Environ. Sci. Technol.* **2003**, 37, (12), 2813-2819.
228. Demoisson, F.; Mullet, M.; Humbert, B., Investigation of pyrite oxidation by hexavalent chromium: Solution species and surface chemistry. *J. Colloid Interface Sci.* **2007**, 316, (2), 531-540.
229. Nesbitt, H. W.; Muir, I. J., X-Ray photoelectron spectroscopic study of a pristine pyrite surface reacted with water-vapor and air. *Geochim. Cosmochim. Acta* **1994**, 58, (21), 4667-4679.
230. Roberts, M. W., Evidence for the role of surface transients and precursor states in determining molecular pathways in surface-reactions. *Appl. Surf. Sci.* **1991**, 52, (1-2), 133-140.
231. Buckley, A. N.; Woods, R., The surface oxidation of pyrite. *Appl. Surf. Sci.* **1987**, 27, (4), 437-452.
232. Rovira, M.; Gimenez, J.; Martinez, M.; Martinez-Llado, X.; de Pablo, J.; Marti, V.; Duro, L., Sorption of selenium(IV) and selenium(VI) onto natural iron oxides: Goethite and hematite. *J. Hazard. Mater.* **2008**, 150, (2), 279-284.
233. Conde, J. E.; Alaejos, M. S., Selenium concentrations in natural and environmental waters. *Chemical Reviews* **1997**, 97, (6), 1979-2003.

234. Frankenberger, W. T.; Benson, S., *Selenium in the environment*. Dekker: New York, 1994; p xiv, 456 p.
235. Lopez-Anton, M. A.; Diaz-Somoano, M.; Spears, D. A.; Martinez-Tarazona, M. R., Arsenic and selenium capture by fly ashes at low temperature. *Environ. Sci. Technol.* **2006**, *40*, (12), 3947-3951.
236. Yang, L.; Shahrivari, Z.; Liu, P. K. T.; Sahimi, M.; Tsotsis, T. T., Removal of trace levels of arsenic and selenium from aqueous solutions by calcined and uncalcined layered double hydroxides (LDH). *Ind. Eng. Chem. Res.* **2005**, *44*, (17), 6804-6815.
237. Agnihotri, R.; Chauk, S.; Mahuli, S.; Fan, L. S., Selenium removal using Ca-based sorbents: Reaction kinetics. *Environ. Sci. Technol.* **1998**, *32*, (12), 1841-1846.
238. GhoshDastidar, A.; Mahuli, S.; Agnihotri, R.; Fan, L. S., Selenium capture using sorbent powders: Mechanism of sorption by hydrated lime. *Environ. Sci. Technol.* **1996**, *30*, (2), 447-452.
239. USEPA. *Wastes from the combustion of fossil fuels*; Report to Congress, Washington, DC, 1999.
240. Ryser, A. L.; Strawn, D. G.; Marcus, M. A.; Johnson-Maynard, J. L.; Gunter, M. E.; Moller, G., Micro-spectroscopic investigation of selenium-bearing minerals from the Western US Phosphate Resource Area. *Geochemical Transactions* **2005**, *6*, (1), 1-11.
241. Breynaert, E.; Bruggeman, C.; Maes, A., XANES-EXAFS analysis of se solid-phase reaction products formed upon contacting Se(IV) with FeS₂ and FeS. *Environ. Sci. Technol.* **2008**, *42*, (10), 3595-3601.
242. Myneni, S. C. B.; Tokunaga, T. K.; Brown, G. E., Abiotic selenium redox transformations in the presence of Fe(II,III) oxides. *Science* **1997**, *278*, (5340), 1106-1109.
243. Loyo, R. L. D.; Nikitenko, S. I.; Scheinost, A. C.; Simonoff, M., Immobilization of selenite on Fe₃O₄ and Fe/Fe₃C ultrasmall particles. *Environ. Sci. Technol.* **2008**, *42*, (7), 2451-2456.
244. Duc, M.; Lefevre, G.; Fedoroff, M., Sorption of selenite ions on hematite. *J. Colloid Interface Sci.* **2006**, *298*, (2), 556-563.
245. Liu, X.; Fattahi, M.; Montavon, G.; Grambow, B., Selenide retention onto pyrite under reducing conditions. *Radiochim. Acta* **2008**, *96*, (8), 473-479.
246. Zhang, N.; Lin, L. S.; Gang, D. C., Adsorptive selenite removal from water using iron-coated GAC adsorbents. *Water Research* **2008**, *42*, (14), 3809-3816.
247. Masset, S.; Monteil-Rivera, F.; Dupont, L.; Dumonceau, J.; Aplincourt, M., Influence of humic acid on sorption of Co(II), Sr(II), and Se(IV) on goethite. *Agronomie* **2000**, *20*, (5), 525-

- 535.
248. Jordan, N.; Lomench, C.; Marmier, N.; Giffaut, E.; Ehrhardt, J. J., Sorption of selenium(IV) onto magnetite in the presence of silicic acid. *J. Colloid Interface Sci.* **2009**, *329*, (1), 17-23.
249. Boyle-Wight, E. J.; Katz, L. E.; Hayes, K. F., Spectroscopic studies of the effects of selenate and selenite on cobalt sorption to gamma-Al₂O₃. *Environ. Sci. Technol.* **2002**, *36*, (6), 1219-1225.
250. Boulton, K. A.; Cowper, M. M.; Heath, T. G.; Sato, H.; Shibutani, T.; Yui, M., Towards an understanding of the sorption of U(V) and Se(IV) on sodium bentonite. *Journal of Contaminant Hydrology* **1998**, *35*, (1-3), 141-150.
251. Zhang, Y. Q.; Wang, J. F.; Amrhein, C.; Frankenberger, W. T., Removal of selenate from water by zerovalent iron. *Journal of Environmental Quality* **2005**, *34*, (2), 487-495.
252. Zhang, Y. Q.; Frankenberger, W. T., Removal of selenate in river and drainage waters by *Citrobacter braakii* enhanced with zero-valent iron. *Journal of Agricultural and Food Chemistry* **2006**, *54*, (1), 152-156.
253. Dash, S. S.; Parida, K. M., Studies on selenite adsorption using manganese nodule leached residues. *J. Colloid Interface Sci.* **2007**, *307*, (2), 333-339.
254. Butler, E. C.; Hayes, K. F., Effects of solution composition and pH on the reductive dechlorination of hexachloroethane by iron sulfide. *Abstracts of Papers of the American Chemical Society* **1997**, *213*, 29-Envr.
255. Jeong, H. Y.; Lee, J. H.; Hayes, K. F., Characterization of synthetic nanocrystalline mackinawite: Crystal structure, particle size, and specific surface area. *Geochim. Cosmochim. Acta* **2008**, *72*, (2), 493-505.
256. Faust, S. D.; Aly, O. M., *Chemistry of water treatment*. 2nd ed.; Ann Arbor Press: Chelsea, Mich., 1998; p xvi, 581 p.
257. Thompstoneagle, E. T.; Frankenberger, W. T.; Karlson, U., Volatilization of selenium by *alternaria-alternata*. *Applied and Environmental Microbiology* **1989**, *55*, (6), 1406-1413.
258. Chung, J.; Nerenberg, R.; Rittmann, B. E., Bioreduction of selenate using a hydrogen-based membrane biofilm reactor. *Environ. Sci. Technol.* **2006**, *40*, (5), 1664-1671.
259. You, Y. W.; Vance, G. F.; Zhao, H. T., Selenium adsorption on Mg-Al and Zn-Al layered double hydroxides. *Applied Clay Science* **2001**, *20*, (1-2), 13-25.
260. Wolthers, M.; Butler, I. B.; Rickard, D., Influence of arsenic on iron sulfide transformations. *Chem. Geol.* **2007**, *236*, (3-4), 217-227.
261. Scott, T. B.; Tort, O. R.; Allen, G. C., Aqueous uptake of uranium onto pyrite surfaces; reactivity of fresh versus weathered material. *Geochim. Cosmochim. Acta* **2007**, *71*, (21), 5044-

5053.

262. Knipe, S. W.; Mycroft, J. R.; Pratt, A. R.; Nesbitt, H. W.; Bancroft, G. M., X-Ray photoelectron spectroscopic study of water-adsorption on iron sulfide minerals. *Geochim. Cosmochim. Acta* **1995**, *59*, (6), 1079-1090.
263. Bonnissel-Gissinger, P.; Alnot, M.; Ehrhardt, J. J.; Behra, P., Surface oxidation of pyrite as a function of pH. *Environ. Sci. Technol.* **1998**, *32*, (19), 2839-2845.
264. American Public Health Association, Standard methods for the examination of water & wastewater. In <http://www.standardmethods.org/Store/index.cfm>, Washington, DC, 2005.
265. Sun, C. M.; Qu, R. J.; Ji, C. N.; Wang, Q.; Wang, C. H.; Sun, Y. Z.; Cheng, G. X., A chelating resin containing S, N and O atoms: Synthesis and adsorption properties for Hg(II). *European Polymer Journal* **2006**, *42*, (1), 188-194.
266. Lee, J. Y.; Ju, Y. H.; Keener, T. C.; Varma, R. S., Development of cost-effective non-carbon sorbents for Hg⁰ removal from coal-fired power plants. *Environ. Sci. Technol.* **2006**, *40*, (8), 2714-2720.
267. Collins, C. R.; Sherman, D. M.; Ragnarsdottir, K. V., Surface complexation of Hg²⁺ on goethite: Mechanism from EXAFS spectroscopy and density functional calculations. *J. Colloid Interface Sci.* **1999**, *219*, (2), 345-350.
268. Macnaugh.Mg; James, R. O., Adsorption of aqueous mercury (II) complexes at oxide-water interface. *J. Colloid Interface Sci.* **1974**, *47*, (2), 431-440.
269. Stumm, W.; Morgan, J. J., *Aquatic chemistry: Chemical equilibria and rates in natural waters*. 3rd ed.; Wiley: New York, 1995; p xvi, 1022 p.
270. EPA. *Mercury study report to congress: Office of air quality planning and standards and office of research and development*. Washington, DC, 1997.
271. Fan, Z. F., Hg(II)-imprinted thiol-functionalized mesoporous sorbent micro-column preconcentration of trace mercury and determination by inductively coupled plasma optical emission spectrometry. *Talanta* **2006**, *70*, (5), 1164-1169.
272. Liu, J.; Feng, X.; Fryxell, G. E.; Chen, X.; Gong, M.; Wang, L.; Kemner, K. M., Self-assembled mercaptan on mesoporous silica for mercury separation. *Abstracts of Papers of the American Chemical Society* **1997**, *214*, 344-PHYS.
273. Kemner, K. M.; Feng, X.; Liu, J.; Fryxell, G. E.; Wang, L. Q.; Kim, A. Y.; Gong, M.; Mattigod, S., Investigation of the local chemical interactions between Hg and self-assembled monolayers on mesoporous supports. *Journal of Synchrotron Radiation* **1999**, *6*, 633-635.
274. Meng, L. Z.; Gong, S. L.; Yin, Y. H.; Chen, Y. Y.; Wang, Y. W., Network crown ether resin with pendent sulfur ether group: Preparation, thermodegradation, and adsorption behavior. *Journal of Applied Polymer Science* **2003**, *87*, (9), 1445-1451.

275. Moses, C. O.; Herman, J. S., Pyrite oxidation at circumneutral pH. *Geochim. Cosmochim. Acta* **1991**, *55*, (2), 471-482.
276. Bonnissel-Gissinger, P.; Alnot, M.; Lickes, J. P.; Ehrhardt, J. J.; Behra, P., Modeling the adsorption of mercury(II) on (hydr)oxides II: Alpha-FeOOH (goethite) and amorphous silica. *J. Colloid Interface Sci.* **1999**, *215*, (2), 313-322.
277. Seals, R. D.; Alexandre, R.; Taylor, L. T.; Dillard, J. G., Core electron binding-energy study of group IIB-VI compounds. *Inorganic Chemistry* **1973**, *12*, (10), 2485-2487.
278. Maithreepala, R. A.; Doong, R. A., Synergistic effect of copper ion on the reductive dechlorination of carbon tetrachloride by surface-bound Fe(II) associated with goethite. *Environ. Sci. Technol.* **2004**, *38*, (1), 260-268.

APPENDIX

1. Computer Program (MATLAB®) to Predict Adsorption Rates of Target Compounds by Nanostructured Adsorbent Media Using Adsorption Kinetic Model

% This coding is for calculating adsorption rate constants and maximum amounts adsorbed on two types of surfaces (fast-reacting sites and slow-reacting sites) in order to separate kinetic effects (how rapidly q increases) from equilibrium effects (how high q becomes after a sufficiently long time).

```

global coeff_global
coeff_global=[100 94 0.01 99.9];
data = load('data_name.txt');

t = data(:,1);
q = data(:,2);

%parameters: k_f, q_f_max, k_s, q_s_eq
% fit sequentially in pairs, first slow coefficients, then fast, then
slow,
% etc. until converge
% to fit slow coefficients:
options=statset('Robust', 'on');

coeff_guess_s= coeff_global(3:4);
[coeff_s,r,j]=nlinfit(t, q ,@kinetics_fs_calc_s,coeff_guess_s, options);
ci_s=nlparci(coeff_s,r,j);
coeff_global(3:4)=coeff_s;

% temp
coeff_global
'finish slow'
% end temp

% to fit fast coefficients
coeff_guess_f=coeff_global(1:2);
[coeff_f,r,j]=nlinfit(t, q ,@kinetics_fs_calc_f,coeff_guess_f, options);
ci_f=nlparci(coeff_f,r,j);
coeff_global(1:2)=coeff_f;

coeff=coeff_global;
[tout, qout]=ode23s(@kinetics_fs,[0 t(end)], [0 0],[],coeff);
qmod=qout(:,1)+qout(:,2);
hold off
plot(tout, qmod);
hold on

```

```

plot(t,q,'o')

% temp
coeff_global
% end temp

% calculate the sum of square error (Numerical Solution - Truncation
Error Expected)
SSE = 0;
for i = 1:size(t,1)
    % numerically calculate y_model corresponding to observation time t
    for j = 1:size(tout,1)-1
        if tout(j,1)<=t(i) && tout(j+1,1)>t(i)
            x1 = tout(j,1);
            x2 = tout(j+1,1);
            y1 = qmod(j,1);
            y2 = qmod(j+1,1);
            break;
        end
    end
    y_model = linear_interpolation(x1,y1,x2,y2,t(i));
    SSE = SSE + (y_model - q(i))^2;
end
% calculate value of GFP (goodness of fit parameter)
GFP = sqrt(SSE/(size(t,1)-2))/mean(q)

```

% This coding is for calculating coefficients at slow-reacting sites

```

function qmod=kinetics_fs_calc_s(coeff_s,t)
global coeff_global
coeff(1:2)=coeff_global(1:2);
coeff(3:4)=coeff_s;
[tout, qout]=ode23s(@kinetics_fs,t,[0 0],[],coeff);
qmod=qout(:,1)+qout(:,2);

```

% This code is for calculating coefficients at fast-reacting sites

```

function qmod=kinetics_fs_calc_f(coeff_f,t)
global coeff_global
coeff(1:2)=coeff_f;
coeff(3:4)=coeff_global(3:4);
[tout, qout]=ode23s(@kinetics_fs,t,[0 0],[],coeff);
qmod=qout(:,1)+qout(:,2);

```

% This code is for solving kinetic equations associated with slow- and fast-reacting sites.

```
function dqdt=kinetics_fs(t,q,coeff)
% q(1) is q_fast, q(2) is q_slow
k_f=coeff(1);
q_f_max=coeff(2);
k_s=coeff(3);
q_s_eq=coeff(4);
dqdt(1)=k_f*(q_f_max - q(1));
dqdt(2)=k_s*(q_s_eq - q(2));
dqdt=dqdt';
```

% This code is related to linear interpolation to calculate sum of squared residual.

```
function y = linear_interpolation(x1,y1,x2,y2,x)
y = (y2-y1)/(x2-x1)*(x-x1) + y1;
```

2. Computer Program (MATLAB®) to Predict Adsorption Equilibrium Isotherm of Target Compounds by Nanostructured Adsorbent Media Using Adsorption Equilibrium Models

% this coding is for non-linear regression of adsorption data using Langmuir isotherm and calculating Langmuir's coefficients with 95 % confidence level.

```
[ced, qed] = initvar('data.txt');
[beta,r,j]=nlinfit(ced,qed,@Langmuir,[1000 0.001]);
betaci = nlparci(beta, r, j);

ced_min = min(ced);
ced_max = max(ced);
xplot = [ced_min:(ced_max-ced_min)/2000:ced_max];
qmod = (beta(1)*beta(2)*xplot)./(1+beta(2)*xplot);
figure, plot(ced, qed, 'o'); hold on; plot(xplot, qmod);

% calculate the sum of square error (Numerical Solution - Truncation
Error
% Expected)
SSE = 0;
xplot = xplot'
qmod = qmod'
for i = 1:size(ced,2)
    % numerically calculate y_model corresponding to observation time t
    for j = 1:size(xplot,1)-1
        if xplot(j,1)<=ced(i) && xplot(j+1,1)>ced(i)
            x1 = xplot(j,1);
            x2 = xplot(j+1,1);
            y1 = qmod(j,1);
            y2 = qmod(j+1,1);
            break;
        end
    end
    y_model = linear_interpolation(x1,y1,x2,y2,ced(i));
    SSE = SSE + (y_model - qed(i))^2;
end
GOF = sqrt(SSE/(size(ced,2)-2))/mean(qed)
```

% Function of Langmuir model

```
function qe=Langmuir(beta,ced)
qmax=beta(1);
b=beta(2);
qe=(qmax*b*ced)./(1+b*ced);
```

% This coding is for non-linear regression of adsorption data using Freundlich isotherm and calculating Freundlich's coefficients with 95 % confidence level.

```
[ced, qed] = initvar('data.txt');
[beta,r,j]=nlinfit(ced,qed,@Freundlich,[0.15 0.7]);
betaci = nlparci(beta, r, j);

ced_min = min(ced);
ced_max = max(ced);
xplot = [ced_min:(ced_max-ced_min)/2000:ced_max];
qmod = beta(1)*xplot.^(1/beta(2));
figure, plot(ced, qed, 'o'); hold on; plot(xplot, qmod);

% calculate the sum of square error (Numerical Solution - Truncation
Error
% Expected)
SSE = 0;
xplot = xplot'
qmod = qmod'
for i = 1:size(ced,2)
    % numerically calculate y_model corresponding to observation time t
    for j = 1:size(xplot,1)-1
        if xplot(j,1)<=ced(i) && xplot(j+1,1)>ced(i)
            x1 = xplot(j,1);
            x2 = xplot(j+1,1);
            y1 = qmod(j,1);
            y2 = qmod(j+1,1);
            break;
        end
    end
    y_model = linear_interpolation(x1,y1,x2,y2,ced(i));
    SSE = SSE + (y_model - qed(i))^2;
end
GOF = sqrt(SSE/(size(ced,2)-2))/mean(qed)
```

% Function of Freundlich model

```
function qe=Freundlich(beta,ced)
k=beta(1);
n=beta(2);
qe=k*ced.^(1/n);
```

% This coding is for non-linear regression of adsorption data using BET isotherm and calculating BET's coefficients with 95 % confidence level.

```
[ced, qed] = initvar('data.txt');
[beta,r,j]=nlinfit(ced,qed,@BET,[200 500]);
betaci = nlparci(beta, r, j);
cs=2000;
ced_min = min(ced);
ced_max = max(ced);
xplot = [ced_min:(ced_max-ced_min)/2000:ced_max];
qmod = (beta(2)*beta(1)*xplot)./((cs-xplot).*(1+(beta(1)-1)*(xplot/cs)));
figure, plot(ced, qed, 'o'); hold on; plot(xplot, qmod);

% calculate the sum of square error (Numerical Solution - Truncation
Error
% Expected)
SSE = 0;
xplot = xplot'
qmod = qmod'
for i = 1:size(ced,2)
    % numerically calculate y_model corresponding to observation time t
    for j = 1:size(xplot,1)-1
        if xplot(j,1)<=ced(i) && xplot(j+1,1)>ced(i)
            x1 = xplot(j,1);
            x2 = xplot(j+1,1);
            y1 = qmod(j,1);
            y2 = qmod(j+1,1);
            break;
        end
    end
    y_model = linear_interpolation(x1,y1,x2,y2,ced(i));
    SSE = SSE + (y_model - qed(i))^2;
end
GOF = sqrt(SSE/(size(ced,2)-2))/mean(qed)
```

% Function of BET Model

```
function qe=BET(beta,ced)
cs=2000;
A=beta(1);
qmax=beta(2);
qe=(qmax*A*ced)./((cs-ced).*(1+(A-1)*(ced/cs)));
```

% Definition of "initvar" used in nonlinear regression of adsorption isotherm data

```
% denifinition of initvar
function [ce_data, qe_data] = initvar(filename);
%INITVAR initialize variable for the use of ILINFIT
% [CE_DATA, QE_DATA] = INITVAR(FILENAME) Filepath is the name of
% the dataset for the use of ILINFIT. INITVAR returns the dataset.
%
% Example:
% [ced, qed] =initvar('pisotherm_mt4.txt');
% [beta,r,j]=nlinfit(ced,qed,@qe_Pisotherm,[308 0.013]);
%
% See also, NLINFIT, QE_PISOTHERM
data1=load(filename);

ce_data=data1(:,1);
ce_data=ce_data';
qe_data=data1(:,2);
qe_data=qe_data';
```

VITA

Name: Dong Suk Han (Shane Han)

Permanent Address: 211-2101 Kolon Haneulchae APT, Chimsan 2-dong, Buk-gu, Daegu, Korea

Mail Address: Department of Chemical Engineering, Texas A&M University at Qatar, PO Box
23874, Doha, Qatar

Email Address: dong_suk.han@qatar.tamu.edu

Education: B.S., Environmental Science, Keimyung University, 1997

M.S., Environmental Science, Keimyung University, 1999

Ph.D., Civil Engineering, Texas A&M University, 2009